

UNIVERSITY OF CATANIA

Department of Electrical, Electronic and Computer Engineering

PhD student: Ing. Aneli Stefano

***MODELING OF INNOVATIVE SOLAR SYSTEMS
INTEGRATED INTO THE BUILDING ENVELOPE FOR
THE PRODUCTION OF THERMO-ELECTRIC ENERGY***

DOCTORAL DISSERTATION

Supervisor:

Prof. Ing. Antonio Gagliano

PhD in engineering of systems, energy, information technology and telecommunications

XXXIII CYCLE

ACKNOWLEDGEMENTS

I dedicate this path to my wife, to whom I would like to acknowledge my deepest gratitude for having always been by my side in every adventure, for always encouraging me to do more, not to give up, for the immense patience shown to me and for having made me the person I am today.

A big thank you goes to my supervisor, prof. Antonio Gagliano, who has always had faith in me, has provided me with an excellent atmosphere and a great opportunity for growth.

I also wish to thank prof. Giuseppe Marco Tina, who with the expertise that distinguishes him has always pushed me to improve.

ABSTRACT

Following the various energy crises, it has been seen that Renewable Energy Sources (RESs) are on the one hand a resource, while on the other a necessity, therefore capable of reducing dependence on fossil fuels and reducing greenhouse gas emissions. Over the years, solar technology has become the most important of the RESs. Proof of this is the large production of scientific articles on the subject, the efforts to improve existing technologies and above all the numerous systems installed around the world. The improvement of existing technology also involves the use of hybrid photovoltaic/thermal (PV/T) systems, which simultaneously produce both electrical and thermal energy, increasing the exploitation of captured solar energy.

This PhD thesis aims to study the performance of solar plants to produce electricity (photovoltaic plant) and thermal energy (solar thermal plant) or their cogeneration (hybrid photovoltaic/thermal plant), as well as the possibility of increasing performance through the use of nanofluids or phase change materials, and the installation of solar RESs in building envelopes.

Through a pilot PV/T plant, installed at the DIEEI of the University of Catania, it was possible to analyse various scenarios. The system, monitored in all its parts, allows with its flexibility, to simulate any thermal or electrical load, but also allows the variation of its configuration: tilt angle, flow rates, electrical and thermal connections (series or parallel), and so on.

An extensive experimental investigation made it possible to compare the thermal and electrical performance of the two PV/T modules making up the pilot plant, depending on the hydraulic configuration, connecting them once in series and another in parallel. In addition, the comparison was also performed by circulating the working fluid in only one panel, leaving the other in stagnation condition. Other analyses made it possible to evaluate the performance of the PV/T at varying thermal levels, and the possibility of managing electricity production to improve the thermal one was explored.

The experimental investigation was subsequently expanded using numerical simulations.

Through an application created in TRNSYS, and validated with experimental data, the performances among a PV/T system and different arrangements of conventional photovoltaic and solar thermal systems (PV-ST) were compared, when both the two solar systems, PV/T and PV-ST, occupies the same surface. Thus, when there could be competition for installing both the surfaces of PV and ST necessary for meet the energy needs of a building due to space scarcity (e.g. in residential tower buildings). The study is carried out considering both the first and second law approach of thermo-dynamic, as well as the economic analysis, having as target a residential unit located in the cities of Catania (IT), Split (HR) and Freiburg (D), which are representative of different geographic areas.

A novel numerical model capable of simulating a complete PV/T system has been developed in Matlab and has been validated using the measured data in the pilot PV/T system. This model is based on the energy balance equations for each component of the PV/T system. The model allows us to study the impact that the various environmental, management and characteristic parameters have on producibility. The analysis carried out made it possible to evaluate the effect of the variation in the flow rate and temperature of the fluid on the performance of the system, as well as the performance over a continuous period of four days (spring season) considering real climatic data. Such information are crucial in PV/T real applications, in fact the validated numerical model is a very useful tool that can be used for the on-line monitoring of real installations to detect immediately faults or inefficient operative conditions through the comparison between calculated and measured variables and performances.

Usually, the PV/T systems have some limitations to fulfil the thermal energy needs; therefore, it is necessary to improve their efficiency with the aim to increase the enthalpy level of the energy produced. Thus, using the Matlab model, the effects of changing the cooling fluid from pure water to a nanofluid composed by water and aluminium oxide (Al₂O₃) in a PV/T system are studied. The analysis is based on the thermodynamics viewpoint, considering both the total energy produced and its quality. Furthermore, the thermal level achievable by changing the heat transfer fluid, as well as the electrical efficiency considering various input conditions has been calculated.

The possibility to improve the performances of the PV plants has been studied using a passive cooling technique, which use the phase change materials (PCMs) to control the PV cell temperature. Using the Fluent simulation software, a CFD model capable of simulating the transfer of heat, mass, and momentum of a PCM connected behind a photovoltaic module was developed. The analyses were carried out considering different periods of the year, and the simulations were performed for several consecutive days in such a way to not overlook the actual degree of solidification obtained during the night. The CFD model has allowed us to compare the thermal behaviour and the electrical performance of PV module equipped with two different types of PCM (PV-PCM) with those of a conventional PV module under the same operative conditions, showing an increase of electrical performance of PV-PCM respect to the conventional PV.

One of the main objectives of nZEBs is to design high performance passive or active building envelope. The high-performance Passive Building Envelopes (PBE)s are facades, windows, roofs, etc., where the efficient design reduces thermal fluxes between outdoor and indoor space, as well as the overheating effect due to solar radiation.

With this aim, it is proposed a comprehensive comparison of the thermal behaviour between an Opaque Ventilated Façade (OVF) and a conventional unventilated Façade (UF), considering both winter and summer period. Moreover, the analysis investigates different façade orientations and several states of windiness. These analyses were developed utilizing fluid-dynamic calculation under dynamic conditions, which allowed to determine the: hourly surface temperatures of the most external layer, temperature profiles for all the facade's layers, airflow profiles inside the cavity and near the façade, and the hourly thermal fluxes that cross the façades.

The installations of solar RESs applied or integrated into the building envelope (the so-called Active Building Envelopes "ABEs") may represent an interesting opportunity to increase the fraction of the building energy demands supplied through solar energy. The performance of the different solar technologies (PV, ST, and PV/T) placed on the building facades were analysed, and the effect that these can generate on the thermal fluxes between indoor and outdoor environment.

In detail, the application of a Building Solar Thermal Façade (BSTF) used for the production of Domestic Hot Water was analysed, considering different Italian climatic locations and two different types of solar collectors (Flat Plate Collector "FPC" and Evacuated Tube Collector "ETC").

Another analysis concerned the integration of a PV/T system in the façade of the building (BIPVT) used to satisfy both thermal and electrical needs. Furthermore, the effect on the thermal fluxes that pass through the envelope was assessed by comparing the energy needs of the building equipped with BIPVT with an equivalent one without BIPVT.

Finally, the addition of PV systems on the facade was analysed. Four scenarios were considered: (i) unventilated active façade with an added single-sided module (BAPV); (ii) ventilated active façade with an added monofacial module (V-BAPV); (iii) ventilated active façade with an added bifacial module (V-

BAbPV); and (iv) ventilated active façade with an added bifacial module and reflective treatment in the internal wall (Vr-BAbPV).

The analysis conducted reveals a good potential for ABE whatever its composition (ST, PV or PV/T), guaranteeing good yields and an improvement in the thermal behaviour of the building envelope.

GENERAL INDEX

ABSTRACT	I
GENERAL INDEX	V
INDEX OF FIGURES.....	VII
NOMENCLATURE.....	X
INTRODUCTION.....	1
1. SOLAR RENEWABLE ENERGY SOURCES	3
1.1 SOLAR THERMAL SYSTEM	3
1.2 PHOTOVOLTAIC SYSTEM.....	6
1.3 PHOTOVOLTAIC/THERMAL SYSTEM (PV/T)	9
1.3.1 PV/T technologies.....	10
1.3.2 Performance and use of PV/T.....	11
1.3.3 Physical Characterization	14
1.4 KEY PERFORMANCE INDICATOR (KPI)	17
1.4.1 Electrical yields	17
1.4.2 Thermal yields.....	18
1.4.3 Overall Energy Yields	19
1.4.4 KPI on the thermal level.....	20
REFERENCES	21
2. EXPERIMENTAL PILOT PV/T PLANT	27
2.1 THERMO-HYDRAULIC SECTION OF THE EXPERIMENTAL SYSTEM.....	28
2.1.1 Thermo-hydraulic layout	28
2.1.2 Thermo-hydraulic components.....	30
2.2 ELECTRIC SECTION OF THE EXPERIMENTAL SYSTEM	32
2.3 DESCRIPTION OF THE MONITORING AND MANAGEMENT SYSTEM.....	33
2.4 EXPERIMENTAL INVESTIGATION	36
2.4.1 Comparison of thermal and electrical performances as the hydraulic configuration changes	36
2.4.2 Performance comparison as the thermal level varies.....	41
2.4.3 Domestic hot water production and simultaneous electricity production.....	43
2.4.4 Electrical and thermal experimental curves	49
REFERENCES	53
3. PERFORMANCE EVALUATION OF SOLAR PLANTS AND TECHNIQUES FOR INCREASING PERFORMANCE, THROUGH MATHEMATICAL MODELS	55
3.1 SIMULATION SOFTWARE.....	55
3.1.1 TRNSYS.....	57
3.1.2 Matlab	57
3.1.3 Fluent.....	58
3.2 PERFORMANCE COMPARISON OF HYBRID PV/T SYSTEMS WITH CONVENTIONAL SOLAR SYSTEMS (PV-ST)	59
3.2.1 Methodology and numerical model	60
3.2.2 Model validation.....	67
3.2.3 Results	69
3.2.4 Economic analysis.....	75
3.3 NUMERICAL MODEL AND EXPERIMENTAL VALIDATION OF THE ELECTRICAL AND THERMAL PERFORMANCES OF PHOTOVOLTAIC/THERMAL PLANT	79

3.3.1 Numerical model	80
3.3.2 Assessment of the numerical model	84
3.3.3 Model Validation	86
3.3.4 Simulations using mathematical model	90
3.4 ANALYSIS OF THE IMPACT OF NANOFUID IN THE ENERGY PRODUCED AND ENERGY QUALITY IN PHOTOVOLTAIC-THERMAL SYSTEMS	95
3.4.1 Methodology	95
3.4.2 Results	96
3.5 ANALYSIS OF THE IMPACT OF PHASE CHANGE MATERIALS IN THE ELECTRICAL YIELDS OF PHOTOVOLTAIC SYSTEMS	100
3.5.1 Phase Change Material	100
3.5.2 Methodology	101
3.5.3 Case Study	104
3.5.4 Results	105
REFERENCES	109
4. STRATEGY FOR ACHIEVING NZEB OBJECTIVES: PASSIVE AND ACTIVE BUILDING ENVELOPE.....	117
4.1 ANALYSIS OF HIGH-PERFORMANCE BUILDING ENVELOPE COMPOSED BY OPAQUE VENTILATED FAÇADE UNDER WINTER AND SUMMER WEATHER CONDITIONS	119
4.1.1 Thermal behaviour of building envelopes.....	119
4.1.2 Methodology and study specifications	122
4.1.3 Results	127
4.2 ANALYSIS OF ACTIVE BUILDING ENVELOPE COMPOSED BY SOLAR THERMAL (ST) SYSTEM	138
4.2.1 Experimental v-BSTF prototype	138
4.2.2 Analysis of the DHW production of the BSTFs	143
4.3 ANALYSIS OF ACTIVE BUILDING ENVELOPE COMPOSED BY PHOTOVOLTAIC/THERMAL (PV/T) SYSTEM	156
4.3.1 Methodology	156
4.3.2 Characterization and validation	160
4.3.3 Results and discussions.....	161
4.4 ANALYSIS OF ACTIVE BUILDING ENVELOPE COMPOSED BY PHOTOVOLTAIC (CONVENTIONAL AND BIFACIAL) SYSTEM.....	167
4.4.1 Method	168
4.4.2 Results and Discussions	172
REFERENCES	177
5. CONCLUSIONS	181
<u>APPENDIX 1</u> - DESCRIPTION AND PERFORMANCE ANALYSIS OF A FLEXIBLE PHOTOVOLTAIC/THERMAL (PV/T) SOLAR SYSTEM	
<u>APPENDIX 2</u> - COMPARATIVE ASSESSMENTS OF THE PERFORMANCES OF PV/T AND CONVENTIONAL SOLAR PLANTS	
<u>APPENDIX 3</u> - NUMERICAL MODEL AND EXPERIMENTAL VALIDATION OF THE ELECTRICAL AND THERMAL PERFORMANCES OF PHOTOVOLTAIC/THERMAL PLANT	
<u>APPENDIX 4</u> - ANALYSIS OF THE ENERGY PRODUCED AND ENERGY QUALITY OF NANOFUID IMPACT ON PHOTOVOLTAIC-THERMAL SYSTEMS	
<u>APPENDIX 5</u> - TRANSIENT ANALYSIS OF PHOTOVOLTAIC MODULE INTEGRATED WITH PHASE CHANGE MATERIAL (PCM)	
<u>APPENDIX 6</u> - ANALYSIS OF THE ENERGY PERFORMANCE OF AN OPAQUE VENTILATED FAÇADE UNDER WINTER AND SUMMER WEATHER CONDITIONS	
<u>APPENDIX 7</u> - ANALYSIS OF THE PERFORMANCE OF A BUILDING SOLAR THERMAL FACADE (BSTF) FOR DOMESTIC HOT WATER PRODUCTION	
<u>APPENDIX 8</u> - ASSESSMENT OF THE ELECTRICAL AND THERMAL PERFORMANCES OF A BUILDING INTEGRATED PHOTOVOLTAIC THERMAL PLANT.	
<u>APPENDIX 9</u> - A NOVEL BUILDING VENTILATED FAÇADE WITH INTEGRATED BIFACIAL PHOTOVOLTAIC MODULES: ANALYSIS OF THE ELECTRICAL AND THERMAL PERFORMANCES	

INDEX OF FIGURES

Figure 1.1 - Theoretical efficiency for commercially solar thermal collectors.	5
Figure 1.2 – characteristic curve of PV plants	7
Figure 1.3 – variation of the I-V curves and P_{el} as the cell temperature changes [8].....	8
Figure 1.4 – spectral properties of a crystalline silicon PV cell [9].	9
Figure 1.5 – different PV/T technologies [10].	11
Figure 1.6 – different PV/T technologies [11].	11
Figure 1.7 – efficiency of the several PVT technologies.	16
Figure 2.1 – main components of the pilot PV/T system and flexible support structure.	27
Figure 2.2 – thermo-hydraulic layout of pilot PV/T system.	28
Figure 2.3 – thermo-hydraulic connection of panels: a) parallel, 2) series, 3) one in stagnation and one active. ...	29
Figure 2.4 – Three-way valve diagram for managing the temperature in the panel	29
Figure 2.5 – circulation pump	31
Figure 2.6 – PV/T system wiring diagram.....	32
Figure 2.7 – data acquisition and management via web browser	33
Figure 2.8 – PV/T plant power and measurement boxes.....	34
Figure 2.9 – architecture of the monitoring and management system	35
Figure 2.10 – Features of the main sensors installed.....	35
Figure 2.11 – Experimental measurements during a typical day with parallel connection	37
Figure 2.12 – Electrical and thermal performance during a typical day with parallel connection.....	37
Figure 2.13 – Experimental measurements during a typical day with parallel connection	38
Figure 2.14 – Electrical and thermal performance during a typical day with parallel connection.....	38
Figure 2.15 – Comparison of experimental measurements between PV/T panel and PV/T in stagnation.....	39
Figure 2.16 – Comparison of electrical and thermal performance between PV/T panel and PV/T in stagnation ...	40
Figure 2.17 – Comparison of electrical and thermal performance when the inlet temperature change	42
Figure 2.18 – Comparison of environment air temperature (left) end solar irradiance (right) for the MPP and SC scenarios	44
Figure 2.19 – example of tank temperature and DHW load	45
Figure 2.20 – Comparison of thermal power produced (on the left) end electricity (on the right) for the MPP and SC scenarios.....	47
Figure 2.21 – Comparison of tank temperature profile for the MPP and SC scenarios	47
Figure 2.22 – Comparison of daily energy produced for the MPP and SC scenarios	48
Figure 2.23 – Comparison of I-V and P-V curves (at left) and of NP (at right) as the solar irradiance varies.....	50
Figure 2.24 – Comparison of I-V and P-V curves (at left) and of NP (at right) as the temperature of the cell varies	50
Figure 2.25 – Experimental performance curve of the PV/T panel.....	51
Figure 3.1 – Layout of PV/T plant.....	60
Figure 3.2 – Sketch of TRNSYS's project.....	61
Figure 3.3 – Flow diagrams for PV/T (at left) and PV+ST (at right).	61
Figure 3.4 – Environmental climate data.	66
Figure 3.5 – DHW daily demand profile.	67
Figure 3.6 - Comparisons between simulated and measured voltage	67
Figure 3.7 - Comparisons between simulated and measured electric power (P_{el})	68
Figure 3.8 - Comparisons between simulated and measured temperatures at the outlet of PV/T panels	68
Figure 3.9 - Comparisons between simulated and measured daily electrical (at left) and thermal (at right) energy produced.....	69

Figure 3.10 - Comparisons of performances between PV and PV/T systems	70
Figure 3.11 - Comparisons of cells temperature between PV/T and PV system on a typical summer day - Catania	71
Figure 3.12 - Annual energy produced by PV-ST and PV/T plants	72
Figure 3.13 – Costs and revenues	77
Figure 3.14 - Cross section and equivalent electrical circuit of the PV/T panel	81
Figure 3.15 - Weather conditions.....	86
Figure 3.16 - Simulated and observed inlet temperatures in the PV/T panel.....	87
Figure 3.17 - Simulated and observed outlet temperatures in the PV/T panel	87
Figure 3.18 - Simulated and observed temperatures in the solar tank.....	88
Figure 3.19 - Simulated and observed voltage in open circuit condition.....	89
Figure 3.20 – Weather conditions of the typical summer day (July).....	90
Figure 3.21 – Performances of PV/T panels when the inlet temperature change.....	91
Figure 3.22 – Performances of PV/T panels when the flowrate change.....	92
Figure 3.23 – PV cells, fluid, absorber plate and environmental temperatures	93
Figure 3.24 – thermal and electrical power (at left) and efficiency (at right) of the PV/T plant.....	93
Figure 3.25 – Weather condition during a typical summer day	97
Figure 3.26 – Outlet temperatures and increase of thermal level.....	97
Figure 3.27 – Average tank temperature during the simulation period for both fluids.	98
Figure 3.28 – Energy fluxes in PV-PCM module.	102
Figure 3.29 – Weather data during summer solstice, autumn equinox and winter solstice	105
Figure 3.30 - PV cells temperature profile (at left) and liquid fraction (at right) during summer solstice.....	106
Figure 3.31 - PV cells temperature profile during autumn equinox (at left) and during winter solstice (at right).	106
Figure 3.32 - Efficiency and electrical power during summer solstice (at left) and during autumn equinox (at right).....	107
Figure 3.33 – Daily electrical yields.	108
Figure 4.1 – Thermal fluxes for the OVF.....	121
Figure 4.2 – Stratigraphy of ventilated and unventilated façades.	123
Figure 4.3 – Geometry and mesh of calculus.	125
Figure 4.4 – Incident irradiance (left) and outdoor temperature (right) for the winter and summer days.....	127
Figure 4.5 – Profiles of air velocity inside the duct (at left) and temperature (at right) for the various wind conditions.....	128
Figure 4.6 – Hourly surface temperatures of the OVF and UF during a winter day.....	130
Figure 4.7 – Velocity (at left) and Temperature profiles (at right) of the OVF and UF at specific hours of the day for façades facing South.....	132
Figure 4.8 – UF and OVF’s hourly thermal fluxes for each scenario during a winter day.	133
Figure 4.9 – hourly surface temperature of the OVF and UF during a summer day for each scenario.....	134
Figure 4.10 – UF and OVF’s hourly thermal fluxes for each scenario during a summer day.	135
Figure 4.11 – Daily energy fluxes and Energy saving for the two façades.	136
Figure 4.12 – Map of the building (left side), photo of the two BSTF prototypes (right side).	138
Figure 4.13 – Features of the main sensors installed.....	139
Figure 4.14 – Section and front view of the v-BSTF façade with the installed sensors.....	140
Figure 4.15 – Experimental data measured on the v-BSTF	141
Figure 4.16 – The monitored data during the 1 st December.....	142
Figure 4.17 – Scheme of the solar system.....	143

Figure 4.18 – TRNSYS assembly of the simulated solar system.	144
Figure 4.19 – Comparison of HDD, average monthly outdoor temperature, and total monthly radiation on BSTF facing South, for the four location analysed.	146
Figure 4.20 – Solar radiation on winter solstice (left-side) and summer solstice (right-side).....	147
Figure 4.21 – Weather data (solar irradiance and ambient temperature) and solar plant operating temperatures (tank and collectors) during a winter week in Ragusa.	148
Figure 4.22 – Weather data (solar irradiance and ambient temperature) and solar plant operating temperatures (tank and collectors) during a winter week in Milan.....	148
Figure 4.23 – Energy fluxes during a winter week in Ragusa.	149
Figure 4.24 – Energy fluxes during a winter week in Milan.	150
Figure 4.25 – Weather data (solar irradiance and ambient temperature) and solar plant operating temperatures (tank and collectors) during a summer week in Ragusa.	151
Figure 4.26 – Weather data (solar irradiance and ambient temperature) and solar plant operating temperatures (tank and collectors) during a summer week in Milan.	151
Figure 4.27 – Energy fluxes during a summer week in Ragusa.	152
Figure 4.28 – Energy fluxes during a summer week in Milan.....	152
Figure 4.29 – Coverage factor of DHW demand for the two scenarios.	153
Figure 4.30 – System layout for building with and without BIPVT.....	157
Figure 4.31 – Thermal curves comparison between experimental and simulated values.....	161
Figure 4.32 – Annual electrical (left) and thermal (right) energy yield per m ² of PV/T panel.....	162
Figure 4.33 – Annual requirements of the building per floor square meter.....	163
Figure 4.34 – Coverage factor of needs (left side) and characteristic temperatures (right side), to varying the specific storage tank volume.....	163
Figure 4.35 – Daily energy needs for the baseline and the BIPVT scenario.	164
Figure 4.36 – Monthly coverage factor.	165
Figure 4.37 – Schematic representation of the modeled configurations: (a) V-BAbPV and Vr-BAbPV, (b) V-BAPV, and (c) BAPV.....	169
Figure 4.38 – Temperature (left) and solar irradiation (right) for the three reference days.	172
Figure 4.39 – daily profiles of cell temperature, efficiency, and electrical power.	173
Figure 4.40 – Temperature into the whole façade at noon, during winter and summer day.....	175
Figure 4.41 – Daily electrical yields and daily thermal fluxes through the façade.	176

NOMENCLATURE

A	collector area, m ²
a ₁	linear thermal heat losses coefficients, W. m ⁻² . K ⁻¹
a ₂	quadratic thermal loss coefficient, W. m ⁻² . K ⁻²
c	speed of light, m. s ⁻¹
c ₁ -c ₆	coefficients for the thermal characterization used in the QDT model
C __	specific heat, J. kg ⁻¹ . K ⁻¹
E	energy, J
E _L	long-wave irradiance, W. m ⁻²
EP	primary energy, J
ES	Energy Saving coefficient, dimensionless
f	demand coverage factor, dimensionless
F	view factor, dimensionless
F'	collector efficiency factor, dimensionless
F _R	collector heat removal factor, dimensionless
G	solar irradiation, W. m ⁻²
H	latent heat, J. kg ⁻¹
h	convection coefficient, W. m ⁻² . K ⁻¹
h _P	Planck constant, J. s
I	current intensity, A
I _{ph}	current flow in the PV cell, A
k	thermal conductivity, W. m ⁻¹ . K ⁻¹
K _b	IAM for beam irradiation, dimensionless
K _d	IAM for diffuse irradiation, dimensionless
L	length of façade, m
ṁ	mass flow rate, kg. s ⁻¹
NP	normalized Power, dimensionless
P __	power, W
PF	Packing Factor, dimensionless
PR	Performance Ratio, dimensionless
q	Heat flux per unit area, W. m ⁻²
Q	Heat flux, W
Q _t	useful thermal power output of a collector, W
r	reflective index, dimensionless
R	thermal resistance, K. m ² . W ⁻¹
R _{pv}	intrinsic resistance of the cell, Ω
R _{sh}	Shunt resistance, Ω
S	solar irradiance absorbed by a collector per unit area, W. m ⁻²
s	surface of the openings in ventilated façade, m ²
T __	temperature, K
t	time, s
TS	surface temperature, K
U	overall heat transfer coefficient, W. m ⁻² . K ⁻¹
u	wind speed, m. s ⁻¹
U _{AbsFluid}	heat transfer coefficient between the absorber and the fluid, W. m ⁻² . K ⁻¹
U _c	constant thermal loss factor (T _{pv} calculate), W. m ⁻² . K
U _L	collector overall heat loss coefficient, W. m ⁻² . K ⁻¹
U _v	wind velocity dependent thermal loss factor (T _{pv} calculate), W. m ⁻³ . s. K
V	voltage, V
V __	volume, m ³
V _s	specific volume, m ³
Y _A	array yield, h
Y _R	reference yield, h
z	altitude, m

Greek symbols

α	absorption coefficient, dimensionless
β	tilt angle, rad
γ	thermal coefficient of electrical efficiency, K ⁻¹
δ	thickness, m
ε	emissivity, dimensionless
ε_T	total efficiency calculated with the second law of thermodynamics, dimensionless
η_0	thermal efficiency at zero-loss, dimensionless
η_{-}	efficiency, dimensionless
η_{power}	electric power generation efficiency for a conventional power plant
θ	incidence angle of irradiance
λ	Wavelength, m
μ	dynamic viscosity, kg. m ⁻¹ . s ⁻¹
ρ	density, kg. m ⁻³
σ_0	Stefan-Boltzmann constant, W. m ⁻² . K ⁻⁴
τ	transmission coefficient, dimensionless
ϕ	volumetric ratio, dimensionless
χ	referred to the exergetic content

Subscripts, acronyms

ABE	Active Building Envelope
abs	absorber
absh	upper absorber plate
absl	lower absorber plate
amb	environment
av	average, refers to temperature of fluid inside the panel
BAPV	Building Added photovoltaic system
bg	Back glass
BIPVT	Building integrated photovoltaic/thermal system
BSTF	Building Solar Thermal Façade
bk	Back side
CFD	Computational Fluid Dynamic
Ch	Chiller
cond	conduction flux
conv	convective flux
CPVT	concentrated PVT collector
e	referred to the outdoor
eff	effective
el	electrical
ETC	Evacuated tube collector
f	fluid
fg	Front glass
FPC	Flat plate collector
fr	Front side
g	Glass cover
i	referred to the indoor
(I)	referred to the primary energy
in	inlet
IAM	Incident Angle Modifier
l	liquid phase
M1	name of the first PV/T panel in pilot plant
M2	name of the second PV/T panel in pilot plant
m	melting
MPP	maximum power point
NOCT	Normal Operating Cell Temperature
oc	open circuit condition

out	outlet
OVF	Opaque Ventilated Façade
p	panel
PCM	Phase Change Material
pm	refers to average temperature of the absorber plate
PV	photovoltaic system
pv	photovoltaic
PV-PCM	photovoltaic equipped with PCM
PVT or PV/T	hybrid photovoltaic/thermal system
PVT _g	Glazed PV/T panel
PVT _{l-e}	Glazed low-emissivity PV/T panel
PVT _{ung}	Unglazed PV/T panel
QDT	Quasi Dynamic Testing
rad	radiative flux
RES	renewable energy source
s	solid phase
SC	short circuit conditions
s.c.	solar circuit
sky	sky dome
sum	summer
sun	Refers to sun
sup	supply water
SST	Steady State Testing
ST	Solar thermal system
ST _{ung}	Unglazed ST collector
STC	standard test conditions
ted	tedlar
th	thermal
tot	overall
UDF	User Defined Function
UF	Unventilated Façade
V-BAPV	Ventilated Building Added Photovoltaic system
V-BAbPV	Ventilated Building Added bifacial Photovoltaic system
Vr-BAbPV	Ventilated Building Added bifacial Photovoltaic system with reflective coating
v-BSTF	Ventilated Building Solar Thermal Façade
w	water
wall	wall
win	winter
WISC	Wind and/or Infrared Sensitive Collectors

INTRODUCTION

After the oil crisis of the 1970s, attention has increasingly grown to the issue of energy efficiency and the development of renewable energies as an alternative to fossil fuels.

The construction sector covers an important part of energy consumption in Europe. In the last decade, around 40% of total consumption is related to the use of the building with about 36% of greenhouse emissions [1].

Several directives have been implemented by the EU to increase the use of renewable energy sources (RES) and reduce final energy consumption: Directive 2009/28/EU has set a target of 20% for the overall share of renewable energy by 2020; Directive 2010/31/EU defined the minimum performance factors for existing and new buildings and introduced the concept of net zero energy building (nZEB), i.e. buildings characterized by very low energy demand and a large percentage of energy renewable produced on-site or nearby. Finally, Directive 2018/2002/EU, sets the "Clean energy for all Europeans" objective, with a further increase in energy efficiency, setting the objective of reducing energy consumption from non-renewable sources of 32.5% within in 2030.

The solar energy that reaches the earth's crust represents a far greater transfer of energy to Earth than fossil energy.

Solar energy can be converted, through natural and technological processes, into other useful forms of energy, i.e. through the chemical process, through photosynthesis, with the electrical process to produce electricity, from the thermal process to produce heat, and from the conversion of solar radiation into mechanical energy, as in the case of wind. However, even with the growing interest in renewable energies in previous decades, global electricity production by solar energy conversion is still below 2% [2].

Thanks to European directives, significant progress has been made in solar energy and other renewable energy equipment, achieving greater efficiency of these technologies, as well as in the discovery of new solutions. This led to the production of primary energy from RES, such as to cover about 19% of the final consumption in Europe.

In recent years, the various directives have been promoting the installation of small RES systems that are widespread in the construction sector. Thus, the end-user consumes self-produced energy on-site. The RES technologies that are most suitable for this purpose are solar systems.

The work includes in the first part the description of the various technologies of solar RESs, including the main parameters that govern energy production, and a small bibliographic analysis for hybrid PV/T systems. Various Key Performance Indicators KPIs are also defined, useful for calculating the characteristic parameters of solar systems, which can be used for the comparison between the various technologies, as well as the indices for calculating production and electrical, thermal and total efficiency, also taking into account the quality of the energy produced by applying the first and second principles of thermodynamics.

The second part shows a highly flexible pilot photovoltaic/thermal (PV/T) plant, installed in the electrical, electronic and computer engineering department of the University of Catania, capable of emulating different scenarios. An extensive experimental investigation has allowed the study of different scenarios both from the plant engineering, management point of view, and the possibility of using hybrid PV/T technology, as well as the calibration and validation of mathematical calculation models

In the third part, the experimental investigations were further expanded using mathematical models, with which the performance of the various solar technologies were compared as the climate changed, and the impact of some operating parameters on the performance of PV/T plants was also analysed, as well as the use of possible strategies to improve the performance of PV/T plants (through nanofluids) and photovoltaic plants (through Phase Change Materials).

Finally, for the scope of achieving the nZEB targets, the performances of passive and active building envelopes are analysed. In detail, the performance of ventilated façades (passive envelope) throughout the whole year are determined, as well as the performance of active envelopes, with integrated or added solar RESs of the type: solar thermal, photovoltaic, and photovoltaic/thermal technologies.

1. SOLAR RENEWABLE ENERGY SOURCES

The main solar RESs used in the construction sector are solar thermal systems, photovoltaic systems, and hybrid photovoltaic/thermal systems.

1.1 Solar thermal system

The solar thermal system (ST) is a system equipped with solar thermal collectors capable of capturing solar energy and transforming it into thermal energy in the form of heated working fluid. This can be used directly, or it can feed a storage tank system where the thermal energy is stored.

The STs can be classified according to the heat transfer fluid (e.g. water, water and glycol mixture, air or heat transfer oil), according to the type of panel (glass floors, uncovered, with vacuum tubes, at concentration) or according to the architecture of the whole system (forced circulation, natural circulation, preheating). The use of thermal energy can cover various cases, for example, production of domestic hot water, heating, solar cooling, or it can even be used for heating industrial processes.

The panels are normally made of a metal absorber, where through a layer of selective material, it can absorb about 95% of the solar radiation and at the same time limits the emissivity of the plate. By means of channels or coils, the heat absorbed by the plate is transferred to the working fluid. To reduce heat losses and to improve the efficiency of the collector, the absorber is equipped with a transparent front cover (flat plate collector) to generate a greenhouse effect, while laterally and on the backside, it is insulated. In vacuum tube collectors each absorber strip is inserted into a glass tube in which the vacuum has been created. This results in excellent insulation which allows to reach even high working temperatures.

The performance of a solar collector is described by the energy balance between the energy incoming and outgoing the system (solar panel). At steady state, the possibility of storing energy by the collector is not considered, therefore the system leads to a balance where the incoming energy flux equals the outgoing flux. The incoming energy flux is represented by the solar radiation absorbed by a collector per unit area of absorber (S), i.e. by the incident solar irradiance reduced by the optical losses, while the thermal energy lost by the collector in the surrounding environment is defined as the heat loss coefficient (U_L) multiplied by the difference between the average temperature of the absorber plate (T_{pm}) and the ambient temperature (T_{amb}). The U_L coefficient includes all heat losses by conduction, convection, and infrared radiation.

Therefore, the useful energy output of a collector of area (A) is defined as:

$$Q_{th} = A[S - U_L(T_{pm} - T_{amb})] \quad (1.1)$$

However, the use of this equation is complex because the average temperature of the absorber plate is difficult to calculate or measure since it depends on the characteristics of the collector, the incident solar radiation and the conditions of the inlet fluid.

By applying a reformulation to equation (eq. 1.1) [3], it is possible to express the useful energy gain in terms of the temperature of the inlet fluid and the incident solar irradiance (G), using the (F_R) parameter, collector heat removal factor, and the optical properties of panel ($\tau\alpha$) called transmittance-absorptance product.

$$Q_{th} = F_R A [G(\tau\alpha) - U_L(T_{in} - T_{amb})] \quad (1.2)$$

The collector heat removal factor can be experimentally measured or analytically evaluated as:

$$F_R = \frac{\dot{m} \cdot C_f}{A \cdot U_L} \left[1 - \exp \left(-\frac{A \cdot U_L \cdot F'}{\dot{m} \cdot C_f} \right) \right] \quad (1.3)$$

Where \dot{m} is the mass flow rate of the fluid, C_f is the specific heat and F' is the collector efficiency factor calculated by:

$$F' = \left(1 + \frac{U_L}{U_{AbsFluid}} \right)^{-1} \quad (1.4)$$

where $U_{AbsFluid}$ represents the heat transfer coefficient between the absorber and the fluid.

Likewise, the useful energy gain transferred to the working fluid from the solar collector is represented by an energy balance between the enthalpy content of the fluid at the inlet and at the outlet of the collector (Eq. 1.5), which is a function of the inlet (T_{in}) and outlet (T_{out}) temperature of the fluid.

$$Q_{th} = \dot{m} \cdot C_f \cdot (T_{out} - T_{in}) \quad (1.5)$$

The thermal efficiency (η_{th}) of the solar collectors is calculated by the ratio between the useful energy transferred to the fluid and the solar energy available in the collector surface:

$$\eta_{th} = \frac{Q_{th}}{A \cdot G} \quad (1.6)$$

Starting from Eq. 1.2, the formula for calculating the thermal efficiency can be written in the form commonly known as Hottel-Whillier-Bliss equation:

$$\eta_{th} = F_R \cdot (\tau\alpha) - F_R \cdot U_L \cdot \frac{(T_{in} - T_{amb})}{G} \quad (1.7)$$

Then, note the characteristics of the collector and the operating conditions of the collector (T_{in} , T_a and G), using Eq. 1.7 and reversing the Eq. 1.6, the thermal efficiency of the collector and the useful energy transferred to the fluid can be easily calculated.

In recent years, the European standard (ISO 9806: 2017) [4] has defined test methods for solar systems and two different methodologies for calculating the performance of solar systems: Steady State Testing (SST) and Quasi Dynamic Testing (QDT).

The SST method determines the efficiency using an equation (see Eq. 1.8) very similar to that of Hottel-Whillier-Bliss, where a quadratic term is simply added and instead of using the temperature of the inlet fluid, it uses the average temperature of the fluid.

$$\eta_{th} = \eta_0 - a_1 \cdot \frac{(T_{av} - T_{amb})}{G} - a_2 \cdot \frac{(T_{av} - T_{amb})^2}{G} \quad (1.8)$$

where η_0 is the zero-loss collector efficiency, a_1 and a_2 are the thermal heat losses coefficients, respectively regard the linear and quadratic term.

The QDT model takes into account the dependence on direct and diffuse radiation, fluid temperature, wind speed, incidence angle effects and capacity, as shows in Eq. 1.9.

$$Q_{th} = \eta_0 \cdot (K_b \cdot G_b + K_d \cdot G_d) - c_1 \cdot (T_{av} - T_{amb}) - c_2 \cdot (T_{av} - T_{amb})^2 + \\ - c_3 \cdot u \cdot (T_{av} - T_{amb}) + c_4 \cdot (E_L - \sigma \cdot T_{amb}^4) - c_5 \cdot \frac{dT_{av}}{dt} - c_6 \cdot u \cdot G \quad (1.9)$$

with

$$K_b = 1 - b_0 \cdot \left(\frac{1}{\cos \theta} - 1 \right) \quad (1.10)$$

where K_b is the IAM for direct radiation, K_d the IAM for diffuse radiation, c_1 - c_4 and c_6 the heat loss coefficient, that respectively represent, c_1 the linear temperature dependence, c_2 the quadratic temperature dependence, c_3 the wind speed dependence, c_4 the sky temperature dependence and c_6 the wind speed dependence of the zero loss efficiency, c_5 represents the effective thermal capacity, u the wind speed in the PV/T plane, E_L the long-wave irradiance, σ the Stefan-Boltzmann constant, b_0 the constant for thermal IAM and θ the incidence angle of beam radiation.

Since only the QDT model includes the differentiation of diffuse and direct radiation, this method is more applicable for collector technologies whose thermal performance is sensitive to the diffuse fraction (e.g. concentration collectors).

By observing the equations described for the efficiency calculation, it can be seen that, as the difference between the temperature of the fluid and the environment increases, or if the solar irradiation decreases, the thermal efficiency decreases, as shown in figure 1.1.

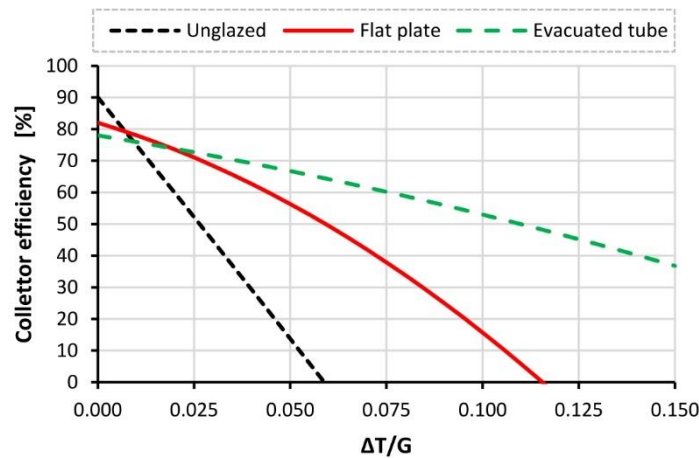


Figure 1.1 - Theoretical efficiency for commercially solar thermal collectors.

Figure 1.1 shows that the trend of efficiency changes for the different technologies of solar thermal collectors. In detail, the efficiency at zero-loss is higher for unglazed collectors because they can absorb a lot of incident solar energy as it directly affects the absorber. Otherwise, the efficiency decreases very quickly for unglazed panels because they are not insulated and the lack of glass does not generate the greenhouse effect that blocks heat losses, while the vacuum panels have more constant efficiencies with good performance even at high temperature differences between fluid and ambient air.

1.2 Photovoltaic system

Photovoltaic (PV) panels are made up of several photovoltaic cells that convert solar energy into electricity.

When sunlight hits the photovoltaic material, the photon energy is absorbed by an electron in the valence band. The energy carried by the photons is given in Eq. 1.11, where λ is the wavelength, h_p is the Planck constant and c is the speed of light.

$$E = \frac{h_p \cdot c}{\lambda} \quad (1.11)$$

If the energy of the photon is greater than the energy of the band gap, it will cause the electron to be excited from the valence band to the conduction band, where it will move producing electric current. However, if the energy of the photon is less than that of the band gap, it will be lost as heat.

Photovoltaic technologies can be grouped into three categories: first, second and third generation. First generation technology photovoltaic cells include both monocrystalline and polycrystalline silicon cells, globally the silicon technology is the one that predominates in the production of solar cells. The second generation, namely thin film, includes amorphous silicon, cadmium telluride, copper indium gallium selenide and gallium arsenide materials cells. Third generations are multi-junction cells, sensitized coloring cells, organic cells (which use organic materials, for example polymers) and inorganic cells (which use inorganic substances).

Photovoltaic cells have a complex relationship between their operating environment and the maximum power they can produce.

The electrical power generated is calculated from the product of the voltage (V) for the current intensity (I).

$$P_{el} = V \cdot I \quad (1.12)$$

The current intensity generated by the PV module can be calculated using Eq. 1.13.

$$I = I_{ph} - I_0 \left(e^{\frac{V + R_s \cdot I}{V_T}} - 1 \right) - \frac{V + R_s \cdot I}{R_{sh}} \quad (1.13)$$

where I_{ph} is the current flow in the cell, I_0 is the saturation current intensity of the diode, V_T is the thermal voltage, R_S is the intrinsic resistance of the cell and R_{sh} is the Shunt resistance.

Therefore, I depends on the construction characteristics, on the voltage and on I_{ph} which is proportional to the solar irradiation.

Figure 1.2 shows the current intensity (left axis) and the electrical power produced (right axis) with the variation of the voltage, considering the constant solar irradiation and temperature.

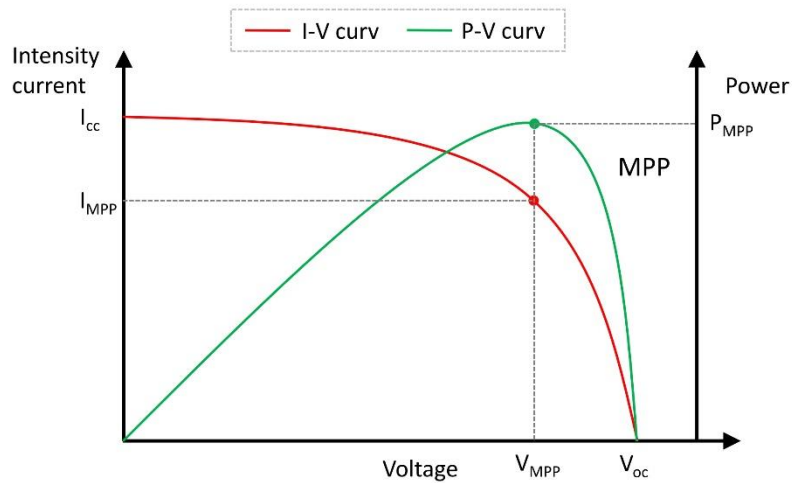


Figure 1.2 – characteristic curve of PV plants

It can be observed that at the knee of the I-V curve the electrical power has the maximum value, commonly called the maximum power point (MPP). The words I_{sc} and V_{oc} respectively indicate the current intensity in short circuit conditions ($V=0$) and the open circuit voltage ($I=0$).

It is important to remember that the solar irradiation that reaches a photovoltaic cell is only partially converted into electricity, whereas a large proportion of the solar irradiation is converted into heat that promotes the temperature increase of the solar cells. Normally the cell temperature is determined using Eq. 1.14 [5] or Eq. 1.15 [6], where in fact the temperature of the cells increases proportionally with the irradiance.

$$T_{pv} = T_{amb} + \frac{(NOCT - 20)}{800} G \quad (1.14)$$

$$T_{pv} = T_{amb} + \frac{G}{U_c + U_v \cdot u} \quad (1.15)$$

Where NOCT represents the cell temperature when the air temperature is equal 20°C and the irradiance is equal to 800 W/m², U_c and U_v are the thermal loss coefficient and for crystalline PV module assume respectively the value of 30.08 W/m²·K and 6.28 W·s/m³·K [7].

The increase in the temperature of the silicon solar cells leads to a reduction in the open circuit voltage and a less pronounced increase in the short circuit current (Figure 1.3), with the

consequent reduction of the electric power at MPP conditions. Therefore, it determines a reduction in electrical efficiency at the point of maximum power, as described in Eq. 1.16:

$$\eta_{el} = \eta_{STC} \cdot [1 - \gamma(T_{pv} - T_{STC})] \quad (1.16)$$

where γ is the thermal coefficient and varies between 0.37%/°C and 0.52%/°C, T_{pv} is the cell temperature and the subscript STC indicate Standard Test Conditions that are referred to cell temperature equal to 25°C and to incident irradiance of 1000 W/m².

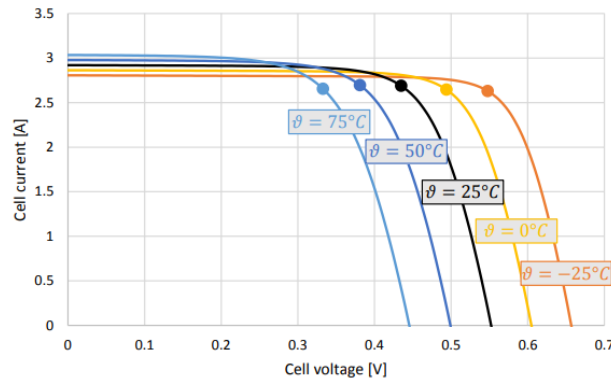


Figure 1.3 – variation of the I-V curves and P_{el} as the cell temperature changes [8].

To counteract this phenomenon, the cells may be cooled by passive or active cooling techniques. Active cooling systems require external power inputs, as the PV modules are equipped with fans or pumps, while passive systems do not require additional power to operate.

The main passive cooling techniques are: use of Phase Change Material inside a tank placed under the photovoltaic cells, use of fins placed behind the cells in order to increase heat dissipation, the use of cotton wick structures that were mounted on the backside surface of PV panels so to utilize the capillary action of the wick structures in order to enhance the heat rejection from the PV panels to the surroundings, or the water immersion method. Passive cooling techniques are simply applicable but have limited impact on performance improvement.

The main active cooling techniques are: use of fans to increase the convection coefficient due to forced convection, use of the water flow on the front of the panels, use of the thermal absorber attached to the rear of the cells where a coolant fluid flows. Active cooling techniques are more suitable to changes in operative conditions, which in general can ensure higher performance improvements but are more demanding from an investment point of view and requires energy for their operation.

1.3 Photovoltaic/thermal system (PV/T)

The use of coolant fluid requires energy for its pumping but allows to generate thermal energy removed from the cells to be used elsewhere, resulting in a hybrid solar equipment with simultaneous generation of electric energy and thermal energy: this is called a Photovoltaic-Thermal collector PV/T. Thus, a PV/T hybrid solar collector is a device formed by a PV module with an attached thermal unit on its back. The importance of this equipment is that it can generate electric and thermal energy simultaneously, with a good level of efficiency and in a smaller area than conventional thermal collectors and photovoltaic modules operating separately.

The fundamental idea of this form of hybrid panel can be illustrated by the optical properties of a typical photovoltaic cell made of crystalline silicon (Figure 1.4).

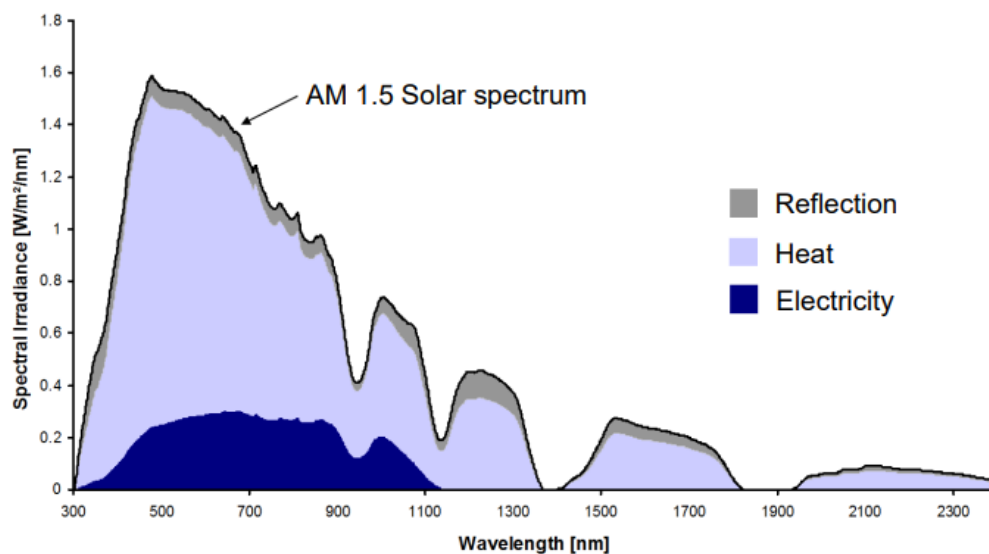


Figure 1.4 – spectral properties of a crystalline silicon PV cell [9].

About 10% of the solar irradiation that hits the crystalline photovoltaic cell is reflected and cannot be used. About 10-20% is absorbed by the cell and is converted into electricity and the remaining part is converted into thermal energy.

The idea behind the PV/T collectors is to use the solar heat produced in the photovoltaic cells instead of releasing it to the environment. To achieve this, a metallic heat absorber filled with heat transfer fluid is attached to the back of a photovoltaic module, allowing the use in the form of thermal energy of solar energy not converted into electricity. Moreover, by extracting the heat produced in the cell, it is possible to simultaneously increase the electric power of the photovoltaic cells, thus obtaining a synergistic effect. For this reason, the PV/T collectors achieve specific surface yields higher than the standard photovoltaic modules or compared to conventional solar collectors.

1.3.1 PV/T technologies

There are various types of PV/T collectors. More than 50 different types of PV/T are produced in Europe, of which about 70% are uncovered liquid-based PV/T collectors.

The classification of the PV/T panels follows the classifications seen for solar thermal collectors and photovoltaic modules. Therefore, a classification is made in agreement to the working fluid used: air-based, liquid-based and bi-fluid. Air-based PV/T systems are characterized by an airflow that flows between the photovoltaic surface and the overlying glass. The coolant fluid can flow in active or passive mode, using a single or double passage and through different configurations of the absorber. Air-based PV/T systems cannot work efficiently at high-temperature region due to some limitations of air like low density, low heat carrying capacity etc. Consequently, liquid-based PV/T collectors are widely used. They use water or a mixture of water and glycol as a coolant fluid. The fluid flows in specific channels or tubes below the cells to subtract the heat from the photovoltaic cells and use the transferred heat. The use of the liquid fluid allows greater usability than the use of air, just think that outside the heating period, in the houses, the use of hot air is not required, while domestic hot water is required every day. The bi-fluid technology consists in the scroll of a liquid working fluid under the cells and the scroll of a gaseous fluid (usually air) above the photovoltaic cells.

Another classification divides the panels into a flat plate, concentrator, and vacuum collectors. Flat plate collectors (FPC) are formed by the insertion in contact of an absorber plate below the PV module. In turn, the flat plate collectors can be divided into covered and uncovered, insulated and uninsulated but also according to the type of absorber (sheet and tube, roll bond, etc.) and the material used to make the absorber (copper, aluminium, stainless steel, polymer). The covered PV/T panels have one or more glasses placed in front of the panel to reduce heat losses on the front of the panel. Insulated panels are created by thermally insulating the panel on the back and side. The panels simultaneously uncovered and uninsulated are called Wind and/or Infrared Sensitive Collectors (WISC) because the lack of thermal insulation and cover glass makes them highly influenced by the wind speed. Besides, the WISC panels on the front of the panel disperse a lot of heat in the field of infrared wavelengths due to the lack of the greenhouse effect normally generated by the glass. The concentrated PV/T collector (CPVT) is composed by the PV/T module and solar concentrators that concentrate the solar radiations on the PV/T panel. Finally, the vacuum PV/T panel is characterized by the presence of a string of photovoltaic cells inside a glass cylinder without air inside. The vacuum allows to reduce heat losses; therefore, these panels can have excellent thermal performances but work with higher cell temperatures.

In summary, Figure 1.5 and 1.6 show the various PV/T technology.

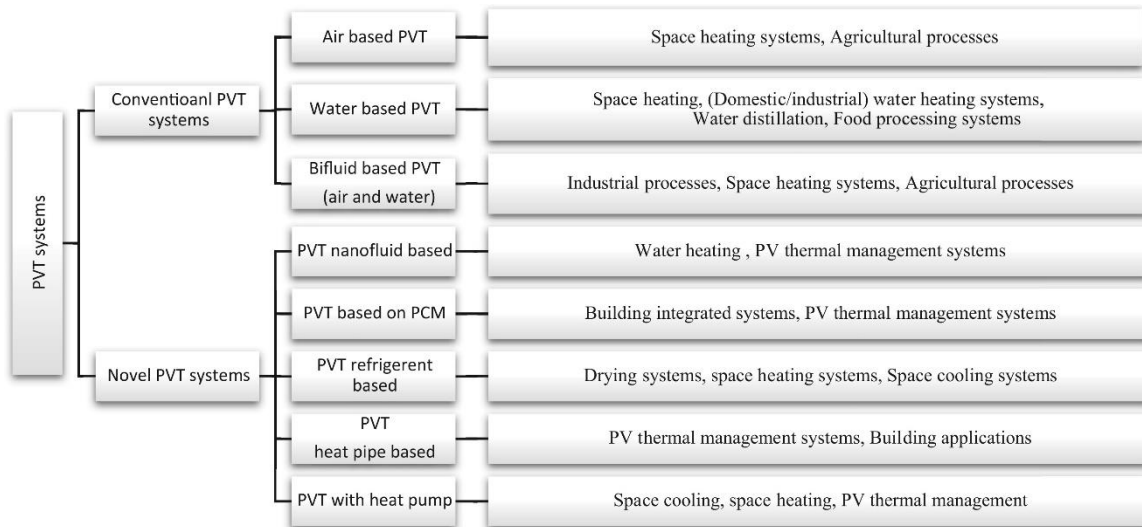


Figure 1.5 – different PV/T technologies [10].

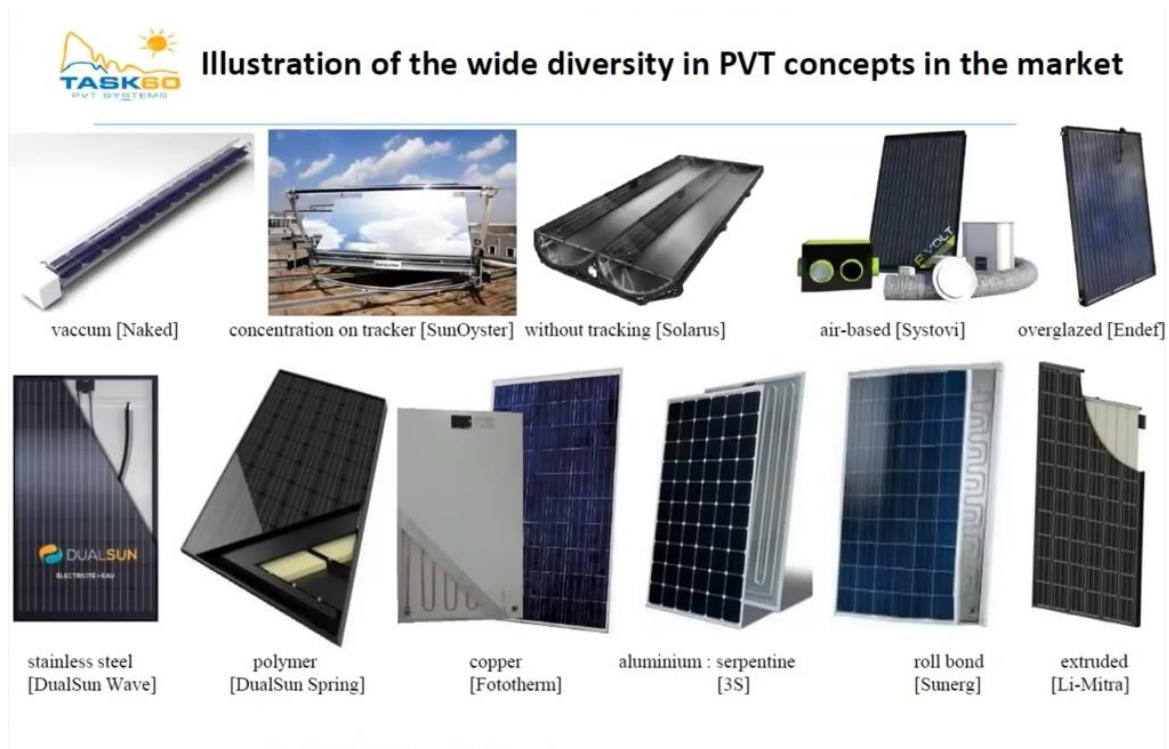


Figure 1.6 – different PV/T technologies [11].

1.3.2 Performance and use of PV/T

The performance and applications of the PV/T system depend on its heat transfer fluid. Conventionally, air and water are used as a thermal fluid in PV/T systems. In the last 3-4 decades, numerous research works have been conducted on the optimization of PV/T systems, varying the geometry of the system, operating conditions, packing factor, etc.

The air-based PV/T design provides a simple and economical solution to cooling the PV cells, and the air can be heated to different temperature levels through forced or natural flow. Forced circulation is more efficient than natural circulation owing to better convective and conductive heat transfer, but the required fan power reduces the net electricity gain. These collectors allow to produce thermal energy in the form of heated air to be used for space heating and the simultaneous cooling effect of the photovoltaic cells allows a greater production of electricity, obtaining about 35-40% of the combined efficiency (thermal plus electrical) [12]. The use double-pass air above the cells allows an increase in performance, both for thermal and electrical yields [13-14]. [15] studied six different configurations of air-based PV/T systems: glazed and unglazed single air channel, glazed and unglazed thin aluminum sheet and glazed and unglazed finned PV/T panel. The results show that the fin arrangement allows to achieve thermal efficiencies far higher than the other configurations as well as for the total yields. The use of micro-channels in glazed PV/T systems allows an increase in overall performance of more than 70% compared to a conventional system [16]. Finally, it has been shown that the performance of an air-based PV/T can be increased by using panels with impinging jets [17-18]. The study of three different configurations of the channel where the air flows: V-groove, honeycomb and stainless steel wool, has shown that the honeycomb absorber allows to achieve very high thermal efficiencies, with overall yields exceeding 90% under certain conditions [19].

The main problem with the air-based system lies in the poor effectiveness of removing heat from the air, due to the low density, low specific heat capacity and low thermal conductivity. Furthermore, the simultaneous production of energy from air-based PV/T systems is limited to the heating season only, while in all other seasons just the production of electricity will be exploited. Alternatively, another use is linked to the cooling of the rooms, if the system is connected with an air solar cooling system, however, the production of thermal energy is not exploited during the whole year. Finally, it is also difficult to store heat in a tank for better management of meeting demand.

The liquid-based PV/T collector is more effective and practical than the air-based collector [20], since the high heat storage capacity of liquids, normally water, allows for much less marked temperature variation compared to air and ensures more cooling uniform of photovoltaic cells [21]. At the same time, the heat subtracted from the fluid can be easily used for different purposes, such as heating domestic water or heating rooms [22], in this way the simultaneous production of thermal and electrical energy is fully exploited during the whole year. Liquid-based PV/T is a very popular technology and has gained increasing application in practical projects. This type of system can achieve an overall efficiency greater than 60% [23]. Its performance largely depends on the temperature and flow rate of the water, the geometric shape and the size of the water flow channels. These collectors can have an external glass cover (glazed collector) with an air gap between the cover and the absorber or without an external cover (unglazed) [24]. The glazed PV/T collector must compromise with electrical efficiency [21] due to the increase in temperature while the other without coverage suffers from lower thermal efficiency but better electrical efficiency [24, 26-27]. The efficiency of the PV/T collectors is also related to the type of absorber. [28] have shown that the roll bond absorber allows higher efficiency compared to the PV/T equipped with a sheet and tube absorber.

Besides, efficiency depends on the distribution of the flow of refrigerants through the channel. The channel design should be optimized to provide maximum heat transfer area and longer retention times for effective heat transfer from the collector to the heat transfer fluid. In this regard, [29] have shown that the performance of the roll-bond manifold is determined not only by the operating conditions and materials but also by the geometric structure of the flow channel network. They compared three types of channel patterns (parallel, fractal T-shape and honeycomb shaped), concluding that the honeycomb roll bond absorber is the best because it shows good temperature uniformity and a small difference between the average panel surface temperature and water temperature. The use of thermal insulation in the PV/T collector allows obtaining better performance than the uninsulated panel [28]. The performance of the PV/T collectors is also influenced by the flow rate, as various literature studies show. The generic conclusion they reached was that thermal and electrical PV/T efficiency increases with increasing flow rate. This is because as the speed of the water in the pipe increases, the heat transfer coefficient also increases, thus maximizing both the cooling of the PV and the transfer of heat to the water [30-31]. Finally, the packing factor has an even greater influence on performance than the flowrate [21].

Recently, some researchers have focused on using both fluids, air and water simultaneously, creating the PV/T system called bi-fluid based. [32-34] carried out an experimental analysis and created a numerical model of the bi-fluid collector. Experimental results have shown that the use of the double thermal vector allows achieving higher efficiencies than the use of single fluid [32]. In addition, the theoretical analysis was conducted considering the simultaneous use of the two fluids, but also the use of a single fluid. This study has shown that the simultaneous use of air and water allows greater efficiency both from a thermal and electrical point of view [33]. The experimental evaluation of the tri-functional PV/T collector (bi-fluid based) was carried out to provide the dual purpose of heating the air and water according to the requirements [35]. Their experimental set-up consists of a top glass cover, monocrystalline silicon solar cells attached to an aluminium absorption plate (painted black), copper pipes, air inlet and outlet arrangement. Steady-state thermal analysis reveals 46% thermal efficiency along with 10.2% electrical efficiency in the air-heating operation mode, while in the water heating operation mode thermal efficiency and electricity are respectively 56.6% and 11.8%. [36] has numerically analyzed the performance of the dual-channel PV/T system using four different fluid configurations, water-air, air-water, air-air, and water-water. The study showed that the water-water based PV/T system allows us to achieve the best electrical and thermal performance, reaching an overall efficiency of about 83% in the best conditions.

To further improve the performance of the PV/T systems, device capable of concentrating solar irradiation onto the PV/T collector, commonly called concentration systems (CPVT), can be used.

Concentration systems allow to reach very high levels of irradiation, consequently very high fluid temperatures are reached [37], to extend the possible uses of PV/T also for industrial purposes. Furthermore, in these systems the photovoltaic part is normally reduced to a strip, therefore it is possible to use expensive multi-junction III-V solar cells to obtain higher efficiencies, i.e. cells with an electrical efficiency of 40-45%, without raising costs.

Currently, there are several configurations of the CPVT system, classified by distribution method and conversion sequence of energy flux: Waste Heat Recovery (WHR CPVT), Spectral Beam Splitting (SBS CPVT) and Energy Distribution Fitting (EDF CPVT). Even more in detail, WHR CPVT systems can be further classified according to the optical concentrators (CR): low concentration system when $CR \leq 10x$ (WHR LCPVT), medium concentration system if $10x < CR \leq 100x$ (WHR MCPVT) and high concentration system for $CR > 100x$ (WHR HCPVT). The portion of diffuse irradiance used changes with the concentration ratio: in low concentration systems, in addition to direct radiation, a high percentage of diffused light is used, while for high concentration devices only direct irradiation converges. High concentration technologies also require a very precise two-axis tracking system, while those with medium concentration need only one-axis tracking.

A complete methodology to characterize, simulate and evaluate the performance of a CPVT has been proposed by [38]. In the study, a parabolic reflector consisting of a silver plastic film laminated on a steel sheet was used, with a concentration ratio of 7.8 and PV cells with an efficiency of about 16%. The analysis shows an electrical efficiency of 6.4% and a thermal efficiency of about 40% if assessed concerning the concentrator area. Otherwise, observing only the net area of the collector achieves an efficiency of about four times higher than that of a conventional system.

Many studies have analyzed concentration systems for PV/T plants based on Fresnel lenses. Using linear Fresnel lenses with two-axis tracking [39], the overall efficiency of over 60% was detected. [40] used a similar configuration lens-Fresnel based, obtaining thermal and electrical efficiency of 48% and 18% respectively. The use of eleven Fresnel lenses arranged vertically [41], has allowed obtaining increases in electrical and thermal efficiency compared to the use of a conventional system, obtaining an increase in electrical generation greater than 4.5 times, while the thermal power ratio takes a value ranging from 1.9 to 2.8 depending on the weather conditions.

Despite the above advantages, the CPVT hybrid system faces several challenges. Due to the precise localization system of 1 or 2 axis concentrators, additional costs may be introduced. Maintenance costs also increase due to the complexity of the system. The loss of discrepancy in the photovoltaic modules, which occurs when the electrical parameters of a solar cell are significantly modified by those of the remaining devices, can deteriorate due to the non-uniform lighting and shading of the structure. Under uneven lighting conditions, the uneven intrinsic temperature on the photovoltaic cells also causes discrepancy losses and hotspot heating.

1.3.3 Physical Characterization

The characterization of the PV/T systems follows what has been seen for the ST and PV systems with some differences related to the mutual dependence of the thermal performance on the electrical performance and vice versa. In fact, the heat transfer mechanisms of PV/T collectors differ from conventional solar collectors only in that a portion of the incoming energy them is converted into electricity by photovoltaic cells. In the same way, the electrical performances of

the PV/T differ from that of a conventional PV only for the temperature of the photovoltaic cells which will also depend on the coolant fluid.

Essentially, the equation for calculating the useful thermal energy (Eq. 1.2) and the equations used to calculate thermal efficiency are modified to take into account the effects of adding photovoltaic cells to the absorber plate of the thermal collector, i.e. the Florschütz method [42].

The changes consist in the replacement of the total radiation incident on the plate “ $G(\tau\alpha)$ ” with the effective value “ $G(\tau\alpha)_{eff}$ ”, that is, reduced by the energy transformed into electricity, as described in eq. 1.17.

$$G(\tau\alpha)_{eff} = G(\tau)(\alpha - \eta_{el} \cdot PF) = G(\tau\alpha) \left(1 - \frac{\eta_{el}}{\alpha} \cdot PF\right) \quad (1.17)$$

where PF is the packing factor, that is the ratio between the surface covered by the PV cells and the total surface of the panel.

Thus, the useful thermal energy in PV/T system is calculated by Eq. 1.18

$$Q_{th} = F_R A [G(\tau\alpha)_{eff} - U_L(T_{in} - T_{amb})] \quad (1.18)$$

Table 1.I shows the average values of the parameters “ $F_R(\tau\alpha)$ ” and “ $F_R \cdot U_L$ ”, derived from the experimentation conducted in [43] without electrical production for PV/T collectors, considering both glazed (PVT_g) and unglazed (PVT_{ung}) panels and for an unglazed solar thermal collector (ST_{ung}).

Table 1.I Average values of the parameters, $F_R(\tau\alpha)$ and $F_R \cdot U_L$ [43].

Parameter	U.M.	PVT _{ung}	PVT _g	ST _{ung}
$F_R(\tau\alpha)$	-	0.76	0.71	0.87
$F_R \cdot U_L$	$W \cdot m^{-2} \cdot K^{-1}$	16.8	8.30	18.2

These data indicate that the photovoltaic cells in the PVT_{ung} reduce the energy absorption and the heat loss coefficient slightly compared to the ST_{ung} and that the glass cover in PVT_g reduces the heat losses in the surrounding environment considerably, but in the meantime reduces the solar energy available due to the reflection of the glass surface.

As regard the PV/T performance, figure 1.7 reports the efficiency of the several PV/T technologies in comparison with standard FPC.

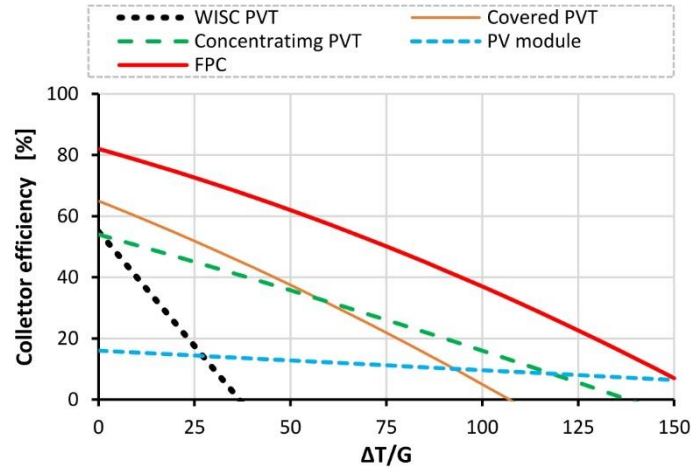


Figure 1.7 – efficiency of the several PVT technologies.

Among the various technologies of PV/T panels, the WISC type has very low thermal efficiencies with a sudden collapse as the temperature difference between the fluid and the surrounding environment increases. This is caused by the high heat losses, due to the lack of thermal insulation and the lack of the greenhouse effect generated by the glass. Consequently, WISC PV/Ts have a narrow field of applicability. Unlike CPVTs, they allow a much wider working range, even for industrial processes, reaching temperature differences of more than 100 K. In any case, any type of PV/T has thermal efficiencies lower than the standard FPC, because part of the incident solar energy is transformed into electricity.

From the point of view of electrical performance, the PV/T panels behave in a completely similar way to the PV, with the only difference that the temperature of the photovoltaic cells also depends on the working conditions of the coolant fluid (temperature, flow rate and characteristics of the fluid). To model the electrical performance of PV/T, it is necessary to find the best compromise between simplicity and detail. A basic approximation used in many models is to set the temperature of the photovoltaic cells equal to the average temperature of the fluid [44]. Other studies [15, 42, 45-46] consider the cell temperature equal to the temperature of the absorber plate, based on the assumption that the heat transfer between photovoltaic cells and absorber is very good. In this way the Hottel Whillier-Bliss equation can be used, taking into account the energy transformed into electricity. Based on experimental observations, [40] proposed the calculation of the cell temperature (Eq. 1.19) as a function of the storage tank temperature, the collector thermal efficiency and the incident radiation, which is a reformulation of the average temperature of the absorber plate calculated by Duffie and Beckman [3].

$$T_{pv} = T_{in} + k \cdot \eta_{th} \cdot G \quad (1.19)$$

where the constant k was determined as:

$$k = \frac{1 - F_R}{F_R U_L} \quad (1.20)$$

Other models [47-50] assume that the temperature difference between the photovoltaic cells and the heat transfer fluid is proportional to the useful heat transferred to the fluid, based on the energy balance derived from one-dimensional models with a single absorber and fluid node. Thus, the mean temperature of the PV cell, which is assumed equal to absorber temperature, is calculated by the following equation:

$$T_{pv} = T_{av} + \frac{Q_{th}}{U_{AbsFluid}} \quad (1.21)$$

During stagnation, Q_{th} is zero and as a consequence of Eq. 1.21 the cell temperature equals the mean fluid temperature. This is an important finding for achieving a high accuracy of the electrical performance model during stagnation conditions.

The value of $U_{AbsFluid}$ can be estimated from the collector efficiency factor F' . [51] determined the values of $U_{AbsFluid}$ and F' for PVT_{ung}, PVT_g, and low-e glazed PV/T (PVT_{l-e}) collector operating in MPP tracking mode.

Table 1.II Average values of the parameters, $U_{AbsFluid}$ and F' [51].

Parameter	U.M.	PVT _{ung}	PVT _g	PVT _{l-e}
$U_{AbsFluid}$	$W. m^{-2}. K^{-1}$	65.1	62.1	61.2
F'	-	0.80	0.88	0.93

1.4 Key Performance Indicator (KPI)

This section summarizes the main indicators that allow to evaluate the performance of PV/T systems and to compare them with other systems or to compare performance with varying working conditions.

1.4.1 Electrical yields

The eq. 1.22 allows to calculate the electricity product ($E_{el,PV/T}$) during a fixed period, where P_{el} is the instantaneous power (calculated with Eq. 1.23), η_{el} represents the electrical efficiency of panel (calculated with Eq. 1.16), A the surface of the panel, and G the total incident irradiance.

$$E_{el,PV/T} = \int_0^t P_{el} dt \quad (1.22)$$

$$P_{el} = \eta_{el} A_{PV} G \quad (1.23)$$

$$\eta_{el} = \eta_{STC} \cdot [1 - \gamma(T_{pv} - T_{STC})] \quad (1.16)$$

Moreover, in order to evaluate the performance of the PV plant over time, IEC standard 61724:1998 introduces the performance ratio PR:

$$PR = \frac{Y_A}{Y_R} \quad (1.24)$$

where, Y_A is the array yield, that indicates the number of equivalent hours in which the PV/T module gives the peak value in the defined time interval (Eq. 1.25) and Y_R is the reference yield, that indicates the number of hours in which PV module works under G_{STC} value in the defined time interval (Eq. 1.26).

$$Y_A = \frac{E_{el}}{P_{peak}} \quad (1.25)$$

$$Y_R = \frac{G}{G_{STC}} \quad (1.26)$$

1.4.2 Thermal yields

The thermal energy ($E_{th,PV/T}$) produced by PV/T panel during a fixed period, is evaluated through the Eq. 1.27, where P_{th} is the instantaneous thermal power, estimated by applying the thermal balance equations to the fluid passing through the panels (Eq. 1.5)

$$E_{th,PV/T} = \int_0^t P_{th} dt \quad (1.27)$$

$$P_{th,PV/T} = Q_{th,PV/T} = \dot{m}_{PV/T} \cdot C_f \cdot (T_{out} - T_{in}) \quad (1.5)$$

where $\dot{m}_{PV/T}$ is the mass flowrate circulating in the PV/T circuit, C_f indicates the specific heat of the coolant fluid, T_{out} and T_{in} the temperature of the fluid at outlet and inlet of the PV/T panels.

However, in a PV/T system, not all the thermal energy coming from the panels is usable, as this is first transferred to the storage tank and then used. Therefore, for the calculation of the useful thermal energy, reference must be made to the balance in the storage tank. The net energy provided by PV/T to cover the thermal needs can be evaluated using Eq. 1.28, where \dot{m}_{load} is the mass flowrate required by users, C_f indicates the specific heat of the working fluid, $T_{t,out}$ and $T_{t,in}$ the temperature of the fluid respectively at outlet of tank (supplied to users) and at the inlet (coming).

$$E_{th,load,PV/T} = \int_0^t \dot{m}_{load} \cdot C_f \cdot (T_{t,out} - T_{t,in}) dt \quad (1.28)$$

While, if the system fails to cover all the requirements, the auxiliary energy required can be calculated as:

$$E_{AUX} = \int_0^t \dot{m}_{load} \cdot C_f \cdot (T_{setpoint} - T_{t,out}) dt \quad (1.29)$$

One of the main Key Performance Indicators (KPI) of energy production plants from renewable sources is the demand coverage factor (f), that is the ratio between the energy supplied by the system and that required by users:

$$f_{th,load} = 100 \cdot \frac{E_{th,load,PV/T}}{E_{th,load}} \quad [\%] \quad (1.30)$$

1.4.3 Overall Energy Yields

The overall performance of PV/T systems can be obtained as a direct summation of electrical and thermal power as given by the following equation:

$$\eta_{tot} = \frac{P_{el} + P_{th}}{A \cdot G} \quad (1.31)$$

$$E_{tot} = E_{th} + E_{el} \quad (1.32)$$

However, the electrical energy is more valuable than thermal energy. Thus, to take into account of the different quality of the thermal and electrical energy, the overall performance must be evaluated based on a thermodynamic approach from the viewpoint of the first and second laws. The first law approach consists in the calculation of the primary energy produced $E_{tot(l)}$ (as described in [51-52]) using the Eq. 1.33:

$$E_{tot(l)} = E_{el}/\eta_{power} + E_{th} \quad (1.33)$$

where η_{power} is the electric power generation efficiency for a conventional power plant.

Nevertheless, to evaluate energy quality in more detail, a second law formulation must be used, therefore exergy must be assessed. The exergy represents the maximum quality of work that can be produced in some given environment.

The overall exergetic efficiency (ε_{tot}) and total exergetic content ($E_{\chi,tot}$) of the PV/T system can be calculated based on the modified equation given by Chow et al. [53]:

$$\varepsilon_{tot} = \frac{E_{\chi,el} + E_{\chi,th}}{E_{\chi,sun} \cdot A} \quad (1.34)$$

$$E_{\chi,tot} = E_{\chi,el} + E_{\chi,th} \quad (1.35)$$

with:

$$E_{\chi,el} = E_{el} \quad (1.36)$$

$$E_{\chi,th} = \int_0^t P_{th} \left(1 - \frac{T_{amb}}{T_{t,max}} \right) dt \quad (1.37)$$

$$E_{\chi,sun} = \int_0^t G \left[1 - \frac{4T_{amb}}{3T_{sun}} (1 - \cos \beta_{sun})^{1/4} + \frac{1}{3} \left(\frac{T_{amb}}{T_{sun}} \right)^4 \right] dt \quad (1.38)$$

where T_{sun} is the equivalent temperature of the Sun as a blackbody (5800 K) and β_{sun} is the half-angle of the cone subtended by the Sun disc where β_{sun} is 0.0047rad on a clear day for a beam sunlight and $\pi/2$ for a diffuse sunlight.

1.4.4 KPI on the thermal level

In a PV/T installation, the electrical performances depend by the temperature of the working cells, which in turn depends on the solar irradiation (G). Thus, it is worth of interest to introduce a KPI, namely $T_{\text{char,PV}}$ (eq. 1.39), which allows evaluating the working temperature of the PV cells weighted by G .

$$T_{\text{char,PV}} = \frac{\int T_{\text{PV}} \cdot G \cdot dt}{\int G \cdot dt} \quad (1.39)$$

Other KPI is the $T_{\text{char,panel}}$, which indicates the coolant thermal level achieved in the panels when the coolant fluid flows, is calculated using eq. 1.40.

$$T_{\text{char,panel}} = \frac{\int T_{\text{av}} \cdot \dot{m} \cdot dt}{\int \dot{m} \cdot dt} \quad (1.40)$$

where T_{av} is the average temperature of the fluid inside the PV/T panels.

Finally, to determine the thermal level of the working fluid supplied by the solar system to satisfy users demand, the KPI $T_{\text{char,th,load}}$, is defined using the eq. 1.41, where the temperature of the fluid coming from the solar tank is weighed for the instantaneous water flow required by the user needs.

$$T_{\text{char,th,load}} = \frac{\int T_{\text{t,out}} \cdot \dot{m}_{\text{load}} \cdot dt}{\int \dot{m}_{\text{load}} \cdot dt} \quad (1.41)$$

References

- [1] Eurostat. Final energy consumption by sector
- [2] RENEWABLES 2019 GLOBAL STATUS REPORT – www.ren21.net
- [3] J. A. Duffie and W. A. Beckman, Solar Engineering of Thermal Processes: Fourth Edition. 2013.
- [4] “ISO 9806, 2013. ISO 9806:2017 Solar energy - Solar thermal collectors - Test methods.”
- [5] D.L. Evans. Simplified method for predicting photovoltaic array output. Solar Energy, Volume 27, Issue 6, 1981, Pages 555-560. [https://doi.org/10.1016/0038-092X\(81\)90051-7](https://doi.org/10.1016/0038-092X(81)90051-7)
- [6] PV SYST software, www.pvsyst.com
- [7] M. Koehl, M. Heck, S. Wiesmeier, J. Wirth. Modeling of the nominal operating cell temperature based on outdoor weathering. Solar Energy Materials and Solar Cells, Volume 95, Issue 7, July 2011, Pages 1638-1646. <https://doi.org/10.1016/j.solmat.2011.01.020>
- [8] D. Zenhäusern, E. Bamberger, A. Baggenstos. PVT Wrap-Up, Energy systems with photovoltaic-thermal solar collectors. Energie schweiz, final report, March 2017.
- [9] P. Dupeyrat, C. Ménézo, S. Fortuin. Study of the thermal and electrical performances of PVT solar hot water system. Energy and Buildings, Volume 68, Part C, January 2014, Pages 751-755. <https://doi.org/10.1016/j.enbuild.2012.09.032>
- [10] T.M. Sathe, A.S. Dhoble. A review on recent advancements in photovoltaic thermal techniques. Renewable and Sustainable Energy Reviews, Volume 76, September 2017, Pages 645-672. <https://doi.org/10.1016/j.rser.2017.03.075>
- [11] IEA SHC Solar Academy: PVT System -Task 60: ISES Webinar 25 March 2020.
- [12] A. Tiwari, M.S. Sodha. Parametric study of various configurations of hybrid PV/thermal air collector: Experimental validation of theoretical model. Solar Energy Materials and Solar Cells, Volume 91, Issue 1, 5 January 2007, Pages 17-28. <https://doi.org/10.1016/j.solmat.2006.06.061>
- [13] K. Sopian, K.S. Yigit, H.T. Liu, S. Kakaç, T.N. Veziroglu. Performance analysis of photovoltaic thermal air heaters. Energy Conversion and Management, Volume 37, Issue 11, November 1996, Pages 1657-1670. [https://doi.org/10.1016/0196-8904\(96\)00010-6](https://doi.org/10.1016/0196-8904(96)00010-6)
- [14] A.A. Hegazy. Comparative study of the performances of four photovoltaic/thermal solar air collectors. Energy Conversion and Management, Volume 41, Issue 8, May 2000, Pages 861-881. [https://doi.org/10.1016/S0196-8904\(99\)00136-3](https://doi.org/10.1016/S0196-8904(99)00136-3)
- [15] J.K. Tonui, Y. Tripanagnostopoulos. Air-cooled PV/T solar collectors with low cost performance improvements. Solar Energy, Volume 81, Issue 4, April 2007, Pages 498-511. <https://doi.org/10.1016/j.solener.2006.08.002>

- [16] S. Agrawal, G.N. Tiwari. Energy and exergy analysis of hybrid micro-channel photovoltaic thermal module. *Solar Energy*, Volume 85, Issue 2, February 2011, Pages 356-370. <https://doi.org/10.1016/j.solener.2010.11.013>
- [17] M. Belusko, W. Saman, F. Bruno. Performance of jet impingement in unglazed air collectors. *Solar Energy*, Volume 82, Issue 5, May 2008, Pages 389-398. <https://doi.org/10.1016/j.solener.2007.10.005>
- [18] S.A. Brideau, M.R. Collins. Development and validation of a hybrid PV/Thermal air-based collector model with impinging jets. *Solar Energy*, Volume 102, April 2014, Pages 234-246. <https://doi.org/10.1016/j.solener.2014.01.022>
- [19] M.Y. Othman, H. Othman, F. Hussain, K. Sopian, B. Yatim, M.H. Ruslan. Performance Study of Air-based Photovoltaic- thermal (PV/T) Collector with Different Designs of Heat Exchanger. *Sains Malaysiana*, Volume 42, September 2013, Pages 1319-1325.
- [20] J. Prakash. Transient analysis of a photovoltaic thermal solar collector for co-generation of electricity & hot air/water. *Energy Conversion and Management*, Volume 35, Issue 11, November 1994, Pages 967-972. [https://doi.org/10.1016/0196-8904\(94\)90027-2](https://doi.org/10.1016/0196-8904(94)90027-2)
- [21] M. Herrando, C.N. Markides, K. Hellgardt. A UK-based assessment of hybrid PV and solar-thermal systems for domestic heating and power: system performance. *Applied Energy*, Volume 122, 1 June 2014, Pages 288-309. <https://doi.org/10.1016/j.apenergy.2014.01.061>
- [22] X. Zhang, X. Zhao, S. Smith, J. Xu, X. Yu. Review of R&D progress and practical application of the solar PV/thermal (PV/T) technologies. *Renewable and Sustainable Energy Reviews*, Volume 16, Issue 1, January 2012, Pages 599-617. <https://doi.org/10.1016/j.rser.2011.08.026>
- [23] T.T. Chow, J. Ji, W. He. Photovoltaic-thermal collector system for domestic application. *Journal of Solar Energy Engineering*, Volume 129, May 2006, Pages 205-209. <https://doi.org/10.1115/1.2711474>
- [24] N. Aste, C. del Pero, F. Leonforte. Water flat plate PV-thermal collectors: a review. *Energy Procedia*, Volume 105, May 2017, Pages 961-966. <https://doi.org/10.1016/j.egypro.2017.03.426>
- [25] G. Fraisse, C. Ménézo, K. Johannes. Energy performance of water hybrid PV/T collectors applied to combisystems of Direct Solar Floor type. *Solar Energy*, Volume 81, Issue 11, November 2007, Pages 1426-1438. <https://doi.org/10.1016/j.solener.2006.11.017>
- [26] T.T. Chow, G. Pei, K.F. Fong, Z. Lin, A.L.S. Chan, J. Ji. Energy and exergy analysis of photovoltaic-thermal collector with and without glass cover. *Apply Energy*, Volume 86, March 2009, Pages 310-316. <https://doi.org/10.1016/j.apenergy.2008.04.016>
- [27] F. Yazdanifard, E. Ebrahimnia-Bajestan, M. Ameri. Investigating the performance of a water-based PV/thermal (PV/T) collector in laminar and turbulent flow regime. *Renewable Energy*, Volume 99, December 2016, Pages 295-306. <https://doi.org/10.1016/j.renene.2016.07.004>

- [28] P. Bombarda, G. Di Marcoberardino, A. Lucchini, S. Leva, G. Manzolini, L. Molinaroli, F. Pedranzini, R. Simonetti. Thermal and electric performances of roll-bond flat plate applied to conventional PV modules for heat recovery. *Applied Thermal Engineering*, Volume 105, 25 July 2016, Pages 304-313. <https://doi.org/10.1016/j.applthermaleng.2016.05.172>
- [29] X. Sun, J. Wu, Y. Dai, R. Wang. Experimental study on roll-bond collector/evaporator with optimized-channel used in direct expansion solar assisted heat pump water heating system. *Applied Thermal Engineering*, Volume 66, Issues 1–2, May 2014, Pages 571-579. <https://doi.org/10.1016/j.applthermaleng.2014.02.060>
- [30] P.G. Charalambous, G.G. Maidment, S.A. Kalogirou, K. Yiakoumetti. Photovoltaic thermal (PV/T) collectors: a review. *Applied Thermal Engineering*, Volume 27, Issues 2–3, February 2007, Pages 275-286. <https://doi.org/10.1016/j.applthermaleng.2006.06.007>
- [31] M.M. Rahman, Md Hasanuzzaman, N. A. Rahim. Effects of operational conditions on the energy efficiency of photovoltaic modules operating in Malaysia. *Journal of Cleaner Production*, Volume 143, 1 February 2017, Pages 912-924. <https://doi.org/10.1016/j.jclepro.2016.12.029>
- [32] M.Y. Othman, S.A. Hamid, M.A.S. Tabook, K. Sopian, M.H. Roslan, Z.Ibrahim. Performance analysis of PV/T Combi with water and air heating system: An experimental study. *Renewable Energy*, Volume 86, February 2016, Pages 716-722. <https://doi.org/10.1016/j.renene.2015.08.061>
- [33] M.N.A. Bakar, M. Othman, M. Hj Din, N.A. Manaf, H. Jarimi. Design concept and mathematical model of a bi-fluid photovoltaic/thermal (PV/T) solar collector. *Renewable Energy*, Volume 67, July 2014, Pages 153-164. <https://doi.org/10.1016/j.renene.2013.11.052>
- [34] H.Jarimi, M.N.A. Bakar, M. Othman, M. Hj Din. Bi-fluid photovoltaic/thermal (PV/T) solar collector: Experimental validation of a 2-D theoretical model. *Renewable Energy*, Volume 85, January 2016, Pages 1052-1067. <https://doi.org/10.1016/j.renene.2015.07.014>
- [35] J. Ji, C. Guo, W. Sun, W. He, Y. Wang, G. Li. Experimental investigation of tri-functional photovoltaic/thermal solar collector. *Energy Conversion and Management*, Volume 88, December 2014, Pages 650-656. <https://doi.org/10.1016/j.enconman.2014.09.030>
- [36] D. Su, Y. Jia, X. Huang, G. Alva, Y. Tang, G. Fang. Dynamic performance analysis of photovoltaic–thermal solar collector with dual channels for different fluids. *Energy Conversion and Management*, Volume 120, 15 July 2016, Pages 13-24. <https://doi.org/10.1016/j.enconman.2016.04.095>
- [37] R. Daneshazarian, E. Cuce, P. M. Cuce, F. Sher. Concentrating photovoltaic thermal (CPVT) collectors and systems: Theory, performance assessment and applications. *Renewable and Sustainable Energy Reviews*, Volume 81, Part 1, January 2018, Pages 473-492. <https://doi.org/10.1016/j.rser.2017.08.013>
- [38] L.R. Bernardo, B. Perers, H. Håkansson, B. Karlsson. Performance evaluation of low concentrating photovoltaic/thermal systems: A case study from Sweden. *Solar Energy*, Volume 85, Issue 7, July 2011, Pages 1499-1510. <https://doi.org/10.1016/j.solener.2011.04.006>

- [39] J.I. Rosell, X. Vallverdu, M.A. Lechon, M. Ibanez. Design and simulation of a low concentrating photovoltaic/thermal system. *Energy Conversion and Management*, Volume 46, Issues 18–19, November 2005, Pages 3034-3046. <https://doi.org/10.1016/j.enconman.2005.01.012>
- [40] C. Feng, H. Zheng, R. Wang, X. Ma. Performance investigation of a concentrating photovoltaic / thermal system with transmissive Fresnel solar concentrator. *Energy Conversion and Management*, Volume 111, 1 March 2016, Pages 401-408. <https://doi.org/10.1016/j.enconman.2015.12.086>
- [41] D. Chemisana, J.I. Rosell, A. Riverola, C. Lamnatou. Experimental performance of a Fresnel-transmission PVT concentrator for building-façade integration. *Renewable Energy*, Volume 85, January 2016, Pages 564-572. <https://doi.org/10.1016/j.renene.2015.07.009>
- [42] L.W. Florschuetz. Extension of the Hottel-Whillier model to the analysis of combined photovoltaic/thermal flat plate collectors. *Solar Energy*, volume 22, Issue 4, 1979, Pages 361-366. [https://doi.org/10.1016/0038-092X\(79\)90190-7](https://doi.org/10.1016/0038-092X(79)90190-7)
- [43] B. Sandnes, J. Rekstad. A photovoltaic/thermal (PV/T) collector with a polymer absorber plate. Experimental study and analytical model. *Solar Energy*, Volume 72, Issue 1, January 2002, Pages 63-73. [https://doi.org/10.1016/S0038-092X\(01\)00091-3](https://doi.org/10.1016/S0038-092X(01)00091-3)
- [44] I. Guarracino, J. Freeman, A. Ramos, S. A. Kalogirou, N. J. Ekins-Daukes, C. N. Markides. Systematic testing of hybrid PV-thermal (PVT) solar collectors in steady-state and dynamic outdoor conditions. *Applied Energy*, Volume 240, 15 April 2019, Pages 1014-1030. <https://doi.org/10.1016/j.apenergy.2018.12.049>
- [45] M. Battaglia, D. Zenhäusern, S. Brunold. Extended Hottel-Whillier Models for uncovered PVT collectors. *EuroSun 2018*, 2018.
- [46] O.M. Hamdoon, O. R. Alomar, B. M. Salim. Performance analysis of hybrid photovoltaic thermal solar system in Iraq climate condition. *Thermal Science and Engineering Progress*, Volume 17, 1 June 2020, 100359. <https://doi.org/10.1016/j.tsep.2019.100359>
- [47] B. Perers, P. Kovacs, M. Olsson, M.P.U. Pettersson. A Tool for Standardized Collector Performance Calculations Including PVT. *Energy Procedia*, Volume 30, 2012, Pages 1354-1364. <https://doi.org/10.1016/j.egypro.2012.11.149>
- [48] M. Stegmann, E. Bertram, G. Rockendorf, S. Janßen. Model of an unglazed photovoltaic thermal collector based on standard test procedures. In *30th ISES Biennial Solar World Congress 2011, SWC 2011*, 2011.
- [49] M. Lämmle, A. Oliva, M. Hermann, K. Kramer, W. Kramer. PVT collector technologies in solar thermal systems: A systematic assessment of electrical and thermal yields with the novel characteristic temperature approach. *Solar Energy*, Volume 155, October 2017, Pages 867-879. <https://doi.org/10.1016/j.solener.2017.07.015>

- [50] M. Lämmle, T. Kroyer, S. Fortuin, M. Wiese, M. Hermann. Development and modelling of highly-efficient PVT collectors with low-emissivity coatings. *Solar Energy*, Volume 130, June 2016, Pages 161-173. <https://doi.org/10.1016/j.solener.2016.02.007>
- [51] A. Gagliano, G.M. Tina, S. Aneli, S. Nižetić. Comparative assessments of the performances of PV/T and conventional solar plants. *Journal of Cleaner Production*, Volume 219, May 2019, Pages 304-315. <https://doi.org/10.1016/j.jclepro.2019.02.038>
- [52] B.J. Huang, T.H. Lin, W.C. Hung, F.S. Sun. Performance evaluation of solar photovoltaic/thermal systems. *Solar Energy*, Volume 70, 2001, Pages 443-448. [https://doi.org/10.1016/S0038-092X\(00\)00153-5](https://doi.org/10.1016/S0038-092X(00)00153-5)
- [53] T.T. Chow, G. Pei, K.F. Fong, Z. Lin, A.L.S. Chan, J. Ji. Energy and exergy analysis of PV/T collector with and without glass cover. *Applied Energy*, Volume 86, March 2009, Pages 310-316. <https://doi.org/10.1016/j.apenergy.2008.04.016>

2. EXPERIMENTAL PILOT PV/T PLANT

The main objective of this chapter is to describe a pilot cogenerative PV/T plant, shown in Fig. 2.1. The pilot plant is installed in the campus of the University of Catania, Italy, (Lat. 37.5256 N, Long. 15.0746 E) on the eastern coast of Sicily, right in the center of the Mediterranean area.

The PV/T panels are installed with an azimuth angle equal to 0° (South-facing), while the tilt angle can be changed manually from 15° to 60° , with an angle step ($\Delta\beta$) equal to 5° , as shown in the lower left of Figure 2.1.



Figure 2.1 – main components of the pilot PV/T system and flexible support structure.

The pilot PV/T system presents a high degree of flexibility, allowing simultaneous management of both the electrical and the thermal load to emulate, on a small scale, different real scenarios. The plant allows to switch the collectors' electrical and hydronic connections in order to modify the operative conditions. In fact, you can easily change the electrical and thermal connection from series to parallel and vice versa or exclude a panel from the extraction of electricity or from the circulation of the coolant fluid (leaving the fluid in stagnation). Moreover, the electrical and thermal load supplied by the PV/T plant can also be managed in order to simulate different energy demand scenarios.

This versatility allows the system to be studied in various operating conditions, allowing various operating hypotheses to be advanced so as to evaluate the potential of a system so made.

2.1 Thermo-hydraulic section of the experimental system

The pilot plant can be divided into several sections: primary thermo-hydraulic section, secondary thermo-hydraulic section, electrical section, and system monitoring and management section.

2.1.1 Thermo-hydraulic layout

The layout of the thermal section of the pilot PV/T plant is shown in Fig. 2.2. The main hydronic components are: two PV/T modules, solar thermal tank with two internal heat exchangers, circulation pump, safety components, water shut-off valves, three-way valves, dry cooler, and pipes.

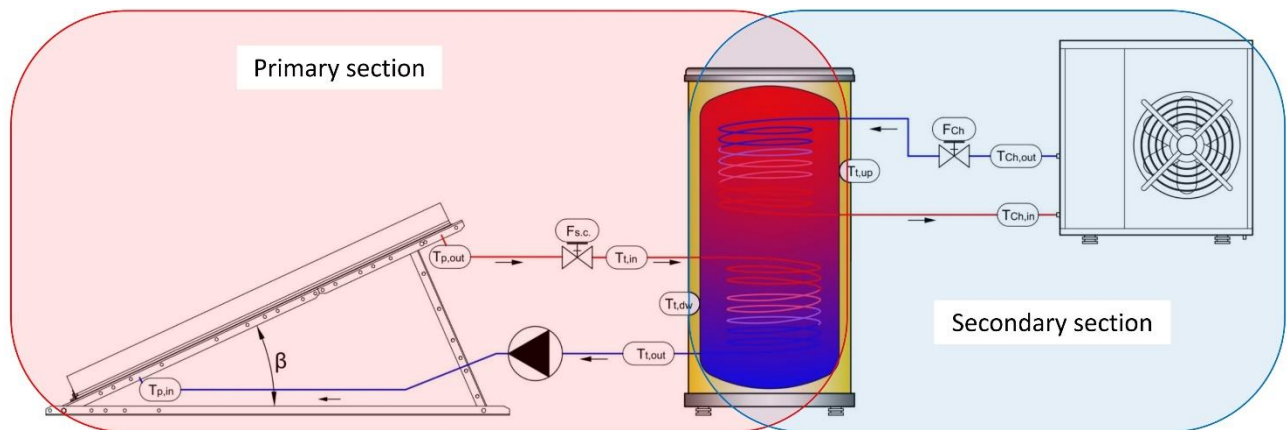


Figure 2.2 – thermo-hydraulic layout of pilot PV/T system.

As shown in figure 2.2, the plant's layout can be split into primary section and secondary section. The primary section or solar circuit (s.c.) is equivalent to a normal solar circuit and is composed by a closed loop where the coolant fluid flows through the PV/T panels, driven by an electric pump, and flows into heat exchanger located inside the solar tank, releases the heat into the storage tank. The main function of the dry cooler loop, or secondary section, is to emulate the thermal energy demand, such as Domestic Hot Water (DHW) production, management of fluid temperature at the inlet of panels, or any other load you want to simulate. At the same time, the chiller can supply thermal energy like a normal auxiliary heater.

The PV/T hydronic system designed allows to connection the panels in series (Fig. 2.3.a), parallel (Fig. 2.3.b), or the stagnation of a panel (Fig. 2.3.c) excluding it from the circulation of the heat transfer fluid, which can be selected by means of flow divider valves. The capability for modifying the configuration of the PV/T plant has several purpose, such as: to test the operation of the two modules subjected to different conditions of shading (parallel connection) and to evaluate the variation of the electrical efficiency due to non-uniform temperature between the modules (series connection).

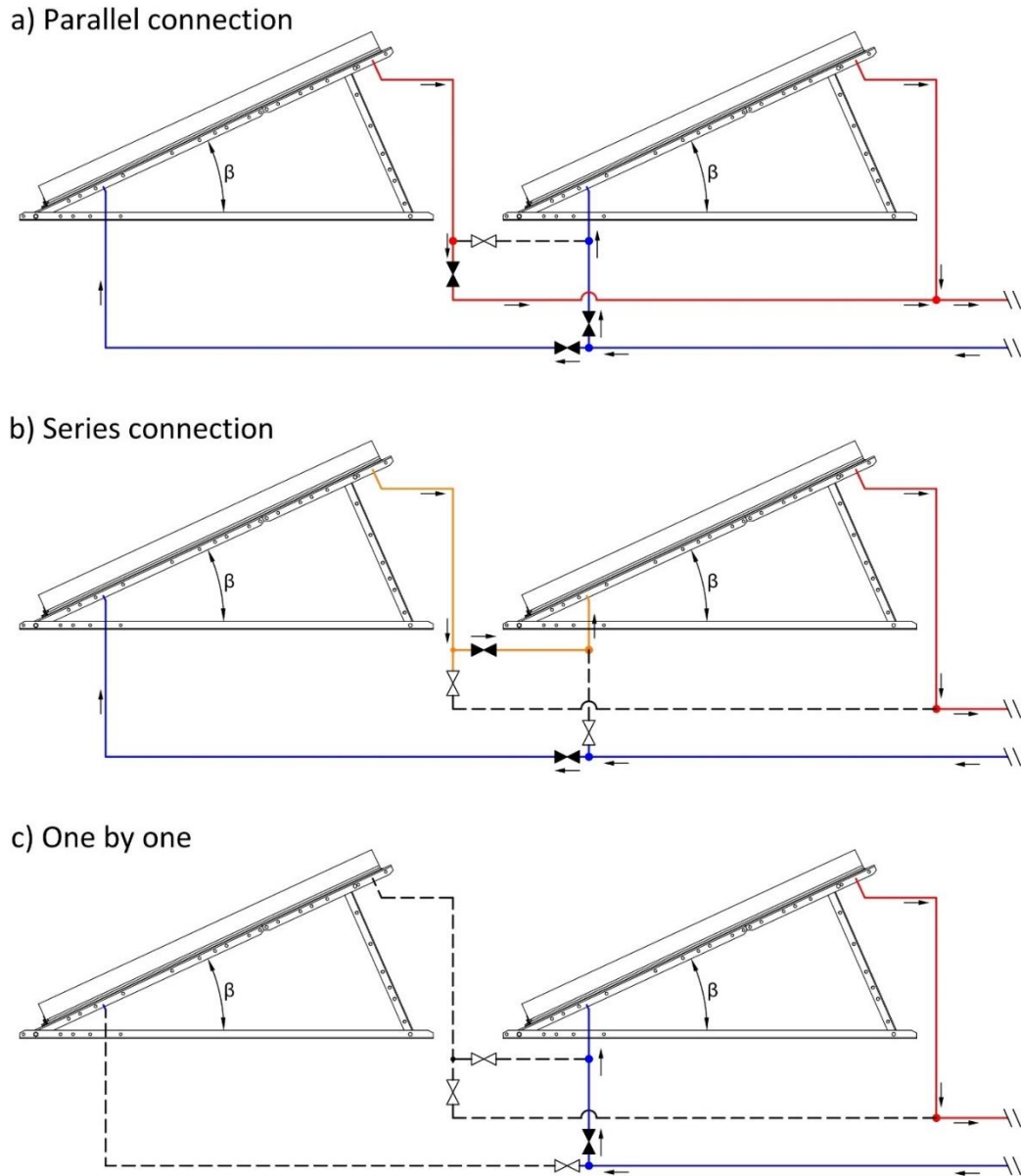


Figure 2.3 – thermo-hydraulic connection of panels: a) parallel, 2) series, 3) one in stagnation and one active.

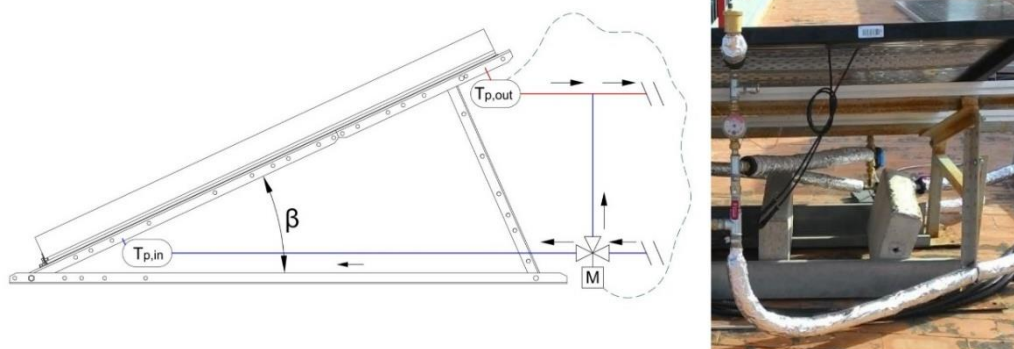


Figure 2.4 – Three-way valve diagram for managing the temperature in the panel

Three-way valves manage the flow rates circulating in the two modules with the aim of controlling their operating temperatures in accordance with weather conditions (irradiance, ambient temperature, wind speed) and thermal energy demand (Fig. 2.4).

2.1.2 Thermo-hydraulic components

The PV/T solar plant consists of two WISC PV/T panels, Wave model, produced by Dualsun™ (France) company. The Wave panel consists of a 250 Wp monocrystalline silicon photovoltaic module, an ultra-thin rigid heat exchanger, completely integrated into the collector, which governs the heat exchange between the front side of the PV/T module and the fluid circulating on the rear side, and is characterized by the absence of the glass cover (unglazed) and the absence of thermal insulation in the back (uninsulated).

Table 2.I reports the main geometric, electric, and thermal characteristics of the panels defined according to EN 12975-1:2006 test methods.

Table 2.I: geometrical and technical characteristics of the PV/T panel

General data			Electrical data		
Length	1667	mm	Number of cells	60	
Width	990	mm	Cell type (dimensions)	Monocrystalline (156mm x 156mm)	
Frame thickness	40	mm	Nominal power, P_{MPP}	250	Wp
Weight when empty/filled	30/31.7	Kg	Module efficiency,	15.4	%
Thermal data			Power tolerance	±3	%
Gross area	1.66	m ²	Rated voltage, V_{MPP}	30.7	V
Aperture area	1.6	m ²	Rated current, I_{MPP}	8.15	A
Heat transfer liquid vol.	1.7	l	Open circuit voltage, V_{oc}	38.5	V
Heat transfer liquid	water		Short circuit current, I_{sc}	8.55	A
Maximum temp.	74.7	°C	Maximum system voltage	1000	V
Max. operating pressure	1.2	Bar	Reverse current load	15	A
Pressure loss per module	6000 Pa at 200 l/h		NOCT	49	°C
Water inlet/outlet	15/21	mm	Connectors	MC4PLUS	
Thermal efficiency			Application class	Class A	
Optical efficiency a_0	55	%	Thermal coeff. V_{oc}	-0.32	%/K
heat loss coefficient a_1	15.76	W/K/m ²	Thermal coeff. I_{sc}	0.048	%/K
heat loss coefficient a_2	0	W/K ² /m ²	Efficiency loss with temperature	-0.44	%/°C

The solar circuit is closed, and the circulation of the heat transfer fluid is entrusted to a circulation pump, model Yonos PARA ST **/7.0 PWM 2 produced by Wilo (Fig. 2.5). It consists of a hydraulic system, a wet rotor motor with a permanent magnet rotor and an electronic control module with integrated frequency converter. The module allows speed control via external PWM signal. It is also equipped with an LED indicator to display the operating status of the pump.

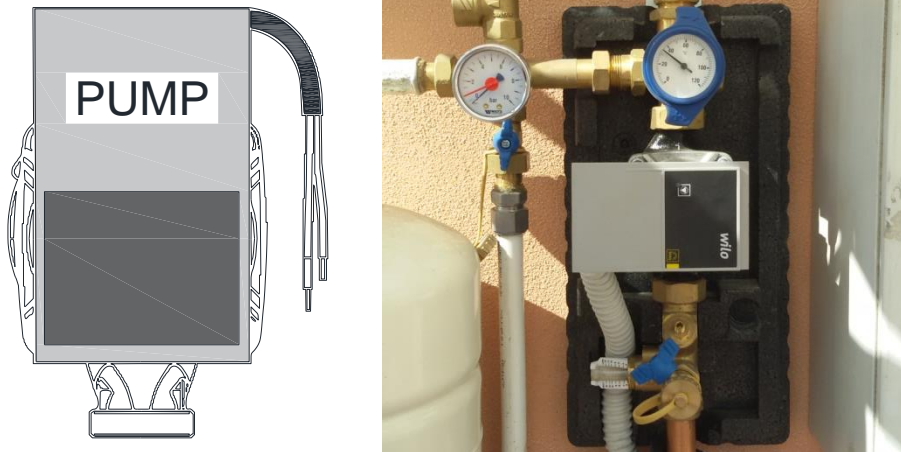


Figure 2.5 – circulation pump

All functions can be set, activated, or deactivated via an external PWM signal which provides the pump with a periodic sequence of pulses (the duty cycle). The control variable is determined by the ratio of the duration of each pulse to the period between two successive pulses. The duty cycle is indicated as a dimensionless coefficient with a value of 0 - 1, or 0% - 100%.

The maximum flow rate allowed by the pump is $3.3 \text{ m}^3/\text{h}$, while the maximum delivery head is equal to 7.3 m of water column.

The storage tank is of the Cordivari type, mod. BOLLY 2 ST. It has an accumulation volume of 200 liters and 2 heat exchange coils placed inside. The heat exchanger, in the lower part of the solar storage tank, is connected with the solar collector circuit, while the heat exchanger, in the upper part of the storage tank, is connected with the chiller (see Fig. 2.1). The chiller used is the 004 NEXPOLAR MN/TN model, produced by Riello. The nominal heat capacity is 4.07 and 4.93 kW respectively for heating and cooling.

Finally, the pipes are made of copper with diameter of 16 mm insulated with 20 mm thick expanded elastomer cups.

2.2 Electric section of the experimental system

The pilot plant consists of two PV/T panels, with a peak power of 250 W (for a total of 500 Wp). These modules are made with 60 monocrystalline silicon photovoltaic cells connected in series with each other. This means that the no-load voltage detected at the ends of a module is given by the sum of the individual voltages generated by the photovoltaic effect by the cells themselves. The modules are equipped with by-pass diodes (three), contained in the junction box that intervene in the event of shading.

As already mentioned, the PV/T modules can be connected both in series and in parallel. Fig. 2.6 shows the wiring diagram of the PV/T electrical circuit in series configuration. The connectors of the PV/T string, or of just one module, and the sensor cable, are connected to two separate sections of the switchboard installed on the roof (QBTP). Then the cables leaving QBTP are connected to another switchboard (QBTS), containing the electrical switching and power distribution gear. The two connectors of the PV/T string are coupled to an Agilent N3300A programmable electronic load (EL).

The EL is connected by means of a GPIB cable/card to a Personal Computer (PC). The PC is programmed with a tool developed in Labview® environment allowing the EL to be controlled in a way that sets a specific operating point for the photovoltaic string. Three different electrical operating modes can be selected: 1) open circuit, 2) I-V curve and 3) Maximum Power Point Tracking (MPPT). This program also controls the electrical output of the modules. Moreover, the measured irradiance on the plane of the PV/T modules, G , and the two back side temperatures, $T_{PVT1,b}$ and $T_{PVT2,b}$ are conveyed to the NI cDAQ 9188, so these data are also shown in real time by means of the Labview® program developed.

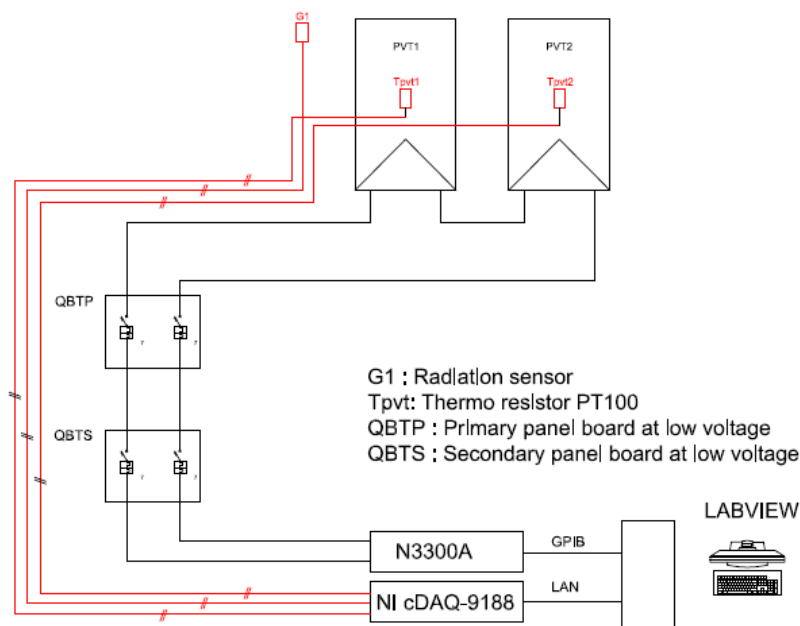


Figure 2.6 – PV/T system wiring diagram

2.3 Description of the monitoring and management system

The management and monitoring of the PV/T system is carried out by means of software capable of acquiring and processing in real time, through the standard MODBUS TCP/IP protocol, the data coming from various sensors using a dedicated SCADA (Supervisory Control and Data Acquisition) system. Furthermore, the processing in real time allows, through the relay card, the management of the various system components, such as switching the circulation pump on/off, switching the chiller on/off, temperature control, and so on.

The adoption of the TCP/IP version of the MODBUS protocol allows the connection of a virtually unlimited number of masters and slaves on local networks and/or World Wide Web. Among the main features, the software is able to store the data of the individual sensors on a database, track the stored data, view the acquired data in real time, carrying out operations on aggregate data, generate periodic graphic reports and/or text files and send them by e-mail, generate email alerts, alarms, and allow remote access to the database via a web browser.

Fig. 2.7 shows the graphical view of monitoring system, where on the left at the bottom the data collected during a fixed period are shown, while on the right the different values measured in real time are shown.

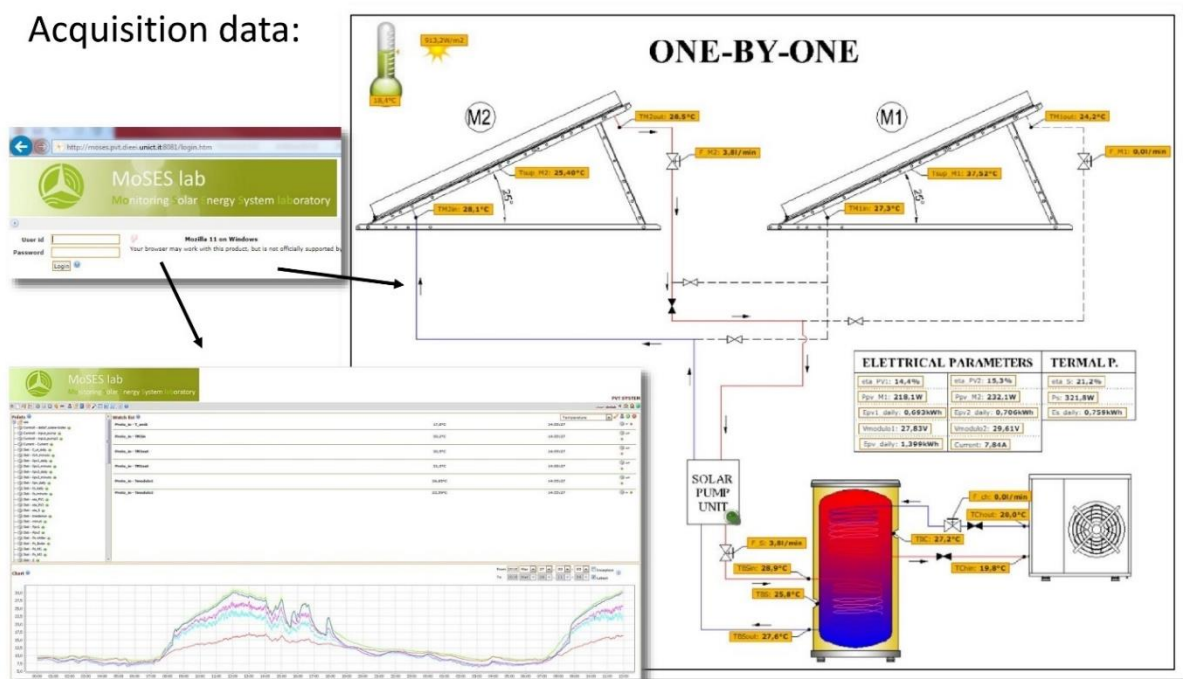


Figure 2.7 – data acquisition and management via web browser

As shown in figure 2.7, the pilot plant is fully monitored, where the acquisition rate is fixed to 1 minute. In detail there are: temperature sensors at the inlet and outlet of each panel, tank and chiller, temperature sensors inside the tank (one in correspondence with the coil of the

primary circuit and one in correspondence with the secondary circuit), surface temperature sensors placed in the back of the panels, flow meters circulating in each panel, primary and secondary circuits, voltage and current in the modules, total radiation in the module plane, air temperature and wind speed near the modules (see left side in fig. 2.1).

The environmental data are compared and integrated with other data taken from a weather station installed near the pilot plant. In particular, the weather station measures total solar radiation on the horizontal plane and on the plane of the panels, direct radiation, diffuse radiation, wind speed and direction, ambient temperature, humidity, and air pressure.

Fig. 2.8 shows a close-up of the power and measurement boxes. The switchboard contains the main switches which supply power to the solenoid valve, the cooling circuit, the pump and all the components for control of the whole system. A remote-controlled relay card is used to manage the three-way valves, circulation pump and chiller. The data acquisition units (DAQ) are installed in the box on the right and acquire the analogic and digital signals measured on the PV/T plant and send them to a PC. The architecture of the monitoring and management system of the pilot plant is shown in detail in Fig. 2.9.

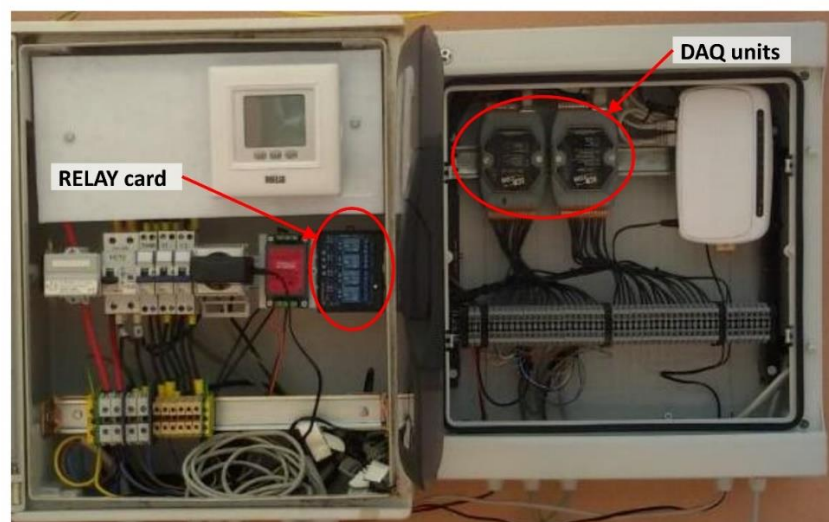


Figure 2.8 – PV/T plant power and measurement boxes

As shown in Fig. 2.9, the core of the system are the two acquisition cards: IP WITH ET-7017-10 and IP WITH ET-7060, for the acquisition of signals from analog sensors (the first) and for the acquisition of signals from digital sensors and the signal outputs (the second).

Fig. 2.10 shows the various sensors present in the monitoring system of the pilot plant (upper part) and the sensors present in the weather station (lower part). The same figure also indicates the measurement ranges, accuracy, and response time.

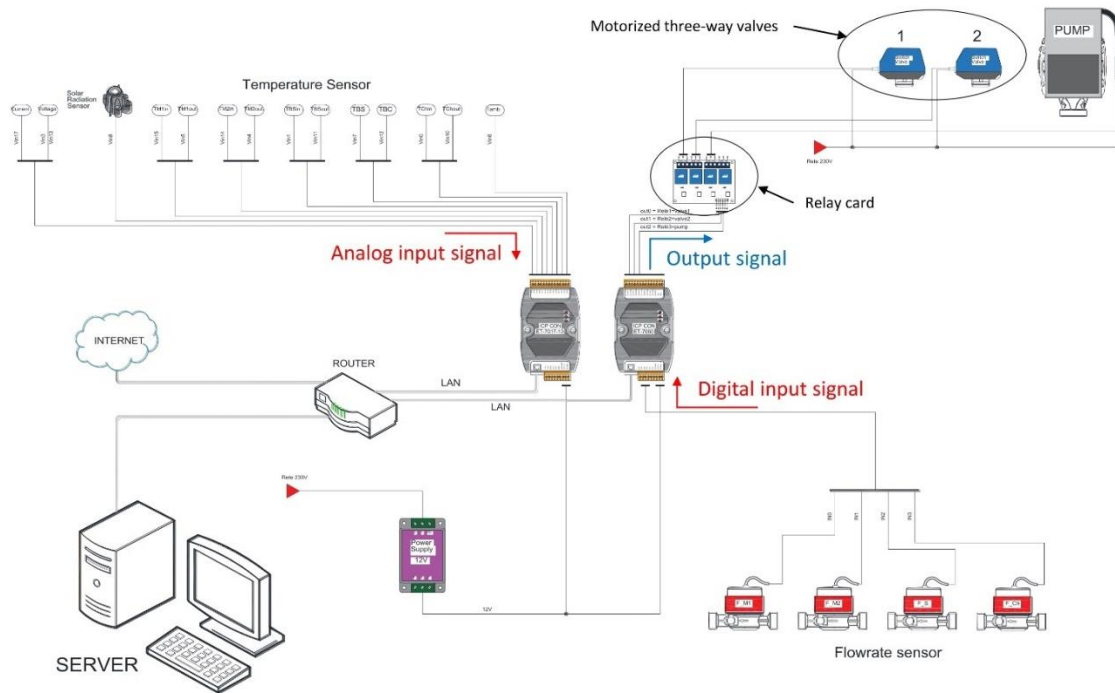


Figure 2.9 – architecture of the monitoring and management system














PV/T monitoring system	Sensors					
	Temperature	Total radiation on tilted plane	Wind speed and direction	Flowmeter	Amperometer	
						
	LM35DZ	CM11 (Kipp&Zonen)	Vantage Pro2 (Davis)	WMT15SV (Watt Ind.)	T201DCH (Seneca)	
Measuring range	0÷100°C	0÷4000 W/m ²	0.5÷89 m/s	0.03÷1.5 m ³ /h	0÷50 A	
Accuracy	±1.0°C	±2%	±3% direction ±5% speed	±5%	±0.3%	
Response time		<5s			<2s	
Weather station	Sensors					
	Temperature and humidity	Wind speed and direction	Total radiation	Flowmeter	Direct irradiation	Barometer
						
	DMA672 (LSI L.)	DNA821 (LSI L.)	DPA154 (LSI L.)	DPA245+DPA154	DPD504 (LSI L.)	DQA240 (LSI L.)
Measuring range	-50÷100°C T. 0÷100% h.	0.26÷50 m/s	0÷4000W/m ²	0÷4000W/m ²	0÷1500W/m ²	800÷1100 hPa
Accuracy	0.1°C Temp. 1% hum.	±1% dir. ±3% speed	±5%	±5%	±15%	0.5 hPa
Response time	10s	0.5s	20s	20s		2s

Figure 2.10 – Features of the main sensors installed

2.4 Experimental investigation

As described above, the plant is fully monitored and very flexible from a management point of view. This flexibility of the system has allowed the carrying out of various experimental analyses.

The following paragraphs show some of the main aspects analysed, where in detail paragraph 2.4.1 shows the results obtained when the hydraulic configuration changes, paragraph 2.4.2 shows the electrical and thermal performance as the thermal level changes, paragraph 2.4.3 shows the performance of the plant for the purposes of Domestic Hot Water (DHW) production considering in an alternative way (i) the simultaneous production of electricity and (ii) the short circuit condition, and finally paragraph 2.4.4 reports the thermal and electrical characterization of the plant.

2.4.1 Comparison of thermal and electrical performances as the hydraulic configuration changes

This section reports the observed data considering three system configurations from the point of view of fluid circulation:

- Parallel connection: the working fluid flows simultaneously into the two panels, then rejoins and goes to the tank;
- Series connection: the working fluid first flows into one panel and then into the other;
- One-by-One: the working fluid flows only in one panel, while the other is in a stagnant condition.

In order not to burden the discussion, only one representative day is reported for each scenario, where the environmental conditions were optimal.

Parallel connection

The parallel hydraulic connection consists in dividing the working fluid before entering the panels and then making it rejoin before entering the storage tank (see Fig. 2.3.a). This configuration allows to reduce the pressure drops of the circuit, but a greater flow rate is required to keep the flow rate in the individual panels unchanged.

Fig. 2.11 reports the external air temperature (T_{amb}), the irradiance on the module plane (G) the inlet and outlet temperature of the collectors (T_{in} and T_{out}) the temperature of the tank in correspondence with the heat exchange coil ($T_{t,dw}$) and the specific flow rate per panel unit (\dot{m}), relative to a typical day (March 31), with hydraulic configuration of the system in parallel.

In detail at left side shows the whole day analyzed, while the right side shows the details of the inlet and outlet temperatures for each panel (M1 and M2) during the central hours of the day.

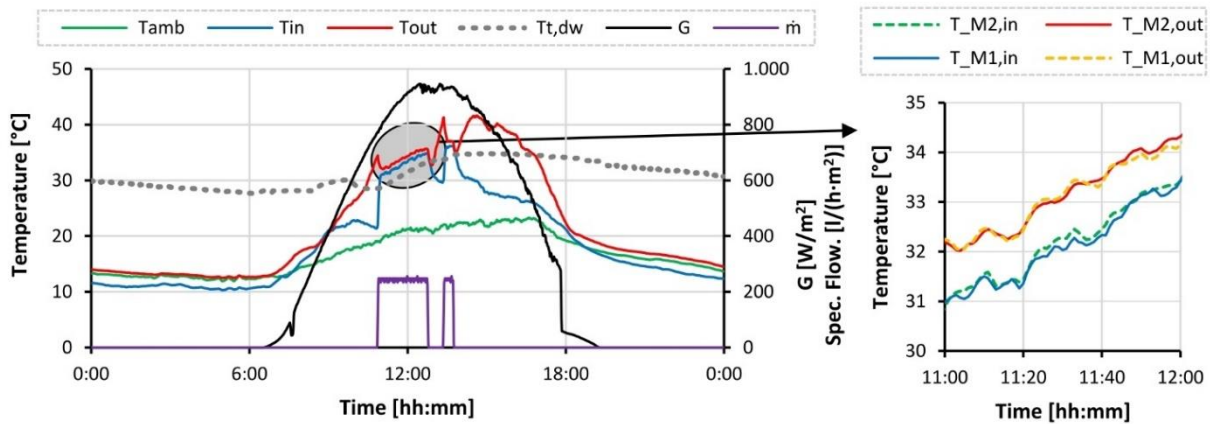


Figure 2.11 – Experimental measurements during a typical day with parallel connection

It can be observed that when the circulation of the fluid is active, the temperatures of the fluid remain below 35°C, while they exceed 40°C when the fluid is in stagnation condition. The detail reported on the right shows that, for these working conditions, the fluid passing through the panels gain 1°C, which corresponds to a thermal power of about 400W.

Fig. 2.12 shows on the left the electrical and thermal power instantaneously produced in both panels, while on the right it shows the efficiencies.

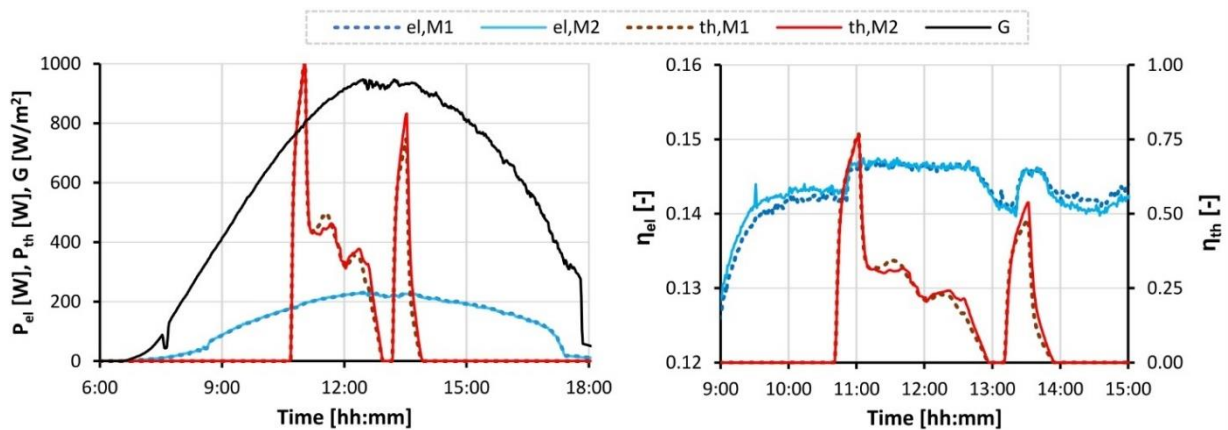


Figure 2.12 – Electrical and thermal performance during a typical day with parallel connection

From Fig. 2.12 it can be noted that since the system is connected in parallel, the two panels work under the same thermal conditions, therefore they have similar performances. Furthermore, in the first moments in which circulation is activated, the thermal powers extracted are very high, even over 1000 W per panel, with thermal efficiency close to 70%, due by the heat accumulated in the panels during the period of stagnation. Finally, in the period where circulation is active (for example between 11:00 and 12:45) the electrical efficiency is maximum (about 14.6%), with a net jump compared to the conditions of stagnation.

Series connection

The hydraulic connection in series consists in circulating the working fluid first in a panel (M1) and then in the second panel (M2), finally the outlet of the second panel will be connected directly with the inlet of the storage tank (see Fig. 2.3.b). This configuration allows to reduce the volumetric flow rates of the heat transfer fluid, but it follows an increase in the pressure drops of the circuit compared to the parallel configuration.

Fig. 2.13 and 2.14 show the main values observed in the pilot system, considering a typical day (May 3) with the hydraulic configuration of the system in series.

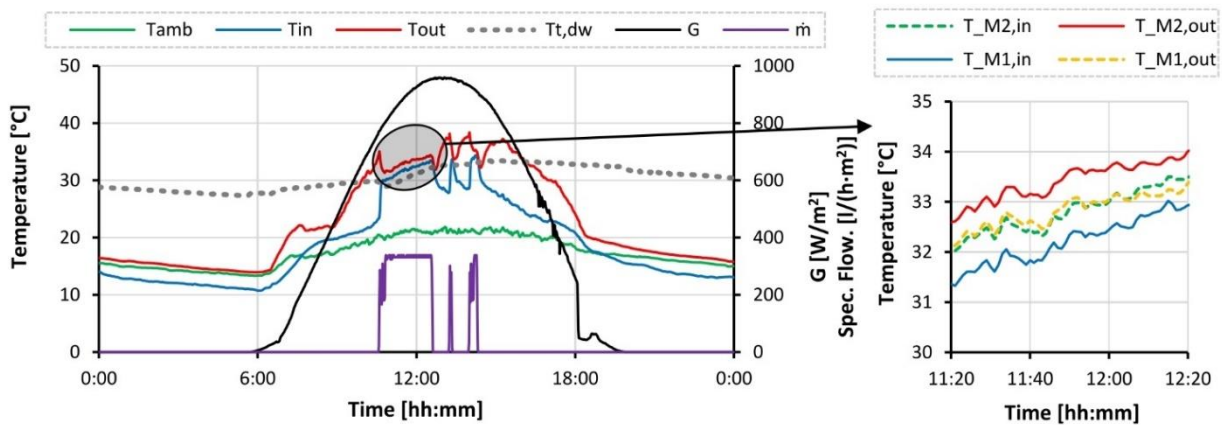


Figure 2.13 – Experimental measurements during a typical day with parallel connection

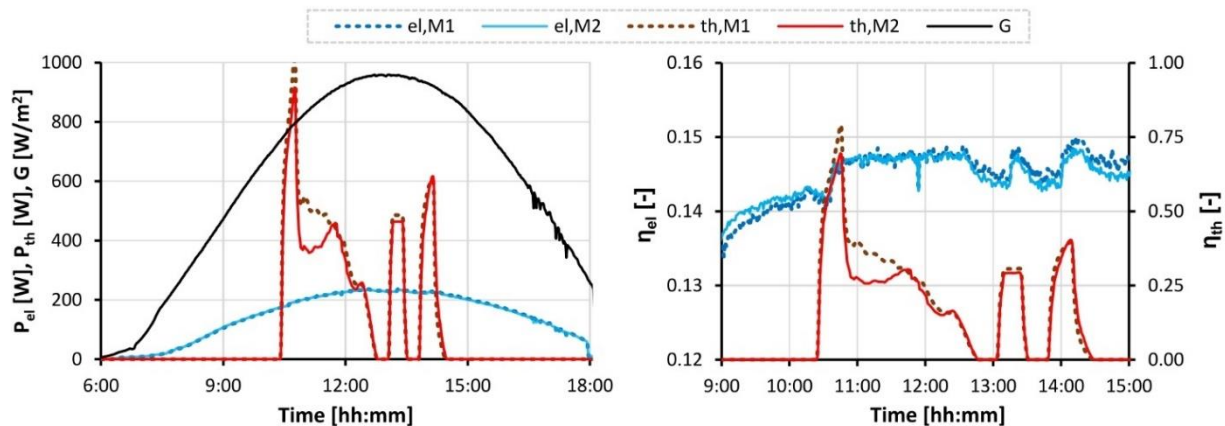


Figure 2.14 – Electrical and thermal performance during a typical day with parallel connection

From Fig. 2.13 it can be observed that, also in this case, when the fluid circulation is active, the temperatures of the fluid remain below 35 ° C, while they exceed 40 ° C when the fluid is stopped. The detail shown on the right shows that, for these working conditions, the fluid passing through the first panel gains about 0.6°C, while passing through the second panel it gains about 0.55°C.

From Fig. 2.14 it can be noted that the hydraulic connection in series generates, albeit minimal, differences between the performances of the two panels. In fact, the power and electrical efficiency are slightly better in the first panel (M1) because it has fluid temperatures that are approximately 0.5°C lower than the second panel. Similarly, the thermal performance of the first panel is better than the second. While the other considerations made for the system connected in parallel are repeated: high thermal power in the first instants of activation of the circulation and better electrical performance with circulation of the working fluid active.

One-by-One

This plant configuration consists in leaving a panel in stagnation (M2), by circulating the working fluid in only one (M1) as shown in Fig. 2.3.c.

This analysis allows to analyze, under the same climatic conditions, the behavior of a PV/T panel with an equivalent PV. In fact, the exclusion of the M2 module from the circulation of the fluid generates a behavior very similar to a normal PV, with the only difference that the PV/T in stagnation has a higher thermal inertia than the conventional PV.

Not being able to correctly measure the temperature of the fluid during stagnation conditions, in Fig. 2.15, in addition to the climatic conditions, the surface temperatures measured at the rear of the panels ($T_{M1,b}$ and $T_{M2,b}$), the electrical voltage (V_{M1} and V_{M2}) and the flow rate of the fluid affecting only the M1 panel are reported.

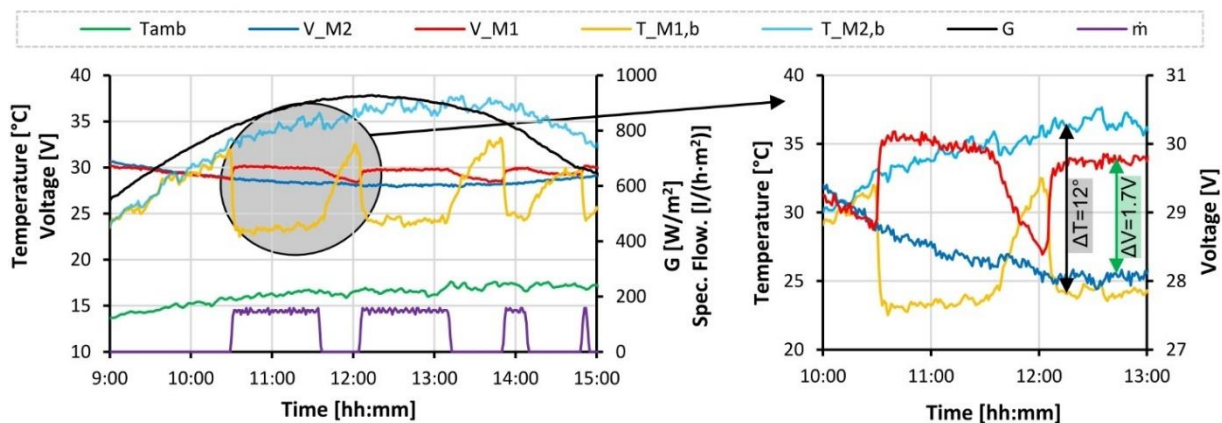


Figure 2.15 – Comparison of experimental measurements between PV/T panel and PV/T in stagnation

From Fig. 2.15 it can be seen that before activating the circulation of the working fluid, the surface temperature at the rear of the panels is very similar, while as soon as the circulation is activated, $T_{M1,b}$ drops by over 10°C . At the same instant, the voltage across module M1 increases. In fact, as shown in the detail on the right, the temperatures of the back module also differ by 12°C with a difference in terms of voltage of about 1.7 V.

The electrical performances shown in figure 2.16 allow to observe an increase in terms of electric power produced of about 6% in the panel where the circulation of the working fluid occurs with respect to the panel in stagnation conditions. Furthermore, the use of the PV/T system (and therefore the circulation of the fluid) allows the production of thermal energy. Therefore, PV/T systems have a double advantage over traditional PV systems: greater production of electricity (increases of about 6%) and simultaneous production of thermal energy.

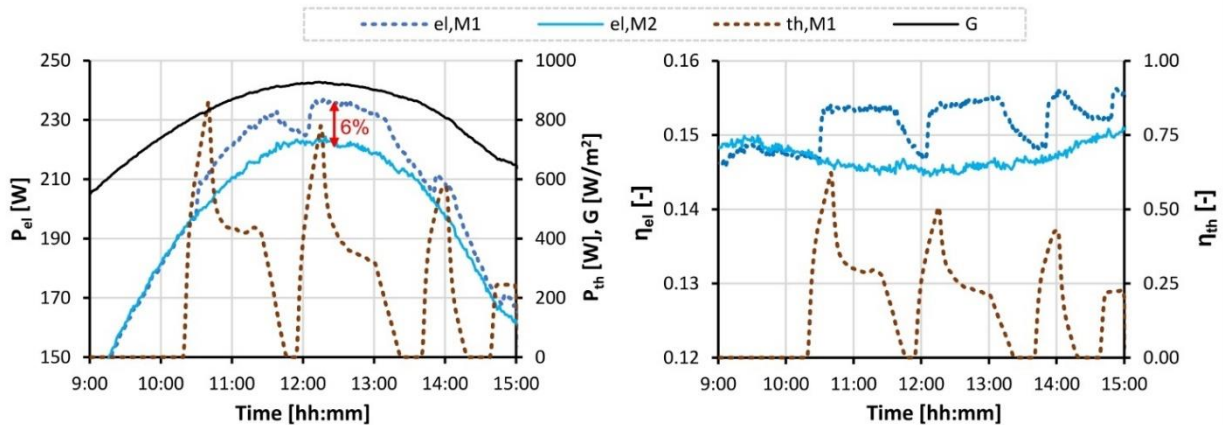


Figure 2.16 – Comparison of electrical and thermal performance between PV/T panel and PV/T in stagnation

Comparison among all scenarios

Table 2.II shows the main KPI for all the scenarios analysed. It is important to note that the monitoring system does not allow the measurement of the temperature of the photovoltaic cells, therefore it was calculated using Eq. 1.21.

From the data shown in the table, it can be seen that the system hydraulically connected in parallel, the performance of the two panels in both electrical and thermal terms are very similar, with electrical and thermal efficiency respectively of approximately 13.8% and 11.0%, with characteristic temperature of the cells slightly above 37°C. Similarly, also the second principle efficiency (ϵ_{tot}) is almost constant and around 14.4%. The system connected in series, on the other hand, presents some differences, with the efficiency of the first module (M1) better than the second module (M2). In fact, the electrical efficiency is about 14.1% for M1 and 13.7 for M2. This is mainly due to the difference in the working temperature of the PV cells ($T_{char,PV}$) where differences of about 1.5°C occur. The thermal efficiency as well as the second principle efficiency are also higher for M1, with values of 11.5% and 14.7% respectively for M1, while M2 records only 10.5% for the thermal efficiency and 14.2% for the total efficiency of second principle.

Finally, the One-by-One scenario allows to compare the performance of a PV/T with a conventional PV, where the PV consists of the PV/T panel in stagnation. This scenario demonstrates that the use of PV/T allows the production of more total energy than a simple

PV, thanks to the simultaneous production of thermal and electrical energy and to the greater efficiencies of electricity production due to the cooling of the cells.

Table 2.II Main KPIs of all hydraulic layouts analyzed.

		Parallel connect		Series connect		One-by-One	
		M1	M2	M1	M2	M1	M2
$T_{amb,av}$	$^{\circ}C$	16.7		17.3		12.7	
E_{sun}	kWh/m^2	6.87		7.36		6.34	
$E_{\chi,sun}$	kWh/m^2	6.84		7.33		6.32	
E_{el}	kWh/m^2	0.95	0.94	1.04	1.01	0.88	0.85
$\eta_{el,av}$	%	13.8	13.7	14.1	13.7	13.8	13.4
E_{th}	kWh/m^2	0.76	0.75	0.85	0.77	0.87	-
$\eta_{th,av}$	%	11.1	10.9	11.5	10.5	13.7	-
$E_{tot(l)}$	kWh/m^2	2.82	2.79	3.51	2.96	2.78	1.85
$T_{char,PV}$	$^{\circ}C$	37.0	37.3	34.5	36.0	30.6	36.7
$T_{char,p}$	$^{\circ}C$	33.8	33.9	32.3	32.9	26.1	-
PR	-	0.91	0.91	0.93	0.91	0.92	0.90
$E_{\chi,th}$	kWh/m^2	0.04	0.04	0.04	0.03	0.03	-
$E_{\chi,el}$	kWh/m^2	0.95	0.94	1.04	1.01	0.88	0.85
$E_{\chi,tot}$	kWh/m^2	0.99	0.98	1.08	1.04	0.91	0.85
ϵ_{tot}	%	14.5	14.3	14.7	14.2	14.4	13.4

2.4.2 Performance comparison as the thermal level varies

As seen above, the performance of solar systems (both ST and PV) depends on the temperatures involved. In fact, the ST systems have decreasing efficiencies as the temperature difference between the fluid and the environment increases (see Eq. 1.7 and 1.8). Similarly, the electricity production efficiency for PV systems decreases as the temperature of the cells increases (see eq. 1.16).

This paragraph analyzes the thermal and electrical performance of the pilot PV/T system as the inlet water temperature varies. Analyzes were conducted using the following settings:

- Circulation of the working fluid in the primary section (solar circuit) active throughout the day provided that the solar irradiance on the module surface is greater than 300 W/m^2 ;
- Hydraulic system in series configuration;
- Tracking of MPP conditions by electronic load in order to extract the maximum amount of electricity;
- Active secondary section with temperature control function at the inlet of the panels.

In order not to burden the graphs, the data of a single panel are shown. Figure 2.17 shows the data observed in the experimental plant considering three inlet temperatures: 30, 40 and $50^{\circ}C$, where the inlet temperatures to the modules are shown at the top left, the irradiance on the

plane of the modules, in the center on the left the electrical power, while on the right the thermal power, and finally at the bottom the electrical and thermal efficiencies.

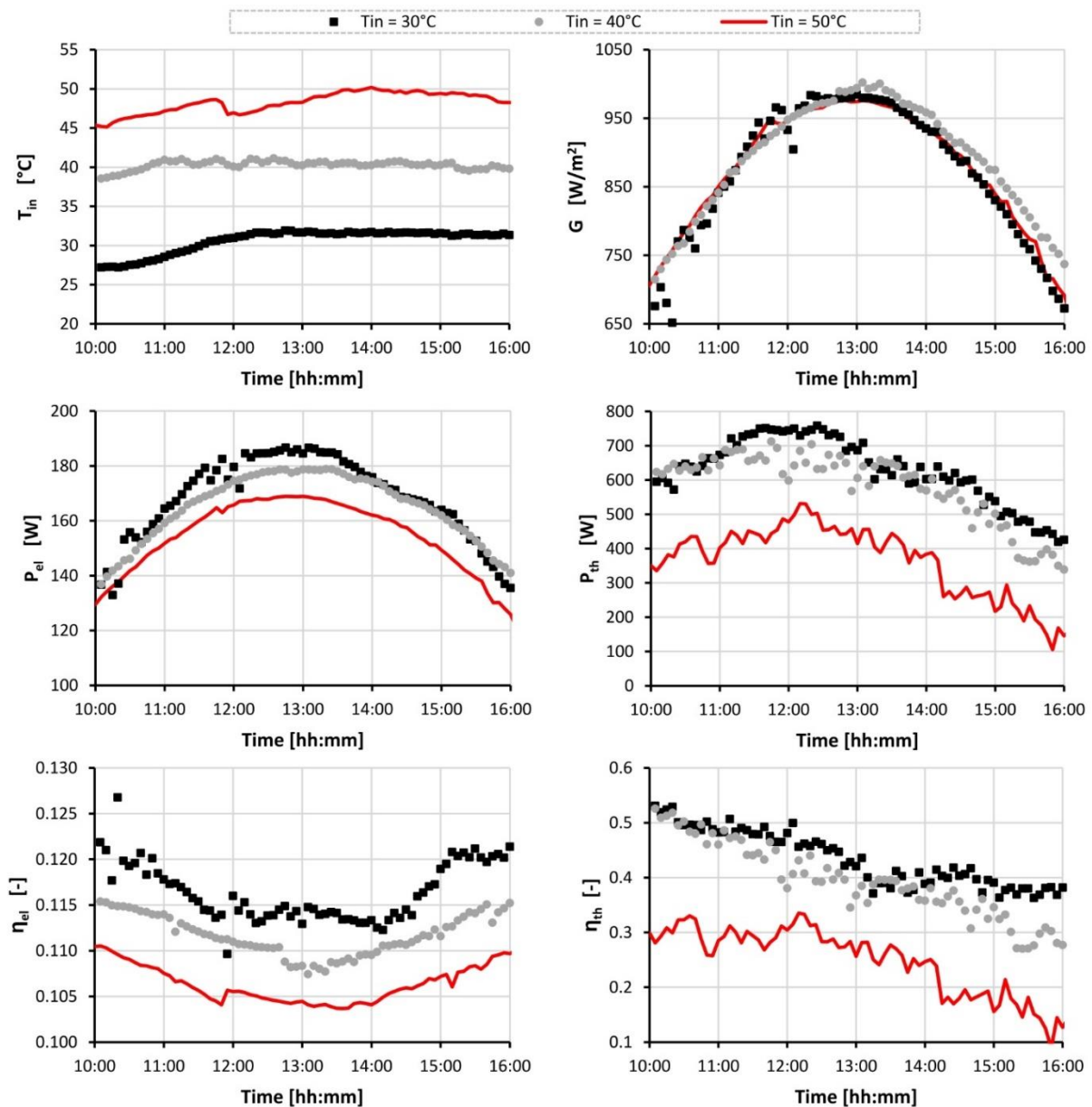


Figure 2.17 – Comparison of electrical and thermal performance when the inlet temperature change

The setpoint temperatures are not kept constant throughout the day, but only during the central hours of the day. By observing the electrical power, it can be seen that it decreases as the inlet temperature increases, with differences of up to 10% in the hours where the maximum electrical production occurs (185 W for $T_{in} = 30^{\circ}\text{C}$ against 165 W for $T_{in} = 50^{\circ}\text{C}$). Also, for the thermal power, it decreases as the temperatures of the inlet fluid increase, with maximum differences of up to 250 W comparing the 30 and 50°C scenarios. However, the scenario with

T_{in} equal to 40°C has reduced thermal powers compared to the scenario with T_{in} equal to 30°C, but the differences are low, because the outside air temperature was lower in the case with T_{in} equal to 40°C, therefore the thermal efficiencies have benefited from it (Eq. 1.8). Similarly, the efficiencies show the same trend seen for the powers.

Table 2.III shows the main KPIs calculated for the various thermal levels analysed.

Table 2.III Main KPI of all scenarios analysed.

		$T_{in} = 30^{\circ}\text{C}$	$T_{in} = 40^{\circ}\text{C}$	$T_{in} = 50^{\circ}\text{C}$
$T_{amb,av}$	$^{\circ}\text{C}$	29.5	28.7	30.8
E_{sun}	kWh/m^2	7.18	7.99	7.36
$E_{\chi,sun}$	kWh/m^2	7.17	7.98	7.36
E_{el}	kWh/m^2	0.96	1.04	0.92
$\eta_{el,av}$	%	13.4	13.0	12.4
E_{th}	kWh/m^2	2.96	2.82	1.56
$\eta_{th,av}$	%	41.2	35.4	21.2
$E_{tot(I)}$	kWh/m^2	5.04	5.08	3.55
$T_{char,PV}$	$^{\circ}\text{C}$	35.4	43.6	48.5
$T_{char,p}$	$^{\circ}\text{C}$	30.0	39.3	47.8
PR	-	0.94	0.91	0.88
$E_{\chi,th}$	kWh/m^2	0.15	0.15	0.07
$E_{\chi,el}$	kWh/m^2	0.96	1.04	0.92
$E_{\chi,tot}$	kWh/m^2	1.11	1.19	0.99
ϵ_{tot}	%	15.5	14.9	13.4

The daily results reported in table 2.III show, once again, decreasing performances as the thermal level increases. While the reduction in electrical efficiency is reduced by one percentage point, going from $T_{in} = 30$ to $T_{in} = 50^{\circ}\text{C}$, the thermal efficiency collapses, reducing to about half (41.2% against 21.2%). Similarly, the overall performances evaluated using the second principle metric, show a reduction of about 2%.

Moreover, the values of the PR index close to 1, in the scenario with $T_{in} = 30^{\circ}\text{C}$, indicate that the PV/T system worked nearest to the optimal operative mode, thanks also to the not too much high PV cell temperature (i.e. less than 35.5°C).

2.4.3 Domestic hot water production and simultaneous electricity production

In the previous sections it was seen that in PV/T systems, the circulation of the working fluid allows to keep the cell temperatures low, increasing the electrical performance of the system. As described in paragraph 1.3.3, thermal performance in turn depends on the solar energy available, which in a PV/T system is reduced by the portion used to produce electricity (Eq. 1.17). Otherwise, if the PV/T system is in short circuit conditions (absence of electricity

production), all the solar irradiance is available to produce thermal energy, varying the performance of the system.

This section compares the performance of the pilot PV/T plant for DHW production by alternatively considering the simultaneous production of electricity and short circuit conditions. The proposed analysis concerns a sunny autumn day. In particular, among the available data collected in situ, there are two days, one with production of electricity under MPP conditions (scenario namely MPP) and one in short circuit conditions (scenario namely SC), where the insolation, the air temperatures and the starting temperature of the tank are very similar and are the 18/11/2019 and 29/11/2019 respectively with and without production of electricity (see fig. 2.18).

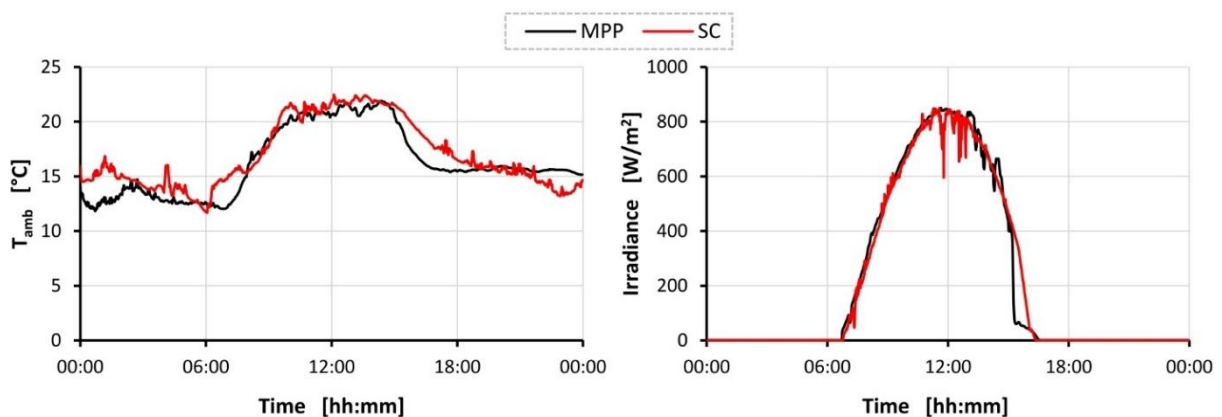


Figure 2.18 – Comparison of environment air temperature (left) and solar irradiance (right) for the MPP and SC scenarios

In particular, in these two days the average air temperature was 16.2 and 16.9° C respectively for MPP and SC, the total solar radiation on the module plane was 5.17 and 5.15 kW/m^2 , while the average tank temperature at 00:00 it was 17.7 and 18.6°C.

Analyses were conducted using the following settings:

- Circulation of the working fluid in the primary section (solar circuit) active when the outlet temperature of the panels exceeds the temperature of the tank at the bottom (in correspondence with the coil of the solar circuit) by at least 4°C and switches off when the temperature difference is less than 2°C;
- Hydraulic system in parallel configuration;
- DHW production with pre-heating scheme;
- Secondary section simulates a DHW thermal load at 12:00 and 18:00 equal to 100 liters.

Simulation of the thermal load

The DHW heat load is simulated by the Chiller, which subtracts energy from the storage tank, which, as mentioned, has a pre-heating scheme. Therefore, once the demand for DHW is fixed, the useful energy for DHW depends on the temperature of the water in the storage tank. Figure 2.19 shows an example of the trend of the water temperature inside the tank, where between the instants t_1 and t_2 there is a request for DHW.

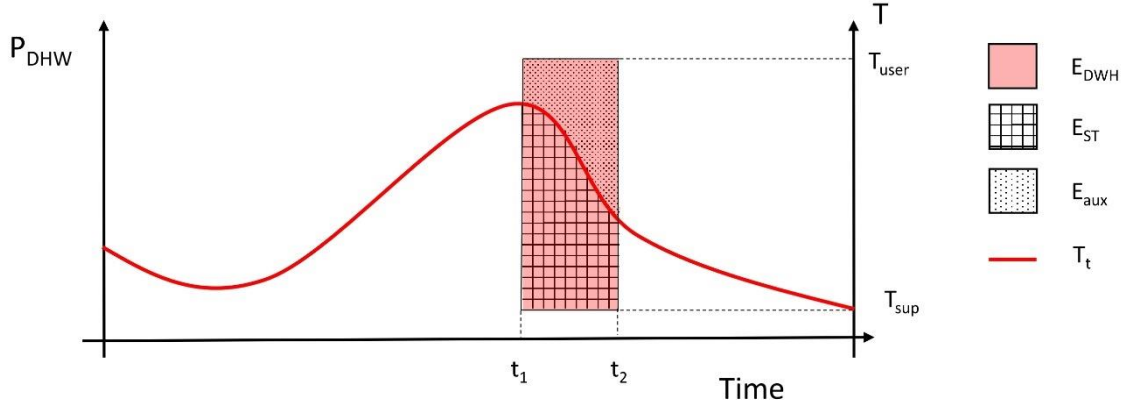


Figure 2.19 – example of tank temperature and DHW load

The energy required to meet the demand for DHW is calculated using the eq. 2.1, where T_{user} and T_{sup} are respectively the temperature required by the user and the temperature of the mains water.

$$E_{DHW} = \int_{t_1}^{t_2} P_{DHW} \cdot dt = \int_{t_1}^{t_2} \dot{m}_{DHW} \cdot c_p \cdot (T_{user} - T_{sup}) dt \quad (2.1)$$

In the pre-heating configuration, if the thermal level of the tank does not exceed the T_{user} , the part of energy required to reach the T_{user} will be provided by an auxiliary heater as described in Eq. 2.2.

$$E_{DHW} = E_{ST} + E_{aux} = \int_{t_1}^{t_2} \dot{m}_{DHW} \cdot c_p \cdot (T_t - T_{sup}) dt + \int_{t_1}^{t_2} \dot{m}_{DHW} \cdot c_p \cdot (T_{user} - T_t) dt \quad (2.2)$$

Where E_{ST} indicates the energy supplied by the solar system, E_{aux} that supplied by the auxiliary heater, t_1 and t_2 respectively the initial and final instant of withdrawal, with T_t and \dot{m}_{DHW} as a function of time.

Assuming constant the water flow rate required by the user, the E_{ST} can be calculated using the eq. 2.3.

$$E_{ST} = \int_{t_1}^{t_2} \dot{m}_{DHW} \cdot c_p \cdot (T_t - T_{supply}) dt = M_{DHW} \cdot c_p \cdot (T_{t,av} - T_{supply}) \quad (2.3)$$

Where M_{DHW} indicates the total amount of water required by the user during withdrawal and where $T_{t,av}$ indicates the average temperature in the tank during withdrawal, calculated with the Eq. 2.4.

$$T_{t,av} = \frac{T_{t,t1} + T_{t,t2}}{2} \quad (2.4)$$

Substituting the 2.4 in the 2.3 and inverting, we obtain:

$$(T_{t,t1} + T_{t,t2}) = \frac{2E_{ST}}{M_{DHW} \cdot c_p} + 2T_{sup} \quad (2.5)$$

During the simulation of the load, the part of energy for DHW coming from the solar tank (E_{ST}) can also be determined by making the thermal balance between the initial and final moments of withdrawal:

$$E_{ST} = V_t \cdot c_p \cdot (T_{t,t1} - T_{t,t2}) \quad (2.6)$$

That by inverting it we can write:

$$(T_{t,t1} - T_{t,t2}) = \frac{E_{ST}}{V_t \cdot c_p} \quad (2.7)$$

Adding the Eq. 2.5 with Eq. 2.7 and by reorganizing it, the E_{ST} can be made explicit, that is the share of energy supplied by the solar system to satisfy the DHW user, making it a function of some constants and only the temperature of the tank at the initial instant:

$$E_{chiller} = \frac{2M_{DHW} \cdot V_t \cdot c_p}{(2V_t + M_{DHW})} (T_{t,t1} - T_{sup}) \quad (2.8)$$

Using the Eq. 2.8 the daily DHW withdrawal of 100 liters was simulated in the experimental plant, divided into two parts, one at 12:00 and one at 18:00.

Results

Fig. 2.20 on the left shows the thermal power produced by the panels using the MPP condition and the SC condition, while on the right the electrical power produced is shown.

Observing the thermal power, an increase in thermal efficiency in SC conditions of about 200 W is noted, due to the fact that under MPP conditions part of the solar energy is used to produce electricity, while in SC conditions all solar energy it is available to produce thermal energy. On the other hand, the MPP scenario produces electricity which otherwise (SC conditions) cannot be produced.

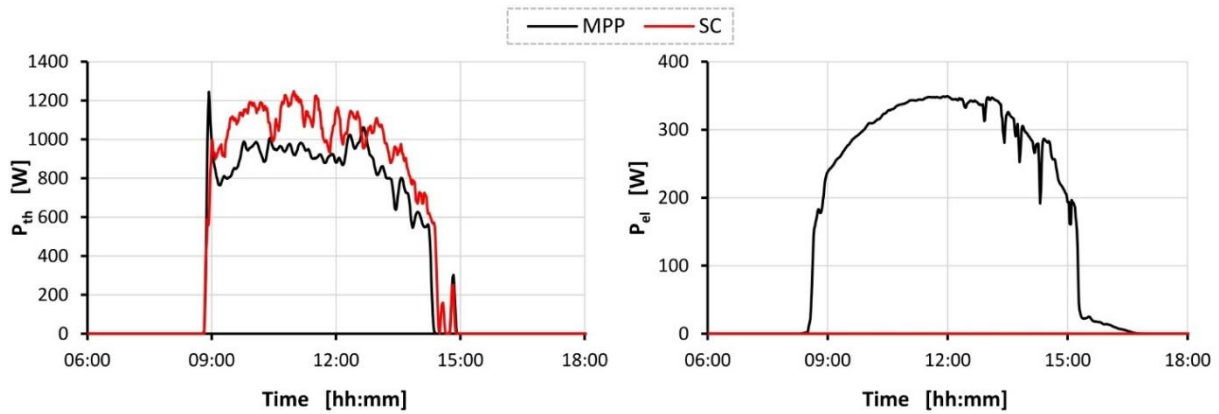


Figure 2.20 – Comparison of thermal power produced (on the left) and electricity (on the right) for the MPP and SC scenarios

Fig. 2.21 shows the average temperature of the tank for the two cases analyzed. The left image shows the daily profile, where, during the morning (from 9:00 to about 12:00) the solar circuit supplies heat to the tank, raising the average temperature by about 8°C in the case of MPP and about 10° for SC. At around 12:00 the first daily withdrawal is activated, which subtracts energy from the tank, subsequently, as soon as the withdrawal stops, the temperatures begin to rise again due to the energy supplied by the solar circuit. Finally, the second pick-up takes place at approximately 18:00.

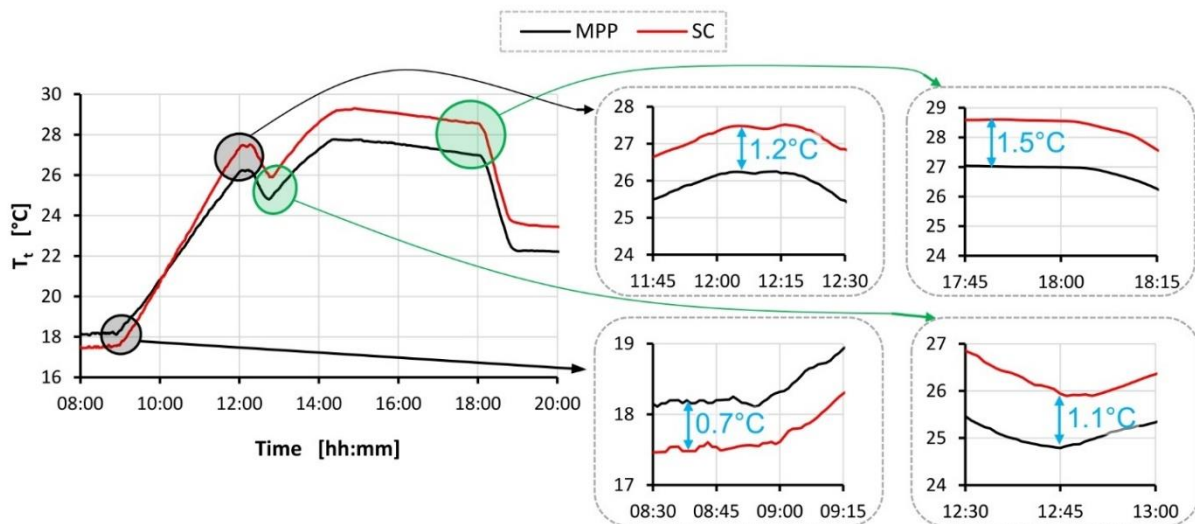


Figure 2.21 – Comparison of tank temperature profile for the MPP and SC scenarios

In the details of fig. 2.21 on the right, it is noted that, although for the SC condition scenario the thermal storage is about 0.7°C lower than the MPP condition scenario (8:45 am), the greater availability of solar irradiance allows to accumulate more energy, bringing the average

temperature in the tank to about 1.2°C higher than that for the MPP scenario (12:00), with a difference of 1.9°C which corresponds to more than 1,200 kJ accumulated.

Following the first withdrawal, the tank temperature for the SC scenario is about 1.1°C higher than the MPP scenario, while in the following hours this difference rises again up to 1.5°C.

Figure 2.22 shows the daily data for both scenarios studied, relating to the thermal energy produced by the panels, the electricity produced (present only for MPP condition) and the net thermal energy used to meet the demand for DHW (E_{ST}).

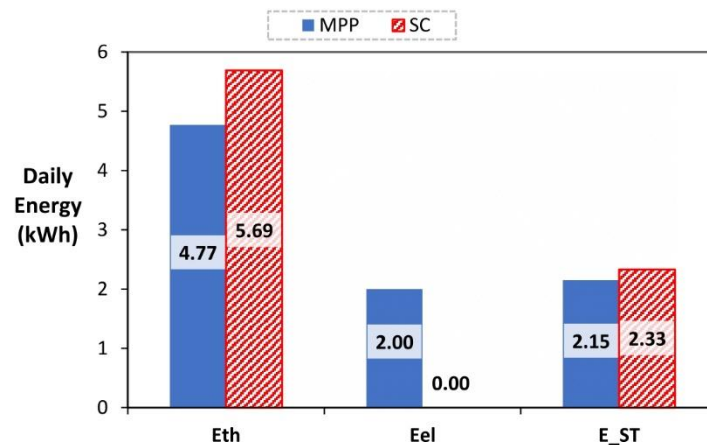


Figure 2.22 – Comparison of daily energy produced for the MPP and SC scenarios

As anticipated, the thermal energy produced for the SC scenario is higher than that produced for the MPP scenario, with an increase of 19%. However, in the SC scenario no electricity is produced, so if we observe the total balance of energy produced, given by the sum of thermal and electrical energy, the MPP scenario produces about 19% more energy than the SC one, not to mention that electric energy has a higher value than thermal energy. Using the revaluation of electricity into thermal energy, through the eq. 1.33, an $E_{tot(l)}$ of 9.12 kWh and 5.69 kWh respectively is obtained for the MPP and SC scenario, respectively.

Table 2.IV reports the main KPIs for both MPP and SC scenarios.

The SC conditions allow an increase in the thermal energy produced, with increases in instantaneous power of about 200 W, i.e. about 20% more than the MPP scenario. This increase in yield also allows for an increase in the demand coverage factor for DHW (f_{DHW}), going from 61.6% to 66.8%.

On the other hand, the overall performance of the PV/T plant at MPP conditions is much better than that at SC conditions, especially if we refer to the second principle metrics, this confirms once again that the strength of the PV/T plant is in the simultaneous production of electrical and thermal energy.

Table 2.IV Main KPI of all scenarios analysed.

		MPP	SC
$T_{amb,av}$	$^{\circ}C$	16.2	16.9
E_{sun}	kWh/m^2	5.17	5.15
$E_{\chi,sun}$	kWh/m^2	5.17	5.15
E_{el}	kWh/m^2	0.60	-
$\eta_{el,av}$	%	11.6	-
E_{th}	kWh/m^2	1.43	1.71
E_{ST}	kWh	2.15	2.33
f_{DHW}	%	61.6	66.8
$\eta_{th,av}$	%	27.7	33.2
$E_{tot(l)}$	kWh/m^2	2.73	1.71
$T_{char,PV}$	$^{\circ}C$	30.3	31.9
$T_{char,p}$	$^{\circ}C$	27.9	29.2
$E_{\chi,th}$	kWh/m^2	0.03	0.05
$E_{\chi,el}$	kWh/m^2	0.60	-
$E_{\chi,tot}$	kWh/m^2	0.63	0.05
ϵ_{tot}	%	12.2	1.0

However, scenarios can be created where, for example, there is no demand for electricity and the electricity grid is saturated, where the possibility of producing a thermal surplus could be exploited using open circuit condition.

2.4.4 Electrical and thermal experimental curves

The characterization of solar systems is a fundamental and useful step in order to compare the different technologies. This also allows us to determine the fundamental variables that affect performance and how to influence them.

This section shows the characterization of the pilot plant under the external environmental conditions, carried out using the monitoring data.

Electrical characterization

The electrical characterization was carried out under the profile of the dependence of the solar irradiance, and of the temperature dependence of the photovoltaic cells.

Fig. 2.23 shows, on the left the curves I-V (dotted lines) and P-V (solid lines) as the solar irradiance varies, while on the right it shows the normalized powers calculated at the point of maximum power (MPP) as the irradiance varies. The various curves relate to cell temperatures between 37 and 39°C.

The normalized powers (*NP*) were determined using Eq 2.9, in this way the direct dependence on irradiance is lost and only the secondary contribution remains.

$$NP = \frac{P_{el} \cdot G_{STC}}{P_{STC} \cdot G} \quad (2.9)$$

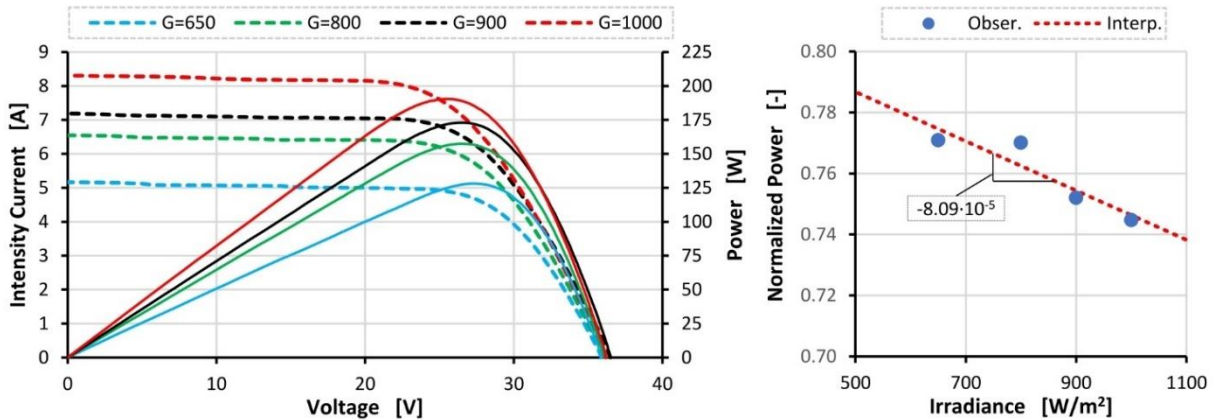


Figure 2.23 – Comparison of I-V and P-V curves (at left) and of NP (at right) as the solar irradiance varies

The I-V curves show that the current intensity (I) grows almost linearly with solar irradiance. Similarly, the P-V curves show an increase in power with increasing of irradiance. The analysis on normalized powers, instead, allows us to see that in addition to the linear dependence on irradiance, there is a second dependence, which reduces the extractable power as solar irradiance increases.

An even more interesting aspect is given by the analysis of the I-V and P-V curves as the temperature of the cells varies. Figure 2.24 shows the dependence of the characteristic curves and the normalized power on the cell temperature.

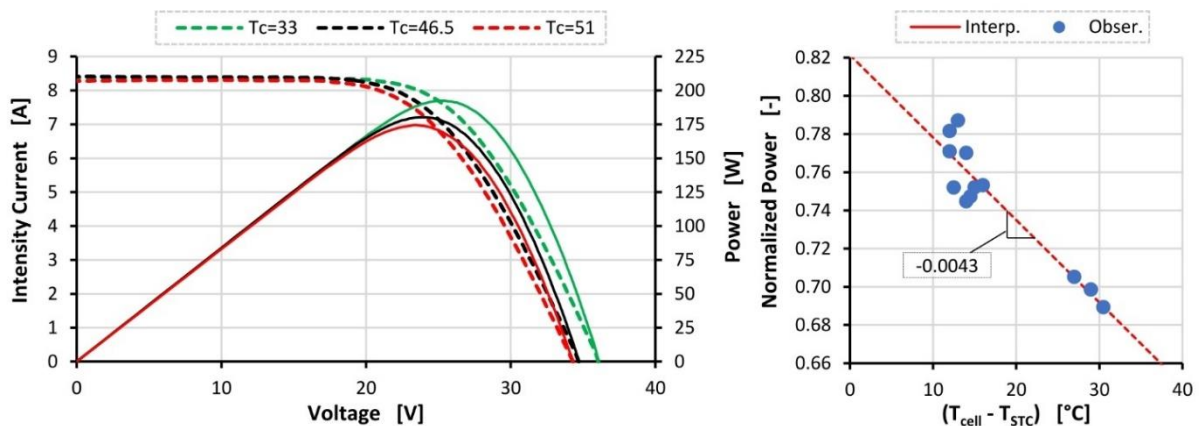


Figure 2.24 – Comparison of I-V and P-V curves (at left) and of NP (at right) as the temperature of the cell varies

In the analysis, the temperature of the cells was calculated using Eq 1.21, the IV and PV curves refer to values observed with irradiance $1000 \pm 20\text{W/m}^2$, while the NP data are obtained at different irradiance levels and normalized using Eq 2.9.

Fig. 2.24 shows that the increase in the temperature of the cells generates a decrease in voltage with the same current, therefore this results in a reduction in the power extracted when the temperature of the cells increases. The normalized values obtained for various levels of insolation show a reduction coefficient of the NP of about 0.0043, therefore for a variation of 10°C in the temperature of the cells a variation of the extracted power of 4.3% is generated.

Thermal characterization

The characterization of the collector efficiency is the fundamental tool for the calculation of thermal performance and for the design of solar systems.

The equations of the Hottel - Whillier - Bliss heat transfer model adapted to PV/T panels were used [1-2] to theoretically represent the panel considering all the heat transfer mechanisms and the electrical equivalent [3]. According to the regulation [4] the performance curve must be obtained when the photovoltaic generation corresponds to the maximum power point (MPP).

In this analysis the instantaneous efficiency curve of the collector as the operating conditions vary (SST method [5]) was used. It provides for the calculation of efficiency using Eq. 2.10, where compared to Eq. 1.18 described above, the quadratic term (a_2) does not appear because for unglazed PV/T it is null and the term G is replaced with G_{eff} calculated according to Eq. 1.17 [6].

$$\eta_{th} = \eta_0 - a_1 \cdot \frac{(T_{av} - T_{amb})}{G_{eff}} \quad (2.10)$$

Figure 2.25 shows the data collected in situ relating to the thermal efficiency of the panels. Where for simplicity, all the terms that multiply the a_1 coefficient are collected in the term called ΔT^*_{eff} .

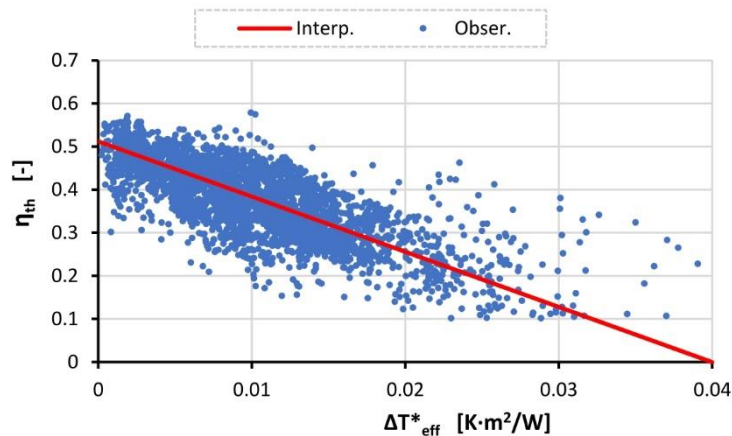


Figure 2.25 – Experimental performance curve of the PV/T panel

The parameters calculated by linear interpolation are respectively 0.512 and $-12.8 \text{ W}\cdot\text{K}^{-1}\cdot\text{m}^{-2}$ for η_0 and a_1 , values that are similar, but not identical to those present in the technical data sheet of the panels.

Other results are shown in the document attached in appendix 1.

References

- [1] J. A. Duffie and W. A. Beckman, Solar Engineering of Thermal Processes: Fourth Edition. 2013.
- [2] H.A. Zondag, D.W. de Vries, W.G.J. van Helden, R.J.C. van Zolingen, A.A. van Steenhoven. The yield of different combined PV–thermal collector designs. Solar Energy, Volume 74, 2003, Pages 253-69. [http://dx.doi.org/10.1016/S0038-092X\(03\)00121-X](http://dx.doi.org/10.1016/S0038-092X(03)00121-X).
- [3] J. Antonanzas, A. del Amo, A. Martinez-Gracia, A.A. Bayod-Rujula, F. Antonanzas-Torres. Towards the optimization of convective losses in photovoltaic–thermal panels, Solar Energy, Volume 116, June 2015, Pages 323-336. <https://doi.org/10.1016/j.solener.2015.04.013>
- [4] “EN 12975-1:2006: Thermal solar systems and components – Solar collectors – Part 2: Test methods.”
- [5] “ISO 9806, 2013. ISO 9806:2017 Solar energy - Solar thermal collectors - Test methods.”
- [6] L.W. Florschuetz. Extension of the Hottel-Whillier model to the analysis of combined photovoltaic/thermal flat plate collectors. Solar Energy, volume 22, Issue 4, 1979, Pages 361-366. [https://doi.org/10.1016/0038-092X\(79\)90190-7](https://doi.org/10.1016/0038-092X(79)90190-7)

3. PERFORMANCE EVALUATION OF SOLAR PLANTS AND TECHNIQUES FOR INCREASING PERFORMANCE, THROUGH MATHEMATICAL MODELS

The use of solar systems, such as photovoltaic (PV), solar thermal (ST) and photovoltaic / thermal hybrid (PV/T) systems, can allow the building sector to achieve ambitious targets, such as zero net energy buildings (nZEB).

The evaluation of the performance of solar plants plays a fundamental role in reaching the pre-established energy targets. It is necessary for the design and prediction of producibility during a predetermined period: season, a year or even the entire life of the plant.

To this end, mathematical models and therefore numerical simulations become an essential tool for estimating the producibility of plants, but they also play an essential role in the search for the improvement of existing technologies by analyzing the effects that some geometric and operational parameters cause on performance.

Below, in paragraph 3.1, some simulation software used to simulate the performance of solar plants are illustrated.

Paragraph 3.2 determines the performance of some solar systems (PV/T, PV and ST), considering a limited surface availability for installation (e.g. roof in residential tower buildings), repeating the analysis in three different climatic locations, as well as the comparison, is carried out both in terms of producibility and efficiency and in terms of economic returns.

Paragraph 3.3 describes a detailed numerical model of a PV/T system equipped with WISC panels. This numerical model is capable of performing parametric analyzes on the main variables that govern the system and is capable of providing various parameters that cannot be measured in real plants, such as the temperature of each layer that makes up the PV/T panel.

Section 4.4 analyzes the effects of changing the cooling fluid from pure water to a nanofluid in a PV/T system. The analysis is based on the thermodynamics viewpoint, considering both the total energy produced and its quality, and the thermal level achievable by changing the heat transfer fluid, considering different hypothetical input conditions and real climatic conditions.

Finally, in paragraph 3.5 through numerical experiments, the possibility to improve the performances of the PV modules through the passive cooling of photovoltaic cells, using two different Phase Change Materials (PCM)s is analyzed. In detail, the dynamic analysis performed for several days of the year allows evaluating the effective performance of the PV-PCM, considering the real degree of solidification achieved during the night.

3.1 Simulation Software

Simulations are "numerical experiments" and can provide the same kinds of performance information as physical experiments. Compared to physical experiments, simulations are relatively fast, cheap and can produce information that changes in design parameters (geometry, layout, type of plant, operating conditions, and so on) generate on system performance. It is possible to reproduce a series of numerical experiments that all use the same

loads and meteorological conditions, making some parameters vary from time to time (parametric simulations). Furthermore, simulations can provide data that is essentially impossible to obtain by other means. In this way, with cost data and appropriate economic analysis, simulation results can be used to find low-cost systems that pay for themselves within a reasonable time.

The parallels between numerical experiments and physical experiments are strong. In principle, it is also possible to calculate what is possible to measure, but it is also possible to calculate what is impossible to measure, such as the measurement of temperatures in parts of a system that are inaccessible for the placement of temperature sensors. Simulations can also be organized to subject systems to extreme conditions and can also be used to intercept faults in a system (for example, a fault in a circulation pump), to see what the effects of the fault would be.

Simulations are therefore powerful tools useful for designing or checking correct operation and can be used for the improvement of existing systems. However, there are limits to what you can do with them. First, the assumption that they are done correctly is implied, as it is easy to make program errors, assume incorrect constants, overlook factors that may be important, and err in a variety of other ways, so a high level of skill and judgment is required to produce useful results.

Second, even though it is possible to model a system at any level, in practice, it can be difficult to detail some of the phenomena that occur, such as clogged pipes, fouling, controller malfunctions, poor equipment installation, and so on.

Therefore, simulations do not replace physical experiments. They must be supported by comparisons with field experiments.

The use of simulation methods in the study of solar processes is a relatively recent development. The first studies date back to 1967 where [1] used a computer to simulate the operation of solar water heaters. Subsequently, [2] developed a model for the thermal performance of natural circulation solar water heater, obtaining good feedback from physical experiments. [3] developed a model of a home heating system, capable of simulating its operation with one year's hourly weather data and applied a pattern search optimization procedure to find optimal designs. And so, it is until today, where the high performances of the computers allow the detailed study of very complex systems.

In the last two decades, hundreds of programs have been written to study energy efficiency, renewable energy, and sustainability in buildings. The common thread of the software is the ability to solve the combinations of algebraic and differential equations that represent the physical behaviour of the equipment.

The main software used for the analyzes presented in this document are: TRNSYS, Matlab and Fluent.

3.1.1 TRNSYS

TRNSYS is one of the most widely used software in the world to evaluate the thermal and electrical performance of solar systems [4-7].

TRNSYS stands for "transient simulation program" and is a quasi-steady simulation model. This program was developed by the University of Wisconsin by members of the Solar Energy Laboratory [8]. It is written in the ANSI Fortran-77 standard. The program consists of many subroutines (called types) that model the subsystem components (e.g. panels, tank, wind turbine, boiler, etc.), and users can write their component subroutines if they are not satisfied with the ones provided. TRNSYS solves the set of algebraic and differential equations that describe the system in a time phase that can be selected by the user and finally, through diagrams or text files, the output results are acquired. Programming is graphical, with simple language, components are "connected" together in a similar way to pipes, ducts, and wiring in a physical system.

It has been demonstrated by analyzing the results of several validation studies that TRNSYS provides results with an average error between simulation and measured results of less than 10%.

3.1.2 Matlab

Matlab (short for Matrix Laboratory) is an environment for numerical computation and statistical analysis written in C, which also includes the programming language of the same name created by MathWorks. MATLAB allows you to manipulate matrices, visualize functions and data, implement algorithms, create user interfaces, and interface with other programs. Matlab is one of the most popular scientific programs, thanks to its numerous applications in fields such as electronics, control engineering, signal analysis, image processing, chemistry, statistics, and many others. There are now numerous scientific publications that use the Matlab environment as mathematical support for the theory. The very first version of Matlab dates back to the late 1970s, written at the University of New Mexico and Stanford University as a software package to support Linear Algebra and Numerical Analysis lessons. Today Matlab is no longer limited to just matrix and numerical calculations but has developed a whole series of functions for the most diverse applications in the scientific field. The simplicity of the language allows you to solve very complex problems without having to develop programs in C or other programming languages.

Besides, Matlab is also associated with graphic programming environments such as Simulink, where the calculation code to be simulated is created simply with a block system such as the one described for the TRNSYS environment. Similarly, the user can create new blocks programmed in "C" or "Fortran".

3.1.3 Fluent

Fluent is one software for CFD (Computational Fluid-Dynamic) analysis, capable of solving the governing equations through the method of finite volumes. Solving a fluid flow problem generally involves solving complex equations called “Navier-Stokes equations”. These equations govern the motion of a viscous, heat-conducting fluid.

The Finite-Volume Method divides the investigated region, the so-called computation domain, into small control volumes, where the governing equations are discretized and solved iteratively. Therefore, the values of each variable at any point in the domain and their time variations are calculated, to be able to monitor and analyze many quantities that characterize the system (temperature, flow flows, heat flows, etc.), even obtaining images visually striking graphics, as well as different types of diagrams and tables.

Each simulation consists of three phases: pre-processing (creation of the digital model and discretization of the domain through the mesh), solving (setting of boundary conditions, appropriate resolution algorithms and solving governing equations), and post-processing (analysis of the outputs and creation of images with the output values).

The governing equations are those of continuity, momentum, and conservation of energy. The solution of the Navier-Stokes equations is carried out following the choice of a turbulence model: Direct Numerical Simulation (DNS), Large Eddy Simulations (LES), and simulation with Reynolds - Averaged Navier - Stokes (RANS) equations [9]. Furthermore, according to the problem, the solver of the equations between pressure based-solver and density based-solver must be chosen.

3.2 Performance comparison of hybrid PV/T systems with conventional solar systems (PV-ST)

The energy needs of buildings concerns heating, cooling, DHW, ventilation, lighting and domestic type appliances. Thus, energy demand consists of both thermal energy and electricity that may be self-produced through RES. Electric energy is generated through photovoltaic systems, while the thermal energy is produced by solar thermal collectors. In high-efficiency buildings, these two solar systems may compete between them, because there is not enough space for their installation. Moreover, conventional photovoltaic modules convert only 10-20% of solar radiation into electricity, while the remainder of solar energy is wasted into heat [10]. Furthermore, as the increase in the operating temperature of the solar cell diminishes the PV cell efficiency. Thus, this efficiency can be increased carrying out the surplus of thermal energy through an active or passive cooling system [11]. Thus, hybrid photovoltaic thermal systems (PV/T) represent an interesting alternative to PV system since they produce simultaneously thermal and electrical energy at the same time also increase the efficiency of electricity production.

The ability to use this untapped energy is the key point for hybrid systems, which increases the energy yield per unit surface occupied [12].

Many studies on solar systems, PV [13-15], ST [16-18] and PV/T [19-21], have been reported in the literature. [22-23] studied various alternative solar energy systems through simulations to achieve nZEB ambitions in Norway. They have shown that the system that comes closest to achieving the zero net energy balance according to this definition was the system with only high-efficiency photovoltaic modules, the second closest was the system with high performance solar thermal collectors and modules PV. However, they point out that the results suggest that PV/T covered could give more output than solar thermal collectors. Although the reduction of efficiency of PV/T plants of is similar to that shown by PV plants, due air temperatures growth, the decrease of efficiency in the PV/T module can be limited if the fluid used to cool the photovoltaic cells has lower temperature than the cells of conventional PV panels.

[24] studied different combinations of solar plants (PV, PV/T, and ST) for different countries in China. Overall, they observed that to maximize net electricity generation, the PV / T and PV system can be the optimal system for residential applications.

However, there is not yet a complete picture regarding the comparison between the performance of various solar systems.

This study concerns the comparison among conventional solar plants (PV and ST) and hybrid PV/T system when space is scarce for installing solar systems to satisfying the building energy load (e.g. residential tower buildings).

The comparison between these energy generation systems proposes a circumstance for which the households decide to use the available surface for generating both thermal and electrical energy, considering the solar plants installed in the cities of Catania (IT), Split (HR) and Freiburg (D). Moreover, the energy performance comparison is developed considering both the first and

second law of thermodynamic, so also taking into account the quality of the energy. Finally, an economic comparative analysis which allows the effect of the cost of energy in different State is proposed.

3.2.1 Methodology and numerical model

The following study determines the performance in terms of energy produced, efficiency and ability to meet energy needs, in homes, considering the different technologies of solar systems: PV, ST and PV/T.

The thermal energy produced by PV/T system and the solar thermal system have the purpose to satisfy an aliquot of the energy needs for DHW production of a single family, while the electricity produced by PV / T and PV is used to meet the home's electricity needs, fixed equal to 3000 kWh/y.

Figure 3.1 shows the layout of co-generative PV/T plant. As regard the conventional plants, the PV presents the layout shown in blue part of fig. 3.1 and ST the same layout shown of red part in fig. 3.1.

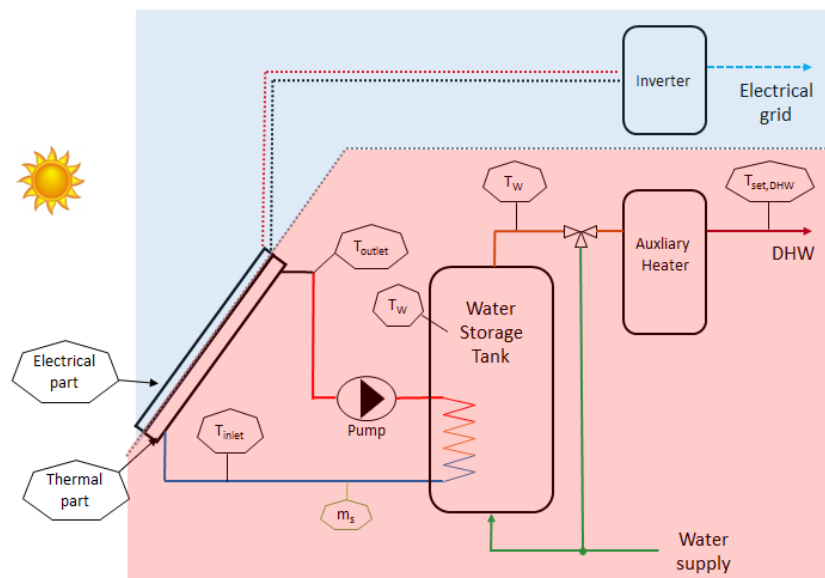


Figure 3.1 – Layout of PV/T plant

As shown in the layout's figure, the thermal part presents the DHW pre-heating configuration scheme, where both the solar ST and PV/T panels are connected to a solar storage tank through pipes equipped with pump and control units (forced circulation system), moreover, the plants are equipped with an auxiliary conventional boiler which will provide the complementary energy request for satisfying the whole DHW needs.

As regards the electrical production, it was hypothesized that both the PV and PV/T plants operate at the maximum power point (MPP) since they are both grid-connected.

The comparison between the various solar plant technologies was conducted by comparing, considering a given available surface, the performance of the PV/T system with different combinations of PV and ST, passing from the available area entirely occupied by the PV to the available area entirely occupied by the ST.

For this purpose, two mathematical models were created in TRNSYS with which the comparative parametric analysis was carried out.

3.2.1.1 Numerical model

For this study, two mathematical models were developed in TRNSYS with which the comparative parametric analysis was carried out.

Fig. 3.2 shows TRNSYS's projects whit the main types and connections used in the simulation tool, while Fig. 3.3 shows the flow diagrams of the two projects developed.

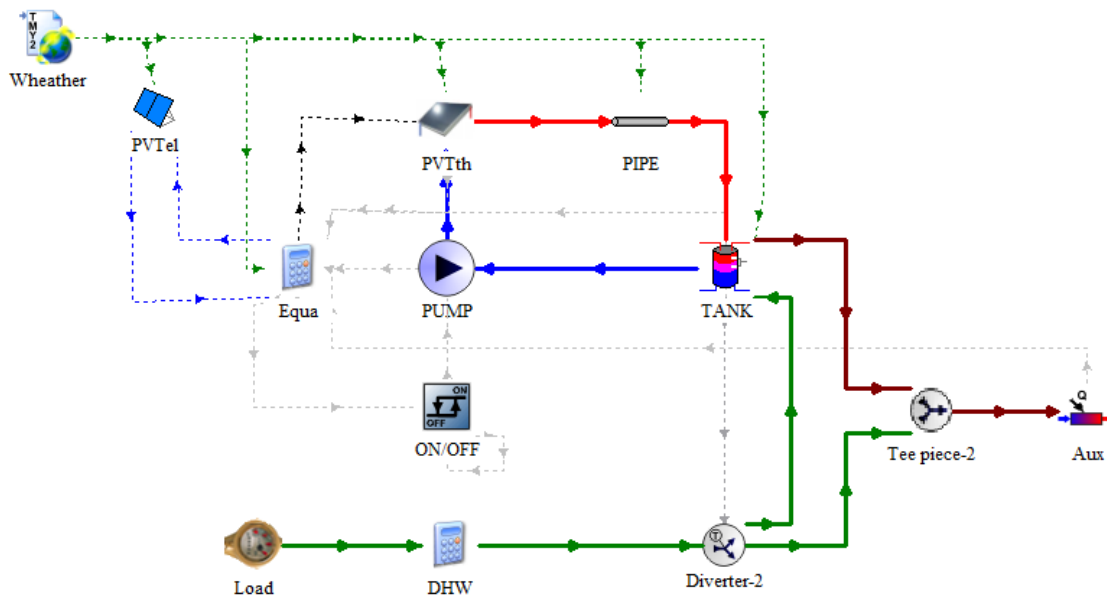


Figure 3.2 – Sketch of TRNSYS's project

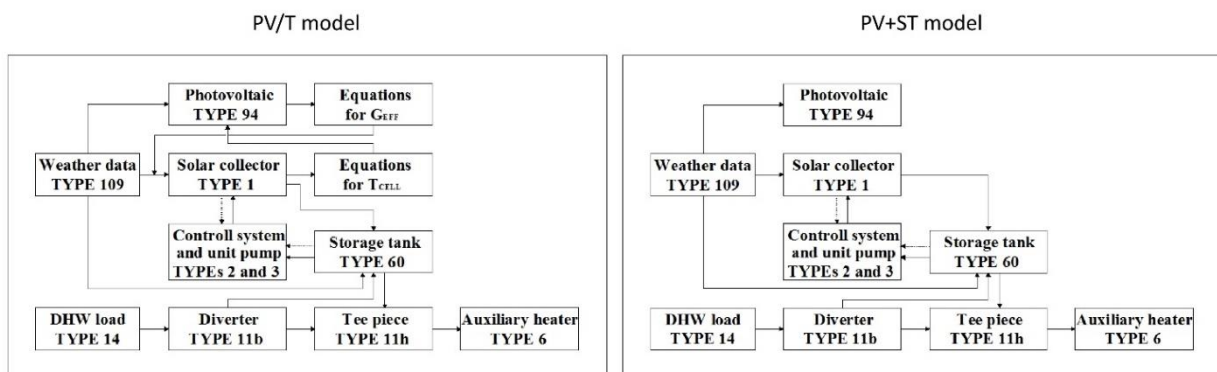


Figure 3.3 – Flow diagrams for PV/T (at left) and PV+ST (at right).

One peculiarity of this PV/T model is the approach used for defining the features of the PV/T module [22]. Therefore, the PV/T module is described using two distinct types, that are a solar thermal collector type (type 1) and a photovoltaic module type (type 94). Thus, the energy produced by the hybrid modules were evaluated taking into account the mutual interaction between the two systems and specifically: the reduction of the solar irradiance on the solar absorber due to the solar energy converted by the photovoltaic effect, calculated from Eq. 3.1, and the PV cells temperature dependence by the average temperature of the working fluid as well the environmental temperature, calculated with Eq. 3.2.

$$G_{eff} = G(1 - \eta_{el}) \quad (3.1)$$

$$T_{pv} = \frac{T_{av} + T_{amb}}{2} \quad (3.2)$$

Eq. 3.1 derives from Eq. 1.17, where in the case in question the PF/ α ratio is equal to 1.

Equation 3.2 coming from expression proposed in [25] and is used to takes into account the heat flux between PV cells and working fluid.

The separate system is described by the same types but in this case, there are not any interaction among the PV and the ST types.

Thermal energy produced by panels are stored in an insulated solar storage tank (type 60) for which the effect of thermal stratification is taken into account. This thermal stratification is calculated using the relation proposed by [TRNSYS manual] which uses the coefficient of de-stratification Δk equal to 0.0576 W/(m²K), calculated as:

$$\Delta k = k_{wall} \frac{A_{wall}}{A_{water}} \quad (3.3)$$

where: k_{wall} is the thermal conductivity of the tank wall, A_{wall} is the cross-section area of tank (including insulation layer) and A_{water} is the cross-section area of water inside the tank.

Type 31 is used to model the pipes between the storage tank and solar panels. Therefore, the heat losses due to the pipes of the solar circuit are taken in account. The coefficient of thermal transmission is 0.18 W/(m²K) and the piping length is 20 m, that is referred to an insulated pipe with 20 mm of thickness.

The flow rate of the solar fluid was set at 50 l/h per square meter of absorber surface. Moreover, the pump ignition is controlled by an on/off controller (type 2), which turn on the pump when the outlet temperature from the panels is 3°C greater than the storage tank.

The DHW load is handled by the type 14, which is connected to a diverter.

The diverter set the flow of water in function of the temperature in the solar tank. When this temperature is higher than the set point temperature (fixed to 45°C), the diverter mixing it with the mains water (15°C). Otherwise, the hot water goes to the auxiliary heater where its temperatures grows up to the set point temperature.

3.2.1.2 Evaluation of performance

The performance of the varies solar plants analyzed are compared regard both thermal, electrical, and overall yields.

The electric power produced by the PV or PV/T panels $P_{el,panel}$, is calculated from previous Eq. 1.23, showed in chapter 1, starting from the electrical efficiency generated from the panel (see Eq. 1.16). To take into account the real electricity coming from PV or PV/T system, the system's losses (from inverter and array) are considered, therefore, the electrical efficiency of system and the total energy produced are evaluated using respectively the Eq. 3.4 and 3.5.

$$\eta_{el,plant} = \eta_{el,panel} \cdot \eta_{inv} \cdot \eta_I \quad (3.4)$$

$$E_{el,plant} = \int_0^t G \cdot A \cdot \eta_{el,plant} dt \quad (3.5)$$

Where: η_{inv} is equal to 0.95 and it is the inverter efficiency and η_I represents the losses in the PV array. This last term depends by several parameter, such as the incident angle [26], and is worth 0.92.

The thermal power conveyed into the storage tank depends by the mass flow rate \dot{m} , the fluid specific heat C_f and the temperature difference between the inlet and the outlet of the fluid in the solar panels, which is calculated through Eq. 1.5 described in chapter 1.

However, in order to evaluate the real energy saving achieved by the solar thermal plant it is important to divide the DHW load (E_{DHW}) into that coming from the RES plant (E_{th}) and that supplied by the auxiliary generator (E_{AUX}), calculated respectively using the Eq. 3.6, 3.7 and 3.8.

$$E_{DHW} = \int_0^t \dot{m}_{DHW} \cdot C_w \cdot (T_{user} - T_{sup}) dt \quad (3.6)$$

$$E_{th} = \int_0^t \dot{m}_{DHW} \cdot C_w \cdot (T_{mx,out} - T_{sup}) dt \quad (3.7)$$

$$E_{AUX} = \int_0^t \dot{m}_{DHW} \cdot C_w \cdot (T_{user} - T_{mx,out}) dt \quad (3.8)$$

where \dot{m}_{DHW} is the instantaneous mass flowrate required by users, C_f indicates the specific heat of the water, $T_{mx,out}$ is the temperature of the fluid coming from the mix valve, T_{sup} the temperature of grid water supply (set equal 15°C), and T_{user} the temperature required by users (set equal 45°C).

An important Key Performance Indicators (KPI) of energy production of solar thermal plants (ST and PV/T) is the DHW energy demand covered by solar energy (f_{DHW}), that is the ratio between the energy supplied by the system and that required by users:

$$f_{DHW} = 100 \cdot \frac{E_{th}}{E_{DHW}} \quad [\%] \quad (3.9)$$

The overall performance of PV/T or combined PV-ST systems can be obtained as a direct summation of electrical and thermal power as given by the following equation:

$$\eta_{tot} = \frac{P_{el} + P_{th}}{A \cdot G} \quad (3.10)$$

$$E_{tot} = E_{th} + E_{el} \quad (3.11)$$

with A total surface of entire plant: surface of collectors for PV/T plant and sum of surface of ST collectors and PV modules for PV-ST plant.

However, the electrical energy is more valuable than thermal energy. Thus, to take into account of the different quality of the thermal and electrical energy, the overall performance can be evaluated based on the primary energy produced $E_{tot(l)}$ using the Eq. 3.12 and 3.13:

$$\eta_{tot(l)} = \frac{P_{el}/\eta_{power} + P_{th}}{A \cdot G} \quad (3.12)$$

$$E_{tot(l)} = E_{el}/\eta_{power} + E_{th} \quad (3.13)$$

where η_{power} is the electric power generation efficiency for a conventional power plant and assumes different values in each country as function of the energetic mix.

Moreover, the primary energy consumptions (EP_0) of a generic user (e.g. residential), due both to the electrical ($E_{el,load}$) and the thermal (E_{DHW}) loads, can be defined as:

$$EP_0 = E_{el,load}/\eta_{power} + E_{DHW}/\eta_{th,b} \quad (3.14)$$

where $\eta_{th,b}$ is the gas boiler efficiency. While the primary energy saving (EP_S) due to the energy produced by co-generative plants can be calculated as:

$$EP_S = E_{el}/\eta_{power} + E_{th}/\eta_{th,b} \quad (3.15)$$

Thus, the rate of primary energy reduction can be calculated as:

$$\Delta EP = \frac{EP_S}{EP_0} \quad (3.16)$$

3.2.1.3 Study specification

PV/T plant consists of unglazed and uninsulated PV/T modules equipped with monocrystalline silicon cells. The e PV-ST system indeed is constituted by distinct ST and PV plants. Both systems (separate and hybrid) are oriented to the south with a tilt angle of 25 degrees. And the modules are connected hydraulically and electrically in series.

The features of PV/T have been defined in accordance with the configuration of the plant installed in the campus of the University of Catania and described in chapter 2. Tables 3.I and 3.II report the characteristics adopted for the solar systems analyzed.

Table 3.I data of PV/T and ST panel.

			PV/T	ST
Gross area		m ²	1.66	1.66
Optical efficiency,	a ₀	%	55.0	82.0
heat loss coefficient,	a ₁	W/K/m ²	15.8	3.2
heat loss coefficient,	a ₂	W/K ² /m ²	0.0	0.0

Table 3.II electrical data of PV/T and PV panel.

			PV/T
Cell type		-	Monocrystalline
Nominal power,	P _{MPP}	W	250
Module efficiency,	η ₀	%	15.4
Rated voltage,	V _{MPP}	V	30.7
Rated current,	I _{MPP}	A	8.15
Open circuit voltage,	V _{OC}	V	38.5
Short circuit current,	I _{SC}	A	8.55
Thermal coefficient,	V _{OC}	%/K	-0.32
Thermal coefficient,	I _{SC}	%/K	0.048
Efficiency loss with temperature,	β	%/K	-0.44
Net area, A _{PV}		m ²	1.58

The analysis was performed in three locations: Catania (IT) lat. 37.5, long. 15.1, Split (HR) lat. 43.5, long. 16.4 and Freiburg (D) lat. 48.0, long. 7.8.

In the scenario of a limited area available for installation of the systems, the analysis was carried out assuming a solar plant surface that meet the electrical consumption of a household.

The analysis was performed for different climatic locations, therefore the reference surface varies from location to location, as shown in table 3.III, where “A_{PV,min}” necessary to satisfy the electrical request, “N_{panel}” is the minimum number necessary of PV panels, “A_{plant,ref}” is the reference surface adopted and “P_{peak,ref}” the effective peak power.

Table 3.III reference characteristic of simulation plants.

		Catania	Split	Freiburg
A _{PV,min}	m ²	11.78	12.07	17.47
N _{panel}	-	8	8	12
A _{plant,ref}	m ²	12.64	12.64	18.96
P _{peak,ref}	kW	2.00	2.00	3.00

All the details of this procedure are shown in the paper [27] present in Appendix 2.

The meteorological data among the three cities, are shown in the follow figures 3.4 [28]. Where respectively at left and right the average monthly irradiation on tilted surface (southern exposure and 25° as tilt angle) and the average monthly temperatures, are shown.

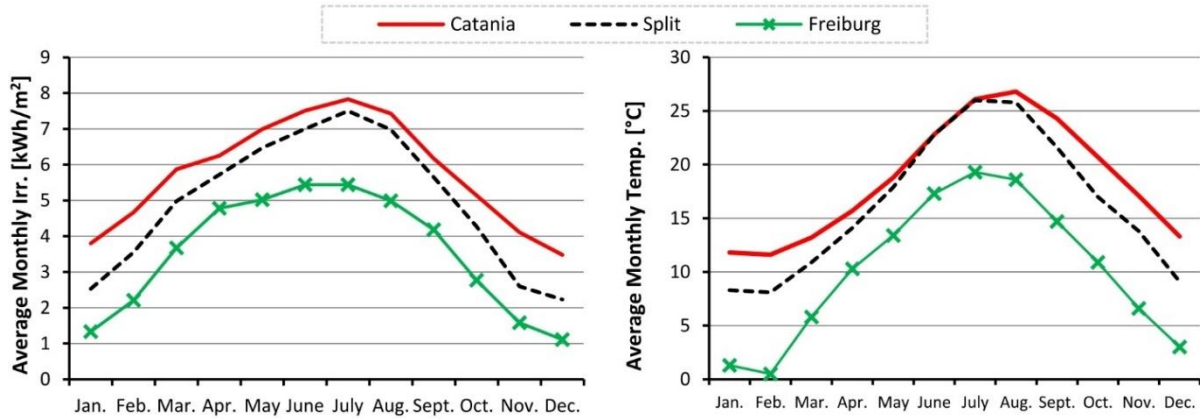


Figure 3.4 – Environmental climate data.

It is important to note that the city of Catania is the sunniest and warmest, while Freiburg is the least sunny and coolest. In fact, the total annual irradiation on the tilted surface is about 2109 kWh/m²y, 1812 kWh/m²y and 1296 kWh/m²y respectively for Catania, Split and Freiburg. Moreover, the different climatic conditions can also be highlight comparing the heating degree day (HDD) for each locality, that are 742, 1388 and 2780 respectively for Catania, Split and Freiburg.

The energy needs concern both electricity and DHW. The electrical energy demand has a wide variation in the EU states. Scandinavian countries have the highest demand for electricity with average consumption of 5000 kWh/y per inhabitant [29-30]. Otherwise, the countries of the Mediterranean surface have much lower electricity consumption ranging from 2500 to 5000 kWh/y per household. The reference annual consumption chosen for electricity is 3000 kWh that is representative of the needs for the less energy intensive European families.

The two generation plants have been considered connected to the grid, therefore the PV and PV/T modules operates at MPP conditions.

Energy consumption for DHW depends on various factors, i.e. consumption patterns: how much hot water is used and the increase in water temperature required (difference between the inlet and outlet temperature). On average, the annual domestic hot water consumption in developed countries is around 1000 kWh per person. In the simulations, the hourly consumption profile for DHW of a single family, depicted in figure 3.5 as suggested by the standard EN 15316:2007, is adopted.

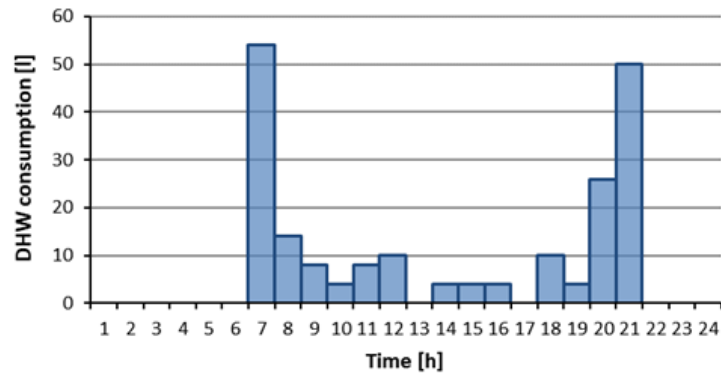


Figure 3.5 – DHW daily demand profile.

3.2.2 Model validation

In this section the simulation results performed using TRNSYS’s model are compared with the experimental data measured with the pilot plant described in chapter 2.

The following figures depict the daily comparisons between the measured and simulated data. Fig. 3.6 compares the simulated and measured voltage. Module voltage is well known to be significantly affected by cell temperature, so this comparison allows assessment of the accuracy of the equation used for calculating T_{PV} . The two sets of data are in good agreement, especially during the central part of the day. However, the experimental values are significantly higher than the simulated ones in the early hours of the day, when the solar irradiation is feeble. These discrepancies may be ascribed to the inaccuracy of the MPPT algorithm at low solar irradiation values. In these conditions, the module voltage tends to reach the open circuit voltage value (V_{oc}).

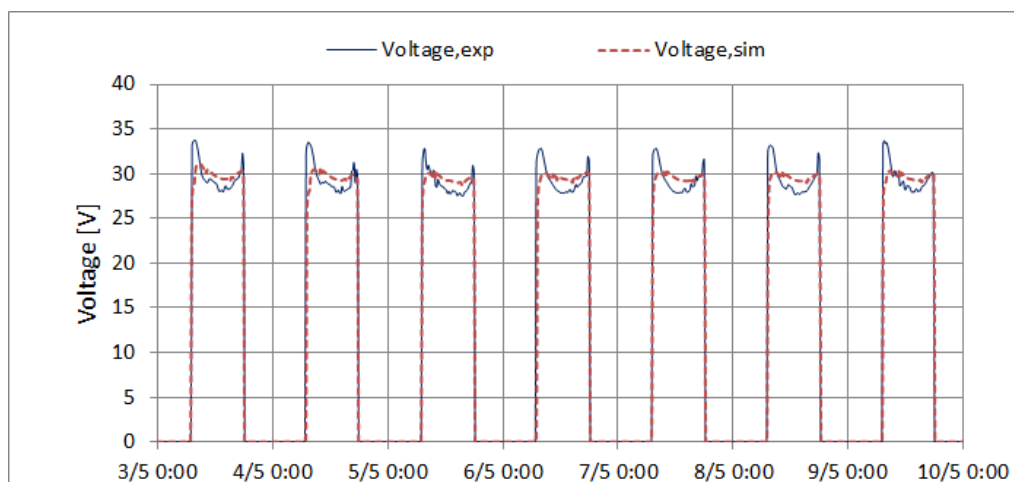


Figure 3.6 - Comparisons between simulated and measured voltage

Fig. 3.7 shows the comparison regards the electrical power (P_{el}). The modelled power presents modest differences, may be due to simplified model adopted for describing the electrical part of the PV/T module, since only thermal losses were considered, leaving aside other losses such as shading, soiling, optical losses, joule losses and MPPT losses.

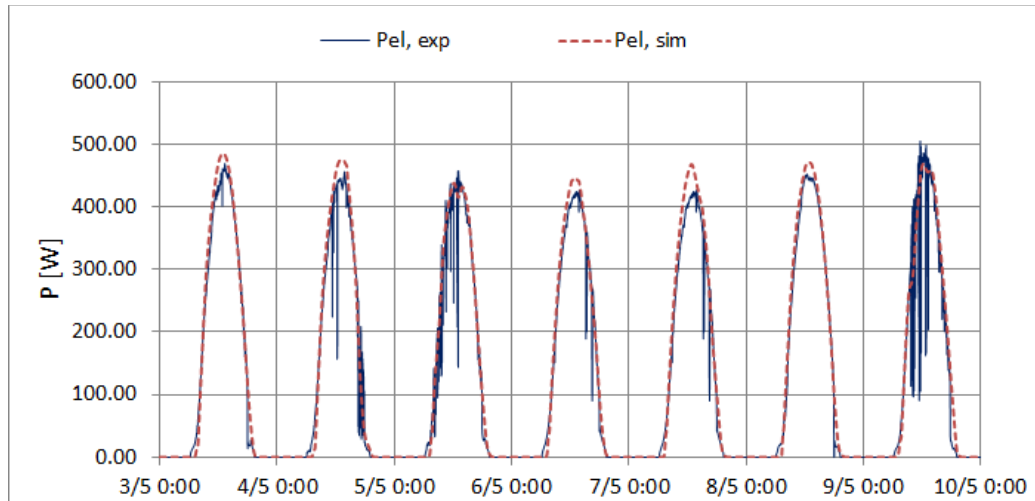


Figure 3.7 - Comparisons between simulated and measured electric power (P_{el})

As regards the thermal features, figure 3.8 displays the comparison between the measured temperature at the outlet of the PV/T module, $T_{out,exp}$, and the simulated value, $T_{out,sim}$, which are the highest hydronic circuit fluid temperatures.

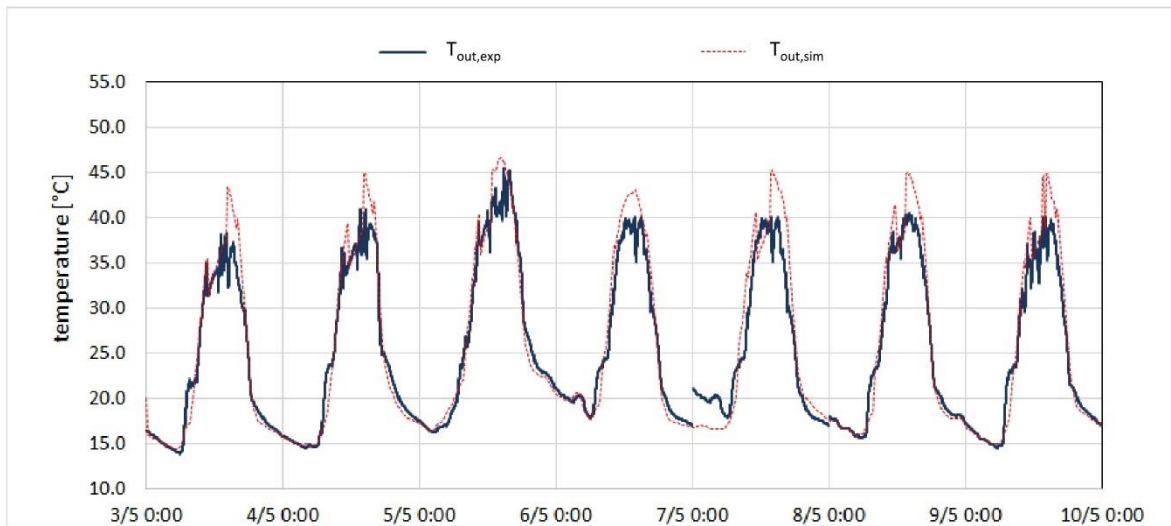


Figure 3.8 - Comparisons between simulated and measured temperatures at the outlet of PV/T panels

The trend of the two temperature sets is fairly comparable, with some significant differences during the second part of the day (after midday), when the increase in the temperature inside

the solar tank causes the pump to stop. After this, it takes some time for the PV/T system to restart the pump, due to its inertia. In contrast, in the simulation, the modular outlet temperature rises rapidly and the pump restarts quickly.

Finally, fig. 3.9 shows the total daily electricity and thermal energy produced in the pilot plant and in the simulation environment.

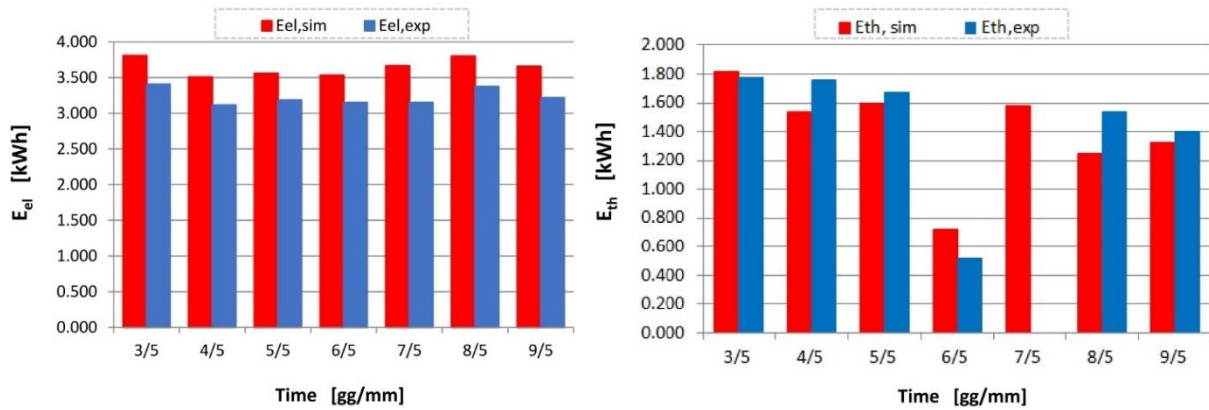


Figure 3.9 - Comparisons between simulated and measured daily electrical (at left) and thermal (at right) energy produced.

Overall, the matching between experimental and simulated data is good. On 6 May, the performance of the PV/T plant was poorer than on the other days. This is because the temperatures inside the solar tank are higher than the solar collector outlet temperatures. This condition turns off the pump and prevents the supply of energy to the solar tank, while due to a malfunction, the thermal energy of the pilot plant is not available during May 7th.

3.2.3 Results

For the cities of Catania, Split and Freiburg, yearly simulations were performed to compare the electrical and thermal performances of solar systems considering the two proposed scenarios.

3.2.3.1 Scenario 1

In this scenario, the comparison between the energy produced by the PV/T system and that produced by the PV system considering the same available surface, that is equal to 12.64 m² for the cities of Catania and Split and 18.96 m² for the city of Freiburg which respectively correspond to a peak electrical power of 2.0 kW and 3.0 kW.

Fig. 3.10 shows the comparison of performances during the year between the PV and PV/T system for the three cities analysed.

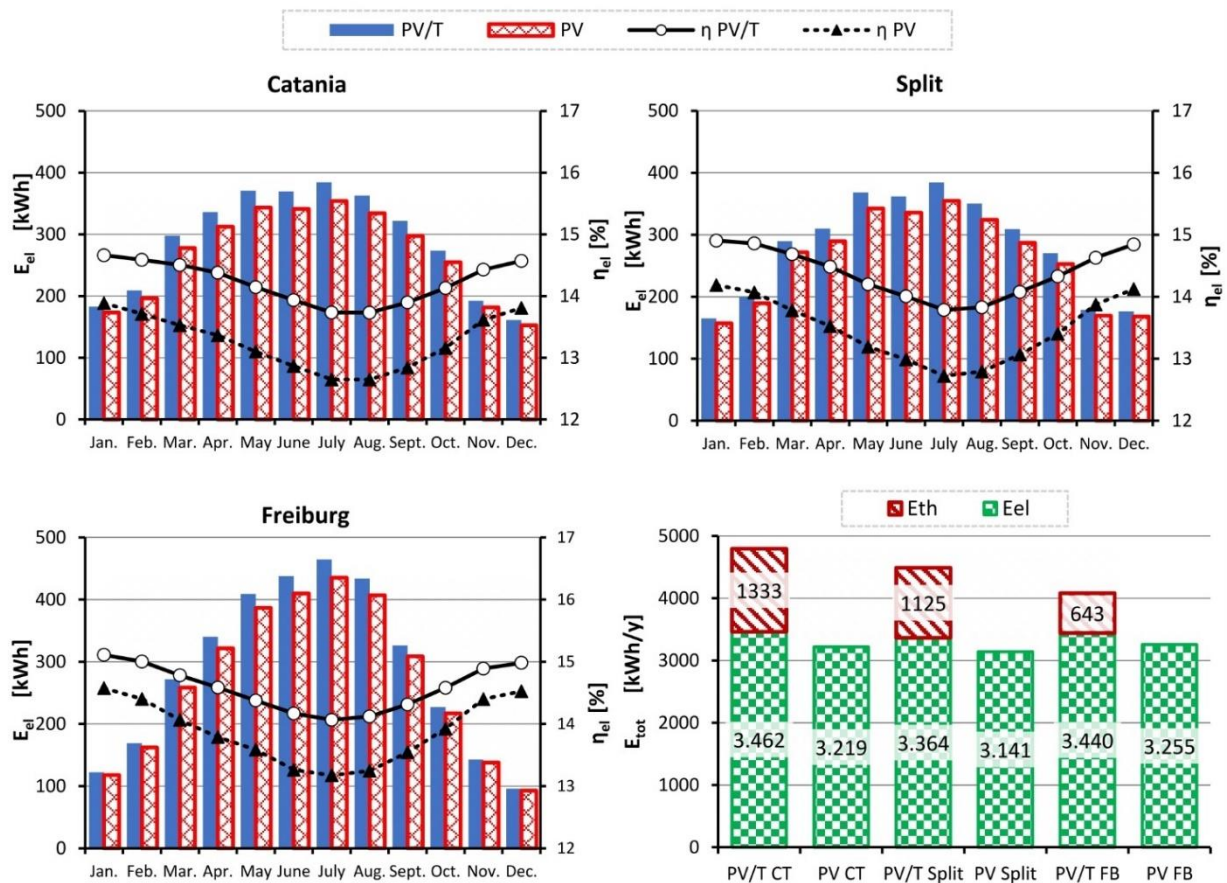


Figure 3.10 - Comparisons of performances between PV and PV/T systems

Comparing the results shows in figure 3.10, it is noted that PV/T plants produce more electricity than conventional PV in all the cities analyzed especially during the summer season. It is quite interesting to observe that during winter month the energy produced by PV and PV/T systems is almost similar. Otherwise, the energy produced by the PV/T plant has a meaningful increase due to both the increase of efficiency and the highest solar irradiation during the summer months.

As well known, the electric production of photovoltaic cells grows as the working temperature decreases. In a PV/T module, the working fluid takes heat away from the cells, making them work at lower temperatures than those of a conventional module, therefore the PV/T plant produces more electricity than a conventional PV plant. In this regard, figure 3.11 shows the temperature profile of the photovoltaic cells on a summer day for the PV and PV/T plants installed in the city of Catania, where the temperature difference of about 26°C is observed.

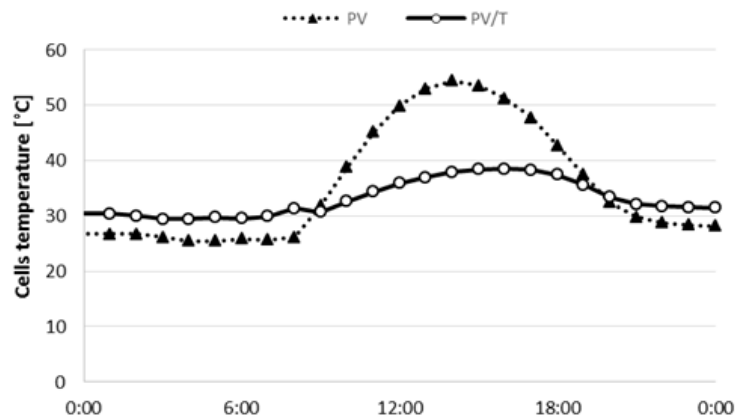


Figure 3.11 - Comparisons of cells temperature between PV/T and PV system on a typical summer day - Catania

If we look the annual production (bottom right graph of fig. 3.10), it can be seen that PV/T systems installed in the cities of Catania and Split achieve an electricity production 7% higher than the PV, while in Freiburg the PV/T system achieve an increase of over 5.5%. The increase of efficiencies of the PV/T compared to the PV is about 0.9% for Catania and Split, and about 0.7% for Freiburg.

Moreover, the PV/T plant in addition to generating more electricity than PV produces thermal energy that can be used to satisfy the energy needs for DHW. Thermal energy generated by PV/T plant allows satisfying the energy demand for DHW higher than 50% for plants installed in Catania and about 44% for plants installed in Split. Otherwise, in Freiburg, just 25% of the annual demand for DHW is satisfied through the PV/T plant. However, this percentage may be increased using most thermal insulated PV/T panels, which reduces the thermal losses during the coldest months.

However, PV/T plant allows increasing the production of total energy (E_{tot}) respect the conventional PV plant of about 40 % in Catania and Split and about 25 % in Freiburg.

3.2.3.2 Scenario 2

The second scenario proposes a circumstance for which the households decide to use the available surface for generating both thermal and electrical energy. Therefore, the annual comparison between conventional PV-ST plants and a PV/T plant is shown. Different proportions between the surface filled with ST and PV modules are investigated. As regards the PV-ST system the energy generated is calculated varying the surface covered by the ST panels from 0 to 100%.

This comparison concerns the evaluation of the production of electrical and useful thermal energy, as well as the efficiencies of the systems calculated also take into account the quality of the energy.

Figure 3.12 shows the annual electrical and thermal (net thermal energy used to satisfy DHW needs Eq. 1.7) energy generated by the PV-ST systems varying the surface filled with PV or ST plant as well as the energy generated by the PV/T plant, considering the solar plant installed in the three cities studied.

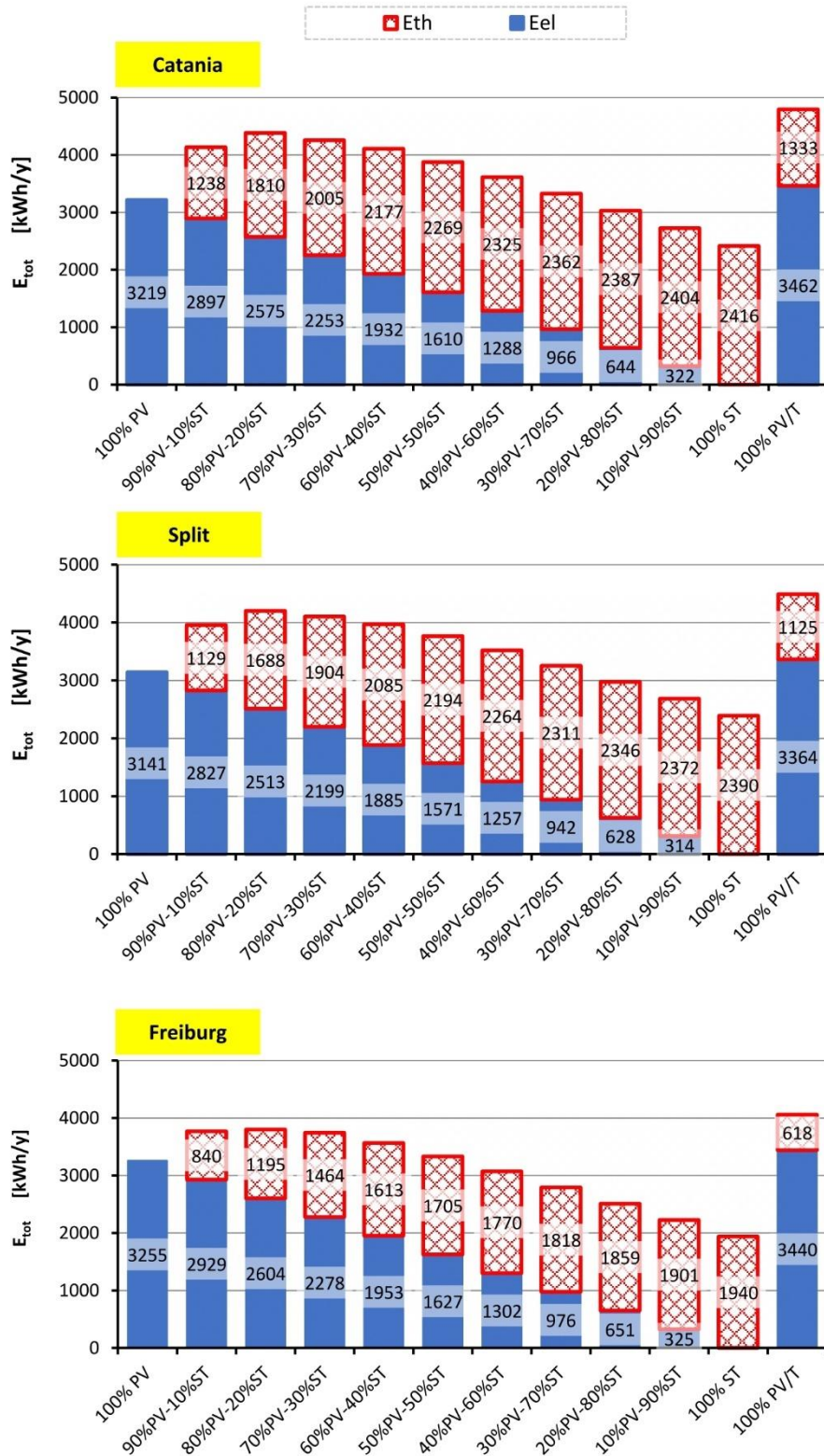


Figure 3.12 - Annual energy produced by PV-ST and PV/T plants

In the analyzed cities, the PV/T plant produces more energy than that one produced by the PV-ST plants for each surface combination.

Plants consisting of only PV panels or only ST panels produce less energy than any combination of the two technologies. The maximum energy generated by the PV-ST plants occurs when the PV panels occupy 80% of the total surface, where achieved the values of 4385, 4201 and 3799 kWh/y respectively for Catania, Split and Freiburg. Thus, the PV/T plant produces at least 10% more total energy than the PV-ST plant in Catania and about 7% for the other cities.

Tables 3.IV, 3.V and 3.VI show the annual result obtained for PV/T installation and for varies combination of PV-ST, respectively for the city of Catania, Split and Freiburg. In detail, the tables report the electricity produced (E_{el}), the net thermal energy used for satisfying DHW needs (E_{th}), the primary energy produced $E_{tot(l)}$, the cover factor of electric (f_{el}) and thermal (f_{DHW}) demand, and the reduction of primary energy (ΔEP). The primary energy produced, and the reduction of primary energy are calculated by eq. 3.13 and 3.16. Where, the terms η_{power} is equal to 0.46 [31], 0.36 [29], and 0.385 [30] respectively for Catania, Split, and Freiburg, while $\eta_{th,b}$ is set equal to 0.85 for all the cities.

Table 3.IV comparison of annual result between PV/T and PV-ST for the city of Catania.

	E_{el} [kWh/y]	E_{th} [kWh/y]	$E_{tot(l)}$ [kWh/y]	f_{el} [%]	f_{DHW} [%]	ΔEP [%]
PV/T	3462	1333	8860	100	52.4	95.6
100% PV	3219	0	6998	100	0.0	73.5
90% PV – 10% ST	2897	1238	7536	96.6	48.6	81.5
80% PV – 20% ST	2575	1810	7409	85.8	71.1	81.2
70% PV – 30% ST	2253	2005	6904	75.1	78.7	76.3
60% PV – 40% ST	1932	2177	6376	64.4	85.5	71.0
50% PV – 50% ST	1610	2269	5768	53.7	89.1	64.8
40% PV – 60% ST	1288	2325	5125	42.9	91.3	58.2
30% PV – 70% ST	966	2362	4462	32.2	92.8	51.3
20% PV – 80% ST	644	2387	3787	21.5	93.7	44.2
10% PV – 90% ST	322	2404	3104	10.7	94.4	37.1
100% ST	0	2416	2416	0.0	94.9	29.9

For Catania, Table 3.IV shows that the maximum of $E_{tot(l)}$ provided by the PV-ST systems is achieved when the PV panels cover the 90% of the total surface, while in the previous analysis (simply the summation of thermal and electrical energy, which is shown in figure 3.12) the maximum value was obtained with 80% of PV. This difference is due to the metric of the second principle which taken into account the superior quality of the electrical energy respect to the thermal energy. The PV/T system has better performances both in terms of $E_{tot(l)}$ as well as of the primary energy reduction. This analysis points out that the PV/T plant in comparison to the conventional technologies, allow attaining an increase of the primary total energy produced around 15%. The PV/T plant with a surface of 12.64 m² meets over 95% of the primary energy

demand against about 80% of the PV-ST plants in its better configurations (i.e. 80% PV and 20% ST). As a rule, the increase of the surface of ST panels dramatically reduces both the $E_{tot(l)}$ and the percentage of primary energy reduction. When the total available surface is occupied with the ST panels, just 30% of primary energy reduction is achieved.

Table 3.V comparison of annual result between PV/T and PV-ST for the city of Split.

	E_{el} [kWh/y]	E_{th} [kWh/y]	$E_{tot(l)}$ [kWh/y]	f_{el} [%]	f_{DHW} [%]	ΔEP [%]
PV/T	3364	1125	10470	100	44.2	94.2
100% PV	3141	0	8726	100	0.0	88.1
90% PV – 10% ST	2827	1129	8982	94.2	44.3	91.0
80% PV – 20% ST	2513	1688	8669	83.8	66.3	88.0
70% PV – 30% ST	2199	1904	8013	73.3	74.8	81.5
60% PV – 40% ST	1885	2085	7321	62.8	81.9	74.5
50% PV – 50% ST	1571	2194	6557	52.4	86.2	66.8
40% PV – 60% ST	1257	2264	5754	41.9	88.9	58.8
30% PV – 70% ST	942	2311	4929	31.4	90.8	50.4
20% PV – 80% ST	628	2346	4092	20.9	92.1	42.0
10% PV – 90% ST	314	2372	3244	10.5	93.1	33.4
100% ST	0	2390	2390	0.0	93.9	24.8

Table 3.VI comparison of annual result between PV/T and PV-ST for the city of Freiburg.

	E_{el} [kWh/y]	E_{th} [kWh/y]	$E_{tot(l)}$ [kWh/y]	f_{el} [%]	f_{DHW} [%]	ΔEP [%]
PV/T	3936	618	9553	100	24.3	89.6
100% PV	3724	0	8454	100	0.0	78.4
90% PV – 10% ST	3352	840	8449	97.6	33.0	79.7
80% PV – 20% ST	2979	1195	7959	86.8	46.9	75.7
70% PV – 30% ST	2607	1464	7382	75.9	57.5	70.8
60% PV – 40% ST	2235	1613	6686	65.1	63.3	64.6
50% PV – 50% ST	1862	1705	5933	54.2	67.0	57.8
40% PV – 60% ST	1490	1770	5151	43.4	69.5	50.6
30% PV – 70% ST	1117	1818	4354	32.5	71.4	43.3
20% PV – 80% ST	745	1859	3550	21.7	73.0	35.9
10% PV – 90% ST	372	1901	2747	10.8	74.7	28.6
100% ST	0	1940	1940	0.0	76.2	21.2

As regards the result for the city of Split (table 3.V), the maximum $E_{tot(l)}$ is generated when the PV panels occupy 90% (as seen for Catania) of the total surface. The PV/T plant produces 10500 kWh/y while the PV-ST produces about 9000 kWh/y, with a difference of about 15%. As regards, the ΔEP of a conventional plant with 90% PV panels is of about 91%, while the PV/T plant achieves a reduction of about 95%. This high performance is related to the value of the

coefficient η_{power} , which emphasize more the electrical energy respect to the thermal energy. Thus, under this constraint the performance between PV/T and PV-ST plants are modest.

Finally, as regards the result for the city of Freiburg (table 3.VI), the PV/T plant produces 9553 kWh/y while the PV-ST (90%PV-10%ST) produces about 8450 kWh/y, with a difference of about 10%. The ΔEP conventional plant with 90% of PV panels is of about 80% of the energy demand, while the PV/T plant achieves a reduction of about 90%. These results are affected by the low value of the η_{power} , as well as the little amount of useful thermal energy generated due to the cold climate of Freiburg.

The complete results of all analyzes are reported in the paper in appendix 2.

3.2.4 Economic analysis

An economic analysis was developed for the solar plants installed, starting from the energy prices of electricity and natural gas in the three cities analysed. It is worth noticing how across the EU Member States the electricity price ranges from 0.1 €/kWh to 0.3 €/kWh, whereas the gas price ranges from 0.035 €/kWh to 0.12 €/kWh [32]. Table 3.VII shows the electricity and prices per kWh for the cities analysed [32].

Table 3.VII prices of the energy.

		Catania	Split	Freiburg
Prices elect.	€/kWh	0.214	0.120	0.305
Prices fuel	€/kWh	0.070	0.036	0.061

The analysis is based on the comparison of the monetary savings R achieved during the life cycle with the costs of the built plants. The annual monetary savings R_y is calculated using Eq. 3.17:

$$R_y = E_{el} \cdot Price_{el} + \frac{E_{th}}{\eta_{th,b}} \cdot Price_{fuel} \quad (3.17)$$

The discounted revenues of the solar systems are calculated using eq. 3.18:

$$R = R_y \frac{(q^n - 1)}{r \cdot q^n} \quad (3.18)$$

where r is the capitalization rate which was set at 3%, and n is the life cycle assumed to be 20 years, and $q=1+r$.

This analysis does not take in account of any possible grants provided by the different Nations.

Table 3.VIII shows the estimated costs of construction of the plants [33].

Table 3.VIII cost of system components.

		PV/T	PV	ST
Panels, structure	€/m ²	300	120	220
Inverter, cable	€/m ²	100	100	-
Hydraulic circuit	€/m ²	100	-	100
Solar tank	€/l	10	-	10
Assembly	€	1000	1000	1000

Figure 3.13 shows the economic analysis for plants installed in Catania, Split and Freiburg.

The cost of construction of the PV/T system is the most expensive respect to any PV-ST configurations. Likewise, the PV/T plant generates more revenue than other solutions. While the construction of the PV system is the cheapest, that is almost less than half the cost of the PV/T plant. It is possible to observe that PV-ST reduces its economic effectiveness increasing the percentage of ST. It is possible to achieve money earnings until the percentage of ST is less than 70%.

In Catania, the discounted revenues of the PV/T are 12660 €, with total money earning of 4340 €. The PV-ST system constituted by 90% PV and 10% ST has revenue of 10740 € and money earnings of 5830 Euro. As regard, the 100% PV arrangements has discounted revenues of 10250 € and total money earning of 6470 €, that is 1.5 times higher than the money earnings of the PV/T system. The PV-ST systems have an economic return higher than PV/T until the PV percentage is higher than 70%.

As regard Split, the revenues of the PV/T fell sharply to 6715 €, as a consequence of the low-price of the energy in Croatia that does not enable to recover the high cost of construction for this solar technology. Indeed, the PV/T plant has a negative economic return of 1605 €. The 100% PV arrangements has revenue of 5610 € and money earning of 1830 €, while PV-ST system achieves money earnings until the percentage of ST is less than 20%. As an example, the PV-ST plant constituted by 90% PV and 10% ST has money earnings of 850 € because of this arrangement has costs of construction that are a little bit higher than 100% PV arrangements.

In Freiburg, the solar plants have about 1.5 times the surface used in Catania and Split. Thus, the costs of construction are of 11480 € for the PV/T plant, that is the most expensive, and 5170 € for the 100% PV that is cheaper. The discounted revenues of the PV/T plant are 16270 €, with money earning of 4790 €, while the 100% PV arrangement has discounted revenue of 14770 € with money earning of 9600 €, which is the arrangement that achieves the highest return of the investments. PV-ST systems allow to achieve money earnings until the percentage of ST is less than 60%, and they have higher economic return than PV/T until the ST percentage is lesser than 30%.

This result demonstrates that the low-cost of the PV panel is the factor that mainly affects the return of the investments, under the terms of this study. However, the higher energy produced by the PV/T system respect to the PV system allows reducing the differences of economic return to just 30%, respect to a difference in the cost of constructions that is more than 50%.

Thus, the solar thermal renewable sources cannot achieve valuable return due to the low-price of the energy under the current economic scenario.

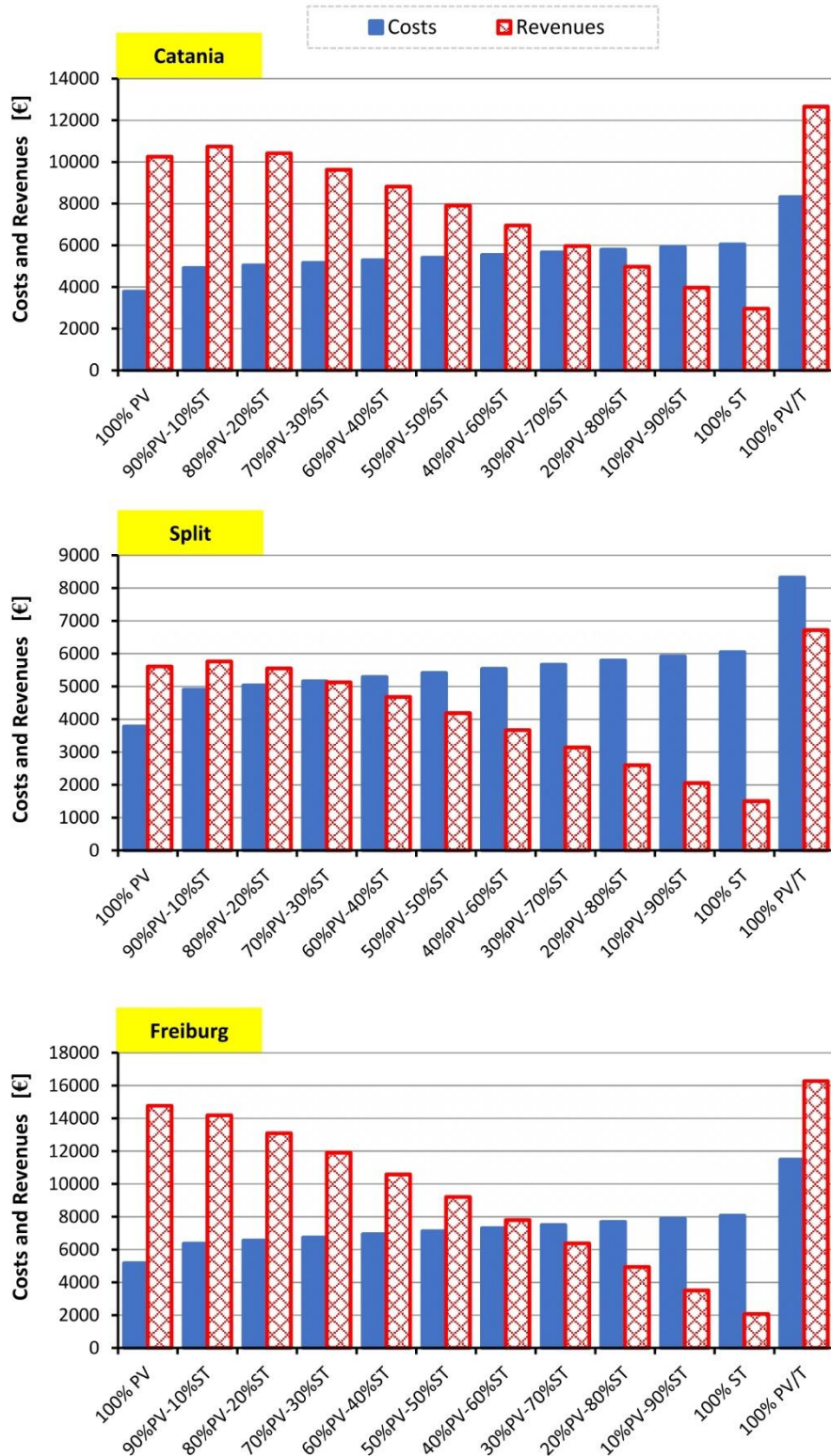


Figure 3.13 – Costs and revenues

This result evidence the low-cost of the PV panel is once again the main factor that influences the economic analysis. Moreover, the cold climate of Freiburg restricts the production of thermal energy through the PV/T system reducing its economic performances.

However, it has to be underlined that the PV/T plants achieve the highest energy savings guaranteeing at the same a valuable economic return.

Surprisingly enough the economic return of both solar systems, in particular the PV plant, has an economic return in Freiburg better than in Catania. Thus, countries that have strong economies draw the highest advantageous in adopting renewable energy source even if they have not an optimal climate for exploiting the solar resource.

3.3 Numerical model and experimental validation of the electrical and thermal performances of photovoltaic/thermal plant

Photovoltaic – thermal (PV/T) collectors can be used to convert solar energy into electricity and heat in a single component allowing, potentially, to increase the overall efficiencies.

Review papers [34-35] have provided a systematic analysis of the historical and recent trend in PV/T technology, concluding that the use of PV/T collectors can lead to both energy and economic benefits.

Several parameters such as the type of fluid, mass flow rate, number of covers and shape of the absorber plate affect the PV/T performance [36].

As regards the electrical yield of PV and PV/T modules, it strongly depends on the temperature of the photovoltaic cells [37]. For modelling of PV/T performances, it is necessary to find the best possible compromise between simplicity and detail. A most basic approximation used in many models is to set the cell temperature equal to the average fluid temperature [38-39]. In other models [40-44], the cell temperature is set equal to the temperature of the absorber plate, based on the assumption that the heat transfer between photovoltaic cells and absorber is very good. In this way, the Hottel Whillier-Bliss equation can be used, while taking into account the energy transformed into electricity. In [45], authors have developed and compared four numerical models, a dynamic 3D model and static 3D, 2D and 1D models. Comparing the numerical and experimental data, they found a maximum error of 5% and that the 1D model, based on the equations of Hottel-Whillier and Klein, was suitable for studies on the annual yield because it presents high computational speed compared to the others. In [46] authors showed that their model (a more detailed version of the Hottel-Willier model) was able to calculate the efficiency of the PV/T system well. In [47] the theoretical cell temperature is calculated as a function of storage tank temperature, the thermal efficiency of the collector and irradiation. The results have been compared with experimental analyzes showing a good correlation. Other models [48-51] assume that the difference in temperature between the photovoltaic cells and the heat transfer fluid is proportional to the useful heat transferred to the fluid. Some literature studies [52-53] evaluated the temperatures of the different layers of a PV/T system through mathematical models.

In this section a validate novel dynamic numerical model developed in Matlab is presented. The model calculates the temperature of the cells by solving the energy balance equation for the various layers that make up the PV/T panel. The proposed model calculates not only the temperatures of each layer of the PV/T module but also the thermal and electrical yields of the plant. The model simulates the behaviour of a complete PV/T plant, constituted by WISC PV/T collectors, hydronic and electric circuits, and thermal solar tank.

The set of equations that constitute the numerical model, is resolved via Runge-Kutta (RK4) numerical method in MATLAB software and are of general application and may be adopted for modelling different PV/T systems that operate under real operative conditions.

3.3.1 Numerical model

The proposed numerical model is based on a pilot PV/T plant, installed at the University Campus of Catania, showed in chapter 2, with which the model was validated.

The overall PV/T plant comprises an active closed-loop system, constituted by two commercially WISC panels DUALSUN Wave©, thermal storage tank, pumping circuit, insulated connection pipes.

The developed numerical models allow to evaluate the thermal behaviour and performance of the PV/T system in dynamic state conditions and are based on energy balance equations.

For each layer (i^{th}) that compose the PV/T plant, the following energy balance has been written:

$$\frac{dE_i}{dt} = \dot{E}_{incoming} - \dot{E}_{outgoing} \quad (3.19)$$

where the first member indicates the stored energy in the layer i^{th} , $\dot{E}_{incoming}$ and $\dot{E}_{outgoing}$ indicate respectively the incoming and the outgoing energy fluxes.

The balance equations are simultaneously solved using the ode45 function in Matlab, modified via the fourth order Runge Kutta method. The simulations were conducted using 1440 daily time steps (time step equal 1 minute).

The climate parameters included in the model are the air temperature, the wind speed and the solar irradiance on the PV/T panel.

The model has been developed under the following assumptions:

- one dimensional (1D) thermal model is used since the thickness of the module is very thin compared with the other two dimensions, thus heat losses at the sides of the PV/T collector are negligible and each layer has a spatially averaged constant temperature;
- the fraction of solar irradiance that is not converted into electrical power by the PV cells is transferred to the system;
- the properties of the materials are considered homogeneous and constant, being the limited temperature range;
- perfect bonding between PV/T components is ensured;
- the heat exchange among cells and EVA is negligible;
- no dust or partial shading on the collector;
- the pipes connecting the PV/T unit with the water storage tank are well insulated, such that there are no heat losses to the environment;
- the water inside the storage tank is fully mixed, that is thermal stratification is neglected.

3.3.1.1 PVT panel

The photovoltaic/thermal (PV/T) panels are uncovered and uninsulated with a roll-bond absorber constituted by two aluminium sheets, joined through a lamination process, where a thin layer of heat transfer fluid is embedded.

The PV/T panel is schematized in the following layers: the front glass, mono-crystalline (c-Si) PV cells, EVA encapsulating film, Tedlar, two aluminium sheet (roll-bond absorber) and the coolant fluid.

Fig. 3.14. shows the cross-section of the module, the equivalent electrical circuit in term of thermal resistances and heat capacities.

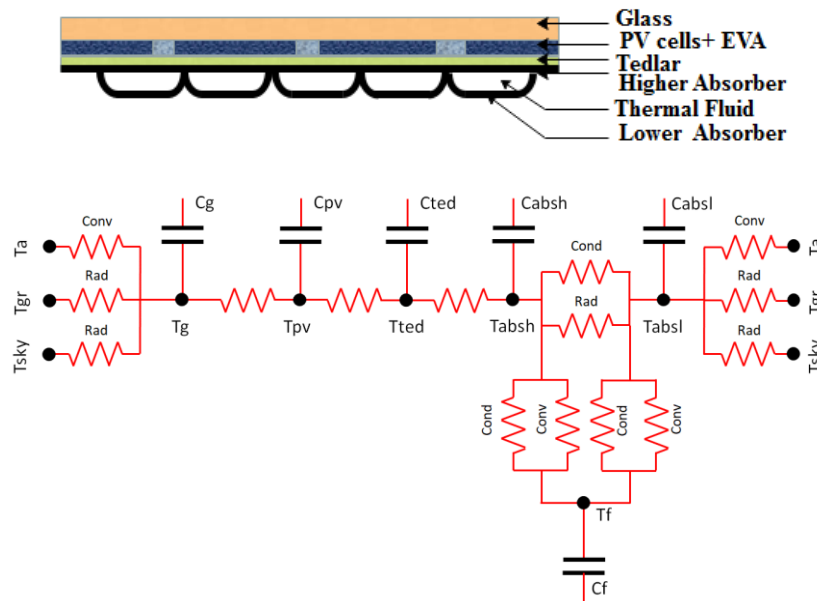


Figure 3.14 - Cross section and equivalent electrical circuit of the PV/T panel

The heat fluxes exchanged among the layers that compose the PV/T panels and the fluxes exchanged with the external environment are governed by the three basic mechanisms of heat transfer: radiation, convection, and conduction.

For the studied PV/T panels, the following thermal fluxes occur:

- convection and thermal radiation between the glass cover “g” of the PV/T panel and the outdoor environment;
- radiation through the glass;
- conduction through the different layers that compose the panel (glass, PV cell “PV”, EVA, tedlar “ted”, upper absorber plate “absh”, and lower absorber plate “absl”);
- convection between the absorber plate and the fluid “f” in the channel;
- radiation between the two absorber plates;
- convection and thermal radiation between the rear part of PV/T module (lower absorber plate) and the outdoor environment.

The conductive heat fluxes are taken into account using Fourier's formulation (Eq. 3.20).

$$Q_{cd} = -kA \frac{\Delta T}{\delta} \quad (3.20)$$

where k , δ and A are the thermal conductivity, layer thickness and surface of the considered layer and ΔT indicates the temperature gradient.

The radiative exchanges have been calculated using the Stefan-Boltzmann law (Eq. 3.21).

$$Q_{rad} = \sigma_0 \varepsilon_i A F (T_i^4 - T_j^4) \quad (3.21)$$

Where i represents the external layer of panel (glass or lower absorber plate), j represents the sky-dome or the ground, σ_0 is the Stefan-Boltzmann constant, ε represent the emissivity of the layer, and F is the view factor calculated using Eq. 3.22 in the case of heat transmission between glass and sky or absorber and ground, while is calculated by Eq. 3.23 in the case of heat transmission between glass and ground and absorber and glass.

$$F = \frac{1 + \cos \beta}{2} \quad (3.22)$$

$$F = \frac{1 - \cos \beta}{2} \quad (3.23)$$

The radiative fluxes between the two absorber plates separated by the fluid (at the channels) are calculated using the view factor for flat and parallel surfaces (Eq. 3.24).

$$F = \frac{1}{\left(\frac{1}{\varepsilon_{absh}} + \frac{1}{\varepsilon_{absl}} - 1\right)} \quad (3.24)$$

The convective exchanges with the outdoor environment are calculated using the Newton formula (Eq. 3.25) where the convective coefficient (h) is calculated using different expressions reported in the document in Appendix 3 [54].

$$Q_{conv} = hA(T_i - T_{amb}) \quad (3.25)$$

As for the working fluid, it remains for a limited time inside the panel, so the formulas in variable rate convection have been used. Therefore, as a function of the residence time (t), the outlet fluid temperature will be given by

$$T_f(t) = T_{abs} + (T_{in} - T_{abs}) e^{\frac{hA}{\rho_f V_f C_f} t} \quad (3.26)$$

While the heat exchanged is equivalent to:

$$Q_{conv} = \dot{m} C_f (T_f(t) - T_{abs}) \quad (3.27)$$

3.3.1.2 Storage tank

In normal operation, the collector outlet flow (flow-rate \dot{m} and temperature T_{out}) enters in the heat exchanger located inside the hot water solar tank (temperature $T_{t,in} = T_{p,out}$) and heats up the water in the tank (mass M_t and temperature T_t). Thus, the fluid reduces its temperature ($T_{t,out}$) and returns to the inlet of the PV/T panel (temperature $T_{p,in} = T_{t,out}$) to be heated again.

The thermal energy coming from the solar panels is transferred to the storage tank for producing domestic hot water. The rate of energy provided by the solar circuit to the tank is calculated from Eq. 3.28,

$$Q_{p \rightarrow t} = \dot{m} C_f (T_{t,in} - T_{t,out}) \quad (3.28)$$

According to Ref. [34], the temperature at the outlet of the solar tank ($T_{t,out}$) is calculated using the effectiveness (ε_H) of the heat exchanger:

$$T_{t,out} = T_{t,in} - \varepsilon_H (T_{t,in} - T_t) \quad (3.29)$$

Moreover, cold water from the mains (temperature T_{sup} and flowrate \dot{m}_l) flows into the tank where it is mixed with the water already contained therein to a temperature T_t . When there is a demand from the household for hot water, water (temperature T_t) is drawn from the tank.

The energy balance of the tank is written considering the heat supplied by the panels, the heat delivered to the user demand and the heat losses with the outside environment and becomes:

$$(M_t C_f) \frac{dT_t}{dt} = \varepsilon_H \dot{m} C_f (T_{t,in} - T_t) - \dot{m}_l C_w (T_t - T_{sup}) - U_t S_t (T_t - T_{amb}) \quad (3.30)$$

Where: C_w is the specific heat of water, U_t is the heat loss coefficient with the outside of the tank ($W \cdot K^{-1} \cdot m^{-2}$), S_t is the external surface of the tank.

3.3.1.3 Overview of the balance equations for the PV/T plant.

In this paragraph are reported the balance equations used in the dynamic model. As regard all the details, see Appendix 3.

In the table 3.IX, the formulas have been synthesized, using the following transformations, respectively for the transmission of heat by radiation, conduction, and convection:

$$hr_{i,j} = \sigma_0 \varepsilon_i A_i F_{i,j} (T_i - T_j) (T_i^2 + T_j^2) \quad (3.31)$$

$$hc_{i,j} = \frac{1}{\frac{\delta_i}{2k_i} + \frac{\delta_j}{2k_j}} A \quad (3.32)$$

$$hv_{i,j} = h_{i,j} A \quad (3.33)$$

Table 3.IX balance equations.

Layers	Equations
Glass	$(\rho_g \delta_g C_g) \frac{dT_g}{dt} = \alpha_g G + hr_{g,sky}(T_{sky} - T_g) + hr_{g,gr}(T_{gr} - T_g) + hv_{g,amb}(T_{amb} - T_g) + hc_{PV,g} PF(T_{PV} - T_g) + hc_{Ted,g}(1 - PF)(T_{Ted} - T_g)$ (3.34)
PV cells	$PF(\rho_{PV} \delta_{PV} C_{PV}) \frac{dT_{PV}}{dt} = [(\tau_g \alpha_{PV} - \eta_{el}) G + hc_{PV,g}(T_g - T_{PV}) + hc_{Ted,PV}(T_{Ted} - T_{PV})] PF$ (3.35)
Tedlar	$(\rho_{Ted} \delta_{Ted} C_{Ted}) \frac{dT_{Ted}}{dt} = (1 - PF) \tau_g \alpha_{Ted} G + (1 - PF) hc_{Ted,g}(T_g - T_{Ted}) + PF \cdot hc_{Ted,PV}(T_{PV} - T_{Ted}) + hc_{absh,Ted}(T_{absh} - T_{Ted})$ (3.36)
Absorber	$(\rho_{absh} \delta_{absh} C_{absh}) \frac{dT_{absh}}{dt} = hc_{absh,Ted}(T_{Ted} - T_{absh}) + (1 - PC) hc_{absl,absh}(T_{absl} - T_{absh}) + PC \cdot hr_{absl,absh}(T_{absl} - T_{absh}) + \dot{m} c_f (T_f - T_{abs})$ $(\rho_{absl} \delta_{absl} C_{absl}) \frac{dT_{absl}}{dt} = hc_{absl,f}(T_f - T_{absl}) + (1 - PC) hc_{absl,absh}(T_{absh} - T_{absl}) + PC \cdot hr_{absl,absh} \cdot (T_{absl} - T_{absh}) + \dot{m} c_f (T_f - T_{abs}) + hr_{sky,absl}(T_{sky} - T_{absl}) + hr_{gr,absl}(T_{gr} - T_{absl})$ (3.38)
Fluid	$(\rho_f \delta_f C_f) \frac{dT_f}{dt} = 2\dot{m} c_f (T_{abs} - T_f) + \dot{m} C_f (T_{out} - T_{in})$ (3.39)
Tank	$(M_t C_t) \frac{dT_t}{dt} = \varepsilon_H \dot{m} C_f (T_{t,in} - T_t) - \dot{m}_l C_w (T_t - T_{sup}) - U_t S_t (T_t - T_{amb})$ (3.30)

3.3.2 Assessment of the numerical model

The validation process entailed a detailed analysis of the behavior of the PV/T panel.

To test the accuracy of the mathematical model, its predictions were compared with the observations obtained from the PV/T pilot plant installed at the university campus of Catania. The PV/T panel modelled in this paper is based on the commercially WISC panel DUALSUN Wave©, as presented in chapter 2. The main features of such panel are reported in table 3.X.

Many technical specifications required for the modelling of this system, though not all, are available in the specifications sheet provided by the manufacturer. The rest of the required parameters have been estimated from [45] and [55].

The module consists of mono-crystalline (c-Si) cells, open-circuit voltage V_{OC} of 38.5 Volt, module efficiency of 15.4% at Standard Test Conditions (STC; $G=1000 \text{ W/m}^2$ and $T_{PV}=25^\circ\text{C}$) and electrical peak power of 250 W. The temperature coefficient (γ) which allow evaluating the decrease of the electrical efficiency used in Eq. 1.16 is equal to 0.44 %/°C. The tilt angle is equal to 25° and azimuth angle is equal to 0° (South-facing). The geometrical and technical specifications of the PV/T module are detailed in Table 3.X.

Table 3.X Characteristic of investigated PV/T module

Layers	Symbol	Parameter	Value
Glazing	A	Aperture area (m ²)	1.66
	L_g	Length (m)	1.677
	W_g	Width (m)	0.99
	δ_g	Thickness (m)	0.003
	C_g	Specific heat (kJ/kg·K)	0.500
	ρ_g	Density (g/cm ³)	2.300
	k_g	Thermal conductivity (W/m·K)	1.0
	α_g	Absorptivity	0.03
	τ_g	Transmittance	0.92
	ε_g	Emissivity	0.95
PV cells	A_{pv}	Area of the PV (m ²)	1.46
	PF	Packing Factor	0.88
	δ_{pv}	Thickness (m)	0.00035
	C_{pv}	Specific heat (kJ/kg·K)	0.757
	ρ_{pv}	Density (g/cm ³)	2.330
	k_{pv}	Thermal conductivity (W/m·K)	168.0
	α_{pv}	Absorptivity	0.93
	η_{ref}	Module efficiency at STC (%)	15.4
Tedlar	δ_{ted}	Thickness (m)	0.0002
	C_{pv}	Specific heat (kJ/kg·K)	1.200
	ρ_{pv}	Density (g/cm ³)	1.500
	k_{Ted}	Thermal conductivity (W/m·K)	0.2
	α_{Ted}	Absorptivity	0.90
Channel Fluid	A_f	Area of channel (m ²)	1.12
	PC	Percentage of channel	0.67
	L_f	Length (m)	1.33
	W_f	Width (m)	0.84
	δ_f	Thickness (m)	0.0015
	C_f	Specific heat (kJ/kg·K)	4.177
	ρ_f	Density (g/cm ³)	0.997
	k_f	Thermal conductivity (W/m·K)	0.606
Absorber plate	δ_{abs}	Thickness(m)	0.001
	C_{abs}	Specific heat (kJ/kg·K)	900
	ρ_{abs}	Density (kg/m ³)	2700
	k_{abs}	Thermal conductivity(W/m·K)	160
	ε_{abs}	Emissivity	0.4

It is possible to notice that the surface where the fluid flows is of about 67% of the total area of the absorber.

In this study, the coolant fluid is still water as in Catania during the period of investigation there is no risk of freezing. However, in cold climate zones, the fluid has to be replaced with a solution

of water and glycol. Consequently, it will be necessary to modify the physical properties of the fluid by considering those of the real coolant fluid.

3.3.3 Model Validation

In this section, the proposed simulation model implemented in MATLAB environment is compared with observed data during the period 7/10 March 2019. The weather variables were set using the data collected by the meteorological station. The thermal load in Eq. 3.30 is not zero only when the tank temperature T_t is higher than 45°C. The mass flow rates used in the simulations are the same as the observed one.

Fig. 3.15 shows the environment temperature (T_a) and the total irradiance on the surface of the PV/T module (G), measured by the weather station located near the pilot PV/T plant.

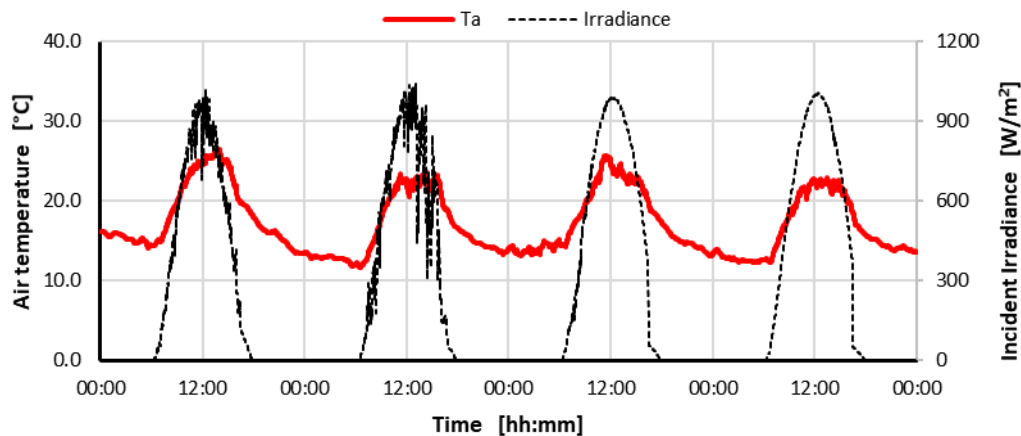


Figure 3.15 - Weather conditions

The following figures show the comparisons between the observed data measured through the monitoring system installed in the PV/T plant and the simulated data during the observation period.

Figures 4 and 5 show respectively the simulated ($T_{c.in,sim}$) and observed ($T_{c.in,exp}$) inlet temperatures in the PV/T collectors and simulated ($T_{c.out,sim}$) and observed ($T_{c.out,exp}$) outlet temperatures in the PV/T collectors.

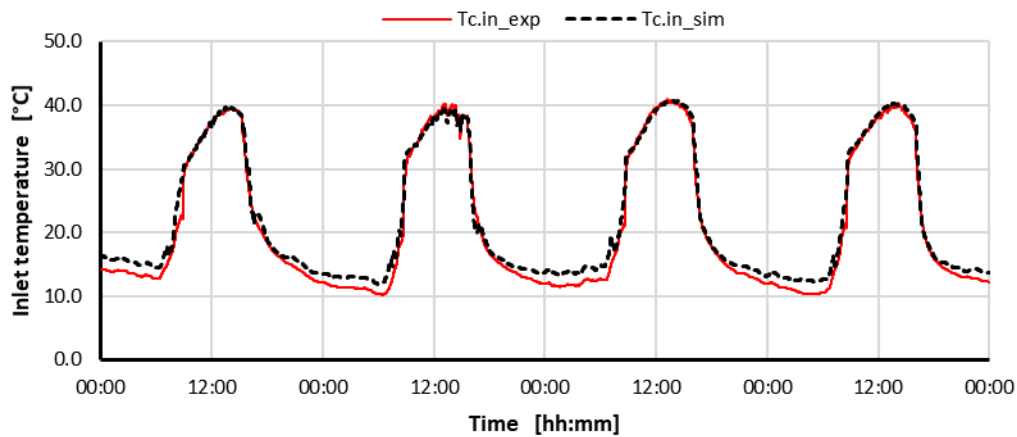


Figure 3.16 - Simulated and observed inlet temperatures in the PV/T panel

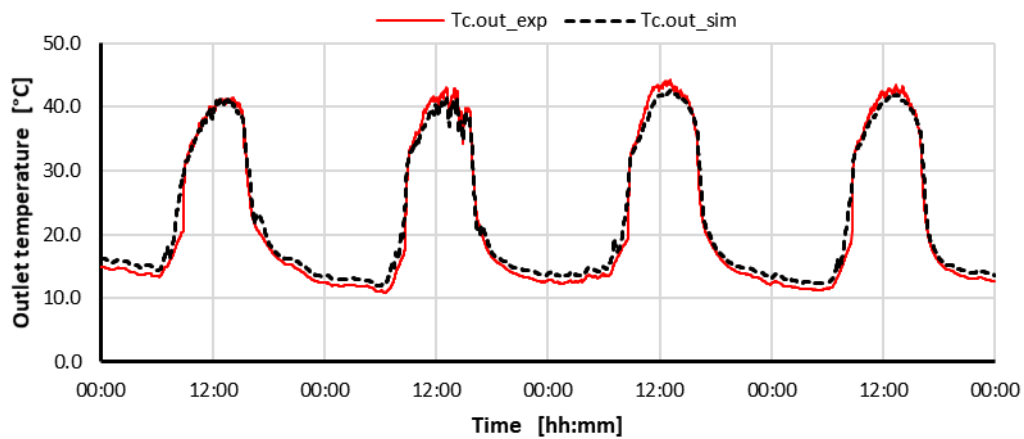


Figure 3.17 - Simulated and observed outlet temperatures in the PV/T panel

As a general result, it can be observed that the inlet water temperature crossing the PV/T panel reaches a maximum average value of about 40.2°C at midday. Likewise, the water at the outlet has a similar trend with a maximum average value of 43.0°C. Thus, a ΔT of about 2.8°C between the inlet and outlet fluid temperatures emerges.

As regards the accuracy of the numerical model, it is possible to observe that during the whole period the two sets of temperatures follow the same pattern with very modest differences. The most significant discrepancies, which appear during the period from sunset to sunrise, may be attributed to the assumptions of neglecting the thermal losses in the hydronic circuit.

Fig. 3.18 shows the simulated and observed mean temperatures of the water inside the solar tank.

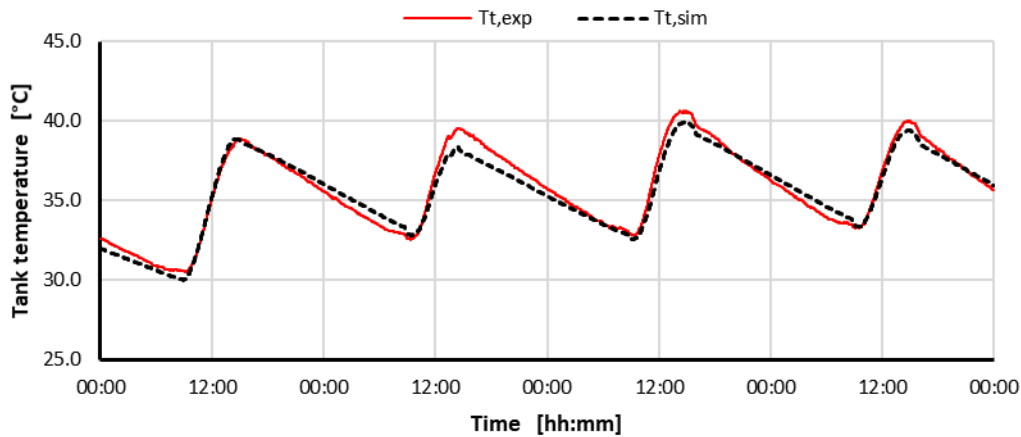


Figure 3.18 - Simulated and observed temperatures in the solar tank

It is possible to highlight that in agreement with the weather data, there is an increase in the tank temperature with the passing of the days. The maximum temperature achieved into the tank is about 40°C and it is attained at about 15:00.

Once again, a good agreement between the simulated and observed data. The biggest differences are observed during the second of the monitored days when the simulated temperature is lower than the observed. These differences could be attributed to the effect of the variable weather conditions, both solar radiation and temperatures, which are more complicated to simulate.

Finally, the analysis of the electrical performance of the PV/T plant is investigated considering the open-circuit conditions. The comparison of the voltage with the panels in open circuit condition (V_{oc}) allows to evaluate the ability of the model to simulate the temperature of the photovoltaic cells, as the V_{oc} directly depends on the temperature:

$$V_{oc} = V_{oc,STC} [1 - \gamma_V (T_{PV} - T_{STC})] \quad (3.40)$$

Fig. 3.19 shows the simulated ($V_{oc,sim}$) and observed ($V_{oc,exp}$) voltage in open circuit condition.

It is possible to highlight that the value of the voltage simulated at open circuit are lower than the observed voltage in the period next sunrise and sunset, when the equation used for evaluating the voltage does not take into account of the effect deriving by the modest solar irradiation, lower than 200 W/m^2 , that hits the solar cell in those period. Otherwise, the comparison between experimental observations and simulation result show a very good agreement during the central part of the day.

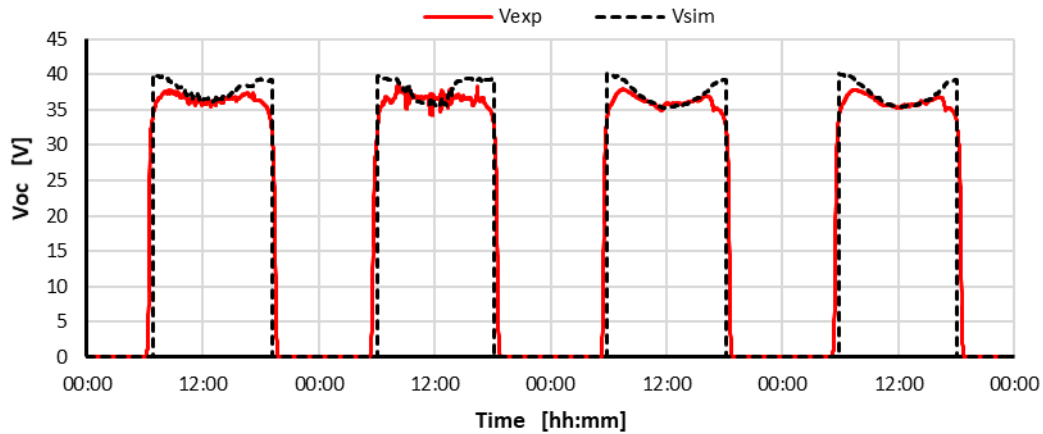


Figure 3.19 - Simulated and observed voltage in open circuit condition

A more detailed analysis for assessing the robustness of the proposed numerical model in evaluating the electrical performance can be carried out through a statistical analysis.

The uncertainty of the PV/T model was assessed using the statistical indicators based on the ASHRAE Guideline 14, which allows to determine the degree of confidence in the true value when using measurement procedures and/or calculations. The accuracy of the presented model is evaluated by means the following indexes Coefficient of Variation of the Root Mean Square Error ($CV(RMSE)$), the coefficient of determination (R^2) and the Normalized Mean Bias Error ($NMBE$). Table 3 shows the values calculated for such indexes, while for the details of the formulas used see Appendix 3.

Table 3.XI Statistical indexes.

Parameter	$CV(RMSE\%)$	R^2	$MBE\%$	$NMBE\%$
$T_{c,in}$	7.0605	0.9934	-5.0758	-1.07765
$T_{c,out}$	6.9935	0.9904	-3.3477	-0.7347
T_t	1.9657	0.9650	-1.4105	-0.4956
V_{oc}	1.0464	0.9981	-1.1479	-6.1403

As the previous results had already highlighted, the proposed numerical model has a good prediction of the thermal parameters with acceptable values of $CV(RMSE\%)$, R^2 , $NMBE$, and MBE . The negative values of both MBE and $NMBE$ indicate the over-estimation of the model. Moreover, it has to be mentioned that these two indexes are subject to cancellation errors especially in the case of a well-calibrated model as in this case. Overall, it is possible to affirm that the proposed model provides quite accurate results. This confirms that the simplifications assumed in the physic models do not diminish the accuracy of its predictions.

3.3.4 Simulations using mathematical model

This section shows some analyzes made with the previously presented and validated mathematical model. In detail, the results of the analysis of the effect of the inlet temperature and the flow rate of the fluid are first shown considering a typical summer day, while the second part shows simulation results performed with real climatic data.

3.3.4.1 Effect of inlet temperature and flow rate on PVT performance

This section shows the effects that the inlet temperature and flow rate generate in terms of the temperature of the fluid at the outlet and the ability to produce energy (thermal and electrical) considering a typical summer day in the city of Catania.

In the simulations typical climatic data for the month of July were used. Fig. 3.20 shows the air temperature and irradiance on the panel plane, while the wind speed is set equal to 1 m/s.

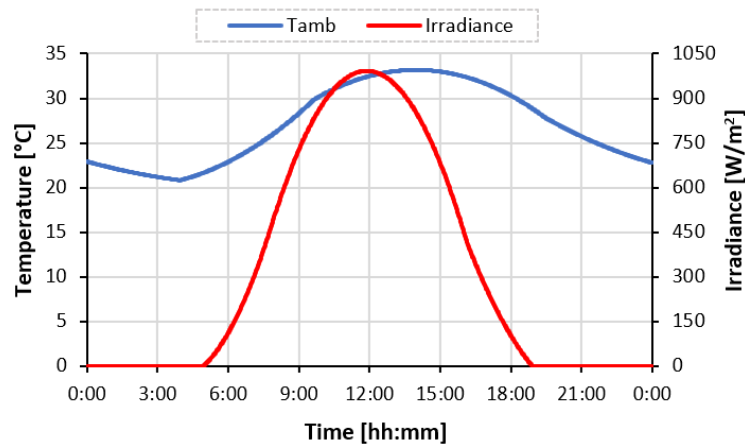


Figure 3.20 – Weather conditions of the typical summer day (July)

Figure 3.21 shows, as the inlet temperature of the fluid varies (from 25 ° C to 45 ° C): top left the efficiency (dashed lines) and electrical power (continuous lines), top right the efficiency (dashed) and the thermal power (continuous), at the bottom, left the efficiency (dashed) and the total power (continuous), calculated respectively using eq. 3.12 and 3.13, and finally at the bottom right the temperature profile of the fluid inside the panel relating to noon.

The results of the simulations show that as the temperature of the inlet fluid increases, the electrical, thermal, and overall efficiencies decrease, as do the instantaneous powers. The electrical efficiency decreases proportionally to the temperature of the cells. Thermal efficiency decreases as the difference between the average temperature of the fluid inside the collector and the ambient temperature increases. Indeed, it can be observed that the thermal efficiency decreases as the inlet temperature increases because this follows the increase in the average temperature of the fluid. In the meantime, with the same T_{in} thermal efficiency tends to increase in the afternoon because the temperature of the external air grows, reducing heat

losses with the environment. Regarding the overall performance, the behaviour reflects what was seen for electric and thermal. However, it can be further observed that the overall efficiency varies from just over 50% for T_{in} equal to 45 °C up to over 80% for T_{in} equal to 25°C. Finally, the fluid temperature profiles show a maximum temperature increase between inlet and outlet of about 15°C with $T_{in}=25^{\circ}\text{C}$, while it results about 8 ° C for $T_{in}=45^{\circ}\text{C}$.

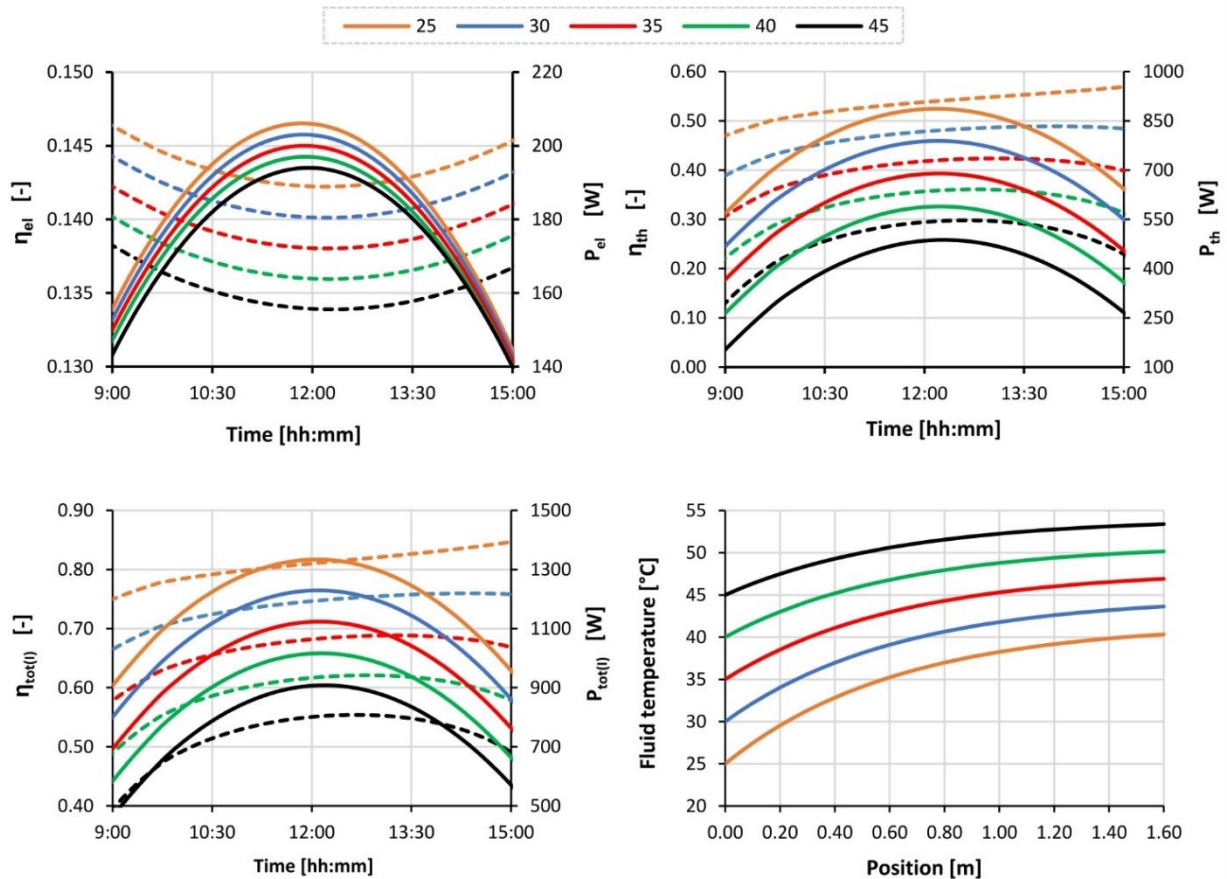


Figure 3.21 – Performances of PV/T panels when the inlet temperature change

Figure 3.22 shows the effect that the flow rate of the fluid generates on the performance of the PV/T.

The simulations were performed for specific fluid flow rates ranging from 30 to 180 kg/(m²h), keeping the $T_{in} = 35^{\circ}\text{C}$. The results show a clear reduction in the temperature of the fluid as the flow rate increases. This generates an increase in performance both in electrical, thermal, and overall terms. However, it should be noted that the effect of increasing the flow rate is very evident for low flow rates, while the passage from 120 to 180 kg/(m²h) hardly produces any advantage, furthermore the increase in flow rates generates an increase in the energy used for pumping, which therefore still reduces the advantages.

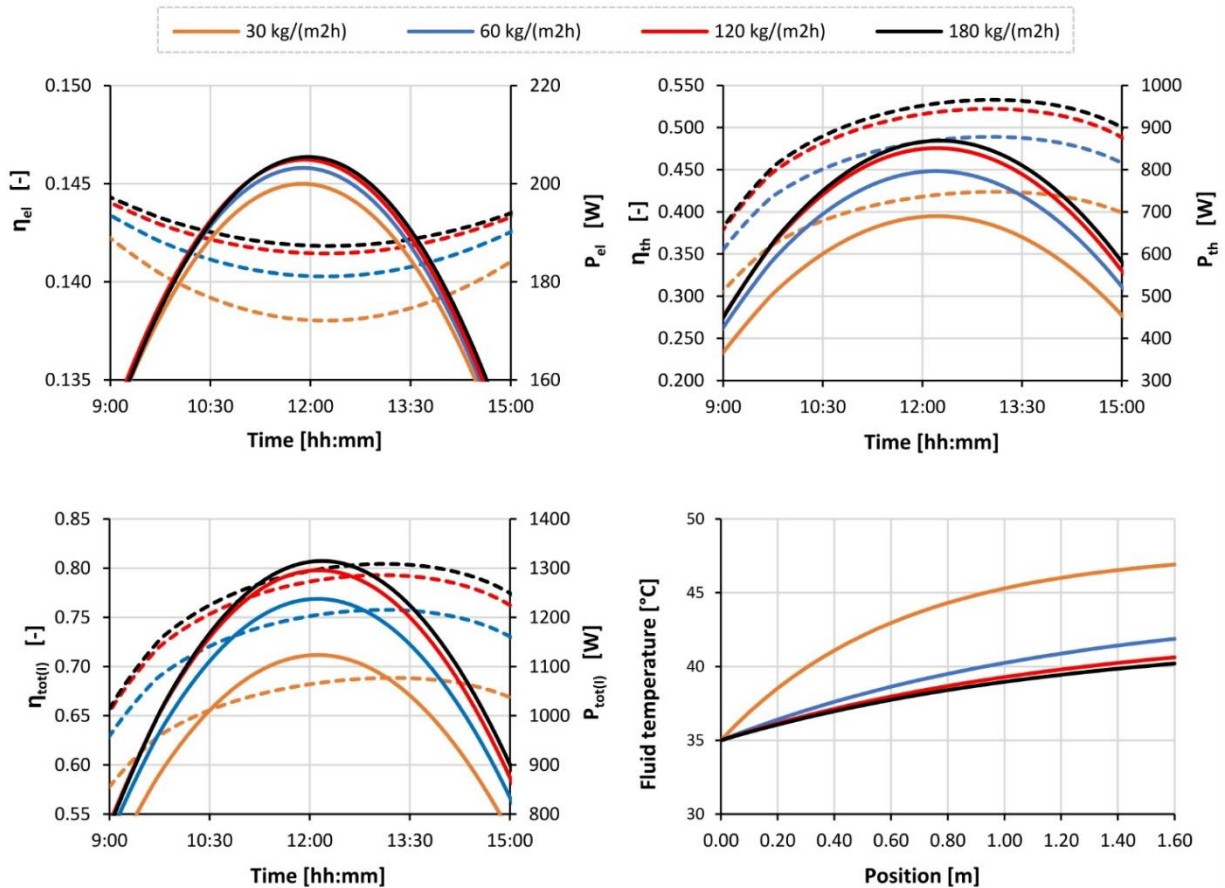


Figure 3.22 – Performances of PV/T panels when the flowrate change

3.3.4.2 Simulations under real in condition

This section shows the temperatures of the various layers and the producibility considering the real climatic conditions showed in the previously Fig. 3.15.

One of the main challenges for predicting the electrical efficiency is the calculation of the PV cells temperature, in particular for the PV/T modules where such temperature is influenced by the temperature of the fluid. Thus, it is worth of interest to observe the mutual relations among the PV cells temperature and the average fluid temperature (T_f).

Fig. 3.23 shows the daily variation of the cells temperature T_{pv} , the mean temperature of the fluid T_f , the temperature of the upper and lower absorber plate (T_{absh}) and (T_{absl}), as well and the environment temperature (T_a) during a clear sky day (9 March). The right side of figure 3.23 shows the enlargement of the above-mentioned temperature during the hottest period of the day.

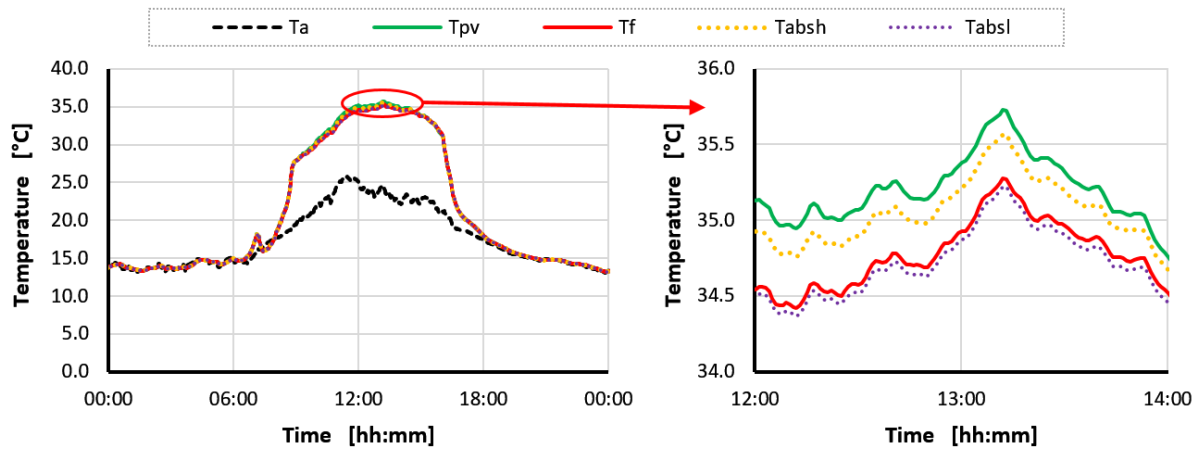


Figure 3.23 – PV cells, fluid, absorber plate and environmental temperatures

The photovoltaic cells reach maximum values of temperatures of about 35.7°C with solar irradiation of about 1000 W/m². This means that the electrical efficiency of the PV/T module should diminish to about 0.7% respect to the reference value.

During the daytime, the temperature of the photovoltaic cells is very close to the mean fluid temperature (Tf). Tpv is 0.7°C higher than the mean fluid temperature during the hottest hours of the day, while such difference diminishes considerably during the other period of the day.

Figure 3.24 shows the daily electrical (EI) and the thermal performance (Th) of the PV/T plant during a clear sky day (9 March), considering the plant at the MPP conditions.

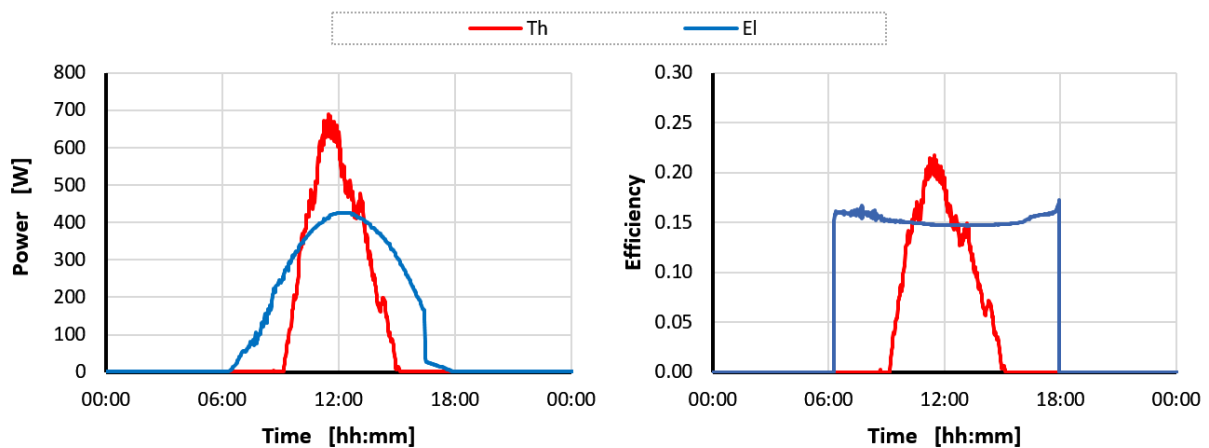


Figure 3.24 – thermal and electrical power (at left) and efficiency (at right) of the PV/T plant

At midday with a value of solar irradiance of about 1000 W/m², the PV/T solar plant provides a power and thermal production of about 430 W and 690 W respectively, to which corresponds an electric and the thermal efficiencies of about 14.7%, and 21.7% respectively.

Thus, this system allows to produce electrical power that is rather close to the peak, that is 500 W. The thermal power could seem modest if compared with the nominal power, that is of about 1650 W, however, it has to be highlighted that the PV/T plant operates with relatively high temperature, of about 35°C, and this power will be lost in a conventional PV plant.

For evaluating the performance of PV/T plant over a period, the energy values in a certain time (day, month, year) have to be evaluated.

Table 3.XII shows the electrical (E_{el}) and the thermal performance (E_{th}) as well as the total performance ($E_{tot(l)}$, $\eta_{tot(l)}$) of the PV/T plant during a clear sky day (7/10 March).

The total performances are calculated valorizing the two different forms of energy. Moreover, the electrical performance of the PV/T plant is also evaluated using the performance ratio PR, which is defined in section 1.4.1.

Table 3.XII Daily results.

Days	G [kWh/m ²]	E_{el} [kWh/m ²]	PR [-]	E_{th} [kWh/m ²]	E_{tot} [kWh/m ²]	η_T [%]
03/07	6.01	0.79	0.872	0.56	2.27	37.8
03/08	6.07	0.80	0.878	0.45	2.19	36.1
03/09	6.61	0.87	0.872	0.65	2.54	38.4
03/10	6.79	0.89	0.875	0.54	2.48	36.6

Data summarized in table 3.XII give a comprehensive outlook of the performances of the PV/T plant. The performance ratio gives speedy information on the amount of electrical energy produced in comparison to STC condition. The values of the PR index close to 1.0 indicate that the PV/T system worked nearest to the optimal operative mode, thanks also to the not too much high PV cell temperature (i.e. less than 36°C). This assessment is confirmed by the low values of the daily thermal energy, which indicates that the WISC PV/T module operated favouring the PV cell electrical performance (MPPT conditions). The average efficiency also shows approximately constant performance of around 37%.

3.4 Analysis of the impact of nanofluid in the energy produced and energy quality in photovoltaic-thermal systems

Several comparative studies [28, 56-57] show that PV/T systems can produce more energy per unit area than any combination of conventional solar systems. Therefore, it is not surprising that in recent years important research has been dedicated to the various parameters that can increase energy production, such as the different geometric design and materials [58-61]. An alternative concern the use of heat transfer fluid with better performance than simple water. Despite the high thermal capacity of the water, which makes it a good heat storage vehicle, its thermal conductivity is low and therefore the heat transfer is limited. Starting from 1995 [62], many researchers have suggested the adoption of nanoparticles to be added to the base fluid to form a suspension with high thermal conductivity, i.e. nanofluids. Nanofluids are solid-liquid composite materials consisting of solid nanoparticles or nanofibers with sizes typically of 1–100 nm suspended in liquid [63]. Various studies have shown that nanofluids have substantially higher thermal conductivities than base fluids [64-67]. Finally, practical studies have shown that nanofluids are preferred over base fluids, as they allow increasing electrical and thermal efficiency [68-71].

In this section, the effects on PV/T performance, by changing the working fluid from pure water to a nanofluid composed by water and aluminium oxide (Al_2O_3) are studied using a validated numerical model shown in section 3.3.

3.4.1 Methodology

The study on the performance of a PV/T system was carried out considering two different heat transfer fluids: pure water and nanofluid. The nanofluid is composed by pure water and nanoparticles of aluminum oxide (3% by weight), with a volumetric ratio (ϕ) calculated by Eq. 3.41.

$$\phi_{nf} = \frac{m_p/\rho_p}{m_p/\rho_p + m_f/\rho_f} \quad (3.41)$$

where m is the mass, ρ is the density and subscripts p , f and nf represent respectively: nanoparticles, fluid (pure water) and nanofluid. All the thermos-physical properties of the water and of the nanofluid are reported in table 3.XIII, which have been calculated using the Eq. 3.42, 3.43, and 3.44 [72].

$$\rho_{nf} = \phi \cdot \rho_p + (1 - \phi) \cdot \rho_f \quad (3.42)$$

$$C_{nf} = \frac{\phi \cdot \rho_p \cdot C_p + (1 - \phi) \cdot \rho_f \cdot C_f}{\rho_{nf}} \quad (3.43)$$

$$k_{nf} = \frac{k_p + 2k_f + 2\phi(k_p - k_f)}{k_p + 2k_f - \phi(k_p - k_f)} k_f \quad (3.44)$$

Table 3.XIII Properties of the fluids.

Properties		<i>Pure water</i>	<i>Nanoparticles</i>	<i>Nanofluid 3%/w.</i>
ρ (density)	[kg/m ³]	0.79	0.872	37.8
C (specific heat capacity)	[J/kg/K]	0.80	0.878	36.1
k (thermal conductivity)	[W/m/K]	0.89	0.875	36.6

The numerical simulation was conducted using the Matlab numerical model explained and validated in section 3.3 and were conducted under dynamic state conditions.

The simulation models the PV/T system installed at University of Catania (IT), so was conduct considering the plant equipped with two commercially WISC panels DUALSUN Wave©, with a total surface of 3.32 m², hydraulically connect in series and connect with a storage tank which has a volume of 170 l. The module consists of mono-crystalline (c-Si) cells, which provide a module efficiency of 15.4% at Standard Test Conditions, with electrical peak power of 250 W. The efficiency loss with temperature coefficient (γ) is 0.44%.

PV/T plant produces simultaneously the thermal and electrical energy. The comparison was based on the thermal and electrical energy produced, respectively E_{th} and E_{el} . However, these two forms of energy have not the same quality, thus this analysis was developed taking into account the second law of thermodynamics, through the primary energy produced ($E_{tot(I)}$), as well as the Overall Exergetic Content (Ex_{tot}), using respectively the Eq. 1.33 and Eq. 1.35 previously defined.

From the thermal quality point of view, it is worth of interest to evaluate the increase of Thermal Level (T^+_{nf}) of the cooling fluid, calculated with the Eq. 3.45.

$$T^+_{nf} = \frac{T_{out,nf} - T_{out,w}}{\Delta T_{out-in}} \times 100 \quad [\%] \quad (3.45)$$

3.4.2 Results

The first part of this study analyses the differences in terms of the temperature of the fluid outlet from the PV/T panels, the temperature of the photovoltaic cells, the difference in electrical efficiency, considering different inlet temperature. In the second part, a comparison is developed in terms of thermal and electrical energy produced as well as the study of the total energy produced considering the first and second principles of thermodynamics, under real climatic data.

3.4.2.1 Thermal comparison during a day type

In this section, the comparison of the working temperatures of the PV/T panel in case of using water or nanofluids as cooling fluid, are discussed. The analyses were carried out considering a typical summer day (showed in fig. 3.25).

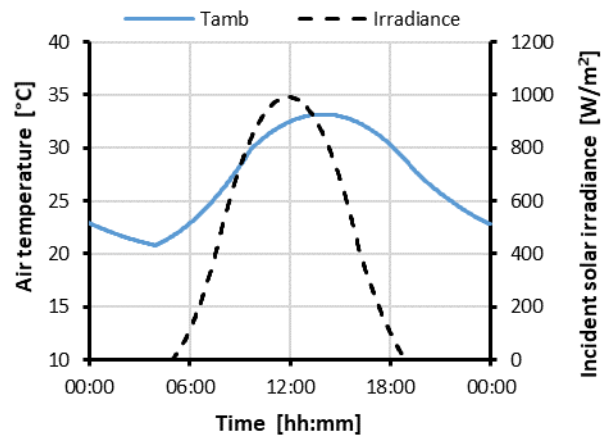


Figure 3.25 – Weather condition during a typical summer day

Fig. 3.26 shows the comparison of the outlet temperatures for the two fluids analyzed and the increase of thermal level, varying the inlet temperatures (T_{in}) from 25 to 45°C and considering a constant flow rate of 30 kg/(h·m²).

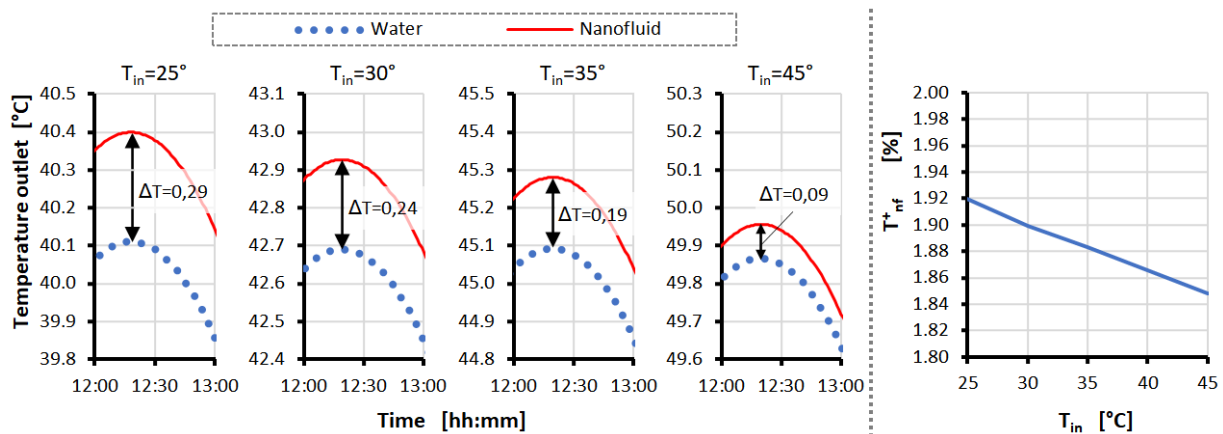


Figure 3.26 – Outlet temperatures and increase of thermal level.

It can be observed that the outlet temperature is greater in the case of use of the nanofluid. Moreover, when the inlet temperature increases, the difference between the two fluids is reduced, from about 0.29° to about 0.09°C. This means that the use of the nanofluid increase the thermal level of about 1.9% respect to pure water.

According to the outlet temperature, T_{PV} increase with a maximum difference of about 0.08°C. Therefore, the electrical efficiency decreases of only 0.04% in the worst case.

3.4.2.2 Effect of the use of nanofluids on PV/T plant performance, under real weather conditions

In this section, the effects when the coolant fluid change in a real plant is analyzed during the period from 7 to 10 March 2019, data already presented previously.

Fig. 3.27 shows the average temperature reached in the thermal storage for both the fluids analysed.

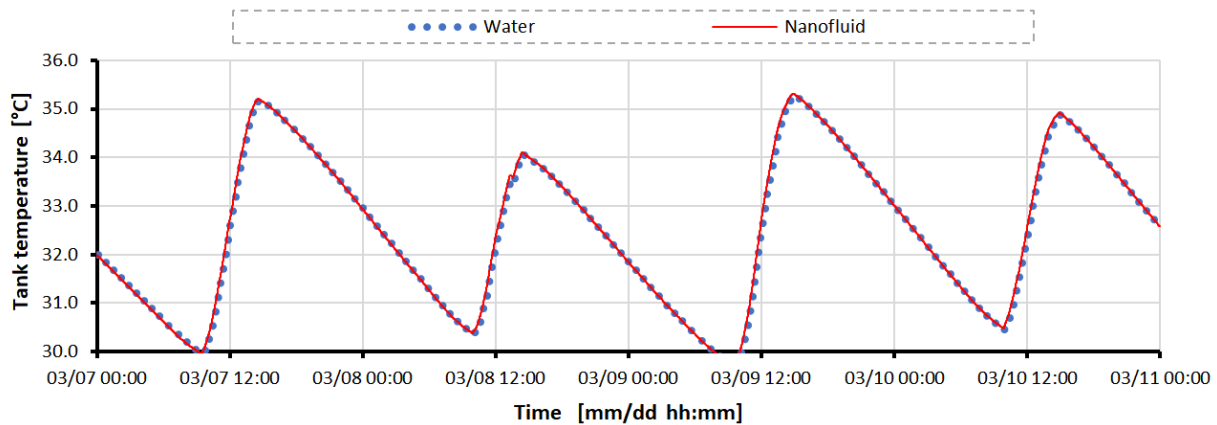


Figure 3.27 – Average tank temperature during the simulation period for both fluids.

It is possible to highlight that the trend of temperature into the thermal storage are quite similar for both fluids. And that the exploitation of the nanofluid allows to slightly increase the daily temperature into the thermal storage.

The daily thermal and electrical energy produced, the primary energy produced ($E_{tot(l)}$), and the Overall Exergetic Content ($E_{\chi,tot}$) are summarized in table 3.XIV.

The results show that the thermal energy produced undergoes a slight increase using nanofluids, while electricity losses are negligible. Indeed, the reference temperature of photovoltaic cells increase in the case to use nanofluid from 0.04 to 0.05°C.

Full considerations, conclusions and future developments are reported in the document reported in Appendix 4.

Table 3.XIV Daily results.

		03/07		03/08		03/09		03/10	
		Water	Nanof.	Water	Nanof.	Water	Nanof.	Water	Nanof.
$T_{amb,av}$	[°C]	18.42		16.52		17.58		16.34	
G	[Wh/m ²]	6013		6070		6607		6794	
$E_{\chi,sun}$	[Wh/m ²]	5781		5842		6356		6540	
$T_{char,PV}$	[°C]	34.59	34.63	33.46	33.50	35.25	35.30	34.35	34.39
E_{el}	[Wh/m ²]	780	780	792	792	855	855	883	883
E_{th}	[Wh/m ²]	310	312	221	221	333	334	263	264
$E_{tot(l)}$	[Wh/m ²]	2006	2007	1943	1944	2191	2192	2184	2184
$E_{\chi,tot}$	[Wh/m ²]	797	797	805	805	874	874	899	899
ε_T	[%]	13.79	13.79	13.78	13.78	13.75	13.75	13.75	13.75

3.5 Analysis of the impact of Phase Change Materials in the electrical yields of photovoltaic systems

As the rise in the temperature of photovoltaic (PV) cells leads to a decrease in the solar to electricity conversion efficiency, many methods have been planned to cool the PV cells [11, 73-75]. They may be differenced into two major categories, active cooling and passive cooling. The active cooling techniques requires energy to operate, while passive cooling techniques do not require energy supply to operate. One of the main passive cooling techniques is the use of phase change materials (PCM). PCMs may enable the PV module to operate with good solar electrical conversion efficiency as they absorb energy as latent heat at a constant phase transition temperature. So, the use of PCM creates a temporary shift in temperature rise [76]. PCM can temporarily store renewable or cheap heat or cold respectively and make it available again later when it is needed.

Several literature studies have shown that the use of PCM inside tanks attached to the rear of the PV panel allows the temperature of the PV cells to be controlled for a certain period [77], the increase in latent heat capacity improves the PV performance [78], the greatest electrical producibility is obtained with PCMs that have fusion temperatures close to the air temperatures [79-80], PCM having a lower melting temperature (near to ambient) can maintain the PV at a lower temperature, bus larger quantity PCM of is necessary [81].

A very important and even neglected topic is the study of the performance of a PV-PCM under real irradiation and ambient temperature.

The following paragraphs will show the study of the effect of using PCM on the performance of PV systems installed in the Mediterranean area. The daily variation of the cell temperatures, as well as the electrical performance of the PV-PCM module, are compared with that one of a conventional PV module considering the winter solstice, autumn equinox and summer solstice.

Using a novel CFD model the non-steady-state conditions were simulated considering the real weather conditions, such as the hourly daily solar irradiation, environment temperature, and wind velocity. The simulations are extended for two days, so in this way, it is possible to take into account the actual degree of PCM solidification/melting that occurs during such period.

3.5.1 Phase Change Material

In the last 15 years, scientists are using PCMs in many and varied applications, the interest in these materials is born because of the possibility to store a great amount of energy maintaining the temperature at a constant value.

Ideal PCMs must have a large latent heat of fusion, usually, it is good to have it greater than 150 J/g, because the greater the latent heat the less the quantity of material needed to store a certain amount of energy high thermal conductivity, the melting temperature must be in the practical range of operations, low cost, non-toxic and non-corrosive and so it is also better than the PCM is as dense as possible [82].

Another important parameter is the thermal conductivity which represents the ability of a substance to transmit heat, therefore the higher the thermal conductivity the faster the heat transfer. Also, the solidification and melting temperature must be the same or in any case with small differences, many PCMs freeze or melt in an interval of different degrees and therefore will present thermal hysteresis, which therefore leads to a loss of energy in a system. Furthermore, the latent heaters of the PCM cannot be exploited if the thermal hysteresis exceeds the operating temperature range. Finally, PCMs must be chemically stable, as they are subject to different melting/freezing cycles and this could affect melting and freezing points and their latent heat.

PCMs find several applications. Everything is based on the principle that when during solidification it emits energy avoiding a sharp reduction in temperature, on the other hand, if the PCM is in solid form, it can subtract a certain amount of heat avoiding overheating. The phase change occurs at a fixed temperature. In the case of constant specific heat capacities for each phase, the temperature field can be defined as:

$$T = \begin{cases} \frac{E}{c_s} & T < T_m & \text{(solid phase)} \\ T_m & T > T_m \text{ and } 0 < E < H & \text{(melt zone)} \\ T_m + \frac{(E - H)}{c_l} & T > T_m \text{ and } E > H & \text{(liquid phase)} \end{cases} \quad (3.46)$$

The use of PCM gives better results in those places where there is a good difference in temperature between day and night, in fact in this way it is possible to guarantee a complete solidification of the PCM overnight and the following day its latent heat can be fully exploited. To achieve this, it is necessary to carefully choose the type of PCM to be used and therefore its melting temperature.

Paraffins and in general organic PCMs are more applicable to PV system cooling, as they have excellent thermal stability with regards to cycling, which is important in a system that heats up and cools down daily [83].

3.5.2 Methodology

The conventional PV modules are composed of glass, PV cells, EVA encapsulating film and Tedlar, where the PV cells absorb solar energy to transform it into electricity. However, the transformation efficiency is strongly influenced by the temperature of the cells themselves and with increasing temperatures the efficiency tends to decline (Eq. 1.16). Furthermore, the layers that make up the panel have a very small thickness and therefore small masses and so low thermal inertia. Thus, as soon as the solar irradiation grows, they heat up quickly, making production efficiency decline [84].

The possibility to improve the performances of the conventional photovoltaic modules through the passive cooling of photovoltaic cells, using phase change materials (PCMs) are performed comparing the thermal behaviour (through PV cell temperature) and the electrical yields.

The study of thermal behaviour and energy performances of PV equipped with PCM (PV-PCM) and conventional PV module (PV), is carried out in dynamic state conditions through Computational Fluid Dynamics (CFD) analysis using the ANSYS Fluent software [85]. This analysis allows evaluating in a detailed way all the heat fluxes occur, the real thermal inertia of the system and the melting process.

Figure 3.28 shows the main thermal fluxes for the PV-PCM, that can be summarized as:

- convection and thermal radiation between the front of module (glass) and the outdoor environment;
- reflection of part of the incident solar irradiation on the glass;
- transmission and absorption of the incident solar irradiation through the glass;
- absorption of the remaining part of the incident solar on the PV cells with the conversion of a part of it into electricity;
- conduction through the different layers;
- heat transfer between the tank wall and the PCM;
- storage or disposal of energy during the phase change by the PCM;
- convection and thermal radiation between the back surface of the PV module and the outdoor environment.

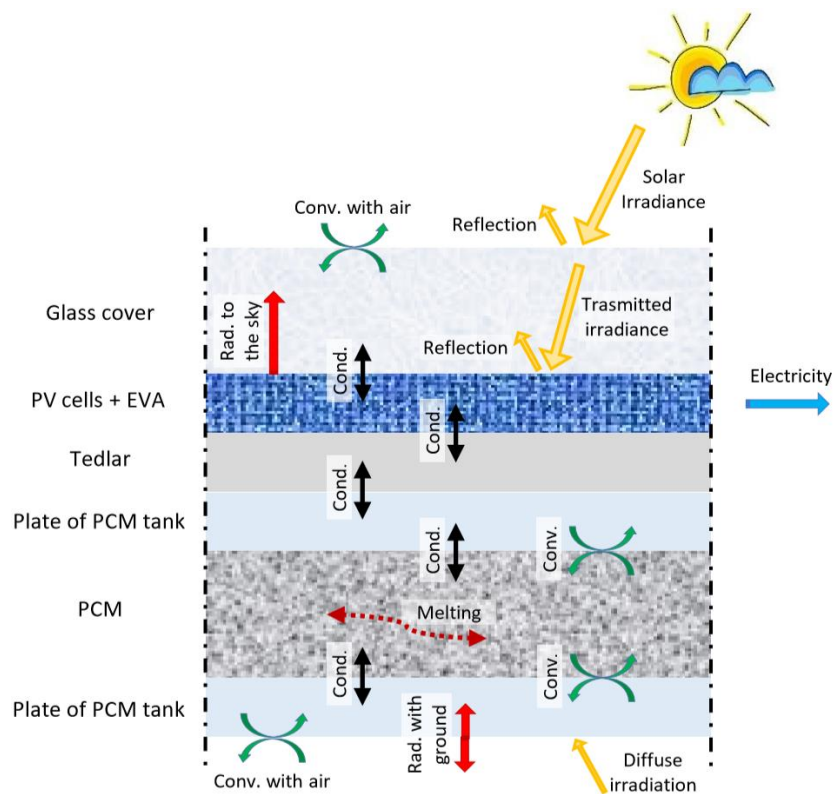


Figure 3.28 – Energy fluxes in PV-PCM module.

The container filled with the PCM is constituted by a tank constituted by aluminium sheets.

Two bi-dimensional model are been developed, one for PV and one for PV-PCM module. The PV's geometry is composed by various layers that compose the PV module, while in the PV-

PCM's geometry the PCM tank, constituted by two aluminium sheets where inside there is the PCM, is added.

Both geometries have a length of 1.0 m. The mesh is of structured type, composed of only quadrangular elements, where the smallest has size 0.0001m x 0.0003m and the largest has size 0.0007m x 0.0008m. Finally, the report orthogonally quality is equal to 1.0 and the ortho skew is 0.0, this means that the mesh is of high quality.

The continuous variation of climatic conditions (air temperature, solar irradiation), as well as the electricity generated, were implemented using specific User Defined Functions (UDFs). The incident solar irradiation available (G_{eff}) on the PV cells is calculated using the Eq. 3.47.

$$G_{eff} = G \cdot \tau_g \cdot \alpha_{PV} \cdot (1 - \eta_{el}) \quad (3.47)$$

where G in the total irradiance on the plane of the module, τ_g is the transmission coefficient of irradiation through the glass cover, α_{PV} represents the absorption coefficient of PV cells and η_{el} is the instantaneous electrical efficiency of the module, calculated using Eq. 1.16 and here reported.

$$\eta_{el} = \eta_{STC} \cdot [1 - \gamma(T_{pv} - T_{STC})] \quad (1.16)$$

The radiative exchanges between the front of PV module and the sky-dome have been implemented with a specific UDF and are calculated using the Stefan-Boltzmann law:

$$Q_{g,sky} = \sigma_0 \varepsilon_g A F (T_g^4 - T_{sky}^4) \quad (3.48)$$

where σ_0 is the Stefan-Boltzmann constant, ε_g represent the emissivity of the glass and F the view factor. Likewise, the radiative fluxes between the rear part of the panel and the ground were calculated, where the glass is replaced with the back of the panel and the sky with the ground.

According with [17] the coefficient of convective flux with the air was calculated using Eq. 3.49, where u represents the wind velocity expressed in m/s.

$$h = 5.7 + 3.8 \cdot u \quad (3.49)$$

As already seen, the instantaneous electrical power (P_{el}) and the energy produced in a period of time by the PV panel are calculated from the irradiance on the collector plane G , the surface of the PV cells A and the electrical efficiency (η_{el}) respectively using Eq. 1.23 and Eq. 1.22:

$$P_{el} = \eta_{el} A_{PV} G \quad (1.23)$$

$$E_{el,PV/T} = \int_0^t P_{el} dt \quad (1.22)$$

3.5.3 Case Study

The scenarios analyzed refer to a PV module with and without PCM container attached at its rear. The reference PV module presents the reference efficiency (η_{STC}) equal to 17% and the thermal coefficient (γ) equal to 0.4%/K.

All the layers properties that compose the reference system are reported in table 3.XV.

Table 3.XV Properties of the layers that make up the PV and PV-PCM modules.

Layer	C [J/(kg·K)]	k [W/(m·K)]	ρ [kg/m ³]	δ [mm]
Glass	500	1.80	3000	4.0
EVA	2090	0.35	960	0.5
Silicon	677	148	2330	0.3
Tedlar	1250	0.20	1200	0.1
Aluminum	903	211	2675	4.0

The container layer is composed by two aluminum sheet which leave a layer available for the PCM with thickness of 6 cm, that is the optimum thickness when the solar radiation and outdoor temperature are high, and the wind velocity is low [86].

The PV-PCM study was conducted considering two different types of PCM, which are: Rubitherm 28 HC and Rubitherm 35 HC. The types of PCMs chosen have good stability and are PCM with high capacity to accumulate energy while maintaining the almost constant temperature during the solidification/melting transformation. Table 3.XVI shows the main properties of the PCMs used.

Table 3.XVI Properties of used PCMs.

		Rubitherm 28 HC	Rubitherm 35 HC
$T_{melting}$	°C	27-29	34-36
$T_{congeling}$	°C	29-27	36-34
H^1	kJ/kg	250	240
C_p	kJ/(kg·K)	2.00	2.00
ρ_{solid}	kg/l	0.88	0.88
ρ_{liquid}	kg/l	0.77	0.77
k	W/(m·K)	0.20	0.20

Notes: 1. Combination of latent and sensible heat in a temperature range, respectively for Rubitherm 28 HC and 35 HC from 21°C to 36°C and from 27°C to 42.

The simulations are carried out considering the modules located in the Mediterranean climate, specifically in the city of Catania (IT) (37° 30' 0" N - 15° 6' 0" E), where are assumed the modules

facing south, with a tilt angle of 30 °C. The weather data, solar irradiance, and air temperature used were taken from PV-GIS database [87].

All comparisons were done considering and evaluating the performance during three “representative” clear days: winter solstice, autumn equinox and summer solstice, for which in figure 3.29 are shown the outdoor temperature (continuous line) and the incident solar irradiation (dashed line).

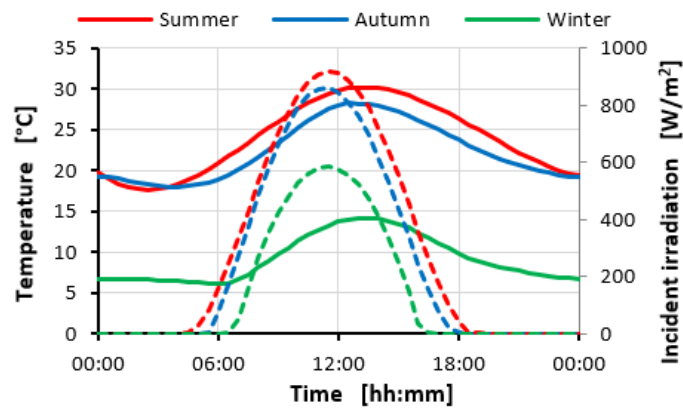


Figure 3.29 – Weather data during summer solstice, autumn equinox and winter solstice

Finally, the wind speed is considered constant for all the scenarios and equal to 1.0 m/s.

3.5.4 Results

This section compares the thermodynamic behaviours and the energy performance of the conventional PV module with the two PV-PCM modules, equipped one with Rubitherm RT 28 HC (PV-RT28) and the other with Rubitherm RT 35 HC (PV-RT35).

To properly evaluate the effective performances of a PV-PCM module it is mandatory taking into account the degree of solidification achieved by the PCM during the night. Thus, the analysis is conducted considering two identical days. In the following, the results showed are referred to the second day of simulation.

Figure 3.30 shows, regarding the summer solstice, at left the comparisons of the temperature of the photovoltaic cells obtained for the three PV-configurations, analyzed and right the rate of liquefaction of the two PCMs at 4:30 and 12:00.

The attachment of the PCMs in the PV module allows decreasing of the cell temperatures. It can be noted that the PV-RT35 leads to attaining a reduction of the cell temperature during the whole day, up to a maximum of 20°C at midday during the summer solstice. PV-RT28 shows the same or even higher reduction of temperature in the first half of the day, then about at noon the temperature raises abruptly as the RT28 loses its capacity to store the heat, the liquefaction process is completed (fig. 3.30 right side), otherwise, the RT35 has a liquid fraction less than

50%. Anyway, the highest temperature of the cells in PV-RT28 is 8 °C lower than the maximum temperature touched by the conventional PV module.

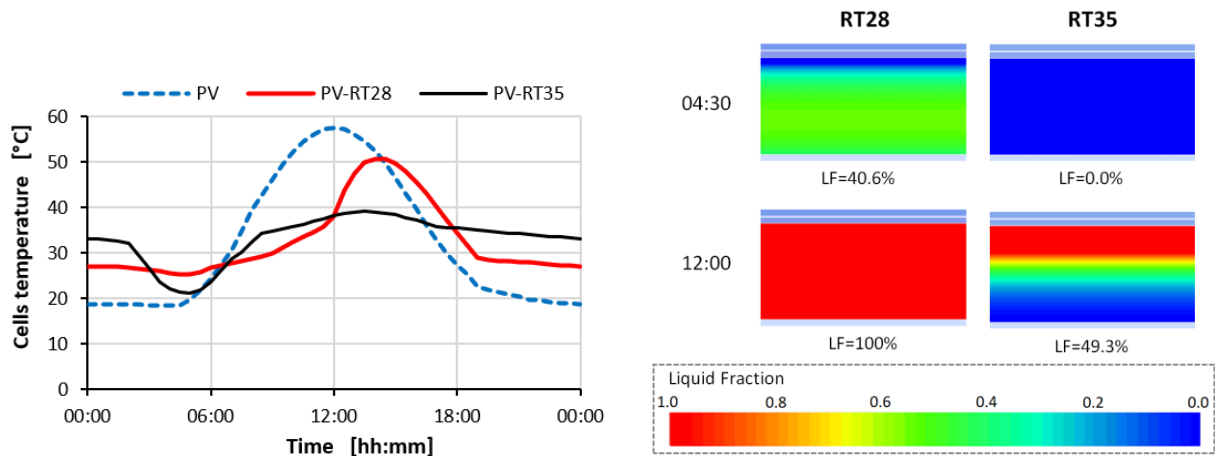


Figure 3.30 - PV cells temperature profile (at left) and liquid fraction (at right) during summer solstice

Moreover, RT35 works all day, reaching the maximum liquid fraction of 93.8% at 16:30. Finally, it is important to note, that RT28 does not solidify completely overnight, which reaches the lowest liquid fraction of 40.6% at 4:30, while RT35 solidifies completely during the night.

Figure 3.31 shows the comparisons of the temperature of the cell respectively at left considering the autumn equinox and at right during the winter solstice.

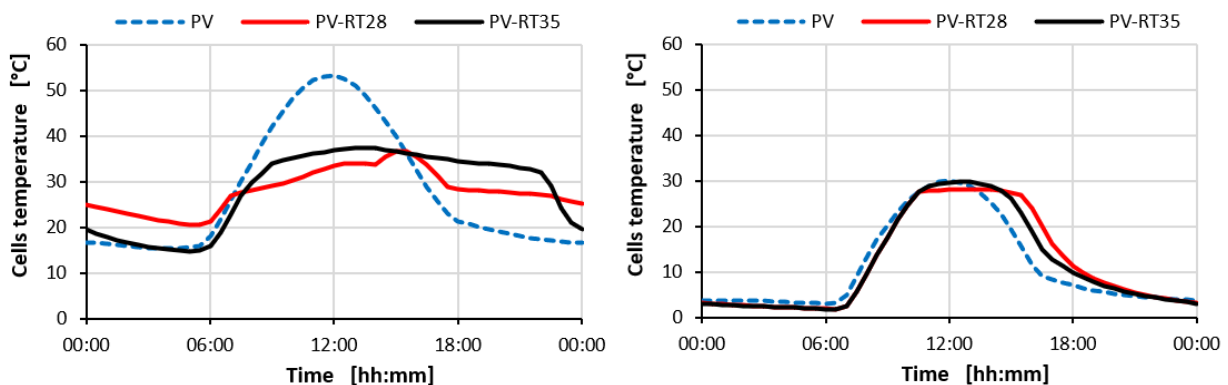


Figure 3.31 - PV cells temperature profile during autumn equinox (at left) and during winter solstice (at right).

On the autumn equinox, the lower outdoor temperature and solar irradiation represent almost ideal conditions for the operation of PV-PCM equipped with RT28. The PV-RT28 module operates effectively for all the daily hours by keeping its temperatures lower than the other

configurations. Otherwise, RT35 is less effective in cooling the panel, PV-RT35 reaches temperatures higher than PV-RT28PCM. This reversal of behaviour is due to the difficulty for RT35 in reaching the solid/liquid transition temperature for these weather conditions. Anyway, also in this period of the year, the conventional PV-module operates at temperatures higher than both PV-PCM modules. Actually, as in the summer, in the last part of the day, the conventional PV module has lower temperatures than both PV-PCM modules, but in that period of the day the solar radiation is very low and, consequently, such drawbacks have scarce relevance.

On the winter solstice, there is no remarkable difference among the cell's temperature of the three module configurations. Indeed, the PV cells of a conventional module are lower than 30°C, so the RT35 do not melt, while the PV-RT28 keeps its temperatures at about 28°C, which is the melting point of this PCM. In the last part of the day, it's possible to notice again an increase in temperature of the PV-PCM modules, due to the increase of the thermal resistance of the PV-PCM modules that delayed the cooling of the PV cells.

Figure 3.32 depicts the electrical efficiency (continuous lines) and the electrical power (dashed lines) during the summer solstice (at left) and during the autumn equinox (at right). The results obtained on the winter solstice are not shown since the efficiency and electrical power are very similar for all the three scenarios due to the very similar cell temperatures.

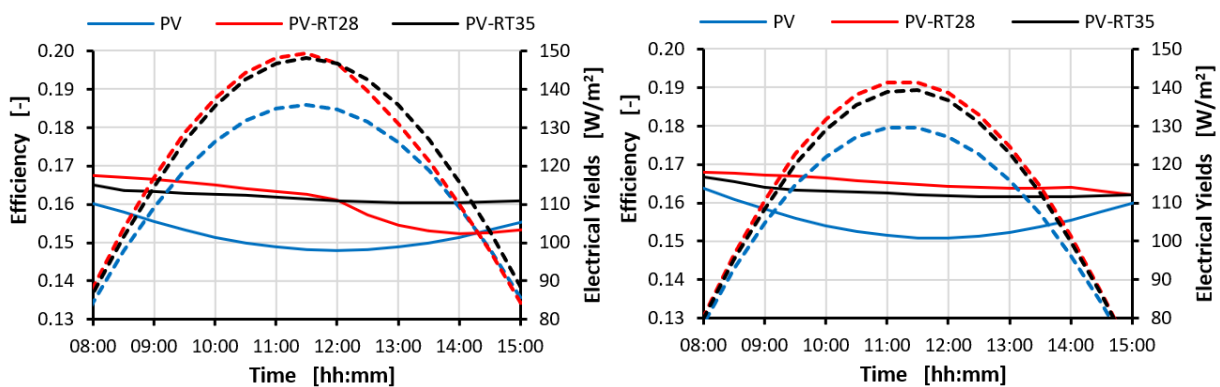


Figure 3.32 - Efficiency and electrical power during summer solstice (at left) and during autumn equinox (at right).

As regards the summer solstice, the conventional PV module presents efficiency and power production lower than both PV-RT28 and PV-RT35 modules. In the first part of the day, the PV-RT28 has the highest efficiency, close to η_{STC} , while after midday due to exhaustion of PCM work, the efficiency decreases quickly. Otherwise, the PV-RT35 maintains fairly high efficiency throughout the day, greater than 16%. This trend is repeated for electrical power production it depends on the available solar irradiance and electrical efficiency. Globally, the use of PCMs allows an increase in the power production of almost 10% during peak hours. On the autumn equinox, the conventional PV module once again attains the lowest efficiency and power production are the smallest using. In this case, the cell temperature profiles of the two PV-

PCMs modules are similar during the whole day. So, it is not repeated the decrease of efficiency for the PV- RT28, that was observed after midday on the summer solstice. On this day the presence of PCMs allows an increase in power production during the peak hours of approximately 9.1% and 7.5% respectively using RT28 and RT35. On the winter solstice, as can be deduced from the temperature of the cell in figure 3.31, there are no remarkable differences between the three PV module, neither in electrical efficiency nor in electrical power.

Figure 3.33 depicts the daily electrical yields on the three analyzed days for the three PV-module configurations.

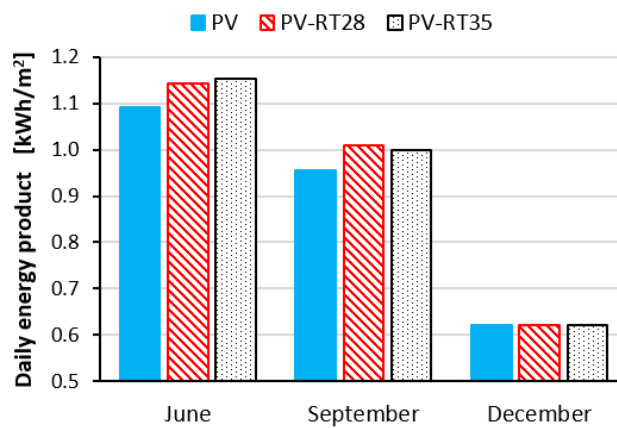


Figure 3.33 – Daily electrical yields.

The daily results reflect what has been already highlighted examining the daily profile of electrical efficiency and power production. The daily electrical yields values, on the winter solstice, are almost the same for the three PV-module configurations, whereas on autumn equinox and summer solstice the lowest daily yields occur in the case of PV-module. The implementation of PCMs improves the performances of PV-modules both on the summer solstice and autumn equinox. On the summer solstice, the daily electrical yields increased by 4.6% using RT28 and by 5.6 % using RT35. Otherwise, on the autumn equinox, this PV- RT28 is the system which has the highest energy production with an increase of about 5.7%, respect to the conventional PV-module, whereas PV-RT35 allows achieving an increase of the daily energy produced of about 4.4%. This finding highlights the importance to carefully choose the type of PCM looking to the climatic conditions of the site of interest. In particular, an important element that has to be observed is the liquefaction temperature of the PCM, and also its complete solidification during the night.

Full considerations, conclusions and future developments are reported in the document reported in Appendix 5.

References

- [1] N.R. Sheridan, K.J. Bullock, J.A. Duffie. Study of solar processes by analog computer. *Solar Energy*, Volume 11, April–June 1967, Pages 69-77. [https://doi.org/10.1016/0038-092X\(67\)90043-6](https://doi.org/10.1016/0038-092X(67)90043-6)
- [2] C.L. Gupta, H.P. Garg. System design in solar water heaters with natural circulation. *Solar Energy*, Volume 12, December 1968, Pages 163-170. [https://doi.org/10.1016/0038-092X\(68\)90003-0](https://doi.org/10.1016/0038-092X(68)90003-0)
- [3] H. Buchberg, J.R. Roulet. Simulation and optimization of solar collection and storage for house heating. *Solar Energy*, Volume 12, September 1968, Pages 31-50. [https://doi.org/10.1016/0038-092X\(68\)90023-6](https://doi.org/10.1016/0038-092X(68)90023-6)
- [4] S.A. Klein, P.I. Cooper, T.L. Freeman, D.M. Beekman, W.A. Beckman, J.A. Duffie. A method of simulation of solar processes and its application. *Solar Energy*, Volume 17, April 1975, Pages 29-37. [https://doi.org/10.1016/0038-092X\(75\)90014-6](https://doi.org/10.1016/0038-092X(75)90014-6)
- [5] J.D. Mondol, Y.G. Yohanis, M. Smyth, B. Norton. Long-term validated simulation of a building integrated photovoltaic system. *Solar Energy*, Volume 78, February 2005, Pages 163-176. <https://doi.org/10.1016/j.solener.2004.04.021>
- [6] S.A. Kalogirou, Y. Tripanagnostopoulos. Hybrid PV/T solar systems for domestic hot water and electricity production. *Energy Conversion and Management*, Volume 47, November 2006, Pages 3368-3382. <https://doi.org/10.1016/j.enconman.2006.01.012>
- [7] B. Quesada, C. Sanchez, J. Canada, R. Royo, J. Paya. Experimental results and simulation with TRNSYS of a 7.2kWp grid-connected photovoltaic system. *Applied Energy*, Volume 88, May 2011, Pages 1772-1783. <https://doi.org/10.1016/j.apenergy.2010.12.011>
- [8] S.A. Klein, W. A. Beckman et al., TRNSYS - A Transient Simulation Program. ASHRAE 82, 1976.
- [9] Z.J. Zhai, Z. Zhang, W. Zhang, Q.Y. Chen. Evaluation of various turbulence models in predicting airflow and turbulence in enclosed environments by CFD: Part 1 – summary of prevalent turbulence models. *HVAC&R Research*, Volume 13, August 2007; Pages 853–870.
- [10] P. Dupeyrat, C. Ménézo, S. Fortuin. Study of the thermal and electrical performances of PVT solar hot water system. *Energy and Buildings*, Volume 68, January 2014, Pages 751–755. <https://doi.org/10.1016/j.enbuild.2012.09.032>
- [11] F.G. Cabo, S. Nizetic, G.M. Tina. Photovoltaic panels: a review of the cooling techniques. *Trans FAMENA*. Volume 40, 2016, Pages 63–74.
- [12] F. Sarhaddi, S. Farahat, H. Ajam, A. Behzadmehr, M. Mahdavi Adeli. An improved thermal and electrical model for a solar photovoltaic thermal (PV/T) air collector. *Applied Energy*, Volume 87, July 2010, Pages 2328-2339. <https://doi.org/10.1016/j.apenergy.2010.01.001>
- [13] J. Ajayan, D. Nirmal, P. Mohankumar, M. Saravanan, M. Jagadesh, L. Arivazhagan. A review of photovoltaic performance of organic/inorganic solar cells for future renewable and

sustainable energy technologies. Superlattices and Microstructures, Volume 143, July 2020.

<https://doi.org/10.1016/j.spmi.2020.106549>

[14] M. Arif Hasan, K. Sumathy. Photovoltaic thermal module concepts and their performance analysis: A review. Renewable and Sustainable Energy Reviews, Volume 14, September 2010, Pages 1845-1859. <https://doi.org/10.1016/j.rser.2010.03.011>

[15] A.S. Joshi, I. Dincer, B.V. Reddy. Performance analysis of photovoltaic systems: A review. Renewable and Sustainable Energy Reviews, Volume 13, Issue 8, October 2009, Pages 1884-1897. <https://doi.org/10.1016/j.rser.2009.01.009>

[16] S. Gorjian, H. Ebadi, F. Calise, A. Shukla, C. Ingraio. A review on recent advancements in performance enhancement techniques for low-temperature solar collectors. Energy Conversion and Management, Volume 222, 15 October 2020. <https://doi.org/10.1016/j.enconman.2020.113246>

[17] E. Vengadesan, R. Senthil. A review on recent development of thermal performance enhancement methods of flat plate solar water heater. Solar Energy, Volume 206, August 2020, Pages 935-961. <https://doi.org/10.1016/j.solener.2020.06.059>

[18] A. Shafieian, M. Khiadani, A. Nosrati. Strategies to improve the thermal performance of heat pipe solar collectors in solar systems: A review. Energy Conversion and Management, Volume 183, 1 March 2019, Pages 307-331. <https://doi.org/10.1016/j.enconman.2018.12.115>

[19] W. Pang, Y. Cui, Q. Zhang, G.J. Wilson, H. Yan. A comparative analysis on performances of flat plate photovoltaic/thermal collectors in view of operating media, structural designs, and climate conditions. Renewable and Sustainable Energy Reviews, Volume 119, March 2020. <https://doi.org/10.1016/j.rser.2019.109599>

[20] F. Yazdanifard, M. Ameri. Exergetic advancement of photovoltaic/thermal systems (PV/T): A review. Renewable and Sustainable Energy Reviews, Volume 97, December 2018, Pages 529-553. <https://doi.org/10.1016/j.rser.2018.08.053>

[21] F. Shan, F. Tang, L.C.G. Fang. Performance evaluations and applications of photovoltaic–thermal collectors and systems. Renewable and Sustainable Energy Reviews, Volume 33, May 2014, Pages 467-483. <https://doi.org/10.1016/j.rser.2014.02.018>

[22] C. Good, I. Andresen, A.G. Hestnes. Solar energy for net zero energy buildings – A comparison between solar thermal, PV and photovoltaic–thermal (PV/T) systems. Solar Energy, Volume 122 December 2015, Pages 986–996. <https://doi.org/10.1016/j.solener.2015.10.013>

[23] Nižetić, S., Papadopoulos, A.M., Tina, G.M., Rosa-Clot, M. Hybrid energy scenarios for residential applications based on the heat pump split air-conditioning units for operation in the Mediterranean climate conditions, Energy and Buildings, Volume 140, April 2017, Pages 110-120. <https://doi.org/10.1016/j.enbuild.2017.01.064>

[24] F. Huide, Z. Xuxin, M. Lei, Z. Tao, W. Qixing, S. Hongyuan. A comparative study on three types of solar utilization technologies for buildings: Photovoltaic, solar thermal and hybrid

photovoltaic/thermal systems. *Energy Conversion and Management*, Volume 140, 15 May 2017, Pages 1-13. <https://doi.org/10.1016/j.enconman.2017.02.059>

[25] A. Gagliano, G.M. Tina, F. Nocera, A.D. Grasso, S. Aneli. Description and performance analysis of a flexible photovoltaic/thermal (PV/T) solar system. *Renewable Energy*, Volume 137, July 2019, Pages 144-156. <https://doi.org/10.1016/j.renene.2018.04.057>

[26] G.M. Tina, C. Ventura, D. Sera, S. Spataru. Comparative assessment of PV plant performance models considering climate effects. *Electric power components and systems*, Volume 45, December 2017, Pages 1381-1392.

<https://doi.org/10.1080/15325008.2017.1362072>

[27] A. Gagliano, G.M. Tina, S. Aneli, S. Nižetić. Comparative assessments of the performances of PV/T and conventional solar plants. *Journal of Cleaner Production*, Volume 219, May 2019, Pages 304-315. <https://doi.org/10.1016/j.jclepro.2019.02.038>

[28] Meteororm. *Solar Engineering Handbook, Part 2, Version 4.0 Theory Part 1: Radiation*. Swiss Federal Office of Energy; 1999.

[29] Enerdata., *Energy Efficiency report – Croatia (2016)*.

[30] E. Molenbroek, E. Stricker, T. Boermans. Primary energy factors for electricity in buildings Toward a flexible electricity supply. *ECOFYS*, July 2011.

[31] UNI TS 11300-2:2008; Prestazioni energetiche degli edifici - Parte2: Determinazione del fabbisogno di energia primaria e dei rendimenti per la climatizzazione invernale e per la produzione di acqua calda sanitaria (2008)

[32] Eurostat, Household energy prices in the EU down compared with 2016, *Energy prices in 2017*, 180 (2017).

[33] C. De Keizer, Available PVT products with focus on the Dutch market: IEA SHC Task 60 - 1st Experts Meeting & PVT Workshop May 16-18, 2018 - Fraunhofer ISE, Freiburg, Germany

[34] A. H. A. Al-Waeli, K. Sopian, H. A. Kazem, M. T. Chaichan. Photovoltaic/Thermal (PV/T) systems: Status and future prospects. *Renewable and Sustainable Energy Reviews*, Volume 77, September 2017, Pages 109-130. <https://doi.org/10.1016/j.rser.2017.03.126>

[35] T. Brahim, A. Jemni. Economical assessment and applications of photovoltaic/thermal hybrid solar technology: A review. *Solar Energy*, Volume 153, September 2017, Pages 540–561. <https://doi.org/10.1016/j.solener.2017.05.081>

[36] K. Moradi, M. Ali Ebadian, C.X. Lin. A review of PV/T technologies: Effects of control parameters. *Int. J. Heat Mass Transf.*, Volume 64, September 2013, Pages 483-500. <https://doi.org/10.1016/j.ijheatmasstransfer.2013.04.044>

[37] S. Priyanka, N.M. Ravindra. Temperature dependence of solar cell performance-an analysis. *Solar Energy Materials and Solar Cells*, Volume 101, June 2012, Pages 36-45. <https://doi.org/10.1016/j.solmat.2012.02.019>

- [38] D. Cabral, J. Gomes, B. Karlsson. Performance evaluation of non-uniform illumination on a transverse bifacial PVT receiver in combination with a CPC geometry. *Solar Energy*, Volume 194, December 2019, Pages 696–708. <https://doi.org/10.1016/j.solener.2019.10.069>
- [39] I. Guarracino, J. Freeman, A. Ramos, S.A. Kalogirou, N. J. Ekins-Daukes, C.N. Markides. Systematic testing of hybrid PV-thermal (PVT) solar collectors in steady-state and dynamic outdoor conditions. *Applied Energy*, Volume 240, April 2019, Pages 1014-1030. <https://doi.org/10.1016/j.apenergy.2018.12.049>
- [40] L.W. Florschuetz. Extension of the Hottel-Whillier model to the analysis of combined photovoltaic/thermal flat plate collectors. *Solar Energy*, Volume 221, 1979, Pages 361–366. [https://doi.org/10.1016/0038-092X\(79\)90190-7](https://doi.org/10.1016/0038-092X(79)90190-7)
- [41] J.K. Tonui, Y. Tripanagnostopoulos. Air-cooled PV/T solar collectors with low cost performance improvements. *Solar Energy*, Volume 81, April 2007, Pages 498–511. <https://doi.org/10.1016/j.solener.2006.08.002>
- [42] M. Battaglia, D. Zenhäusern, S. Brunold. Extended Hottel-Whillier Models for uncovered PVT collectors. in *EuroSun 2018*, 2018.
- [43] O. Ahmed, S. Bawa. The combined effect of nanofluid and reflective mirrors on the performance of PV/thermal solar collector. *Thermal Science*, Volume 23, 2019, Pages 573-587. <https://doi.org/10.2298/TSCI171203092A>
- [44] O.M. Hamdoon, O.R. Alomar, B.M. Salim. Performance analysis of hybrid photovoltaic thermal solar system in Iraq climate condition. *Thermal Science and Engineering Progress*, Volume 17, June 2020, 100359. <https://doi.org/10.1016/j.tsep.2019.100359>
- [45] H.A. Zondag, D.W. de Vries, W.G.J. van Helden, R.J.C. van Zolingen, A.A. van Steenhoven. The thermal and electrical yield of a PV-thermal collector. *Solar Energy*, Volume 72, February 2002, Pages 113–128. [https://doi.org/10.1016/S0038-092X\(01\)00094-9](https://doi.org/10.1016/S0038-092X(01)00094-9)
- [46] T. Bergene, O.M. Løvvik. Model calculations on a flat-plate solar heat collector with integrated solar cell. *Solar Energy*, Volume 55, 1995, Pages 453–462, 1995. [https://doi.org/10.1016/0038-092X\(95\)00072-Y](https://doi.org/10.1016/0038-092X(95)00072-Y)
- [47] B. Sandnes, J. Rekstad. A photovoltaic/thermal (PV/T) collector with a polymer absorber plate. Experimental study and analytical model. *Solar Energy*, Volume 72, January 2002, Pages 63–73, 2002. [https://doi.org/10.1016/S0038-092X\(01\)00091-3](https://doi.org/10.1016/S0038-092X(01)00091-3)
- [48] B. Perers, P. Kovacs, M. Olsson, M.P.U. Pettersson. A Tool for Standardized Collector Performance Calculations Including PVT. *Energy Procedia*, Volume 30, 2012, Pages 1354–1364. <https://doi.org/10.1016/j.egypro.2012.11.149>
- [49] M. Stegmann, E. Bertram, G. Rockendorf, S. Janßen. Model of an unglazed photovoltaic thermal collector based on standard test procedures. in *30th ISES Biennial Solar World Congress 2011*, SWC 2011.
- [50] M. Lämmle, A. Oliva, M. Hermann, K. Kramer, W. Kramer. PVT collector technologies in solar thermal systems: A systematic assessment of electrical and thermal yields with the novel

characteristic temperature approach. *Solar Energy*, Volume 155, October 2017, Pages 867–879. <https://doi.org/10.1016/j.solener.2017.07.015>

[51] D. Jonas, G. Frey, D. Theis. Implementation and Experimental Validation of a Photovoltaic-Thermal (PVT) Collector Model in TRNSYS. in *EuroSun 2018*, 2018.

[52] F. Calise, R.D. Figaj, L. Vanoli. Experimental and Numerical Analyses of a Flat Plate Photovoltaic/Thermal Solar Collector. *Energies*, Volume 10, April 2017, Page 491. <https://doi.org/10.3390/en10040491>

[53] N. Aste, C. Del Pero, F. Leonforte. Water PVT collectors performance comparison, *Energy Procedia*, Volume 105, May 2017, Pages 961-966.

<https://doi.org/10.1016/j.egypro.2017.03.426>

[54] C. El Fouas, B. Hajji, A. Gagliano, G.M. Tina, S. Aneli. Numerical model and experimental validation of the electrical and thermal performances of a photovoltaic/thermal plant. *Energy Conversion and Management*, Volume 220, September 2020, 112939. <https://doi.org/10.1016/j.enconman.2020.112939>

[55] A.R. Kumar, H.P. Garg. Study of a photovoltaic-thermal system–thermosyphonic solar water heater combined with solar cells. *Energy Conversion and Management*, Volume 35, July 1994, Pages 605-620. [https://doi.org/10.1016/0196-8904\(94\)90044-2](https://doi.org/10.1016/0196-8904(94)90044-2)

[56] B. Boumaaraf, K. Touafek, M.S. Ait-cheikh, M. El Amine Slimani. Comparison of electrical and thermal performance evaluation of a classical PV generator and a water glazed hybrid photovoltaic–thermal collector. *Mathematics and Computers in Simulation*, Volume 167, January 2020, Pages 176-193. <https://doi.org/10.1016/j.matcom.2018.09.003>

[57] E. Sakellariou, P. Axaopoulos. Simulation and experimental performance analysis of a modified PV panel to a PVT collector. *Solar Energy*, Volume 155, October 2017, Pages 715-726. <https://doi.org/10.1016/j.solener.2017.06.067>

[58] M. Herrando, A. Ramos, I. Zabalza, C.N. Markides. A comprehensive assessment of alternative absorber-exchanger designs for hybrid PVT-water collectors. *Applied Energy*, Volume 235, February 2019, Pages 1583-1602. <https://doi.org/10.1016/j.apenergy.2018.11.024>

[59] J.J. Michael, S. Iniyar, R. Goic. Flat plate solar photovoltaic-thermal (PV/T) systems: A reference guide. *Renewable and Sustainable Energy Reviews*, Volume 51, November 2015, Pages 62-88. <https://doi.org/10.1016/j.rser.2015.06.022>

[60] J. Antonanzas, A. del Amo, A. Martinez-Gracia, A.A. Bayod-Rujula, F. Antonanzas-Torres. Towards the optimization of convective losses in photovoltaic–thermal panels. *Solar Energy*, Volume 116, June 2015, Pages 323-336. <https://doi.org/10.1016/j.solener.2015.04.013>

[61] H.A. Zondag, D.W. de Vries, W.G.J. van Helden, R.J.C. van Zolingen, A.A. van Steenhoven. The yield of different combined PV-thermal collector designs. *Solar Energy*, Volume 74, March 2003, Pages 253-269. [https://doi.org/10.1016/S0038-092X\(03\)00121-X](https://doi.org/10.1016/S0038-092X(03)00121-X)

- [62] S. Chol, J. Estman. Enhancing thermal conductivity of fluids with nanoparticles. ASME-Publications-Fed Volume 231, 1995, Pages 99-106.
- [63] V. Sridhara, L.N. Satapathy. Al₂O₃-based nanofluids: a review. Nanoscale Research Letters, Volume 6, July 2011, Page 456. DOI: [10.1186/1556-276X-6-456](https://doi.org/10.1186/1556-276X-6-456)
- [64] A.A. Minea. Hybrid nanofluids based on Al₂O₃, TiO₂ and SiO₂: numerical evaluation of different approaches. International Journal of Heat and Mass Transfer, Volume 104, January 2017, Pages 852-860. <https://doi.org/10.1016/j.ijheatmasstransfer.2016.09.012>
- [65] E. Ebrahimi-Bajestan, M. Charjouei Moghadam, H. Niazmand, W. Daungthongsuk, S. Wongwises. Experimental and numerical investigation of nanofluids heat transfer characteristics for application in solar heat exchangers. International Journal of Heat and Mass Transfer, Volume 92, January 2016, Pages 1041-1052.
<https://doi.org/10.1016/j.ijheatmasstransfer.2015.08.107>
- [66] M. Hemmat Esfe, A. Karimipour, W.-M. Yan, M. Akbari, M.R. Safaei, M. Dahari. Experimental study on thermal conductivity of ethylene glycol based nanofluids containing Al₂O₃ nanoparticles. Int. Communications in Heat and Mass Transfer, Volume 88, September 2015, Pages 728-734. <https://doi.org/10.1016/j.ijheatmasstransfer.2015.05.010>
- [67] T. Yousefi, F. Veysi, E. Shojaeizadeh, S. Zinadini. An experimental investigation on the effect of Al₂O₃-H₂O nanofluid on the efficiency of flat-plate solar collectors. Renewable Energy, volume 39, March 2012, Pages 293-298. <https://doi.org/10.1016/j.renene.2011.08.056>
- [68] A. Kasaeian, A.T. Eshghi, M. Sameti. A review on the applications of nanofluids in solar energy systems. Renewable and Sustainable Energy Reviews, Volume 43, March 2015, Pages 584-598. <https://doi.org/10.1016/j.rser.2014.11.020>
- [69] S. Alous, M. Kayfeci, A. Uysal. Experimental investigations of using MWCNTs and graphene nanoplatelets water-based nanofluids as coolants in PVT systems. Applied Thermal Engineering, Volume 162, November 2019, 114265.
<https://doi.org/10.1016/j.applthermaleng.2019.114265>
- [70] A.H.A. Al-Waeli, M.T. Chaichan, H.A. Kazem, K. Sopian. Comparative study to use nano-(Al₂O₃, CuO, and SiC) with water to enhance photovoltaic thermal PV/T collectors. Energy Conversion and Management, Volume 148, 15 September 2017, Pages 963-973. <https://doi.org/10.1016/j.enconman.2017.06.072>
- [71] M. Sardarabadi, M. Passandideh-Fard, S.Z. Heris. Experimental investigation of the effects of silica/water nanofluid on PV/T (phot. thermal units). Energy, Volume 66, March 2014, Pages 264-272. <https://doi.org/10.1016/j.energy.2014.01.102>
- [72] J. Avsec, M. Oblak. The calculation of thermal conductivity, viscosity and thermodynamic properties for nanofluids on the basis of statistical nanomechanics. International Journal of Heat and Mass Transfer, Volume 50, October 2007, Pages 4331-4341. <https://doi.org/10.1016/j.ijheatmasstransfer.2007.01.064>

- [73] S.A. Zubeer, H.A. Mohammed, M. Ilkan. A review of photovoltaic cells cooling techniques. E3S Web of Conferences 22, November 2017. <https://doi.org/10.1051/e3sconf/20172200205>
- [74] J. Siecker, K. Kusakana, B.P.Numbi, "A review of solar photovoltaic systems cooling technologies", Renewable and Sustainable Energy Reviews, Volume 79, November 2017, Pages 192-203. <https://doi.org/10.1016/j.rser.2017.05.053>
- [75] A.G. Lupu, V.M. Homutescu, D.T. Balanescu, A. Popescu. A review of solar photovoltaic systems cooling technologies. 8th International Conference on Advanced Concepts in Mechanical Engineering, Materials Science and Engineering 444, 2018.
- [76] P. Atkin, M.M. Farid. Improving the efficiency of photovoltaic cells using PCM infused graphite and aluminum fins. Solar Energy, Volume 114, April 2015, Pages 217-228. <https://doi.org/10.1016/j.solener.2015.01.037>
- [77] M.J. Huang, P.C. Eames, B. Norton. Thermal regulation of building-integrated photovoltaics using phase change materials. International Journal of Heat and Mass Transfer, Volume 47, June 2004, Pages 2715-2733. <https://doi.org/10.1016/j.ijheatmasstransfer.2003.11.015>
- [78] T. Ma, J. Zhao, J. Han. A parametric study about the potential to integrate phase change material into photovoltaic panel. Energy Procedia, Volume 142, December 2017, Pages 648-654. <https://doi.org/10.1016/j.egypro.2017.12.107>
- [79] M.A. Kibria, R. Saidur, F.A. Al-Sulaiman, M.M.A. Aziz. Development of a thermal model for a hybrid photovoltaic module and phase change materials storage integrated in buildings. Solar Energy, Volume 124, February 2016, Pages 114-123. <https://doi.org/10.1016/j.solener.2015.11.027>
- [80] S. Khanna, K.S. Reddy, T.K. Mallick. Performance analysis of tilted photovoltaic system integrated with phase change material under varying operating conditions. Energy, Volume 133, 15 August 2017, Pages 887-899. <https://doi.org/10.1016/j.energy.2017.05.150>
- [81] R. Stropnik, U. Stritih. Increasing the efficiency of PV panel with the use of PCM. Renewable Energy, Volume 97, November 2016, Pages 671-679. <https://doi.org/10.1016/j.renene.2016.06.011>
- [82] M.M. Farid, A.M. Khudhair, S.A.K. Razack, S. Al-Hallaj. A review on phase change energy storage: materials and applications. Energy Conversion and Management, Volume 45, June 2004, Pages 1597-1615. <https://doi.org/10.1016/j.enconman.2003.09.015>
- [83] B. Gibbs, S. Hasain. DSC study of technical grade phase change heat storage materials for solar heating applications. International Solar Energy Conference, Part 2, Proceedings of the 1995 ASME/JSME/JSEJ, 1995
- [84] G.M. Tina, A. Gagliano. An improved multilayer thermal model for photovoltaic modules. In 2016 International Multidisciplinary Conference on Computer and Energy Science (SpliTech), SJuly 2016. DOI: [10.1109/SpliTech.2016.7555927](https://doi.org/10.1109/SpliTech.2016.7555927)
- [85] ANSYS Fluent User's guide, release Fluent 16.1, ANSYS, Inc., 2015 - www.ansys.com

[86] S. Khanna, K.S. Reddy, T.K. Mallick. Optimization of solar photovoltaic system integrated with phase change material. *Solar Energy*, Volume 163, March 2018, Pages 591–599.

<https://doi.org/10.1016/j.solener.2018.01.002>

[87] JRC European Commission, “Photovoltaic Geographical Information System (PVGIS),” *Jt. Res. Cent. - Inst. Energy Transp.*, 2017. <https://ec.europa.eu/jrc/en/pvgis>

4. STRATEGY FOR ACHIEVING NZEB OBJECTIVES: PASSIVE AND ACTIVE BUILDING ENVELOPE

Tackling climate change is a common priority, due to ethical issues related to the general concept of sustainability and a viable future.

Reducing GHG emissions and energy waste are two of the main objectives of international policy. The International Energy Agency estimated that in the United States energy consumption in the building sector is 45% and in Europe, it is around 40 %, where for example in the United Kingdom it is around 42% whereas, in Italy, it is 40% [1]. In Europe, the energy consumption of buildings built before 1990 played a higher impact, i.e. before adopting a common energy-saving policy [2].

The World energy outlook 2019 highlights that under the current scenario the energy demand yet will rise by 1.3% each year up to 2040.

In most industrial sectors, as well as in residential buildings, the energy needs concern heating, cooling, DHW, ventilation, lighting and domestic type appliances. An ambitious goal for the building sector is to achieve the target of zero net energy buildings (nZEB).

The energy performance of buildings directive [3] emphasized the urgency of adopting strategies that contribute to improving the performance of new and existing buildings.

The concept of nZEBs focuses on firstly improving the energy performance of the building envelope and then, integrating Renewable Energy Sources (RESs) to cover the remaining energy demand.

Although the energy demand of energy-intensive buildings could be, partially or totally, balanced by the widespread use of renewable energy sources, this nevertheless represents a waste of clean energy and does not meet the problem of the urban heat islands [4]. For this reason, one of the main objectives of nZEBs is to design high performance passive or active building envelope.

The high performance Passive Building Envelopes (PBE)s are facades, windows, roofs, etc., where the high performance is entrusted to the exploitation of the thermophysical characteristics of the material used, and of the construction techniques, sensitive to the climate [5]. The efficient design reduces thermal fluxes between outdoor and indoor space, as well as the overheating effect due to solar radiation [6-7].

The use of RES, as solar plants, can finally allow the achievement of the nZEB target.

However, due to the lack of available spaces, different kinds of RESs could not find the necessary surfaces where install them. Therefore, it becomes more and more necessary to think about the integration of solar systems into the building envelope and to use systems that allow a high conversion rate of solar radiation into primary energy, giving rise to the so-called Active Building Envelopes (ABE)s.

Integration of solar panels (PV, PV/T, or ST), in literature is subdivided into two basic categories: added and integrated. In Building-Added (BA) the panels are not incorporated into building architecture but are added as an additional Building-Added component. While, in Building-

Integrated the panels are part of the building structure and replace certain building elements (roof, cladding, façade, etc.).

The use of renewable energies in the building envelope is very diverse and opens up many opportunities for creative designers. Many architects have already successfully integrated photovoltaics into their buildings.

The International Energy Agency, Solar Heating and Cooling Programme has supported the task Solar Energy and Architecture (IEA SHC Task 41), which led to providing design criteria and guidelines for achieving high-quality architecture for buildings integrating solar energy systems [8].

In this chapter, first, a strategy for reducing the energy needs of buildings will be analyzed through the application of high-performance passive building envelope (ventilated façade). Subsequently, some solutions of solar system applied on the building's façade (ABE) to produce renewable energy will be analyzed, to evaluate the performance of these systems and the impact on the performance of the building envelope.

4.1 Analysis of High-Performance Building Envelope composed by Opaque Ventilated Façade under winter and summer weather conditions

Nowadays, there is continuing worrying about energy efficiency and the reduction of GHG emissions in the building sector.

The features of the building envelope have a direct influence of both the annual energy consumption and the operating costs for heating, cooling, and for the humidity control.

The most common retrofit intervention on the building envelope is the laying of an external thermal insulation coating system (ETICS), which allows a significant reduction in the thermal transmittance of the opaque façades and the consequent reduction of energy consumptions [9-11]. On the other hand, the thermal coat can increase the energy requirement during the cooling period and create problems of transpiration of the façades if not properly designed [12-13].

Therefore, it is encouraged the advancement of refurbished buildings into very low energy buildings, emphasizing the importance of avoiding overheating during the summer season, not only in warm climate countries but also throughout Europe.

Currently, there are a multiplicity of construction techniques, which allow the improvements of the thermal performances of the building envelopes giving the great chance of reducing the buildings energy demand [14-16].

It has been claimed that ventilated building envelopes help to reduce energy use in buildings and improve occupant comfort. Indeed, they allow reducing the peak cooling load and the energy needs of buildings [17-18], especially in regions with high levels of solar radiation, such as southern Europe [19-22].

This section proposes an energy performance comparison between the Opaque Ventilated Façade (OVF) with that one of a conventional Unventilated Façade (UF). The analyses have been developed having as reference the real weather conditions of a city located in the Mediterranean climate, for both a winter and a summer day, and were performed considering the effect of the façade orientation and the surrounding wind on the energy performances.

4.1.1 Thermal behaviour of building envelopes

The building envelope has to protect and separate as much as possible the indoor space from the climate-forcing, which during the year presents great variations concerning temperature, solar radiation, wind, air humidity [23].

The heat fluxes exchanged between the building façades and the external environment are governed by the three basic mechanisms of heat transfer: radiation, convection, and conduction, that for a conventional unventilated façade consist in:

- convection and thermal radiation between the inner slab of the façade and the indoor environment;
- conduction through the different layers of the façade;
- convection and thermal radiation between the outer slab of the building wall and the outdoor environment.

These heat fluxes differ greatly in the case of the so-called opaque ventilated facades (OVF). The main difference between a ventilated and an unventilated façade (UF) lies in the presence of an additional layer (counter-wall) which forms a channel where the air can circulate freely.

The counter wall has the function of constituting a shield for the radiative heat fluxes as well as for the incident solar irradiation. The airflow within the cavity forms a sort of barrier that allows keeping the internal layers of the building envelope dry. Thus, the combined effects of the counter wall and the airflow in the channel create a most muffled microclimate.

The fluid dynamic processes that occur within the ventilated cavity, as well as the screen effect of the counter-wall, are the main causes of the different thermal behaviour of UF and OVF.

Convection inside the channel is fundamentally caused by the airflow rates and the difference of temperatures between the wall surfaces and the air stream. In the absence of wind, the airflow through the air gap is only driven by the temperature gradient, which generates a chimney effect due to buoyancy forces, free-convection. Otherwise, when wind velocity is higher than zero, the airflow rates within the air gap is due both to mechanical and buoyancy forces. Moreover, the airflow rate will depend even by the intensity and the main wind direction. The counter-wall absorb a portion of the incident solar irradiance, as the function of its absorption coefficient, increasing its temperature. Thus, a part of the stored energy is reemitted as thermal radiation to the outdoor environment and the internal wall, and through convection to the airflow in the channel and the outdoor air. Consequently, a reduction of the solar gain of the building envelope is attained.

This could appear as a controversial outcome because during the winter period the solar gains reduce the energy needs for space heating while in summer period solar gains increase the energy need for space cooling. However, as will be shown in the following, globally the installation of an OVF allows reducing the energy demands for space heating thanks to the reduction of the thermal losses through the building façade.

The thermal fluxes involved in an Opaque Ventilating Facade are depicted in figure 4.1.

Under hypothesis of steady-state condition the heat flux through an unventilated façade (UF) is calculated by eq. 4.1

$$Q = \frac{(T_o - T_i)}{R} A \quad (4.1)$$

where the thermal resistance R is calculated by equation 4.2, T_o and T_i are the outdoor and indoor temperature and A is the surface of the façade.

$$R = \frac{1}{h_i} + \sum_{j=1}^n \frac{\delta_j}{k_j} + \frac{1}{h_e} \quad (4.2)$$

with δ_j and k_j thickness and thermal conductivity of the j^{th} layer of the façade, n the number of layers, h_i and h_e respectively indoor and outdoor heat transfer coefficients.

These coefficients, h_i and h_e , which include both the convection and radiation thermal exchange, conventionally are assumed to be 7.7 and 25.0 W/m²K [24].

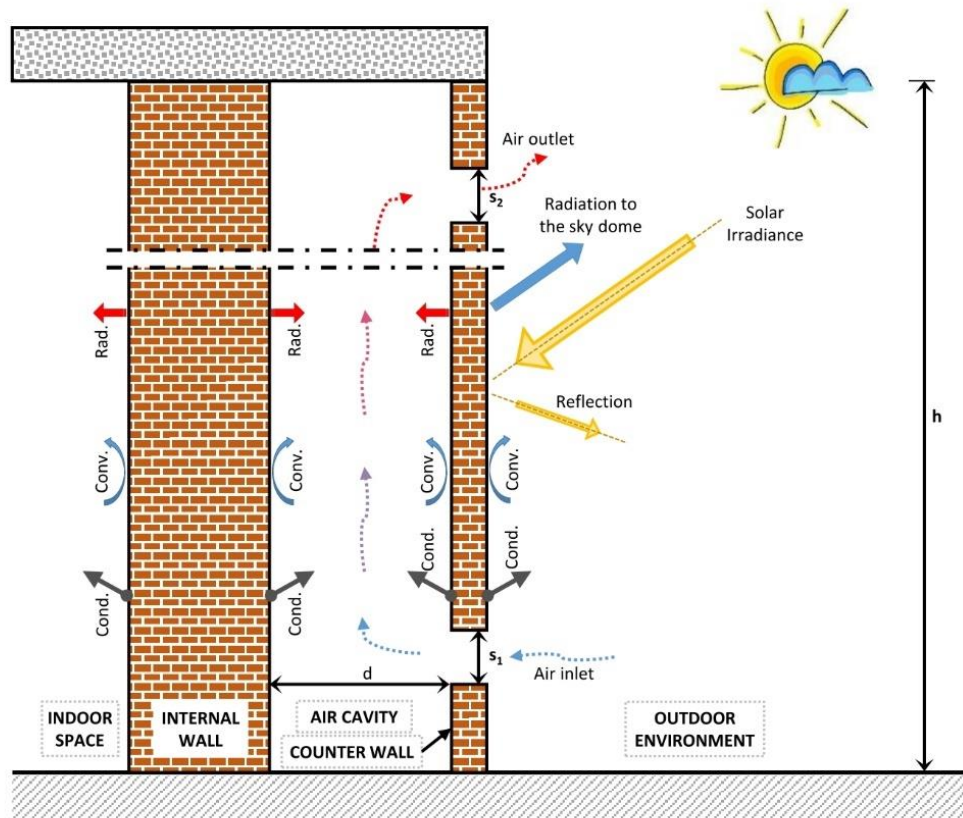


Figure 4.1 – Thermal fluxes for the OVF.

Unlike, for OVFs the thermal resistance calculation procedure is more complex [25-26] since it is necessary to consider the ventilation of the interspace, which also depends on the size of the openings.

The OVFs can be classified in very weakly ventilated, weakly ventilated and strongly ventilated, using the ratio between the surface of the openings (s) and that of the length of the façade (L), as shown in table 4.1.

Table 4.1 classification of ventilated façades [25-26].

Ratio $X = s/L$	Classification of OVF
$X < 0.002$	very weakly ventilated
$0.002 < X < 0.05$	weakly ventilated
$X \geq 0.05$	strongly ventilated

For very weakly ventilated façades, the thermal resistance is calculated using eq. 4.2 considering the cavity as unventilated. In this case, the counter-wall and the air gap contribute to increasing the total thermal resistance of the façade.

In the case of weakly ventilated façades, the thermal resistance is calculated using the follows equation:

$$R = \frac{1}{U_0 + J \left(\frac{U_0}{U_e} \right)^2} \quad (4.3)$$

where:

- U_0 is the overall heat transfer coefficient considering the cavity not ventilated;
- U_e is the heat transmission coefficient of the counter wall;
- J is a coefficient function of the ratio s/L , U_0/U_e and sum $(U_i + U_e)$;
- U_i is the heat transfer coefficient of the internal wall.

For strongly ventilated façades the thermal resistance is calculated using eq. 4.2 neglecting the counter-wall and modifying the values of the heat transfer coefficients as follows:

$$\frac{1}{h_i} + \frac{1}{h_e} = 0.22 \quad (4.4)$$

Thus, comparing an unventilated façade and a very strong ventilated facade with the same stratigraphy, the thermal resistance R of the two facades differs of about 0.05 m²K/W.

It is worth of interest to underline that, for a building façade with a thermal resistance of about 2.0 m²K/W ($U = 0.5$ W/m²K), such difference is just of 2.5 % of the thermal resistance of such facade.

This means that the steady-state analysis for a very strongly ventilated façade gives place to a reduction of the thermal fluxes of about 2.5%, which is incomparable with the not steady-state analysis that evaluates energy savings from 20.0 to 50.0 % during summer days. Therefore, the performances of ventilated facades cannot be analysed through a steady-state analysis but it is mandatory a transient analysis (i.e. using CFD tools).

4.1.2 Methodology and study specifications

The comprehensive comparison of the thermal behaviour between an Opaque Ventilated Façade (OVF) and a conventional unventilated Façade (UF) is performed to evaluate the impact of wind speed and the exposure effects on the thermal behaviour and performances, considering both winter and summer period.

Thus for the two façades were calculated: (I) the hourly surface temperatures of the most external, (II) the temperature profiles for all the facade's layers; (III) the airflow profiles inside the cavity and near the façade; (IV) the hourly thermal fluxes that cross the façade. Finally, the daily energy fluxes and the energy-saving, achievable through the adoption of the OVF, is calculated for the different façade exposures and the conditions of windiness.

These analyses are performed using computational fluid dynamic (CFD) simulations calculation under dynamic conditions.

Figure 4.2 shows the sketch of the two façades (OVF and UF), which differ between them only for the counter wall that creates the ventilated air channel of the OVF. The thermal insulation layer is placed on the most external layer of both façades. The dimensions and physical characteristics of the layers that make up the façades are summarized in table 4.II.

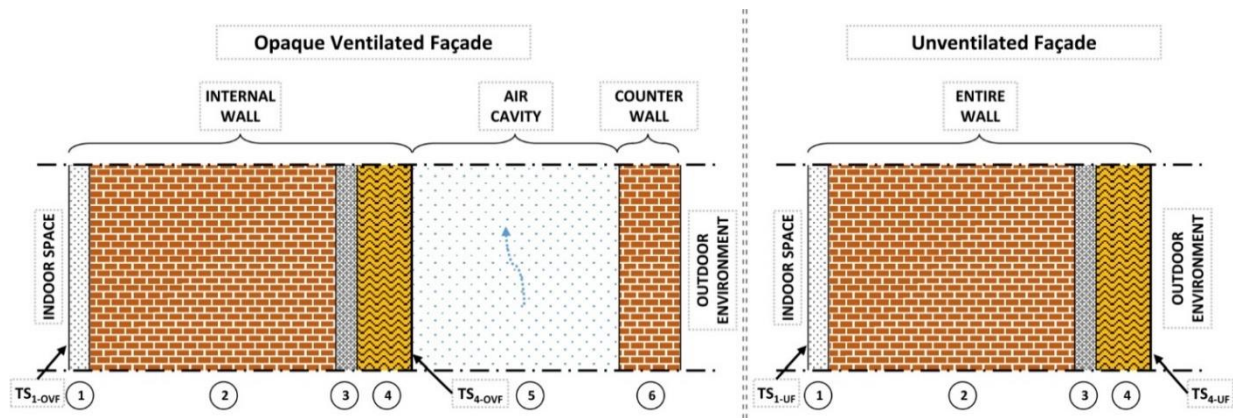


Figure 4.2 – Stratigraphy of ventilated and unventilated façades.

Table 4.II Properties of the layers that make up the PV and PV-PCM modules.

N. of layer	Description	k [W/(m·K)]	ρ [kg/m ³]	δ [m]
1 (inside)	Gypsum plaster	0.900	1800	0.015
2	Brick in hollow blocks	0.590	1600	0.180
3	Cement mortar	1.400	2000	0.015
4	Rigid fibreglass panels	0.038	100	0.040
5	Air (ventilation duct)	0.560	-	0.150
6 (outside)	Brick slabs	0.300	800	0.045

The stratigraphy of the OVF has been defined in such a way to enhance the buoyancy effect and to exploit the thermal inertia of the counter wall [17, 27].

The most external layer of the investigated OVF is made up of bricks with large thermal capacity and low thermal conductivity allowing to attenuate and delay the weather forcing (i.e. solar irradiation) in summer days [27]. The ventilated air gap has two openings with a height of 10.0 cm (0.10 m²/m), placed at the bottom and the top of the facade so to increase the chimney effect. The height of both façades is 6.0 m. The investigated ventilated façade has a ratio between the surface of the openings and that of the entire façade equal to 0.10 m²/m, therefore, it can be classified as a strongly ventilated façade.

Consequently, the thermal resistances of the UF and OVF calculated respectively with Eqs. 4.2 and 4.4, are respectively 1.55 W/m²K and 1.60 W/m²K. Thus, under a steady-state approach, the ventilation layer allows achieving an increase of just 3% for the thermal resistance.

It is worth to observe that a steady-state analysis does not allow considering the thermal inertia of the wall, which may be accounted for only performing a transient analysis.

An option for comparing the heat fluxes through the two facades towards the outdoor environment ($Q_{OVF/UF}{}_{outdoor}$) is the utilization of the temperature on the most external layer of the inner wall for the OVF facade OVF (TS_{4-OVF}), and on the external layer for the UF facade (TS_{4-UF}).

The temperature TS_1 (i.e. the temperature on the most internal layer for both the facades) is used for calculating the heat fluxes towards the indoor environment ($Q_{OVF/UF}{}_{indoor}$).

Such approach allows to attain results that are almost independent by the specific stratigraphy of the façade, and the difference between the thermal fluxes through the two façades depend mostly by the mutual effect of the ventilation cavity and counter wall.

The energy performances of the two facades are compared introducing as an indicator the energy-saving rate (ES)_{win} and (ES)_{sum} defined respectively by Eq 4.5 and Eq. 4.6, where the subscripts (*win, sum*) stand respectively for winter and summer days.

$$(ES)_{win} = \frac{(\sum Q_{OVF} - \sum Q_{UF})_{outgoing,win}}{(\sum Q_{UF})_{outgoing,win}} \quad (4.5)$$

$$(ES)_{sum} = \frac{(\sum Q_{OVF} - \sum Q_{UF})_{incoming,sum}}{(\sum Q_{UF})_{incoming,sum}} \quad (4.6)$$

The ES is defined in such way to take into account only of the outgoing thermal fluxes (i.e thermal losses) for the winter days ($Q_{OVF/UF}{}_{outgoing,win}$), whereas only the incoming thermal fluxes (i.e heat gains) are taken into account for the summer days ($Q_{OVF/UF}{}_{incoming,sum}$). During the winter days, the solar gains are neglected because they do not constantly give rise to effective energy saving but they could generate just overheating phenomena. During the summer days, the heat fluxes from the room to the environment, which occur mostly during night-time, are neglected because they are unimportant compared with the cooling effect obtainable through natural ventilation.

4.1.2.1 Mathematica Model

A Computational Fluid Dynamics (CFD) analysis can be applied for evaluating the thermal behaviour of both the opaque ventilated façade as well as the unventilated facade under variable weather conditions.

In this study, the ANSYS Fluent software [28] is used for assessing the dynamic thermal behaviour and the energy performances for both ventilated and unventilated façades.

The governing equations are solved through the Finite Volume Method (FVM), adopting the second-order upwind discretization scheme and the standard RNG k-epsilon model among the available RANS turbulence models complex [29-30].

Then, the discrete ordinates (DO) radiation model converts the radiative transfer equation (RTE) into transport equations for radiation intensity in the spatial coordinates. Further specification on these transport equations can be found in the software manual.

In the light of experimental and simulation literature studies [30], which indicate that for a given height the temperature difference along the width of the façade was not significant, a two-dimensional geometric model of the building façades is adopted.

Fig. 4.3 shows the mesh used for the OVF.

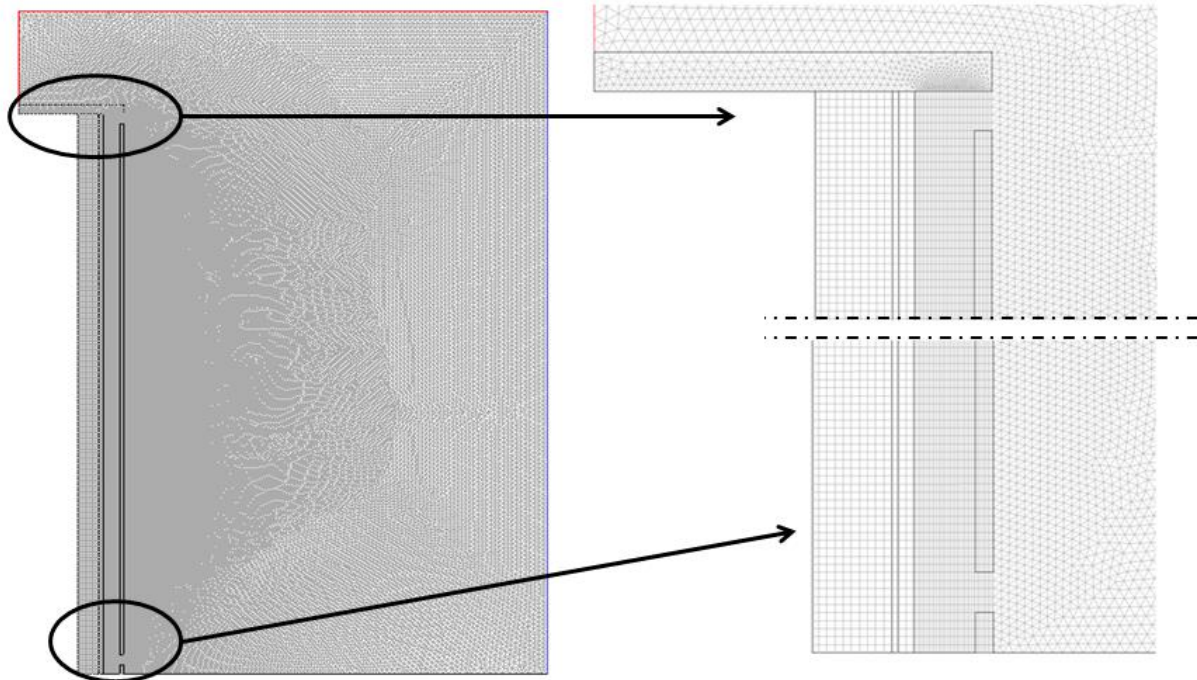


Figure 4.3 – Geometry and mesh of calculus.

To take into account the not negligible effects of the wind on the building facade, the two-dimensional computational domain must be extended to a portion of the outdoor environment for evaluating the barrier effects of the façade on the wind field (see fig. 4.3). A preliminary analysis indicated that it is sufficient to stretch the calculation domain at least 4.00 m beyond the façade, that is about $\frac{3}{4}$ of the façade's height.

The mesh in the calculation domain is constituted by quad and triangular elements. In particular, the different layers belonging the façade, solid and fluid, are discretized through a "structured" mesh, with a width from 0.5 to 1.5 cm and height of 2.0 cm. An "unstructured" mesh is used in the near-wall zones, where more complex fluid structures and heat transfer processes occur, since such mesh allows varying the size of the cells from 2.0 to 10.0 cm, respectively adjacent to the wall and far away from the solid surface.

The hourly variation of the weather conditions (air temperature, solar irradiation), as well as the wind shear, which are the boundary conditions, are defined setting-up a specific User Defined Functions (UDF) that can be dynamically loaded in ANSYS Fluent.

The principal assumptions adopted in the numerical models are summarized in the follows.

The air viscosity is calculated referring to an isobaric transformation for a perfect gas using Eq. 4.7

$$\mu(T) = \mu_0 \sqrt{\frac{T_{amb}}{300}} \quad (4.7)$$

where μ_0 is the dynamic viscosity, being 1.85×10^{-5} kg/(m·s) (at 300 K) and T_{amb} is the air temperature:

The vertical profile of wind velocity is calculated through Eq. 4.8

$$u(z) = u \left(\frac{z}{z_r} \right)^{c_o} \quad (4.8)$$

where u is the wind velocity measured at 10 m by ground, z is the altitude considered, z_r is the reference altitude where the wind velocity is measured (equal to 10 m), and c_o is a coefficient that takes into account orography and roughness of the surrounding environment.

The radiative heat fluxes between the outer surface of the façades and the sky are taken into account by Stefan-Boltzmann law (Eq. 3.21) previously defined in section 3.3.1.1., where the view factor is posed equal to 0.5, and the sky temperature is calculated by the follows formulation [31].

$$T_{sky} = 0.037536T_{amb}^{1.5} + 0.32T_{amb} \quad (4.9)$$

Moreover, the indoor temperature is fixed (air-conditioned room) being 293 K for the winter and 297 K for the summer, the coefficient h_i is posed equal to $7.7 \text{ W/m}^2\text{K}$, while he is assumed variable with the wind velocity [24].

The solid layers are defined through the following parameters: thickness, density, thermal conductivity, and specific heat. The variation of such parameters with temperature is neglected.

The numerical convergence of the CFD model is checked using the scaled numerical residuals of all the computed variables. Usually, the value of 10^{-3} is adequate for continuity, velocity, and turbulence residuals, while energy and radiation residuals the value of 10^{-6} is necessary.

4.1.2.2 Weather data

This study is carried out considering two sunny days, one for the winter period (21st January) and other for the summer period (21st July). The weather data are assumed considering the façades located in the city of Catania ($37^\circ 30' 0'' \text{ N} - 15^\circ 6' 0'' \text{ E}$). Figure 4.4 shows the daily outdoor temperature and solar incident irradiance on the façades for winter (January) and summer (July) sunny day for the East, South and West exposure [32].

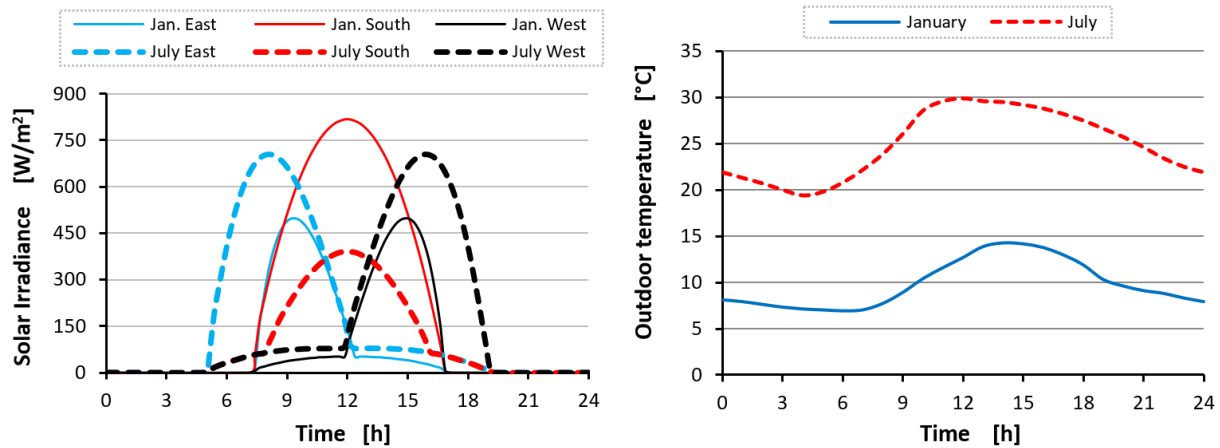


Figure 4.4 – Incident irradiance (left) and outdoor temperature (right) for the winter and summer days.

The East and West façades collect the highest solar radiation during summer days while the South facades collect the highest solar radiation during the winter day.

In order to evaluate the impact of the wind speed, the analyses following three different scenarios: Calm Wind condition ($U_0 = 0.0$ m/s), upwind ($U_0 = 2.5$ and 5.0 m/s), and downwind ($U_0 = 2.5$ m/s).

It is important to highlight that the thermal behavior of an OVF facing West should be substantially symmetric respect to the midday in conformity with the diurnal path of the sun.

4.1.3 Results

In this section, first, the impact of the several wind scenarios on the thermal behaviour of OVF is analysed. Subsequently, the thermal behaviour and the thermal performance comparisons are analysed considering both winter and summer seasons, as well as different façade exposure.

4.1.3.1 Impact of wind speed on the thermal behaviour of OVF

The air velocity inside the air gap of the ventilated façade depends by the effects of buoyancy and wind forces. Thus, in this section, limited for a summer day and façade facing South, several scenarios of wind conditions will be shown:

- Calm wind
- Up wind, two scenarios are considered, respectively with U_0 equal 2.5 and 5.0 m/s
- Downwind, with U_0 equal 2.5.

Figure 4.5 shows the wind profiles (at left) and the temperature profiles (at right) from 6:00 to 21:00, for the several wind conditions analysed. In the graphs, the left side of the ventilated

cavity is closer to the indoor environment while the right side is closer to the outdoor environment.

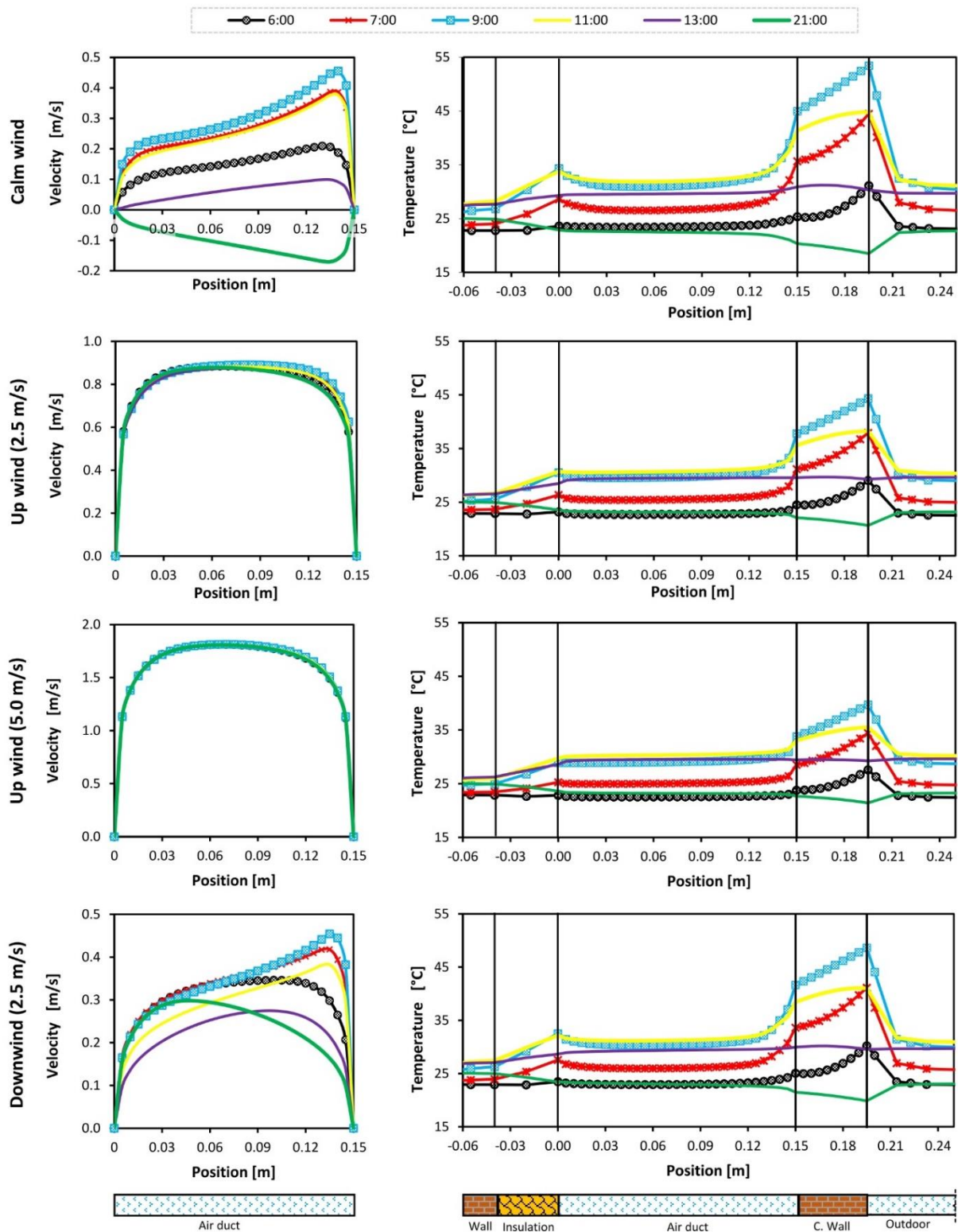


Figure 4.5 – Profiles of air velocity inside the duct (at left) and temperature (at right) for the various wind conditions.

As regards the calm wind scenario, the upward motion of the air within the cavity starts at 6:00 a.m. when the solar irradiance strikes the counter-wall of the OVF and heat the outer layer of the ventilated channel. In the following hours, the solar radiation increases causing the growth of the temperature of the counter-wall which strengthens of both the buoyancy forces and the air velocity.

The maximum values of both air temperature and velocity are reached between 9:00 - 10:00 a.m., in phase with the highest incident solar irradiance on a vertical plane EAST oriented. Later, the air velocity begins to diminish due to the attenuation of incident solar irradiance. At 13:00 it can be observed that the temperature of the inner layer of the OVF is almost equal with the outdoor air temperature, consequently, the velocity within the cavity progressively tends to zero.

At 21:00, the radiative heat flux between the façade and the sky cools the counter-wall, which reaches temperatures lower than the outdoor environment temperatures. Consequently, also the air inside the cavity cools and moves from the top downwards (the air density increases). Such inversion of the air stream within the duct allows pulling out the stored heat into the wall during the day.

It is possible to highlight that the profiles of velocity are intimately related to the profiles of temperature since the air stream is generated only by the buoyancy effect.

In upwind scenarios, the airflow inside the cavity depends substantially by the value of the wind velocity and, the profiles of velocity assume the classical aspect of the forced laminar regime. It means that the buoyancy effects are almost negligible for this scenario.

It is possible to highlight as the two wind velocities generate well-differentiated profiles of air velocity, with an air velocity of about 0.9 and 1.75 m/s respectively for U_0 equal to 2.5 and 5.0 m/s. During the daytime, the variation of those profiles of velocity is very modest they are almost overlapped for any cases.

Therefore, we can observe that the air velocity within the duct is directly affected by the speed of the external wind [33], for high wind velocities correspond high air velocities within the duct and, consequently less important are the effects of the buoyancy forces.

Moreover, the results of simulations allow to extrapolate a first correlation between the outdoor wind velocity (U_0) and the maximum value of velocity reached by air within the ventilated channel ($U_{max,int}$), that is reported in the following equation:

$$U_{max,int} = 0.35 U_0 \quad (4.10)$$

Consequently, high wind velocities generate high heat flux between the external layer of the ventilated channel and the air inside, in accordance with the increase of the convection coefficient.

As regards the downwind condition, it is quite evident that the profiles of velocity depend on both the outdoor wind velocity and by the buoyancy forces, so it is generated a condition of mixed convection.

It can be observed that when the incident solar irradiance reaches the highest values ($500 \div 600 \text{ W/m}^2$) from 7:00 - 13:00, the profiles of velocity indicate that the action of the buoyancy forces are predominant, while before 7:00 and after 13:00 when the incident irradiance on the façade has low values, mixed profiles of velocity are generated. Moreover, in the night hours, it does not occur reversal airflow conditions in the cavity as in the case of calm wind.

By comparing the temperatures in the hours with the maximum insolation, in principle, decreasing temperature gradients are observed between the cavity and the indoor area as the speed of the external air increases.

4.1.3.2 Comparisons between the OVF and UF during the winter season

In this section, the comparisons between the OVF and UF, during the winter season, are shown, through the analysis of the hourly temperatures of the more external layer of the two façades, that are the inner wall of the OVF and external layer of the UF (i.e. TS_{4-UF} , and TS_{4-OVF}), and the hourly heat flux profiles. The comparison will be shown for the façades facing South and East, considering the calm wind scenario and the up-wind scenario with U_0 equal to 5.0 m/s.

Figure 4.6 depicts the hourly external surface temperatures for the UF (TS_{4-UF}) and the OVF, (TS_{4-OVF}) as well as the outdoor temperature for the different windiness and façade exposure.

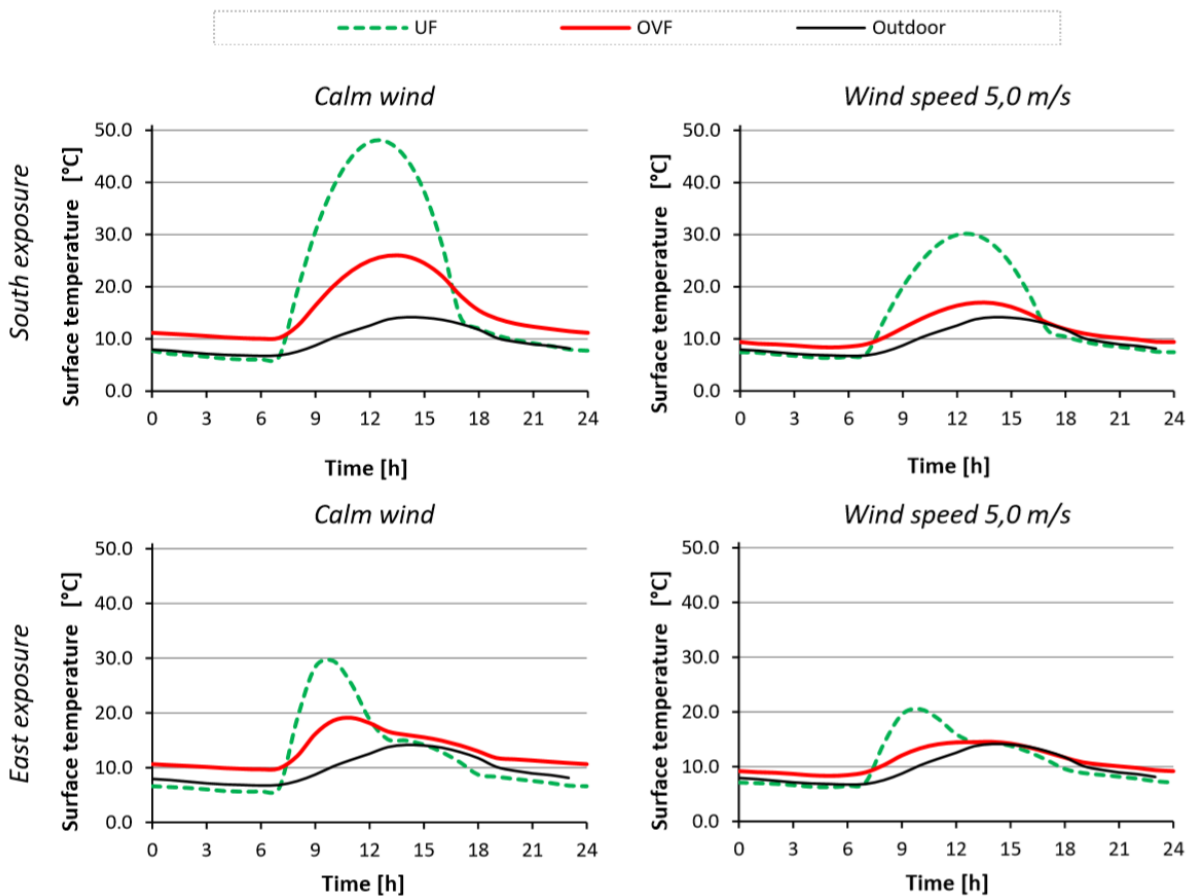


Figure 4.6 – Hourly surface temperatures of the OVF and UF during a winter day.

It is possible to evidence that the façade exposure, likewise the wind velocity, greatly affect the thermal behaviour of both UF and OVF facades. By looking to the South exposure, the OVF has temperatures lower than UF during the daytime period, with differences that reach 23 °C for calm-wind conditions. Such differences diminish to about 13 °C for the up-wind scenario.

During the night, a reverse behaviour is observed, where the OVF presents temperature slightly higher than the UF. In particular, the temperatures on the outermost layer of the inner wall of the OVF do not go down below the outdoor air temperature. This is a consequence of the reduction of the radiative thermal losses with the sky-dome. The UF with South exposure could benefit of higher solar gains than an OVF during winter sunny day. Otherwise, the OVF allows reducing the heat losses during the night period.

Globally, the facade facing East has similar behaviour of the South façade. The main difference is the reduced solar radiation that hit this façade.

The counter wall plays an important role in thermal flows, in fact, during the day it intercepts solar radiation and warms up, transferring only a small part of heat towards the interior. Similarly, during the nighttime, the counter wall reduces heat losses towards the sky, guaranteeing temperature on the internal wall higher than the UF. The surface temperature on the insulation of the UF is 4 °C lower than the one that occurs in OVF in calm wind conditions.

The shielding effect of the counter wall is very visible by comparing the temperature profiles along the wall that occurred for the OVF with those of the UF. In this regard, figure 4.7 shows the temperature and velocity profiles for the façades facing South and for both wind conditions.

The velocity and temperature profile are referred at noon and at 6:00, that are respectively the time with the highest solar irradiance and the time with the lowest outdoor temperature.

As regards the velocity profile (left side in figure 4.7), is referred to the air duct for the OVF, while it is referred to the region near the wall for the UF.

The profile of velocity, within the cavity of the OVF and for the region near to the UF, points out significant differences as a function of the wind status, as well as the time of the day.

Intense wind generates into the cavity an air velocity profile typical of forced convection, independently by the time of the day. Consequently, the airflow more effectively cools the surfaces facing the channel. Similar observations can be done for the UF, the increase of the external wind causes the increases of the velocity on the façade (orange and light-blue continue lines) and consequently the cooling effect.

Otherwise, for the calm wind condition the profile of velocity into the channel has noteworthy dependence by the time of the day (red and blue dotted lines).

The velocity profiles show that both during the day and the night times, an upward airflow is generated into the cavity. During the daytime, the airflow into the channel generates two distinct profiles of velocity, one on the external and the other on the inner side of the wall-channel. Indeed, the two surfaces facing the cavity have temperatures higher than the outdoor air, so a twofold buoyancy effect is generated [12, 29]. The most intense velocity is reached on the external side since it has the highest temperature.

During the night-time, a single upward profile of velocity is observed within the channel due to the higher temperature on the inner wall (TS_{4-OVF}) in comparison to the outdoor air.

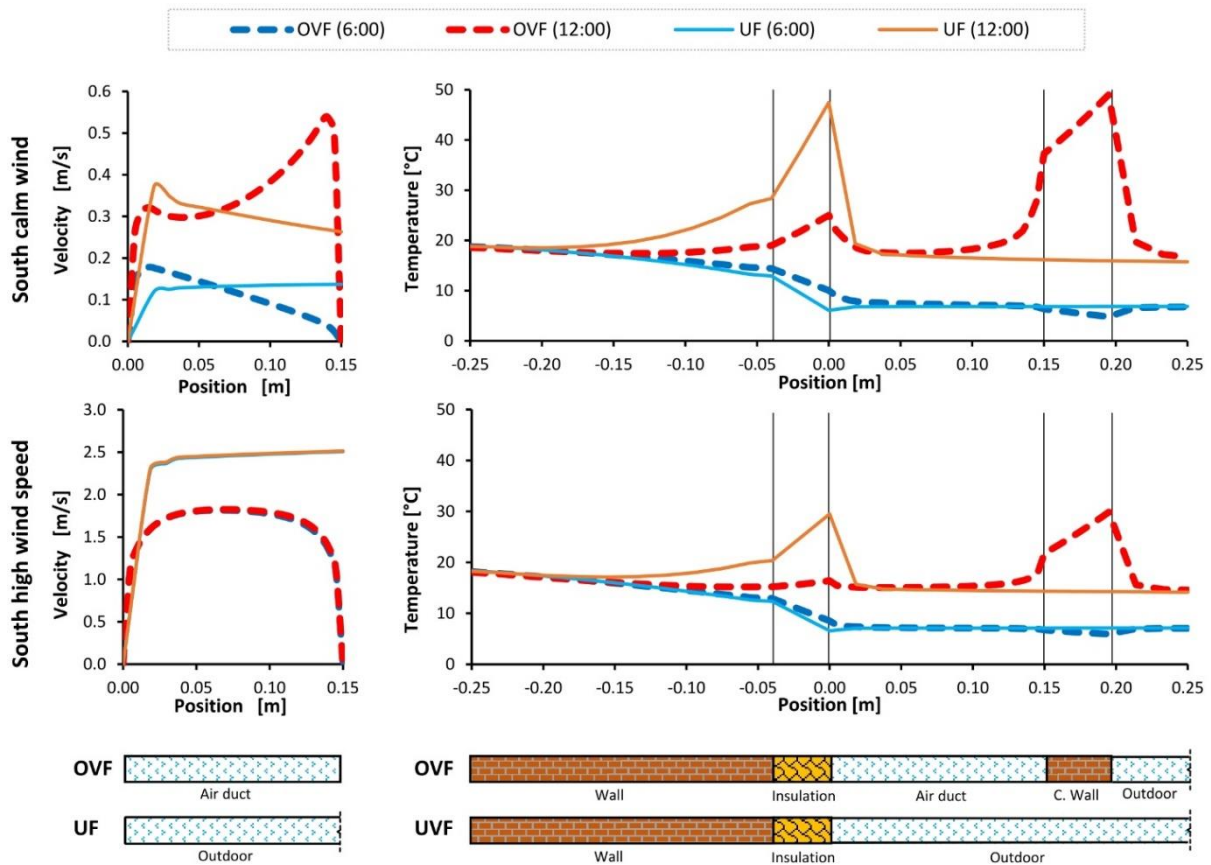


Figure 4.7 – Velocity (at left) and Temperature profiles (at right) of the OVF and UF at specific hours of the day for façades facing South.

The previous analysis indicates that the OVF, in comparison to the UF, leads to a reduction of the solar gain during the daytime, while it allows maintaining higher temperature during nighttime.

Detail about the East exposure are shown in the document reported in the appendix 6 [34].

Finally, fig. 4.8 shows the performances of the OVF and UF through evaluating the heat fluxes which flow through both the facades, where the daily heat fluxes, $(Q_{OVF/UF})_{indoor}$ (dashed lines) as well $(Q_{OVF/UF})_{outdoor}$ (continuous lines) are depicted as a function of the exposure and the status of wind. In Fig. 4.8 the incoming heat fluxes have a positive sign whereas the outgoing heat fluxes have a negative sign.

It is possible to observe that the two exposures give rise to different heat flux timelines coherently with the solar path. The differences between $(Q_{OVF/UF})_{outdoor}$ and $(Q_{OVF/UF})_{indoor}$

depend by the thermal inertia of the façade, which generates the time lag and the attenuation of the heat fluxes transferred to the indoor.

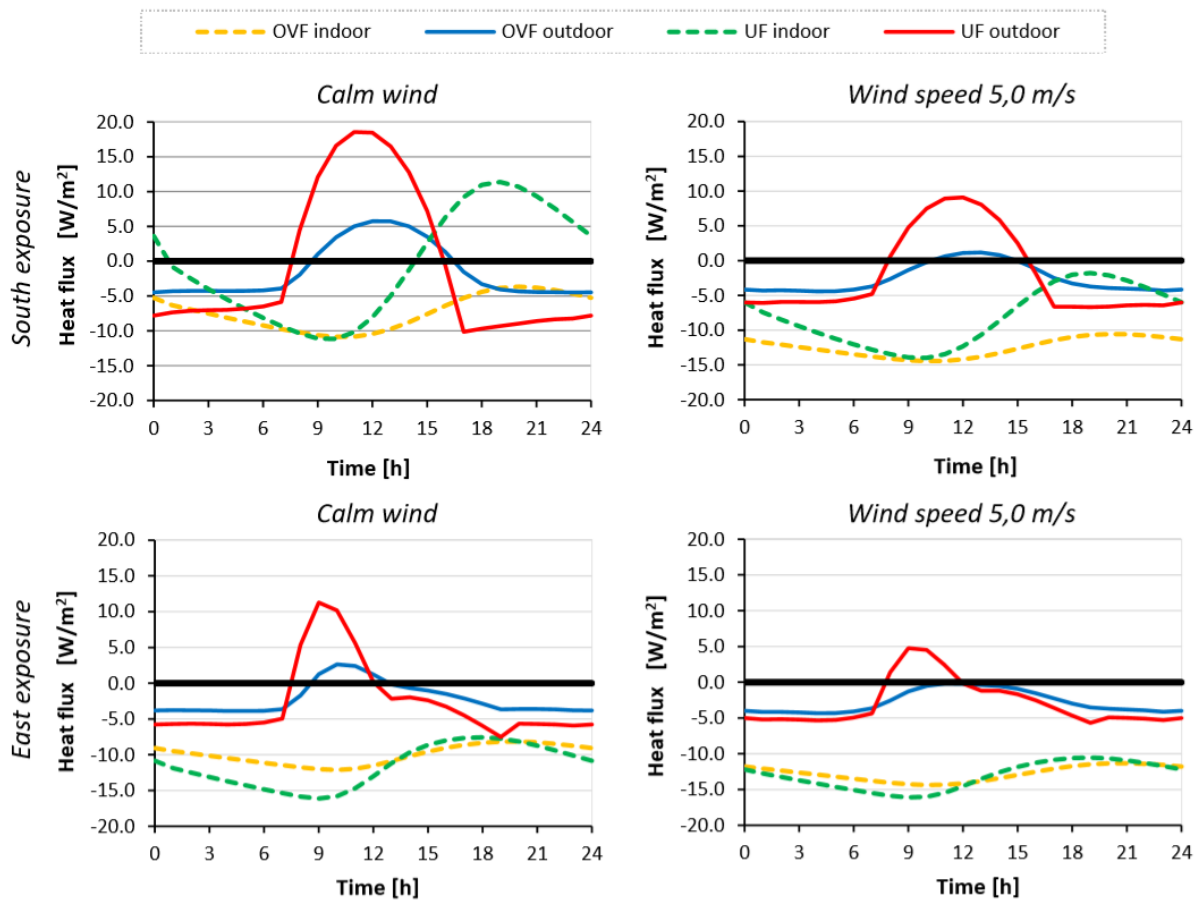


Figure 4.8 – UF and OVF’s hourly thermal fluxes for each scenario during a winter day.

In general, the heat fluxes are most powerful for the UF, so the counter-wall of the OVF shields the internal wall of the façade ensuring greater separation from the external environment.

The most strength wind reduces the magnitude of the heat fluxes towards the outdoor for both the exposures.

The screen effect of the external skin diminishes the solar gains during the daylight hours, the highest decrease happens for the South exposure and the status of calm wind, being of 17.9 and 5.1 W/m² respectively for the UF and OVF at noon, with a difference of 12.8 W/m².

It has to be remarked that the solar gains are not always converted in an effective energy saving as they may lead just to an overheating of the indoor space during the daytime period in winter.

Most intense winds reduce the solar gains, of about 50.0% for the UF and about 80.0% for the OVF in comparison to the status of calm wind. The OVF shows the highest solar gains decrease because of the counter wall transfer the solar energy by radiation to the internal wall, and consequently, the decrease of the temperature on the external surface has a higher impact.

During the nighttime, the thermal losses of the UF $(Q_{UF})_{outgoing,win}$ are always higher than that one of the OVF $(Q_{OVF})_{outgoing,win}$. The difference among $(Q_{UF})_{outgoing}$ and $(Q_{OVF})_{outgoing}$ are the highest for the South façade and for calm wind day, whereas this difference is minimal for the East façade and windy day.

As an example, for the South Exposure and a calm wind day, the thermal losses of the OVF $(Q_{OVF})_{outgoing}$ are approximately 4.5 W/m^2 , whereas for the same scenario the thermal losses of the UF $(Q_{UF})_{outgoing}$ are about 10.1 W/m^2 , with a reduction of the energy needs of almost 50%, which guarantees a reduction of the peak energy demand for space heating.

4.1.3.3 Comparisons between the OVF and UF during the summer season

As observed for the winter period, during the summer period the thermal behaviour of both the facades depends on their exposure as well as the wind status are presented.

Figure 4.9 depicts the hourly external surface temperatures for the UF (TS_{4-UF}) and the OVF (TS_{4-OVF}), as well as the outdoor temperature for the different windiness and façade exposure.

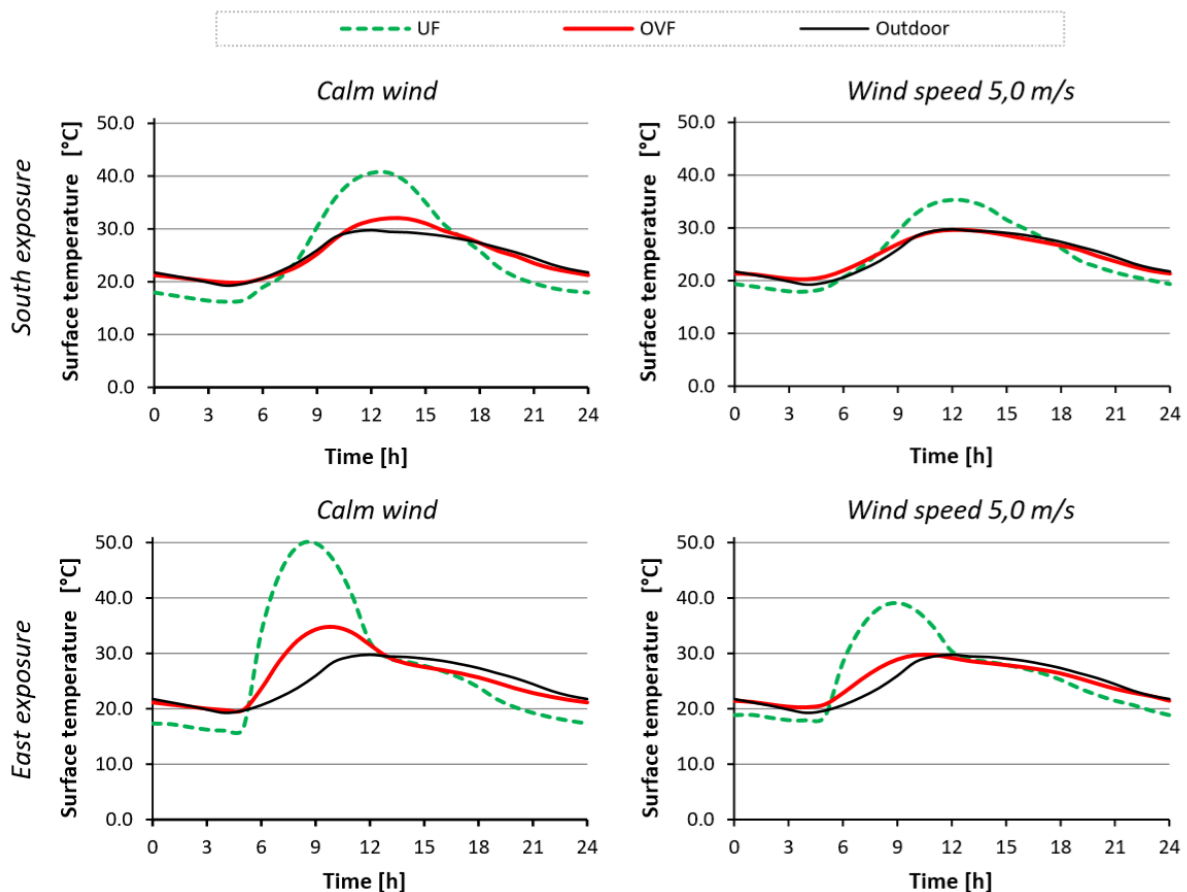


Figure 4.9 – hourly surface temperature of the OVF and UF during a summer day for each scenario.

By looking to the East exposure, the superficial temperatures of the OVF are lower than the superficial temperatures of the UF during the daytime period, with differences that reach a maximum of 15 °C for calm-wind conditions. Otherwise, the temperatures of the UF are slightly lower than the temperatures of the OVF during the night period.

In general, higher wind velocity, i.e. 5.0 m/s, reduces the superficial temperature of both UF and OVF, besides, the maximum temperature difference between the two facades diminishes to about 10 °C. The facade facing South has similar behaviour of the facade facing East. The main differences are generated by the reduced solar irradiance that hits the South façade during the summer period.

Thus, the OVF allows to remarkably reduces the solar gains in comparison to the UF during the hot summer days.

More details regard the velocity and temperature profiles are shown in appendix 6.

The daily heat fluxes, $(Q_{OVF,UF})_{indoor}$ (dashed lines) as well $(Q_{OVF,UF})_{outdoor}$ (continuous lines) are depicted as a function of the exposure and the windiness in fig. 4.10, where the incoming heat fluxes have a positive sign whereas the outgoing heat fluxes have a negative sign.

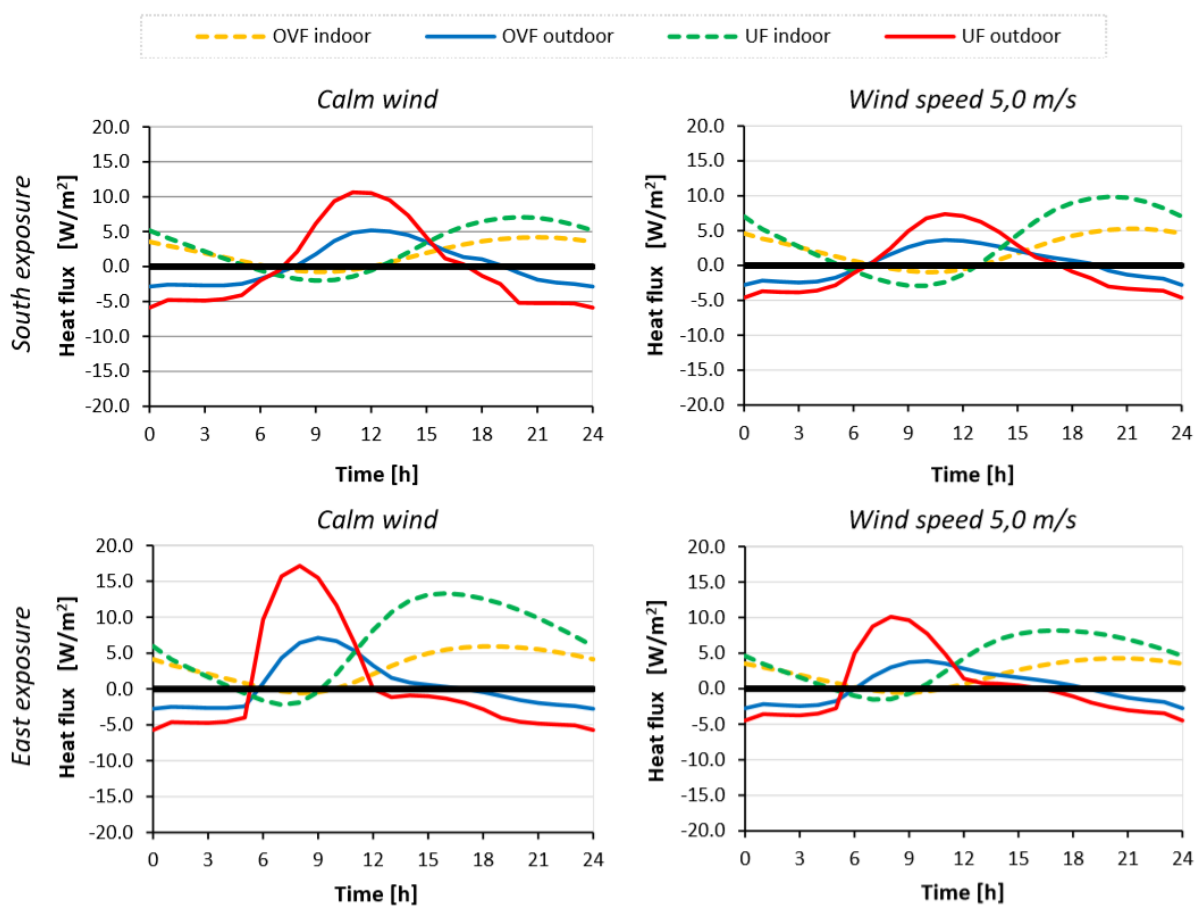


Figure 4.10 – UF and OVF’s hourly thermal fluxes for each scenario during a summer day.

In general, the thermal behaviour of the two façades follows a similar trend of that one described during the winter period. One of the main differences is that the East façades are subjected to the highest heat fluxes.

The $(Q_{OVF/UF})_{outdoor}$ is transferred to the indoor space $(Q_{OVF/UF})_{indoor}$ attenuated and delayed as a function of the thermal inertia of the internal wall.

Due to the effect of the counter-wall, the heat fluxes are more powerful for the UF than the OVF. This means that the external layer of the internal wall of the OVF has a less intense fluctuation of its temperature during the day. For the East exposure and the status of calm wind, the OVF allows achieving the highest reduction of the solar gains $(Q_{OVF})_{incoming}$, being 10.0 W/m^2 , thanks to the ventilated channel and the screen effect of the counter wall. It is evident that for all scenarios, the OVF allows diminishing the incoming heat fluxes guarantying the reduction of the peak energy demand necessary for space cooling.

4.1.3.4 Energy Savings

In this section, the daily heat fluxes, which crosses the two façades and the energy saving, calculated by Eqs. 4.5 and 4.6, respectively for winter and summer season, are shown.

As previously mentioned, the analysis of the daily heat fluxes $(Q_{OVF/UF})_{outdoor}$ that crosses the outermost layer of the two façades allows enhancing the different performances between the OVF and UF deriving by the ventilated cavity and the screen effect of the counter-wall.

For the right interpretation of the reported results, it has to be remarked that the daily heat fluxes taken into account are, the outgoing thermal fluxes $(Q_{OVF/UF})_{outgoing,win}$ during the winter day, so the solar heat gains are not reckoned, and the incoming heat fluxes $(Q_{OVF/UF})_{incoming,sum}$ during the summer day, thus the night cooling is not reckoned.

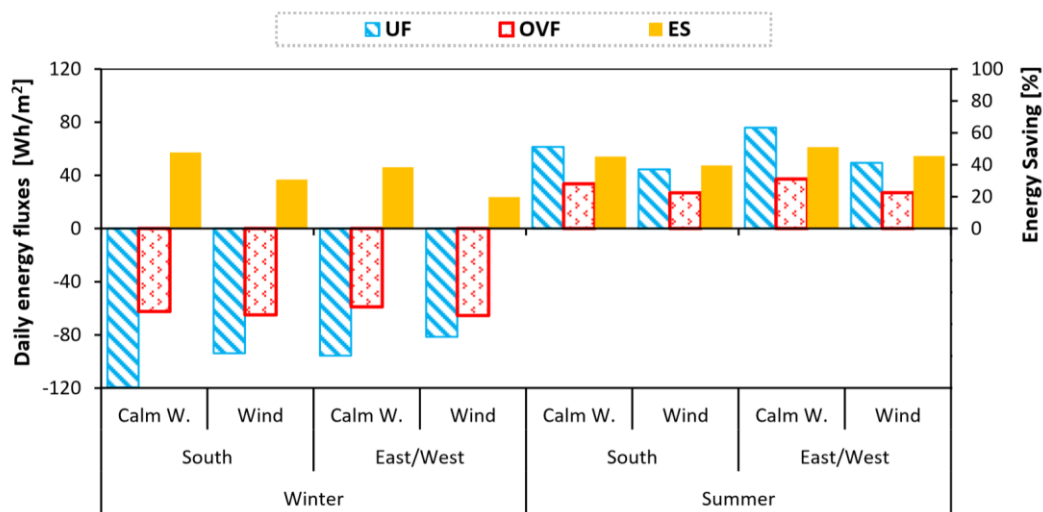


Figure 4.11 – Daily energy fluxes and Energy saving for the two façades.

It is possible to highlight that, under the previous settings, the OVF gives rise to daily thermal fluxes lesser than the UF for all the examined scenarios. However, for the winter days, the positive sign of the heat fluxes indicates that the UF has heat gains higher than the UVF.

The energy fluxes through the OVF are rather constant for both the winter and the summer days independently by the façade orientation and the wind status, which are around 60.0 and 30.0 Wh/(day·m²) respectively for winter and summer day.

This outcome highlights the role of the combined effect of the counter wall and the ventilation to protecting the internal wall by the environmental forcing.

As a rule, wind calm conditions enhance the energy-saving achievable by the OVF both in winter and summer days, which ranges from 20.0 to 55.0%. The highest ES is achieved during a summer day for the façade facing East/West. On the contrary during a winter day the façade facing South give rise to the highest ES.

These results indicate that for the façades facing from East to West, the adoption of an OVF gives rises to remarkable Energy Saving. More specifically the façades facing South attain the better performance during the winter day, while the façades facing East or West attain the better performance during the summer day.

4.2 Analysis of Active Building Envelope composed by solar thermal (ST) system

The installation of solar collectors applied or integrated into the building envelope may represent an interesting opportunity to increase the fraction of the building energy demands supplied through solar energy.

A general methodology to evaluate the economic benefits of building integrated solar thermal systems is presented in [35]. They demonstrated that any thermal energy offset by the BIST generates a saving that reduces the building's operational cost. Moreover, the BIST system can reduce the overall construction material costs and may offer additional revenue in the form of financial incentives and tax credits.

Building Solar Thermal Facades (BSTFs) could be very useful in high-rise buildings, which do not have sufficient spaces to install a solar plant.

This section first presents a preliminary investigation on a prototype of Ventilated Building Solar Thermal Facade (v-BSTF) built in Ragusa.

Subsequently, the objective aims at evaluation of the energy performances to the purpose the Domestic Hot Water (DHW) production of the BSTFs, constructed with two distinct types of solar collectors, flat plate (FPC) and evacuated solar collectors (ETC), through transient simulations carried out with TRNSYS software, under different climate conditions.

An economic and LCA analysis on the two types of examined BSTFs were developed and shown in the document annex in appendix 7 [36].

4.2.1 Experimental v-BSTF prototype

Under the research project "Solar Collector Continue Façade" (FCCS), funded by the POR FERS Sicilia 2007/2013- Research line 4.1.1.1, two BSTF prototypes were designed and tested.

These two BSTF prototypes, depicted in figure 4.12, are installed into the industrial building of the EUROINFISSI Company, in Ragusa.



Figure 4.12 – Map of the building (left side), photo of the two BSTF prototypes (right side).

4.2.1.1 Prototype design

The two BSTFs are constructed with an aluminium frame specifically designed to be coupled with the solar plate collector type Viessmann Vitosol 200-FM. The designed BSTF may be integrated or merely overlaid into the façade in case of building renovation.

One of the two BSTF prototype, namely v-BSTF, is mounted leaving a ventilated gap between the FPC and the building envelope.

The ventilated solar thermal façade (v-BSTF) has a total gross surface of 7.50 x 2.40 m and it is constituted by six solar panels, subdivided into two arrays. The v-BSTF is north-west oriented.

The v-BSTF is part of a solar thermal plant, designed for DHW production, equipped with a solar storage tank with a capacity of 1000 litres. The hydronic circuit is managed through a control system that switches on/off the solar pump by controlling the outlet temperature from the solar collector and the temperature in the lowest part of the solar storage tank.

Nearby the pilot v-BSTF, a meteorological station equipped with a set of sensors for the measurements of the outdoor air temperature, total irradiance on the vertical plane, wind speed and direction was installed. Moreover, the superficial temperatures on the back of the solar collectors and the building wall and the air velocity are measured at different heights into the air gap. The air pressure difference between the inlet and outlet sections of the air gap, the superficial temperature on the front of the solar collector and the air temperature in the indoor space were also measured. All the measured parameters were recorded in a data logger.

In Fig. 4.13 are shown the different sensors installed, where the measuring range, accuracy and response time are reported.






	Outdoor air temperature	Air temperature	Total radiation	Wind speed and direction	Surface temperature
					
Measuring range	-50÷70°C	-50÷70°C	0÷2000W/m ²	>0.36m/s	-50÷70°C
Accuracy	0.10°C	0.10°C	±5%	1.5%	0.15°C
Response time	30s	30s	23s	0.48s	35s

Figure 4.13 – Features of the main sensors installed.

Figure 4.14 depicts the cross section and the front view of the v-BSTF installed, where are indicated the positions and the name of the sensors.

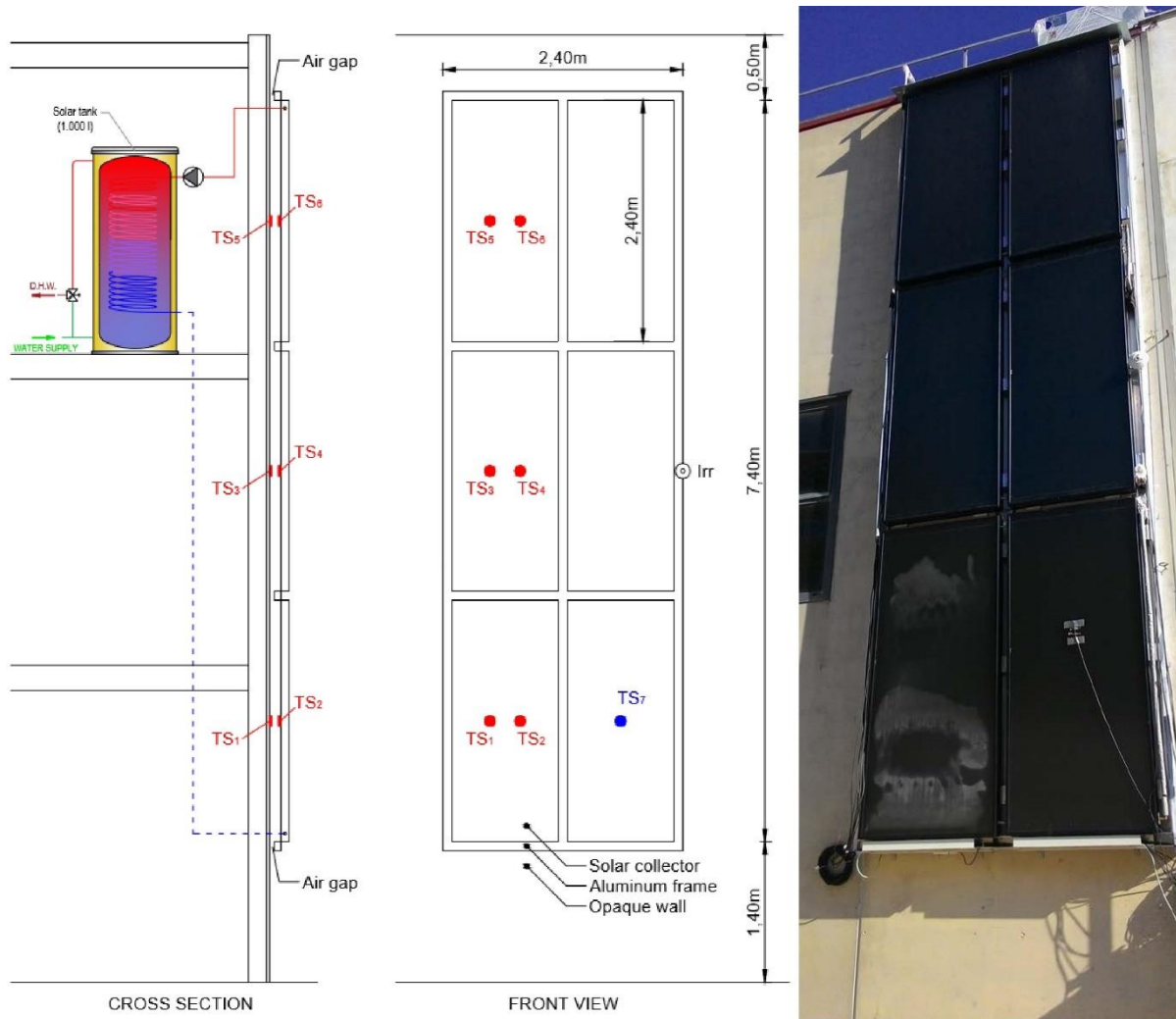


Figure 4.14 – Section and front view of the v-BSTF façade with the installed sensors.

The placement of the temperature sensors was conceived for the purpose to evaluate the vertical gradient of the temperatures, on the surface façade and the rear of the v-BSTF, generated by the airflow in the air gap.

The sensors that measure the surface temperature are called TS_{*i*} (*i* = 1, 2 7). They are installed in the middle part of each solar panel, three in adherence to the building wall (TS₁, TS₃, and TS₅), others three in the back of the solar plate panel (TS₂, TS₄, and TS₆). The sensor TS₇ is installed into the front face of the lower solar panel of the v-BSTF.

The comparison of the temperatures measured with sensor TS₇ with the temperatures measured on the building façade (TS₁, TS₃, and TS₅) allows evaluating the difference of temperature of a surface directly exposed to the sun rays and a shaded surface. Moreover, the time shift between the peaks of temperatures in those surfaces may be pointed out.

4.2.1.2 On-Site Measurements

Figure 4.15 depicts the data collected through the monitoring system for six winter days. The upper part of this figure shows the solar irradiance and the environmental temperature, while the lower part shows the temperatures measured by the sensors.

It is possible to observe that during these sunny days the thermal behavior of the v-BSTF is quite similar.

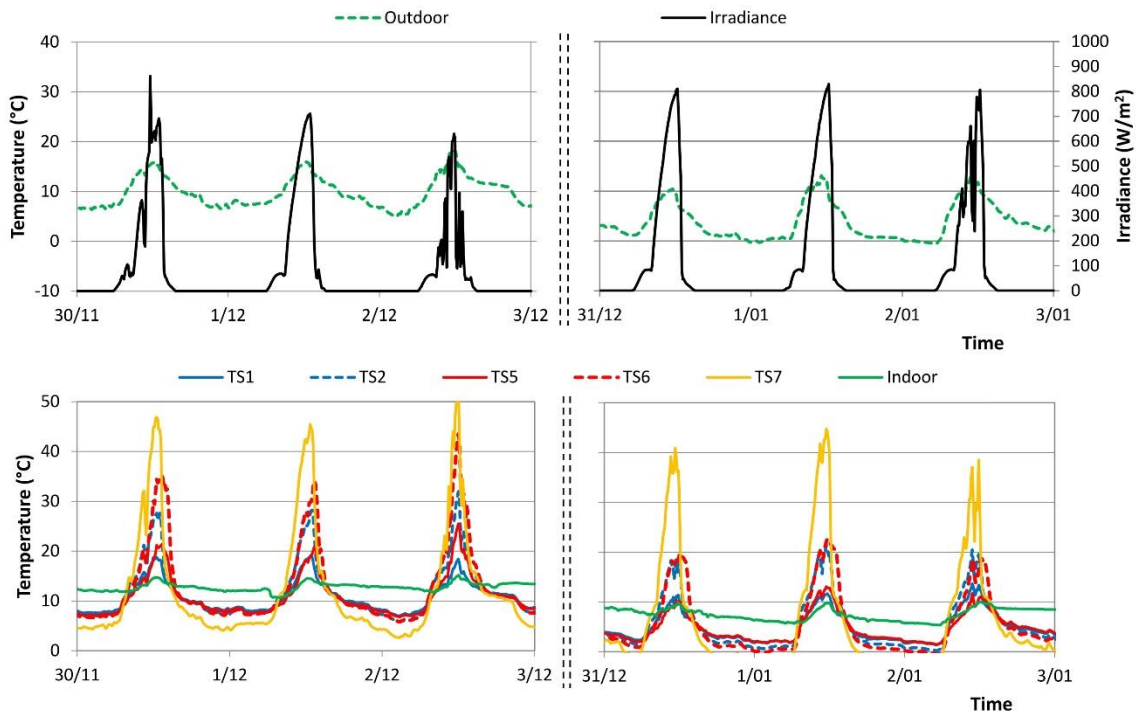


Figure 4.15 – Experimental data measured on the v-BSTF

Figure 4.16 shows the details of the monitored data during one of these days (1st December)

It is possible to notice that the superficial temperature (TS₇) on the front of the solar panel is the highest during day-time (the surface is heated by the solar irradiance) and it is the lowest during night-time (the surface is cooled by radiative losses versus the sky-dome). Such temperature has the highest thermal drop.

On the back of the solar collectors, the highest temperature is reached in the upper part of the solar facades (TS₆). This means that the surrounding air is heated flowing out in the ventilated air gap. The temperatures differences between the highest and the lowest sensor (TS₆ – TS₂) increase during the daytime reaching a maximum of about 10°C about at 13:30.

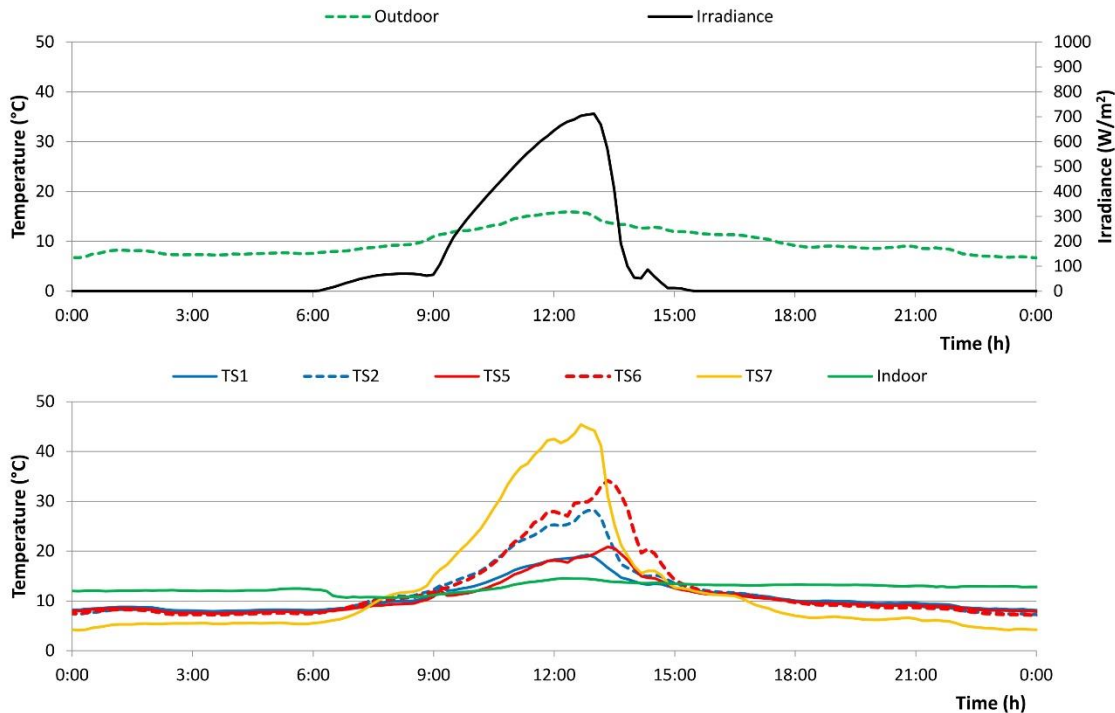


Figure 4.16 – The monitored data during the 1st December

The temperatures measured on the building facade, (TS₁ and TS₅), once again increase moving from the bottom up of the building façade, reaching a temperature difference of about 5°C (TS₅ – TS₁) at 13:30. During daytime, these temperatures are permanently higher than the outdoor air temperatures. During nighttime, a reversal behaviour occurs since the superficial temperatures on the building façade (TS₁ and TS₅) are about 5°C higher than TS₇ and close to the outdoor temperature. This result designates a reduction of the radiative heat-losses from the wall surface to the sky-dome in comparison with a façade directly exposed to the sky-dome.

Finally, it has to be remarked that the solar façade causes a decrease of the solar gains during the winter period, since a part of the solar energy that strikes the façade is used for heating the fluid in the solar circuit.

However, as well known this shortcoming may be neglected considering that only a low percentage of the solar radiation that strikes the opaque façade is useful for reducing the building thermal load. And also, that during night-time the v-BSTF allows reducing the heat losses through the building envelope as previously mentioned.

During the summer period, the combined effect of shading and ventilation deriving by the adoption of v-BSTF allows achieving remarkable energy savings, up to 50.0% as shown in paragraph 4.1 and in [34, 37].

4.2.2 Analysis of the DHW production of the BSTFs

Through un-steady state simulations, the thermal producibility of solar thermal systems installed on the façade (BSTF) was analysed. For the analysis, the preheating plant layout was considered (Fig. 4.17), where the heat produced is stored in a thermal storage tank in the form of heated water and used for Domestic Hot Water (DHW).

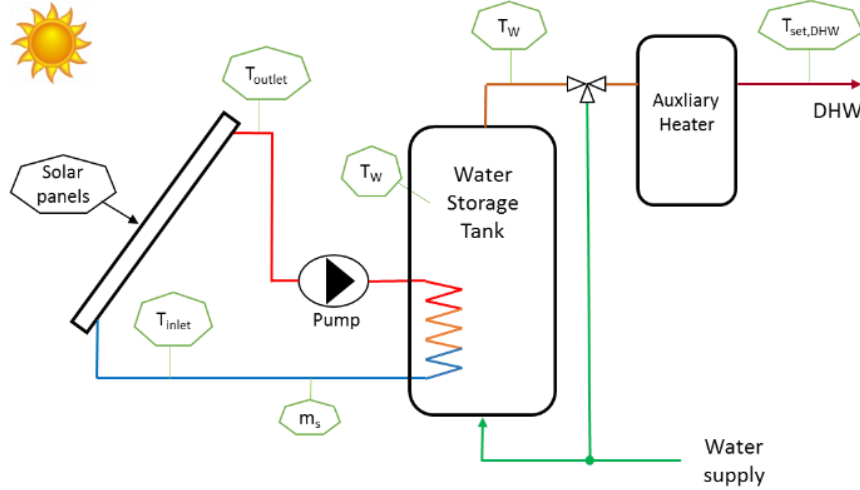


Figure 4.17 – Scheme of the solar system

Therefore, in the solar circuit, from the solar collectors the working fluid with temperature T_{out} is sent to the heat exchanger present in the storage tank, giving it heat and return to the panels with T_{in} temperature. The DHW production circuit consists of the storage tank, a mixing valve, and an auxiliary boiler. When the user requests DHW with flowrate " \dot{m}_{DHW} " and temperature " $T_{set,DHW}$ ", the water is taken from the tank with temperature $T_{t,out}$. If $T_{t,out}$ is less than $T_{set,DHW}$, an auxiliary heater will provide the remaining part of energy to bring the water to $T_{set,DHW}$, otherwise if $T_{t,out}$ is greater than $T_{set,DHW}$ the mixing valve will use part of the mains water to send water with temperature equal to $T_{set,DHW}$.

Thus, the DHW load (E_{DHW}) calculated with Eq. 4.11, can be divide into that coming from the RES plant (E_{th}) and that supplied by the auxiliary generator (E_{AUX}), calculated respectively using the Eq. 4.12, and 4.13.

$$E_{DHW} = \int_0^t \dot{m}_{DHW} \cdot C_w \cdot (T_{set,DHW} - T_{sup}) dt \quad (4.11)$$

$$E_{th} = \int_0^t \dot{m}_{DHW} \cdot C_w \cdot (T_{mx,out} - T_{sup}) dt \quad (4.12)$$

$$E_{AUX} = \int_0^t \dot{m}_{DHW} \cdot C_w \cdot (T_{set,DHW} - T_{mx,out}) dt \quad (4.13)$$

Where C_w indicates the specific heat of the water, $T_{mx,out}$ is the temperature of the fluid coming from the mix valve, T_{sup} the temperature of grid water supply, and $T_{set,DHW}$ the temperature required by users.

Finally, the effectiveness of BSTF to produce DHW can be evaluated through the fraction of the energy demand supplied:

$$f_{DHW} = 100 \cdot \frac{E_{th}}{E_{DHW}} \quad [\%] \quad (4.14)$$

4.2.2.1 Numerical model

The model of the solar system was created in TRNSYS software environment [38]. In the model, distinct components describe the solar thermal loop (i.e. solar panels, storage tank, unit pump, and controller) as well as the management of the energy demand (i.e. DHW load, thermal mixing, and auxiliary heater). Figure 4.18 shows the flow diagram of the solar system created in TRNSYS.

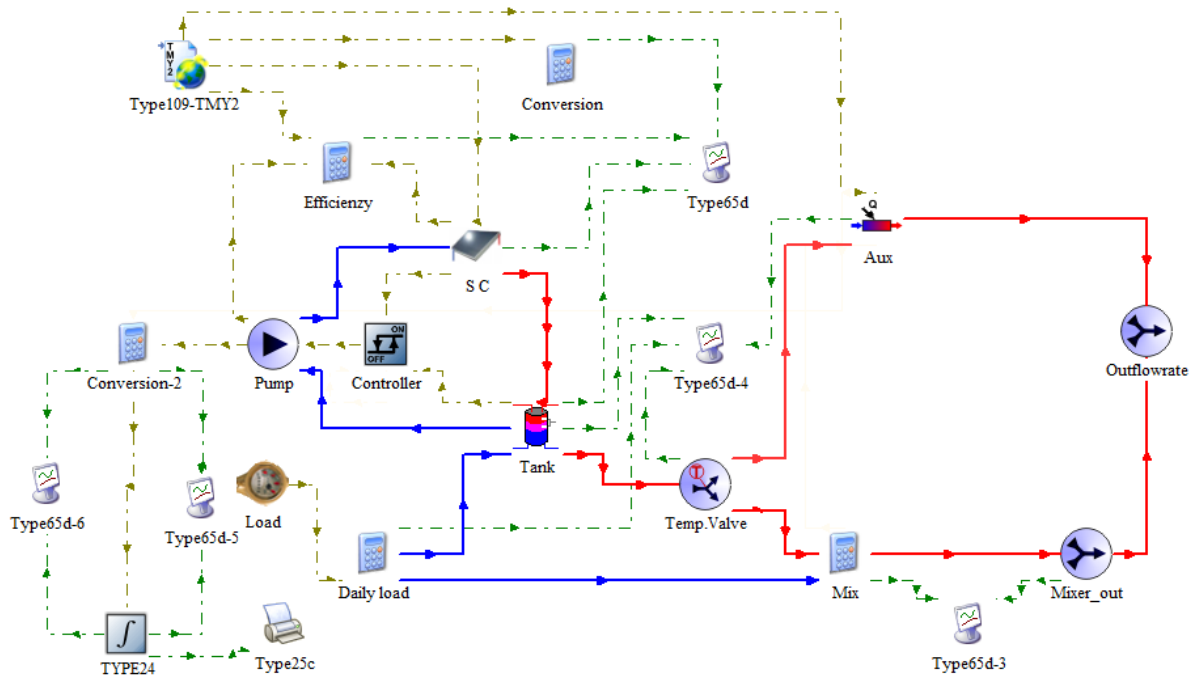


Figure 4.18 – TRNSYS assembly of the simulated solar system.

The solar collector receives hourly meteorological data as inputs from the Type 109 data reader in the standard TMY2 format. The On/Off controller receives inputs of the fluid temperature that exits the collector and the temperature of the fluid at the bottom of the storage tank. The output control function is connected with the pumps, thus switching it on or off, allowing or not the charging of the tank (Type 60).

The DHW tank subsystem includes the components that define the request for DHW (Type 4c), as well as a temperature-controlled flow diverter (Tempering Valve - Type 11b) used to regulate the flow stream at the required temperature $T_{set,DHW}$. When the enthalpy level from the solar tank is insufficient for achieving the minimum required temperature, the flow stream goes to the auxiliary heating system.

As previously explained two distinct BSTF configurations are simulated, in the first the solar collectors used are flat plate model (scenario 1), while in the second configuration the solar collectors used are evacuated tube model (scenario 2). Consequently, Type 1 describes the solar collector subsystem, under scenario 1, while Type 71 describes the evacuated tube collector, under scenario 2.

4.2.2.2 Study specifications

The analysis of BSTF's performance are performed considering two technologies of solar thermal collector, installed in façade facing South, and located in four different Italian cities, that are Ragusa, (lat. 36°55') Catania (lat. 37°30'), Rome (lat. 41°53') and Milan (lat. 45°28').

For both two distinct typologies of solar collectors, FPC (scenario 1) and ETC (scenario 2), the BSTFs have an area of 4.0 m², which was chosen as a reference for an Italian residential unit with a DHW consumption of about 200 l/day. The hourly consumption profile is that suggested by the standard EN 15316:2007.

Table 4.III shows the technical data of commercial solar collectors available in the Italian market that were used in the simulations.

Table 4.III Features of the two typologies of thermal collectors.

Panel type	η_0 [-]	α_1 [W/m ² K]	A_2 [W/m ² K ²]
Glazed flat plate	0.803	3.55	0.035
Evacuated tube	0.789	1.55	0.007

4.2.2.3 Environmental climate data

The climatic differences among the four cities can be pointed out comparing the average monthly radiation and temperature data, as well the number of heating degree-days. These data were obtained from the PV-GIS monthly radiation tool [39].

Figure 4.19 depicts for the various locations, the heating degree days at the top left, the average monthly temperature at the top right, and the total radiation on the BSTF at the bottom.

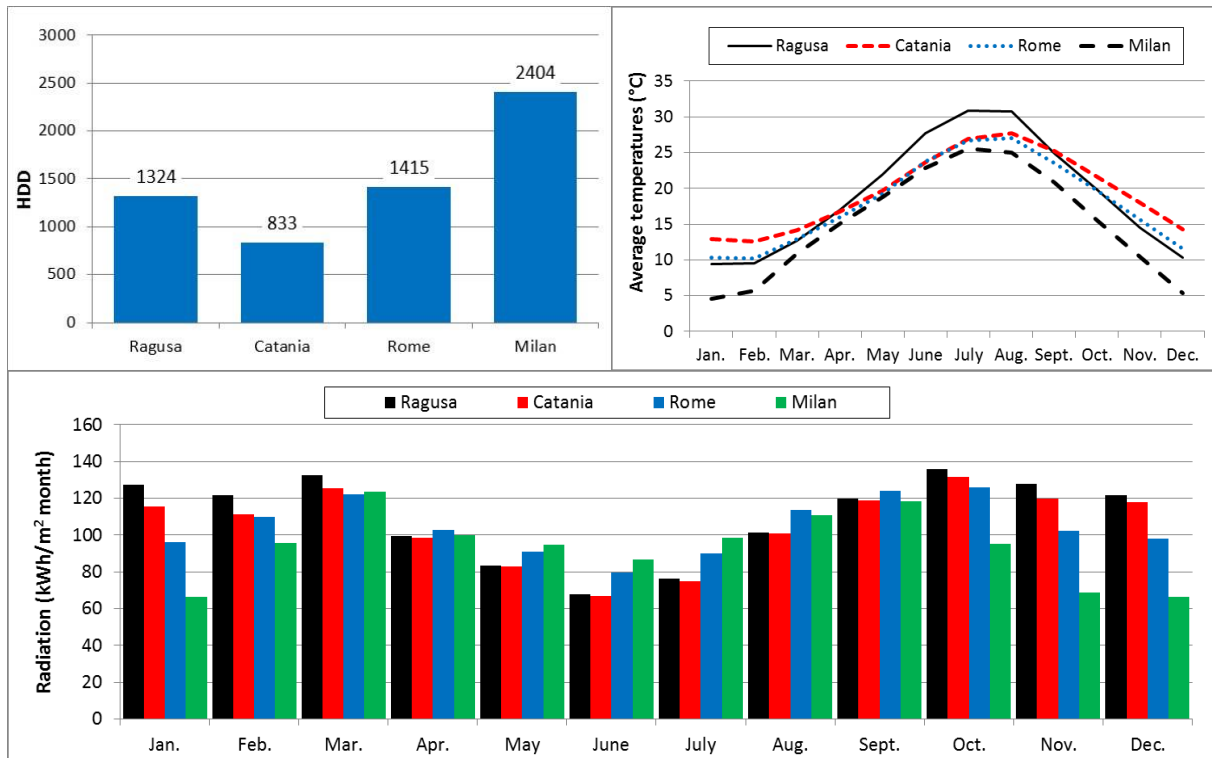


Figure 4.19 – Comparison of HDD, average monthly outdoor temperature, and total monthly radiation on BSTF facing South, for the four location analysed.

As regard, the number of Heating Degree Day, Milan has the highest HDD (2404), which are about two times higher than that one of Rome and Ragusa (1415 and 1324) and almost three times the HDD of Catania (833). As regards the air temperature, the greatest differences of temperature among the cities emerge during the winter period, when up to 10°C between Milan and Catania is observed. It is important to note, that the values of solar radiation do not reach the highest values during the summer months, except for Milan that during the cold season presents the most frequent worst meteorological conditions which causes the reduction of the beam irradiance available.

During the summer period, a vertical solar façade has modest performance especially in the sites with the lowest latitudes. As shown in figure 4.20, the solar irradiance that hits a vertical south-facing façade during a sunny winter day (left side) is higher than the solar irradiance on a summer day (right side), where the maximum daily solar irradiance in winter is even twice the maximum daily solar irradiance in summer.

The solar irradiance has quite modest differences among the four cities both in winter and summer days. This means that such position of the solar collectors smooths the dependence of the solar radiation by the latitude. During summer days, the solar irradiance reaches the highest values in Milan and the lowest in Catania and Ragusa, so the southern cities are the most penalized during the hot season.

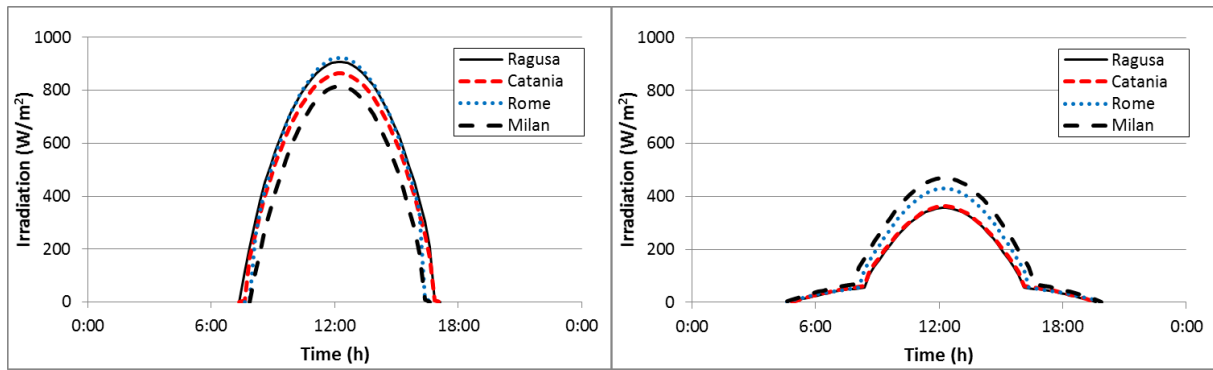


Figure 4.20 – Solar radiation on winter solstice (left-side) and summer solstice (right-side).

4.2.2.4 Results

This section shows some results of transient simulations carried out for the two scenarios.

In this section, the thermal fluxes occurring between the solar thermal façade and the building envelope are not investigated.

Winter period

The transient simulations allow calculating the main parameters that characterize the performances of the BSTF per each month, city, and scenario.

As an example, the results obtained during a winter week (January 20-27) in Ragusa and Milan, which respectively could be assumed as representative for temperate and cold climate, are shown in the following.

Figures 4.21 and 4.22 depict the outlet temperatures from the solar collectors under scenario 1 " $T_{O,S1}$ " (dashed red line) and scenario 2 " $T_{O,S2}$ " (dashed blue line), the ambient air temperatures " T_{amb} " (green line), the solar irradiance " G " (black line), as well as the temperatures in the solar tank for scenario 1 " $T_{t,S1}$ " (orange line) and for scenario 2 " $T_{t,S2}$ " (light blue line), respectively for system installed in Ragusa and in Milan.

During this week, it is possible to observe the effect of different sky conditions on the thermal behaviour of these solar systems.

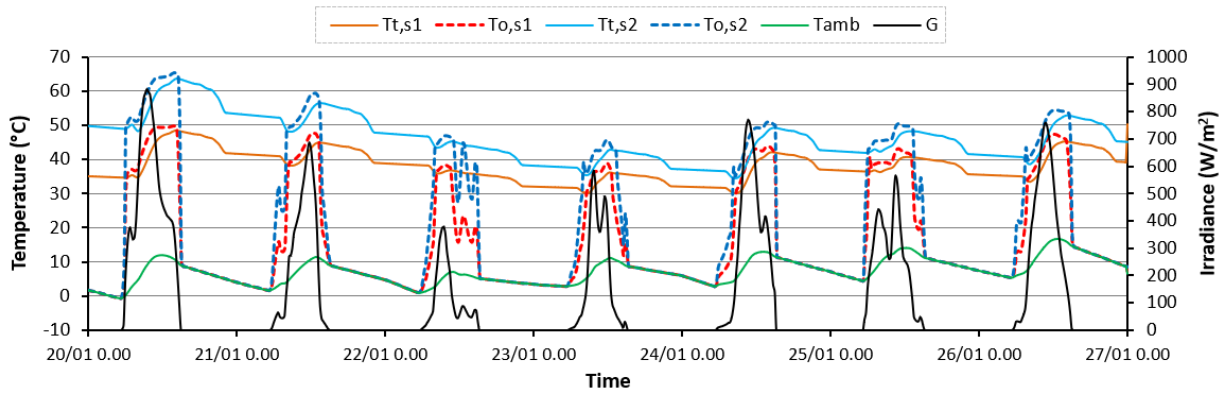


Figure 4.21 – Weather data (solar irradiance and ambient temperature) and solar plant operating temperatures (tank and collectors) during a winter week in Ragusa.

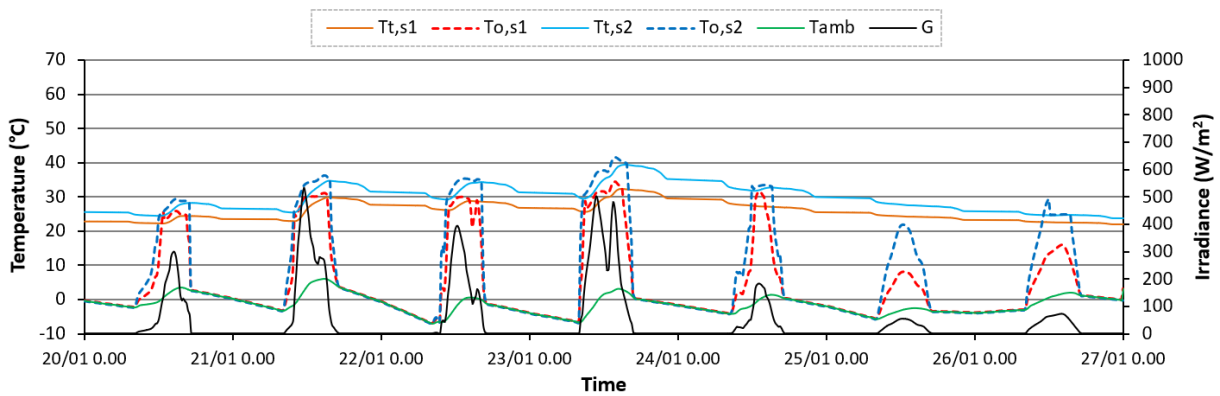


Figure 4.22 – Weather data (solar irradiance and ambient temperature) and solar plant operating temperatures (tank and collectors) during a winter week in Milan.

As regards Ragusa, under scenario 1 the temperatures in the solar tank ($T_{t,s1}$) are constantly higher than 30°C, with the highest values that do not exceed 50°C. While, under scenario 2 the temperatures in the solar tank ($T_{t,s2}$) are constantly higher than 35°C, with the highest values of about 65°C. The daily variation of the temperatures in the solar tank is quite similar in both scenarios with differences of almost 10°C, during the whole period. Analogous considerations may be pointed out for the outlet temperatures from the solar collectors, it is confirmed that $T_{o,s2}$ is always higher than $T_{o,s1}$.

As regards Milan, during the same observed winter week the solar irradiance as well as the outdoor temperatures are lower than that in Ragusa. In particular, the last three days represent very cloudy sky conditions for which only the diffuse component of the solar irradiance is present. Consequently, the two solar systems do not produce any useful energy. Once again, the daily variation of the temperatures in the solar tank during the whole period is quite similar in both scenarios.

Thus, comparing equivalent scenarios, a BSTF installed in Ragusa allows reaching solar tank temperatures that are at least 10°C higher than that attained in Milan.

Figures 4.23 and 4.24 show, respectively for BSTC installed in Ragusa and in Milan, the hourly thermal energy provided by the solar plants (E_{th}) and that one supplied by the auxiliary heater (E_{aux}), considering both scenario1 and 2. In the graphs the areas subtended by the curves correspond to the daily energy needs for DHW production.

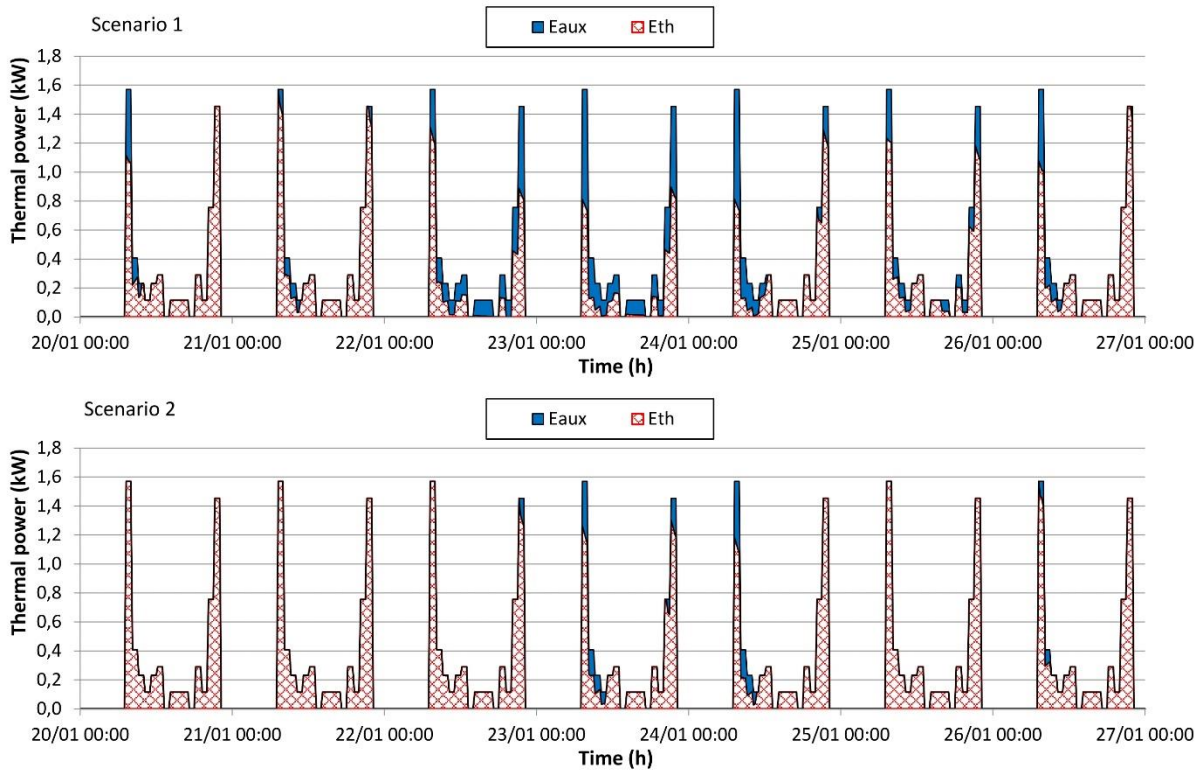


Figure 4.23 – Energy fluxes during a winter week in Ragusa.

In Ragusa, under scenario 1, although the energy supplied by the solar system guarantees great daily coverage factors, higher than 0.7, the auxiliary heater has to function all the days. In particular the morning and in the late hours of the day. Otherwise, under scenario 2 the daily coverage factors significantly increase. In fact, for three days the DHW energy requirements are totally supplied through the solar system ($f=100\%$), and in the other four days, the energy supplied by the auxiliary heater is very small.

The performances of the BSTF installed in Milan are modest compared with that one of Ragusa. Under the scenario 1, the thermal power supplied by the solar plant is very scarce, just in one day, the solar system provides of about 0.65 kW, which is about 40.0% of the peak value for the DHW demand. Under scenario 2, the performances of the system, although remain modest, increase significantly reaching a thermal power of about 1.1 kW that is about 70.0% of the peak value for the DHW demand. This outcome evidences that the ETC solar collectors exploit better their features in the coldest climates.

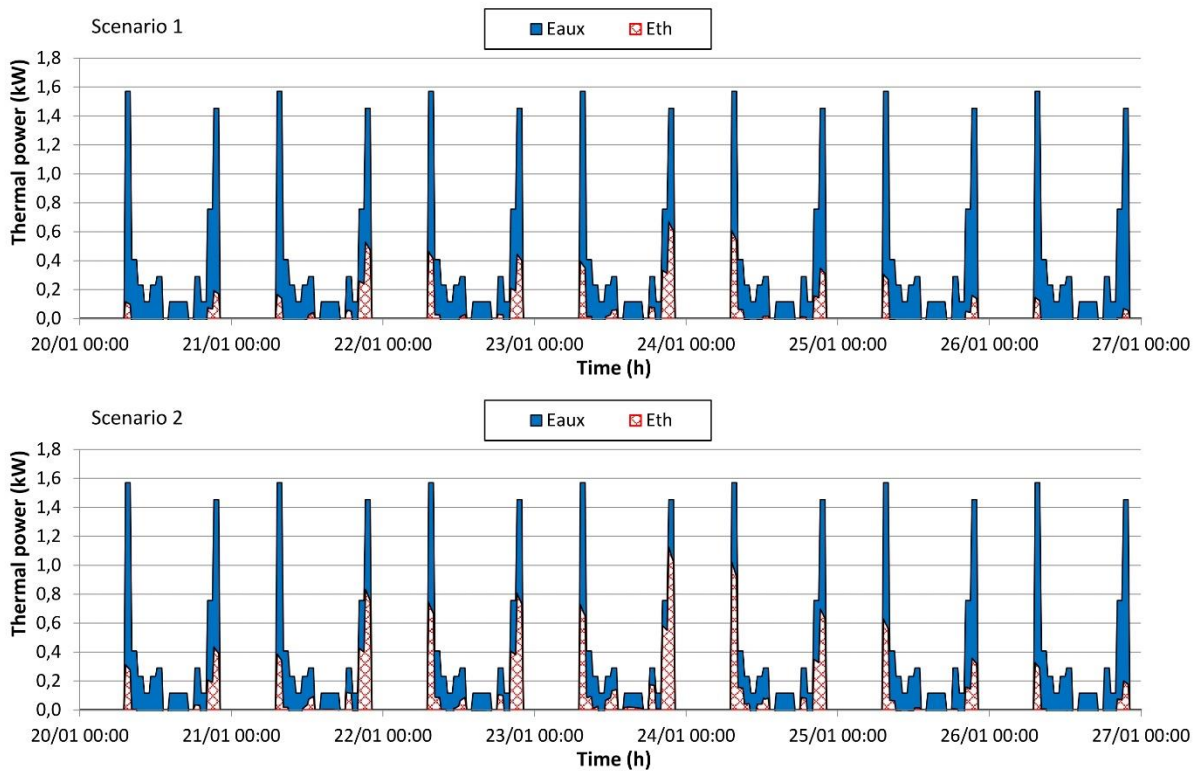


Figure 4.24 – Energy fluxes during a winter week in Milan.

Generally, the scarce performances obtained from both the two solar systems are related to the low values of solar radiation and air temperatures as previously highlighted.

It is interesting to underline that the energy provided by the solar plant is strictly coupled with the daily trend of the DHW needs, which have peaks values in the early morning and in the late evening.

Summer

Similarly, the same analysis showed for the winter season are proposed in the summer period (20-27 June).

Figure 4.25 and 4.26 depict the weather data and the operating temperature for both scenarios, respectively for BSTF installed in Ragusa and in Milan.

As regards Ragusa, under scenario 1 the $T_{t,s1}$ ranges from 32.0 to 42.0°C, while under scenario 2, $T_{t,s2}$ ranges from 35.0 to 45.0°C. The daily variation of the temperatures in the solar tank is quite similar in both scenarios with differences less than 5.0°C, during the whole period. Analogous considerations may be pointed out for the outlet temperatures from the solar collectors, it is confirmed that $T_{o,s2}$ is always higher than $T_{o,s1}$. These outcomes confirm that the two BSTFs have energy performances that are not so different between the winter and the summer period in Ragusa. This is due to the reduced irradiance that strikes a vertical surface

south exposed during the summer period. The maximum daily values of irradiance are of about 50.0% lesser than that observed during a sunny winter day.

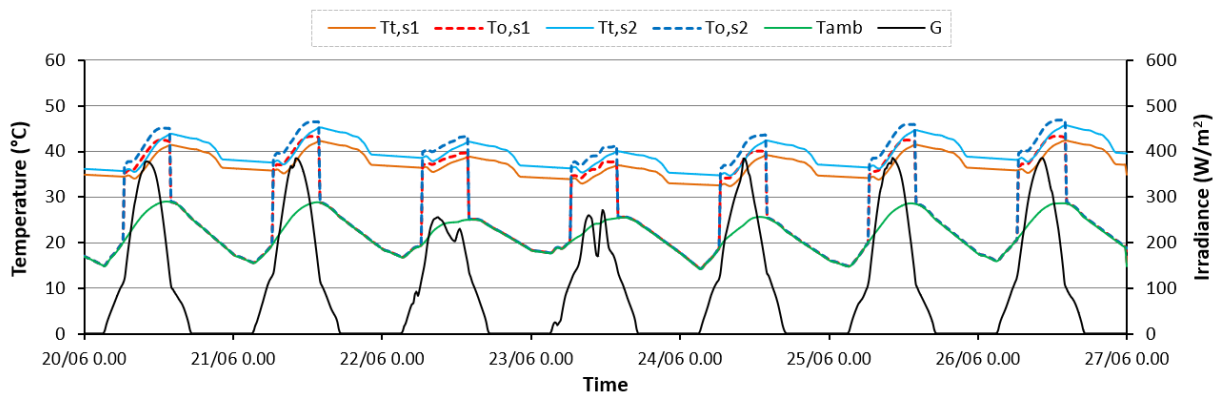


Figure 4.25 – Weather data (solar irradiance and ambient temperature) and solar plant operating temperatures (tank and collectors) during a summer week in Ragusa.

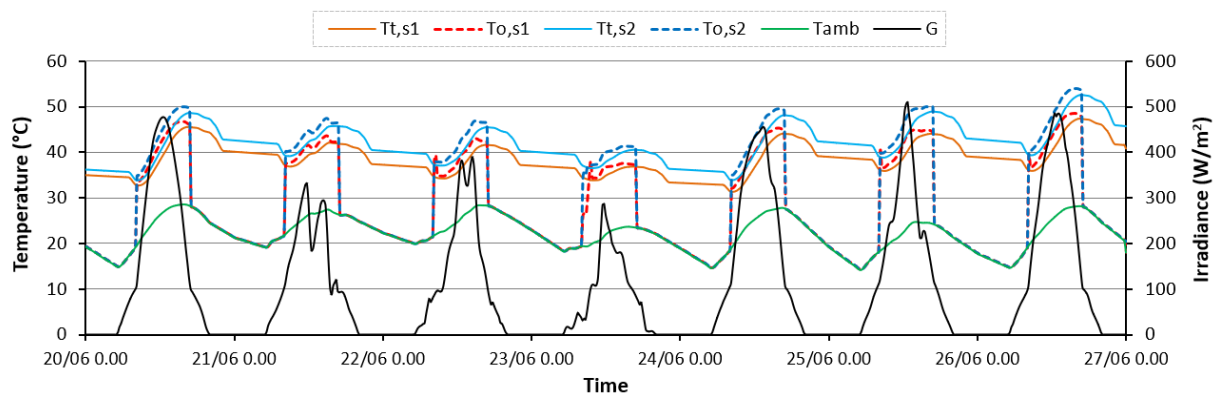


Figure 4.26 – Weather data (solar irradiance and ambient temperature) and solar plant operating temperatures (tank and collectors) during a summer week in Milan.

As regards Milan, during the same observed summer week the solar irradiance that strikes the solar façade is higher than in Ragusa, while the outdoor temperatures are similar. Once again, the daily variation of the temperatures in the solar tank is quite similar in both scenarios, during the whole period. Under the scenario 1 the $T_{t,s1}$ is continuously higher than 32.0°C , with peak values that reach 47.0°C , while under the scenario 2 the temperature achieved in the solar tank, $T_{t,s2}$, is permanently higher than about 5.0°C respect to the scenario 1. Thereby, rather unexpectedly, the solar tank temperatures in Milan are 5.0°C higher than that one achieved in Ragusa. As previously discussed, this outcome indicates that the reductions of the performances of a vertical solar façade are greatest in cities with low latitude (e.g. Ragusa).

Figures 4.27 and 4.28 show the hourly thermal power supplied by the solar plants (E_{th}) and that one supplied by the auxiliary heater (E_{aux}), during the summer week (June 20-27), respectively for Ragusa and Milan.

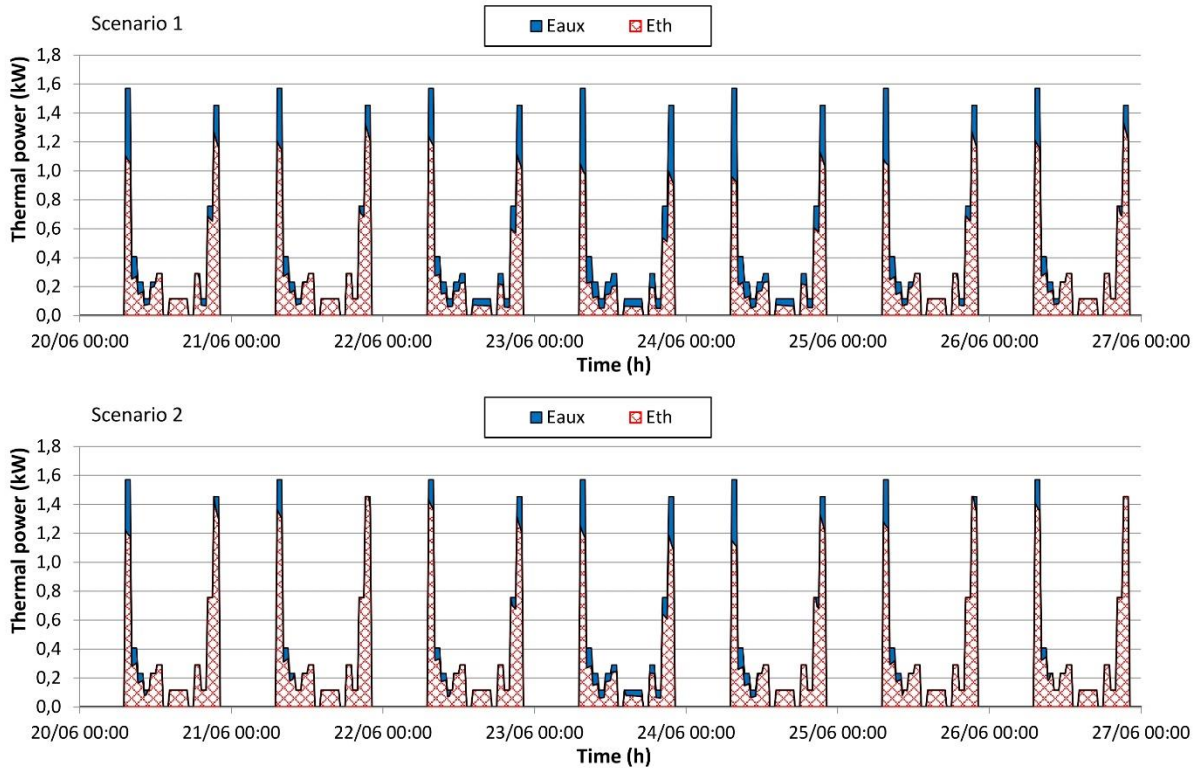


Figure 4.27 – Energy fluxes during a summer week in Ragusa.

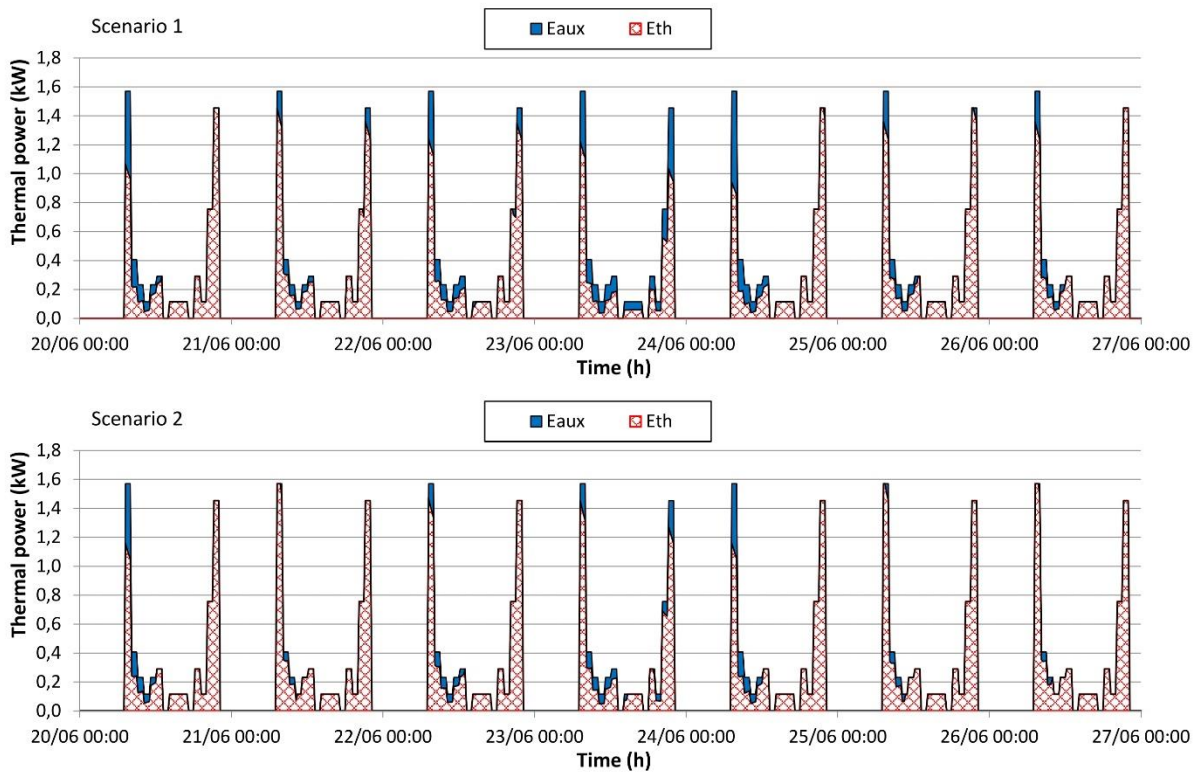


Figure 4.28 – Energy fluxes during a summer week in Milan.

As regards the BSTF installed in Ragusa, under scenario 1, although the energy supplied by the solar system guarantees great daily coverage factors, higher than 0.8, the auxiliary heater has to function all the days. Under scenario 2 the daily coverage factors further increase, but anyway in all days it is necessary to supply a little amount of energy by the auxiliary heater. These outcomes confirm that the two BSTFs have energy performances that are not so different between the winter and the summer period in Ragusa.

For plant installed in Milan, during the summer season, the daily coverage factors show substantial increase respect to the winter season thanks to the high values of the irradiances and the air temperatures. Under scenario 2 the performances of the BSTF are a bit better respect to scenario 1. Even in Milan, the solar plants do not allow fully balancing the energy demand for DHW. This reveals the mandatory use of an auxiliary energy source.

It is worth of interests to underline that during such summer week, the solar plants in Ragusa and Milan achieve almost similar performances.

Yearly performances

In this section of the study, the yearly performances of the solar façade are presented.

Figure 4.29 shows the monthly coverage factor values “*f*” for both the scenarios analysed.

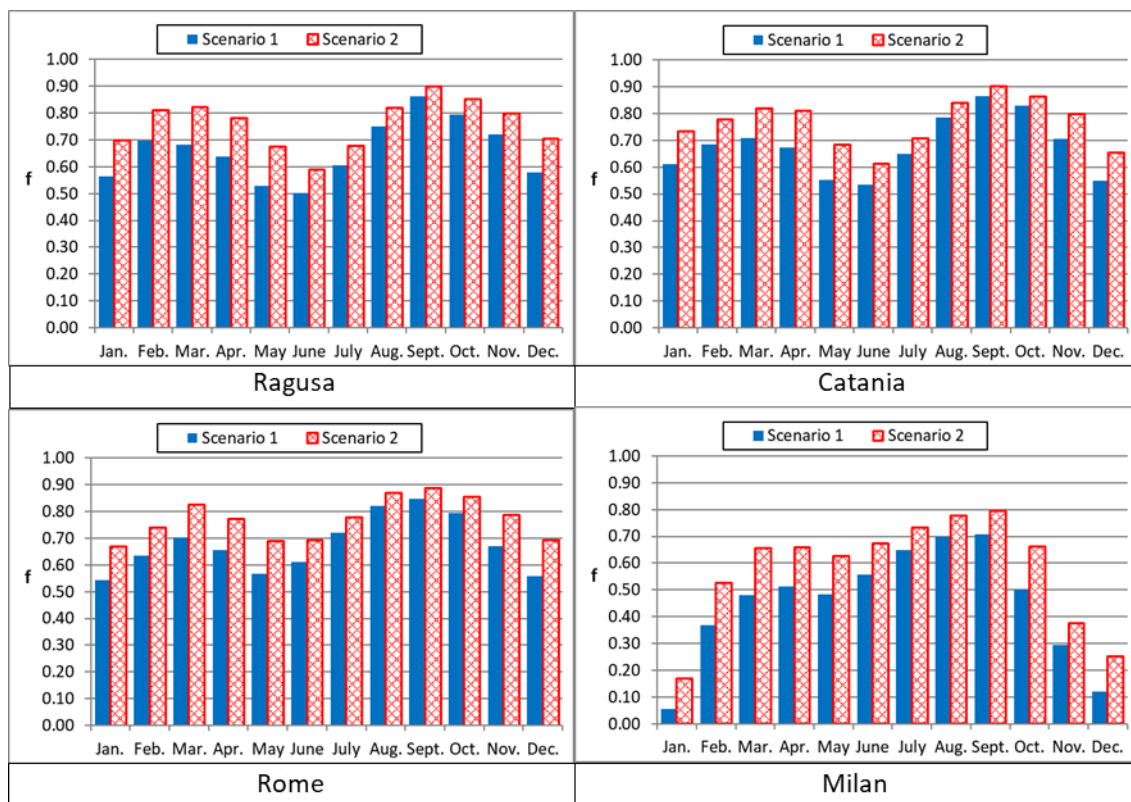


Figure 4.29 – Coverage factor of DHW demand for the two scenarios.

It can be observed that the coverage factors in Catania, Ragusa, and Rome are quite similar during the whole year. As regards, Milan, under scenario 1 the coverage factor has modest values during the winter period. Coverage factors less than 10% are achieved during the coldest months. Otherwise, under scenario 1 during the mid and the summer seasons the coverage factors reach values of about 60%, while under scenario 2 a value of about 70% is achieved.

As expected, the higher values of f are reached during the mid-season and the use of the ETC allows achieving the highest performance.

It is important to note that solar systems installed on the south-facing façade allow reducing the fluctuations of the coverage factor throughout the year, especially when evacuated tube collectors are used. Moreover, during the summer, the reduced solar irradiance that hits the vertical surfaces avoids overproduction and therefore energy waste.

Table 4.IV shows the yearly thermal energy supplied by the solar panels (E_{th}), the auxiliary energy supplied by the auxiliary system (E_{aux}) as well as the coverage factor (f), for the different scenarios and cities. The percentage differences in the energy yields between the two scenarios are also indicated.

Table 4.IV Annual result for the analysed scenarios.

	Scenario 1 (FPC)			Scenario 2 (ETC)			Difference		
	E_{th} [kWh]	E_{aux} [kWh]	f [%]	E_{th} [kWh]	E_{aux} [kWh]	f [%]	ΔE_{th} [%]	ΔE_{aux} [%]	Δf [%]
Ragusa	1943	1028	65	2247	724	76	12.5	-29.5	15.6
Catania	1999	972	67	2263	708	76	13.2	-27.2	13.2
Rome	1994	977	67	2281	690	77	14.4	-29.3	14.4
Milan	1312	1659	44	1685	1286	57	28.4	-22.5	28.4

In Ragusa, Catania, and Rome a vertical BSTF constructed with 4.0 m² of flat plate collectors allows to satisfy up to 65.0% of the energy needs for DHW requirements. On the other hand, in Milan just about 44.0% of the DHW demand is satisfied. This quite modest outcome is due to multiple factors, such as limited solar radiation, cool air temperatures and few days with clear sky compared to the other cities, during the winter months.

The use of ETC improves the performances of the solar facades of about 15.0 % in Ragusa, 13.0% in Catania and 14.0% in Rome, it allows reaching a yearly “ f ” factor of 76%.

In Milan, where the coldest climate limits the efficiency of flat plate collectors, the use of ETC allows boosting the yearly “ f ” factor up to 57% with an increment of 28.0%.

It is possible to highlight that the differences among the performances of the solar facades are not directly related to the values of the HDD. Indeed, in Ragusa and Roma, the coverage factor is about the same of Catania, although the HDD of Ragusa and Roma are about 1.5 times the number HDD of Catania.

In appendix 7, a simplified economic analysis is proposed, which highlights that the installation of the ETC instead of the FPC involves payback time of about 20.0 years in Catania, Ragusa and Roma, which does not justify the adoption of the ETC in such cities. In Milan, the payback time is less than 15 years that may be acceptable under the economic point of view instead.

Furthermore, the LCIA (Life-Cycle Impacts Assessment) reported in appendix shows for both BSTF an energy and emission payback times less than 2 years, which are very short in comparison with the life cycle of such solar systems.

The high fraction of the DHW energy requirements supplied through the BSTF, as well as the short energy and CO₂ payback times, allow affirming that a vertical solar façade represents a suitable system for DHW production with great environmental conveniences.

4.3 Analysis of Active Building Envelope composed by photovoltaic/thermal (PV/T) system

In most industrial sectors, as well as in residential buildings, energy needs consist of both thermal and electrical energy. An ambitious goal for the building sector make is to meet the buildings energy needs through renewable energy sources (RESs). However, due to the lack of available spaces, different kinds of RESs could not find the necessary surfaces where install them. Therefore, it becomes more and more necessary to think about the integration of solar systems into the building envelope and to use systems that allow a high conversion rate of solar radiation into primary energy.

As shown in paragraph 3.2 the hybrid photovoltaic/thermal (PV / T) system produce more total energy per unit of installed surface than conventional plants, therefore they constitute a very interesting technology for increasing the distributed generation and the integration of renewable energy in building façades.

In the following sections, the performances of an ABE are analysed, consisting of a PV/T system integrated into the facade of the "BIPVT" building (i.e. replacing the last layer of the facade).

The present analysis investigates the thermal behaviour and the energy yield considering the operating temperature of the BIPVT plant considering different design solutions, i.e. varying the ratio between the surface of the PVT water collector and the volume of the thermal storage. Moreover, the comparison of the heating and cooling energy needs, as well as the annual withdrawal of electricity from the electrical grid for the building with and without the BIPVT plant, is evaluated.

4.3.1 Methodology

This study aims to evaluate the performance of a solar energy source (PV/T systems) installed in the building facades. This could be a suitable solution for multi-storey buildings where the roof surface maybe not enough to install solar plants for all the residential units present.

4.3.1.1 System layout and model description

This study proposes the comparison between a building equipped with BIPVT system and the same building that is not provided with a solar plant, that is the baseline configuration.

In the baseline configuration, it is assumed that the various energy needs (DHW production, space heating and cooling, artificial lighting and other requirements) are provided by an electrical boiler for the DHW production, electrical heat pumps/chillers for space heating and cooling, whilst the electricity is provided by the national grid.

The BIPVT system integrated into the façade is put in place without any ventilated chamber between the PV/T panels and the building façade. The electrical energy produced will be used to satisfy the electrical requirements while the thermal energy is devoted to DHW production. If the thermal energy produced is less than the demand an auxiliary electrical heater provides the complementary energy requested.

Figure 4.30 shows the layout adopted for the reference building and the building equipped with BIPVT.

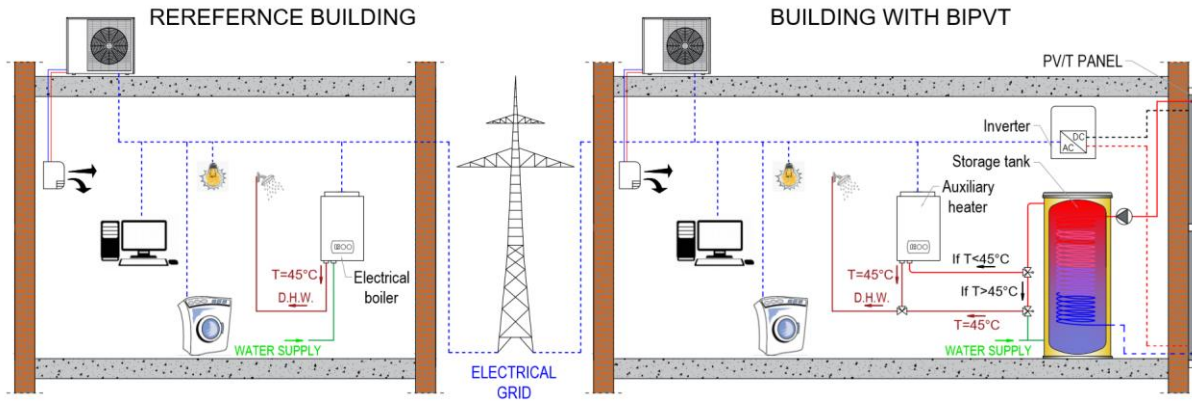


Figure 4.30 – System layout for building with and without BIPVT.

As shown in figure 4.30, the PV/T panels are connected to a solar storage tank through pipes equipped with a pump and a control unit (forced circulation system). The storage tank is a vertical type with the serpentine heat exchanger placed in the lower part of the tank. Tap water from the mains (T_{sup}) enters at the bottom of the tank, while hot water is drawn from the higher part of the tank ($T_{t,out}$). If $T_{t,out}$ is greater than the temperature required by the user ($T_{setpoint}$), the adjustment devices mix it with tap water from the aqueduct. Otherwise, if $T_{t,out}$ is less than $T_{setpoint}$, the auxiliary heater provides the energy necessary to reach the setpoint temperature.

Finally, the electricity supplied by the PV/T panels is converted by an inverter device that operates at the maximum power point (MPP) and it is used directly for the building electrical needs or conveyed to the electrical grid.

The topic was studied considering a quasi-steady state approach implemented by TRNSYS software [38].

4.3.1.2 Energy yields and Key Performance Indicators

The electrical and thermal energy produced by a PV/T source can be evaluated using a metric based on the First Law of Thermodynamics.

Eq. 4.15 allows to calculate the net electricity product ($E_{el,PV/T}$) during a fixed period, where the η_{inv} is the efficiency of the inverter device fixed equal 95%, η_{el} represents the electrical efficiency of panel calculated with Eq. 1.16 and above reported, A is the surface of the panel, G the total incident irradiation and P_{pump} the power for pumping the coolant fluid.

$$E_{el,PVT} = \int_0^t (\eta_{inv} \cdot \eta_{el} \cdot A \cdot G - P_{pump}) dt \quad (4.15)$$

$$\eta_{el} = \eta_{STC} \cdot [1 - \gamma(T_{pv} - T_{STC})] \quad (4.16)$$

As previously indicates, the energy saving obtained by RES for the DHW production can be calculate dividing the DHW load (E_{DHW}) into the part coming from the RES plant ($E_{DHW,PV/T}$) and the part supplied by the auxiliary generator (E_{AUX}), calculated respectively using the Eq. 4.12, and 4.13.

$$E_{DHW,PV/T} = \int_0^t \dot{m}_{DHW} \cdot C_w \cdot (T_{mx,out} - T_{sup}) dt \quad (4.12)$$

$$E_{AUX} = \int_0^t \dot{m}_{DHW} \cdot C_w \cdot (T_{set,DHW} - T_{mx,out}) dt \quad (4.13)$$

with the meaning of the symbols previously identified in the section 4.2.2.

To assess the ability of a solar system to meet energy demand, the main Key Performance Indicators (KPI) is the demand coverage factor (f), that is the ratio between the energy supplied by the system and that required by users. Therefore, the coverage factors are calculated for electricity (f_{el}), DHW (f_{DHW}) and global demand (f_{TOT}), using the following equations.

$$f_{el} = 100 \cdot \frac{E_{el,PV/T}}{E_{el,load}} \quad [\%] \quad (4.16)$$

$$f_{DHW} = 100 \cdot \frac{E_{DHW,PV/T}}{E_{DHW,load}} \quad [\%] \quad (4.17)$$

$$f_{TOT} = 100 \cdot \frac{E_{el,PV/T} + E_{DHW,PV/T}}{E_{el,load} + E_{DHW,load}} \quad [\%] \quad (4.18)$$

where $E_{DHW,load}$ and $E_{el,load}$ are respectively the DHW and the total electrical needs. $E_{el,load}$ is the sum of several contributions, which are energy required for heating, cooling, and appliances.

$$E_{el,load} = \frac{E_{el-Heating}}{COP} + \frac{E_{el-Cooling}}{EER} + E_{el-apps} \quad (4.19)$$

Furthermore, in a PV/T installation, the electrical performances depend by the temperature of the working cells, which in turn depends on the solar irradiation (G). Thus, it is worth of interest to introduce a KPI, namely $T_{char,PV}$ (eq. 4.20), which allows evaluating the working temperature of the PV cells weighted by G .

$$T_{char,PV} = \frac{\int T_{PV} \cdot G \cdot dt}{\int G \cdot dt} \quad (4.20)$$

To determine the thermal level of the water supplied by the solar system to satisfy users demand, the KPI $T_{char,DHW}$, is defined using the eq. 4.21, where the temperature of the water coming from the solar system is weighed for the instantaneous water flow required by the user for the DHW needs.

$$T_{char,DHW} = \frac{\int T_{m,out} \cdot \dot{m}_{DHW} \cdot dt}{\int \dot{m}_{DHW} \cdot dt} \quad (4.21)$$

Finally, the $T_{char,panel}$, which indicates the coolant thermal level achieved in the panels, is calculated using eq. 4.22.

$$T_{char,panel} = \frac{\int T_{f,av} \cdot G \cdot dt}{\int G \cdot dt} \quad (4.22)$$

where $T_{f,av}$ is the average temperature of the fluid inside the PV/T panels.

4.3.1.3 Case study

The case study refers to a multi-family house, well-representative of conventional Italian constructions, located in the South-Italy (Catania).

The features of the building envelope were chosen according to those of the buildings built in the period 1970-2000 in southern Italy, which correspond to about 50% of the building stock.

The analysis of the building energy needs is referred to an apartment placed on intermediate floors, with a floor area of 100 m² and net volume of 300 m³.

This apartment has three walls facing the outdoor environment, to East, South and West orientation, each with an area of 30 m², of which 9 m² constituted by glazed surfaces.

Table 4.V shows the main features of the components of the building envelope.

Table 4.V main features of the components of the building envelope.

Description	U.M.	Value
U_{wall}	W/(m ² ·K)	0.587
Surface mass of wall	Kg/m ²	227
U_{glass}	W/(m ² ·K)	2.83
SHG	-	0.755
Air infiltrations	vol/h	0.52
Sensible heat gain	W/person	75
Latent heat gain	W/person	55

The number of dwellers is equal to 0.04 occupants per square meter [UNI 10339].

According to the Italian regulation, the heating period goes from December 1st to March 31st, the cooling period is set from June 1st to September 30th, the setpoint temperature are set respectively to 20°C and 26°C.

The total consumption for DHW is 152.5 l/day, according to the Italian regulation [UNITS11300-2], with the daily profile defined by the standard EN 15316:2007. Finally, the T_{setpoint} is fixed at 40 °C and the T_{sup} is 15 °C.

The BIPVT plant is realized with twelve water WISC PV/T collectors constituted by mono-crystalline (c-Si) cells, which have an electrical peak power of 250 W. The module efficiency is 15.4% at Standard Test Conditions, and the temperature coefficient (γ) is 0.44%.

The BIPVT is installed in the façade facing south and has a net surface of 19.92 m², with an installed peak power of 3.0 kW.

The electrical energy demand for the common household appliances $E_{\text{el,app}}$ is fixed equal to 3000 kWh/y [40], to which the electric consumption due to the air conditioning system has to be added.

4.3.2 Characterization and validation

The Wave PV/T panel produced by DualSun was taken as a reference in this study, as they were used in the pilot PV/T plant installed at the Department of Electrical Electronics and Informatic Engineering of the University of Catania. All the characteristics of this plant and the monitoring system are described in chapter 2. Therefore, there is the availability of huge experimental data that are used to validate the results carried out through the simulations.

The BIPVT system is described using the type 563 available into TRNSYS software libraries. It simulates the thermal fluxes exchanged with the external environment and the building behind it, and also calculates the thermal and electrical energy produced. The input parameters are the main geometric characteristics, thermal resistances of the various layers that make it up and the electrical characteristics of the module. The outputs available are the thermal and electrical efficiency, the outlet fluid temperature and so on.

The collector efficiency curve of the PV/T panels can be calculated as described in section 2.4.4, using Eq. 2.10 above reported.

Where starting from the equations of the Hottel - Whillier – Bliss [41], replacing G with G_{eff} calculated according to Eq. 1.17 [42], and neglecting the quadratic term “ a_2 ” (only for unglazed PV/T collector), it becomes:

$$\eta_{th} = \eta_0 - a_1 \cdot \frac{(T_{av} - T_{amb})}{G_{eff}} \quad (2.10)$$

Figure 4.31 shows the comparison between experimental and simulated values of efficiency as a function of the ratio $\Delta T^*/G_{\text{eff}}$, where ΔT^* is the difference between the average temperature of the fluid inside the PV/T panels and the ambient temperature.

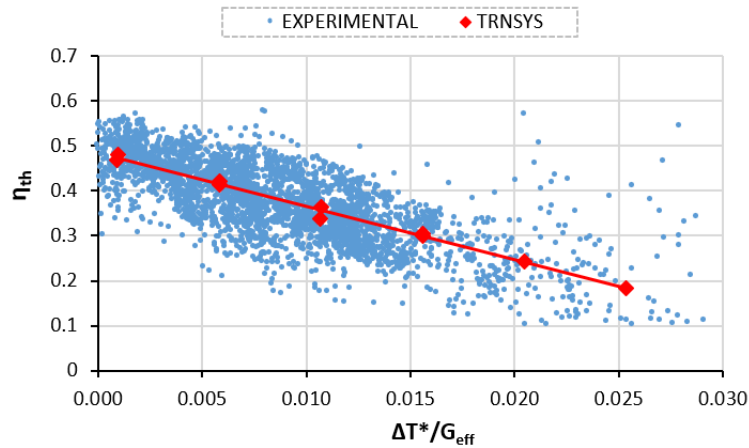


Figure 4.31 – Thermal curves comparison between experimental and simulated values.

As it can be observed, the simulated data provide an accurate evaluation of the efficiency curve of the investigated PV/T collector.

4.3.3 Results and discussions

The analyses were divided into two parts. The first part analyses the effect on the energy yield provided by BIPVT when the flow rate and the volume storage change. While in the second part the all-year-round energy requirements of the building with and without the BIPVT system are compared.

All the simulations have been performed utilising the weather data of Catania.

4.3.3.1 Sensitivity analysis on flow rate and storage tank in BIPVT system

In PV/T systems, the performances can be depending on the flow rate and volume of the thermal storage.

Systems placed on the façade (tilt angle equal to 90°) do not receive the same amount of solar radiation as systems placed with optimal tilt angles (20-40° in the Mediterranean area), therefore the flow rate and storage tank must be chosen to account of the reduced solar energy available.

With the aim to find the parameters that maximize the overall performances, the sensitive analysis of flow rate and volume of storage tank in BIPVT system were conducted.

Figure 4.32 shows the sensitivity analysis carried out in terms of electrical and thermal annual yields, as well as the thermal energy supplied to the user for DHW. As regards the thermal energy ($E_{th,panel}$) produced by PV/T panel can be estimated by applying the thermal balance equations to the fluid passing through the panels (Eq. 1.27 of section 1.4.2). In detail, the upper part of the figure shows the result of analysis on the flow rate when it is varied from 0.10 to

0.50 kg/min per square meter of PV/T panel, while the lower part shows the result of sensitivity analysis of storage volume when it varies from 10 to 50 litres per square meter of PV/T panel.

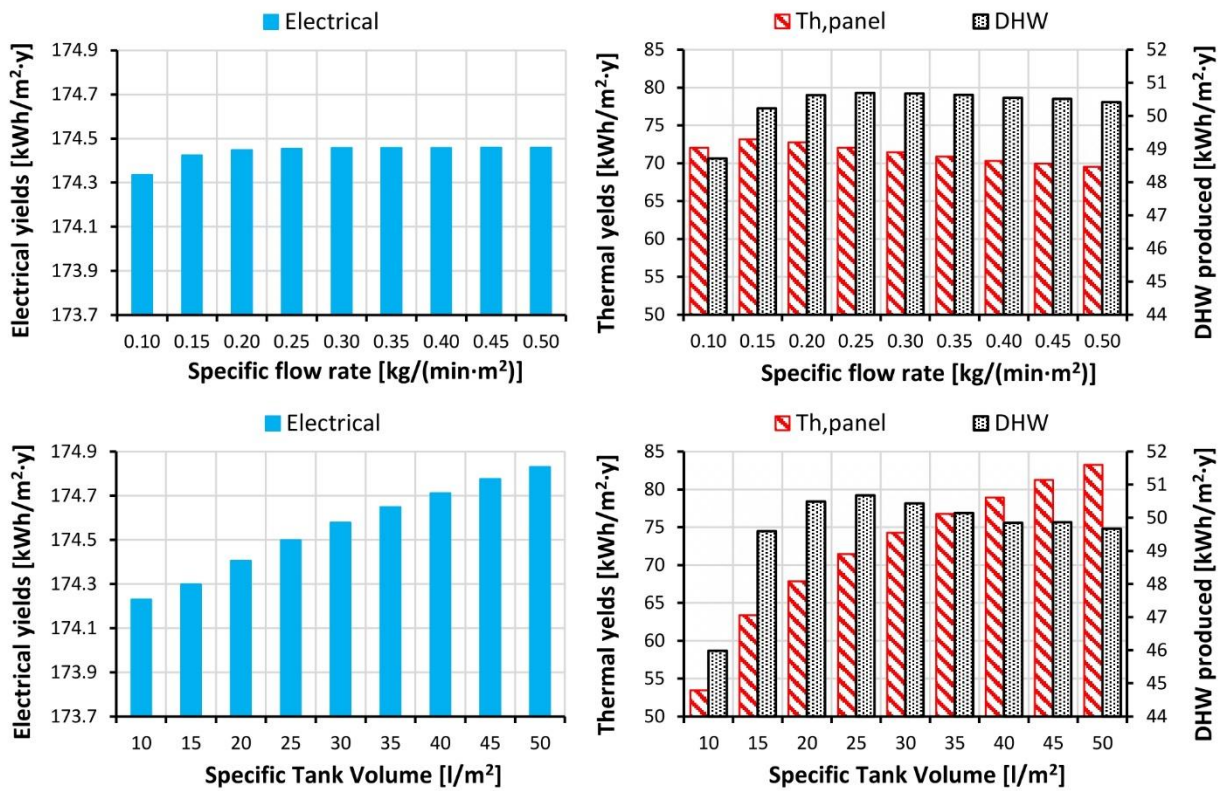


Figure 4.32 – Annual electrical (left) and thermal (right) energy yield per m² of PV/T panel.

The sensitivity analysis of flow rate shows a small increase in the electricity produced by increasing the specific mass flow rate from 0.10 to 0.25 kg/(min·m²) and then remaining constant. The thermal energy initially produced tends to increase as the flow rate increases, after which, once the specific flow rate of 0.30 kg/(min·m²) is exceeded, it begins to decrease.

Differently, it is observed that both the electrical and the thermal energy increases with the increase of the storage volume. This result is quite obvious since the higher is the volume of the tank the lower are the operating temperatures and consequently both the electrical and the thermal efficiency increase. Otherwise, focusing the analysis on the thermal energy derivable for DHW, which take into account of the enthalpy of the hot water, it is observed that E_{DHW} has a maximum for the specific volume of 25 l/m². The decreases of E_{DHW} is mainly due to the increase in the thermal losses from the storage tank as well from the PV/T collectors.

This first analysis has shown that the electrical and thermal performance are strongly influenced by the volume of the storage, while the flow rate does not affect considerably.

Figure 4.33 shows the building's annual needs per square meter of the apartment's floor as a function of the specific volume tank.

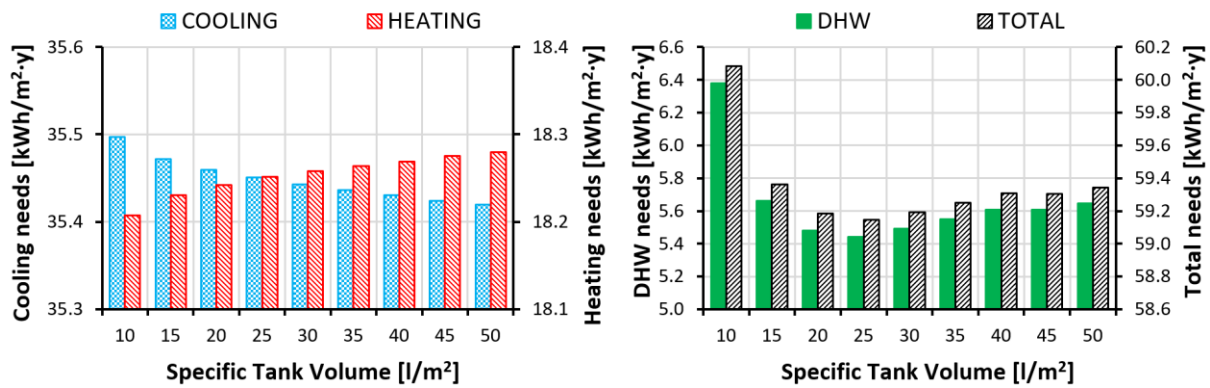


Figure 4.33 – Annual requirements of the building per floor square meter.

It can be highlighted that the specific energy needs for space cooling ($E_{Cooling}$) and heating ($E_{Heating}$), as predictable, have an opposite behaviour, $E_{Cooling}$ decreases as the volume of the tank increases while $E_{Heating}$ increases. This is due to the decrease in the average temperatures of the coolant fluid inside the BIPVT facade as the tank volume increases. Otherwise, the energy provided by the auxiliary source (E_{AUX}) has a minimum for the specific volume of 25 l/m². The total energy needs, given by the summation of these three different energy needs, (E_T), has its minimum value, of 59.15 kWh/y m² of climatized when the specific volume of the tank is equal to 25 l/m² of PV/T panels. Finally, figure 4.34 shows at left the coverage factor and at right the characteristic temperatures for the PV cell ($T_{char,PV}$), the coolant fluid ($T_{char,PVT}$) and the DHW ($T_{char,DHW}$), as a function of the specific volume of the storage tank.

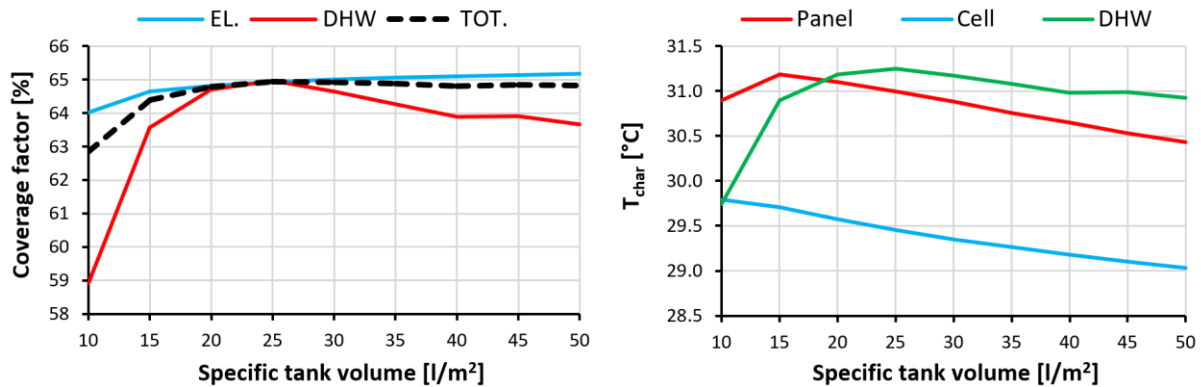


Figure 4.34 – Coverage factor of needs (left side) and characteristic temperatures (right side), to varying the specific storage tank volume.

The variation of the coverage factor as a function of the volume of storage, the trends showed in the previous analysis are confirmed, i.e. the electrical f-factor increases with specific tank volume (V_{St}) up to 65.2%, while the f-factor for DHW reaches the maximum of 65% for $V_{St} = 25$ l/m². The combination of these two trends determines that the f-factor for the total energy is almost constant for $V_{St} > 25$ l/m².

As regards the characteristic temperatures, it can be observed that the KPI $T_{char,panel}$ has its maximum value for the specific tank volume (V_{st}) of 0.15 l/m^2 and for $V > 0.15 \text{ l/m}^2$ decreases almost linearly. In the range of V_{st} investigated, even the KPI $T_{char,cell}$ decreases almost linearly. Consequently, the increase in electrical efficiency and power produced is attained. Finally, the $T_{char,DHW}$ has its maximum for the specific volume of the tank of 25 l/m^2 of panels.

Therefore, for the investigated BIPVT façade, which utilises WISC PV/T panels, the analysis conducted highlight that a thermal tank with a specific volume of 25 l/m^2 of PV/T panel allows maximising the overall producibility of the system, the thermal level of the water produced for DHW and minimizes the overall needs of the building.

4.3.3.2 Energy needs of the building with and without BIPVT

This section compares the all-year-round energy requirements of the building with and without the BIPVT system. The BIPVT plant is been designed utilising the optimized value defined in the previous for which the thermal storage volume, which is assumed being 500 litres.

Figure 4.35 shows the daily electrical and thermal energy needs for the two-building configurations. In particular, the yellow area depicts the electric needs for typical households appliances (e.g. lighting, TV, dishwasher and so on) supposed constant during the year, the green area indicates the energy consumption for DHW, assumed as constant for the baseline configuration; the red and the blue area indicates the energy needs for space heating and cooling. Finally, the black dotted curve indicates the electricity produced by the BIPVT plant.

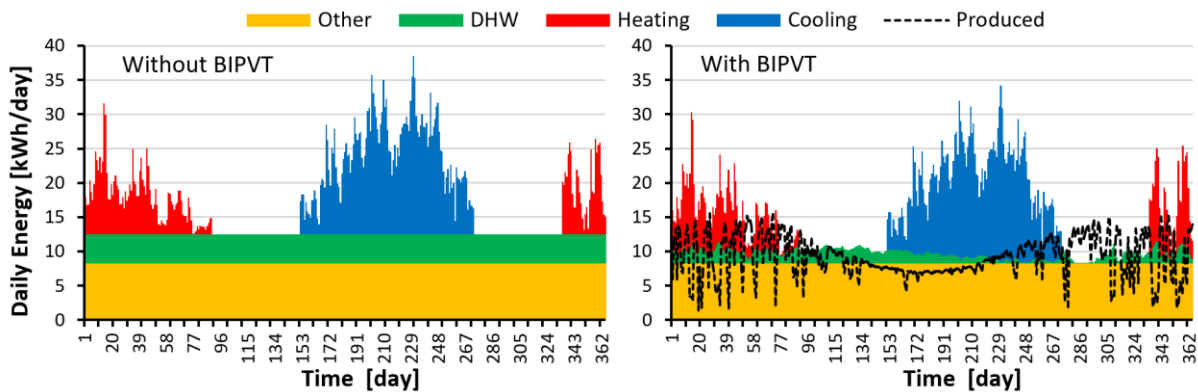


Figure 4.35 – Daily energy needs for the baseline and the BIPVT scenario.

It is possible to observe as the total daily electrical demand for space heating and cooling is extremely variable during the days and according to the seasons.

The dotted black line, which represents the power production of the BIPVT plant is also extremely variable, with minimum values of 1.4 kWh/day happened on a cloudy day and maximum of 15.5 kWh/day happened on a clear day.

It can be highlighted as the daily energy needs for DHW production for the building with the BIPVT plant are significantly reduced in comparison with the baseline configuration.

As previously underlined the energy requirements for space heating and cooling between the two configurations are very modest, as evidenced in the follow table 4.VI.

During the midseason, the daily electricity produced exceeds the electrical demand of the building. Otherwise, during summer the electricity demand is more than twice the energy produced, due to the modest availability of solar radiation on the south-facing façade compared with the large electrical demand for satisfying the cooling load.

Globally, the BIPVT plant generates 3354 kWh of electric energy and 1009 kWh of thermal energy for DHW production. This means that a BIPVT plant installed on a façade facing South allow to attain 168 kWh/m² (1118 kWh/kWp) of power production and 50.5 kWh/m² of thermal energy for DHW production.

Figure 4.36 shows the monthly coverage factors for electrical, thermal, and total energy needs achieved by using the proposed BIPVT system.

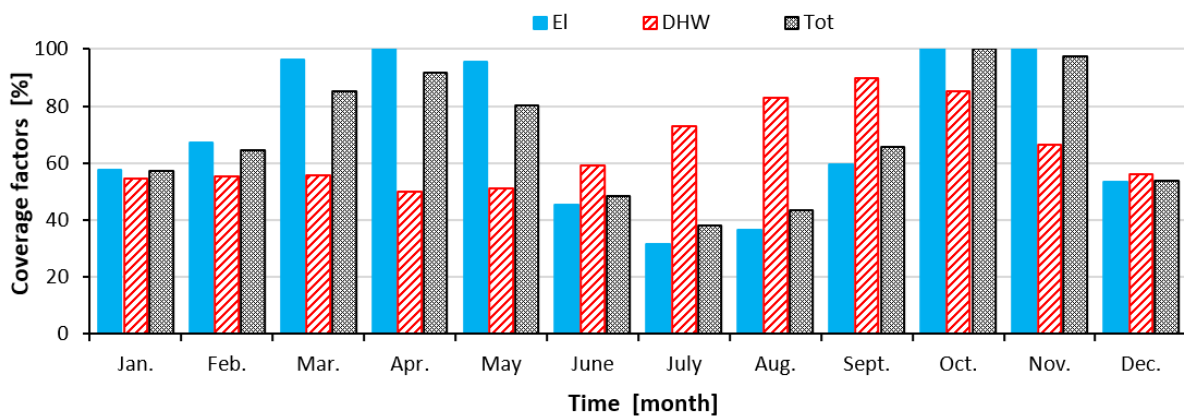


Figure 4.36 – Monthly coverage factor.

The electrical coverage factor varies from about 35% during the summer, up to the total fulfilment of the electric demand during the mid-seasons, when there is no demand of electricity for heating or cooling. The f_{DHW} is always above 50%, with peaks close to 90% in the months between August and October, thanks to either the high solar radiation, which hit the south façade and the outdoor air temperatures. Looking at f_{tot} , in spring and autumn, it exceeds 80%, with the highest yearly peak in October. Otherwise, in summer, the BIPVT system has the worst performance because the amount of solar radiation that hit the vertical wall facing south is quite limited and the needs of electricity for cooling is very high. In Table 4.VI, the annual electric requirements for air conditioning, differenced for space heating and cooling ($E_{el-Heating}$ and $E_{el-Cooling}$), electrical household appliances (E_{el-app}), the annual energy for DHW production (E_{DHW}), and the electricity drawn from the grid, for the two configurations are stated. It is also specified the percentage difference between the two configurations, calculated using Eq. 4.23.

$$\Delta E = \frac{E_{BIPVT} - E_{baseline}}{E_{baseline}} 100 \quad (4.23)$$

Table 4.VI Comparison of the energy needs for the two-building configurations.

	<i>E_{el-Heating}</i> [kWh]	<i>E_{el-Cooling}</i> [kWh]	<i>E_{el-app}</i> [kWh]	<i>E_{el-grid}</i> [kWh]	<i>E_{DHW}</i> [kWh]
Baseline	712	1442	3000	5159	1553
BIPVT	730	1418	3000	1805	544
<i>E_{BIPVT}</i> - <i>E_{baseline}</i>	18	-24	-	-3354	-1009
ΔE (%)	2.51	-1.68	-	-65.01	-64.97

Globally, the installation of BIPVT increases the energy requirement for heating by about 18 kWh, that is 2.5% and decreases the cooling needs of about 24 kWh, that is 1.7%.

These results indicate that the BIPVT does not meaningful modify the building energy needs. But the energy needs for DHW production and electrical needs are reduced by about 65%.

Moreover, it is interesting to observe that the electricity produced with the studied BIPVT façade fulfils the energy needs for the common household electrical appliances (i.e. 3000 kWh) with a modest surplus. The highest deficit between the electrical needs happens during the summer period when the south façade has the lowest efficiency.

Finally, it must be highlighted these results are obtained with the ratio between the peak power of the BIPVT and the annual electricity demand of 0.58 W/kWh.

Full considerations, conclusions and future developments are reported in the document reported in Appendix 8.

4.4 Analysis of Active Building Envelope composed by photovoltaic (conventional and bifacial) system

The concept of nZEBs focuses on firstly improving the energy performance of the building envelope and then installation of Renewable Energy Sources to cover the remaining energy demand. In this context, photovoltaic (PV) systems provide a reliable solution for electricity supply either in existing or new buildings. Building Added or Integrated Photovoltaic (BAPV and BIPV) systems have the twofold advantage of increasing the prospects of renewable energy in the built environment, whilst providing savings in materials and construction time by replacing traditional building elements.

The most common photovoltaic panels are opaque and can, therefore, act as shading devices [43]. A more recent technology that is making its way into buildings are semi-transparent PVs that can be incorporated into the glass [44-45]. The advantages of semi-transparent photovoltaic systems include an increase in daytime lighting compared to more opaque façades, a reduced heat gain compared to double transparent glass and on-site electricity generation.

Recently, bifacial PV cells have attracted interest because of their potential to increase PV modules power production [46]. Integration of bifacial PV modules into a building façade represents a significant step forward in the application of this relatively new technology.

Moreover, the performances of bifacial PV can be increased collecting the albedo irradiance coming from the roof and surrounding surfaces closest to the PV module, using a concentration device that increases albedo irradiance [47].

Finally, such façade can serve not only as a renewable source of electricity acting as an active building envelope but also it could contribute to reducing the building cooling needs acting as a passive system.

In the following sections, the performances of different alternatives of ABE equipped with PV module are analysed, under the point of view of (i) thermal behaviour of PV module, (ii) electrical yields and (iii) impact of PV technology on the thermal flux through the building envelope.

In detail, four active façades systems were considered:

- unventilated active façade with an added single-sided module, (BAPV);
- ventilated active façade with an added monofacial module (V-BAPV);
- ventilated active façade with an added bifacial module (V-BAbPV);
- ventilated active façade with an added bifacial module and reflective treatment in the internal wall (Vr-BAbPV) with a reflection coefficient r_{wall} equal to 0.7.

The main goal of this research is to identify the type of active façade which maximizes electricity production considering different periods of the year, but in the meantime, we want to highlight how the different active façades influence the thermal fluxes exchanged through the building envelope.

4.4.1 Method

The study of performance and thermal behaviour of several active façades was conducted using numerical models developed in Matlab® environment.

The features of the active façades were chosen starting from the characteristics of two pilot façades which are going to be realized in the laboratories of the DIEEI department of the University of Catania (Italy). Therefore, the geometric configuration, the exposure of the façades, the characteristics of the photovoltaic modules as well as the property of internal wall, replicate the features of the ongoing experimental system.

4.4.1.1 Numerical models

The developed numerical models allow to evaluate the thermal behaviour and performance of the active façade system in dynamic state conditions and are based on energy balance equations.

The heat fluxes exchanged among the layers that compose the active façades and the fluxes exchanged with the external environment are governed by the three basic mechanisms of heat transfer: radiation, convection, and conduction. For the studied active façades, the following thermal fluxes occur:

- convection and thermal radiation between the inner slab of the façade and the indoor environment;
- conduction through the different layers of the inner wall;
- convection between the outer slab of the inner wall and the air in the cavity;
- convection between the rear part of PV module and the air in the cavity;
- thermal radiation between the outer slab of the inner wall and the rear side of PV module;
- conduction through the different layers that make up the PV module;
- convection and thermal radiation between the front side of PV module and the outdoor environment.

The main difference between a ventilated and an unventilated active façade lies in the air gap. Indeed, in the ventilated active façade the air can circulate freely, as the interspace is in contact with the outside through an opening.

Figure 4.37 shows a graphic representation of the unventilated active façade and the ventilated active façade. In the case of unventilated active façade (BAPV) it has been assumed that the monofacial PV module is installed in adherence to the wall of the building and that the air present between the tedlar and the external layer of the wall is trapped inside the frame of the PV panel. Moreover, three alternatives active ventilated façades were studied. The V-BAPV is realised with opaque monofacial PV modules, in which the rear layer is made of tedlar material. The V-BAbPV is realised with a semi-transparent bifacial PV module, in which the rear layer is made up of a layer of glass. Finally, the Vr-BAbPV is again realized with a semi-transparent bifacial PV module differs with the addition of a high reflection paint posed on the outermost surface of the interior wall.

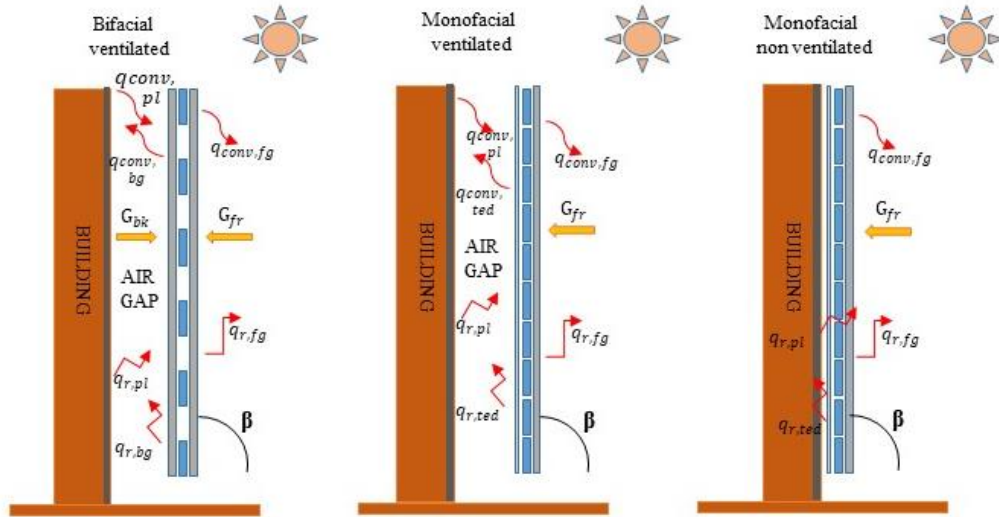


Figure 4.37 – Schematic representation of the modeled configurations: (a) V-BAbPV and Vr-BAbPV, (b) V-BAPV, and (c) BAPV.

In Figure 4.37 the terms q_{conv} and q_r refer to the heat fluxes on both sides of the PV module, described by the subscripts “fg”, “bg”/“ted”, due to the convection and radiation phenomena respectively. G_{fr} and G_{bk} represent the solar irradiance that hit the module on the front and the backside respectively.

As shown in the section 3.3.1 for PV/T numerical model, for each layer (i^{th}) that compose the active façade, the model solves the energy balance the incoming ($\dot{E}_{incoming}$) and the outgoing ($\dot{E}_{outgoing}$) energy fluxes:

$$\frac{dE_i}{dt} = \dot{E}_{incoming} - \dot{E}_{outgoing} \quad (4.24)$$

The balance equations are simultaneously solved using the ode45 function in Matlab, modified via the fourth order Runge Kutta method, and the simulations were conducted using 1440 daily time steps (time step equal 1 minute).

The conductive, radiative, and convective heat flux are calculated using respectively the equation of Fourie, Stefan-Boltzmann and Newton [48].

As regard the radiative heat fluxes, are considered both the fluxes with sky-dome and with ground, where the ground temperature is calculated with Eq. 4.25

$$T_{gro} = T_{air} + \frac{\alpha_{gr} G_H}{h_{gr}} \quad (4.25)$$

Where α_{gr} represents the absorption coefficient, G_H is the irradiance on horizontal surface and h_{gr} the convective coefficient.

According with [49], the convective exchanges of the surfaces that face the ventilated chamber are calculated using the eq. 4.26.

$$Q_{conv} = 0.85 \left(1.959 + 1.517 |T_i - T_{airgap}|^{\frac{1}{3}} + 1.33 u_{airgap} \right) \quad (4.26)$$

where T_i is the temperature of the i^{th} layer facing the airgap, T_{airgap} is the average temperature of the air inside the gap, u_{airgap} is the average air velocity in the chamber.

In the case of unventilated cavity, the Newton formula was used where the convection coefficient is set equal to 11.1 W/(m²K) in accordance with [24].

As regards the irradiation incident on the façade (G_{fr}), it is given by the sum of the radiation incident on the tilted (vertical) surface “ G_{β} ” plus the reflected part by the ground (eq. 4.27).

$$G_{fr} = G_{\beta} + a_{gr} G_H \quad (4.27)$$

In the case of semi-transparent (bifacial) PV modules, the part of solar irradiation entering the chamber that hits the internal wall is calculated through eq. 4.28, where τ_{fg} is the transmission coefficient of the glass and PF is the packing factor, i.e. ratio between the total PV cells area and the PV module area.

$$G_t = \tau_{fg} G_{fr} (1 - PF) \quad (4.28)$$

Finally, the incident solar irradiance on the rear of the semi-transparent module (G_{bk}) is calculated using eq. 4.29, where r_{wall} indicates the reflective coefficient of the internal wall.

$$G_{bk} = r_{wall} G_t \quad (4.29)$$

The electrical efficiency of the PV module has been calculated starting from the cell temperature as previously shown using eq. 1.16.

$$\eta_{el} = \eta_{STC} \cdot [1 - \gamma(T_{pv} - T_{STC})] \quad (1.16)$$

While the electrical power is calculated using eq. 4.30 and eq. 4.31 respectively for monofacial and bifacial modules.

$$P_{el,m} = \eta_{el} \cdot A \cdot G_{fr} \quad (4.30)$$

$$P_{el,b} = \eta_{el} \cdot A \cdot G_{fr} + \eta_{el} \cdot BF \cdot A \cdot G_{bk} \quad (4.31)$$

Where BF is the bifaciality factor and is defined as follows:

$$BF = \frac{\eta_{STC,back}}{\eta_{STC,front}} \quad (4.32)$$

4.4.1.2 Case studies

The scenarios analysed refer to an active façade with or without a ventilation chamber, and with different types of the PV modules (monofacial and bifacial) and reflective coefficient of the internal wall.

The ventilated active façades have an air gap of 10 cm thickness, where the air is free to circulate in any climatic condition.

For the scenario, V-BAbPV, the reflective coefficient of the internal wall was assumed of 0.2 and 0.7 for the Vr-BAbPV scenario where a highly reflective paint is posed on the internal side of the air gap.

In all scenarios, the façade has dimensions of 1.0 m wide and height equal to the length of the PV module (about 2.0 m).

The building wall is made up of 20 cm of brick and 2 cm of plaster. To take into account the variation of the temperature into the wall, it is divided into 6 homogeneous layers. Two of them are constituted by plaster with a thickness of 1cm and the other four are constituted by a section of 5 cm of brick. The temperature inside the building is kept at 20 ° C during the wintertime, 26°C during the summertime. The surface thermal resistance on the internal side of the building is posed to 0.13 m²K/W [50].

The physical properties of each layer are shown in Table 4.VII

Table 4.VII Properties of the layers that make up the ABE.

Description	L [m]	δ [mm]	A [m ²]	C [J/(kg·K)]	k [W/(m·K)]	ρ [kg/m ³]	α [-]	τ [-]	ε [-]
Front/back glass	1.979	3	1.979	980	1.0	2300	0.03	0.90	0.89
PV cells		0.35	1.797	757	168.0	2330	0.93	0.00	0.90
Tedlar	1.979	0.20	1.979	1200	0.2	1500	1.00	0.00	0.95
Air gap	1.979	*	1.979	1005	0.026	1.2	0.00	1.00	
Plaster	1.979	20	1.979	1000	1.0	1800	**	0.00	0.70
Brick	1.979	200	1.979	1000	0.4	600	1.0	0.00	0.90

*: air gap presents a thickness equal to 100mm in the case of ventilated envelope and 20mm in the case of unventilated envelope (thickness of PV frame);

**: absorptivity coefficient is equal to 0.8 for normal plaster (reflective index equal to 0.2) and equal to 0.3 for plaster with reflective coating (reflective index equal to 0.7)

Both monofacial and bifacial module are considered equipped with monocrystalline silicon (c-Si) cells, which have a Packing factor (PF) of 0.908, efficiency of 17.0% at Standard Test Conditions, temperature coefficient (γ) of 0.38%, and for bifacial is assumed a bifaciality factor (BF) of 0.85.

4.4.1.3 Weather data

This study was carried out considering the active façades located in the city of Catania (37° 30' 0" N - 15° 6' 0" E). The weather data (i.e. solar irradiation, wind speed, and air temperature) used for the implementation of the numerical model were taken from PV-GIS database [32].

All comparisons were done considering the façades facing south and evaluating the performance during three “representative” clear days: winter solstice, spring equinox and summer solstice. Figure 4.38 shows the daily outdoor temperature, the daily incident solar irradiation on the façades (continuous line) and the solar irradiation on the horizontal plane (dashed line). The wind speed is considered equal to 1 m/s in each cases studied.

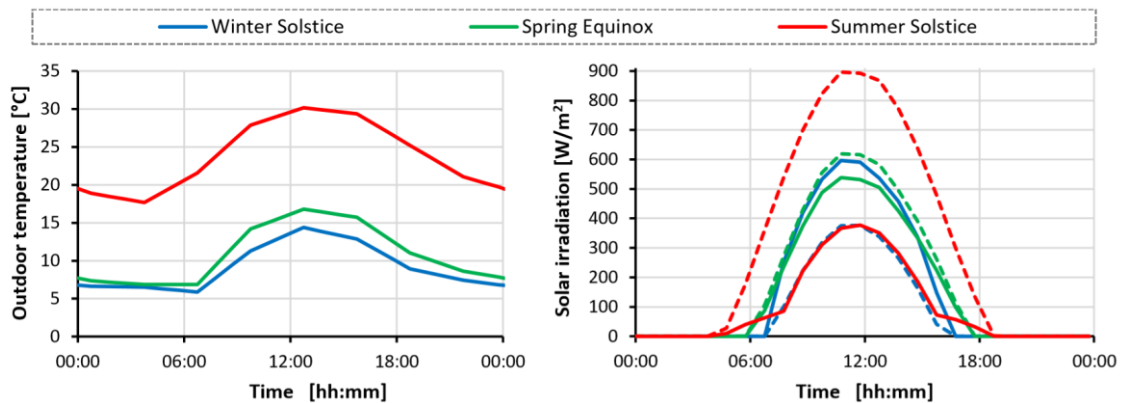


Figure 4.38 – Temperature (left) and solar irradiation (right) for the three reference days.

4.4.2 Results and Discussions

This section compares the thermodynamic behaviours and the energy performance for the studied technologies of active façades.

4.4.2.1 Thermal and performance behaviour of the integrated PV modules

Figure 4.39 shows the main results obtained for the four technologies analysed considering the three climatic seasons described above. In detail, on the left side, the comparisons of the temperature of the photovoltaic cells are shown, while on the right side the electrical efficiencies (dashed lines) and the electric power (continuous lines) are shown.

The patterns of the plotted variables do not depend evidently on the considered studied days (equinox and solstices) whereas the numerical values are different (see for example the values at sunrise and sunset time and noon).

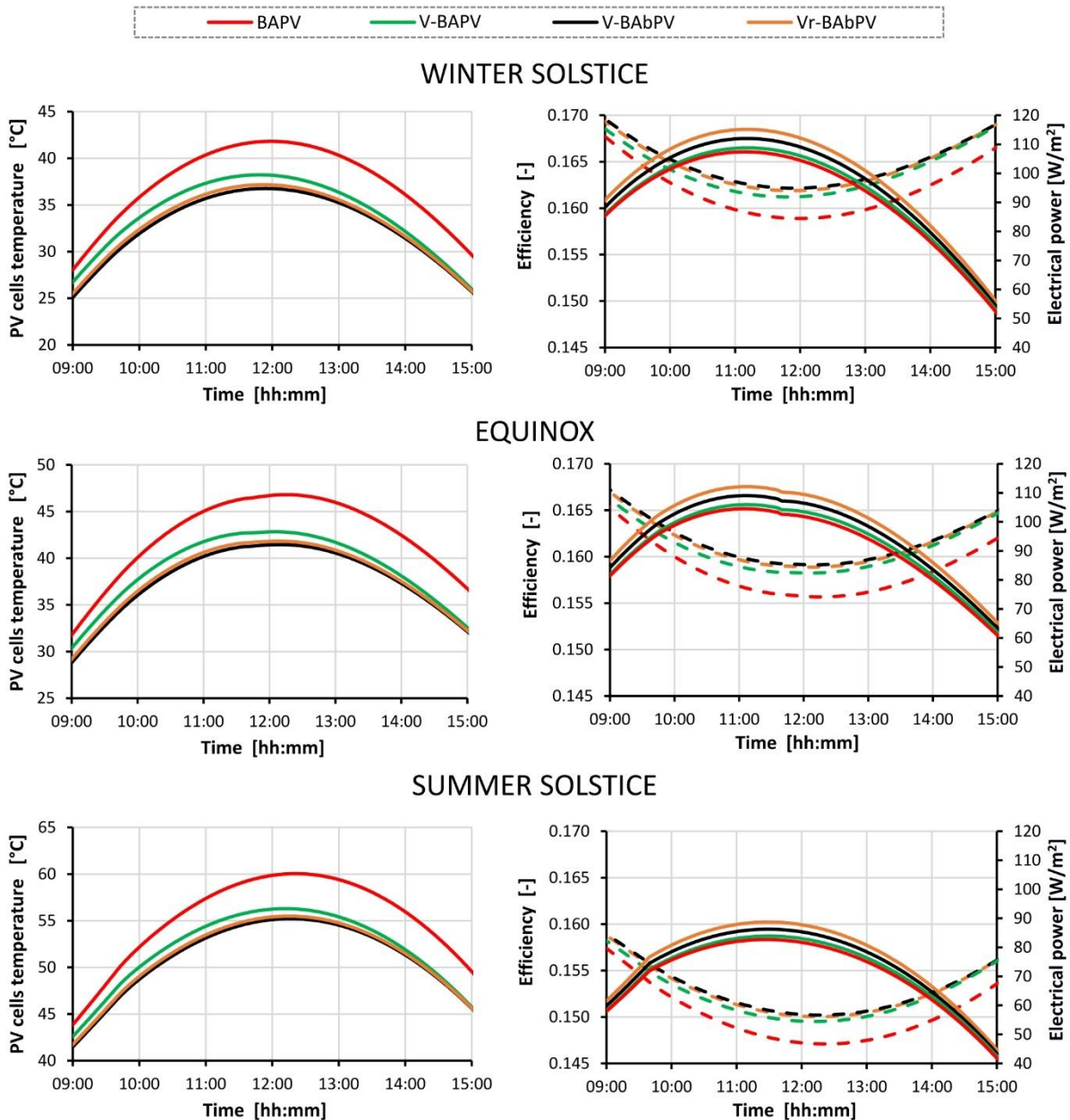


Figure 4.39 – daily profiles of cell temperature, efficiency, and electrical power.

Observing the cell temperatures, it is noted that the BAPV has the maximum values because there is no ventilation behind the modules since they are directly integrated into the building envelope. In the ventilated active façades, the cell temperatures are much lower than in the BAPV with differences sometimes even higher than 5°C. For the V-BAbPV, the lowest temperatures are achieved. In fact, in the V-BAPV technology, the tedlar layer blocks much of the solar radiation incident on it, heating up, while in the bifacial panels, the rear glass (which replaces the tedlar) allows most of it to pass, guaranteeing temperatures of about 1-2°C lower than the same geometry equipped with a conventional PV panel. Finally, V-BAbPV and Vr-BAbPV have very similar cell temperatures, with a temperature increase in the case of

maximum Vr-BAbPV of 0.5°C, caused by the higher solar radiation incident on the back of bifacial modules.

The electrical efficiency is strongly influenced by the temperature of the cells; therefore, a similar behaviour can be observed but opposite to that seen for the temperature of the modules. In the case of BAPV, the modules have the lowest efficiency, while rear ventilation increases their efficiency in the case of V-BAPV. Finally, the adoption of the bifacial module generates, albeit minimal, a further increase in efficiency compared to the case of the V-BAPV.

The electric power produced depends on the available solar irradiation and the electrical efficiency (eq. 4.30 and 4.31), therefore in line with what was previously seen, in the case of BAPV the lower values are obtained, while the ventilation in the V-BAPV allows an increase of approximately 1.5% during peak hours compared to the same module installed without an air gap, thanks to the increase in electrical efficiency. The use of the bifacial modules allows a further increase in the produced power, as the module benefits from the increase in incident solar irradiation in the backside, with an increase in power in the peak hours of 2.9% compared to the same geometry with a conventional module (V-BAPV) and 4.4% compared to BAPV. Finally, the adoption of reflective material in the outer envelope of the wall allows the Vr-BAbPV to further increase performance, with an increase in peak power of 7.4%, 5.7% and 2.9% compared, respectively, to BIPV, V-BAPV and V-BAbPV.

4.4.2.2 Thermal behaviour of the "active façade" system

The difference in the thermal behaviour of the "active façade" system affects the heat flux through the wall, as well as the profile of the temperatures within the wall and the layers of the active facades.

Figure 4.40 shows the temperature profiles for the three days analysed at the centre of the wall, observed during the two solstices at noon.

In the case of ventilated active façades, the superficial temperature on the internal side of the air gap is significantly lower than that one of the unventilated façade (BAPV), thanks to airflow that cools the wall, so a modest amount of heat is transferred to the building wall.

Otherwise, in the case of BAPV, the lack of ventilation in the backside of the panel generates an increase of the temperatures of the panel (as previously highlighted). This behaviour allows active ventilated façades to reduce thermal loads during the summer season, but which can also lead to the reduction of solar gains during the winter season. By comparing in detail the three active ventilated façades, it is noted that the maximum temperatures of the building envelope occur in the case of V-BAbPV, since the back glass allows that from it a part of solar radiation hit directly the wall. In the case of Vr-BAbPV, the use of the reflective surface reflects part of the incident irradiation on the wall, thus reducing the heat absorption. Finally, the use of the conventional module (V-BAPV) achieves the lowest temperatures because it completely enables the solar radiation to directly hit the wall.

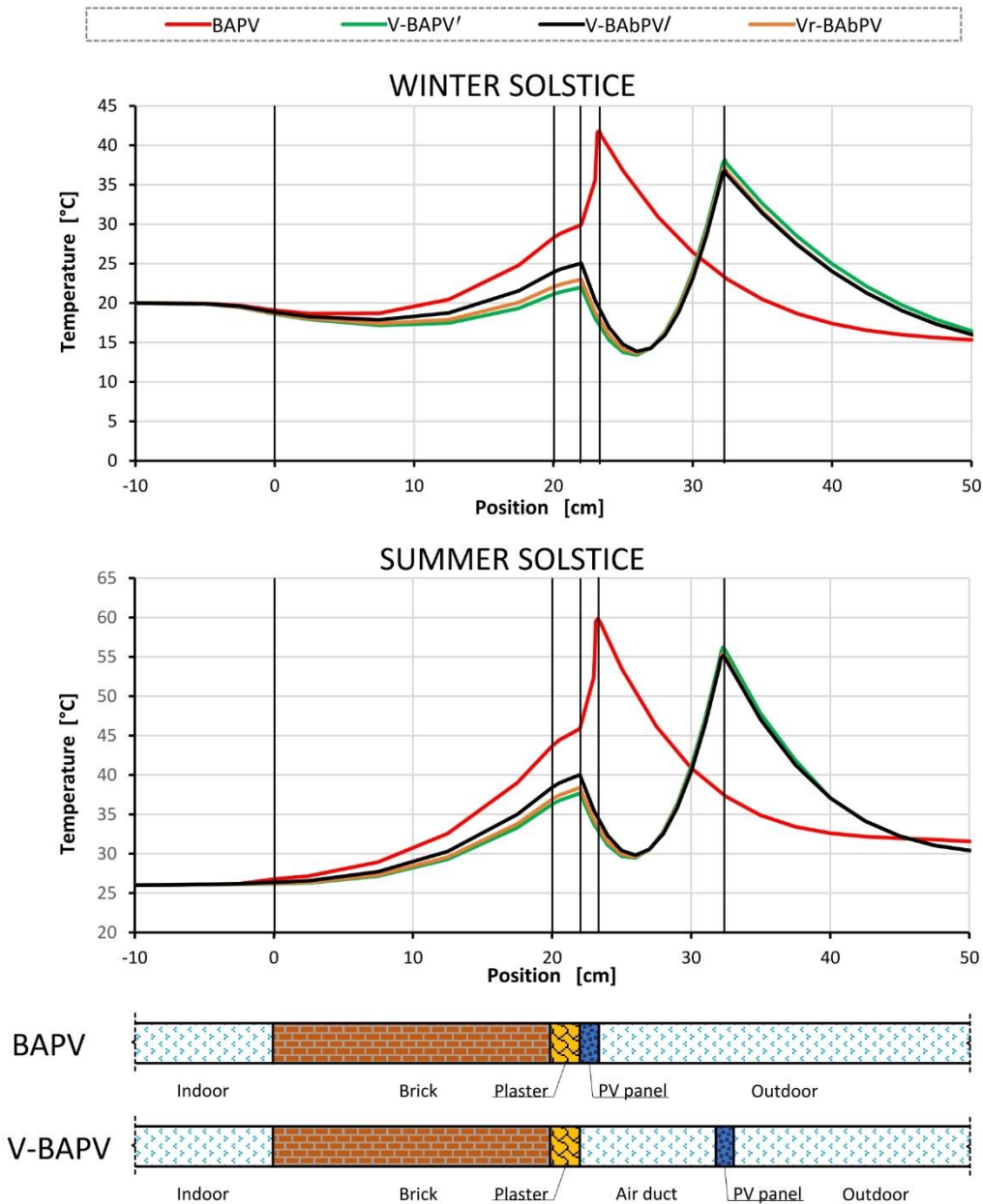


Figure 4.40 – Temperature into the whole façade at noon, during winter and summer day.

4.4.2.3 Energy production and thermal energy requirements

As the technology adopted varies, the performance in terms of the power generated, as well as the thermal fluxes through the walls of the building.

Figure 4.41 shows the comparison of the four technologies analysed, considering the daily electrical energy produced (at left) and the daily thermal fluxes through the wall (at right), where the negative value corresponds to outgoing flux (heat losses) and positive if the flux is towards inside (gains).

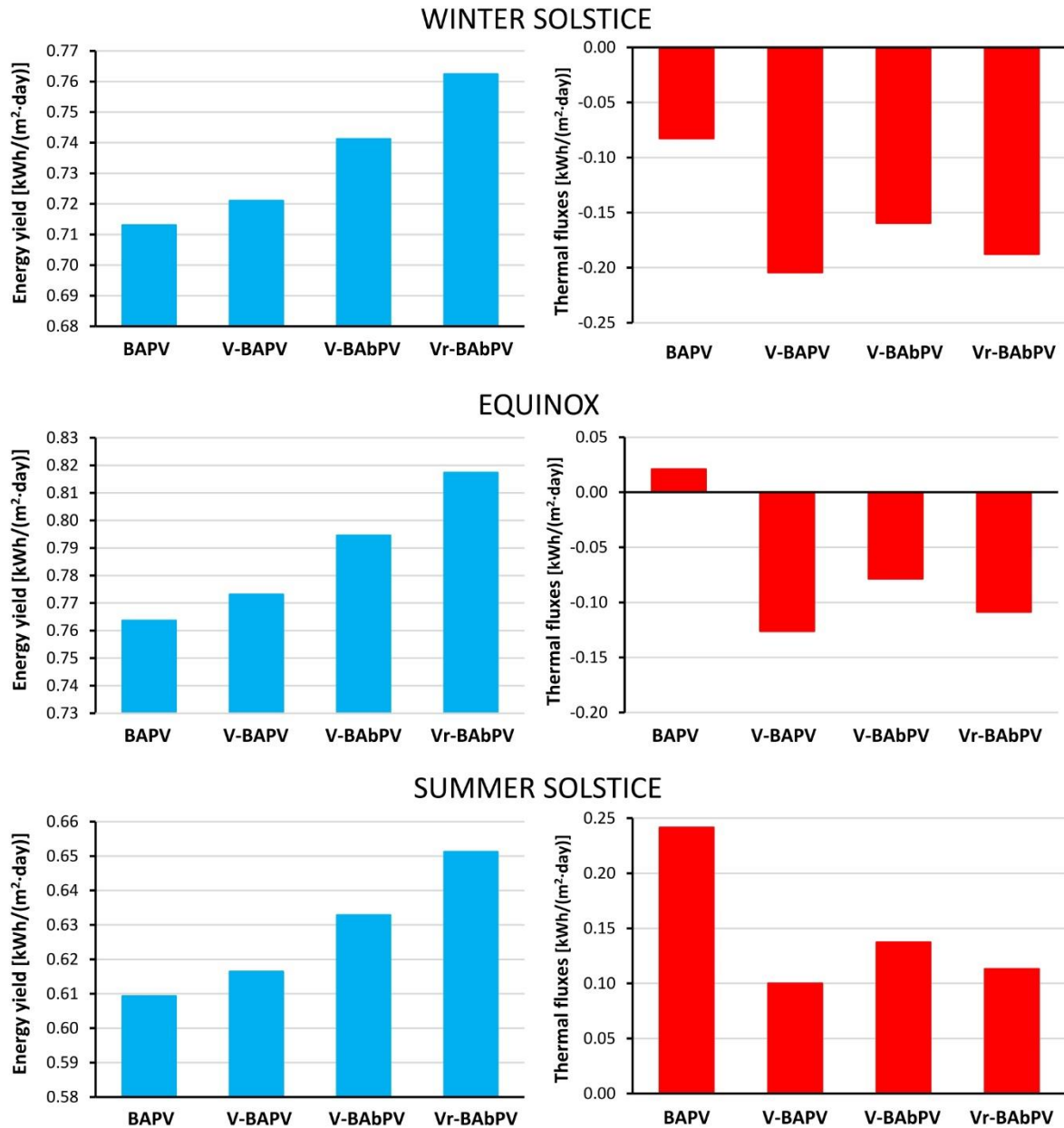


Figure 4.41 – Daily electrical yields and daily thermal fluxes through the façade.

The results on the daily power yields reflect what has been already highlighted examining the instantaneous powers, thus among the four scenarios, the lowest power production occurs in the case of BAPV. The ventilated active façades exceed the power production compared to the BAPV scenario of about 1.2% in the case of V-BAPV, about 3.9% in the case of V-BAbPV and of about 7% in the case of Vr-BAbPV. Moreover, the ventilated active façades compared with the BAPV scenario cause an increase of the heat losses during the winter season, while strongly reduce the heat gains during the summer season. Therefore, the choice of the most appropriate system must be calibrated looking to the needs of the building user and the climatic conditions of the site. Full considerations, conclusions and future developments are reported in Appendix 9.

References

- [1] IEA, International Energy Agency. Energy Technology Perspectives 2012. Pathways to a Clean Energy System.
- [2] European Environment Agency, Annual European Union Greenhouse Gas Inventory 1990-2012 and Inventory Report, 2014
- [3] Directive 2012/27/EU of the European Parliament and of the Council of 25 October 2012 on energy efficiency, Amending Directives 2009, Directives 2009/125/EC and 2010/30/EU and repealing Directives 2004/8/EC and 2006/32/EC, 2009
- [4] F. Ascione. Energy conservation and renewable technologies for buildings to face the impact of the climate change and minimize the use of cooling. *Solar Energy*, Volume 154, 15 September 2017, Pages 34-100. <https://doi.org/10.1016/j.solener.2017.01.022>
- [5] W.D. Seo, K.G. Lee. Application plan for an intelligent façade and interactive design of environment-friendly buildings. *Advanced Materials Research*, Volume 689, Pages 18-21. <https://doi.org/10.4028/www.scientific.net/AMR.689.18>
- [6] E. Giancola, M. Nuria Sánchez, M. Friedrich, O.L. Larsen, A. Nocente, S. Avesani, F. Babich, F. Goia. Possibilities and Challenges of Different Experimental Techniques for Airflow Characterization in the Air Cavities of Façades. *Journal of Facade Design and Engineering*, Volume 6, November 2018, Pages 34-48. 10.7480/jfde.2018.3.2470
- [7] J. Arce, M.J. Jiménez, J.D. Guzmán, M.R. Heras, G. Alvarez, J. Xamán. Experimental study for natural ventilation on a solar chimney. *Renewable Energy*, Volume 34, December 2009, Pages 2928-2934. <https://doi.org/10.1016/j.renene.2009.04.026>
- [8] M.C. Munari Probst, C. Roecker. Towards an improved architectural quality of building integrated solar thermal systems (BIST). *Solar Energy*, Volume 81, Issue 9, September 2007, Pages 1104-1116. <https://doi.org/10.1016/j.solener.2007.02.009>
- [9] D.I. Kolaitis, E. Malliotakis, D.A. Kontogeorgos, I. Mandilaras, D.I. Katsourinis, M.A. Founti. Comparative Assessment of Internal and External Thermal Insulation Systems for Energy Efficient Retrofitting of Residential Buildings. *Energy and Buildings*, Volume 64, September 2013, Pages 123-131. <https://doi.org/10.1016/j.enbuild.2013.04.004>
- [10] C. Alonso, I. Oteiza, J. García-Navarro, F. Martín-Consuegra. Energy consumption to cool and heat experimental modules for the energy refurbishment of façades. Three case studies in Madrid, *Energy and Buildings*, Volume 126, 15 August 2016, Pages 252-262. <https://doi.org/10.1016/j.enbuild.2016.04.034>
- [11] I. Mandilaras, I. Atsonios, G. Zannis, M. Founti. Thermal performance of a building envelope incorporating ETICS with vacuum insulation panels and EPS. *Energy and Buildings*, Volume 85, December 2014, Pages 654-665. <https://doi.org/10.1016/j.enbuild.2014.06.053>

- [12] R. Garay, B. Arregi, P. Elguezabal. Experimental Thermal Performance Assessment of a Prefabricated External Insulation System for Building Retrofitting. *Procedia Environmental Sciences*, Volume 38, 2017, Pages 155-161. <https://doi.org/10.1016/j.proenv.2017.03.097>
- [13] ENEA, National Agency for New Technologies, Energy and Sustainable Economic Development, *Energy Efficiency Tips for Citizens and Professionals*, 2015
- [14] A. Gagliano, F. Nocera, M. Detommaso, F. Patania. Design solutions for reducing the energy needs of residential buildings. 6th International Renewable Energy Congress, IREC 2015. DOI: 10.1109/IREC.2015.7110898
- [15] Y. Xing, N. Hewitt, P. Griffiths. Zero carbon buildings refurbishment—A Hierarchical pathway. *Renewable and Sustainable Energy Reviews*. Volume 15, Issue 6, August 2011, Pages 3229–3236. <https://doi.org/10.1016/j.rser.2011.04.020>
- [16] C. Lamnatou, J.D. Mondol, D. Chemisana. Modelling and simulation of Building-Integrated solar thermal systems: Behaviour of the system. *Renewable and Sustainable Energy Reviews*. Volume 45, May 2015, Pages 36–51. <https://doi.org/10.1016/j.rser.2015.01.024>
- [17] M. Ciampi, F. Leccese, G. Tuoni. Ventilated facades energy performance in summer cooling of buildings. *Solar Energy*, Volume 75, December 2003, Pages 491-502. <https://doi.org/10.1016/j.solener.2003.09.010>
- [18] E. Gratia, A. De Herde. Natural cooling strategies efficiency in an office building with a double-skin façade. *Energy and Buildings*, Volume 36, November 2004, Pages 1139-1152. <https://doi.org/10.1016/j.enbuild.2004.05.004>
- [19] J. Yu, J. Yang, C. Xiong. Study of dynamic thermal performance of hollow block ventilated wall. *Renewable Energy*, Volume 84, December 2015, Pages 145–151. <https://doi.org/10.1016/j.renene.2015.07.020>
- [20] S. Tong, H. Li. An efficient model development and experimental study for the heat transfer in naturally ventilated inclined roofs. *Building and Environment* Volume 81, November 2014, Pages 296–308. <https://doi.org/10.1016/j.buildenv.2014.07.009>
- [21] M. Labat, M. Woloszyn, G. Garnier, G. Rusaouen, J.J. Roux. Impact of direct solar irradiance on heat transfer behind an open-jointed ventilated cladding: Experimental and numerical investigations. *Solar Energy* Volume 86, Issue 9, September 2012, Pages 2549–2560. <https://doi.org/10.1016/j.solener.2012.05.030>
- [22] A. Gagliano, F. Patania, F. Nocera, A. Ferlito, A. Galesi. Thermal performance of ventilated roofs during summer period. *Energy and Buildings*, Volume 49, June 2012, Pages 611-618. <https://doi.org/10.1016/j.enbuild.2012.03.007>
- [23] A. Castell, M.M. Farid. Experimental validation of a methodology to assess PCM effectiveness in cooling building envelopes passively. *Energy and Buildings*, Volume 81, October 2014, Pages 59-71. <https://doi.org/10.1016/j.enbuild.2014.06.011>
- [24] ISO 6946:2017, *Building components and building elements - Thermal resistance and thermal transmittance -- Calculation methods*, 2017

- [25] UNI 11018:2003 - Rivestimenti e sistemi di ancoraggio per facciate ventilate a montaggio meccanico - Istruzioni per la progettazione, l'esecuzione e la manutenzione - Rivestimenti lapidei e ceramici. 2003
- [26] DTU P50-702 janvier 1997. Règles Th – K: Règles de calcul des caractéristiques thermiques utiles parois de construction. 1997
- [27] F. Patania, A. Gagliano, F. Nocera, A. Ferlito, A. Galesi. Thermofluid-dynamic analysis of ventilated facades. *Energy and Buildings*, Volume 42, Issue 7, July 2010, Pages 1148-1155. <https://doi.org/10.1016/j.enbuild.2010.02.006>
- [28] ANSYS Fluent User's guide, release Fluent 16.1, ANSYS, Inc., 2015
- [29] C. Sanjuan, M.J. Suárez, M. González, J. Pistono, E. Blanco. Energy performance of an open-joint ventilated façade compared with a conventional sealed cavity façade. *Solar Energy*, Volume 85, Issue 9, September 2011, Pages 1851-1863. <https://doi.org/10.1016/j.solener.2011.04.028>
- [30] G. Diarce, Á. Campos-Celador, K. Martin, A. Urresti, A. García-Romero, J.M. Sala. A comparative study of the CFD modeling of a ventilated active façade including phase change materials. *Applied Energy*, Volume 126, 1 August 2014, Pages 307-317. <https://doi.org/10.1016/j.apenergy.2014.03.080>
- [31] M.K. Fuentes. A simplified thermal model for flat-plate photovoltaic arrays, Sandia Report: SAND85-0330-UC-63, Albuquerque
- [32] Photovoltaic Geographical Information System (PV-GIS), Photovoltaic-software.com. 2020
- [33] P. Seferis, P. Strachan, A. Dimoudi. Investigation of the performance of a ventilated wall. *Energy and Buildings*, Volume 43, September 2011, Pages 2167–2178. <https://doi.org/10.1016/j.enbuild.2011.04.023>
- [34] A. Gagliano, S. Aneli. Analysis of the energy performance of an Opaque Ventilated Façade under winter and summer weather conditions. *Solar Energy*, Volume 205, July 2020, Pages 531-544. <https://doi.org/10.1016/j.solener.2020.05.078>
- [35] C. Maurer, C. Cappel, T.E. Kuhn. Simple models for building-integrated solar thermal systems. *Energy and Buildings*, Volume 103, 15 September 2015, Pages 118-123. <https://doi.org/10.1016/j.enbuild.2015.05.047>
- [36] A. Gagliano, S. Aneli, F. Nocera. Analysis of the performance of a building solar thermal facade (BSTF) for domestic hot water production. *Renewable Energy*, Volume 142, November 2019, Pages 511-526. <https://doi.org/10.1016/j.renene.2019.04.102>
- [37] A. Gagliano, F. Nocera, S. Aneli. Thermodynamic analysis of ventilated façades under different wind conditions in summer period. *Energy and Buildings*, Volume 122, June 2016, Pages 131-139. <https://doi.org/10.1016/j.enbuild.2016.04.035>
- [38] S.A. Klein, W.A. Beckman, et al., TRNSYS - A Transient Simulation Program. ASHRAE 82, 1976.

- [39] JRC European Commission, "Photovoltaic Geographical Information System (PVGIS)," Jt. Res. Cent. - Inst. Energy Transp., 2017. <https://ec.europa.eu/jrc/en/pvgis>
- [40] A. Gagliano, F. Patania, F. Nocera, A. Capizzi, A. Galesi, GIS-based decision support for solar photovoltaic planning in urban environment. Sustainability in Energy and Buildings, 2013
- [41] J. A. Duffie and W. A. Beckman, Solar Engineering of Thermal Processes: Fourth Edition. 2013.
- [42] L.W. Florschuetz. Extension of the Hottel-Whillier model to the analysis of combined photovoltaic/thermal flat plate collectors. Solar Energy, volume 22, Issue 4, 1979, Pages 361-366. [https://doi.org/10.1016/0038-092X\(79\)90190-7](https://doi.org/10.1016/0038-092X(79)90190-7)
- [43] S.H. Yoo, E.T. Lee. Efficiency characteristic of building integrated photovoltaics as a shading device. Building and Environment, Volume 37, June 2002, Pages 615-623. [https://doi.org/10.1016/S0360-1323\(01\)00071-3](https://doi.org/10.1016/S0360-1323(01)00071-3)
- [44] Y.T. Chae, J. Kim, H. Park, B. Shin. Building energy performance evaluation of building integrated photovoltaic (BIPV) window with semi-transparent solar cells. Applied Energy, Volume 129, 2014, pages 217–227. <https://doi.org/10.1016/j.apenergy.2014.04.106>
- [45] K. Park, G. Kang, H. Kim, G. Yu, J. Kim. Analysis of thermal and electrical performance of semi-transparent photovoltaic (PV) module. Energy, Volume 35, 2010, Pages 2681–2687. <https://doi.org/10.1016/j.energy.2009.07.019>
- [46] T. Liang, M. Praveettoni, C. Deline, J.S. Stein, R. Kopecek, J. Prakash Singh, W. Luo, Y. Wang, A.G. Aberlea, Y. Sheng Khoo. A review of crystalline silicon bifacial photovoltaic performance characterisation and simulation. Energy & Environmental Science, Volume 12, January 2019, Pages 116-148. <https://doi.org/10.1039/C8EE02184H>
- [47] R. Guerrero-Lemus, R. Vega, T. Kim, A. Kimm, L. Shephard. Bifacial solar photovoltaics – A technology review. Renewable and Sustainable Energy Reviews, Volume 60, July 2016, Pages 1533-1549. <https://doi.org/10.1016/j.rser.2016.03.041>
- [48] Y.A. Cengel. Introduction to Thermodynamics and Heat Transfer. McGraw-Hill, 2009
- [49] V.M.S. Francés, E.J. Sarabia Escriva, J.M. Pinazo Ojer, E. Bannier, V.C. Soler, G.S. Moreno. Modeling of ventilated façades for energy building simulation software. Energy and Buildings, Volume 65, October 2013, Pages 419-428. <https://doi.org/10.1016/j.enbuild.2013.06.015>
- [50] COMMISSION REGULATION (EU) 2016/2281 of 30 November 2016.

5. CONCLUSIONS

The use of solar systems, such as photovoltaic (PV), solar thermal (ST) and hybrid photovoltaic/thermal (PV/T) systems, can allow the building sector to achieve ambitious targets, such as net Zero Energy Buildings (nZEB).

The activity carried out in this thesis aims at evaluating the performance of different solar RESs, the possibility of increasing the performance of these systems, as well as the integrability of solar systems in the building envelopes.

A large survey carried out with the use of a pilot WISC PV/T system, installed at the DIEEI of the University of Catania, showed that PV/T technology allows taking advantage of solar energy, first of all, producing electricity with higher yields than conventional PV, and also producing at the same time thermal energy that can be used for Domestic Hot Water (DHW) or space heating. The cooling fluid reduces the temperature of the PV cells compared to a conventional PV (or PV/T in stagnation), guaranteeing an increase in electrical performance even higher than 6%.

Furthermore, it has been shown that in PV/T systems it is necessary to find the right compromise between a high thermal level and the total performance of the system the study shows that an increase of about 20°C in the thermal level generates a fall in the overall yields by more than 20%. Otherwise, the careful management of electricity production can allow an increase in the production of thermal energy and its enthalpy content. This scenario, although unusual, is possible in the case in which there is no electricity demand and the electricity grid capacity is overcome. Nevertheless, observing the total energy produced, it is shown that simultaneous energy production allows better exploitation of solar energy.

Novel developed mathematical models have shown that the hybrid PV/T plant allows producing about 7% more electricity than the conventional PV system, moreover, the simultaneous production of thermal energy results in an increase in the total energy produced by the PV/T between 20 and 30% compared to that produced by conventional PV, depending on the site.

In the scenario of limited availability of space for the installation of solar systems, the combination of conventional solar RESs (PV-ST) that allows the maximum energy yields are made up of 80% of PV and 20% of ST, nevertheless even this configuration showed lower performances compared to the PV/T system. The economic analysis shows that PV/T system has the highest revenues, but the economy of the PV allows the system to be repaid in less time than the PV/T or the various combinations of PV-ST.

The possibility of improving the performance of solar plants was investigated through the use of Nanofluids and Phase Change Materials (PCM), noting that nanofluids allow an increase in the thermal performance of PV/T systems of almost 2%, generating only a small increase in the working temperatures of the PV cells and therefore a negligible decrease in terms of electricity produced. Otherwise, the use of PCMs allows the temperature control of the PV cells, allowing an increase in terms of electric power produced even higher than 9% and an increase of the daily energy yield of about 5.5%. However, it was observed the necessity to carefully choose the type of PCM, observing the climatic conditions of the site throughout the year, because,

during the hot season, PCMs with low melting temperatures can soon run out of functionality due to the difficulty of solidification overnight.

Finally, the performances of solar plants were analysed according to an innovative approach. Due to the lack of available spaces (e.g. in multi-storey buildings) RES sources often do not find the surfaces necessary for installation, it, therefore, becomes necessary to think about the integration of solar systems in the building envelope, giving rise to the so-called Active Building Envelopes (ABEs).

The analyses conducted in this thesis on the performances of solar RESs (ST, WISC PV/T, conventional PV, bifacial PV) installed on the façade reveals a good potential for any ABEs, also the intelligent integration of ABEs, through the creation of a ventilated cavity allows the simultaneous increase of the thermal performance of the envelope and therefore the reduction of the energy requirement.

In this regard, through experimental analyses, it has been shown that the Ventilated Building Solar Thermal Façade (V-BSTF) generates a shielding effect against solar radiation, capable of reducing the surface temperature of the internal wall by up to 25°C. Similarly, the simulations of the addition of PV panels in the façade of the building placed with a ventilated cavity, show a clear reduction in the surface temperature of the envelope compared to the same ABE without a ventilated cavity. It has been shown that the shielding effect, evaluated by comparing the thermal behaviour of an Opaque Ventilated Façade (OVF) with a conventional unventilated (UF), generates advantages even during the winter, reducing dispersions towards the sky-dome during the night and thus allowing energy savings during the whole year; they also limit thermal stresses in the materials and the formation of condensation. Otherwise, it has been shown that a PV/T system integrated into the building envelope (BIPVT) slightly increases the winter heat requirement but compensates for it during the summer season.

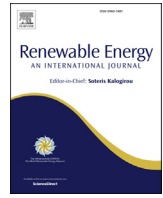
The survey on energy producibility showed a very high potential for ABEs. Indeed, the yearly analysis highlights that the BSTF constituted by just 4.0 m² of FPC allows to satisfy over 65% of the DHW of a family in Rome, Catania, and Ragusa, and 44% in Milan. While a BSTF equipped with 4.0 m² of ETC satisfies 57% of the demand for the city of Milan and over 75% for the other locations. Even more important is the ability to reduce the fluctuations of the demand coverage factor throughout the year, where the reduced amount of solar radiation that hits the vertical surface facing south during the summer avoids thermal energy overproduction and therefore the risk of overheating and the consequent energy waste.

It was also noted that the installation of a BIPVT system with a peak power of 3.0 kW allows a reduction of the total building requirement (including energy for heating, cooling, DHW and appliances), of about 65%, with total coverage of the needs in the autumn and spring season.

As regards the production of electricity through PV modules placed on the façade, the analysis carried out showed that the construction of the ventilated cavity (V-BAPV) allows the production of electricity to be increased by about 1.2% compared to the unventilated system (BAPV), as the rear ventilation of the panel reduces the heating of the cells. Besides, the performance can be further improved by using bifacial PV modules (V-BAbPV), which allow an increase in the electricity produced by about 4.4% compared to the BAPV and about 2.9%

compared to the ventilated solution (V-BAPV). Finally, the adoption of reflective material in the outer envelope of the wall allows to further increase the performance of bifacial module, with an increase in peak power of 7.4%, 5.7% and 2.9% compared, respectively, to BAPV, V-BAPV and V-BAbPV.

As a general conclusion, it can be stated that the choice of the most appropriate system must be calibrated looking to the needs of the building user and the climatic conditions of each site.



Description and performance analysis of a flexible photovoltaic/thermal (PV/T) solar system



Antonio Gagliano, Giuseppe M. Tina^{*}, Francesco Nocera, Alfio Dario Grasso, Stefano Aneli

University of Catania, Electric, Electronics and Computer Engineering Department, V.le A.Doria n.5, 95125 Catania, Italy

ARTICLE INFO

Article history:

Received 10 August 2017

Received in revised form

4 April 2018

Accepted 16 April 2018

Available online 25 April 2018

Keywords:

Solar energy

Photovoltaic/thermal system

Modelling

Experimental tests

ABSTRACT

The main objectives of the present paper are to describe a pilot cogenerative PV/T plant and discuss its preliminary electrical and thermal experimental data. The PV/T plant is installed in the campus of the University of Catania, (Catania, Italy) on the eastern coast of Sicily, right in the centre of the Mediterranean area. The operative conditions of the experimental PV/T plant can be modified to implement parallel and series electrical and hydronic connections to the PV/T modules. The electrical and thermal load supplied by the PV/T plant can also be managed in order to simulate different energy demand scenarios. This study reports the main thermal and electrical operating parameters of the PV/T plant on the basis of experimental measurements, with the PV/T modules connected in series. A good level of correspondence was found between the measurements and the simulations obtained from a model of the system, particularly as regards electrical features.

© 2018 Elsevier Ltd. All rights reserved.

1. Introduction

In the few last years, the development of solar power systems has been led by the Photovoltaic (PV) technology, which is experiencing rapid, solid growth. Indeed, in 2016 global installed PV capacity reached a peak of over than 300 GW, corresponding to annual energy output of 365-TWh. At present, PV technology is used worldwide: in 2016, 24 countries exceeded the 1-GW power level, six countries reached more than 10 GW of total capacity, four attained more than 40 GW (Japan 42.8 GW, Germany 41.2 GW, USA 40.3 GW) and China alone reached 78 GW [1]. The Si-wafer based PV technology accounted for about 93% of total output in 2015. Multi-crystalline technology now generates about 68% of total output. In the last 10 years, the average efficiency of commercial wafer-based silicon modules has increased from about 12% to 17%. At the same time, CdTe module efficiency has increased from 9% to 16% [2]. This means that only less than 20% of solar energy can be converted into electricity, while more than 50% of incident solar radiation is dissipated as heat. Moreover, the main source of energy losses for a PV plant is the high operating temperature of PV cells (shading losses are not considered as they are almost exclusively dependent on array design and the presence of obstacles [3]).

Obviously, module electrical efficiency can be improved by removing the excess heat using active or passive cooling systems [4]. This latter consideration, together with the reduction in the number of useful surfaces available for installation of solar thermal systems due to the widespread adoption of small and medium size PV plants on the roofs of buildings (), has renewed interest in hybrid Photovoltaic/Thermal (PV/T) collectors. Recent review papers [5,6] have provided a systematic analysis of the historical and recent trend in PV/T technology, highlighting the performance and economic feasibility of PV/T systems using different heat transfer fluids and designs and for different application areas.

A large number of theoretical and experimental studies on PV/T collectors and systems have also been reported in the literature. The first study on a PV/T system was presented by Wolf in 1976 [7]. In 2001, Kalogirou [8] simulated a hybrid photovoltaic–thermal plant installed in Cyprus using TRNSYS. The results demonstrated that the hybrid system can increase the mean annual efficiency of the PV solar system from 2.8% to 7.7%. In addition, the PV/T plant can cover up to 49% of a house's hot water needs, thus increasing the system's mean annual efficiency to 31.7%.

In 2005, M. Bakker et al. [9] simulated PV/T collectors and a ground coupled heat pump in TRNSYS 25-m2. The results showed that their system was able to meet 100% of the total heat demand for a typical newly-built one-family dwelling, while covering nearly all its electric energy demand and keeping the long-term average ground temperature constant.

^{*} Corresponding author.

E-mail address: giuseppe.tina@dieei.unict.it (G.M. Tina).

In meantime, Notton et al. [10] have developed a finite-differences simulation model. This model was validated using experimental data and let to estimate the cell temperature with a root mean square error of 1.3 °C. The work was proposed as an alternative to TRNSYS in order to model new hybrid PV/T collectors and estimate their thermal and electrical performances.

In 2008, Dubey and Tiwari [11] designed one of the first integrated photovoltaic (glass-to-glass) thermal solar water heater systems and tested it in outdoor conditions in India. They also came up with an analytical expression for the characteristic equation of PV/T collectors, experimentally validated for evaluating system performance for various configurations.

Similarly, Erdil et al. [12] have designed and tested a hybrid PV/T system for energy collection in Cyprus, with water used as the cooling fluid. They reported that 2.8 kWh of thermal energy could be stored as pre-heated water for domestic utilization with 11.5% electrical energy loss.

In 2010, Corbin and Zhai [13] suggested a new application for PV/T systems. They proposed integrating PV/T systems into the building façade. These collectors were capable of providing hot water for domestic use or hydronic space heating with total efficiency of 34.9% and no additional roof space requirements.

In 2012, Huang et al. [14] carried out an experimental study on a PV/T system composed of a 240-W poly-crystalline silicon collector, a 120-L storage tank and a pump. The results showed system thermal efficiency and photovoltaic conversion efficiency as high as 35.33% and 12.77%, respectively.

In meantime, Ozgoren et al. [15] studied a system made up of a 190-W PV module and a 190-W PV/T commercial water collector linked to a 175-L storage tank. They experimentally measured a PV/T collector thermal efficiency of 51% and maximum electrical efficiency of 13.6% for a mass flow rate of 0.03 kg/s. The electrical efficiency fell to 8% when the PV module temperature was 65 °C. They also observed that for each 100-W/m² increase in solar radiation value the cell temperature increased about 1.2 °C for the PV/T system and 5.4 °C for the PV system, respectively.

In 2014, Dupeyrat et al. [16] built a new prototype of a PV/T system that was tested under the same conditions and requirements for certification tests of thermal collectors. The parameters extracted from their tests were used in TRNSYS simulations. The results showed that a PV/T system on a limited roof area provides not only higher total PV and energy output but also higher primary energy saving than side-by-side installations with conventional ST and PV components. The increase in electrical output for the equivalent roof area for the PV/T/PV combination was around 12.7% in Paris, 12.6% in Lyon and 10.7% in Nice.

The research of Herrando et al. [17] tried to maximize the supply of both electricity and hot water in the scenario of an average 3-bedroom terraced house in London, UK, while also maximizing the total CO₂ emission savings. They found out that with a completely covered collector and a flow-rate of 20 l/h, 51% of the total electricity demand and 36% of the total hot water demand over a year could be covered by a hybrid PV/T system with a saving of up to 16.0 tons of CO₂. In addition, the electricity demand coverage was slightly higher than the PV-only system equivalent (49%).

In 2015, Huang and Hsu [18] investigated the performance of a PV/T system made up of six 240-W PV modules with copper pipes circulating water on the back of a 500-L water tank. Electrical efficiency was 13.26% and thermal efficiency 17.34% in the zero-reduction condition. The average performance ratio of the PV/T system was 86%.

Aste et al. [19] developed a PV/T system simulation model and evaluated its accuracy by means of an experimental monitoring campaign on a prototype. The collector was installed at the

Politecnico di Milano, Italy, experimental station, with tilt angle of 30° and azimuth equal to 0°. The 125-W unglazed PV/T collector was connected to an insulated 200-L storage tank. They measured thermal and electrical performance in December. They found a daily mean PV/T electrical efficiency of 6.0% and thermal energy efficiency of 25%.

Allan J et al. [20] developed a new methodology to characterize the performance of PV/T collectors using an indoor solar simulator. In particular, they studied different PV/T system configurations and, in agreement with other studies, they found that serpentine collectors have the highest combined efficiency in comparison with other configurations.

In 2017, Bianchini et al. [21] started to monitor the potential of a commercial PV/T solar collector for supplying electricity and thermal energy for domestic hot water (DHW) production in central Italy (or central-southern Europe in general).

Ramos et al. [22] started to assess the technical potential and basic economic implications of integrating PV/T systems in the domestic sector, specifically regarding the provision of combined heating, cooling and electricity. They proposed different solutions for 4–5 person households, with a 100 m² floor area and 50 m² rooftop area available for installation of solar collectors, in ten selected European locations with distinct climatic conditions, using annualized data of varying temporal resolution. They found out that the most efficient system configuration involves the coupling of PV/T to water-to-water heat pumps. In addition, TRNSYS analyses indicated that PV/T systems were capable of covering 60% of the combined heating demands and almost 100% of the cooling demands of the households examined in middle and low European latitude regions.

The studies reported in the literature have therefore shown that PV/T systems offer some advantages as compared with PV or solar thermal systems alone.

However, the literature survey revealed that, although many studies have investigated the PV/T system, there are relatively few works based on experimental research [10,12–15,19,21–25]. In particular, only two of these studies [14,24] refer to unglazed PV/T systems.

The present study investigates the performance of a pilot plant constructed using unglazed PV/T panels installed in the campus of the University of Catania (Catania, Italy).

Therefore, since the existing experimental studies [14] and [19] were performed in Taiwan and Milan respectively, one of the novelties of this research is the study of an unglazed PV/T system in a typical Mediterranean climate. Moreover, the PV/T modules used are not thermally insulated.

This characteristic should allow the achievement of a good compromise between the thermal and electrical performances of PV/T panels in a mild climate. This means accepting higher heat losses in winter and lower PV cell temperatures in summer.

Therefore, we believe that this study could help to increase knowledge of the performances of unglazed, uninsulated PV/T plants in the Mediterranean area.

With the aim of enriching the state of the art of PV/T systems, this paper reports the implementation, simulation and preliminary experimental validation of a pilot water-cooled PV/T plant. The system is described from a hardware point of view, providing details on both the hydronic and the electrical sections. The software adopted to monitor and control the plant is also described. The system was modelled using TRNSYS and simulation results were compared with the experimental data collected during a one-week period.

The preliminary results indicate that the model developed in TRNSYS is quite reliable for simulating the behaviour of a PV/T system in the climatic conditions and with the design solutions

Table 1
Technical characteristics of the PV/T module.

General data			Electrical data		
Length	1667	mm	Number of cells	60	
Width	990	mm	Cell type (dimensions)	Monocrystalline (156 mm × 156 mm)	
Frame thickness	40	mm	Nominal power, P_{MPP}	250	Wp
Weight when empty/filled	30/31.7	Kg	Module efficiency,	15.4	%
Thermal data			Electrical data		
Gross area	1.66	m ²	Power tolerance	±3	%
Aperture area	1.6	m ²	Rated voltage, V_{MPP}	30.7	V
Heat transfer liquid vol.	1.7	l	Rated current, I_{MPP}	8.15	A
Heat transfer liquid	water		Open circuit voltage, V_{oc}	38.5	V
Maximum temp.	74.7	°C	Short circuit current, I_{sc}	8.55	A
Max. operating pressure	1.2	Bar	Maximum system voltage	1000	V
Pressure loss per module	6000 Pa at 200 l/h		Reverse current load	15	A
Water inlet/outlet	15/21	mm	NOCT	49	°C
Thermal efficiency			Connectors		
Optical efficiency a_0	55	%	Application class	Class A	
heat loss coefficient a_1	15.76	W/K/m ²	Thermal coeff. V_{oc}	-0.32	%/K
heat loss coefficient a_2	0	W/K ² /m ²	Thermal coeff. I_{sc}	0.048	%/K
			Efficiency loss with temperature	-0.44	%/°C

used in this study.

2. PV/T solar plant description

One of the distinctive features of the proposed PV/T system is its high degree of flexibility, allowing simultaneous management of both the electrical and the thermal load to emulate different energy demand scenarios. Moreover, it is possible to switch the collectors' electrical and hydronic connections in order to modify the plant's operative conditions from parallel to series connection of the PV/T modules in terms of both subsystems.

In a PV/T plant, the hybrid modules constitute the connection point between the electrical and the hydronic subsystems.

The PV/T solar plant consists of two Dualsun™ (France) modules. Table 1 contains the main geometric, electric and thermal characteristics of the modules defined according to EN 12975–1:2006 test methods.

Thermal energy is transferred to the fluid by means of a rigid ultra-thin heat exchanger, completely integrated into the collector, which governs the heat transfer between the PV/T module front side and the fluid circulating on the back side.

The modules are installed on the roof of building 13 of the University Campus of Catania (Lat. 37.5256 N, Long. 15.0746 E), with a tilt angle $\beta = 25^\circ$ and azimuth angle $\gamma = 0^\circ$ (South-facing). The tilt angle can be changed manually from 15° to 60° , with an angle step, $\Delta\beta$, equal to 5° . Fig. 1 shows the deployed PV/T array and a detail of the structure allowing to modification of the tilt angle.

The outline of the thermal section of the PV/T solar plant is shown in Fig. 2. The main components of the hydronic circuit are: two PV/T modules; one solar thermal tank with two heat exchangers; one water pump; ten temperature sensors; four flow meters (although in case of series connection only two are used); one data acquisition system; safety components; water shut-off valves; three-way valves; one dry cooler. The function of the dry cooler loop, or secondary circuit, is to emulate the energy demand for domestic hot water production.

The PV/T hydronic system designed allows series or parallel connection of the two modules, which can be selected by means of flow divider valves. The capability for modifying the configuration of the PV/T plant has a dual purpose: to test the operation of the two modules subjected to different conditions of shading (parallel connection) and to evaluate the variation of the electrical efficiency



Fig. 1. Mounting structure: a) PV/T modules – b) Tilt angle setting structure, β .

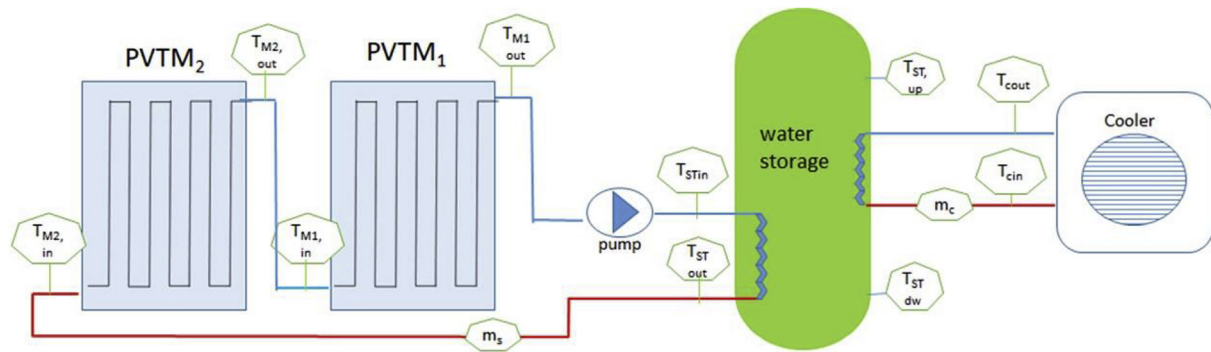


Fig. 2. Diagram of the hydronic section of the PV/T plant with the measured variables.

Table 2

Main characteristics of the hydronic circuit.

Pump		Solar Thermal tank		Cooling device	Pipes	
Maximum flow rate 55 l/min	Power 3–45 W	water tank 0.185 m ³	Water thermal capacity 4.174 (kJ/kg.K)	Nominal power 5000 W	Pipe length 40 m	Pipe diameter 16 mm

due to non-uniform temperature between the modules (series connection).

Three-way valves manage the flow rates circulating in the two modules with the aim of controlling their operating temperatures in accordance with weather conditions (irradiance, ambient temperature, wind speed) and thermal energy demand.

The hydronic circuit variables measured are: inlet and outlet temperatures of the operative fluid (water) at the inlet and outlet of each module, namely $T_{M1,in}$ and $T_{M1,out}$, at the inlet and outlet of the thermal solar tank, $T_{ST,in}$ and $T_{ST,out}$, at the bottom and in the top of the solar tank, $T_{ST,up}$ and $T_{ST,dw}$, as well as the fluid volumetric flowrate, m_s . The temperatures, T_{Cout} and T_{Cin} , and cooling volumetric flowrate, m_c , are also measured in the cooling circuit. The temperatures in the back of the modules ($T_{M1,b}$ and $T_{M2,b}$) are measured as well.

Table 2 contains the main characteristics of the hydronic circuit. Fig. 3 shows the installed hydronic section of the PV/T plant.

Fig. 4 shows a close-up of the power and measurement boxes. The switchboard contains the main switches which supply power to the solenoid valve, the cooling circuit, the pump and all the components for control of the whole system. A remote-controlled relay card is used to manage the three-way valves. The data acquisition units (DAQ) are installed in the box on the right and acquire the analogic and digital signals measured on the PV/T plant and send them to a PC with a Supervisory Control and Data Acquisition (SCADA) system, as detailed in Section 5.

The Hydronic circuit is managed using the strategy commonly adopted to control conventional solar thermal systems, based on monitoring of the temperature in the solar thermal tank. The primary circuit pump is turned on when $T_{M1,out}$ is 5-°C higher than the



Fig. 3. View of the hydronic section of the PV/T plant.

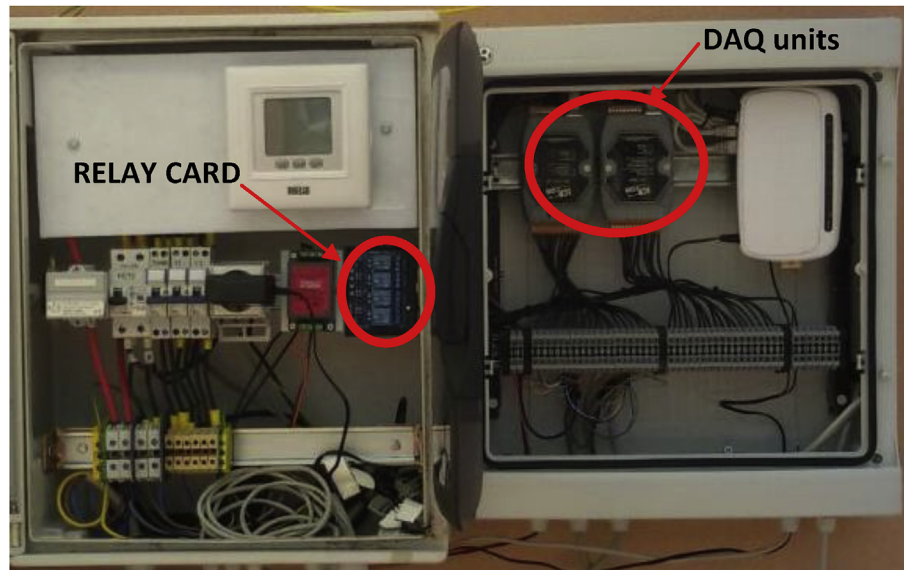


Fig. 4. PV/T plant power and measurement boxes.

Table 3

Module electrical values (measured at STC conditions) in series and parallel configuration.

	Isc (A)	Voc(V)	Impp (A)	Vmpp (V)	Pp (W)
module M_1	8.664	38.645	8.089	31.376	253.813
module M_2	8.654	38.607	8.103	31.545	255.597
Series	8.55	77	8.15	61.4	500
Parallel	17.1	38.5	16.3	30.7	500

temperature in the lower part of the solar thermal tank, and is switched off when $T_{ST,dw} - T_{M1out}$ is lower than 2 °C. Finally, when the temperature inside the solar thermal tank reaches a given set-up value, the dry cooler is turned on.

Environmental data, such as global and diffuse solar radiation, wind speed and direction, ambient temperature, humidity and air pressure, are measured by a weather station placed close to the PV/T modules. All the sensors are connected to the control unit, placed in an external box, which transfers the sensor data to the PC

through Ethernet [26]. Data from the PV/T solar plant and local weather station are stored in a dedicated SCADA with 1 min acquisition rate. A web page was created to allow the users to remotely monitor or set the parameters governing the PV/T plant, as detailed in Section 5.

Therefore, the plant described is an effective research tool, allowing the study of PV/T systems with different configurations and different application scenarios.

3. Hardware and software setup for electrical performance analysis

The main electrical characteristics of the PV/T modules, measured by the manufacturer in Standard Test Conditions (STC) and of the string, with modules series or parallel connected, are contained in Table 3.

As already mentioned, the PV/T modules can be connected both in series and in parallel. Fig. 5 shows the wiring diagram of the PV/T electrical circuit in series configuration. The connectors of the PV/T string, or of just one module, and the sensor cable, are connected to two separate sections of the switchboard installed on the roof (QBTP). Then the cables leaving QBTP are connected to another switchboard (QBTS), containing the electrical switching and power distribution gear. The two connectors of the PV/T string are coupled to an Agilent N3300A programmable electronic load (EL).

The EL is connected by means of a GPIB cable/card to a Personal Computer (PC). The PC is programmed with a tool developed in Labview® environment allowing the EL to be controlled in a way that sets a specific operating point for the photovoltaic string. Three different electrical operating modes can be selected: 1) open circuit, 2) I-V curve and 3) Maximum Power Point Tracking (MPPT). This program also controls the electrical output of the modules.

Moreover, the measured irradiance on the plane of the PV/T modules, G , and the two back side temperatures, $T_{M1,b}$ and $T_{M2,b}$ are conveyed to the NI cDAQ 9188, so these data are also shown in real time by means of the Labview® program developed.

Selection of one of the different operating modes available allows the performance of experimental tests to evaluate the impact of the electrical operating point on the module working temperatures. For standard PV modules, it was evaluated that PV module temperatures can vary by up to 5 °C in response to the switch from

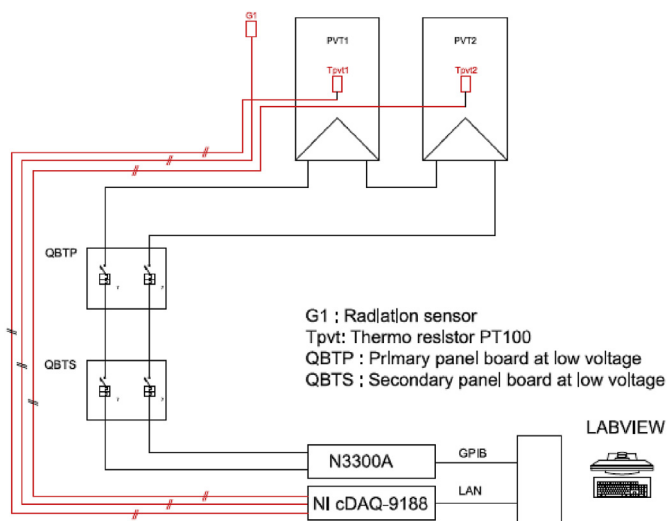


Fig. 5. PV/T system wiring diagram.

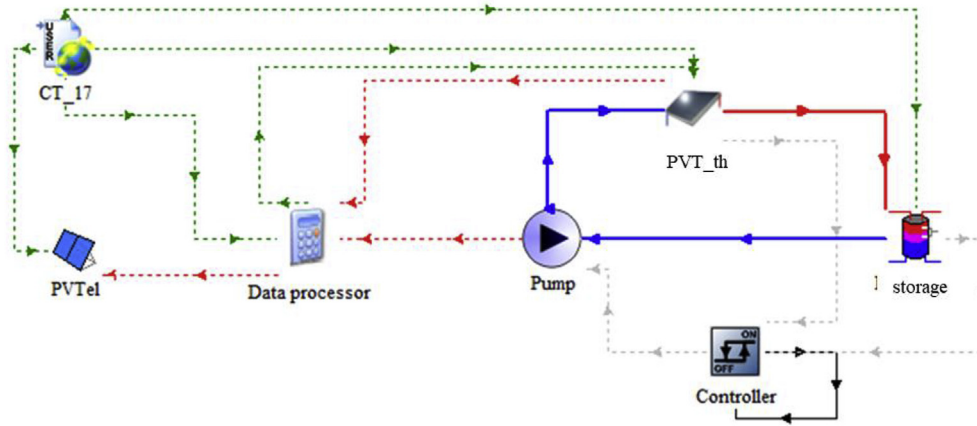


Fig. 6. Model of the PV/T plant.

Table 4

Type used for the PV/T modelling.

Type	109	1b	94a	3d	60d	2b	92	24
Name	Weather data	Solar collector	PV module	Pump	Storage Tank	Controller	Cooling circuit	Integral operator

the no-load to the maximum power condition [27,28]. PV module temperature is therefore a crucial parameter for optimal management of the PV/T system.

4. Model of the PV/T system in TRNSYS

A numerical study was developed using the TRNSYS 17 software in order to evaluate the thermal and electrical energy, the relative efficiencies and the transient behaviour of the PV/T plant.

As shown in Fig. 6, the system consists of two main circuits:

- solar loop (PV/T systems with a hot water storage tank)
- cooling circuit (including storage and energy demand).

The TRNSYS user interface allows the connection of single components (called types) available in the program library, e.g. solar collector, pump, controller, heat exchanger. The model developed in TRNSYS mainly consist of the type shown in Table 4. TRNSYS solves the set of algebraic or differential equations that govern the different components with a user-selectable time step.

The mathematical description of each type can be found in the TRNSYS manuals.

One peculiarity of this PV/T model is the approach used for defining the features of the PV/T module.

The type available in the TRNSYS library (type 50), needs values of τ , α , U_L and F' as input data to characterize the thermal performance the PV/T module.

Currently, some PV/T modules, such as Dualsun modules, are tested in accordance with UNI EN 12975, which provides values of η_0 , a_1 and a_2 . This hitch could be overcome converting data based on one standard (η_0 , a_1 and a_2) with another (based on τ , α , U_L and F') [solar collecting testing], or by fitting available experimental data.

However, even if such a procedure is feasible it could be subject to some inaccuracies compared to data obtained from laboratory tests.

Therefore, the PV/T module was defined using two distinct systems: one consisting of a solar thermal collector and the other of a photovoltaic module, operating in parallel. The performances of the thermal and photovoltaic modules were then evaluated, taking

the mutual interference between the two systems into account.

This approach also allows use of the output of the photovoltaic type, i.e. current and voltage, for testing the plant's electrical performance.

It has to be pointed out that the approximation involved in the ways in which this study models two different components might lead to deviations between the experimental and the theoretical results.

As far as the photovoltaic system is concerned, the efficiency was calculated using the data provided by the producer and the temperature dependence of the photovoltaic cells, which in turn is coupled with the temperature of the thermal fluid (see eq. (7)).

The efficiency of the thermal system was calculated with the aid of a simplified model using the modified solar radiation G_T [28]. G_T is calculated from the solar radiation "G" by subtracting the amount of solar energy converted by the photovoltaic effect (see eq. (3)).

4.1. Weather data

The study was carried out using the weather data measured by the weather station mentioned in Section 2, from 3 to 9 May 2017. The data, originally collected in a Microsoft Office Excel® file, was converted into text format using a Matlab® script and then implemented within Type 109.

4.2. Solar collector (Type 1b)

The thermal efficiency of the solar thermal collector, η_{th} , was calculated through eq. (1) in steady-state conditions, while the thermal power is given in (2).

$$\eta_{th} = a_0 - a_1 \cdot \Delta T_m^+ - a_2 \cdot G_T \cdot (\Delta T_m^+)^2 \quad (1)$$

$$P_{th} = A_{ST} - G_T \cdot \eta_{th} \quad (2)$$

where

$a_0 = 0.55$, $a_1 = 15.76 \text{ W/(m}^2 \text{ K)}$, $a_2 = 0 \text{ W/(m}^2 \text{ K}^2)$ and ΔT_m^+ is the true mean fluid temperature difference [29]. G_T is the modified

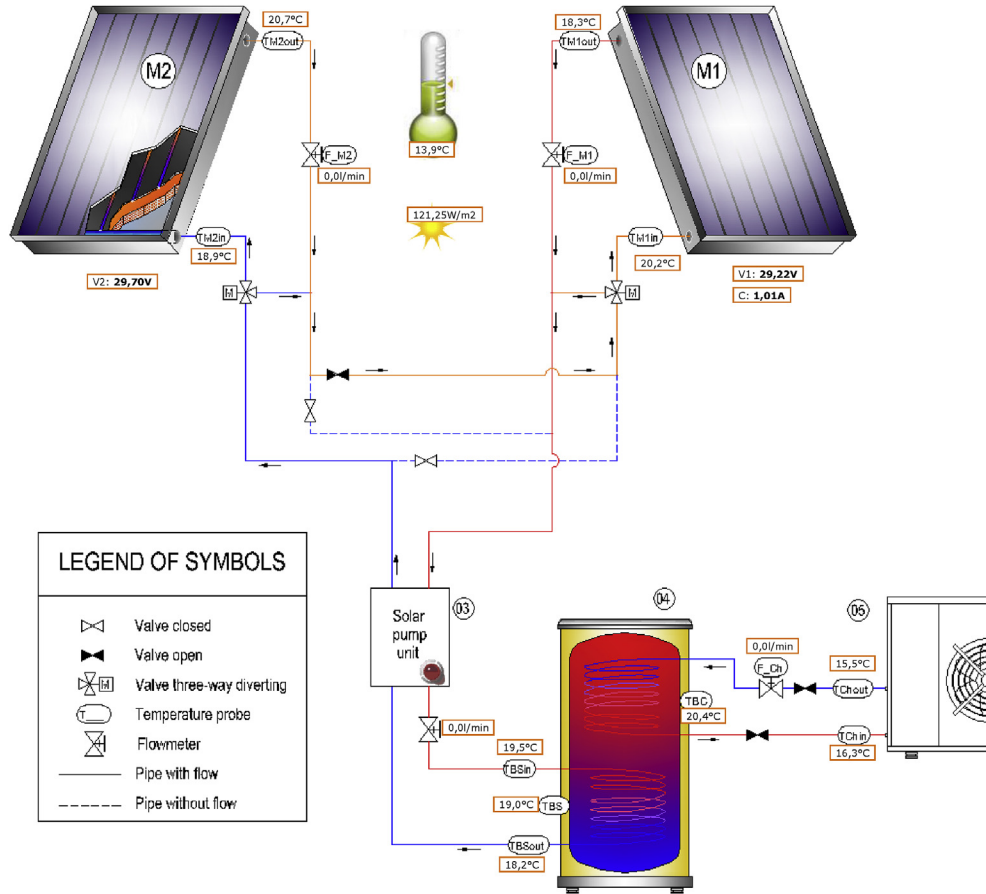


Fig. 7. Graphical view of the SCADA system.

solar radiation calculated by subtracting from the solar radiation, G , the amount of solar energy converted by the photovoltaic effect, thus expressed by eq. (3),

$$G_T = G \cdot (1 - \eta_{el}) \quad (3)$$

Assessment of the thermal efficiency in quasi-dynamic conditions also takes into account the wind effect and the thermal inertia of the PV/T solar system (ISO 9806:2013). However, for wind velocity lower than 4 m/s, the quasi-dynamic and steady-state models give comparable results for most collector designs.

In addition, the thermal power, P_{th} , produced by the PV/T solar plant in Fig. 2 can be expressed as a function of the temperature difference between the water inlet and the outlet as

$$P_{th} = m \cdot C \cdot (T_{M1,out} - T_{M2,in}) \quad (4)$$

where m_s is the mass flowrate and C is the fluid specific heat.

4.3. PV module

In Table 3 the electrical values of the PV modules are referred to STC ($G_{STC} = 1000 \text{ W/m}^2$ of global solar radiation PV module temperature of 25°C). However, as we are all aware PV modules do not usually work at STC, and the electrical features provided in Table 3 vary when they operate under different environmental conditions. Consequently, the actual DC power, P_{el} , differs from the nominal one, P_{nom} , due to variations in the module temperature, T_{PV} , and/or solar radiation, G . Therefore, the efficiency, η_{el} , is defined as the ratio between measured P_{el} and the product of the solar radiation G

and the surface area of modules A_{PV} :

$$\eta_{el} = \frac{P_{el}}{A_{PV} \cdot G} \quad (5)$$

In the model designed, an external operator is introduced with the aim of calculating electrical efficiency as a function of module cell temperature, T_{PV} (see eq. (6)).

Module cell temperature is in turn defined as a function of the average of the inlet and outlet temperatures of the thermal fluid in the solar collector. The electrical efficiency is then calculated by

$$\eta_{el} = 0.154 \cdot [1 - 0.0044 \cdot (T_{PV} - 25)] \quad (6)$$

where T_{PV} is calculated as

$$T_{PV} = \frac{\left[\frac{(T_{M,in} + T_{M,out})}{2} + T_a \right]}{2} \quad (7)$$

Equation (7) was derived by modifying the models available in the literature [30], which adopt the mean temperature of the cooling fluid, in accordance with results obtained from our experimental survey on this PV/T plant.

In order to evaluate the performance of the PV plant over time, IEC standard 61724:1998 introduces the array yield, Y_A , and the reference yield, Y_R . Y_A is defined as the ratio between the electrical energy produced in a defined time interval, E_{el} , and the nominal electrical power, P_{nom} . The array yield represents the number of hours in which the PV modules work at their peak value in the defined time interval:

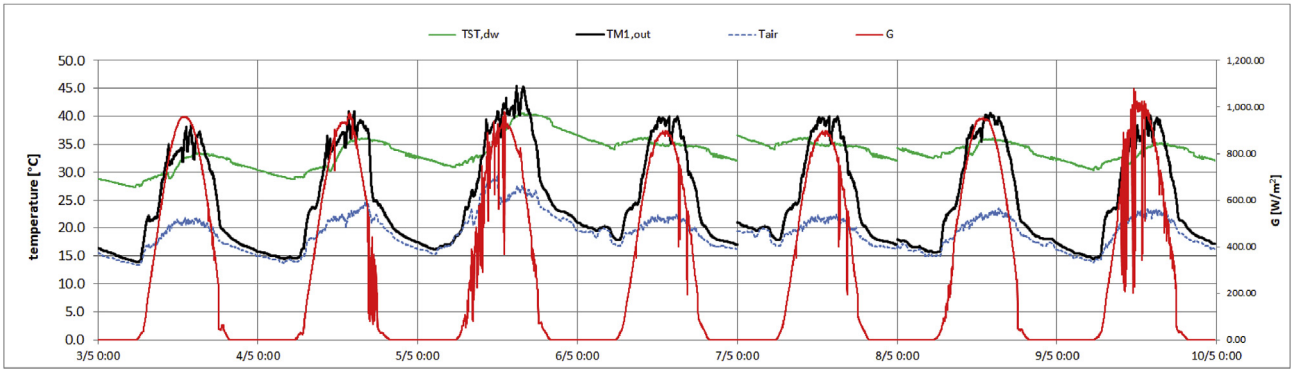


Fig. 8. Solar radiation (G), air temperature (T_{air}), M1 outlet temperature ($T_{M1,out}$), solar tank temperature ($T_{ST,dw}$).

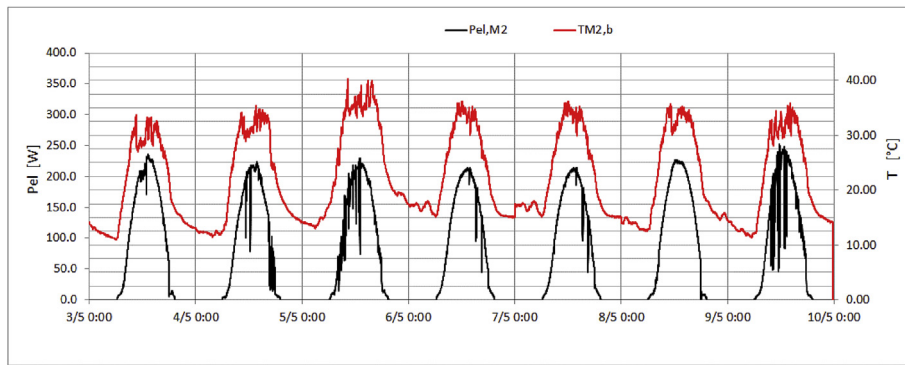


Fig. 9. Photovoltaic temperature and electrical power of PV/T module M2.

$$Y_A = \frac{E_{el}}{P_{nom}} \quad (8)$$

Y_R is defined as the ratio between the solar radiation energy per surface unit, H , evaluated in the considered time interval and G_{STC} :

$$Y_R = \frac{H}{G_{STC}} \quad (9)$$

Finally, the performance ratio, PR , is defined as the ratio between the array yield Y_A and the reference yield Y_R :

$$PR = Y_A/Y_R \quad (10)$$

Therefore, PR provides the ratio between the nominal and actual

efficiency of the PV plant.

4.4. Solar Storage Tank (Type 60d)

Type 60d allows modelling of a stratified cylindrical vertical storage tank with an inlet and an outlet flow rate and two internal heat exchangers (inlet 1 and 2). The heat exchanger, in the lower part of the solar storage tank, is connected with the solar collector circuit, while the heat exchanger, in the upper part of the storage tank, is connected with the auxiliary device. The inputs required are the flow rates at inlets 1 and 2 and the tank volume, which is 0.189 m^3 . The average temperature of the tank is used as input for the ON/OFF controller that operates the pump. The type was set without considering thermal stratification.

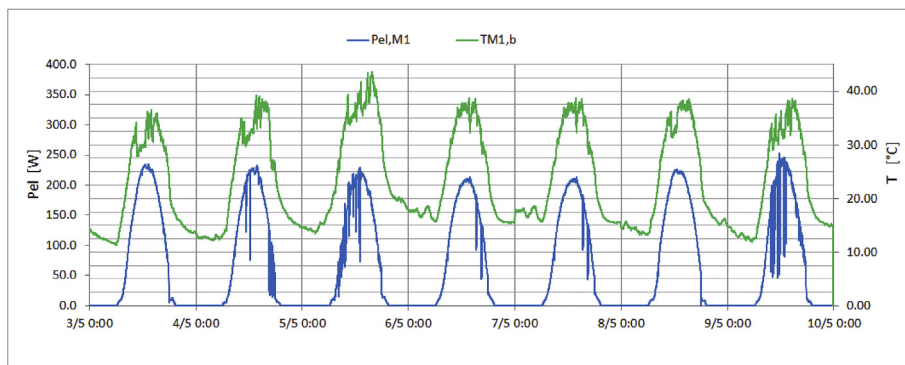


Fig. 10. Photovoltaic temperature and electrical power of PV/T module M1.

Table 5
Percentage error between simulated and experimental data.

	Min (%)	Mean (%)	Max (%)
$\Delta T_{M1,out}$	0.009	6.53	27.58
ΔV_{M1}	0.03	4.35	23.49
ΔE_{th}	2.22	12.04	28.31
ΔE_{el}	4.23	5.29	8.02

4.5. Auxiliary cooling device (Type 92)

In this study, the auxiliary cooling device simulates DHW energy demand. The operating principle requires the cooling device to remove energy from the solar tank until a given temperature value (e.g., 40 °C) is reached inside the solar tank. The thermal energy extracted by the solar tank is the useful thermal energy produced by the PV/T plant at the selected thermal level.

4.6. Integral operator (Type 24)

The thermal energy transferred to the thermal storage E_{th} and the electricity produced, during the time period t_1 – t_2 , E_{el} are calculated by means of the integral operator,

$$E_{th} = \int_{t_1}^{t_2} \dot{m} \cdot C \cdot \Delta T \cdot dt \quad (11)$$

where \dot{m} = water flow rate

$$C = 4.186 \frac{kJ}{kg \cdot K}$$

$$\Delta T = (T_{ST_in} - T_{ST_out})$$

$$E_{el} = \int_{t_1}^{t_2} G \cdot A_{PV} \cdot \eta_{el} \cdot dt \quad (12)$$

5. Experimental results

The PV/T plant is monitored in real time by means of a dedicated SCADA system. The SCADA adopts low-cost commercial off-the-shelf sensors and components. The data acquisition board is the ICPDAS ET-7017 (20 analog single-ended channels with programmable input range). The information provided by the data acquisition board is acquired by a web-based application. The system can be interfaced to any device through the standard MODBUS TCP/IP protocol. The adoption of the TCP/IP version of MODBUS protocol allows the connection of a virtually unlimited number of masters and slaves over local networks and/or the World Wide Web. Among the main features, the software is capable of storing data from the individual sensors on a database; plotting stored data; viewing the captured data in real time; carrying out operations on aggregate data; generating periodic graphical and/or text file reports and sending them via e-mail; generating e-mail alerts and alarms and allowing remote access to the database via a web browser.

Fig. 7 shows a screenshot of the web page of the PV/T plant (accessible at <http://moses.pvt.dieei.unict.it:8081>), where the current configuration and the value of the operative variables (thermal, electrical and environmental) are reported in real time (inside the red boxes).

The architecture of the PV/T plant allows the temperature inside the storage tank to be managed by defining the temperature set-point that switches on the cooling device. Different scenarios of daily heat demand curves may be simulated by choosing the set points of the temperature inside the hot water storage tank [31]. Consequently, the global efficiency (thermal plus electrical efficiency) of the PV/T modules can be evaluated as a function of the different enthalpic level of the water in the solar tank. In fact, the global efficiency of a PV/T plant strongly depends on the operating temperatures. In other words, when the thermal level of the user demand is low, the PV module works at its maximum power point; in contrast, when the requested thermal level is high, electricity production is reduced due to the increase in PV cell temperature.

Below, the preliminary results obtained during a week of operation of the system in a single scenario are reported and discussed. The PV/T plant was set with the two modules connected in series, and the set-point temperature of 45 °C in the upper part of the hot water storage tank (T_{ST_up}) had to be exceeded to switch on the cooling device.

Fig. 8 shows the plots of a week of measurements, from 3 to 9 May 2017, of the following variables: irradiance on the plane of the modules (G); ambient temperature (T_{air}); temperature of the lower part of the storage tanks ($T_{ST,dw}$); and temperature at the outlet of module 1 ($T_{M1,out}$). In the period over 7–8 May there is an interruption in the recorded data due to a malfunction of a couple of thermal sensors.

During the monitored period, the temperature in the upper part of the hot water storage tank (T_{ST_up}) never exceeded 45 °C, the temperature set point that activated the cooling device, so thermal energy was not extracted from the solar tank.

Regarding the electrical configuration, the two series-connected modules are operated at the maximum power point. The monitoring system acquires both the voltage and the current of each PV/T module, so the performances of the two modules are available separately.

Figs. 9 and 10 show the weekly variation of the electrical power ($P_{el,Mi}$) and the module back side temperature ($T_{Mi,b}$) of PV/T modules M2 and M1, respectively.

It can be seen that M2 has lower back side temperature than M1. This result is in agreement with the series-connection of the modules, which implies that the circulating fluid first enters M2 and then flows to M1. The maximum difference in the back temperatures is 3.0–4.0 °C, so the impact on the amount of electricity generated is quite low. Indeed, considering that the thermal power coefficient of the PV modules is $-0.44\%/^{\circ}C$ (see Table 1), the increase in the electrical power generated is almost 1.5%.

6. Comparison with simulation results

In this section the experimental data are compared with the results of the simulation performed using TRNSYS. This makes it possible to evaluate the accuracy of the model of the PV/T plant simulated in TRNSYS environment.

The percentage error between experimental and simulation data for some representative variables was calculated. The parameters considered were the thermal (ΔE_{th}) and electrical (ΔE_{el}) energy produced by the PV/T plant, the outlet temperature ($\Delta T_{M1,out}$) and the voltage (ΔV_{M1}) of module 1. Table 5 shows the percentage error between simulated and experimental data.

It can be seen that there is a wide range of variation in the percentage errors, with minimum values that are rather small, while the maximum values are rather high. Reflecting the complexity of the two sub-systems, the errors of the electrical parameters are lower than the errors observed for the thermal parameters. However, the mean errors may be acceptable

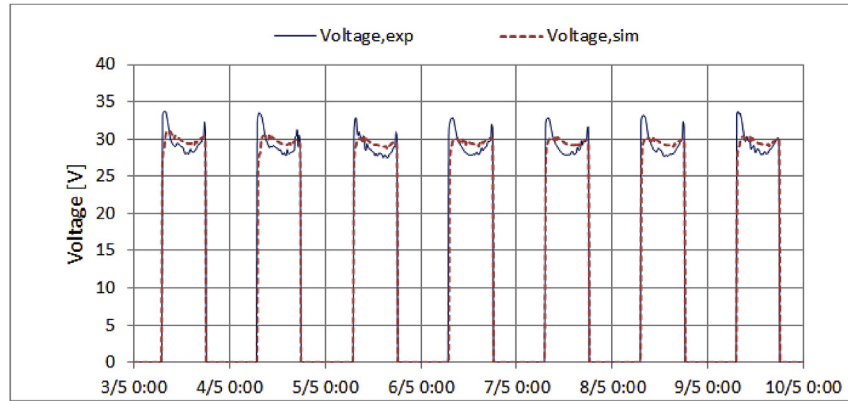


Fig. 11. Comparisons between simulated and measured voltage of PV/T module M1.

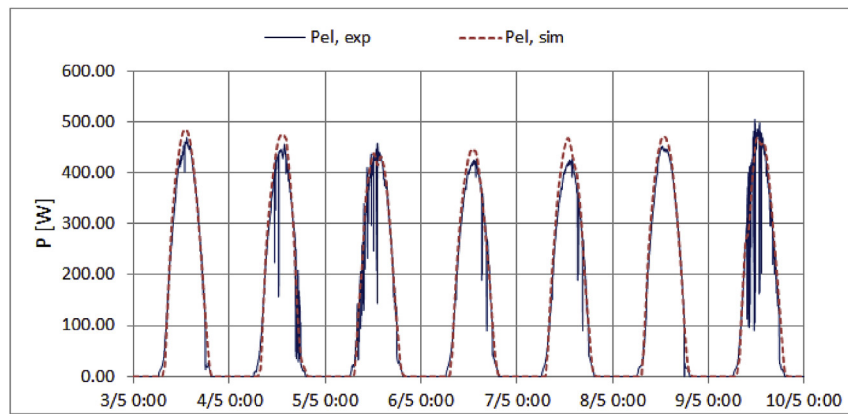


Fig. 12. Comparisons between experimental and simulated electric power (P_{el}).

considering the approximation affecting both the experimental and the simulation data.

The following figures depict the daily comparisons between the measured and simulated data. Fig. 11 compares the simulated and measured voltage of module M1. Module voltage is well known to be significantly affected by cell temperature, so this comparison allows assessment of the accuracy of the equation used for calculating T_{PV} (eq. (7)). The two sets of data are in good agreement, especially during the central part of the day. However, the experimental values are significantly higher than the simulated ones in

the early hours of the day, when the solar radiation is feeble. These discrepancies may be ascribed to inaccuracy of the MPPT algorithm at low solar radiation values. In these conditions, the module voltage tends to reach the open circuit voltage value (V_{oc}).

Figs. 12 and 13 show the comparisons between electrical power (P_{el}) and electrical efficiency (η_{el}). The modelled efficiency fits the experimental data quite well, whereas greater differences emerge between the two sets of electrical power values. This may be due to simplified model adopted for describing the electrical part of the PV/T module, since only thermal losses were considered, leaving

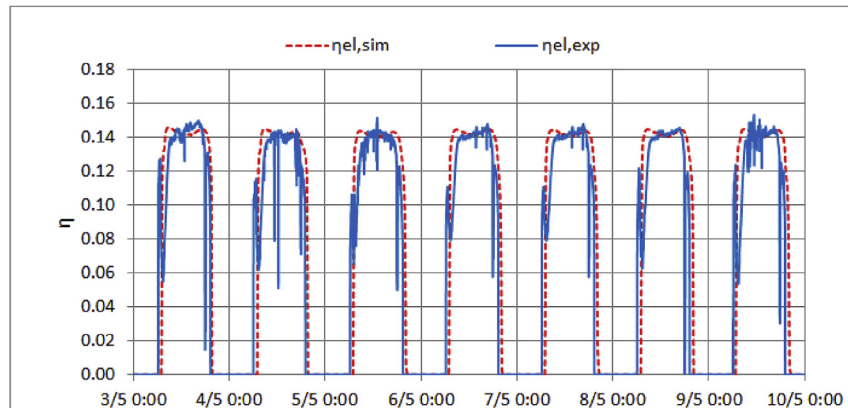


Fig. 13. Comparisons between experimental and simulated electric efficiency (η_{el}).

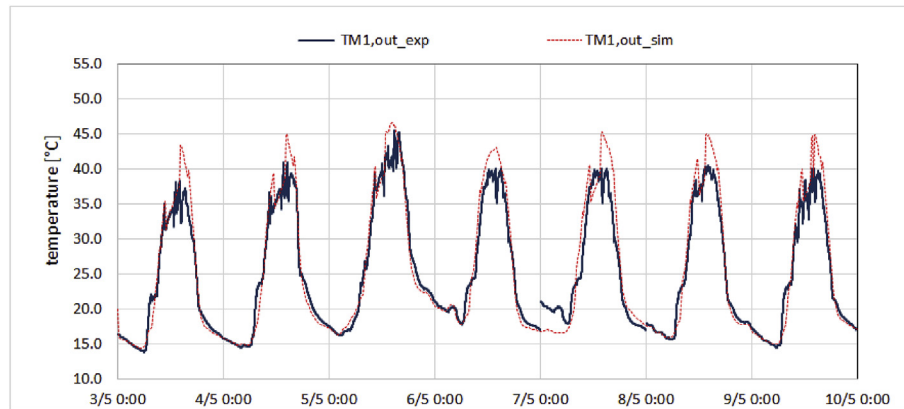


Fig. 14. Comparisons between experimental and simulated temperatures at the outlet of PV/T module M1.

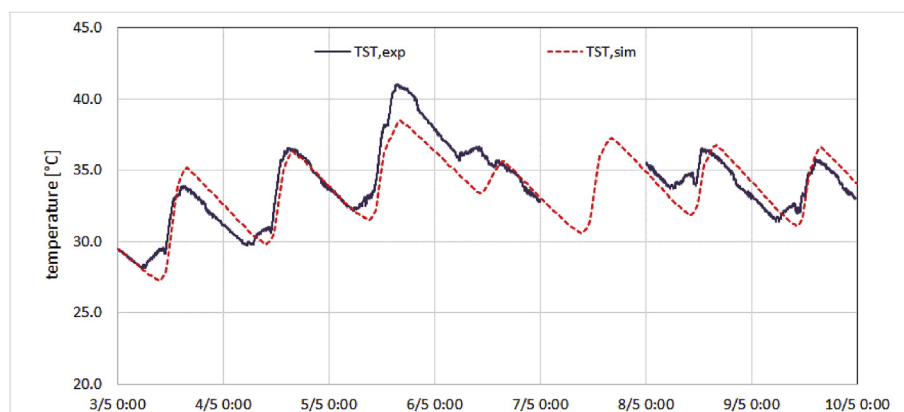


Fig. 15. Comparisons between experimental and simulated temperatures in the solar tank T_{ST} .

aside other losses such as shading, soiling, optical losses, joule losses and MPPT losses.

As regards the thermal features, Fig. 14 displays the comparison between the measured temperature at the outlet of the PV/T module, T_{M1out_exp} , and the simulated value, T_{M1out_sim} , which are the highest hydronic circuit fluid temperatures.

The trend of the two temperature sets is fairly comparable, with some significant differences during the second part of the day (after midday), when the increase in the temperature inside the solar tank causes the pump to stop. After this, it takes some time for the PV/T system to restart the pump, due to its inertia. In contrast, in the simulation, the modular outlet temperature rises rapidly and the pump restarts quickly. Obviously, it will be necessary to define a different control strategy to realign the model with the experimental plant.

Fig. 15 shows the comparison between the mean temperature measured inside the solar thermal tank, T_{ST_exp} , and the simulated value, T_{ST_sim} , where T_{ST_exp} is calculated by

$$T_{ST_exp} = \frac{(T_{ST_up} + T_{ST_dw})}{2} \quad (13)$$

Once again, the trends of the two temperature sets are fairly comparable. However, on some days obvious differences emerge between the experimental and simulated data, which may be partially attributed to the discrepancies in the module outlet temperature already highlighted. Moreover, temperature sensor measurement errors may play an important role. On 7 May, the experimental values of T_{ST} are not reported due to a fault in the

temperature sensors.

Finally, the energy production of the PV/T plant is reported. Fig. 16 displays the comparison of the daily thermal energies exchanged between the PV/T modules and the solar storage tank.

Overall, the matching between experimental and simulated data is good. On 6 May, the performance of the PV/T plant was poorer than on the other days. This is because the temperatures inside the solar tank are higher than the solar collector outlet temperatures. This condition turns off the pump and prevents the supply of energy to the solar tank.

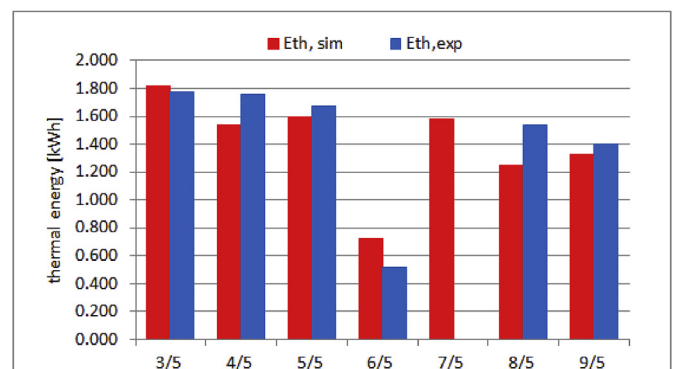


Fig. 16. Comparison of daily thermal energies: simulated ($E_{th,sim}$) and experimental ($E_{th,exp}$).

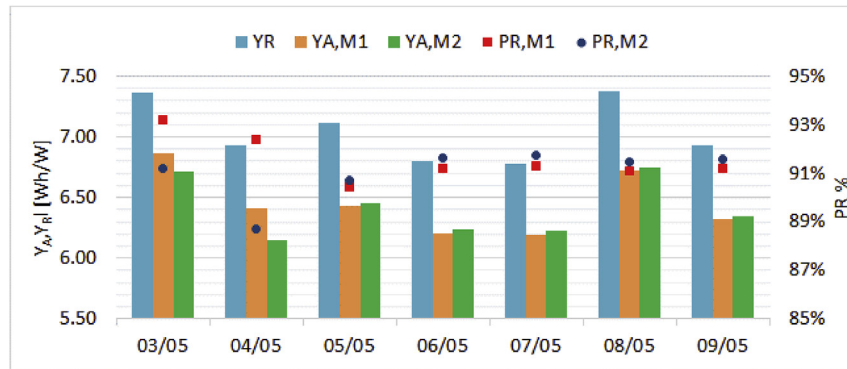


Fig. 17. Daily value of the array yield, YA, reference yield, YR and performance ratio (PR) of the two modules.

Fig. 17 shows the daily values of the array yield, YA, reference yield, YR, and performance ratio, P_R , of the two modules.

P_R is calculated as a function of both YA and YR by eqs. (9) and (10). During the first two days, the hottest module M1 performed better, but this is due to a shading problem, since the difference in power is not justified by the difference in the TPV temperatures, whereas for the last five days the performances of the two modules are in accordance with the thermal analysis. It is worth noting that the PV/T modules always have a P_R value higher than 88%, this means that the effective efficiency of the module is about 10% less than the nominal one. This result is comparable with that observed by Ref. [21].

7. Conclusions

This paper describes a pilot cogenerative PV/T plant installed in the campus of the University of Catania (Catania, Italy).

The energy demand may be varied through management of the cooler device and the electronic load (controlled and monitored by a specially developed software). This feature makes the system flexible in determining the electrical and thermal operating points of the PV/T modules. Although the PV/T plant is able to operate in both series and parallel configuration, this study only reports on preliminary tests conducted with the modules connected in series. The experimental survey provides useful data on the system's behaviour and energy performances.

A TRNSYS model of the PV/T plant was also produced and the results of the simulations are reported. The comparison between the numerical data and the measurements is also presented. From this point of view, it was observed that the two sets of data are fairly comparable, with average errors of 12.04% and 5.29% respectively for the thermal and electrical energy produced by the system. Although the reported results are limited to a very short period, they provide some useful indications on the performances of a PV/T plant installed in the Mediterranean area.

The further development of this study is in the direction of extending the monitored period to one year, to obtain a complete analysis of the system also during the winter, and also to check the precision of the TRNSYS model in different weather conditions.

Acknowledgements

This research received a specific grant from the University of Catania: progetto di Ateneo, FIR 2014 (DC90C1): "L'integrazione degli impianti fotovoltaici e fotovoltaici/termici nei sistemi edilizi in area mediterranea: studio numerico e sperimentazioni sull'efficienza e sulla compatibilità costruttiva".

References

- [1] 2016-SNAPSHOT of GLOBAL PHOTOVOLTAIC MARKETS, 2017. Report IEA PVPS T1-31.
- [2] PHOTOVOLTAICS REPORT, Fraunhofer Institute for Solar Energy Systems, ISE, 2016.
- [3] G.M. Tina, Simulation model of photovoltaic and photovoltaic/thermal module/string under nonuniform distribution of irradiance and temperature, ASME. J. Sol. Energy Eng 139 (2) (2016), <https://doi.org/10.1115/1.4035152>, 021013–021013-12.
- [4] F.G. Cabo, S. Nizetic, G.M. Tina, Photovoltaic panels: a review of the cooling techniques, Trans. FAMENA 40 (2016) 63–74.
- [5] A.H.A. Al-Waeli, K. Sopian, H.A. Kazem, M.T. Chaichan, PV/T (Photovoltaic/Thermal): status and future prospects, Renew. Sustain. Energy Rev. 77 (2017) 109–130.
- [6] T. Brahim, A. Jemni, Economical assessment and applications of photovoltaic/thermal hybrid solar technology: a review, Sol. Energy 153 (2017) 540–561, <https://doi.org/10.1016/j.solener.2017.05.081>.
- [7] M. Wolf, Performance analyses of combined heating and photovoltaic power systems for residences, Energy Convers. 16 (1–2) (1976) 79–90, [https://doi.org/10.1016/0013-7480\(76\)90018-8](https://doi.org/10.1016/0013-7480(76)90018-8).
- [8] S.A. Kalogirou, Use of TRNSYS for modelling and simulation of a hybrid pv-thermal solar system for Cyprus, Renew. Energy 23 (2001) 247–260, [https://doi.org/10.1016/S0960-1481\(00\)00176-2](https://doi.org/10.1016/S0960-1481(00)00176-2).
- [9] M. Bakker, H.A. Zondag, M.J. Elswijk, K.J. Strootman, M.J.M. Jong, Performance and costs of a roof-sized PV/thermal array combined with a ground coupled heat pump, Sol. Energy 78 (2005) 331–339, <https://doi.org/10.1016/j.solener.2004.09.019>.
- [10] G. Notton, C. Cristofari, M. Mattei, P. Poggi, Modelling of a double-glass photovoltaic module using finite differences, Appl. Therm. Eng. 25 (2005) 2854–2877, <https://doi.org/10.1016/j.applthermaleng.2005.02.008>.
- [11] Swapnil Dubey, G.N. Tiwari, Thermal modeling of a combined system of photovoltaic thermal (PV/T) solar water heater, Sol. Energy 82 (7) (2008) 602–612.
- [12] E. Erdil, M. Ilkan, F. Egelioglu, An experimental study on energy generation with a photovoltaic (PV)-solar thermal hybrid system, Inside Energy 33 (8) (2008) 1241–1245, <https://doi.org/10.1016/j.energy.2008.03.005>.
- [13] C.D. Corbin, Z.J. Zhai, Experimental and numerical investigation on thermal and electrical performance of a building integrated photovoltaic-thermal collector system, Energy Build. 42 (1) (2010) 76–82, <https://doi.org/10.1016/j.enbuild.2009.07.013>.
- [14] C.Y. Huang, H.C. Sung, K.L. Yen, Experimental study of photovoltaic/thermal (PV/T) hybrid system, International Journal of Smart Grid and Clean Energy 2 (2) (2013) 148–151.
- [15] M. Ozgoren, M.H. Aksoy, C. Bakir, S. Dogan, Experimental Performance Investigation of Photovoltaic/Thermal (PV-t) System EPJ Web of Conferences, vol. 45, 2013, <https://doi.org/10.1051/epjconf/20134501106>.
- [16] P. Dupeyrat, C. Ménézo, S. Fortuin, Study of the thermal and electrical performances of PVT solar hot water system, Energy Build. 68 (C) (2014) 751–755, <https://doi.org/10.1016/j.enbuild.2012.09.032>.
- [17] M. Herrando, C.N. Markides, K. Hellgardt, A UK-based assessment of hybrid PV and solar-thermal systems for domestic heating and power: system performance, Appl. Energy 122 (1) (2014) 288–309, <https://doi.org/10.1016/j.apenergy.2014.01.061>.
- [18] C.-Y. Huang, K.-C. Hsu, Performance Monitoring of Photovoltaic Thermal Hybrid System the 14th IFToMM World Congress, 2015. Taipei, Taiwan, October 25–30.
- [19] N. Aste, F. Leonforte, C. Del Pero, Design, modelling and performance monitoring of a photovoltaic–thermal (PVT) water collector, Sol. Energy 112 (2015) 85–99.
- [20] J. Allan, Z. Dehouche, S. Stankovic, L. Mauricette, Performance testing of thermal and photovoltaic thermal solar collectors, Energy Science &

- Engineering 3 (4) (2015) 310–326, <https://doi.org/10.1002/ese3.75>.
- [21] A. Bianchini, A. Guzzini, M. Pellegrini, C. Sacconi, Photovoltaic/thermal (PV/T) solar system: experimental measurements, performance analysis and economic assessment, *Renew. Energy* 111 (2017) 543–555.
- [22] A. Ramos, et al., Hybrid photovoltaic-thermal solar systems for combined heating, cooling and power provision in the urban environment, *Energy Convers. Manag.* 150 (2017) 838–850.
- [23] T.T. Chow, W. He, J. Ji, An experimental study of facade-integrated photovoltaic/water-heating system, *Appl. Therm. Eng.* 27 (2007) 37–45.
- [24] N. Aste, C. Del Pero, F. Leonforte, M. Manfren, Performance monitoring and modelling of an uncovered photovoltaic-thermal (PVT) water collector, *Sol. Energy* 135 (2016) 551–568.
- [25] N. Aste, G. Chiesa, F. Verri, Design, development and performance monitoring of a photovoltaic-thermal (PVT) air collector, *Renewable Energy Volume 33, Issue 5 (May 2008)* 914–927.
- [26] G.M. Tina, A.D. Grasso, A. Gagliano, Monitoring of solar cogenerative PVT power plants: overview and a practical example, *Sustain. Energy Technol. Assess* 10 (2015) 90–101.
- [27] G.M. Tina, A coupled electrical and thermal model for photovoltaic modules., *J. Sol. Energy Eng.* 132 (2010) 1–5, <https://doi.org/10.1115/1.4001149>.
- [28] L.W. Florschuet, Extension of the Hottel- Whillier model to the analysis of combined photovoltaic/thermal flat plate collectors, *Sol. Energy* 22 (1979), [https://doi.org/10.1016/0038-092X\(79\)90190-7](https://doi.org/10.1016/0038-092X(79)90190-7), 361–36.
- [29] J.A. Duffie, et al., *Solar Engineering of Thermal Processes*, John Wiley & Sons, 1974. ISBN: 0-471-22371-9.
- [30] S.A. Kalogirou, Y. Tripanagnostopoulos, Hybrid PV/T solar systems for domestic hot water and electricity production, *Energy Convers. Manag.* 47 (2006) 3368–3382.
- [31] G. Tina, A. Gagliano, F. Nocera, A. Grasso, The Pilot Photovoltaic/Thermal Plant at the University of Catania: Description and Preliminary Characterization, BIREs, Dublin, Ireland, 2017.

Nomenclature

A_{PV} : area of the PV modules (m^2)
 A_{ST} : area of the solar thermal absorber (m^2)
 a_0 : ratio between the thermal power produced and a given solar radiation when there are not heat losses
 a_1 : linear coefficient of thermal dispersion
 a_2 : quadratic coefficient of thermal dispersion
 C : specific heat ($kJ/kg^\circ C$)
 E_{el} : electrical energy (kWh)
 E_{th} : thermal energy (kWh)
 G : solar irradiation (W/m^2)
 G_{STC} : solar irradiation at STC (W/m^2)
 G_T : modified solar radiation (W/m^2)
 H : Solar Radiation (kWh/m^2)
 k_θ : Incident Angle Modifier (IAM)

\dot{m}_c : mass flow rate of cooler circuit (kg/s)
 \dot{m}_s : mass flow rate of solar circuit (kg/s)
 P_{nom} : nominal electrical power (kW)
 P_{PV} : electrical power (kW)
 P_{th} : thermal power (kW)
 T_{air} : outdoor temperature ($^\circ C$)
 $T_{c,in}$: water temperature at the inlet of cooling circuit ($^\circ C$)
 $T_{c,out}$: water temperature at the outlet of cooling circuit ($^\circ C$)
 $T_{Mi,in}$: water temperature at the inlet of PV/T module “i” ($^\circ C$)
 $T_{Mi,out}$: water temperature at the outlet of PV/T module “i” ($^\circ C$)
 $T_{Mi,b}$: temperature measured at the back PV/T module “i” ($^\circ C$)
 T_{PV} : temperature of PV cells ($^\circ$)
 T_{ST} : average temperature in the storage solar tank
 $T_{ST,in}$: water temperature at the inlet of storage solar tank ($^\circ C$)
 $T_{ST,out}$: water temperature at the outlet of storage solar tank ($^\circ C$)
 $T_{ST,dw}$: water temperature in the lower part of storage solar tank ($^\circ C$)
 $T_{ST,up}$: water temperature in the upper part of storage solar tank ($^\circ C$)
 Y_A : array yield (Wh/W)
 Y_R : reference yield (Wh/W)

Greek symbols

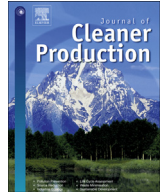
B : tilt angle of the PV/T module ($^\circ$)
 Γ : azimuth angle ($^\circ$)
 ΔT^m : true mean fluid temperature difference ($^\circ C$)
 H : efficiency

Subscript

C: cooling
 el : electrical
 exp : experimental
 i : index of PV/T modules [1, 2]
 s : solar
 sim : simulated
 ST : solar tank
 $Therm$: thermal

Acronyms

DHW: domestic hot water
 EL : electronic load
 PR : Performance Ratio
 $QBTP$: primary panel at low voltage
 $QBTS$: secondary panel board at low voltage electrical board
 $SCADA$: Supervisory Control and Data Acquisition
 STC : Standard Test Condition



Comparative assessments of the performances of PV/T and conventional solar plants



Antonio Gagliano ^{a,*}, Giuseppe M. Tina ^a, Stefano Aneli ^a, Sandro Nižetić ^b

^a DIEEI- Department of Electric, Electronics and Computer Engineering, University of Catania, Viale A. Doria 6, 95125 Catania, Italy

^b LTEF- Laboratory for Thermodynamics and Energy Efficiency, Faculty of Electrical Engineering, Mechanical Engineering and Naval Architecture, University of Split, Rudjera Boskovicica 32, 21000 Split, Croatia

ARTICLE INFO

Article history:

Received 1 October 2018

Received in revised form

22 January 2019

Accepted 4 February 2019

Available online 7 February 2019

Keywords:

Solar energy

Hybrid PV/T plant

Quality of energy

Economic analysis

Renewable energy

TRNSYS simulation

ABSTRACT

The building's energy demand consists of both thermal energy and electricity that may be provided through solar energy sources. Typically, the electrical energy needs are satisfied by photovoltaic plants (PV)s, while the thermal energy needs are satisfied by solar thermal plants (ST)s. However, there is the possibility to produce simultaneously electrical and thermal energy by hybrid photovoltaic/thermal (PV/T) plants.

This study presents the comparison of the performances of a hybrid photovoltaic/thermal (PV/T) plant with those of a systems made by a PV plant plus a ST plant (PV + ST).

Such comparisons are interesting in those buildings where there is not enough available surface for installing both PV and ST plants as much as necessary for satisfying the energy needs of such buildings (e.g. in residential tower buildings).

This research is carried out having as target a residential unit situated in different geographic areas: Catania (IT), Split (HR) and Freiburg (D).

The outcomes of the energy analysis, calculated following the first and the second thermodynamic law approach, highlight that a PV/T plant produces more energy than a conventional solar system (PV-ST) in the three cities. Otherwise, the results of the economic analysis show that the PV plants allow to achieve the most economic benefits due to the cheaper cost of this technology.

© 2019 Elsevier Ltd. All rights reserved.

1. Introduction

To achieve the target of zero net energy building (nZEB) (European Parliament, 2010), the energy needs, in the new buildings, have to be fulfilled as much as possible through renewable energy sources (RES), which have to be installed next to the building boundaries (Marszal et al., 2011).

Since energy needs of buildings concerns heating, cooling, DHW, ventilation, lighting and domestic type appliances, both thermal and electrical energy are necessary.

Photovoltaic systems could satisfy the electric energy demand through and solar thermal systems could satisfy the thermal energy demand. In some circumstances (e.g. multi-story buildings), there is not enough space where install both PV and ST system.

Thereby, the designer has to define a criterion for defining

which, or how many, of these two RES systems should be installed. Conventional photovoltaic modules convert only 10–15% of solar radiation into electricity, while the remaining amount of solar energy is wasted in heat and causes the increase of the operating temperature of the solar cell (Dupeyrat et al., 2014), and consequently the decrease of the efficiency of the PV module. Hybrid photovoltaic thermal systems (PV/T) represent an interesting alternative to PV and ST systems since they allow to produce simultaneously electricity and heat. And also increase the efficiency of electricity production as the surplus of thermal energy is carried out by a cooling fluid (Cabo et al., 2016).

The ability to use this untapped energy is the key point of hybrid systems, which increases the energy yield per unit surface of roof or façade used by a solar plant (Sarhaddi et al., 2010).

Bergene and Løvvik (1995) have developed a transient model and concluded that the water-cooled PV/T can achieve global efficiencies between 60% and 80%. Other studies (He et al., 2006) have shown that for PV/T systems, electrical and thermal performances are significantly reduced when the operating temperature

* Corresponding author.

E-mail address: antonio.gagliano@dieei.unict.it (A. Gagliano).

increases. It is worth noticing that the simultaneous production of heat and electricity has to be analysed starting from the Second Law of Thermodynamics, considering both of energy and exergy balances to get crucial information on the performance of a PV/T system (Tina et al., 2018).

The energy performances and also the cost effectiveness of PV/T systems, as well any RES, are site dependent, as demonstrated by G. Vokas et al (Vokas et al., 2006). for three locations in Greece (Athens, Heraklion and Thessaloniki).

C. Good et al. and Nizetić et al. (Good et al., 2015; Nizetić et al., 2017) studied distinct alternative of solar energy systems through simulations in order to achieve the nZEB ambitions for a single-family building in Norway. They analysed a system with only uncovered PV/T panel, a combination of PV/T and PV and a system with only PV. They have shown that the system that comes closest to achieving the zero net energy balance according to this definition was the that one with only high efficient photovoltaic modules, the second closest was the system with high performant solar thermal collectors and modules PV. However, they pointed out that PV/T covered panel give more energy output than solar thermal collectors.

Although the reduction of efficiency of PV/T plants of is similar to that of PV plants, due to the cells temperature growth, the decrease of efficiency of PV/T can be limited if the cooling fluid has a temperature lower than the temperature of the cells of the conventional PV panels.

The interest in PV/T system of stakeholder as well the scientific community has encouraged the IEA to dedicate Task 60 to this topic (PVT Systems).

However, there is a scarcity of studies, which compare the effectiveness of PV/T plant with those of a conventional plant composed by a solar photovoltaic and a solar thermal plant.

This study concerns the comparison among alternative solar energy systems under constraints that there is a scarcity of space (e.g. residential tower buildings) for installing both PV and ST plants (PV + ST).

In such circumstances, designers have to choose how much surface may be spent for installing a PV plant, for producing electricity, and/or ST plants, for producing thermal energy, (PV + ST). As an alternative, the designer can choose a hybrid PV/T system that produces contemporary both electricity and heating using less space.

The comparison between these two energy generation systems (PV/T and PV + ST) was carried out exploring two scenarios.

The first scenario represents a situation for which the households decide to employ the entire available surface for producing only electrical energy by a conventional PV plant. Therefore, the comparison between the performances of a PV and a PV/T plants is proposed.

The second scenario proposes a circumstance for which the households decide to employ the available surface for generating both thermal and electrical energy. Therefore, the comparison between a PV/T plant and a PV + ST plant, composed of different percentages of the available surface filled with ST and PV modules, is investigated. The TRNSYS simulation software is used for calculating the performances of the different solar plants when they are installed in the cities of Catania (IT), Split (HR) and Freiburg (D).

The energy performance comparison was performed considering both the first and second thermodynamic law for taking into account the different energy quality of electricity and heat. Moreover, an economic analysis of the different energy plants is proposed. Such analysis allows highlighting the consequences of the different cost of energy in the different Countries.

2. Methodology

In this section, the main features of conventional solar plants (solar thermal ST and photovoltaic PV), as well as hybrid systems, are described.

Moreover, the computational model developed in TRNSYS environment, the energy needs and the climatic characteristics in the three cities are described.

2.1. Description of the thermal plants

In this study, the PV/T system and the solar thermal system have the purpose to satisfy a portion of the energy needs for DHW production of a single-family unit.

The plants are equipped with an auxiliary conventional boiler which provides the complementary energy request to satisfy the DHW demand.

Regarding the plant design, both the solar ST and PV/T panels are connected to a solar storage tank through pipes equipped with pump and control units (forced circulation system).

The scheme of the PV/T plant is depicted in Fig. 1.

The upper part of Fig. 1 depicts the electrical section while the lower part depicts the thermal section of the plant.

The panels are hydraulically connected in series. This configuration allows to obtain a higher differential temperature between inlet and outlet water.

The storage tank is a vertical type with a serpentine heat exchanger placed in its lower part for exploiting the thermal stratification. The inlet of cold water (supposed a temperature of 15 °C) is in the bottom and the outlet is in the higher part of the tank so as to supply the heated water at the highest temperature.

When the temperature of the water in the upper part of the tank is lower than the set point temperature of 45 °C, an auxiliary heater provides the energy necessary to heat the water up to this temperature.

The thermal power conveyed into the storage tank depends by the mass flow rate m_s , the fluid specific heat C and the difference of temperature between the inlet and the outlet fluid in the solar panels, which is calculated through eq. (1).

$$P_{sol} = m_s \cdot C \cdot (T_{in} - T_{out}) \quad (1)$$

Thus, thermal efficiency is calculated by equation (2).

$$\eta_{sol} = \frac{P_{sol}}{G_{eff} \cdot A_{abs}} \quad (2)$$

where A_{abs} is the absorber surface and G_{eff} is the useful incident solar irradiation exploitable by the thermal circuit of the PV/T or ST panels.

For ST panels G_{eff} is the incident solar irradiation, while for PV/T panels, it is reduced by the amount of solar energy converted in the PV module into electrical energy.

G_{eff} is calculated by equation (3).

$$G_{eff} = G \cdot (1 - PF \cdot \eta_{el,mod}) \quad (3)$$

Where $\eta_{el,panel}$ is the electrical efficiency of panels and PF is the packing factor defined as the ratio of the total surface of the PV cells to the overall absorber surface.

$$PF = \frac{A_{pV}}{A_{abs}} \quad (4)$$

The energy needs for domestic hot water is calculated by equation (5), while the energy provided by the auxiliary is

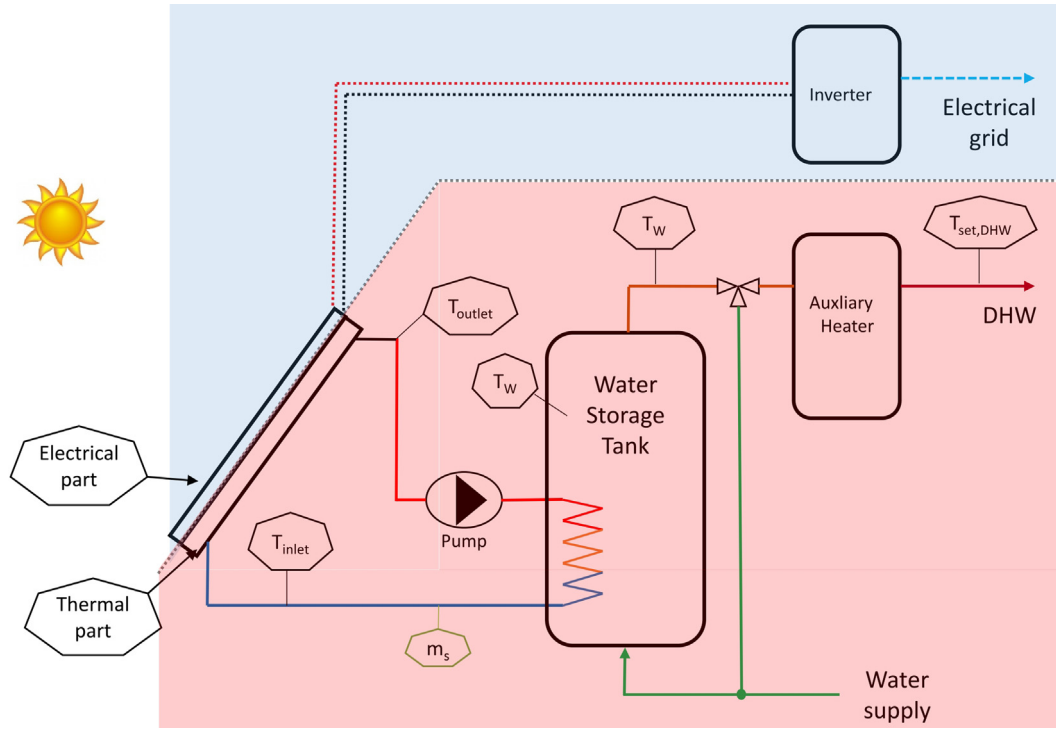


Fig. 1. Scheme of PV/T plant.

calculated by equation (6).

$$E_{DHW} = \int m \cdot C \cdot (45 - T_{cw}) \cdot dt \quad (5)$$

$$E_{aux} = \int m \cdot C \cdot (45 - T_w) \cdot dt \quad (6)$$

where m is the flow rate of DHW required by the user, T_w is the temperature of the outlet water from the storage tank (upper part of tank) and T_{cw} is the temperature of tap water (set equal 15 °C).

The energy saving, E_{th} , provided by the solar system is calculated by equation (7), which allows to assess the “quality” of the thermal energy generated through a solar system:

$$E_{th} = E_{DHW} - E_{aux} \quad (7)$$

The thermal losses in the hydronic components (pipes, solar tank and heat exchanger) are taken into account using such equation.

The effective energy saving therefore represents the actual contribution of the solar thermal system in reducing the energy by fossil fuels necessary for DHW production. In this way.

According to Nualboonrueng et al. (2011), the percentage of the monthly DHW energy demand covered by solar energy, coverage factor f_{DHW} , was calculated using equation (8):

$$f_{DHW} = \frac{E_{DHW} - E_{aux}}{E_{DHW}} \cdot 100 \quad (8)$$

2.2. Description of the photovoltaic plants

As regards the electric production, it was supposed that both the PV and PV/T plants operate at the maximum power point (MPP)

since they are both grid connected.

The electric power $P_{el,mod}$ and $\eta_{el,mod}$ the electrical efficiency of the photovoltaic modules are calculated by equations (9) and (10).

$$P_{el,mod} = G \cdot A \cdot \eta_{el} \quad (9)$$

$$\eta_{el,mod} = \eta_{el,0} \cdot [1 - \beta(T_C - 25)] \quad (10)$$

Where: $\eta_{el,0}$ is the module efficiency at the reference conditions, β is the efficiency loss with temperature (both supplied by the manufacturer) and T_C is the temperature of PV cells described in equation (20).

The efficiency, η_{el} , and the electrical energy, E_{el} , produced by a photovoltaic plant are calculated using respectively equations (11) and (12), where the losses of inverter and array are taken into account.

$$\eta_{el} = \eta_{el,mod} \cdot \eta_{inv} \cdot \eta_l \quad (11)$$

$$E_{el} = \int G \cdot A \cdot \eta_{el} \cdot dt \quad (12)$$

Where: η_{inv} is equal to 0.95 and it is the inverter efficiency and η_l represents the losses in the PV array. This last term depends on several parameters, such as the incident angle, his worth is 0.92 (Tina et al., 2017).

2.3. Thermodynamic analysis

Following a metric based on the first law of thermodynamics, the comparison of the total energy produced $E_T(I)$, and the total efficiency $\eta_T(I)$, of the two systems (PV/T vs PV + ST) can be performed by equations (13) and (14).

$$E_T(I) = E_{el} + E_{th} \quad (13)$$

$$\eta_T(I) = \frac{P_{el} + P_{th}}{G \cdot A_t} \quad (14)$$

Where: A_t is the total surface of the plant, which is the surface of collectors for a PV/T plant and the sum of the surface of ST collectors and PV modules for PV + ST plant.

The efficiency calculated by equation (14) does not take into account the different thermodynamic “quality” of thermal and electrical energy.

Otherwise, the second law of thermodynamic allows considering the more quality electrical energy respect to thermal energy.

For the proper evaluation of the quality of each energy flux, the net energy output of a co-generative system is calculated converting the electrical output into equivalent thermal energy.

Thus, a new efficiency parameter, called primary efficiency (Huang et al., 2001), $\eta_T(II)$, is calculated by equation 15

$$\eta_T(II) = \frac{P_{el}/\eta_{power} + P_{th}}{G \cdot A_t} \quad (15)$$

where η_{power} is the electric power generation efficiency for a conventional power plant. This efficiency assumes different values in each country as a function of its energetic mix.

In the same way, the total primary energy, $E_T(II)$, produced by a co-generative plant (PV/T or PV + ST) is calculated by equation (16). Electricity produced is emphasized dividing it by the power generation efficiency.

$$E_T(II) = \frac{E_{el}}{\eta_{power}} + E_{th} \quad (16)$$

It is also possible to evaluate the primary energy saving E_{PS} , that is calculated from equation (16) introducing the gas boiler efficiency $\eta_{th,b}$, as follows

$$PE_S = \frac{E_{el}}{\eta_{power}} + \frac{E_{DHW} - E_{aux}}{\eta_{th,b}} \quad (17)$$

Finally, the ratio of primary energy reduction is calculated as:

$$PE_R = \frac{PE_S}{PE} \quad (18)$$

Where PE is the primary energy consumptions of the generic user (e.g. residential), due to the electrical ($E_{el,load}$) and the thermal (E_{DHW}) energy demand, defined as

$$PE = \frac{E_{el,load}}{\eta_{power}} + \frac{E_{DHW}}{\eta_{th,b}} \quad (19)$$

2.4. TRNSYS simulations

Several computational tools have been developed for the numerical evaluation of the performance of solar systems. In recent years, one of the most used software for evaluating thermal and electrical performances of solar systems is TRNSYS (Mondol et al., 2005; A Kalogirou and Tripanagnostopoulos, 2006; Quesada et al., 2011; Mondol et al., 2007; Choi et al., 2011).

TRNSYS, that is the acronym of “transient simulation program, was developed by the Solar Energy Laboratory of Wisconsin University (A Klein Beckman et al., 1976).

In the present study, two TRNSYS models were designed to investigate solar systems performances:

- hybrid photovoltaic thermal system;
- separate photovoltaic and solar thermal system

Fig. 2 shows the flow diagram of the projects developed in TRNSYS for the hybrid power generation plant (PV/T). The description of each type can be found in TRNSYS manuals.

2.4.1. PV/T module (TYPE 1 + TYPE 94)

The PV/T module is described using two distinct types (Gagliano et al., 2018), that are the TYPE 1, which models a solar thermal collector, and TYPE 94, which models a photovoltaic module. Thus, the energy yield of the hybrid modules was assessed taking into account the mutual interference between the two systems. Specifically, it was evaluated the effect of the cooling fluid on the temperature of the photovoltaic cell $T_{C,PV/T}$, which is a function of the average temperature of the fluid as well the environmental temperature, by equation (20).

$$T_{C,PV/T} = \frac{\left[\frac{(T_{M,in} + T_{M,out})}{2} + T_a \right]}{2} \quad (20)$$

Thus $T_{C,PV/T}$ is used for calculating the electrical efficiency of the PV/T by equation (10).

Moreover, the effective solar radiation incident on the absorber of the thermal collector, G_{eff} , calculated subtracting from the solar radiation, G , the amount of solar energy converted by the PV effect, calculated through equation (3).

Equation (21) is used for calculating the cell temperature of a conventional PV module (A Klein Beckman et al., 1976).

$$T_{C,PV} = T_a + G \left(\tau\alpha / U_L \right) \left[\left(1 - \left(\eta_{el,0} / \tau\alpha \right) \right) \right] \quad (21)$$

where $\tau\alpha$ represents the module transmittance-absorbance product and U_L is the array thermal loss coefficient.

2.4.2. Solar storage tank (TYPE 60)

The effect of thermal stratification in the solar storage tank is evaluated introducing the coefficient of de-stratification Δk (A Klein Beckman et al., 1976), calculated by equation (22).

$$\Delta k = k_{wall} \frac{A_{c,wall}}{A_{c,water}} \quad (22)$$

where: k_{wall} is the thermal conductivity of the tank wall, $A_{c,wall}$ is the cross section area of tank (including insulation layer) and

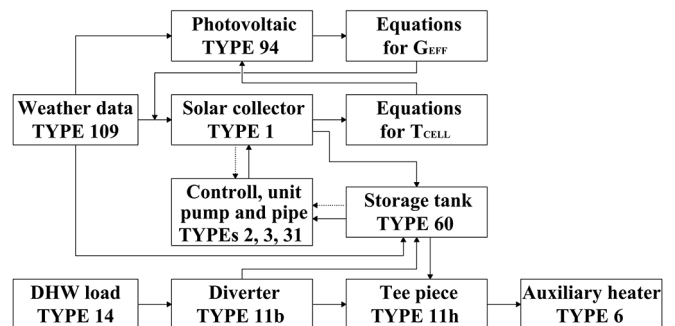


Fig. 2. TRNSYS flow diagram for PV/T system.

$A_{c,water}$ is the cross section area of water inside the tank.

A value of $0.0576 \text{ W}/(\text{m}^2\text{K})$ was calculated for the de-stratification coefficient.

2.4.3. Solar circuit (TYPE 31)

The type 31 allows modelling the pipes that connected the storage tank with solar panels. The heat losses in the pipes of the solar circuit are taken into account through the coefficient of thermal transmission, that is $0.18 \text{ W}/(\text{m}^2\text{K})$, and the piping length, that is 20.0 m.

The flow rate of the solar fluid was set at 50 l/h per square meter of the absorber surface.

2.4.4. Control unit and pump (TYPE 2)

An on/off controller controls the pump ignition, which turns on the pump when the outlet temperature from the panels is 3°C higher than the temperature in the lower part of the storage tank.

2.4.5. Diverter (TYPE 11b)

The diverter set the flow of water, handled by the type 14, in function of the temperature in the solar tank. When the temperature in the upper part of the solar tank is higher than the set point temperature (45°), the diverter mixing the heated water coming from the solar tank with the tap water (set at 15°). Otherwise, the pre-heated water goes to the auxiliary heater where it is heated up to the set point temperature.

2.5. Study specifications

Both systems (separate and hybrid) are oriented to the south with a tilt angle of 25° .

The features of the PV/T module are the same of that one used in the plant installed at the campus of the University of Catania (Gagliano et al., 2018). Tables 1 and 2 summarize the data of the solar modules used in the simulations.

2.5.1. Thermal energy demand

Energy consumption for domestic hot water depends on various factors, on average, the annual domestic hot water consumption in developed countries is around 1000 kWh per person.

The hourly consumption profile for DHW, specified in the standard EN 15,316:2007, depicted in Fig. 3, was used in the simulation.

2.5.2. Electrical energy demand

The electrical energy demand has a wide variation in the EU states. Scandinavian countries have the highest demand for electricity with an average consumption of 5000 kWh/y per inhabitant (Eurostat Statistics Explained, 2016; de Almeida et al., 2011). Otherwise, the countries of the Mediterranean surface have much lower electricity consumption ranging from 2500 to 5000 kWh/y per household.

The annual consumption of 3000 kWh, which is representative of the needs for the less energy intensive European families, was assumed.

Table 1
Data of PV/T and solar thermal panel.

		PV/T	ST
Gross area	m^2	1.66	1.66
Optical efficiency, a_0	%	55.0	82.0
heat loss coefficient, a_1	$\text{W}/\text{K}/\text{m}^2$	15.8	3.18
heat loss coefficient, a_2	$\text{W}/\text{K}^2/\text{m}^2$	0	0

Table 2
Electrical data of PV/T and PV module.

		PV/T and PV
Cell type	–	Monocrystalline
Nominal power, P_{MPP}	W	250
Module efficiency, $\eta_{el,0}$	%	15.4
Rated voltage, V_{MPP}	V	30.7
Rated current, I_{MPP}	A	8.15
Open circuit voltage, V_{OC}	V	38.5
Short circuit current, I_{SC}	A	8.55
Thermal coefficient, V_{OC}	%/K	–0.32
Thermal coefficient, I_{SC}	%/K	0.048
Efficiency loss with temperature, β	%/K	–0.44
Net area, A_{PV}	m^2	1.58

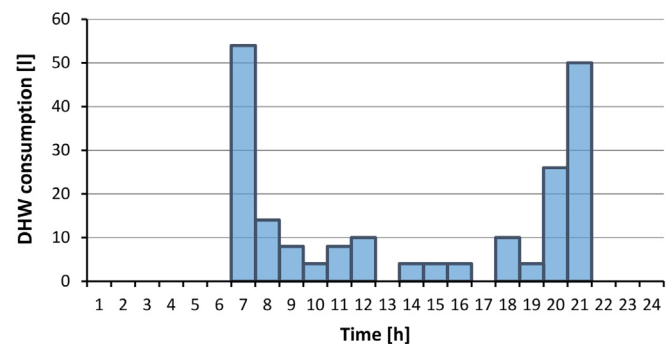


Fig. 3. DHW daily demand profile.

2.5.3. Weather data

This study was conducted in three cities that are: Catania (IT), lat. 37.5° , long. 15.1° ; Split (HR), lat. 43.5° , long. 16.4° ; Freiburg (D), lat. 48.0° , long. 7.8° .

The main weather data of these cities are shown in Figs. 4 and 5 (Meteonorm, 1999). Fig. 4 shows the average monthly irradiation on a tilted south oriented surface (25° of tilt angle).

Fig. 5 shows the average monthly ambient temperatures.

It is evident that Catania is the sunniest and warmest city, while Freiburg is the least sunny and the coolest city among the three cities. Specifically, Catania has total annual irradiation of about $2109 \text{ kWh}/\text{m}^2\text{y}$ and an average temperature of about 18.5°C . The city of Split has annual irradiation of about $1812 \text{ kWh}/\text{m}^2\text{y}$ and an average temperature of about 16.3°C , while in Freiburg the irradiation is about $1296 \text{ kWh}/\text{m}^2\text{y}$ and the average temperature is 10.1°C .

The different climatic conditions of such cities can be also highlighted comparing the heating degree days (HDD) for each

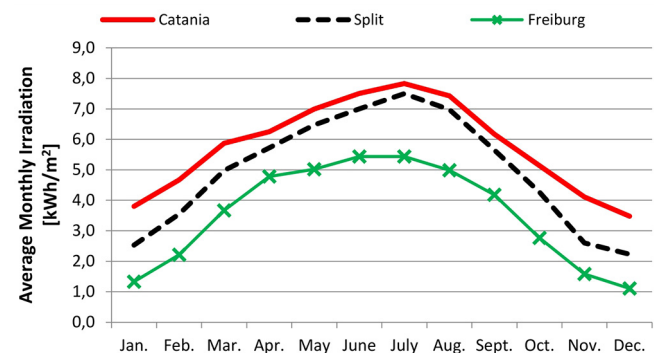


Fig. 4. Average monthly irradiation on a tilted south oriented surface.

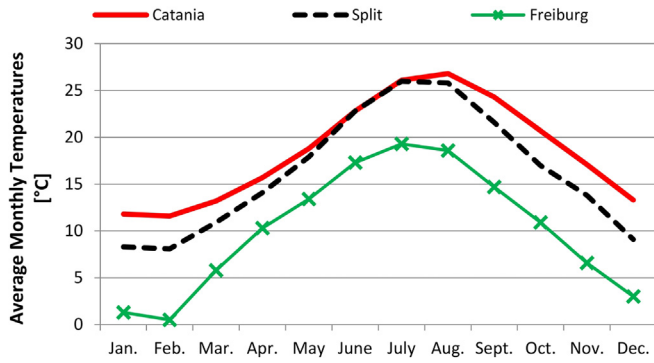


Fig. 5. Average monthly ambient temperatures.

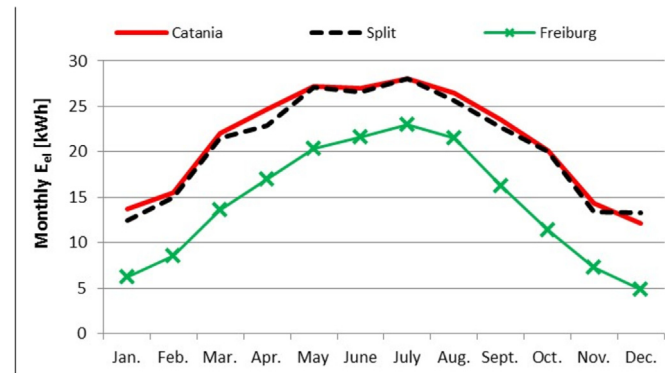


Fig. 7. Monthly electrical energy per square meter of PV plant.

locality (Fig. 6).

It can be noticed that Freiburg's HDD are about two times Split's HDD and almost four times Catania's HDD. The previous data highlight that in Freiburg, due to its cold climate especially during winter season, there is the most critical condition for exploiting solar systems.

2.5.4. Solar plant surface

The design of the solar systems was carried out assuming as reference a household electrical consumption of 3000 kWh/y. Starting from the monthly production of electricity per square meter (Fig. 7) of PV module, the PV surface, necessary for satisfying the above-mentioned household electrical consumption for each city, was determined.

In Catania and Split the PV modules provide almost equal electricity productions all year around, that is of about 250 kWh/m²y. While the electricity production in Freiburg is of about 172 kWh/m²y.

Consequently, the surfaces “ $A_{PV,min}$ ” necessary for producing as much energy as the yearly electrical demands for Catania, Split and Freiburg are: 11.8 m²; 12.1 m² and 17.5 m².

Thus, in function of the characteristics of the used PV modules the number of panels “ N_{panels} ”, the reference surface “ $A_{plant,ref}$ ” and the effective peak power “ $P_{peak,ref}$ ” were defined. Table 3 shows the characteristics of simulated plants.

In Freiburg, $A_{plant,ref}$ for producing 3000 kWh/y is 1.5 times the $A_{plant,ref}$ required in Catania and Split. It is of interest to know the percentage of the electrical demand satisfied by such PV plants when the available surface is lesser than the reference surface previous defined (e.g. a portion of the surface is filled with ST panels).

Fig. 8 shows the percentage of the electrical demand satisfied by the PV plants varying the surface occupied by the PV modules.

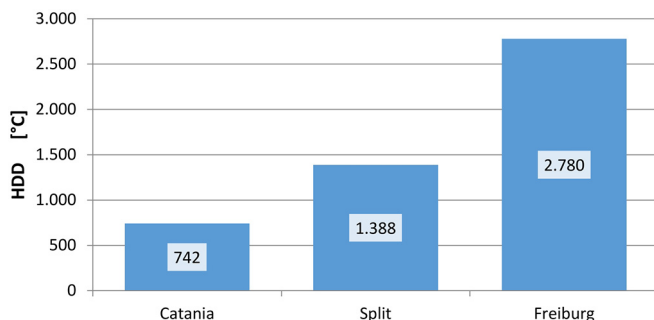


Fig. 6. Heating Degree Days for the analysed cities.

Table 3
Reference characteristic of simulated plants.

		Catania	Split	Freiburg
$A_{PV,min}$	m ²	11.78	12.07	17.47
N_{panel}	–	8	8	12
$A_{plant,ref}$	m ²	12.64	12.64	18.96
$P_{peak,ref}$	kW	2.00	2.00	3.00

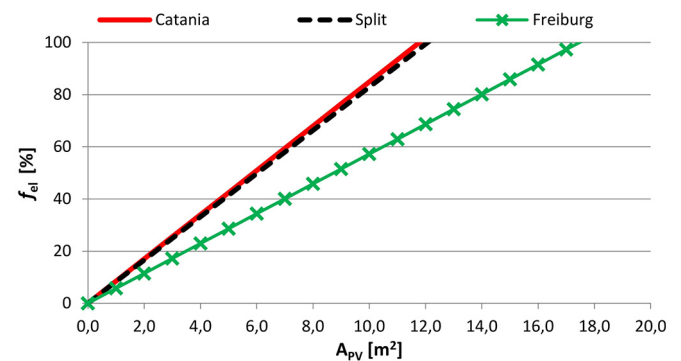


Fig. 8. Electricity demand satisfied by different PV surface.

This graph evidences the reduction of energy production as function of the surface. It is evident the gap of energy generation among the three cities.

3. Results and discussions

The useful thermal energy savings, as well as the electrical energy produced by the two systems, PV + ST and PV/T, were calculated through transitory simulations, in the cities of Catania, Split and Freiburg.

3.1. Scenario 1

3.1.1. Electrical production

Tables 4 and 5 show the monthly electricity production and the monthly efficiency of the PV (Table 4) and PV/T plant (Table 5) installed in Catania (CT), Split (ST) and Freiburg (FR).

In these tables, the last row reports the annual electricity production and the average annual efficiency.

In agreement with the pre-design analysis, the PV plants allow satisfying the annual electrical load of 3000 kWh in the three cities, without significant surplus.

Table 4
Electrical energy and efficiency for PV plants.

	Electrical energy [kWh]			Efficiency [%]		
	Catania	Split	Freiburg	Catania	Split	Freiburg
Jan	173.3	157.1	117.8	13.9	14.2	14.6
Feb	196.6	189.3	162.2	13.7	14.1	14.4
Mar	278.0	271.7	258.5	13.5	13.8	14.1
Apr	312.4	289.5	321.7	13.4	13.5	13.8
May	343.3	342.3	386.5	13.1	13.2	13.6
June	341.1	335.6	409.8	12.9	13.0	13.3
July	354.0	354.6	435.1	12.6	12.7	13.2
Aug	334.1	324.2	407.0	12.6	12.8	13.2
Sept	297.4	287.1	308.7	12.8	13.1	13.5
Oct	254.7	252.7	216.9	13.2	13.4	13.9
Nov	181.6	169.4	137.9	13.6	13.9	14.4
Dec	152.7	167.9	92.7	13.8	14.1	14.5
Year	3219	3142	3255	13.3	13.5	13.9

Table 5
Electrical energy and efficiency for PV/T plants.

	Electrical energy [kWh]			Efficiency [%]		
	Catania	Split	Freiburg	Catania	Split	Freiburg
Jan	183.0	165.1	122.2	14.7	14.9	15.1
Feb	209.1	200.0	168.9	14.6	14.9	15.0
Mar	298.0	289.5	271.7	14.5	14.7	14.8
Apr	336.1	310.1	340.3	14.4	14.5	14.6
May	370.7	368.4	409.0	14.1	14.2	14.4
June	369.4	361.9	437.8	13.9	14.0	14.2
July	384.3	384.3	464.6	13.7	13.8	14.1
Aug	362.8	350.5	433.9	13.7	13.8	14.1
Sept	321.8	309.3	326.3	13.9	14.1	14.3
Oct	273.5	270.2	227.1	14.1	14.3	14.6
Nov	192.5	178.6	142.6	14.4	14.6	14.9
Dec	161.1	176.5	95.7	14.6	14.8	15.0
Year	3462	3364	3440	14.2	14.4	14.6

The electrical efficiency of the PV modules increases going from Catania to Freiburg. This result is due to the difference of air temperature among the three cities, being Catania the hottest and Freiburg the coldest cities.

Table 5 shows the results of energy and electrical efficiency for PV/T plants.

The PV/T plants produce more electricity than conventional PV plants in the three studied cities. In Catania and Split, PV/T plants provide an energy production of about 7% higher than the PV energy production, while in Freiburg an increase of over 5.5% is achieved. The efficiencies of the PV/T module are in average about 1% greater than the PV module efficiency (e.g. in Catania 13.3% vs 14.2).

The best performances of the PV/T plants are strictly related to the lower temperatures of the photovoltaic cells in the PV/T modules. In this regard, Fig. 9 shows the temperatures of the photovoltaic cells during a summer day for the PV and PV/T module, in Catania.

It can be observed a difference of the cell temperatures up to 26 °C between the two modules (Gagliano et al., 2018).

Figures from 10–12 show the monthly electricity production and the efficiencies of the PV and PV/T plants in Catania, Split and Freiburg.

During winter months, PV and PV/T plants have almost equal energy production. Instead, the energy production of PV/T plant is meaningfully higher than the one of the PV plant during the summer months, that is due to the increase of the efficiencies of the PV/T modules when solar radiation and the air temperatures are high.

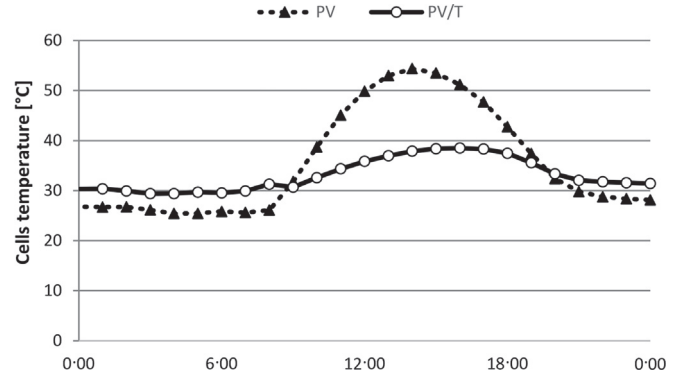


Fig. 9. Temperature of photovoltaic cells on a typical summer day - Catania.

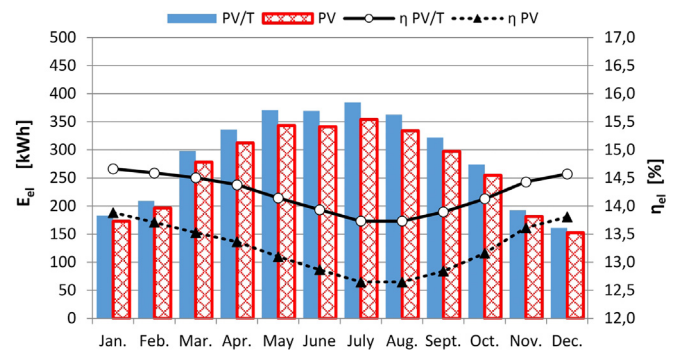


Fig. 10. PV/T and PV monthly electricity production and efficiency in Catania.

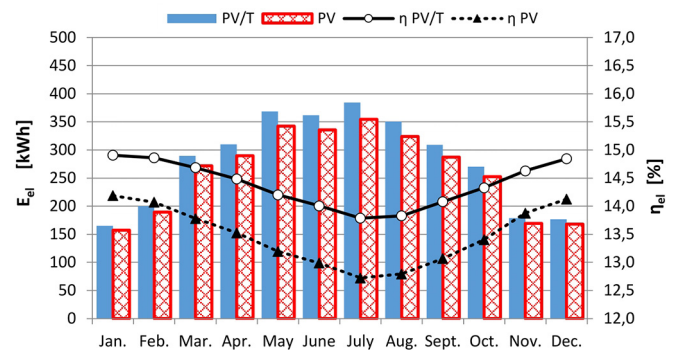


Fig. 11. PV/T and PV monthly electricity production and efficiency in Split.

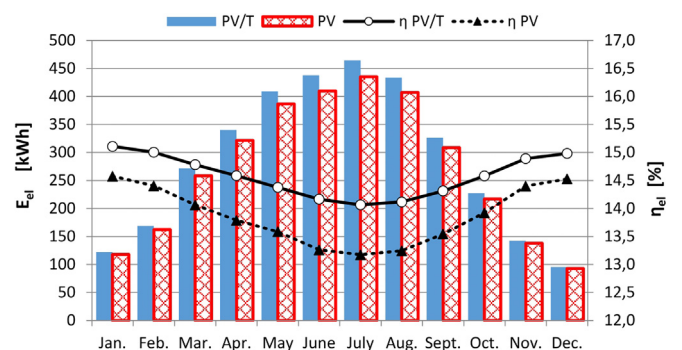


Fig. 12. PV/T and PV monthly electricity production and efficiency in Freiburg.

This result is very useful for PV/T system coupled with an electrical air conditioning system since vapor compressed chillers increase their energy needs in the hottest period.

3.1.2. Thermal energy production

The PV/T plant other than to produce more electricity than PV plant, provide thermal energy that can be used for space heating or DHW production.

Table 6 shows the monthly values of the energy savings, E_{th} , achieved by the PV/T plant and the coverage factor of the demand for DHW (f_{DHW}).

In Catania, the PV/T plant provides more than of 50% of the annual energy demand for DHW, in Split, the f-factor is of about 44% and in Freiburg it is just about 25%. However, during summer months the PV/T plant provides rather the 50% of the energy demand for DHW, also in Freiburg.

This percentage may be increased using PV/T panels with more thermal insulation, which allows reducing the thermal losses during the coldest months.

3.1.3. Total energy production

The energy comparison between PV/T plant and PV plant is based on the total energy production $E_T(I)$.

Fig. 13 shows $E_T(I)$, for the studied cities, it is split into the two contributions electricity E_{el} and thermal energy E_{th} .

The PV/T plants produce 4795 kWh/y in Catania, 4489 kWh/y in Split and 4083 in Freiburg of total energy. The main difference about $E_T(I)$ among the three cities is due to the thermal energy production, which in Catania and Split is almost two times that one produced in Freiburg.

The PV/T plants show evident advantages respect to a conventional PV plant, in fact, $E_T(I)$ of PV/T is greater than about 33.0% and 20.0% in Catania and Freiburg respectively.

However, the previous comparisons do not take into account the different “quality” of thermal and electrical energy. This aspect will be pointed out in paragraph 3.2.

3.2. Scenario 2

In this scenario, the households decide how much surface has to be used for generating both thermal and electrical energy. Therefore, the comparison between a PV/T plant and PV + ST plants, with different proportions of the available surface filled with ST and PV modules, is analyzed. In the PV + ST plant, the surface covered by ST panels varies from 0 to 100%.

The production of electrical energy, the thermal energy saving as well as the efficiencies of the different solar plants are calculated

Table 6 Useful thermal energy and f-factor for PV/T plant.

	E_{th} [kWh]			f_{DHW} [%]		
	Catania	Split	Freiburg	Catania	Split	Freiburg
Jan	47.3	21.1	0.0	21.9	9.8	0.0
Feb	56.5	33.2	0.0	28.9	17.0	0.0
Mar	84.8	64.1	25.0	39.2	29.6	11.5
Apr	102.9	85.1	54.6	49.2	40.7	26.1
May	133.0	124.4	86.0	61.5	57.5	39.8
June	153.0	143.1	104.9	73.1	68.4	50.1
July	180.3	172.0	125.1	83.4	79.5	57.8
Aug	176.6	166.3	121.0	81.7	76.9	55.9
Sept	153.1	133.3	82.2	73.1	63.7	39.3
Oct	122.7	100.7	42.5	56.7	46.6	19.6
Nov	73.6	50.3	1.5	35.2	24.0	0.7
Dec	49.2	31.1	0.0	22.8	14.4	0.0
Year	1333	1125	643	52.2	44.0	25.1

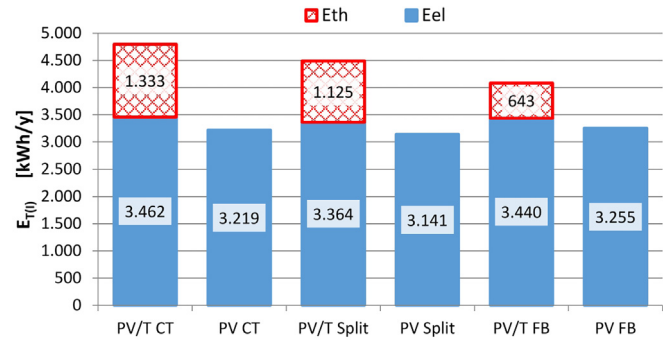


Fig. 13. PV/T and PV yearly energy production plants.

following the metrics of the first and the second law of thermodynamics (eqs. (14) and (15)).

3.2.1. Solar systems installed in Catania

Fig. 14 shows the yearly energy generated by the different configurations of the PV + ST plants and by the PV/T plant.

The 80%PV+20% ST plants produce the maximum $E_T(I)$, that is 4385 kWh/y. The PV/T plant produces 4795 kWh/y, which is greater than the total energy produced by any other PV + ST configurations (10% more than the 80% PV+20% ST).

Fig. 15 shows, the total energy, $E_T(II)$, calculated in accordance to the second law of thermodynamics (eq. (16)), and the primary energy reduction PE_R (eq. (19)). The electricity power generation efficiencies η_{power} and $\eta_{th,b}$, in eqs. (16) and (19), are respectively, 0.46 and 0.85 (UNI TS 11300-2, 2008).

The configuration 90%PV+10%ST plant provides the maximum of $E_T(II)$. Thereby, adopting the metric of the second thermodynamic principle a different result is obtained.

The PV/T plant achieves the best performances both in terms of $E_T(II)$ and of primary energy reduction PE_R (about 95%) respect to any PV + ST configurations (about 80% with 80% PV + 20% ST).

The increase of the surface of ST panels dramatically reduces both $E_T(II)$ and PE_R (about 30% with 100% ST).

Fig. 16 compares the efficiencies $\eta_T(I)$ and $\eta_T(II)$ of the PV-ST and PV/T plants.

The PV/T plant achieves efficiencies $\eta_T(I)$ and $\eta_T(II)$ of 19.6% of 36.2%, that are greater than the maximum efficiencies achievable by any configuration of the PV + ST plants, which are $\eta_T(I)$ of 17.9% and $\eta_T(II)$ of 30.8%.

For the same PV + ST configuration, $\eta_T(II)$ are always greater than $\eta_T(I)$ as the second principle overestimated, through the η_{power} coefficient, the electrical energy generated by the PV module.

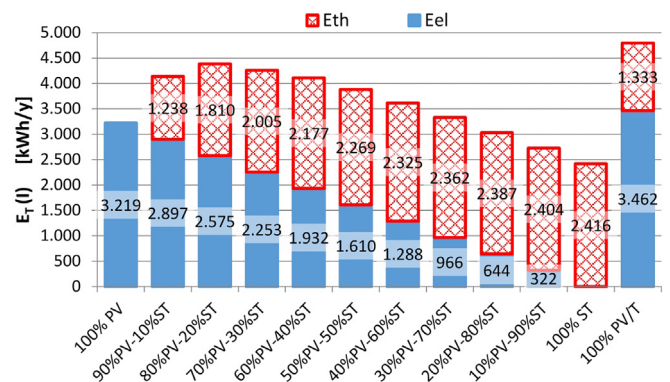


Fig. 14. Yearly electrical energy production and thermal energy saving.

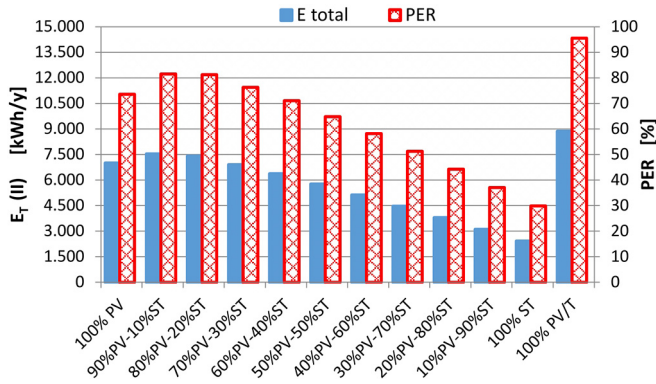


Fig. 15. Total energy $E_T(II)$ and primary energy reduction PE_R .

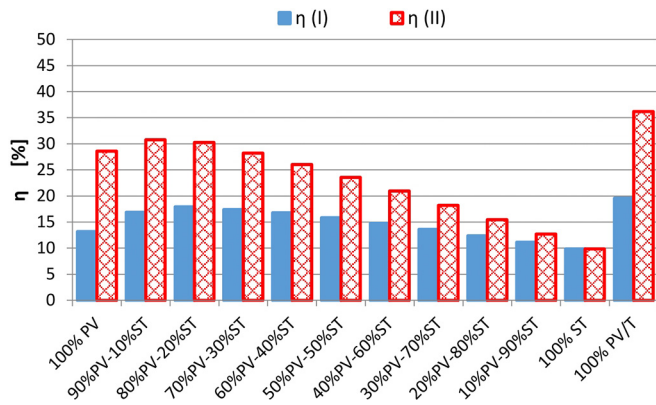


Fig. 16. First and Second laws efficiencies.

The efficiency $\eta_T(II)$ decreases sharply with the rise of the surface filled with ST panels, which provide less treasured thermal energy.

3.2.2. Solar systems installed in Split

Fig. 17 shows the annual energy produced by the different configurations of the PV + ST plants and by the PV/T plant.

The electrical energy production and thermal energy saving are rather similar to that one observed in Catania.

Once again, the 80%PV+20% ST plants produce the maximum of $E_T(I)$, that is 4201 kWh/y. The PV/T plant energy production, that is 4489 kWh/y, is at least 10% greater than the total energy produced by any other configurations of PV + ST plants.

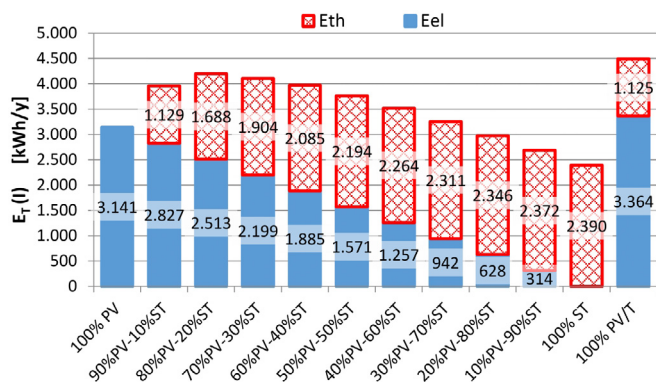


Fig. 17. Yearly electrical energy production and thermal energy saving.

Fig. 18 depicts the total energy $E_T(II)$ and the primary energy reduction PE_R . It has to be highlighted that electric power generation efficiency η_{power} and $\eta_{th,b}$ are respectively, 0.36 and 0.85 (Enerdata., 2016) in Split. Fig. 19 shows the first and second laws efficiencies.

It is confirmed that the 90%PV+10%ST plants provide the maximum of $E_T(II)$, (9000 kWh/y, that is about 15% lesser than the energy produced by PV/T plant (10,500 kWh/y).

In comparison with the results obtained in Catania, substantial differences were found as regards the reduction of the needs of primary energy PE_R . In fact, the 90%PV+10% ST plant allows attaining a PE_R of about 91% in Split and of about 80% in Catania.

This difference is due to the values of η_{power} , which is lower in Split than in Catania. Consequently, in Split, there is a more accentuate valorization of electrical energy respect to thermal energy, which reduces the difference of performance between PV/T and PV-ST plants.

The PV/T plant obtains the maximum performances with efficiencies of $\eta_T(I)$ and $\eta_T(II)$ of 19.1% and of 44.4% respectively. Otherwise, the efficiencies $\eta_T(I)$ and $\eta_T(II)$ of the PV + ST plants do not exceed 17.8 and 38.1%.

Thus, also in terms of efficiencies, small values of η_{power} reduces the gap between the PV/T and the PV + ST systems.

3.2.3. Solar systems installed in Freiburg

Fig. 20 shows the annual energy produced by the different configurations of the PV + ST plants and by the PV/T plant.

The $E_T(I)$ produced by the PV/T plant is 4058 kWh/y, that is greater than the one produced by any other PV + ST configuration. Also in Freiburg, the 80%PV+20%-ST configuration produces the maximum $E_T(I)$ that is 3799 kWh/y. However, a very slight decreasing in the total energy occurs when the ST surface varies from 10% to 30%.

The $E_T(II)$ and the primary energy reduction are shown in Fig. 21. It has to be underlined that in this case, the coefficient η_{power} is 0.385 (Molenbroek et al., 2011).

The 90%PV+90%ST plant provide the maximum of $E_T(II)$, that is 8450 kWh/y, also in Freiburg.

The PV/T plant produces 9553 kWh/y, which is 10% greater than the energy produced by the configuration 90%PV+10%ST plant. Moreover, the PV/T plant allows achieving a PE_R of about 90%, whereas the maximum PE_R of the PV + ST plants is of 80%.

This result is the same as the one found in Catania, although η_{power} is quite different. In fact, the cold climate of Freiburg penalizes the performances of the ST collectors and, consequently does not allow reaching a great reduction of ΔE_p .

Fig. 22 compares the efficiencies $\eta_T(I)$ and $\eta_T(II)$ of the PV-ST and PV/T plants.

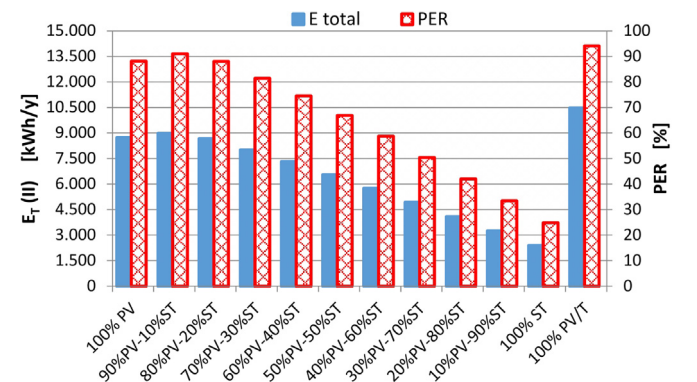


Fig. 18. Total energy $E_T(II)$ and primary energy reduction.

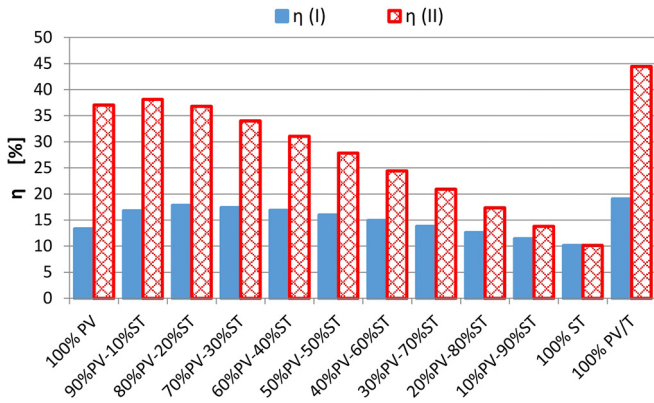


Fig. 19. First and Second laws efficiencies.

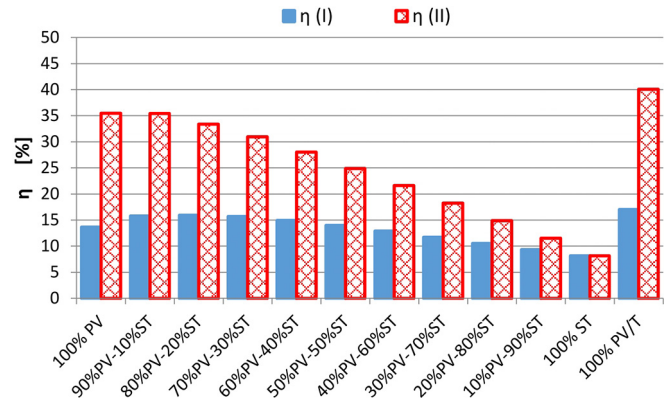


Fig. 22. First and second laws efficiencies.

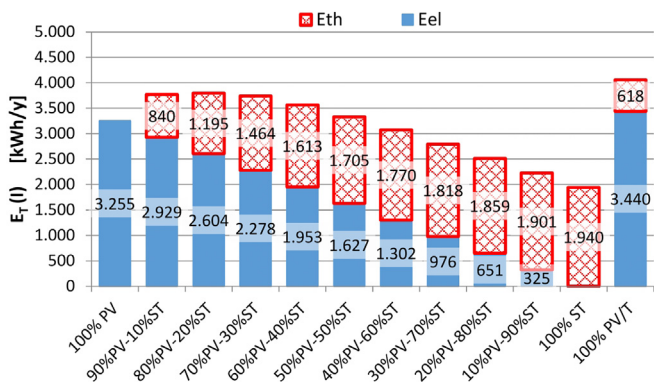


Fig. 20. Yearly electrical energy production and thermal energy saving.

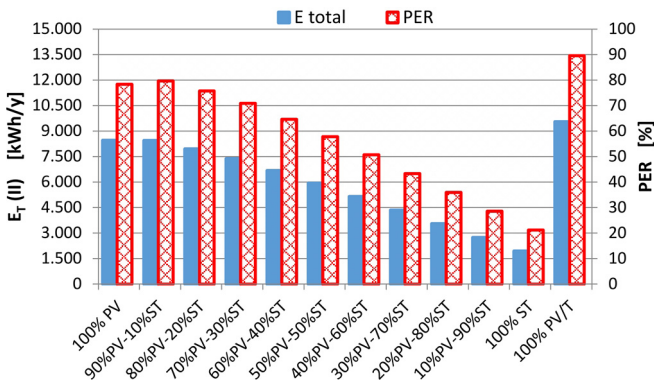


Fig. 21. Total energy $E_T(II)$ and primary energy reduction.

The PV/T plant has the best performances achieving first and second law efficiency of 17.0 and 40.1% respectively. Otherwise, the efficiencies $\eta_T(I)$ and $\eta_T(II)$ of the PV + ST plants do not exceed 15.9 and 35.4%

4. Economics analysis

An economic analysis was developed for the considered solar plants starting from the electricity and natural gas prices in the three cities analysed. It is worth noticing how across the EU Member States the electricity price ranges from 0.12 €/kWh to 0.30 €/kWh, whereas the gas price ranges from 0.036 €/kWh to 0.07 €/kWh (Eurostat, 2017). Table 7 shows the electricity and gas prices

per kWh for the cities analysed (Eurostat, 2017).

The annual money savings, R_y , as well as their discounted sum, R (revenues), achievable by the solar plants are calculated using equations (23) and (24)

$$R_y = E_{el} \cdot Price_{el} + \frac{E_{DHW} - E_{aux}}{\eta_{th,b}} Price_{fuel} \quad (23)$$

$$R = \sum_{i=1}^n R_y \frac{(q^n - 1)}{r \cdot q^n} \quad (24)$$

where r is the capitalization rate which was set at 3%, and n is the life cycle assumed to be 20 years, and $q = 1 + r$. This analysis does not take in account governmental incentives.

Table 8 shows the costs of construction of the different components that constitute the solar plants (De Keizer, 2018), as well the total cost (C_c).

The total costs in Freiburg are higher since the solar plants have about 1.5 times the surface used in Catania and Split. The PV/T plants are the more expensive plants, whereas the 100% PV system is the cheapest one.

Figs. 23–25 show respectively, for Catania, Split and Freiburg, the variable C_c and R , versus the different combination of PV + ST plants. The last entry in each graph is the case of the PV/T plant.

The PV/T plant has positive difference between revenues and cost of construction in Catania and Freiburg, whereas in Split this difference is negative.

The configurations constituted by only PV allow to achieve the

Table 7 Prices of energy.

		Catania	Split	Freiburg
Prices elect.	€/kWh	0.214	0.120	0.305
Prices fuel	€/kWh	0.070	0.036	0.061

Table 8 Cost of the system components.

		PV/T	PV	ST
Panels, structure.	€/m ²	300	120	220
Inverter, cable	€/m ²	100	100	–
Hydraulic circuit	€/m ²	100	–	100
Solar tank	€/l	10	–	10
Assembly	€	1000	1000	1000
Total costs (Catania and Split)	€	8320	3780	6000
Total costs (Freiburg)	€	11,480	5670	8000

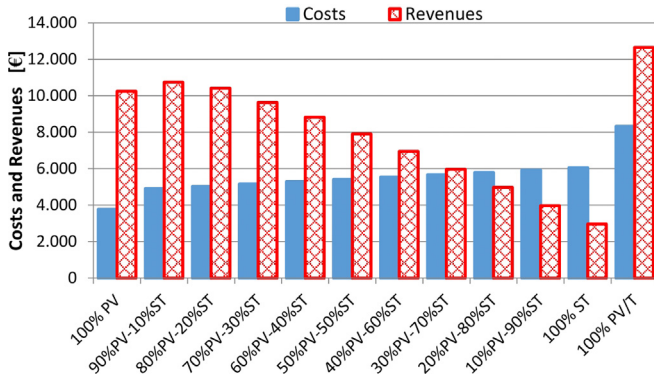


Fig. 23. Costs and revenues in Catania.

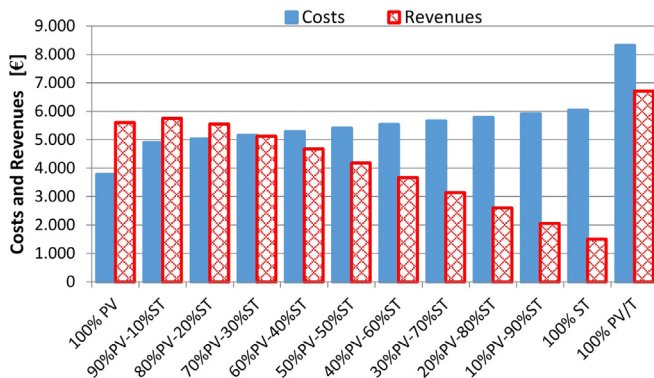


Fig. 24. Costs and revenues in Split.

biggest differences between C_c and R . In all the cities examined, the PV + ST plants reduce their economic effectiveness when the percentages of ST increase.

As an example, the PV + ST plants provide better economic benefits than PV/T until the PV percentage is higher than 70%, in Catania.

This analysis highlights that the low-cost of the PV plant and the costly of electricity are the factors that mainly affects the return of the investments, under the terms of this study.

However, it has to be underlined that the PV/T plants achieve economic benefits not only in Catania but also in Freiburg, even though its cold climate.

In Split, the negative economic performances of the PV/T plants are due to the cheap cost of the energy that does not allow

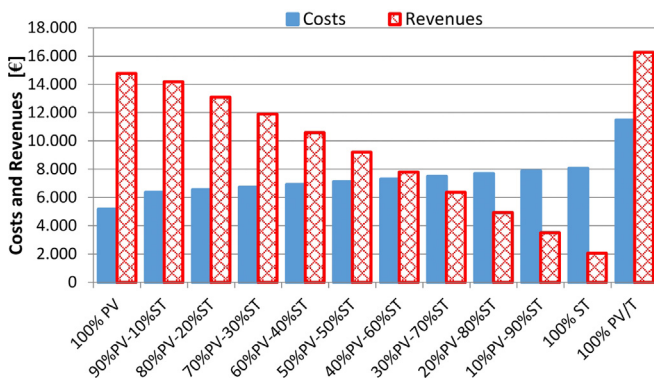


Fig. 25. Costs and revenues in Freiburg.

recovering the money of the greatest investment requested for the PV/T plant.

Surprisingly enough the economic investment of both solar systems, in particular, the PV plant, provide economic benefits in Freiburg better than in Catania.

Thus, countries that have strong economies draw the highest advantages in exploiting renewable energy sources even if they have not favorable climates for the solar resource.

5. Conclusions

The energy performances of conventional solar plant constituted by both PV modules and solar collectors (PV + ST) and the performance of a solar plant constituted by hybrid solar panels (PV/T) were evaluated in Catania, Split and Freiburg.

The performances of these two typologies of solar plants were calculated using the metric of both the first and second principle of thermodynamics, so also taking into account of the different quality of the thermal and electrical energy.

Two different scenarios were investigated. In the first scenario, the energy performances of a PV/T plant and the one of conventional PV plant were compared; in the second scenario, a PV/T plant and solar plants constituted by different proportions of PV panels and solar collectors (PV + ST) were compared.

The first scenario's results highlight that PV/T plants produce more total energy, " $E_T(I)$ ", than PV systems, of about 33% in Catania and of about 20% in Freiburg.

The second scenario's results highlight the PV/T plants provide more total energy $E_T(I)$ than the best PV + ST configuration (80% PV+20%ST), with an increase of 8.5% and 7.0% in Catania and Freiburg respectively.

The analysis of the second principle points out the PV/T plant has second-law efficiency $\eta_T(II)$, total energy production $E_T(II)$ as well as primary energy reduction EP_R always higher than any PV + ST configuration.

The PV/T plant allows achieving a primary energy reduction of about 95%, in Catania and Split, and an increase of $E_T(II)$ of about 10–15% in the three cities.

The proposed economic analysis highlights that the PV plants realize the biggest economic benefits, thanks to the low-cost of the PV plant and the costly of electricity that are the factors that mainly affects the effectiveness of the investments in solar systems.

However, even though the PV/T plants have the greatest cost of constructions, they allow achieving economic benefits both in Catania and Freiburg.

Otherwise, in Split, the negative economic results are due to the cheap cost of the energy that does not allow recovering the biggest investment requested for installing the PV/T plant.

Thereby, under the current economic scenario, the PV plant maintains a supremacy deriving by their low-cost technology.

However, when both thermal and electrical energy are requested and there is a scarcity of surface where install a solar system, PV/T plants represent a very effective solution that provides better performance than conventional PV + ST plants.

Acknowledgements

This research is funded by "the Notice 12/2017 for financing the Ph.D. regional grant in Sicily" as part of Operational Programme of European Social Funding 2014-2020 (PO FSE 2014–2020). The results also contribute to the work and discussion of IEA SHC Task 60 - PVT systems.

References

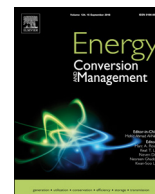
- A Kalogirou, S., Tripanagnostopoulos, Y., 2006. Hybrid PV/T solar systems for domestic hot water and electricity production. *Energy Convers. Manag.* 47, 3368–3382.
- A Klein, S., Beckman, W.A., et al., 1976. TRNSYS - a transient simulation program. ASHRAE 82.
- Bergene, T., Løvvik, O.M., 1995. Model calculations on a flat-plate solar heat collector with integrated solar cells. *Sol. Energy* 55, 453–462.
- Cabo, F.G., Nizetic, S., Tina, G.M., 2016. Photovoltaic panels: a review of the cooling techniques. *Trans. FAMENA* 40, 63–74.
- Choi, Y., Rayl, J., Tammineedi, C., Brownson, J.R.S., 2011. PV Analyst: Coupling ArcGIS with TRNSYS to Assess Distributed Photovoltaic Potential in Urban Areas. *Solar Energy*.
- de Almeida, A., Fonseca, P., Scholmann, B., Feilberg, N., 2011. Characterization of the household electricity consumption in the EU, potential energy savings and specific policy recommendations. *Energy and Buildings* 43, 1884–1894.
- C. De Keizer, Available PVT Products with Focus on the Dutch Market: IEA SHC Task 60 - 1st Experts Meeting & PVT Workshop May 16-18, 2018 - Fraunhofer ISE, Freiburg, Germany.
- Dupeyrat, P., Ménéz, C., Fortuin, S., 2014. Study of the thermal and electrical performances of PVT solar hot water system. *Energy Build.* 68, 751–755.
- Enerdata, 2016. Energy Efficiency Report – Croatia.
- European Parliament, 2010. Directive 2010/31/EU of the European Parliament and of the Council of 19 May 2010 on the Energy Performance of Buildings. Directive 2010/31/EU, Brussels.
- Eurostat, 2017. Household Energy Prices in the EU Down Compared with 2016. Energy prices in 2017, p. 180.
- Eurostat Statistics Explained, 2016. Household consumption of electricity per capita.
- Gagliano, A., Tina, G., Nocera, F., Grasso, A., Aneli, S., 2018. Description and Performance Analysis of a Flexible Photovoltaic/thermal (PV/T) Solar System. Renewable Energy available online. <https://doi.org/10.1016/j.renene.2018.04.057>.
- Good, C., Andresen, I., Hestnes, A.G., 2015. Solar energy for net zero energy buildings – a comparison between solar thermal, PV and photovoltaic–thermal (PV/T) systems. *Sol. Energy* 122, 986–996.
- He, W., Chow, T., Ji, J., Lu, J., Pei, G., Chan, L., 2006. Hybrid photovoltaic and thermal solar collector designed for natural circulation of water. *Appl. Energy* 83, 199–210.
- Huang, B.J., Lin, T.H., Hung, W.C., Sun, F.S., 2001. Performance evaluation of solar photovoltaic/thermal systems. *Sol. Energy* 70, 443–448.
- Marszal, A.J., Heiselberg, P., Bourrelle, J.S., Musall, E., Voss, K., Sartori, I., Napolitano, A., 2011. Zero energy building – a review of definitions and calculation methodologies. *Energy Build.* 43, 971–979.
- Meteonorm, 1999. Solar Engineering Handbook, Part 2, Version 4.0 Theory Part 1: Radiation. Swiss Federal Office of Energy.
- Molenbroek, E., Stricker, E., Boermans, T., 2011. Primary Energy Factors for Electricity in Buildings toward a Flexible Electricity Supply. *ECOFYS*.
- Mondol, J.D., Yohanis, Y.G., Smyth, M., Norton, B., 2005. Long-term validated simulation of a building integrated photovoltaic system. *Sol. Energy* 78, 163–176.
- Mondol, J.D., Yohanis, Y.G., Norton, B., 2007. Comparison of measured and predicted long term performance of grid a connected photovoltaic system. *Energy Convers. Manag.* 48, 1065–1080.
- Nizetic, S., Papadopoulos, A.M., Tina, G.M., Rosa-Clot, M., 2017. Hybrid energy scenarios for residential applications based on the heat pump split air-conditioning units for operation in the Mediterranean climate conditions. *Energy Build.* 140, 110–120.
- Nualboonrueng, T., Tuenpusa, P., Ueda, Y., Akisawa, A., 2011. The performance of PV-T systems for residential application in Bangkok. *Progress in Photovoltaics* 21, 1204–1213.
- PVT Systems: Application of PVT Collectors and New Solutions in HVAC Systems. IEA SHC. task60.iea-shc.org/.
- Quesada, B., Sanchez, C., Canada, J., Royo, R., Paya, J., 2011. Experimental results and simulation with TRNSYS of a 7.2kWp gridconnected photovoltaic system. *Appl. Energy* 88, 1772–1783.
- Sarhaddi, F., Farahat, S., Ajam, H., Behzadmehr, A., Mahdavi Adeli, M., 2010. An improved thermal and electrical model for a solar photovoltaic thermal (PV/T) air collector. *Appl. Energy* 87, 2328–2339.
- Tina, G.M., Ventura, C., Sera, D., Spataru, S., 2017. Comparative assessment of PV plant performance models considering climate effects. *Electr. Power Compon. Syst.* 45.
- Tina, G.G.M., Grasso, A.D., Gagliano, A., 2018. Monitoring of solar cogenerative PVT power plants: overview and a practical example. *Sustainable Energy Technologies and Assessments* 10, 90–101.
- UNI TS 11300-2, 2008. Prestazioni energetiche degli edifici - Parte2: Determinazione del fabbisogno di energia primaria e dei rendimenti per la climatizzazione invernale e per la produzione di acqua calda sanitaria (2008).
- Vokas, G., Christandonis, N., Skittids, F., 2006. Hybrid photovoltaic-thermal systems for domestic heating and cooling - a theoretical approach. *Sol. Energy* 80, 607–615.

Nomenclature

- A: area of the plant (m^2)
- $A_{plant,ref}$: reference surface of panel (m^2)
- A_{PV} : area of the PV modules (m^2)
- A_{abs} : area of the solar thermal absorber (m^2)
- $A_{c,wall}$: cross section area of tank including insulation layer (m^2)
- $A_{c,water}$: cross section area of water inside the tank (m^2)
- a_0 : ratio between the thermal power produced and a given solar radiation when there are not heat losses
- a_1 : linear coefficient of thermal dispersion (W/m^2K)
- a_2 : quadratic coefficient of thermal dispersion (W/m^2K^2)
- C: specific heat ($kJ/kg^\circ C$)
- E_{aux} : auxiliary energy required for DHW
- E_{DHW} : DHW demand (kWh)
- E_{el} : electrical energy (kWh)
- PE: primary energy consumption (kWh)
- PE_S : primary energy saving (kWh)
- EP_R : rate of primary energy reduction (kWh)
- E_{th} : useful thermal energy (kWh)
- $E_T(I)$: total energy calculated by metric based on first law of thermodynamics (kWh)
- $E_T(II)$: total energy calculated by metric based on second law of thermodynamics (kWh)
- f_{DHW} : percentage of the monthly DHW energy demand covered by solar energy
- G: solar irradiation (W/m^2)
- G_{eff} : solar effective irradiation (W/m^2)
- HDD: heating degree days
- I_{MPP} : rated current (A)
- I_{SC} : short circuit current (A)
- k_{wall} : thermal conductivity of the tank wall
- m: instantaneous flow rate of DHW required (kg/s)
- m_s : mass flow rate of solar circuit (kg/s)
- N_{panel} : number of PV panels
- PF: packing factor
- P_{MPP} : electrical power at MPP (W)
- $P_{Peak,ref}$: effective peak power (kW)
- P_{sol} : thermal power in the panel (kW)
- $Price_{el}$: price of electrical energy ($€/kWh$)
- $Price_{fuel}$: price of thermal energy ($€/kWh$)
- R: money saving during the useful life of plant ($€$)
- R_y : annual money saving ($€$)
- T_a : outdoor temperature ($^\circ C$)
- T_{in} : temperature of the fluid at the inlet of panel ($^\circ C$)
- T_{out} : temperature of the fluid at the outlet of panel ($^\circ C$)
- T_C : temperature of the PV cell ($^\circ C$)
- T_{CW} : temperature of cold water by grid ($^\circ C$)
- T_w : temperature of water at the outlet of solar tank ($^\circ C$)
- U_L : array thermal loss coefficient (W/m^2K)
- V_{MPP} : rated voltage (V)
- V_{OC} : open circuit voltage (V)
- β : efficiency loss with temperature
- Δk : de-stratification coefficient (W/m^2K)
- η_{sol} : thermal efficiency of the panel
- η_{el} : electrical efficiency of the PV or PV/T plant
- $\eta_{el,mod}$: electrical efficiency of the PV module
- $\eta_{el,0}$: module efficiency at the reference conditions
- η_{inv} : efficiency of the inverter
- η : efficiency of array
- $\eta_T(I)$: efficiency calculated by metric based on first law of thermodynamics (kWh)
- $\eta_T(II)$: efficiency calculated by metric based on second law of thermodynamics (kWh)
- η_{power} : national electricity power generation efficiency
- $\eta_{th,b}$: efficiency of gas boiler
- $\tau\alpha$: module transmittance-absorptance product

Acronyms

- DHW: domestic hot water
- MPP: maximum power point
- PV-ST: plant constituted by photovoltaic panel and solar thermal panel
- ST: solar thermal



Numerical model and experimental validation of the electrical and thermal performances of photovoltaic/thermal plant

C. El Fouas^a, B. Hajji^a, A. Gagliano^{b,*}, G.M. Tina^b, S. Aneli^b

^a *Laboratory of Renewable Energy, Embedded System and Information Processing, National School of Applied Sciences, Mohammed First University, Oujda, Morocco*

^b *Department of Electric, Electronics and Computer Engineering, University of Catania, Catania, Italy*

ARTICLE INFO

Keywords:

Photovoltaic-thermal technology
Pilot plant
Numerical model
Thermal energy
Electrical energy
Energy performance

ABSTRACT

The technology of photovoltaic-thermal solar collectors offers an attractive option for the simultaneous production of electrical and thermal energies. This technology finds interesting applications in the fields of desalination, sensitive heating/cooling and other related industrial processes. In this paper, we study the performance of a photovoltaic-thermal solar power plant operating in a Mediterranean city (Catania, Italy). A novel numerical model for a solar plant, constituted by uncovered photovoltaic-thermal solar collectors, the hydronic and electric circuits, and thermal solar tank, is presented and validated with experimental data. The developed model, based on energy balance equations for each Photovoltaic-Thermal Solar plant component, allows determining the state and dynamic behaviour of the system. The set of equations attained is resolved via the Runge-Kutta (RK4) numerical method in MATLAB software. Moreover, the built model allows considering the effects of solar radiation, outdoor temperature, wind velocity, the temperature in the thermal storage, flow rate and features of the photovoltaic-thermal solar panel, on the electrical and thermal energy production. The performances of the photovoltaic-thermal solar power plant have been evaluated and analysed. In particular, hourly temperatures achieved in the solar tank as well as the voltage in open circuit condition are calculated and compared with the observed experimental data.

Furthermore, such analysis highlights a very good correlation between experimental and simulated results with a coefficient of determination higher than 0.96 and a root mean square error lower than 7%. During the period of survey, the investigated Photovoltaic-Thermal Solar plant provide an average daily energy production of 0.83 kWh/m² of electrical energy and 0.53 kWh/m² of thermal energy.

1. Introduction

In the last decades, there is a significant and continuing desire to diversify and decarbonize the energy supply, since this means a reduction of the emissions associated with fossil fuel that leads to wider environmental and health concerns.

Photovoltaic technology is one of the most widely used renewable power sources all around the world. Currently, the increase of PV installations has been remarkable (globally about 402.5 GW in 2017, especially in China, and in the USA [1], which are the countries that lead the ranking of installed PV capacity with 131.0 and 51.0 GW respectively).

As it is widely known, PV solar technology converts into electricity only a limited percentage of primary energy (i.e. solar radiation), from 6.0 to 25.0% for typical commercial PV solar cell at reference testing conditions [2], whereas there is large industrial research to improve

such efficiency. The PV cell efficiency degrades in conjunction with rising temperatures, especially for c-Si PV technologies [3].

The increase of the PV cell temperature is mainly related with the local climate, wind speed, the ambient temperature, and solar radiation so countries characterized by the hottest climate conditions experience an evident reduction of the yearly electricity production [4].

To keep low the PV module temperatures different active and passive cooling solutions have been proposed [5]. One growing solution for maintaining low PV cell temperature is represented by hybrid Photovoltaic/Thermal (PV/T) technology, which allow to take advantages of the thermal energy wasted by the PV modules [6]. This active cooling system represents a very interesting and flexible solution that allows to simultaneously generate electric and thermal energy from solar radiation.

Many studies are proposed in literature for evaluating the performance of PV/T plants in different context. Gagliano et al. [7] compared the performances of PV/T and conventional solar plants having as

* Corresponding author.

E-mail address: antonio.gagliano@dieei.unict.it (A. Gagliano).

Nomenclature

A	area [m ²]
CC	specific heat [kJ/kg °C]
E_e	electrical energy [Wh]
E_{th}	thermal energy [Wh]
E_T	overall energy [Wh]
$E_{(II)}$	overall primary energy [Wh]
E_T	overall energy [Wh]
$F_{j,k}$	view factor between layer j and k
G	solar irradiance [W/m ²]
Gr	Grashof number
G_{STC}	irradiance at the STC conditions
$hc_{j,k}$	conductive heat transfer coefficient between layer j and k [W/m ² K]
$hr_{j,k}$	radiative heat transfer coefficient between layers i and j [W/m ² K]
$hv_{i,j}$	convective heat transfer coefficient between layer j and k [W/m ² K]
L	Length [m]
m_i	measured value
\bar{m}	mean of measured values
\dot{m}	mass flow rate [kg/s]
\dot{m}_l	mass flow rate of thermal load [kg/s]
Nu	Nusselt number
PC	percentage of collector occupy by channel
P_e	electrical power [W]
PF	packing factor
P_{peak}	peak power
Pr	Prandlt number
PR	performance ratio
P_{th}	thermal power [W]
Ra	Rayleigh number
Re	Reynolds number
s_i	simulated value
S_t	external surface of the tank [m ²]
STC	standard test conditions
t	time step [s]
T	temperature [°C]
T_a	outdoor temperature [°C]
$T_{c,in}$	temp. of fluid at inlet of PV/T panels [°C]
$T_{c,out}$	temp. of fluid at outlet of PV/T panels [°C]
T_f	average fluid temperature inside of PV/T panels [°C]
T_{sup}	temperature of water from the mains [°C]
T_t	average tank temperature [°C]
$T_{t,in}$	temp. of the fluid at inlet of tank [°C]
$T_{t,out}$	temp. of the fluid at outlet of tank [°C]
U_t	overall heat losses of tank [W/m ² K]
V	voltage [V]
V_{OC}	open circuit voltage [V]

w	wind speed [m/s]
w_{bc}	wind speed at the back of PV/T [m/s] WISC Wind and/or Infrared Sensitive Collec.

Scripts

a	ambient
abs	absorber plate
$absh$	high absorber plate
$absl$	low absorber plate
c	conductive
f	fluid
$forced$	forced convection regime
$free$	natural convection
g	glass
gr	ground
in	inlet
$incoming$	incoming heat flux
$mixed$	mixed convection regime
oc	open circuit
out	outlet
$outcoming$	outcoming thermal flux
PV/T	photovoltaic/thermal panel
PV	photovoltaic cells
r	radiative
sky	sky
t	tank
Ted	Tedlar
v	convective

Greek symbol

α	absorptivity
β	temperature coefficient for efficiency
β_V	temperature coefficient for voltage
δ	thickness [m]
ε	emissivity
ε_H	effectiveness of heat exchanger
η_e	PV efficiency
η_{ref}	reference efficiency
η_{power}	national efficiency for electric products
η_{th}	thermal efficiency [%]
η_T	overall efficiency [%]
$\eta_{(II)}$	primary efficiency [%]
θ	tilt angle
P	density [kg/m ³]
Λ	conductivity [W/m K]
Σ	Stefan-Boltzmann constant
T	transmissivity

target a residential unit situated in different geographic areas Catania (IT), Split (HR) and Freiburg (DE). This study evidences that a PV/T plant produces more energy than a conventional PV plant in those cities.

Herrando et al. [8] have studied the energetic and economic performance of PV/T used to covering the energy demands of single-family reference households in three European cities, Athens (EL), London (UK) and Zaragoza (ES). The results of this study highlight that these systems are capable of satisfying about 65% of electricity needs and between 30% and 60% of thermal needs.

Kalogirou et al [9] performed a TRNSYS simulation of two PV/T water systems at three different locations: Nicosia, Athens and Madison. The PV/T systems considered are based on pc-Si and a-Si PV modules,

with thermosiphon and active system for domestic hot water applications. As well a test of the developed model was performed based on the prototype at the University of Patras, Greece. The results show a meaningful increase on the thermal and electrical production.

Bianchini et al [10] presented an extensive monitoring activities performed on PV/T solar power plant at HEnergy research centre in Forlì, Italy. They also evaluated the PV/T offered potential in Central, Italy. They observed that the electricity and heat generation are respectively 835 kWh/m² and 1600 kWh/m², for a mean operative temperature of 40 °C. From the economical assesment, they found that the PV/T solar plant reached an investment cost vary among 3700–4700 €/kWp.

Bahaidarah [11] reported the effectiveness of water PV/T system

used in the hot climate region of Dhahran, Saudi Arabia. Results proved that PV temperatures reduced by 20.0% using a water-cooling system and PV efficiency is increased by 9.0%.

A wide investigation on real applications of Energy Systems with Photovoltaic-Thermal Solar Collectors can be found in the study commissioned by Swiss Energy [12].

Calise et al [13] developed a dynamic model for a novel tri-generation PV/T solar system, which provides electricity, thermal energy for domestic hot water and space heating, and cooling energy. The results of this study highlight that the analysed PV/T system represents an interesting option from energetic and economic points of view.

One of the drawbacks of PV/T technology is the mismatch between the electricity generation and hot water demand [14]. For instance, in summer there is a high production of both electricity and thermal energy but usually, there is a low demand for hot water needs [15].

Some applications, however, such as swimming pools [16], air conditioning of sport centre [17] and the desalination process [18], have a good matching between these two types of energy demand.

Therefore, the PV/T technology is evolving in the direction of increasing the enthalpy of the hot fluid with the aim to be suitable for the above mentioned applications (e.g. cooling and desalination). So, with the aim to develop and optimize PV/T systems different technologies are studied. Bombarda et al. [19] tested two insulated and non-insulated roll-bond PV/T design with commercial conventional sheet-and tubes design at SolarTechLAB. They found that with a good insulation PV/T roll-bond can achieve higher thermal performances by 8% than the PV/T sheet-and-tubes. Xiaolin investigated the optimization of the roll-bond collector Sun et al. [20]. This study pointed out as an optimized channel pattern enhances the performance of the roll-bond panel.

Jinshun et al. [21] proved that micro-channel heat pipe, extruded and roll-bond heat exchanger, and cotton wick structure are promising alternative with respect to sheet-and-tube structure. Indeed, they could provide significant enhancement in terms of efficiency, structure, weight, and cost, etc. Moreover, they suggest that the ethylene-vinyl acetate (EVA) based lamination method seems the best option for the integration of PV layer.

However, with the aim to evaluate in precisely the performance of a PV/T system is of crucial importance to evaluate the temperature of the cooling fluid as well as the PV cell temperature.

Many literature studies evaluated the temperatures of the different layers of a PV/T system through mathematical models. Calise et al. [22] developed one-dimensional roll-bond PV/T model based on control volume numerical approach.

Aste et al. [23] proposed a dynamic model for the prediction of roll-bond PV/T system performances in different weather conditions.

Recent studies on mathematical models of a PV/T system are presented in Ref. [24], where a lumped parameter model for PV/T solar collector is developed in TRNSYS.

Nine different designs of combined PV-thermal collectors to obtain a clearer view on the expected yield of the various concepts, were evaluated in Ref. [25].

However, very few researches have investigated the performance of PV/T plants that produce concurrently thermal and electrical energy under real operative conditions. Thus, they do not provide a comprehensive evaluation of the performances of PV/T module/plants in terms of thermal and electrical yield, since they usually do not investigate the electrical behaviour and the interaction between the electrical and thermal operating points.

Moreover, it has to be highlighted that there is a lack of information on the performance of PV/T systems equipped with wind and/or infrared sensitive collectors (WISC) panel operating in central Mediterranean area (Csa Koppen Zone classification).

This paper aims to contribute in this area of research proposing a novel dynamic numerical model, where the modelled system is not merely constituted by a single PV/T module but it considers a string of PV/T modules, the hydronic and electric circuits, as well as the thermal solar tank. Thus the proposed model, calculates not only the temperatures of each layer of the PV/T module, in particular the PV cell temperatures, but also the thermal and electrical yields of the plant. The set of equations that constitute the numerical model, resolved via Runge-Kutta (RK4) numerical method in MATLAB software, are of general application and may be adopted for modelling different PV/T systems that operates under real operative conditions.

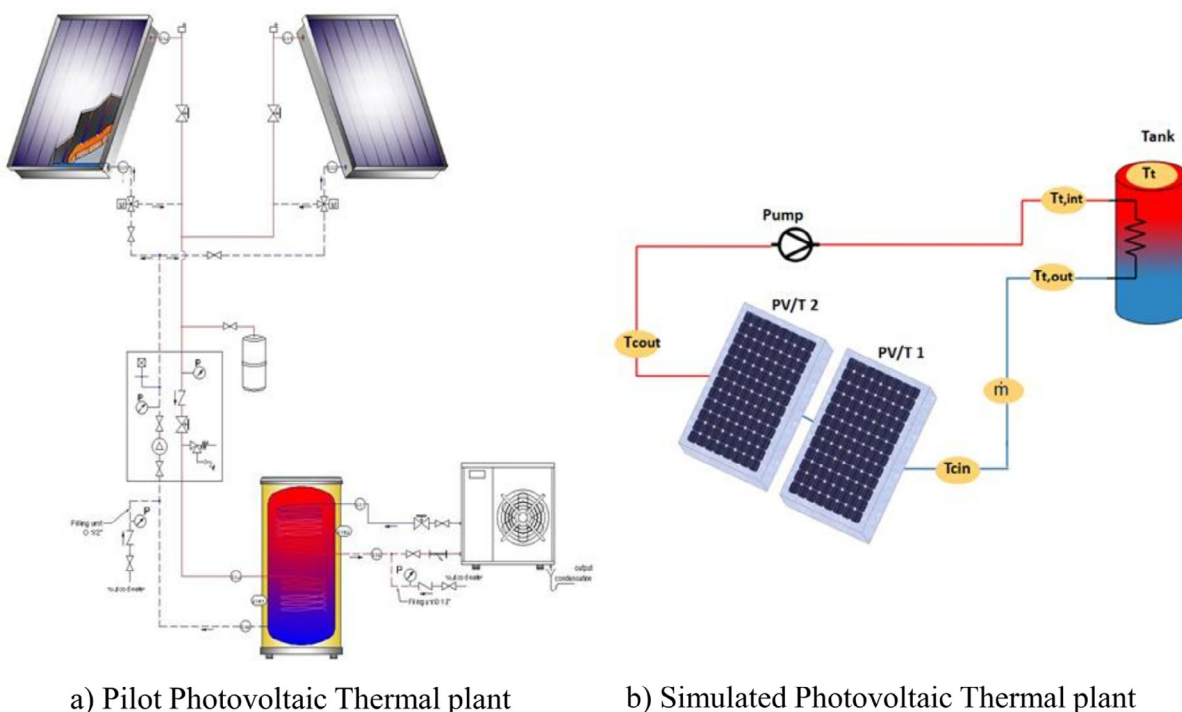


Fig. 1. Descriptive diagram of the PV/T plant components a) real system, b) simulated system.

The model has been experimentally tested using the measurements taken in the pilot plant installed at the University of Catania. Several tests under real meteorological conditions have been carried out in order to evaluate through statistical indicators the precision of the proposed mathematical model

2. Materials and method

The proposed numerical model is based on a pilot PV/T plant, installed on the roof of building 13 of the University Campus of Catania (Lat. 37.5256 N, Long. 15.0746 E), with a tilt angle $\beta = 25^\circ$ and azimuth angle $\gamma = 0^\circ$ (South-facing). The plant is constituted by two commercially WISC panels DUALSUN Wave©, thermal storage tank, pumping circuit, insulated connection pipes (Fig. 1). A more complete description of this pilot plant can be found in Ref. [26].

As shown in Fig. 1, the overall PV/T plant comprises an active closed-loop system in which, in normal operation, the collector outlet flow (flow-rate \dot{m} and temperature $T_{c,out}$) enters in the heat exchanger located inside the hot water solar tank (temperature $T_{t,in} = T_{c,out}$) and heats up the water in the tank (mass M_t and temperature T_t).

Thus, the fluid reduces its temperature ($T_{t,out}$) and returns to the inlet of the PV/T collector (temperature $T_{c,in} = T_{t,out}$) to be heated again.

The thermal energy coming from the solar panels is transferred to the storage tank for producing domestic hot water.

In the Pilot plant, the following variables are measured: inlet and outlet temperatures of the operative fluid (water) at the inlet and outlet of each PV/T module, at the inlet and outlet of the thermal solar tank, at the bottom and the top of the solar tank, as well as the fluid volumetric flowrate, m_s .

The weather station placed close to the PV/T modules allows to measure the global and diffuse solar radiation, wind speed and direction, ambient temperature, humidity and air pressure. All the sensors are connected to the control unit, placed in an external box, which transfers the sensor data to the PC through Ethernet. Data from the PV/T solar plant and local weather station are stored in a dedicated SCADA with 1 min. acquisition rate.

2.1. Photovoltaic/thermal panel

The photovoltaic/thermal (PV/T) panels are uncovered and un-insulated with a roll-bond absorber constituted by two aluminum sheets, joined through a lamination process, where a thin layer of heat transfer fluid is embedded.

The PV/T panel is schematized in the following layers: the front glass, mono-crystalline (c-Si) PV cells, EVA encapsulating film, Tedlar, two aluminum sheet (roll-bond absorber) and the coolant fluid (see Fig. 2).

2.2. Numerical model

Similarly, to previous PV/T literature models [27], in order to calculate the temperatures throughout the solar panel, energy balance equations were made explicit separately in each layer [28]. Such energy balance equations include radiative, convective and conductive thermal exchanges among each PV/T layer (glass cover, PV cells, Tedlar, upper absorber, the cooling thermal fluid, lower absorber), and the environment. The radiative heat fluxes exchanged between the front and the back surface of the panel (respectively glass cover and lower absorber) with the sky and the ground are considered.

The climate parameters included in the model are the air temperature, the wind speed and the solar irradiance on the PV/T panel.

The proposed numerical model has been developed under the following assumptions:

- one dimensional (1D) thermal model is used since the thickness of the module is very thin compared with the other two dimensions, thus heat losses at the sides of the PV/T collector are negligible and each layer has a spatially averaged constant temperature;
- the fraction of solar irradiance that is not converted into electrical power by the PV cells is transferred to the system;
- the optical properties of the glass cover, the PV cells and of the EVA layer are constant;
- the properties of the materials are considered homogeneous and constant, being the limited temperature range;
- perfect bonding between PV/T components is ensured;
- the heat exchange among cells and EVA is negligible;
- no dust or partial shading on the collector;

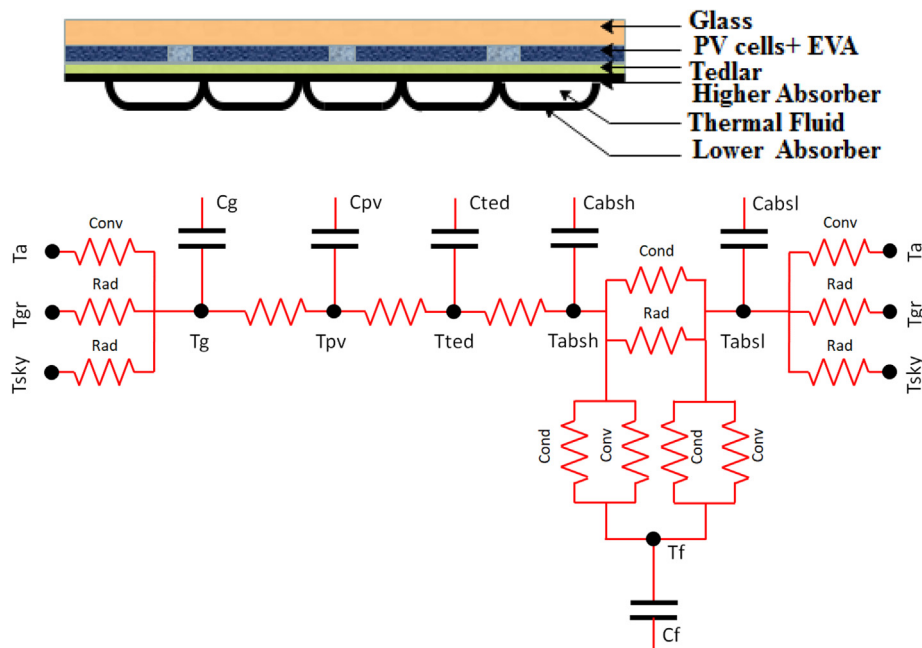


Fig. 2. Cross section and equivalent electrical circuit of the PV/T panel.

- the pipes connecting the PV/T unit with the water storage tank are well insulated, such that there are no heat losses to the environment;
- the water inside the storage tank is fully mixed, that is thermal stratification is neglected

Thus, the energy balance for unsteady state are determined for each i -th layer.

The balance equations, which are detailed in the proceeding sections below, are solved at 1440 daily time steps (time step equal 1 min).

2.2.1. Glass energy balance

The energy balance of the glass is established according to the energy accumulated by the glass, solar irradiance absorbed and energy lost by convection, radiation, and conduction. Respecting to previous assumption, and considering the unitary surface, it becomes:

$$(\rho_g \delta_g C_g) \frac{dT_g}{dt} = \alpha_g G + hr_{g,sky}(T_{sky} - T_g) + hr_{g,gr}(T_{gr} - T_g) + hv_{g,a}(T_a - T_g) + hc_{PV,g} P F(T_{PV} - T_g) + hc_{Ted,g}(1 - PF)(T_{Ted} - T_g) \quad (1)$$

where $\alpha_g G$ is the absorbed solar irradiance by the glass (W/m^2); $hr_{i-1,i+1}$, $hr_{i-1,i}$ and $hc_{i-1,i+1}$ are respectively the radiative, convective and conductive heat transfer coefficients ($W/m^2 K$) occur between the previous ($i - 1$) and next ($i + 1$) layer.

The PV cells do not cover the entire surface of the panel, therefore the packing factor (PF) that is the ratio between the surface covered by the PV cells and the total surface of the panel has been considered. Moreover, since the thermal conductivity and the radiation transmission coefficient of the EVA are very high, this layer was not considered.

The radiative exchange coefficients depend by T_{sky} , T_{gr} and view factors $F_{g,sky}$ and $F_{g,gr}$ as:

$$\begin{cases} hr_{g,sky} = \sigma \varepsilon_g F_{g,sky} A (T_{sky} + T_g) \cdot (T_{sky}^2 + T_g^2) & (2) \\ hr_{g,gr} = \sigma \varepsilon_g F_{g,gr} A (T_{gr} + T_g) \cdot (T_{gr}^2 + T_g^2) & (3) \\ F_{g,sky} = \frac{1 - \cos\theta}{2} & (4) \\ F_{g,gr} = \frac{1 + \cos\theta}{2} & (5) \end{cases}$$

The glass-ambient convective heat transfer coefficient hv is calculated using different expressions depending on the convection regime. The convection has been evaluated forced if $Gr/Re^2 \ll 1$ and free if $Gr/Re^2 \gg 1$. Through Cole correlation [29], in forced convection regime this coefficient is written as:

$$hv_{forced} = 5.7w + 11.4 \quad (6)$$

In natural convection case, the correlation of Bejan is considered [30]:

$$hv_{free} = \frac{Nu_{free} \lambda a}{L} \quad (7)$$

where λa , Nu are respectively thermal conductivity of air and Nusselt number given by:

$$Nu_{free} = 0.14 \left[(GrPr)^{\frac{1}{3}} - (Gr_{cr} Pr)^{\frac{1}{3}} \right] + 0.56 (Gr_{cr} Pr \cos\theta) \quad (8)$$

Otherwise, in mixed convection regime, the correlation [31] is introduced:

$$hv_{mixed} = (hv_{forced}^3 + hv_{free}^3)^{1/3} \quad (9)$$

2.2.2. PV cells energy balance

The second layer is made up of the PV cells. They are affected by solar radiation transmitted through the glass ($\tau_g G$), by the conversion of solar radiation into electrical energy ($\eta_e G$), and by heat transfer by conduction with the adjacent layers.

$$\begin{aligned} PF(\rho_{PV} \delta_{PV} C_{PV}) \frac{dT_{PV}}{dt} \\ = [(\tau_g \alpha_{PV} - \eta_e)G + hc_{PV,g}(T_g - T_{PV}) + hc_{Ted,PV}(T_{Ted} - T_{PV})]PF \end{aligned} \quad (10)$$

2.2.3. Tedlar energy balance

The following thermal balance regards the Tedlar layer. In the upper face, for one part it is in contact with the PV cells and for the remaining part ($1 - PF$) it is considered in contact with the glass, while the underlying face is totally in contact with the aluminum absorber. Therefore, a part of Tedlar is directly affected by the solar radiation that passes through the glass layer (and the empty space among the PV cells).

$$\begin{aligned} (\rho_{Ted} \delta_{Ted} C_{Ted}) \frac{dT_{Ted}}{dt} \\ = (1 - PF)\tau_g \alpha_{Ted} G + (1 - PF)hc_{Ted,g}(T_g - T_{Ted}) + PF \cdot hc_{Ted,PV} \\ (T_{PV} - T_{Ted}) + hc_{absh,Ted}(T_{absh} - T_{Ted}) \end{aligned} \quad (11)$$

2.2.4. Absorber energy balance

The roll-bond absorber is schematized as a channel delimited by two different layers, namely upper ($absh$) and lower absorber layer ($absl$) respectively, where the fluid flows.

For the upper absorbent plate, the energy balance regards the heat transmitted by conduction with the Tedlar layer, the energy exchanged between this plate and the fluid, as well as the heat transfers between the upper plate and the lower plate of the absorber. The interactions between the upper and the lower layer of the absorber are radiative in correspondence of the channels housing the fluid and of the conductive type in the remaining parts.

The ratio between the surface where the fluid flows and the total surface of the absorber is indicated below with PC (percentage of the channel).

$$\begin{aligned} (\rho_{absh} \delta_{absh} C_{absh}) \frac{dT_{absh}}{dt} \\ = hc_{absh,Ted}(T_{Ted} - T_{absh}) + (1 - PC)hc_{absl,absh}(T_{absl} - T_{absh}) + PC \\ \cdot hv_{absl,absh}(T_{absl} - T_{absh}) + hc_{f,absh}(T_f - T_{absh}) \end{aligned} \quad (12)$$

The radiative heat transfer coefficient between the two aluminum plates are calculated according to Ben Cheikh correlation [32]:

$$hr_{absl,absh} = \frac{4\sigma T^3}{\left(\frac{1}{\varepsilon_{abs}} + \frac{1}{\varepsilon_{abs}} - 1\right)} \quad (13)$$

where σ , T , and ε_{abs} are Stefan-Boltzmann constant, mean plate temperature and plate emissivity.

The energy balance related to low absorber plate is performed considering the amount of energy transferred with the fluid, the high absorber plate and the heat exchange with the outside (ground and air):

$$\begin{aligned} (\rho_{absl} \delta_{absl} C_{absl}) \frac{dT_{absl}}{dt} \\ = hc_{absl,f}(T_f - T_{absl}) + (1 - PC)hc_{absl,absh}(T_{absh} - T_{absl}) + PC \cdot hr_{absl,absh} \\ (T_{absh} - T_{absl}) + hv_{a,absl}(T_a - T_{absl}) + hr_{sky,absl}(T_{sky} - T_{absl}) + hr_{gr,absl} \\ (T_{gr} - T_{absl}) \end{aligned} \quad (14)$$

The convective heat transfer coefficient between low absorber plate and ambient is calculated as a function of thermal air conductivity and Nusselt number in case of free convection using [33]:

$$Nu_{free} = \left\{ 0.825 + \frac{0.387Ra^{1/6}}{\left[1 + \left(\frac{0.492}{Pr}\right)^{9/16}\right]^{8/27}} \right\}^2 \quad (15)$$

While in forced convection $h_{v, absl}$, a is expressed by:

$$h_{v_{a,absl}} = 5.7w_{bc} \tag{16}$$

The radiative exchange coefficients depend by T_{sky} , T_{gr} and view factors $F_{sky,absl}$, and $F_{gr,absl}$ as:

$$\left\{ \begin{aligned} hr_{sky,absl} &= \sigma \epsilon_{absl} F_{sky,absl} A (T_{sky} + T_{absl}) \cdot (T_{sky}^2 + T_{absl}^2) \tag{17} \\ hr_{gr,absl} &= \sigma \epsilon_{absl} F_{gr,absl} A (T_{gr} + T_{absl}) \cdot (T_{gr}^2 + T_{absl}^2) \tag{18} \end{aligned} \right.$$

$$F_{sky,absl} = \frac{1 - \cos\theta}{2} \tag{19}$$

$$F_{gr,absl} = \frac{1 + \cos\theta}{2} \tag{20}$$

2.2.5. Fluid energy balance

The heat transfer coefficient between the absorber and fluid flow depends on the nature of the flow condition and the conduction thermal resistance.

In the field of use of the panels and using traditional fluids, the flow condition is always laminar since the Reynolds number is less than 3000.

The fluid inside the absorber has a thickness of 1.5 mm, consequently the contribution of convection is negligible and the thermal flux in mainly driven by conduction.

The heat exchange between the coolant fluid and the absorber is governed by the follows equation:

$$(\rho_f \delta_f C_f) \frac{dT_f}{dt} = hc_{f,absh} (T_{absh} - T_f) + hc_{absl,f} (T_{absl} - T_f) + \dot{m}C_f (T_{out} - T_{in}) \tag{21}$$

where \dot{m} is the mass flow rate (kg/s), C_f is the fluid heat capacity (J/kg K); $T_{c,in}$ and $T_{c,out}$ are respectively the inlet and outlet fluid temperature (K). The mean fluid temperature is assumed as the average value between its inlet and outlet temperature:

$$T_f = \frac{T_{c,out} + T_{c,in}}{2} \tag{22}$$

2.3. Water storage tank model

Cold water from the mains (temperature $T_{sup} = 15^\circ\text{C}$) flows into the tank where it is mixed with the water already contained therein to a temperature T_r . When there is a demand from the household for hot water, water (temperature T_j) is drawn from the tank.

The energy balance of the tank is written considering the heat supplied by the panels, the heat delivered to the user demand and the heat losses with the outside environment.

Moreover, no one gains solar heat are considered and the water inside the storage tank is fully mixed.

The rate of energy provided by the solar circuit to the tank is calculated from Eq. (24),

$$\dot{q}_{c \rightarrow t} = \dot{m}C_f (T_{t,in} - T_{t,out}) \tag{23}$$

According to Ref. [34], the temperature at the outlet of the solar tank ($T_{t,out}$) is calculated using the effectiveness (ϵ_H) of the heat exchanger

$$T_{t,out} = T_{t,in} - \epsilon_H (T_{t,in} - T_t) \tag{24}$$

thus, the energy balance equation becomes:

$$(M_t C_f) \frac{dT_t}{dt} = \epsilon_H \dot{m}C_f (T_{t,out} - T_t) - \dot{m}_l C_w (T_t - T_{sup}) - U_t S_t (T_t - T_a) \tag{25}$$

where: \dot{m}_l is the mass flow rate of the thermal load, C_w is the specific heat of water, U_t is the heat loss coefficient with the outside of the tank (W/K m²), S_t is the external surface of the tank.

The main equations of the numerical model are reported in Table 1. So, it is necessary to solve a system of 7 non-linear equations.

Table 1
Overview of the balance equations for the PV/T layers and tank.

Layers	Equations
Glass	$(\rho_g \delta_g C_g) \frac{dT_g}{dt} = \alpha_g G + hr_{g,sky} (T_{sky} - T_g) + hr_{g,gr} (T_{gr} - T_g) + hv_{g,at} (T_a - T_g) + hc_{pv,g} PF (T_{pv} - T_g) + hc_{red,g} (1 - PF) (T_{red} - T_g)$ (1)
PV cells	$PF (\rho_{pv} \delta_{pv} C_{pv}) \frac{dT_{pv}}{dt} = [(\tau_g \alpha_{pv} - \eta_e) G + hc_{pv,g} (T_g - T_{pv}) + hc_{red,pv} (T_{red} - T_{pv})] PF$ (10)
Tedlar	$(\rho_{red} \delta_{red} C_{red}) \frac{dT_{red}}{dt} = (1 - PF) \tau_g \alpha_{red} G + (1 - PF) hc_{red,g} (T_g - T_{red}) + PF \cdot hc_{red,pv} (T_{pv} - T_{red}) + hc_{absh,red} (T_{absh} - T_{red})$ (11)
Absor-ber	$(\rho_{absh} \delta_{absh} C_{absh}) \frac{dT_{absh}}{dt} = hc_{absh,red} (T_{red} - T_{absh}) + (1 - PC) hc_{absh,absh} (T_{absh} - T_{absh}) + PC \cdot hr_{absh,absh} (T_{absh} - T_{absh}) + hc_{f,absh} (T_f - T_{absh})$ (12)
	$(\rho_{absl} \delta_{absl} C_{absl}) \frac{dT_{absl}}{dt} = hc_{absl,f} (T_f - T_{absl}) + (1 - PC) hc_{absl,absh} (T_{absh} - T_{absl}) + PC \cdot hr_{absl,absh} (T_{absh} - T_{absl}) + hc_{sky,absl} (T_{sky} - T_{absl}) + hr_{gr,absl} (T_{gr} - T_{absl})$ (14)
Fluid	$(\rho_f \delta_f C_f) \frac{dT_f}{dt} = hc_{f,absh} (T_{absh} - T_f) + hc_{absl,f} (T_{absl} - T_f) + \dot{m}C_f (T_{out} - T_{in})$ (21)
Tank	$(M_t C_t) \frac{dT_t}{dt} = \epsilon_H \dot{m}C_f (T_{t,out} - T_t) - \dot{m}_l C_w (T_t - T_{sup}) - U_t S_t (T_t - T_a)$ (25)

2.4. Assessment of the electrical and thermal performance

In this section, the equations for calculating both electrical and thermal energy yields, as well as the efficiencies are presented.

2.4.1. Electrical yields

The electrical power (P_e) produced by a PV/T plant is calculated from the irradiance on the collector plane G , the total surface of the PV cells and the electrical efficiency:

$$P_e = \eta_e A_{pV} G \quad (26)$$

where the electrical efficiency is calculating by the following equation:

$$\eta_e = \eta_{ref} [1 - \beta(T_{pV} - T_{ref})] \quad (27)$$

η_{ref} is the efficiency at STC condition, β is a characteristic of the PV cell and T_{pV} is calculated by Eq. (11).

The reduction of the electrical efficiency is mainly due to the decrease of the voltage as a function of the temperatures of the cell as per Eq. (28)

$$V_{oc} = V_{oc,STC} [1 - \beta_V (T_{pV} - T_{ref})] \quad (28)$$

Thus, the electric energy yield is evaluated as:

$$E_e = \int_0^t P_e dt \quad (29)$$

2.4.2. Thermal yields

The thermal power (P_{th}) can be estimated by applying the thermal balance equations to the fluid passing through the panels:

$$P_{th} = \dot{m} C_f (T_{c,out} - T_{c,in}) \quad (30)$$

And the thermal efficiency as:

$$\eta_{th} = \frac{P_{th}}{A_{abs} G} \quad (31)$$

Thus the Thermal energy yield is evaluated as:

$$E_{th} = \int_0^t P_{th} dt \quad (32)$$

2.4.3. Overall Energy yields

The overall performance of PV/T systems can be obtained as a direct summation of electrical and thermal power as given by the flowing equation:

$$\eta_t = \frac{P_e + P_{th}}{A_t \cdot G} \quad (33)$$

$$E_T = E_{th} + E_e \quad (34)$$

The electrical energy, however, is more valuable than thermal energy. Thus, to take into account of the different quality of the thermal and electrical energy a primary efficiency $\eta_{(II)}$, as described by Ref. [35], can be calculated as:

$$\eta_{(II)} = \frac{P_e / \eta_{power} + P_{th}}{G \cdot A_t} \quad (35)$$

where η_{power} is the electric power generation efficiency for a conventional power plant. Thus the overall energy produced is calculated as:

$$E_{T(II)} = E_{th} + \frac{E_e}{\eta_{power}} \quad (36)$$

2.5. Statistical indicators

The uncertainty of the PV/T model can be evaluated using statistical indicators based on the ASHRAE Guideline 14, which is one of the main sources that explain how to determine the degree of confidence in the

true value when using measurement procedures and/or calculations.

The uncertainty indices used are the Coefficient of Variation of the Root Mean Square Error ($CV(RMSE)$), the coefficient of determination (R^2) and the Normalized Mean Bias Error ($NMBE$).

The coefficient of variation of the Root Mean Square Error $CV(RMSE)$ and the coefficient of determination R^2 are calculated as follow:

$$CV(RMSE) = \frac{1}{m} \sqrt{\left(\frac{\sum_{i=1}^n (m_i - s_i)^2}{n} \right)} \quad (37)$$

$$R^2 = \left(\frac{n \cdot \sum_{i=1}^n m_i \cdot s_i - \sum_{i=1}^n m_i \cdot \sum_{i=1}^n s_i}{\sqrt{(n \cdot \sum_{i=1}^n m_i^2 - (\sum_{i=1}^n m_i)^2) \cdot (n \cdot \sum_{i=1}^n s_i^2 - (\sum_{i=1}^n s_i)^2)}} \right)^2 \quad (38)$$

where m_i , s_i and n denoted respectively measured and simulated values and number of the measured data point.

$CV(RMSE)$ indicates the variability of the errors between measured and simulated values. The coefficient of determination indicates how simulated values approximate the regression line of the measured values.

Values of the R^2 to 1.0 indicate that the model matches the prototype perfectly and 0 implies that there is no agreement between predicted values and measured ones.

The Mean Bias Error (MBE) is calculated by.

$$MBE = \frac{\sum_{i=1}^n (m_i - s_i)}{n} \quad (39)$$

MBE describes the direction of the error bias. A negative MBE occurs when predictions are smaller in value than observations. However, this index is subject to cancellation errors, indeed the sum of positive and negative values could reduce the value of MBE. In fact, when a model is calibrated or near calibrated, the regression line of the sample is so close to the simulated one that the cancellation effect increases considerably [36].

The $NMBE$ [36] is the normalized MBE index, calculate dividing the MBE by the mean of measured values (m). It describes the overall behavior of the predictions against measured values regression line.

$$NMBE = \frac{1}{m} \frac{\sum_{i=1}^n (m_i - s_i)}{n} \times 100(\%) \quad (40)$$

As in the case of MBE, positive and negative values mean the under- or over-prediction of this normalization. $NMBE$ is also subject to cancellation errors; consequently, the use of this index alone is not recommended.

3. Assessment of the numerical model

The validation process entailed a detailed analysis of the behavior of the PV/T panel.

In order to test the accuracy of the mathematical model, its predictions were compared with the observations obtained from the PV/T pilot plant installed at the University campus of Catania.

In such system, the temperatures of the fluid at the inlet and outlet of the two panels, the temperatures in the rear part of each panel (low absorber plate), as well as the inlet and outlet temperatures from the solar tank are monitored.

The weather data are measured by a meteorological station placed near the PV/T system.

The PV/T panel modeled in this paper is based on the commercially WISC panel DUALSUN Wave©, as presented in Ref. [26]. The main features of such panel are reported in Table 2.

Many technical specifications required for the modeling of this system, though not all, are available in the specifications sheet provided by the manufacturer. The rest of the required parameters have been estimated from Refs. [37,38].

The module consists of mono-crystalline (c-Si) cells, open circuit

Table 2
Characteristic of investigated PV/T module.

Layers	Symbol	Parameter	Value	
Glazing	A	Aperture area (m ²)	1.66	
	L_g	Length (m)	1.677	
	W_g	Width (m)	0.99	
	δ_g	Thickness (m)	0.003	
	C_g	Specific heat (kJ/kg·K)	0.500	
	ρ_g	Density (g/cm ³)	2.300	
	λ_g	Thermal conductivity (W/m·K)	1.0	
	α_g	Absorptivity	0.03	
	τ_g	Transmittance	0.92	
	ε_g	Emissivity	0.95	
	PV cells	A_{pv}	Area of the PV (m ²)	1.46
PF		Packing Factor	0.88	
δ_{pv}		Thickness (m)	0.00035	
C_{pv}		Specific heat (kJ/kg·K)	0.757	
ρ_{pv}		Density (g/cm ³)	2.330	
λ_{pv}		Thermal conductivity (W/m·K)	168.0	
α_{pv}		Absorptivity	0.93	
η_{ref}		Module efficiency at STC (%)	15.4	
Tedlar		δ_{ted}	Thickness (m)	0.0002
		C_{pv}	Specific heat (kJ/kg·K)	1.200
	ρ_{pv}	Density (g/cm ³)	1.500	
	λ_{ted}	Thermal conductivity (W/m·K)	0.2	
	α_{ted}	Absorptivity	0.90	
Channel fluid	A_f	Area of channel (m ²)	1.12	
	PC	Percentage of channel	0.67	
	L_f	Length (m)	1.33	
	W_f	Width (m)	0.84	
	δ_f	Thickness (m)	0.0015	
	C_f	Specific heat (kJ/kg·K)	4.177	
	ρ_f	Density (g/cm ³)	0.997	
	λ_f	Thermal conductivity (W/m·K)	0.606	
Absorber plate	δ_{abs}	Thickness (m)	0.001	
	C_{abs}	Specific heat (kJ/kg·K)	900	
	ρ_{abs}	Density (kg/m ³)	2700	
	λ_{abs}	Thermal conductivity (W/m·K)	160	
	ε_{abs}	Emissivity	0.4	

voltage V_{OC} of 38.5 Volt, module efficiency of 15.4% at Standard Test Conditions (STC; $G = 1000 \text{ W/m}^2$ and $T_{PV} = 25 \text{ }^\circ\text{C}$) and electrical peak power of 250 W.

The temperature coefficients (β) and (β_v), which allow to evaluate the decrease of the electrical efficiency and the open circuit voltage used in Eqs. (27) and (28), are 0.44%/°C and 0.32%/°C. The geometrical and technical specifications of the PV/T module are detailed in Table 2.

It is possible to notice that the surface where the fluid flows is of about 67% of the total area of the absorber.

In this study, the coolant fluid is still water as in Catania during the period of investigation there is no risk of freezing. However, in cold

climate zones the fluid has to be replaced with a solution of water and glycol. Consequently, it will be necessary to modify the physical properties of the fluid by considering those of the real coolant fluid.

4. Result and discussion

In the first part of this section, to validate the numerical model, the simulated results are compared with the experimental data carried out from a real plant. In the second section, the most important outputs are shown.

4.1. Model validation

In this section, the proposed simulation model implemented in MATLAB environment is compared with observed data during the period 7/10 March 2019. The weather variables were set using the data collected by the meteorological station. The thermal load in Eq. (26) is not zero only when the tank temperature T_t is higher than 45 °C. The mass flow rates used in the simulations are the same as the observed one.

Fig. 3 shows the environment temperature (T_a) and the total irradiance on the surface of the PV/T module (G), measured by the weather station located near the pilot PV/T plant.

The following figures shows the comparisons between the observed data measured through the monitoring system installed in the PV/T plant and the simulated data during the observation period.

Fig. 4 shows the simulated ($T_{c_{in,sim}}$) and observed ($T_{c_{in,exp}}$) inlet temperatures in the PV/T collectors.

Fig. 5 shows the simulated ($T_{c_{out,sim}}$) and observed ($T_{c_{out,exp}}$) outlet temperatures in the PV/T collectors.

As a general result, it can be observed that the inlet water temperature crossing the PV/T panel reaches a maximum average value of about 40.2 °C at midday. Likewise, the water at the outlet has a similar trend with a maximum average value of 43.0 °C. Thus, a ΔT of about 2.8 °C between the inlet and outlet fluid temperatures emerges.

As regards the accuracy of the numerical model, it is possible to observe that during the whole period the two set of temperatures follow the same pattern with very modest differences.

The most significant discrepancies, which appear during the period from sunset to sunrise, may be attributed to the assumptions of neglecting the thermal losses in the hydronic circuit. fast variation of temperature during the second day of simulations, which is characterized by a continuous fluctuation of the solar radiation.

Fig. 6 shows the simulated and observed mean temperatures of the water inside the solar tank.

It is possible to highlight that in agreement with the weather data, there is an increase of the tank temperature with the passing of the days. The maximum temperature achieved into the tank is about 40 °C and it is attained at about 15:00.

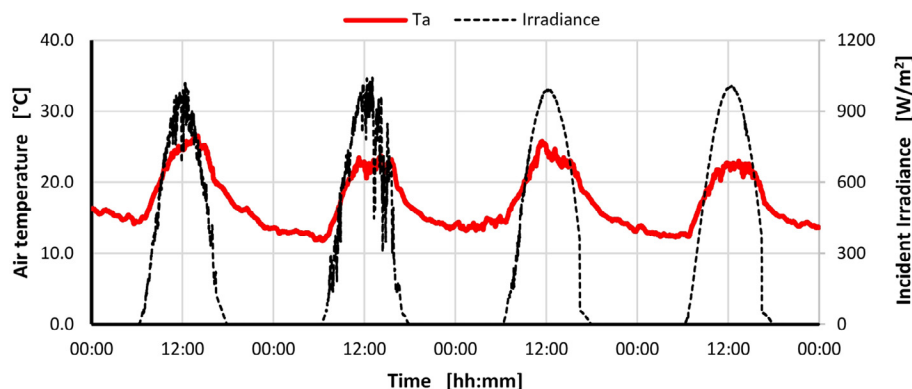


Fig. 3. Weather conditions: air temperature (T_a) and solar irradiance (G).

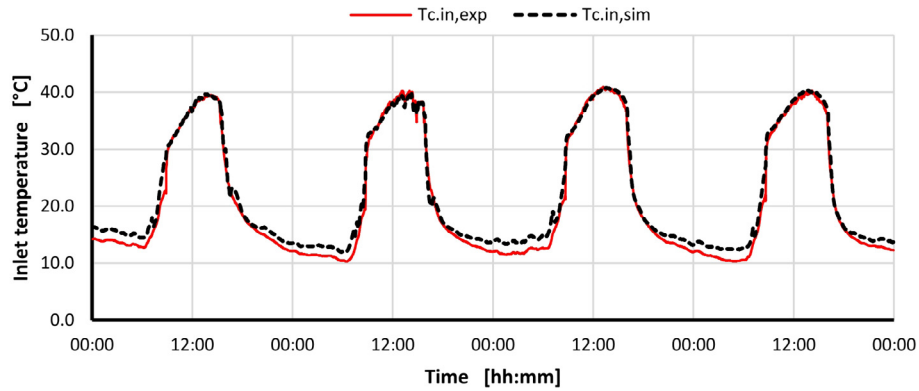


Fig. 4. Simulated and observed inlet temperatures in the PV/T panel.

Once again a good agreement between the simulated and observed data. The biggest differences are observed during the second of the monitored days, when the simulated temperature are lower than the observed. These differences could be attributed to the effect of the variable weather conditions, both solar radiation and temperatures, which are more complicate to simulate. A more detailed analysis for assessing the robustness of the proposed numerical model will be presented through a statistical analysis in the Section 4.2.

Finally, the analysis of the electrical performance of the PV/T plant are investigated.

Fig. 7 shows the simulated ($V_{oc,sim}$) and observed ($V_{oc,exp}$) voltage in open circuit condition.

It is possible to highlight that the value of the voltage simulated at open circuit ($V_{oc,sim}$) are lower than the observed voltage. The main differences emerge next sunrise and sunset, when the equation used for evaluating the voltage does not take into account of the effect deriving by the modest solar irradiation, lower than 200 W/m^2 , that hits the solar cell in those period.

Otherwise, the comparison between experimental observations and simulation result show a very good agreement during the central part of the day.

A more detailed analysis for assessing the robustness of the proposed numerical model in evaluating the electrical performance will be presented through a statistical analysis in the follow

4.2. Comparison between predictions and experimental results

The uncertainty of the PV/T model was assessed using the statistical indicators based on the ASHRAE Guideline 14, which allows to determine the degree of confidence in the true value when using measurement procedures and/or calculations. The accuracy of the presented model is evaluated by means the following indexes Coefficient of Variation of the Root Mean Square Error ($CV(RMSE)$), the coefficient of

determination (R^2) and the Normalized Mean Bias Error ($NMBE$). Table 3 shows the values calculated for such indexes.

As the previous results had already highlighted, the proposed numerical model has a good prediction of the thermal parameters with acceptable values of $CV(RMSE\%)$, R^2 , $NMBE$, and MBE . The negative values of both MBE and $NMBE$ indicate the over-estimation of the model. Moreover, it has to be mentioned that these two indexes are subject to cancellation errors especially in the case of a well-calibrated model as in this case. Overall, it is possible to affirm that the proposed model provides quite accurate results. This confirms that the simplifications assumed in the physic models do not diminish the accuracy of its predictions.

4.3. Temperature profiles

One of the main challenge for predicting the electrical efficiency is the calculation of the PV cells temperature, in particular for the PV/T modules where such temperature is influenced by the temperature of the fluid.

Thus, it is worth of interest to observe the mutual relations among the PV cells temperature and the average fluid temperature (T_f).

Fig. 7 shows the daily variation of the cells temperature T_{pv} , the mean temperature of the fluid T_f , the temperature of the upper and lower absorber plate (T_{absh} and T_{absl}), as well and the environment temperature (T_a).

The right side of Fig. 8 shows the enlargement of the above-mentioned temperature during the hottest period of the day.

The photovoltaic cells reach maximum values of temperatures of about $35.7 \text{ }^\circ\text{C}$ with a solar irradiation of about 1000 W/m^2 . This means that the electrical efficiency of the PV/T module, calculated through Eq. (27), should diminish of about 0.7% respect to the reference value.

During the daytime, the temperature of the photovoltaic cells is very close to the mean fluid temperature (T_f). Actually, T_{pv} are $0.7 \text{ }^\circ\text{C}$ higher

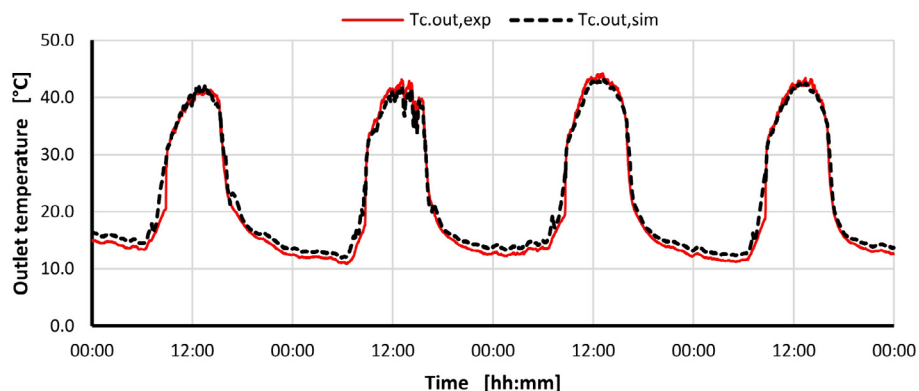


Fig. 5. Simulated and observed outlet temperatures in the PV/T panel.

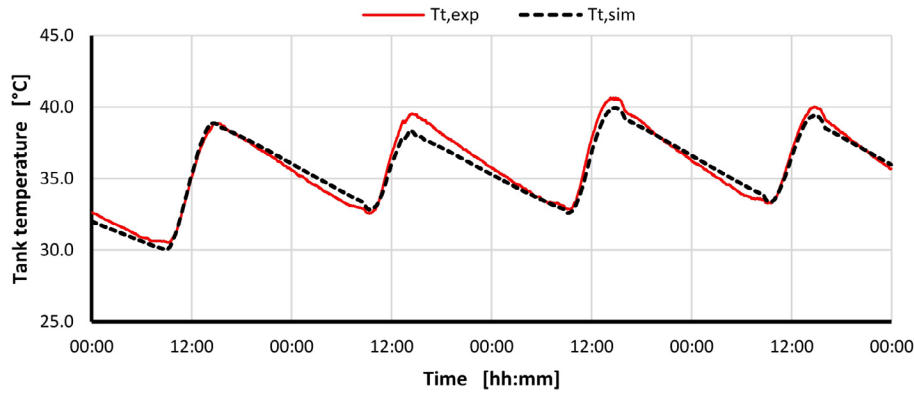


Fig. 6. Simulated and observed temperatures in the solar tank T_t .

than the mean fluid temperature during the hottest hours of the day, while such difference diminishes considerably during the other period of the day.

One of the simplest hypothesis that is proposed in literature studies [9] is to evaluate the temperature of the PV cells as a function of the temperature of the coolant fluid (e.g. the mean temperature).

Thus, the comparison of the PV cell temperatures calculated by the proposed model with that one calculate assuming the PV cells temperature as the mean value of the coolant fluid is proposed in Fig. 8. Such comparison evidences that the assumptions to set the cell temperatures coincident to the mean fluid temperatures can be considered rather acceptable for the PV/T collector investigated in this study.

4.4. Energy production

Fig. 9 shows the daily electrical (EL) and the thermal performance (Th) of the PV/T plant during a clear sky day (9 March).

At midday with a value of solar irradiance of about 1000 W/m^2 , the PV/T solar plant provides a power and thermal production of about 430 W and 690 W respectively, to which corresponds an electric and the thermal efficiencies of about 14.7%, and 21.7% respectively.

Thus, this system allows to produce electrical power that is rather close to the peak, that is 500 W. The thermal power could seem modest, if compared with the nominal power, that is of about 1650 W, however it has to be highlighted that the PV/T plant operates with relatively high temperature, of about $35 \text{ }^\circ\text{C}$, and this power will be totally lost in a conventional PV plant.

For evaluating the performance of PV/T plant over a period, the energy values in a certain time (day, month, year) have to be evaluated.

Table 4 shows the electrical (E_e) and the thermal performance (E_{th}) as well as the total performance (E_{Tot} , η_T) of the PV/T plant during a clear sky day (9 March).

As regard the total performances, they are calculated by Eqs. (35)

Table 3

Statistical indexes.

Parameter	CV (RMSE%)	R ²	MBE%	NMBE %
$T_{c,in}$	7.0605	0.9934	-5.0758	-1.07765
$T_{c,out}$	6.9935	0.9904	-3.3477	-0.7347
T_t	1.9657	0.9650	-1.4105	-0.4956
V_{oc}	1.0464	0.9981	-1.1479	-6.1403

and (36), which allow correctly valorizing the two different forms of energy.

Moreover, the electrical performance of the PV/T plant are also evaluated using the performance ratio PR, which is defined as the ratio between YA and YR.

PR is calculated by the following equation.

$$PR = \frac{YA}{YR} \tag{41}$$

YA indicates the number of equivalent hours in which the PV/T module gives the peak value in the defined time interval.

$$YA = \frac{E_e}{P_{peak}} \tag{42}$$

YR indicates the number of hours in which PV module works under G_{STC} value in the defined time interval

$$YR = \frac{G}{G_{STC}} \tag{43}$$

Data summarized in Table 4 give a comprehensive outlook of the performances of the PV/T plant. The performance ratio gives a speedy information on the amount of electrical energy produced in comparison to STC condition. The values of the PR index close to 1.0 indicate that the PV/T system worked nearest to the optimal operative mode, thanks

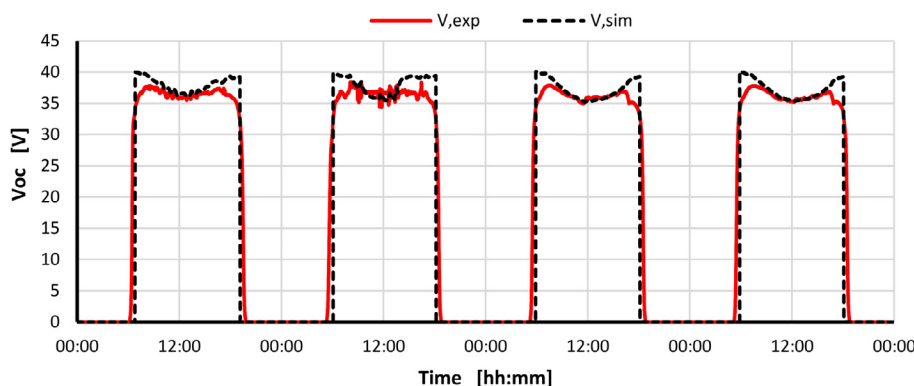


Fig. 7. Simulated and observed voltage in open circuit condition.

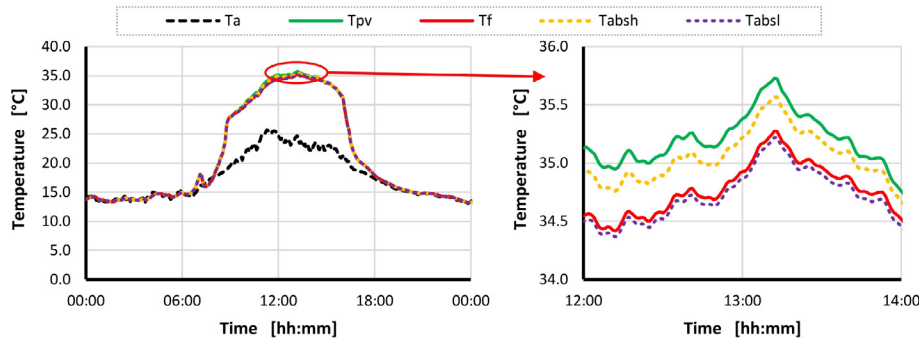


Fig. 8. PV cells, fluid, absorber plate and environmental temperatures.

also to the not too much high PV cell temperature (i.e. less than 36 °C). This assessment is confirmed by the low values of the daily thermal energy, which indicates that the WISC PV/T module operated favouring the PV cell electrical performance (MPPT conditions).

Mainly, the proposed model allows characterizing the performances of the PV/T system in terms of thermal, electrical, and total energy production, as well as the total efficiency.

Such information are crucial in PV/T real applications not only for having data useful for evaluating the yield of energy produced, but also for comparing the performances of a PV/T plant with other conventional solar plant (i.e. PV and solar thermal plant).

Consequently, the output of the proposed model can be also used to evaluate the gains derived by the installation of PV/T plants in comparison with conventional solar systems.

Moreover, the availability of a validated numerical model represents a very useful tool for the on line monitoring a real PV/T installation in such a way to detect immediately faults or inefficient operative conditions through the comparison between calculated and measured variables and performances [39].

5. Conclusion

This work proposes a novel dynamic numerical model that allows characterizing thermal and electrical performances of a WISC PV/T panel as well as a complete PV/T power plant. The main outputs of this model are the temperatures of the PV cells, the inlet and outlet temperatures of the solar panel, the temperature in the storage tank and the yield of electrical and thermal energy.

The comparison among the simulation results and the observed data highlights the very good accuracy of the proposed model during the testing days. The numerical output matched the measurements with a root mean square error $CV(RMSE\%)$ less than 7.00% and a coefficient of determination R^2 more than 0.99.

During the observation period (spring season) the energy performance analysis of the modelled plant shows an average daily electrical yield of 0.84 kWh/m², a thermal yield of 0.59 kWh/m² and a total

Table 4

Daily results.

Days	G (kWh/m ²)	E _{el} (kWh/m ²)	PR	E _{th} (kWh/m ²)	E _{tot} (kWh/m ²)	η _T
03/07	6.01	0.79	0.872	0.56	2.27	0.378
03/08	6.07	0.80	0.878	0.45	2.19	0.361
03/09	6.61	0.87	0.872	0.65	2.54	0.384
03/10	6.79	0.89	0.875	0.54	2.48	0.366
Average	6.37	0.84	0.874	0.548	2.372	0.372

energy production of 2.27 kWh/m². This last data takes into account of the different quality of the thermal and electric energy. The average total efficiency of the PV/T plant is 37.22%, this means that by means of the PV/T technology is possible to reach a twofold objective, that is increase the percentage of used energy per square and increase the efficiency of PV modules.

Such information are crucial in PV/T real applications not only for having data useful for evaluating the yield of energy produced, but also for comparing the performances of a PV/T plant with other conventional solar plant (i.e. PV and solar thermal plant).

Consequently, the output of the proposed model can be also used for evaluating the advantages deriving by the installation of PV/T plants in comparison with conventional PV solar systems.

Moreover, validated numerical models are very useful tool that can be used for the on line monitoring of real PV/T installations to detect immediately faults or inefficient operative conditions through the comparison between calculated and measured variables and performances.

Future works foresee analysis regarding the optimization of the electrical and thermal performance of a PV/T plant in function of the most influencing factors (i.e. solar irradiation, ambient temperature, and mass flow rate are). This is a very complex task because in hybrid PV/T systems the total energy output depends on several factors and typically there is an antithetical behaviour between the electrical and thermal performance.

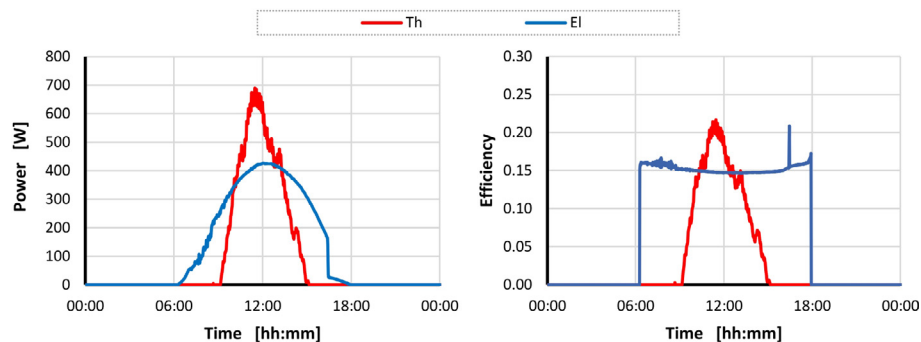


Fig. 9. Thermal and electrical power (at left) and efficiency (at right) of the PV/T plant.

Declaration of Competing Interest

The authors declare that they have no known competing financial interests or personal relationships that could have appeared to influence the work reported in this paper.

Acknowledgment

This work was supported by University of Catania “FUNDS FOR UNIVERSITY PLAN FOR RESEARCH 2016/2018 – line 2”.

This work was supported by the Notice 12/2017 for financing the Ph.D. regional grant in Sicily” as part of Operational Programme of European Social Funding 2014-2020 (PO 2014-2020). These results also contribute to the work and discussion of IEA SHC Task 60 – PV/T systems.

References

- [1] 2018 SNAPSHOT OF GLOBAL PHOTOVOLTAIC MARKETS Report IEA PVPS T1-33:2018.
- [2] Urbanetz J, Zomer CD, R  ther R. Compromises between form and function in grid-connected, building-integrated photovoltaics (BIPV) at low-latitude sites. *Build Environ* 2011;46(10):2107–13.
- [3] Priyanka S, Ravindra NM. Temperature dependence of solar cell performance-an analysis. *Sol Energy Mater Sol Cells* 2012;101:36–45.
- [4] Adham M, Siddig O, Hisham S. Advancements in hybrid photovoltaic systems for enhanced solar cells performance. *Renew Sustain Energy Rev* 2015;41:658–84.
- [5] Daisuke S, Noboru Y. Review of photovoltaic module cooling methods and performance evaluation of the radiative cooling method. *Renew Sustain Energy Rev* 2019;104:151–66.
- [6] Kern JEC, Russell MC. Combined photovoltaic and thermal hybrid collector systems. *Proc. 13th IEEE photovoltaic specialist* Washington DC, USA. 1978. p. 1153–7.
- [7] Gagliano A, Tina GM, Aneli S, Nizetic S. Comparative assessments of the performances of PV/T and conventional solar plants. *J Cleaner Prod* 2019;304–315:2019.
- [8] Herrando M, Ramosa A, Freeman J, Zabalza I, Markides CN. Technoeconomic modelling and optimisation of solar combined heat and power systems based on flat-box PVT collectors for domestic applications. *Energy Convers Manage* November 2018;175(1):67–85.
- [9] Kalogirou SA, Tripanagnostopoulos Y. Hybrid PV/T solar systems for domestic hot water and electricity production. *Energy Convers Manage* 2006;47:3368–82.
- [10] Bianchini A, Guzzini A, Pellegrini M, Sacconi C. Photovoltaic/thermal (PV/T) solar system: experimental measurements, performance analysis and economic assessment. *Renew Energy* 2017;111:543–55.
- [11] Bahaidaraha H, Subhana A, Gandhidasana P, Rehmanb S. Performance evaluation of a PV (photovoltaic) module by back surface water cooling for hot climatic conditions. *Energy* 2013;59:445–53.
- [12] Zenh  user D, Bamberger E, Baggenstos A, H  berle A. PVT wrap-up: energy systems with photovoltaic-thermal solar collectors – technology, market, Experiences ISES Solar World Congress; 2017.
- [13] Calise F, Dentice d’Accadia M, Vanoli L. Design and dynamic simulation of a novel solar trigeneration system based on hybrid photovoltaic/thermal collectors (PVT). *Energy Convers Manage* 2012;60:214–25.
- [14] Sandeep SJ, Ashwinkumar SD. Photovoltaic -Thermal systems (PVT): technology review and future trends. *Renew Sustain Energy Rev* 2018;92:848–82.
- [15] Mellor A, Alonso AD, Guarracino I, Ramos A, Riverola LA, Ferre LL, et al. Roadmap for the next-generation of hybrid photovoltaic-thermal solar energy collectors. *Sol Energy* 2018;174:386–98.
- [16] Buonomano A, De Luca G, Figaj RD, Vanoli L. Dynamic simulation and thermo-economic analysis of a PhotoVoltaic/thermal collector heating system for an indoor–outdoor swimming pool. *Energy Convers Manage* July 2015;99(15):176–92.
- [17] Wang K, Herrando M, Pantaleo AM, Markides CN. Techno economic assessments of hybrid photovoltaic-thermal vs. conventional solar-energy systems: case studies in heat and power provision to sports centres. *Appl Energy* 2019;254:113657.
- [18] Mahmoud A, Maher C. Design of a PV/T based desalination plant Concept and assessment. The 5th EEE international renewable energy congress (IREC) 2014. <https://doi.org/10.1109/IREC.2014.6827025>.
- [19] Bombarda P, Di Marcoberardino G, Lucchini A, Leva S, Manzolini G, Molinari L, et al. Thermal and electric performances of roll-bond flat plate applied to conventional PV modules for heat recovery. *Appl Therm Eng* 2016;105:304–13.
- [20] Sun X, Wu J, Dai Y, Wang R. Experimental study on roll-bond collector/evaporator with optimized-channel used in direct expansion solar assisted heat pump water heating system. *Appl Therm Eng* 2014;66(1–2):571–9. <https://doi.org/10.1016/j.applthermaleng.2014.02.060>.
- [21] Jinshun W, Xingxing Z, Jingchun S, Yupeng W, Karen C, Tong Y, et al. A review of thermal absorbers and their integration methods for the combined solar photovoltaic/thermal (PV/T) modules. *Renew Sustain Energy Rev* 2017;75:839–54.
- [22] Calise F, Figaj RD, Vanoli L. Experimental and numerical analyses of a flat plate photovoltaic/thermal solar collector. *Energies* 2017;10:491. <https://doi.org/10.3390/en10040491>.
- [23] Aste N, Del Pero C, Leonforte F. Water PVT collectors performance comparison. *Energy Procedia* 2017;105:961–6.
- [24] Zarrella A, Emmi G, Viviani J, Croci L, Besagni G. The validation of a novel lumped parameter model for photovoltaic thermal hybrid solar collectors: a new TRNSYS type. *Energy Convers Manage* 2019;188:414–28.
- [25] Zondag HA, de Vries DW, van Helden WGJ, van Zolingen RJC, van Steenhoven AA. The yield of different combined PV-thermal collector designs. *Sol Energy* 2003;74:253–69.
- [26] Gagliano A, Tina GM, Nocera F, Grasso AD, Aneli S. Description and performance analysis of a flexible photovoltaic/thermal (PV/T) solar system. *Renew Energy* 2018;137:144–56.
- [27] Bhattarai S, Oh J, Euh S, Kafle GK, Kim DH. Simulation and model validation of sheet and tube type photovoltaic thermal solar system and conventional solar collecting system in transient states. *Sol Energy Mater Solar Cells* 2012;103:184–93.
- [28] Notton G, Cristofari C, Mattei M, Poggi P. Modelling of a double-glass photovoltaic module using finite differences. *Appl Therm Eng* 2005;25:2854–77.
- [29] Cole RJ, Sturrock NS. The convective heat exchange at external surface of buildings. *Build Environ* 1997;12:207–14.
- [30] Bejan A, Kraus AD. Heat transfer handbook. Wiley-IEEE; 2003.
- [31] Churchill SW. A comprehensive correlating equation for laminar, assisting, forced and free convection. *J Am Inst Chem Eng* 1976;23(1):10–6.
- [32] Ben Cheikh HH, Touafek K, Kerrour F, Haloui H, Khelifa A. Model validation of an empirical photovoltaic thermal (PV/T) collector. *Energy Procedia* 2015;74:1090–9.
- [33] Incropera FP, DeWitt DP. Fundamentals of heat and Mass transfer. John Wiley & Sons; 2002.
- [34] Lunde PJ. Solar thermal engineering: space heating and hot water systems. New York, Chichester: Wiley; 1980.
- [35] Huang BJ, Lin TH, Hung WC, Sun FS. Performance evaluation of solar photovoltaic/thermal systems. *Sol Energy* 2001;70:443–8.
- [36] Germ  n Ra R, Carlos FB. Validation of calibrated energy models: common errors. *Energies* 2017;10(10):1587. <https://doi.org/10.3390/en10101587>.
- [37] Zondag HA, De Vries DW, Van Helden WGJ, Van Zolingen RJC, Van Steenhoven AA. The thermal and electrical yield of a PV-thermal collector. *Sol Energy* 2002;72:113–28.
- [38] Kumar AR, Garg HP. Study of a photovoltaic-thermal system–thermosiphonic solar water heater combined with solar cells. *Energy Convers Manage* 1994;620.
- [39] Tina GM, Grasso AD, Gagliano A. Monitoring of solar cogenerative PVT power plants: overview and a practical example. *Sustain Energy Technol Assess* 2015;10:90–101.

Analysis of the energy produced and energy quality of nanofluid impact on photovoltaic-thermal systems

Stefano Aneli¹, Antonio Gagliano¹, Giuseppe M. Tina¹, Bekkay Hajji²

¹ University of Catania, viale Andrea Doria 6 Catania 95125, Italy

² National School of Applied Sciences, Mohammed First University, Oujda, Morocco
antonio.gagliano@dieei.unict.it

Abstract. To limit climate change, the use of renewable energy is mandatory. PV/T systems generate renewable energy, simultaneously satisfy both the thermal and electrical energy requests. Usually, these systems have some limitations to fulfill the thermal energy needs; therefore, it is necessary to improve their efficiency with the aim to increase the enthalpy level of the energy produced. In this paper, the effects of changing the cooling fluid from pure water to a nanofluid composed by water and aluminum oxide (Al_2O_3) in a PV/T system are studied. The analysis is based on the thermodynamics viewpoint, considering both the total energy produced and its quality. The thermal level achievable by changing the heat transfer fluid, as well as the electrical efficiency considering various input conditions has been calculated. Finally, the energy yield produced by a conventional PV/T plant, which use pure water (PV/T_w) and the proposed improved PV/T plant, which use pure the nanofluid (PV/T_{nf}), under real climate conditions have been compared. Such comparison was developed taking into account the second law of thermodynamics as well as the exergy analysis.

Keywords: WISC PV/T collector, Nanofluid; numerical model.

1 Introduction

The world energy requirement shows a constantly increasing trend, where the necessary energy concerns both the electrical and thermal form. To produce the two forms of energy, photovoltaic and solar thermal systems must therefore be installed. Alternatively, there are PV/T systems able of simultaneously generating both forms of energy, thus producing a lot of renewable energy. Several comparative studies [1-3] show that PV/T systems are capable of producing more energy per unit area than any combination of conventional solar systems. Therefore, it is not surprising that in recent years important research has been dedicated to the various parameters that can increase energy production, such as the different geometric design and materials [4-7]. An alternative, concerns the use of heat transfer fluid with better performance than simple water. Despite the high thermal capacity of the water, which makes it a good heat storage vehicle, its thermal conductivity is low and therefore the heat transfer is limited. Starting from 1995 [8], many researchers have suggested the adoption of nanoparticles to be added to the base fluid to form a suspension with high thermal conductivity, i.e. nanofluids. Nanofluids are solid-liquid composite materials consisting of solid nanoparticles or

nanofibers with sizes typically of 1–100 nm suspended in liquid [9]. Various studies have shown that nanofluids have substantially higher thermal conductivities than base fluids [10-13]. Practical studies have shown that nanofluids are preferred over base fluids, as they allow increasing electrical and thermal efficiency [14-17].

In this paper, the effects of changing the heat transfer fluid from pure water to a nanofluid composed by water and Al_2O_3 are studied using a numerical model.

Such model, developed with Matlab®, was validated using experimental data coming from the pilot plant installed at the University of Catania [18].

The first part of this study analyses the differences in terms of temperature of the fluid outlet from the PV/T panels, temperature of the photovoltaic cells, difference in electrical efficiency, considering different inlet temperature. In the second part, a comparison is developed in terms of thermal and electrical energy produced as well as the study of the total energy produced considering the first and second principles of thermodynamics, under real climatic data.

2 Methodology

2.1 PV/T numerical model

The numerical model used in this paper was explained and validated in [19]. It works in dynamic state conditions and is based on the energy balance equations. The model is based on the PV/T system installed at University of Catania (IT) equipped with two commercially WISC panels DUALSUN Wave©, as presented in Ref. [18], with total surface of 3.32 m². The panels are connected in series and are connected with a storage tank, which has a volume of 170 l. The module consists of mono-crystalline (c-Si) cells, which provide a module efficiency of 15.4% at Standard Test Conditions, with electrical peak power of 250 W. The efficiency loss with temperature coefficient (β) is 0.44%.

2.2 Coolant fluids

The study on the performance of a PV/T system was carried out considering two different heat transfer fluids: pure water and nanofluid. The nanofluid is composed by pure water and nanoparticles of aluminum oxide (3% by weight), with a volumetric ratio (ϕ) calculated by eq. (1).

$$\phi_{nf} = \frac{m_p/\rho_p}{m_p/\rho_p + m_f/\rho_f} \quad (1)$$

where m is the mass, ρ is the density and subscripts p , f and nf represent respectively: nanoparticles, fluid (pure water) and nanofluid. All the thermos-physical properties of the water and of the nanofluid are reported in table 1, which have been calculated using the equations proposed by [20].

Table 1. Properties of the fluids.

Properties		Pure water	Nanoparticles	Nanofluid 3%/w.
ρ (density)	[kg·m ⁻³]	997.0	3970.0	1019.2
C (specific heat capacity)	[J·kg ⁻¹ ·K ⁻¹]	4177.0	765.0	4077.6
λ (thermal conductivity)	[W·m ⁻¹ ·K ⁻¹]	0.606	40.0	0.619

2.3 Key Performance indicator

In a PV or PV/T installation, the electrical performances depend by the working cells temperature, which in turn depends by the solar irradiation (G).

Thus, it is worth of interest to introduce a KPi, namely $T_{char,PV}$, which allows to evaluate the working temperature of the PV cells weighted by G.

$$T_{char,PV} = \frac{\int T_{PV} \cdot G \cdot dt}{\int G \cdot dt} \quad (2)$$

The increase of Thermal Level (T^+_{nf}) of the cooling fluid trough the PV/T module is calculated by eq. 3:

$$T^+_{nf} = \frac{T_{out,nf} - T_{out,w}}{\Delta T_{out-in}} \times 100 \quad [\%] \quad (3)$$

The overall performance of a PV/T system must be evaluated based on a thermodynamic approach from the viewpoint of the first and second laws. The KPi(s) useful for calculating the Overall Energy Yields are the primary energy produced ($E_{T(I)}$) [1, 21]) and the Overall Exergetic Content ($E_{\chi T}$) [22], calculated by eq. 4 and 5:

$$E_{T(I)} = \frac{P_e}{\eta_{power}} + P_{th} \quad (4)$$

$$E_{\chi T} = E_{\chi e} + E_{\chi th} \quad (5)$$

3 Result and discussions

3.1 Thermal comparison during day a type

In this section, the comparison of the working temperatures of the PV/T panel in case of using water or nanofluids as cooling fluid, are discussed. The simulations were carried out considering a typical summer day. The flow rate of 30 kg/(h·m²) was chosen in accordance with the solar collector fluid flow rates suggested by [23].

Fig. 1 shows the comparison of the outlet temperatures for the two fluids analyzed and the increase of thermal level, varying the inlet temperatures (T_{in}) from 25 to 45°C.

It can be observed that the outlet temperature is greater in the case of use of the nanofluid. Moreover, when the inlet temperature increases, the difference between the two fluids is reduced, from about 0.29° to about 0.09°C. This means that the use of the nanofluid increase the thermal level of about 1.9% respect to pure water.

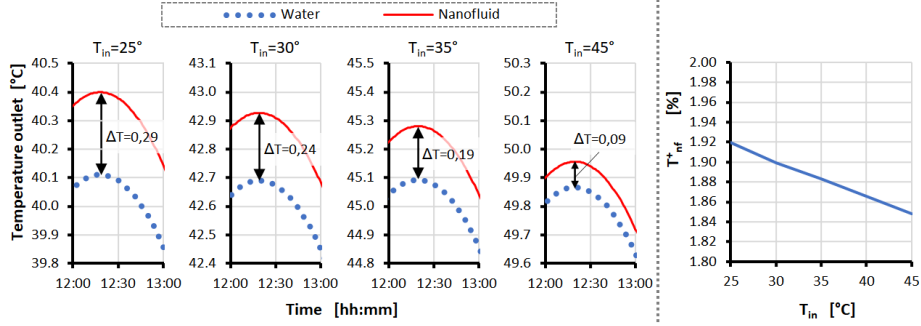


Fig. 1. Outlet temperatures and increase of thermal level.

According to the outlet temperature, T_{PV} increase with a maximum difference of about 0.08°C . Therefore, the electrical efficiency decrease of 0.04% in the worst case.

3.2 PV/T system under real weather conditions

In this section, the performances of the PV/T plant operating with nanofluid are analyzed during the period from 7 to 10 March 2019 as in this period experimental data are available for the PV/T plant operating with pure water [19]. Fig. 2 shows the average temperature reached in the thermal storage for both the fluids analyzed. It is possible to highlight that the trend of temperature into the thermal storage are quite similar for both fluid. The exploitation of the nanofluid allows to slightly increasing the daily temperature into the thermal storage.

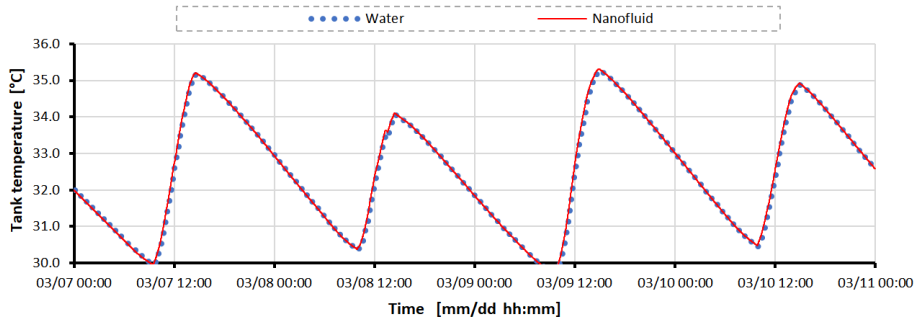


Fig. 2. Average tank temperature during the simulation period for both fluids.

The daily thermal and electrical energy produced and the overall energy calculated using eq. 4, and the total exergy content are summarized in table 2.

The results show that the thermal energy produced undergoes a slight increase using nanofluids, while electricity losses are negligible. Indeed, the reference temperature of photovoltaic cells ($T_{\text{char,PV}}$), which can be assumed as an indicator of the temperature effects on the electrical efficiency, have a maximum increases of 0.05°C , using the nanofluid (Nfluid).

Table 2. Daily results.

Day	03/07		03/08		03/09		03/10	
	Water	Nfluid.	Water	Nfluid.	Water	Nfluid.	Water	Nfluid.
$T_{\text{outd,av}}$ [°C]	18.42		16.52		17.58		16.34	
G_{TOT} [Wh/m ²]	6013		6070		6607		6794	
$E_{\chi,\text{sun}}$ [Wh/m ²]	5781		5842		6356		6540	
$T_{\text{char,PV}}$ [°C]	34.59	34.63	33.46	33.50	35.25	35.30	34.35	34.39
E_{el} [Wh/m ²]	780	780	792	792	855	855	883	883
E_{th} [Wh/m ²]	310	312	221	221	333	334	263	264
$E_{\text{T(1)}}$ [Wh/m ²]	2006	2007	1943	1944	2191	2192	2184	2184
$E_{\chi\text{T}}$ [Wh/m ²]	797	797	805	805	874	874	899	899
ε_{T} [%]	13.79	13.79	13.78	13.78	13.75	13.75	13.75	13.75

4 Conclusions

The paper shows the effects of changing the coolant fluid from pure water to a nanofluid composed by water and aluminum oxide in a PV/T system.

The use of the nanofluid allows reaching higher thermal levels than the use of pure water. As the inlet temperature increases, the differences in outlet temperature between the two fluids decrease, while maintaining a relationship with the temperature difference between the inlet-outlet almost constant, with an increase in performance obtained by using the nanofluid of approximately 1.9%. Furthermore, the increase in the thermal level generates a small increase in the working temperatures of the PV, generating a negligible decrease in terms of electricity produced.

Observing a complete system, the nanofluid slightly increases the thermal energy produced and the total energy produced, while the exergetic content remains rather constant. Future study should evaluate to optimize all the operative parameters (e.g. the mass flow rate, the specific volume of the thermal storage) for a further improvement of the performance of the (PV/T)_{nf} plant.

References

1. A. Gagliano, G.M. Tina, S. Aneli, S. Nižetić. Comparative assessments of the performances of PV/T and conventional solar plants. *J. of Cleaner Production* (219), 304-315 (2019)
2. B. Boumaaraf, K. Touafek, M.S. Ait-cheikh, M. El Amine Slimani. Comparison of electrical and thermal performance evaluation of a classical PV generator and a water glazed hybrid photovoltaic-thermal collector. *Math. and Comp. in Simulation* (167), 176-193 (2020)
3. E. Sakellariou, P. Axaopoulos. Simulation and experimental performance analysis of a modified PV panel to a PVT collector. *Solar Energy* (155), 715-726 (2017)
4. M. Herrando, A. Ramos, I. Zabalza, C.N. Markides. A comprehensive assessment of alternative absorber-exchanger designs for hybrid PVT-water collectors. *Applied Energy* (235), 1583-1602 (2019)

5. J.J. Michael, S. Iniyar, R. Goic. Flat plate solar photovoltaic-thermal (PV/T) systems: A reference guide. *Renewable and Sustainable Energy Reviews* (51), 62-88 (2015)
6. J. Antonanzas, A. del Amo, A. Martinez-Gracia, A.A. Bayod-Rujula, F. Antonanzas-Torres. Towards the optimization of convective losses in photovoltaic-thermal panels. *Solar Energy* (116), 323-336 (2015)
7. H.A. Zondag, D.W. de Vries, W.G.J. van Helden, R.J.C. van Zolingen, A.A. van Steenhoven. The yield of different combined PV-thermal collector designs. *Solar Energy* (74), 253-269 (2003)
8. S. Chol, J. Estman. Enhancing thermal conductivity of fluids with nanoparticles. *ASME-Publications-Fed* (231), 99-106 (1995)
9. V. Sridhara, L.N. Satapathy. Al₂O₃-based nanofluids: a review. *Nanoscale Research Letters* (6), 456 (2011)
10. A.A. Minea. Hybrid nanofluids based on Al₂O₃, TiO₂ and SiO₂: numerical evaluation of different approaches. *International J. of Heat and Mass Transfer* (104), 852-860 (2017)
11. E. Ebrahimnia-Bajestan, M. Charjouei Moghadam, H. Niazmand, W. Daungthongsuk, S. Wongwises. Experimental and numerical investigation of nanofluids heat transfer characteristics for application in solar heat exchangers. *International J. of Heat and Mass Transfer* (92), 1041-1052 (2016)
12. M. Hemmat Esfe, A. Karimipour, W.-M. Yan, M. Akbari, M.R. Safaei, M. Dahari. Experimental study on thermal conductivity of ethylene glycol based nanofluids containing Al₂O₃ nanoparticles. *Int. Communications in Heat and Mass Transfer* (68), 248-251 (2015)
13. T. Yousefi, F. Veysi, E. Shojaeizadeh, S. Zinadini. An experimental investigation on the effect of Al₂O₃-H₂O nanofluid on the efficiency of flat-plate solar collectors. *Renewable Energy* (39), 293-298 (2012)
14. A. Kasaeian, A.T. Eshghi, M. Sameti. A review on the applications of nanofluids in solar energy systems. *Renewable and Sustainable Energy Reviews* (43), 584-598 (2015)
15. S. Alous, M. Kayfeci, A. Uysal. Experimental investigations of using MWCNTs and graphene nanoplatelets water-based nanofluids as coolants in PVT systems. *Applied Thermal Engineering* (162), (2019)
16. A.H.A. Al-Waeli, M.T. Chaichan, H.A. Kazem, K. Sopian. Comparative study to use nano-(Al₂O₃, CuO, and SiC) with water to enhance photovoltaic thermal PV/T collectors. *Energy Conversion and Management* (148), 963-973 (2017)
17. M. Sardarabadi, M. Passandideh-Fard, S.Z. Heris. Experimental investigation of the effects of silica/water nanofluid on PV/T (phot. thermal units). *Energy* (66), 264-272 (2014)
18. A. Gagliano, G.M. Tina, F. Nocera, A.D. Grasso, S. Aneli. Description and performance analysis of a flexible photovoltaic/thermal (PV/T) solar system. *Renewable Energy* (137), 144-156 (2019)
19. C. El Fouas, B. Hajji, A. Gagliano, G.M. Tina, S. Aneli. Numerical model and experimental validation of the electrical and thermal performances of a pilot PV/T plant. *Energy Conversion and Management*, in press
20. J Avsec, M. Oblak. The calculation of thermal conductivity, viscosity and thermodynamic properties for nanofluids on the basis of statistical nanomechanics. *International Journal of Heat and Mass Transfer* (50), 4331-4341 (2007)
21. B.J. Huang, T.H. Lin, W.C. Hung, F.S. Sun. Performance evaluation of solar photovoltaic/thermal systems. *Solar Energy* (70), 443-448 (2001)
22. T.T. Chow, G. Pei, K.F. Fong, Z. Lin, A.L.S. Chan, J. Ji. Energy and exergy analysis of PV/T collector with and without glass cover. *Applied Energy* (86), 310-316 (2009)
23. S. Furbo, L. J. Shah. Optimum solar collector fluid flow rates, EuroSun '96 - Freiburg, Germany, (1996)



Transient Analysis of Photovoltaic Module Integrated with Phase Change Material (PCM)

Stefano Aneli, Roberta Arena, Antonio Gagliano*

University of Catania, DIEEI, Viale Andrea Doria, 6-95125 Catania, Italy

Corresponding Author Email: antonio.gagliano@unict.it

<https://doi.org/10.18280/ti-ijes.642-409>

ABSTRACT

Received: 25 March 2020

Accepted: 3 June 2020

Keywords:

PCM, PV performances, cells temperature, efficiencies, solidification/melting

This paper focuses on the possibility to improve the performances of the photovoltaic (PV) modules through the passive cooling of photovoltaic cells, using phase change materials (PCMs.) In particular, the use of two organic PCM to reduce the temperature rise in PV module has been investigated by numerical simulations. A two-dimensional fluid dynamic simplified model has been developed in Ansys Fluent software to characterize the thermal behavior of the PV module where the PCM is incorporated (PV-PCM), as well as for a benchmark PV module. The results show that PCMs allow to achieve better performance if compared to PV modules without PCM, with an increase in terms of peak electric power even higher than 9% and in terms of daily energy of about 5% all year round, except for winter. Moreover, the dynamic analysis performed for several days allows to evaluate the effective performance of the PV-PCM, taking into account the real degree of solidification achieved during the night. This analysis shows that the use of PCM with low melting temperature does not guarantee complete solidification during the night and this limits its effectiveness during the day.

1. INTRODUCTION

As the rise in the temperature of photovoltaic (PV) cells leads to a decrease in the solar to electricity conversion efficiency, many methods have been planned to cool the PV cells [1, 2], as well as for increasing their efficiency [3].

They may be differentiated into two major categories, active cooling and passive cooling. The active cooling techniques requires energy to operate, while passive cooling techniques are preferable because they do not require energy supply to operate and less maintenance.

One of the main passive cooling techniques is the use of phase change materials (PCM).

PCMs may enable the PV module to operate with good solar electrical conversion efficiency as they absorb energy as latent heat at a constant phase transition temperature. So, the use of PCM creates a temporary shift in temperature rise [4].

PCM can temporarily store renewable or cheap heat or cold respectively and make it available again later when it is needed, so they may be used in combination with electrical storage [5, 6].

The numerical model and experimental tests developed in [7] has highlighted that a tank of 40 mm of PCM attached to the rear of the PV panel allows controlling the temperature of PV for about 150 min under a solar 2 insolation of 750 W m^{-2} .

Usually, for PV-PCM systems, the melting temperature is about $20\text{--}40^\circ\text{C}$. Using a transitory one-dimensional energy balance model, Kibria et al. [8] studied the effect of the variation of the melting point, obtaining an increase in the performance of the PV-PCM of 5% compared to the standard PV.

It is a fact that the energy flow due to convection inside the melted PCM affects the system's performance significantly [9]. A CFD analysis performed keeping the air temperatures and

solar radiation constant, showing that the greatest electrical producibility is obtained with PCMs that have fusion temperatures close to the air temperatures [10]. Several PCMs analyzed in the paper [11] shown that the increase in latent heat capacity improves the PV performance.

The optimum depth of PCM container to keep the PV cool has been calculated under various daily solar radiation levels in the paper [12]. This study highlights that PCM having a lower melting temperature (near to ambient) can maintain the PV at a lower temperature. Larger quantity PCM of is necessary as ambient temperature increases the optimum depth of PCM container increases and, as wind velocity increases the optimum depth decreases. A very important topic is the study of a PV-PCM performance under real irradiance and environment temperature.

A numerical study using CFD simulation was developed in COMSOL to compare the PV temperature with different PCMs varying solar irradiation and ambient temperature, for two summer days [13]. The results of that study show that the PCM works differently over the two days, even if the working conditions do not change as the PCM does not complete the solidification process overnight due to its low melting temperature. This phenomenon highlights that neglect of the solidification process will lead to inaccurate simulation results, which is an aspect that is not yet deeply considered in the literature.

However, there is a scarcity of both theoretical and experimental studies on PV-PCM system in the Mediterranean area, where more important is the importance to maintain cool the temperature of the PV cells.

To cover this lack of knowledge, this study proposes an unsteady CFD study on a PV module equipped with two different types of PCM installed in Catania (IT).

The daily variation of the cell temperatures, as well as the

electrical performance of the PV-PCM module, are compared with that one of a conventional PV module considering the winter solstice, autumn equinox and summer solstice.

To simulate non-steady state conditions a novel CFD model has been built that allows taking into account of real weather conditions, such as the hourly daily solar irradiation environment temperature, and wind velocity.

The simulations are extended for two days, so in this way, it is possible to verify the actual degree of PCM solidification/melting that occurs during such period.

2. PHASE CHANGE MATERIAL

In the last 15 years, scientists are using PCMs in many and varied applications, the interest in these materials is born because of the possibility to store a remarkable amount of energy maintaining the temperature at a constant value.

Ideal PCMs must have a large latent heat of fusion, usually, it is good to have it greater than 150 J/g, because the greater the latent heat the less the quantity of material needed to store a certain amount of energy high thermal conductivity, the melting temperature must be in the practical range of operations, low cost, non-toxic and non-corrosive. Consequently, it is convenient to have PCM as dense as possible [14]. Another important parameter is the thermal conductivity which represents the ability of a substance to transmit heat, therefore the higher the thermal conductivity the faster the heat transfer. Besides, the solidification and melting temperature must be the same or in any case with small differences, many PCMs freeze or melt in an interval of different degrees and therefore will present thermal hysteresis, which therefore leads to a loss of energy in a system. Furthermore, the latent heaters of the PCM cannot be exploited if the thermal hysteresis exceeds the operating temperature range. Finally, PCMs must be chemically stable, as they are subject to different melting/freezing cycles and this could affect melting and freezing points and their latent heat.

PCMs applications are based on the principle that during solidification PCM emits energy avoiding a sharp reduction in temperature, on the other hand, if the PCM is in solid form, it can subtract a certain amount of heat avoiding overheating. In the case of constant specific heat capacities for each phase, the temperature field, which during the phase change is constant, can be defined as:

$$T = \begin{cases} \frac{E}{c_s} & T < T_m \quad (\text{solid phase}) \\ T_m & T > T_m \text{ and } 0 < E < H \quad (\text{melt zone}) \\ T_m + \frac{(E - H)}{c_l} & T > T_m \text{ and } E > H \quad (\text{liquid ph.}) \end{cases} \quad (1)$$

The use of PCM gives better results in those places where there is a good difference in temperature between day and night, in fact in this way it is possible to guarantee a complete solidification of the PCM overnight and the following day its latent heat can be fully exploited. Obviously, to achieve this, it is necessary to carefully choose the type of PCM to be used and therefore its melting temperature.

Paraffins and in general organic PCMs are more applicable to PV system cooling, as they have excellent thermal stability with regards to cycling, which is important in a system that heats up and cools down daily [15].

3. METHODOLOGY

This study compares the thermal behaviour and the electrical yields of a conventional photovoltaic module (PV) with that one of the same PV module equipped with Phase Change Material (PV-PCM).

The efficiency of PV cells is strongly influenced by the temperature of the cells themselves, temperatures increasing cause the decrease of the efficiency. Furthermore, the layers that make up the panel have a very small thickness and therefore small masses and low thermal inertia. Thus, as soon as the solar irradiation grows, they heat up quickly, making production efficiency decline [16].

One way to keep the module temperature low for longer is to use Phase Change Materials (PCM). In a PV-PCM module, the variation of the temperature of the cells is determined by the behaviour of the PCM, which during the melting process absorb heat without changing its temperature. Figure 1 shows the main thermal fluxes for the PV-PCM, which can be summarized as follows:

- convection and thermal radiation between the front of the PV module (glass) and the outdoor environment;
- reflection of part of the incident solar irradiation on the glass
- transmission and absorption of the incident solar irradiation through the glass
- absorption of the remaining part of the incident solar on the PV cells with the conversion of a part of it into electricity;
- conduction through the different layers;
- heat transfer between the tank wall and the PCM
- storage or disposal of energy during the phase change by the PCM;
- convection and thermal radiation between the back surface of the PV module and the outdoor environment.

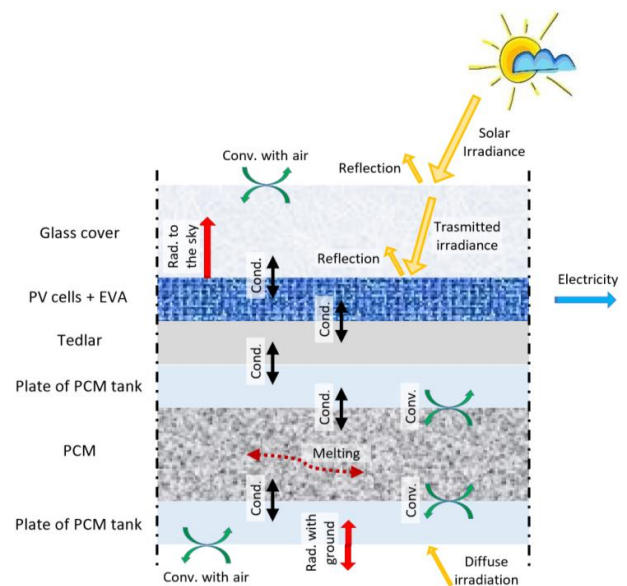


Figure 1. Energy fluxes in PV-PCM module

The container filled with the PCM is constituted by a tank constituted by aluminium sheets.

3.1 CFD simulation

The study of the PV-PCM module through an unsteady state Computational Fluid Dynamics (CFD) analysis allows

evaluating the heat fluxes which occur into the PV module taking into account of the effective thermal inertia of the system, as well as of the melting process.

In this research, the ANSYS Fluent software [17] has been used for simulating the thermal behaviour of both a PV-PCM and a conventional PV module, under dynamic conditions.

The PV panels are simulated considering a bi-dimensional geometry being a length of 1.0 m, which allows to include all the layers that compose the PV module. The mesh is of structured type, composed of only quadrangular elements, where the smallest has size $10^{-4} \times 3 \cdot 10^{-4}$ m and the largest has size $7 \cdot 10^{-4}$ m \times $8 \cdot 10^{-4}$ m.

To check the quality of the mesh the report orthogonally quality and the ortho skew have been detected finding values of 1.0 and 0.0, which indicates that the mesh has a high quality.

The weather conditions (air temperature, solar irradiance and wind velocity) are implemented through User Defined Functions (UDFs), which are assembled for the specific case. The incident solar irradiation used for defining the equations of thermal balance (G_{eff}) is calculated using Eq. (2).

$$G_{eff} = G \cdot \tau_g \cdot \alpha_{PV} \cdot (1 - \eta_{el}) \quad (2)$$

where, G is the total irradiance on the plane of the module, τ_g is the transmission coefficient of irradiation through the glass cover, α_{PV} represents the absorption coefficient of PV cells and η_{el} is the electrical efficiency of the module, calculated using Eq. (3).

$$\eta_{el} = \eta_{STC} [1 - \gamma(T_{PV} - T_{STC})] \quad (3)$$

where, η_{STC} and T_{STC} are respectively the efficiencies and the temperature at Standard Test Condition and γ is the thermal coefficient of the PV panel.

The radiative exchanges between the front of the PV module and the sky-dome have been implemented with a specific UDF and are calculated using the Stefan-Boltzmann law [18]:

$$\dot{q}_{rad,g-sky} = \sigma_0 \cdot \varepsilon \cdot F(T_g^4 - T_{sky}^4) \quad (4)$$

where, σ_0 is the Stefan-Boltzmann constant, ε represent the emissivity of the glass and F is the view factor calculated with Eq. (5), where β is the tilt angle of the PV module.

$$F = \frac{1 + \cos \beta}{2} \quad (5)$$

The radiative exchanges between the rear part of the panel and the ground are calculated once again through Eq (4), where the glass is replaced with the back of the panel and the sky with the ground.

According to the paper [19], the coefficient of convective flux with the air is calculated using Eq. (6), where w represents the wind velocity expressed in m/s.

$$h = 5.7 + 3.8 \cdot w \quad (6)$$

3.2 Energy performance

The electrical efficiency of the photovoltaic panel calculated by Eq. (3), is a function of the temperature of the cells, which in turns is calculated through the CFD simulation.

Thus, the electrical power (P_{el}) produced by the PV panel is calculated from the irradiance on the collector plane G , the

surface of the PV cells and the electrical efficiency:

$$P_{el} = \eta_{el} \cdot A_{PV} \cdot G \quad (7)$$

Finally, the electric energy product is evaluated as:

$$E_{el} = \int P_{el} \cdot dt \quad (8)$$

4. CASE STUDY

The scenarios analyzed refer to a PV module with and without PCM container attached at its rear.

The reference PV module has an STC efficiency (η_{STC}) of 17% and the thermal coefficient (γ) of 0.4%/K.

The features of the layers that compose the PV module are specified in Table 1.

Table 1. Properties of the layers that make up the PV and PV-PCM modules

	C	k	ρ	Thickness
	J/kgK	W/mK	kg/m ³	mm
Glass	500	1.8	3000	4.0
EVA	2090	0.35	960	0.5
Silicon	677	148	2330	0.3
Tedlar	1250	0.2	1200	0.1
Aluminium	903	211	2675	4.0

The PCM's container, composed of two aluminium sheet, has a thickness of 6.0 cm. Such thickness is suggested by Ma et al. [11] when the solar radiations and outdoor temperatures are high, and the wind velocities are low.

Two different types of PCM are investigated in this study: Rubitherm 28 HC and Rubitherm 35 HC. These PCMs have chosen since they have good stability and high capacity to accumulate energy during the solidification/melting transformation. Table 2 shows the main properties of the PCMs used.

Table 2. Properties of the used PCM materials

		Rubitherm28 HC	Rubitherm 35 HC
$T_{melting}$	°C	27-29	34-36
$T_{congeling}$	°C	29-27	36-34
H^1	kJ/kg	250	240
C_P	kJ/kgK	2.00	2.00
ρ_{solid}	kg/l	0.88	0.88
ρ_{liquid}	kg/l	0.77	0.77
k	W/mK	0.20	0.20

Notes: 1 Combination of latent and sensible heat in a temperature range, respectively for Rubitherm 28 HC and 35 HC from 21°C to 36°C and from 27°C to 42.

The simulations are carried out considering the two investigated PV modules, with and without the addition of the PCM, located in Catania (IT) (37° 30' 0" N - 15° 6' 0" E). It was assumed that the modules facing south, with a tilt angle of 30 degrees. The weather data, solar irradiation and air temperature were derived from the PV-GIS database [20] considering clear days.

All the analyses are developed considering three annual "representative" days: the winter solstice, autumn equinox and summer solstice.

Figure 2 shows the outdoor temperature (continuous line)

and the incident solar irradiation (dashed line) during those three days.

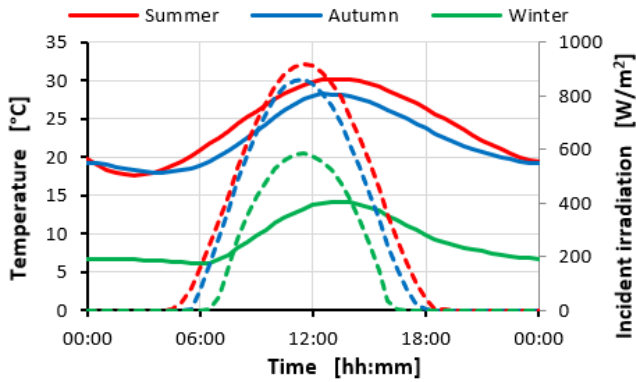


Figure 2. Weather data on the summer solstice, autumn equinox and winter solstice

As regards the wind speed it is assumed constant and equal to 1.0 m/s.

5. RESULTS

This section compares the thermodynamic behaviours and the energy performance of the conventional PV module with the two PV-PCM modules, equipped one with Rubitherm RT 28 HC (PV-RT28) and the other with Rubitherm RT 35 HC (PV-RT35).

To properly evaluate the effective performances of a PV-PCM module it is mandatory taking into account the degree of solidification achieved by the PCM during the night. Thus, the analysis is conducted for a simulation time of 48 h.

In the following, the results showed are referred to the second day of simulation.

Figure 3 shows the comparisons of the temperature of the photovoltaic cells obtained for the three PV-configurations analyzed during the summer solstice.

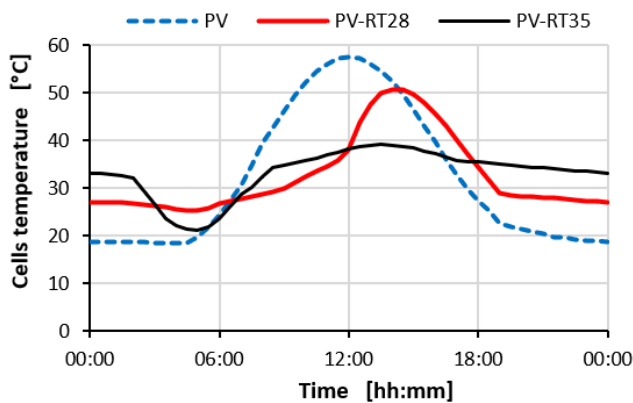


Figure 3. PV cells temperature during the summer solstice

It is evident that the attachment of the PCMs in the PV-module allow decreasing of the cell temperatures. It can be noted that the PV-RT35 leads to attaining a reduction of the cell temperature during the whole day, up to a maximum of 20°C at midday. PV-RT28 shows the same or even higher reduction of temperature in the first half of the day, then about at noon the temperature raises abruptly as the RT28 loses its

capacity to store the heat, the liquefaction process is completed. The highest temperature of the cells PV-RT28 is 8 °C lower than the maximum temperature touched by the conventional PV module. However, in the second part of the afternoon, after 16:30 for the PV-RT35, and at least one hour before for the PV-RT28, the cell temperatures are higher than that one of the conventional PV module.

Figure 4 shows the rate of liquefaction of the two PCMs at 4:30 and 12:00.

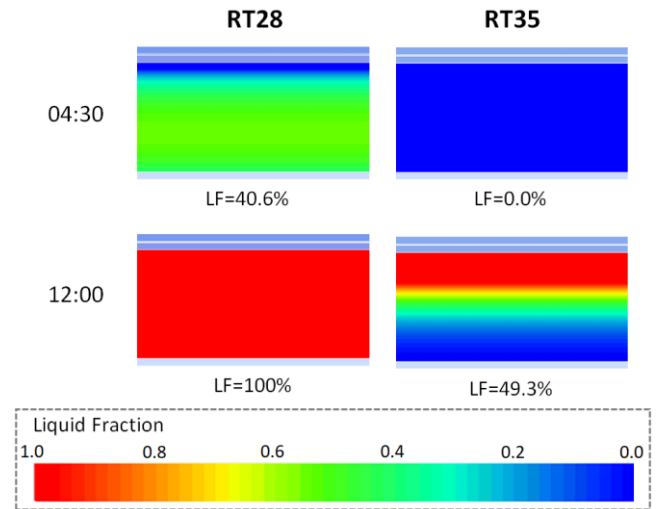


Figure 4. Liquid fraction on the summer solstice

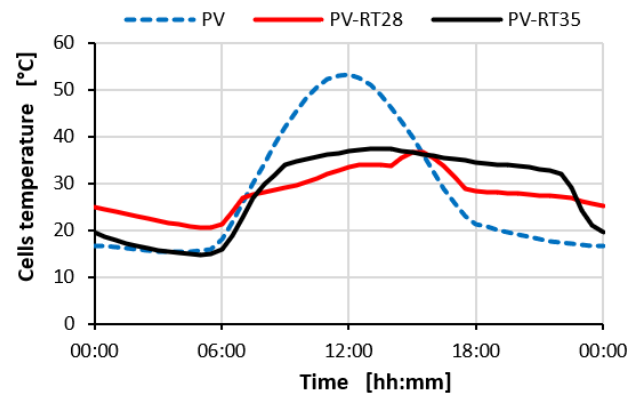


Figure 5. PV cells temperature profile on the autumn equinox

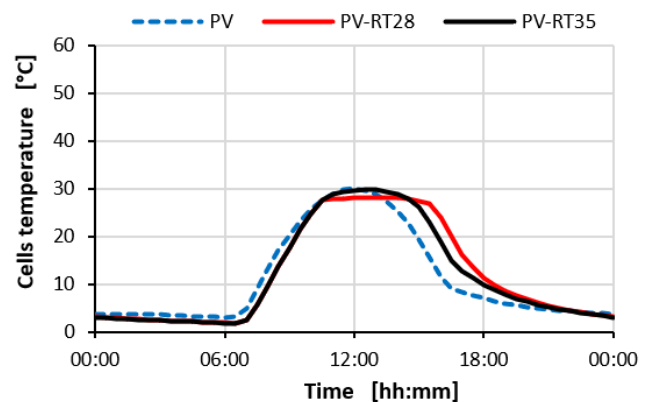


Figure 6. PV cells temperature profile on the winter solstice

It can be observed that at midnight the RT28 is completely melted otherwise, the RT35 has a liquid fraction of 49.3%.

Moreover, RT35 works all day, reaching the maximum liquid fraction of 93.8% at 16:30. Finally, it is important to note, that RT28 does not solidify completely overnight, which reaches the lowest liquid fraction of 40.6% at 4:30, while RT35 solidifies completely during the night.

Figures 5 and 6 depict the temperature of the cells respectively for the autumn equinox and winter solstice.

On the autumn equinox, the lower outdoor temperature and solar irradiation represent almost ideal conditions for the operation of PV-PCM equipped with RT28.

The PV-RT28 module operates effectively for all the daily hours by keeping its temperatures lower than the other configurations. Otherwise, RT35 is less effective in cooling the panel, PV-RT35 reaches temperatures higher than PV-RT28PCM. This reversal of behaviour is due to the difficulty for RT35 in reaching the solid/liquid transition temperature for these weather conditions. Anyway, also in this period of the year, the conventional PV-module operates at temperatures higher than both PV-PCM modules. Actually, as in the summer, in the last part of the day, the conventional PV module has lower temperatures than both PV-PCM modules, but in that period of the day the solar radiation is very low and, consequently, such drawbacks have scarce relevance.

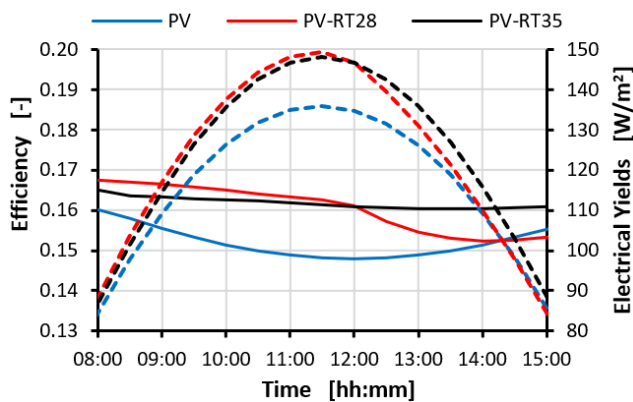


Figure 7. Efficiency and electrical power on the summer solstice

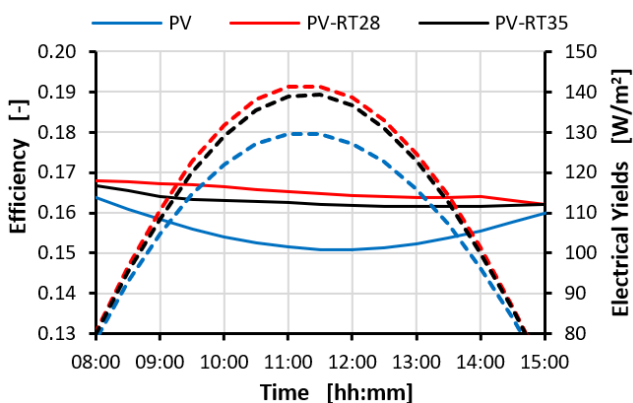


Figure 8. Efficiency and electrical power on the autumn equinox

Results in Figure 6 highlights that on the winter solstice, there is no remarkable difference among the cell's temperature of the three module configurations. Indeed, the PV cells of a conventional module are lower than 30°C, so the RT35 do not melt, while the PV-RT28 keeps its temperatures at about 28°C,

which is the melting point of this PCM. In the last part of the day, it's possible to notice again an increase in temperature of the PV-PCM modules, due to the increase of the thermal resistance of the PV-PCM modules that delayed the cooling of the PV cells.

Figures 7 and 8 depict the electrical efficiency (continuous lines) and the electrical power (dashed lines) during the summer solstice and the autumn equinox.

The results obtained on the winter solstice are not shown since the efficiency and electrical power are very similar for all the three scenarios due to the very similar cell temperatures.

As shown in Figure 7 the conventional PV module has efficiency and power production lower than both PV-RT28 and PV-RT35 modules. In particular, on the summer solstice in the first part of the day, the PV-RT28 has the highest efficiency, close to η_{STC} , while after midday due to exhaustion of PCM work, the efficiency decreases quickly.

Otherwise, the PV-RT35 maintains fairly high efficiency throughout the day, greater than 16%. This trend is repeated for electrical power production it depends on the available solar irradiation and electrical efficiency. Globally, the use of PCMs allows an increase in power production greater than 10.00 W/m², which is about 10%, during peak hours.

On the autumn equinox, the conventional PV module once again attains the lowest efficiency and power production are the smallest using. In this case, the cell temperatures of the two PV-PCMs modules are very similar during the whole day. So, it is not repeated the decrease of efficiency for the PV-RT28, that was observed after midday on the summer solstice. On this day the presence of PCMs allows an increase in power production during the peak hours of approximately 9.1% and 7.5% respectively using RT28 and RT35. On the winter solstice, as can be deduced from the temperature of the cell in figure 6, there are no remarkable differences between the three PV module, neither in electrical efficiency nor in electrical power.

Figure 9 reports the daily electrical yields on the three analyzed days for the three PV-module configurations.

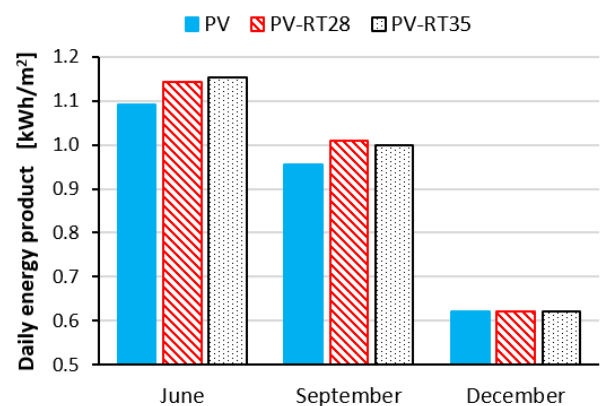


Figure 9. Daily electrical yields

These results reflect what has been already highlighted examining the daily profile of electrical efficiency and power production. The daily electrical yields values, on the winter solstice, are almost the same for the three PV-module configurations, whereas on autumn equinox and summer solstice the lowest yields occur in the case of PV-module. The implementation of PCMs improves the performances of PV-modules both on the summer solstice and autumn equinox. On the summer solstice, the daily electrical yields rose by

4.6% using RT28 and by 5.6 % using RT35. Otherwise, on the autumn equinox, this PV- RT28 is the system which has the highest energy production with an increase of about 5.7%, respect to the conventional PV-module, whereas PV- RT35 allows achieving an increase of the daily energy produced of about 4.4%. This finding highlights the importance to carefully choose the type of PCM looking to the climatic conditions of the site of interest. In particular, an important element that has to be observed is the liquefaction temperature of the PCM, and also its complete solidification during the night.

6. CONCLUSIONS

In this study, through CFD analysis, the thermal behavior and the electrical performance of PV-PCM module equipped with two different types of PCM have been evaluated and their performances are compared with that one of a conventional PV module under the same operative conditions.

Using the Fluent simulation software, a model capable of simulating the transfer of heat, mass and momentum of a PCM connected behind a photovoltaic module was developed.

The analyzes were carried out considering the weather conditions of the city of Catania (IT) for different periods of the year.

The simulations were carried out for several consecutive days in such a way to not overlook the actual degree of solidification obtained during the night.

The results of simulations highlight that the use of PCM allows an increase in electrical performance compared to the conventional PV module except on the winter solstice when the cell temperatures and therefore the photovoltaic efficiency are very similar for all the configurations studied.

In detail, the adoption of PV-PCMs allows an increase in terms of peak electric power even higher than 9% compared to PV modules without PCM and an increase of the daily energy yield of about 5.5%.

In general, the use of RT28, which has melting temperatures lower than RT-25 improves the efficiency thanks to its globally greater cooling effect.

However, during the summer days, during very hot days the RT28 runs out of its functionality and the RT-35 perform better in particular after midday. This is also due to the difficulty of solidifying completely during the night for RT 28.

Therefore, it is necessary to carefully choose the type of PCM to be used, observing the climatic conditions of the site of interest throughout the year.

ACKNOWLEDGMENT

This research is funded by “the Notice 12/2017 for financing the Ph.D. regional grant in Sicily” as part of Operational Program of European Social Funding 2014-2020 (PO FSE 2014-2020).

This work was also financed by the University of Catania within the project "Piano della Ricerca Dipartimentale 2016–2018" of the Department of Electric, Electronics and Computer Engineering of the University of Catania.

REFERENCES

[1] Zubeer, S.A., Mohammed, H.A., Ilkan, M. (2017). A

- review of photovoltaic cells cooling techniques. In E3S Web of Conferences, 22: 00205. <https://doi.org/10.1051/e3sconf/20172200205>
- [2] Siecker, J., Kusakana, K., Numbi, B.P. (2017). A review of solar photovoltaic systems cooling technologies. *Renewable and Sustainable Energy Reviews*, 79: 192-203. <https://doi.org/10.1016/j.rser.2017.05.053>
- [3] Scavo, F.B., Tina, G.M., Gagliano, A., Nižetić, S. (2020). An assessment study of evaporation rate models on a water basin with floating photovoltaic plants. *International Journal of Energy Research*. <https://doi.org/10.1002/er.5170>
- [4] Atkin, P., Farid, M.M. (2015). Improving the efficiency of photovoltaic cells using PCM infused graphite and aluminium fins. *Solar Energy*, 114: 217-228. <https://doi.org/10.1016/j.solener.2015.01.037>
- [5] Gagliano, A., Nocera, F. (2017). Analysis of the performances of electric energy storage in residential applications. *International Journal of Heat and Technology*, 35(S1): S41-S48. <https://doi.org/10.18280/ijht.35Sp0106>
- [6] Buonomo, B., Cirillo, L., Diana, A., di Pasqua, A., Ercole, D., Fardella, V., Manca, O., Nardini, S. (2020). Thermal Energy Storage Systems, 64: 39-44. <https://doi.org/10.18280/ti-ijes.640108>
- [7] Huang, M.J., Eames, P.C., Norton, B. (2004). Thermal regulation of building-integrated photovoltaics using phase change materials. *International Journal of heat and mass transfer*, 47(12-13): 2715-2733. <https://doi.org/10.1016/j.ijheatmasstransfer.2003.11.015>
- [8] Kibria, M.A., Saidur, R., Al-Sulaiman, F.A., Aziz, M.M.A. (2016). Development of a thermal model for a hybrid photovoltaic module and phase change materials storage integrated in buildings. *Solar Energy*, 124: 114-123. <https://doi.org/10.1016/j.solener.2015.11.027>
- [9] Kant, K., Shukla, A., Sharma, A., Biwole, P.H. (2016). Heat transfer studies of photovoltaic panel coupled with phase change material. *Solar Energy*, 140: 151-161. <https://doi.org/10.1016/j.solener.2016.11.006>
- [10] Khanna, S., Reddy, K.S., Mallick, T.K. (2017). Performance analysis of tilted photovoltaic system integrated with phase change material under varying operating conditions. *Energy*, 133: 887-899. <https://doi.org/10.1016/j.energy.2017.05.150>
- [11] Ma, T., Zhao, J., Han, J. (2017). A parametric study about the potential to integrate phase change material into photovoltaic panel. *Energy Procedia*, 142: 648-654. <https://doi.org/10.1016/j.egypro.2017.12.107>
- [12] Strith, U. (2016). Increasing the efficiency of PV panel with the use of PCM. *Renewable Energy*, 97: 671-679. <https://doi.org/10.1016/j.renene.2016.06.011>
- [13] Nouira, M., Sammouda, H. (2018). Numerical study of an inclined photovoltaic system coupled with phase change material under various operating conditions. *Applied Thermal Engineering*, 141: 958-975. <https://doi.org/10.1016/j.applthermaleng.2018.06.039>
- [14] Farid, M.M., Khudhair, A.M., Razack, S.A.K., Al-Hallaj, S. (2004). A review on phase change energy storage: materials and applications. *Energy conversion and management*, 45(9-10): 1597-1615. <https://doi.org/10.1016/j.enconman.2003.09.015>
- [15] Gibbs, B.M., Hasnain, S.M. (1995). DSC study of technical grade phase change heat storage materials for solar heating applications (No. CONF-950336-).

American Society of Mechanical Engineers, New York, NY (United States).

- [16] Tina, G.M., Gagliano, A. (2016). An improved multi-layer thermal model for photovoltaic modules. In 2016 International Multidisciplinary Conference on Computer and Energy Science (SpliTech), 1-6.
- [17] Ansys, I.N.C. (2020). ANSYS FLUENT user's guide. Canonsburg, PA.
- [18] Gagliano, A., Aneli, S. (2020). Analysis of the energy performance of an Opaque Ventilated Façade under winter and summer weather conditions. *Solar Energy*, 205: 531-544. <https://doi.org/10.1016/j.solener.2020.05.078>
- [19] Skoplaki, E., Boudouvis, A., Palyvos, J. (2008). A simple correlation for the operating temperature of photovoltaic modules of arbitrary mounting. *Solar Energy Materials and Solar Cells*, 92(11): 1393-1402. <https://doi.org/10.1016/j.solmat.2008.05.016>
- [20] <https://ec.europa.eu/jrc/en/pvgis>, accessed on 20 March 2020.

NOMENCLATURE

C	specific heat, J. kg ⁻¹ . K ⁻¹
E	energy, J
F	dimensionless view factor
G	solar irradiation, W. m ⁻²
H	latent heat, J. kg ⁻¹
H	convection coefficient, W. m ⁻² . K ⁻¹
LF	dimensionless liquid fraction

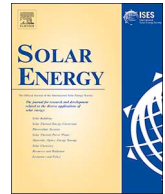
K	Thermal conductivity, W. m ⁻¹ . K ⁻¹
P	power, W
q̇	heat flux, W. m ⁻²
T	temperature, °C
w	wind speed, m. s ⁻¹

Greek symbols

α	dimensionless absorption coefficient
β	tilt angle, rad
γ	thermal coefficient, K ⁻¹
ε	dimensionless emessivity
η	dimensionless, efficiency
ρ	density, kg. m ⁻³
σ ₀	Stefan-Boltzmann constant, W. m ⁻² . K ⁻⁴
τ	dimensionless transmission coefficient

Subscripts

eff	effective, available
el	electrical
g	glass cover
l	liquid phase
m	melting
PV	photovoltaic cells
rad	radiative flux
s	solid phase
sky	sky dome
STC	standard test conditions



Analysis of the energy performance of an Opaque Ventilated Façade under winter and summer weather conditions

A. Gagliano*, S. Aneli

Department of Electrical Electronic and Informatics Engineering, Viale Andrea Doria 6, 95125 Catania, Italy

ARTICLE INFO

Keywords:

Ventilated facade
Computational fluid dynamic
Energy saving

ABSTRACT

Nowadays, there is continuing worrying about energy efficiency and the reduction of GHG emissions in the building sector. It has been claimed that ventilated building envelopes help to reduce energy use in buildings and improve occupant comfort.

This study proposes a comprehensive comparison of the thermal behaviour between an Opaque Ventilated Façade (OVF) and a conventional unventilated Façade (UF) considering two reference days for the winter and summer period. The analysis is developed investigating different façade orientations and two states of windiness, which are a state of calm wind and a state with wind velocity higher than zero (i.e. 5.0 m/s at 10 m of height) are taken into account.

These analyses were developed utilizing fluid-dynamic calculation under dynamic conditions. Thus for the two façades were calculated: (I) the hourly surface temperatures of the most external, (II) the temperature profiles for all the facade's layers; (III) the airflow profiles inside the cavity and near the façade; (IV) the hourly thermal fluxes that cross the façade.

Finally, the daily energy fluxes and the energy-saving, achievable through the adoption of the OVF, is calculated for the different façade exposures and the conditions of windiness.

The outcomes of this study highlight that the OVF guarantees an energy-saving ranging from 20 to 55%, with the highest rate during the summer day for the façade facing East/West.

1. Introduction

Tackling climate change is a common priority, due to ethical issues related to the general concept of sustainability and a viable future. In recent years, a global warming process is underway that will surely make the evolution of the quality of life on earth alarming.

Reducing GHG emissions and energy waste are two of the main objectives of international policy. The International Energy Agency estimated that in the United States energy consumption in the building sector is 45% and in Europe, it is around 40%, where for example in the United Kingdom it is around 42% whereas, in Italy, it is 40% (IEA, 2012). In Europe, the energy consumption of buildings built before 1990 played a higher impact, i.e. before adopting a common energy-saving policy (European Environment Agency, 2014).

EU countries are promoting the development of more efficient cities where an important role is played by the figure of net-zero-energy buildings. One of the main objectives of the energy design of buildings is to take advantages of the thermophysical characteristics of the material used, which should be climate-responsive (W.D. Seo et al., 2013).

The efficient design reduces thermal fluxes between outdoor and indoor space, as well as the overheating effect due to solar radiation (Arce et al., 2009; Giancola et al., 2014). The energy performance of buildings directive (EU Directive, 2012) emphasized the urgency of adopting strategies that contribute to improving the thermal performance of new and existing buildings.

Although the energy demand of energy-intensive buildings could be, partially or totally, balanced by the widespread use of renewable energy sources, this nevertheless represents a waste of clean energy and does not meet the problem of the urban heat islands (Ascione, 2017).

The most common retrofit intervention on the building envelope is the laying of an external thermal insulation coating system (ETICS), which allows a significant reduction in the thermal transmittance of the opaque façades and the consequent reduction of energy consumptions (Kolaitis et al., 2013; Alonso et al., 2016; Gagliano et al., 2017; Mandilaras et al., 2014). On the other hand, the thermal coat can increase the energy requirement during the cooling period and create problems of transpiration of the façades if not properly designed (Garay et al., 2017; ENEA, 2015).

* Corresponding author.

E-mail address: antonio.gagliano@unict.it (A. Gagliano).

Nomenclature

C_p	specific heat at pressure constant, [J kg ⁻¹ K ⁻¹]
ES	energy saving rate, [%]
F_{W-sky}	wall sky view factor, [-]
h_i	heat transfer coefficient at the inside of the internal wall, [W/m ² K]
$Q_{(OVF,UF) incoming}$	heat fluxes incoming through the façade, [W/m ² K]
$Q_{(OVF,UF) outgoing}$	heat fluxes outgoing through the façade, [W/m ² K]
OVF	Opaque Ventilated Façade,
UF	unventilated façade,
R_{OVF}	thermal resistance of the layer of the ventilated façade starting from the ventilated cavity, [m ² K/W]
R_{UF}	thermal resistance of the layer of the unventilated façade starting from the external layer, [m ² K/W]
T_o	air temperature of the outdoor environment, [K]
T_i	air temperature of the indoor environment, [K]
TS_1	indoor superficial temperature, [K]
$TS_4 (OVF)$	superficial temperature of the outer layer of the ventilated

	cavity, [K]
$TS_4 (OVF)$	superficial temperature of the outer layer of the ventilated cavity, [K]
T_{sky}	sky temperature, [K]
U_r	wind speed at reference height, [m/s]
$U(z)$	wind speed at “z” height, [m/s]
z	height, [m]
z_r	reference height, [m]

Greek symbols

β	tilt angle of the surface measured from horizontal [-]
γ	coefficient that takes into account the features of the surrounding environment [-]
ε	emissivity, [-]
λ	thermal conductivity [W m ⁻¹ K ⁻¹]
μ	dynamic viscosity [kg m ⁻¹ s ⁻¹]
ρ	density [kg m ⁻³]
σ	Stefan-Boltzmann constant [W m ⁻² K ⁻⁴]
τ	time [hour]

Ventilated facades and ventilated roofs can be used in addition to the thermal coat (Barbosa et al., 2014; Soutullo et al., 2016), so increasing the thermal resistance of the opaque envelope (Sanjuan et al., 2011; De Gracia et al., 2013), and significantly reduce the thermal loads during the cooling period (Bianco et al., 2016; Gagliano et al., 2016). Besides, ventilated façades reduce building humidity problems: rain penetration, frost damage, decomposition, corrosion, mould growth and discolouration of building materials (Yang et al., 2019; Collinart et al., 2019; Leccese et al., 2019; Nizovtsev et al., 2014).

The main parameters that influence the thermal performance of Opaque Ventilated Facades (OVFs) are discussed in (Ibañez-Puy et al., 2017). The most appropriate OVF configuration have to be defined climate by climate and building by building (Elarga et al., 2015).

The analysis of the performance of the OVFs as a function of the climate indicates that the warmer the climatic region the greater is the energetic advantage of the ventilated façades (Fernandes et al., 2019).

This research is also focused on the study of the parameters that influence the performance of the OVFs.

The experimental study on the position of a mass in the cavity shows that the greatest efficiency about cooling is obtained by increasing the thermal capacity of the outermost layer (Stazi et al., 2018). Another important factor is the position and the size of the openings that connect the air channel to the outside (Buratti et al., 2018).

Several studies are devoted to the characterizations of the airflow in open joint ventilated facades (OJVF), for which the ventilation is attained through the open joints between the panels composing the outer layer. (Sánchez et al., 2017) observed experimentally for an open joint ventilated facade that the characteristics of the openings determine the airflow in the ventilated cavities. Although the air-flow is always turbulent, the velocity profile along the cavity assumes different shapes. In particular, at the entrance where the horizontal joints generate recirculation vortices.

(Sánchez et al., 2020) assessed the airflow in an open OJVF both by a numerical model and experimental tests.

The reliability of current different experimental methodologies and the most relevant monitoring techniques for characterisation of airflow in the ventilated cavities are discussed in (Giancola et al., 2018).

In the mission to improve the thermal performance of ventilated façades, the effect of emissivity was analyzed in a double-wall façade with a closed cavity (Aketouane et al., 2016). It is pointed out that low emissivity drastically reduces the heat transfer coefficient by radiation, and consequently, the cooling load diminished of 24%.

The performances of ventilated envelopes during the whole year, so

including also the heating period, are mainly devoted to envelope equipped with “active” airflow control and or energy recovery systems (Astorqui et al., 2017; Diallo et al., 2017). Other researchers have evaluated the performances of solar systems integrated into a ventilated envelope (Liang et al., 2018; Gagliano et al., 2019). A Ventilated Active Thermoelectric Envelope (VATE) module designed to be installed in the building façade as an alternative solution for providing heating and cooling in Net Zero Energy Building is presented in (Zuazu-Rosa et al., 2018). However, in literature, there is a lack of studies regarding the analysis of the thermal behaviour of opaque ventilated facades both for winter and summer days as well as on the effects of the wind action.

This study proposes a novel approach for analysing the thermal behaviour of an Opaque Ventilated Façade (OVF) in the summer and the winter period, as well as the comparison of the OVF energy performance with that one of a conventional Unventilated Façade (UF). Moreover, the effect of the façade orientation and the surrounding wind on the energy performances of the OVF has been investigated.

These comparisons have been developed having as reference the real weather conditions of an Italian city, located in the south of Italy, for both a winter and a summer day.

This study has been carried out by means transitory fluid-dynamic simulations developed through the software FLUENT. For performing realistic transitory fluid-dynamic simulations, it is indispensable to draw-up a specific procedure, which allows to include into the governing equations the variation of the weather conditions (e.g. solar radiation, air temperature, wind velocity and direction).

Thus, for the two façades, OVF and UF (I) the hourly external surface temperatures; (II) the temperature profiles in the façade’s layers; (III) the airflow profiles inside the cavity and near the façade; (IV) the hourly thermal fluxes that cross the façades, were evaluated.

Finally, the daily energy fluxes attainable through the implementation of an OVF is calculated for the different façade exposures, wind status and the energy-saving as well.

This paper is structured as follows. The first section proposes a general analysis of the ventilated facades and describes the studied system and the methodological approach followed. The second section illustrates the main findings of the investigated case study. The third section reports the results of the thermal behaviour for the winter and summer period as a function of the façade orientation and windiness for both the OVF and UF. Then, the Energy Savings for the different examined scenarios is assessed.

In the end, the discussion of the results and the conclusions of this study are proposed.

2. Methodology

2.1. Thermal behaviour of ventilated building envelopes

The building envelope has to protect and separate as much as possible the indoor space from the climate-forcing, which during the year presents great variations concerning temperature, solar radiation, wind, air humidity (Castell et al., 2014).

The heat fluxes exchanged between the building façades and the external environment are governed by the three basic mechanisms of heat transfer: radiation, convection, and conduction.

For a conventional unventilated façade, the following thermal fluxes occur:

- convection and thermal radiation between the inner slab of the façade and the indoor environment;
- conduction through the different layers of the facade;
- convection and thermal radiation between the outer slab of the building wall and the outdoor environment;

These heat fluxes differ greatly in the case of the so-called opaque ventilated facades (OVF).

The main difference between a ventilated and an unventilated façade (UF) lies in the presence of an additional layer (counter-wall) which forms a channel where the air can circulate freely.

The counter wall has the function of constituting a shield for the radiative heat fluxes as well as for the incident solar irradiation. The airflow within the cavity forms a sort of barrier that allows keeping the internal layers of the building envelope dry. Thus, the combined effects of the counter wall and the airflow in the channel create a most muffled microclimate.

The fluid dynamic processes that occur within the ventilated cavity, as well as the screen effect of the counter-wall, are the main causes of the different thermal behaviour of UF and OVF.

Convection inside the channel is fundamentally caused by the air-flow rates and the difference of temperatures between the wall surfaces and the air stream.

In the absence of wind, the airflow through the air gap is only driven by the temperature gradient, which generates a chimney effect due to buoyancy forces, free-convection. Otherwise, when wind velocity is higher than zero, the airflow rates within the air gap is due both to mechanical and buoyancy forces. Moreover, the airflow rate will depend even by the intensity and the main wind direction.

The counter-wall absorbs a portion of the incident solar irradiation, as the function of its absorption coefficient, increasing its temperature. Thus, a part of the stored energy is reemitted as thermal radiation to the outdoor environment and the internal wall, and through convection to the airflow in the channel and the outdoor air. Consequently, a reduction of the solar gain of the building envelope is attained.

This could appear as a controversial outcome because during the winter period the solar gains reduce the energy needs for space heating while in summer period solar gains increase the energy need for space cooling. However, as will be shown in the following, globally the installation of an OVF allows reducing the energy demands for space heating thanks to the reduction of the thermal losses through the building facade.

The thermal fluxes involved in an Opaque Ventilated Facade are depicted in Fig. 1.

2.2. Thermal fluxes in steady-state conditions

As well known under the steady-state condition the heat flux through an unventilated façade (UF) is calculated by Eq. (1)

$$Q = \frac{(T_o - T_i)}{R} A [W] \tag{1}$$

where the thermal resistance R is calculated by Eq. (2), T_o and T_i are the outdoor and indoor temperature and A is the surface of the façade

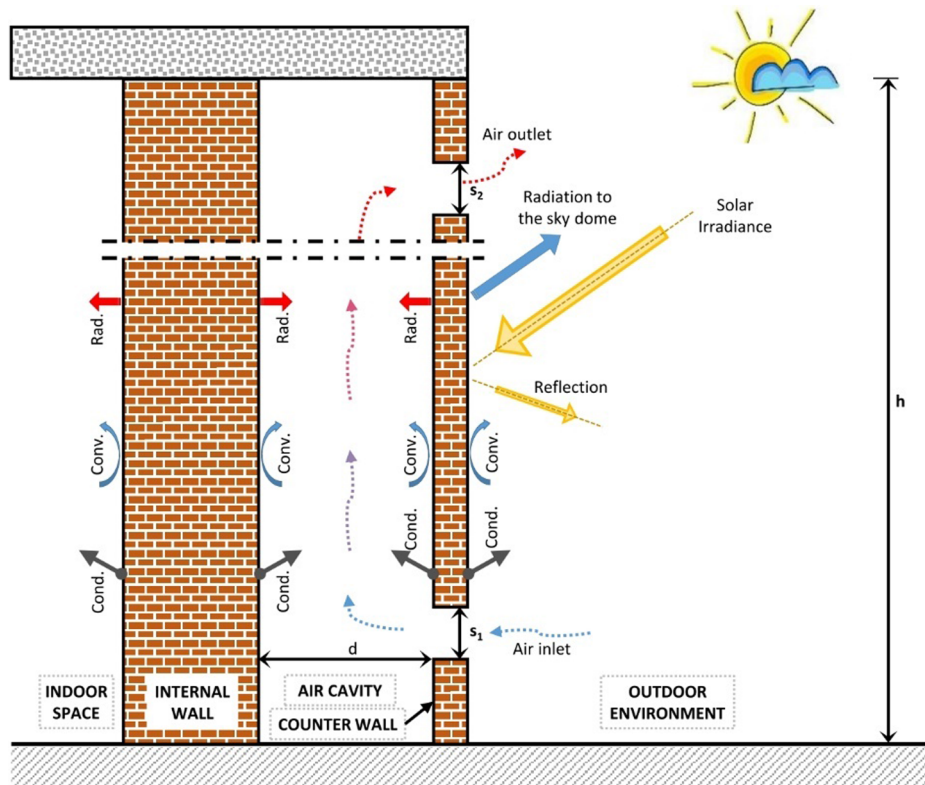


Fig. 1. Thermal fluxes for the OVF.

$$R = \frac{1}{h_i} + \sum_{j=1}^n \frac{s_j}{k_j} + \frac{1}{h_e} \left[\frac{K \cdot m^2}{W} \right] \quad (2)$$

where s_j and k_j are the thickness and thermal conductivity of the j_{th} layer of the façade, n is the number of layers, h_i and h_e are the indoor and outdoor heat transfer coefficients.

These coefficients, h_i and h_e , which include both the convection and radiation thermal exchange, conventionally are assumed to be 7.7 and 25.0 W/m²K (UNI EN ISO 6946, 2008).

Unlike, for OVs the thermal resistance calculation procedure is more complex (UNI 11018,2003; DTU P50-702, 1997) since it is necessary to take into account the ventilation of the interspace, which also depends on the size of the openings.

The OVs can be classified in very weakly ventilated, weakly ventilated and strongly ventilated, using the ratio between the surface of the openings (s) and that of the length of the façade (L), as shown in Table 1.

For very weakly ventilated façades, the thermal resistance is calculated using Eq. (2) considering the cavity as unventilated. In this case, the counter-wall and the air gap contribute to increasing the total thermal resistance of the facade.

In the case of weakly ventilated façades, the thermal resistance is calculated using the follows equation:

$$R = \frac{1}{U_0 + J \left(\frac{U_0}{U_e} \right)^2} \left[\frac{K \cdot m^2}{W} \right] \quad (3)$$

where:

- U_0 is the overall heat transfer coefficient considering the cavity not ventilated
- U_e is the heat transmission coefficient of the counter wall
- J is a coefficient function of the ratio s/L , U_0/U_e and sum ($U_i + U_e$);
- U_i is the heat transfer coefficient of the internal wall

For strongly ventilated façades the thermal resistance is calculated using Eq. (2) neglecting the counter-wall and modifying the values of the heat transfer coefficients as follows:

$$\frac{1}{h_i} + \frac{1}{h_e} = 0.22 \left[\frac{K \cdot m^2}{W} \right] \quad (4)$$

Thus, comparing an unventilated façade and a very strong ventilated facade with the same stratigraphy, the thermal resistance R of the two facades differs of about 0.05 m²K/W.

It is worth of interest to underline that, for a building façade with a thermal resistance of about 2.0 m²K/W ($U = 0.5$ W/m²K), such difference is just of 2.5% of the thermal resistance of such facade.

This means that the steady-state analysis for a very strongly ventilated facade gives place to a reduction of the thermal fluxes of about 2.5%, which is incomparable with the not steady-state analysis that evaluates energy savings from 20.0 to 50.0% during summer days. Therefore, the performances of ventilated facades cannot be analysed through a steady-state analysis but it is mandatory a transient analysis (i.e. using CFD tools).

2.3. CFD analysis

A Computational Fluid Dynamics (CFD) analysis can be applied for evaluating the thermal behaviour of both the Opaque Ventilated Façade as well as the unventilated facade under variable weather conditions.

In this study, the ANSYS Fluent software (ANSYS Fluent, 2015, a) is used for assessing the dynamic thermal behaviour and the energy performances for both ventilated and unventilated façades.

The governing equations are solved through the Finite Volume Method (FVM), adopting the second-order upwind discretization scheme and the standard RNG k-epsilon model among the available

RANS turbulence models complex (Sanjuan et al., 2011; Diarce et al., 2014).

Then, the discrete ordinates (DO) radiation model converts the radiative transfer equation (RTE) into transport equations for radiation intensity in the spatial coordinates. Further specification on these transport equations can be found in the software manual (ANSYS Fluent, 2015b).

In the light of experimental and simulation literature studies (Diarce et al., 2014; Patania et al., 2010), which indicate that for a given height the temperature difference along the width of the façade was not significant, a two-dimensional geometric model of the building façades is adopted.

To take into account the not negligible effects of the wind on the building facade, the two-dimensional computational domain must be extended to a portion of the outdoor environment for evaluating the barrier effects of the façade on the wind field (Gagliano et al., 2016).

A preliminary analysis indicated that it is sufficient to stretch the calculation domain at least 4.00 m beyond the façade, that is about 3/4 of the façade's height.

The mesh in the calculation domain is constituted by quad and triangular elements.

In particular, the different layers belonging the façade, solid and fluid, are discretized through a “structured” mesh, with a width from 0.5 to 1.5 cm and height of 2.0 cm.

An “unstructured” mesh is used in the near-wall zones, where more complex fluid structures and heat transfer processes occur, since such mesh allows varying the size of the cells from 2.0 to 10.0 cm, respectively adjacent to the wall and far away from the solid surface.

The hourly variation of the weather conditions (air temperature, solar irradiation), as well as the wind shear, which are the boundary conditions, are defined setting-up a specific User Defined Functions (UDF) that can be dynamically loaded in ANSYS Fluent.

The numerical convergence of the CFD model is checked using the scaled numerical residuals of all the computed variables. Usually, the value of 10⁻³ is adequate for continuity, velocity and turbulence residuals, while energy and radiation residuals the value of 10⁻⁶ is necessary.

2.3.1. Model assumptions

The principal assumptions adopted in the numerical models are summarized in the follows.

The air viscosity is calculated referring to an isobaric transformation for a perfect gas using Eq. (5),

$$\mu(T) = \mu_0 \sqrt{\frac{T_a}{300}} \quad (5)$$

where μ_0 is the dynamic viscosity, being 1.85 × 10⁻⁵ kg m⁻¹ s⁻¹ (at 300 K) and T_a is the air temperature:

The vertical profile of wind velocity is calculated through Eq. (6),

$$U(z) = U \left(\frac{z}{z_r} \right)^\gamma \quad (6)$$

where U is the wind velocity measured at 10 m by ground, z and z_r are respectively the current and the altitude where the wind velocity is measured (10 m), and γ is a coefficient that takes into account orography and roughness of the surrounding environment.

Table 1
classification of ventilated façades (UNI 11018,2003; DTU P50-702, 1997).

Ratio $X = s/L$	Classification of OVF
$X \leq 0.002$	very weakly ventilated
$0.002 < X < 0.05$	weakly ventilated
$X \geq 0.05$	strongly ventilated

The radiative heat fluxes between the outer surface of the façades and the sky are taken into account by Eq. (7),

$$q_{rad} = \varepsilon \sigma F_{w-sky} (T_{so}^4 - T_{sky}^4) \left[\frac{W}{m^2} \right] \quad (7)$$

where F_{w-sky} is the wall-sky view factor, T_{so} is the surface temperature of the outer surface of the façade and T_{sky} is the sky temperature calculated by the follows formulation (Fuentes, 1987).

The indoor temperature is fixed (air-conditioned room) being 293 K for the winter and 297 K for the summer; the coefficient h_i is posed equal to 7.7 W/m²K, while h_e is assumed variable with the wind velocity (UNI EN ISO 6946,2008).

The solid layers are defined through the following parameters: thickness, density, thermal conductivity and specific heat. The variation of such parameters with temperature is neglected.

2.4. Energy saving of OVF

Fig. 2 shows the sketch of the two façades, which differ between them only for the counter wall that creates the ventilated air channel of the OVF. The thermal insulation layer is placed on the most external layer of both façades.

For both the façades the following parameters are calculated: (I) the temperature profiles for all the layers of the two façades; (II) the daily variation of the temperatures on the external face of the insulation layer (TS_4); (III) the daily variation of the thermal fluxes between the façade and the external environment; (IV) the profile of the air velocity within the cavity.

It is worth to observe that a steady-state analysis does not allow taking into account of the thermal inertia of the wall, which may be accounted only performing a transient analysis (Gagliano et al., 2014).

An option for comparing the heat fluxes through the two façades towards the outdoor environment ($Q_{OVF/UF}^{outdoor}$) is the utilization of the temperature on the most external layer of the inner wall for the OVF facade OVF (TS_{4-OVF}), and on the external layer for the UF facade (TS_{4-UF}).

The temperature TS_1 (i.e. the temperature on the most internal layer for both the façades) is used for calculating the heat fluxes towards the indoor environment ($Q_{OVF/UF}^{indoor}$).

Such approach allows to attain results that are almost independent by the specific stratigraphy of the façade, and the difference between the thermal fluxes through the two façades depend mostly by the mutual effect of the ventilation cavity and counter wall.

The energy performances of the two façades are compared introducing as an indicator the energy-saving rate (ES)_{w,s}, defined by Eq. (8), where the subscripts (w,s) stand respectively for winter and summer days.

$$(ES)_w = \frac{(\sum Q_{OVF} - \sum Q_{UF})_{outgoing,w}}{(\sum Q_{UF})_{outgoing,w}} \quad (8)$$

$$(ES)_s = \frac{(\sum Q_{OVF} - \sum Q_{UF})_{in,s}}{(\sum Q_{UF})_{incoming,s}} \quad (9)$$

The (ES)_{w,s} is defined in such way to take into account only of the outgoing thermal fluxes (i.e thermal losses) for the winter days ($Q_{OVF/UF}^{outgoing,w}$) whereas only the incoming thermal fluxes (i.e heat gains) are taken into account for the summer days ($Q_{OVF/UF}^{incoming,s}$). During the winter days, the solar gains are neglected because they do not constantly give rise to effective energy savings but they could generate just overheating phenomena.

During the summer days, the heat fluxes from the room to the environment, which occur mostly during night-time, are neglected because they are unimportant compared with the cooling effect obtainable through natural ventilation.

3. Case study

3.1. Features of the two façades

This study analyzes and compares the thermal performances of an opaque ventilated and an unventilated façade, whose stratigraphy are shown in Fig. 2. Dimensions and physical characteristics of the layers that make up the façades are summarized in Table 2.

The stratigraphy of the OVF has been defined in such a way to enhance the buoyancy effect and to exploit the thermal inertia of the counter wall (Patania et al., 2010; Ciampi et al., 2003).

The most external layer of the investigated OVF is made up of bricks with large thermal capacity and low thermal conductivity allowing to attenuate and delay the weather forcing (i.e solar irradiation) in summer days (Patania et al., 2010). The ventilated air gap has two openings with a height of 10.0 cm (0.10 m²/m), placed at the bottom and the top of the façade so to increase the chimney effect. The height of both façades is 6.0 m. The investigated ventilated façade has a ratio between the surface of the openings and that of the entire façade equal to 0.10 m²/m, therefore, it can be classified as a strongly ventilated façade.

Consequently, the thermal resistances of the UF and OVF calculated respectively with Eqs. (2) and (4), are respectively 1.55 W/m²K and 1.60 W/m²K. Thus, under a steady-state approach, the ventilation layer allows achieving an increase of just 3% for the thermal resistance.

3.2. Weather data

This study is carried out considering two sunny days, one for the

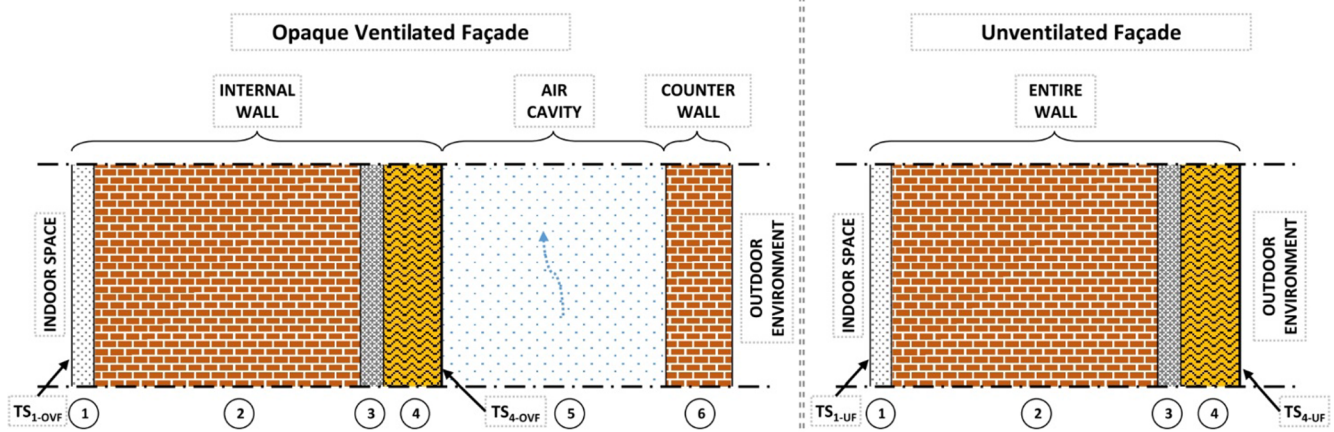


Fig. 2. Stratigraphy of ventilated and unventilated façades.

Table 2
Dimension and physical characteristics of the ventilated façade.

Property		Layer					
		1 (inside)	2	3	4	5	6 (outside)
Description of layer		Plaster	Brick wall	Cement mortar	Rock wool	Air (cavity)	Brick slabs
Thickness (s)	[m]	0.015	0.180	0.015	0.040	0.150	0.045
Density (ρ)	[kg m ⁻³]	1800	1600	2000	100	$\rho = f(p,T)$	800
Thermal conductivity (k)	[W m ⁻¹ K ⁻¹]	0.900	0.590	1.400	0.038	0.024	0.300
Specific heat (C)	[J kg ⁻¹ K ⁻¹]	910	840	670	1030	1006	840

winter period, 21st January, and other for the summer period, 21st July. The weather data are assumed the one of the city of Catania (37° 30' 0" N – 15° 6' 0" E). Fig. 3 shows the daily outdoor temperature and solar incident irradiance on the façades for winter (January) and summer (July) sunny day for the East, South and West exposure (PVGIS, 2020).

The East and West façades collect the highest solar radiation during summer days while the South façades collect the highest solar radiation during the winter day.

4. Results and discussion

This section shows the profiles of temperatures and the thermal fluxes through the walls of both the OVF and UF as a function of the exposures, wind velocity and weather conditions. Specifically:

- exposure: façades facing to East and South (façades facing West and East are considered substantially symmetric (see Fig. 3));
- windiness: calm wind and wind speed of 5.0 m/s at 10.0 m;
- weather conditions: winter and summer days.

4.1. Winter performances

In this section, the hourly temperatures of the more external layer of the two façades, that are the inner wall of the OVF and external layer of the UF (i.e. TS_{4-UF} and TS_{4-OVF}) are compared.

Moreover, the profile of temperature for all the layers, as well as the heat fluxes through the two façades, for the different wind status and exposures, are showed.

4.1.1. External daily superficial temperature

Fig. 4 depicts the hourly external surface temperatures for the UF (TS_{4-UF}) and the OVF, (TS_{4-OVF}) as well as the outdoor temperature for the different windiness and façade exposure.

It is possible to evidence that the façade exposure, likewise the wind velocity, greatly affect the thermal behaviour of both UF and OVF

façades. By looking to the South exposure, the OVF has temperatures lower than UF during the daytime period, with differences that reach 23 °C for low-wind conditions. Such differences diminish to about 13 °C for a wind velocity of 5.0 m/s.

During the night a reverse behaviour is observed, the OVF has temperature slightly higher than the UF. In particular, the temperatures on the outermost layer of the inner wall of the OVF do not go down below the outdoor air temperature. This is a consequence of the reduction of the radiative thermal losses with the skydome. The UF with South exposure could benefits of higher solar gains than an OVF during winter sunny day. Otherwise, the OVF allows reducing the heat losses during the night period.

Globally, the façade facing East has similar behaviour of the South façade. The main difference is the reduced solar radiation that hit this façade.

4.1.2. Profile of temperature across the wall

Fig. 5 shows the temperature and velocity profiles for the different façade orientations and wind conditions.

As regards the profile of temperature (right side in Fig. 5), it is represented at certain times of the day, that is for the South exposure, at noon when the façade is hit by the highest solar irradiance and at 6:00 a.m. when the outdoor temperature is the lowest. While for the EAST exposure, the profiles of temperature are depicted at 9:00, when the façade is hit by the highest solar irradiance, and once again at 6:00 a.m. It is possible to highlight the profiles of temperature varies considerably as a function of the exposure and windiness. During the daytime, the intense solar irradiance that hits the façades cause a significant increase in the temperatures of the outer layer of both the façades.

It is evident that during the daytime the temperature on the outer layer of the UF façade (TS_{4-UF}) is meaningfully higher than the comparable temperature on the OVF (TS_{4-OVF}).

However, the incoming energy is partly dissipated towards the outside by convection and re-emission and partly transferred to the indoor space generating solar gains.

Two distinct profiles of temperature are generated on each side of

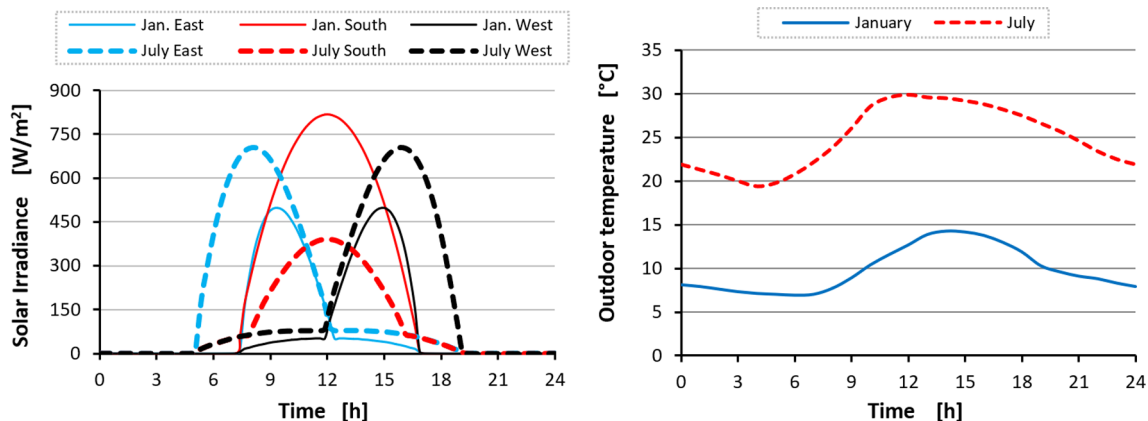


Fig. 3. Incident irradiance (left) and outdoor temperature (right) for the winter and summer days.

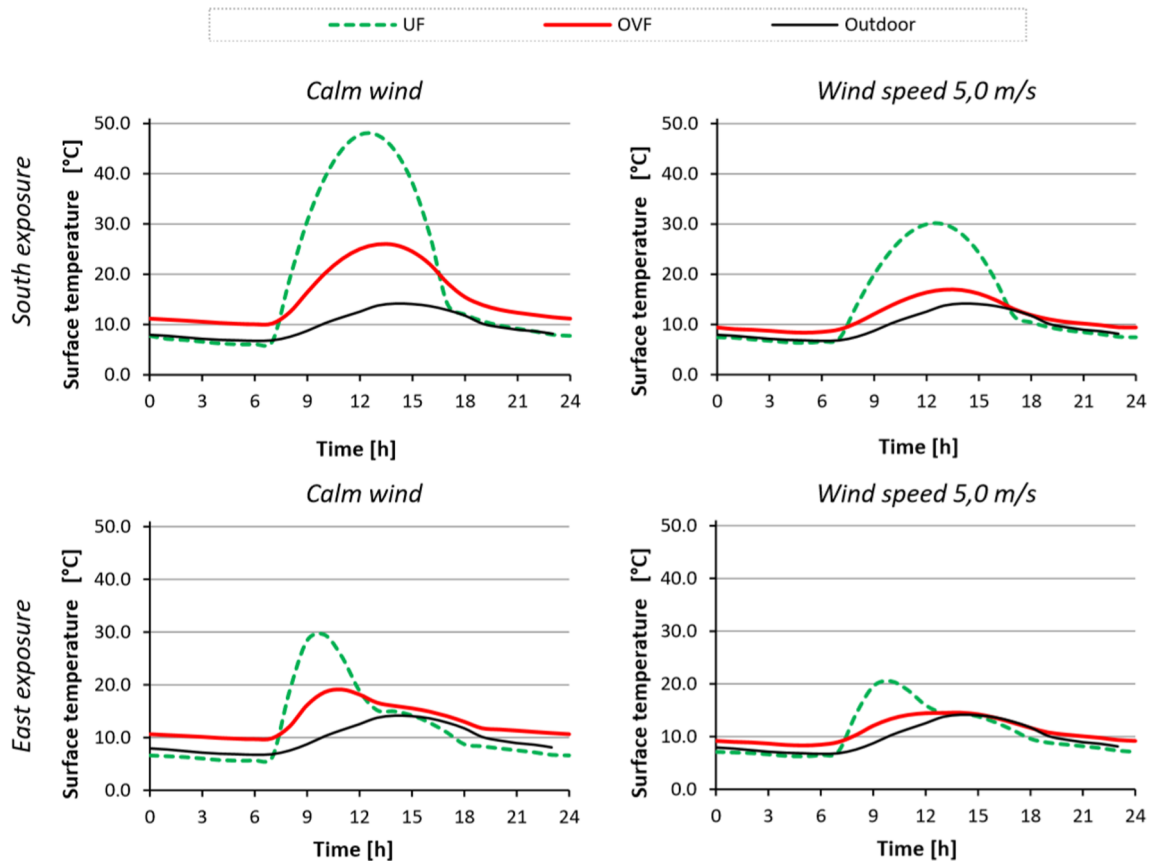


Fig. 4. Hourly surface temperatures of the OVF and UF for each scenario during a sunny winter day.

the channel.

Qualitatively, the East-facing façades behave like those facing South, but the reduced amount of solar irradiance that hits the East façade keeps its surface temperatures far lower than the South façade.

During the nighttime, the counter wall of OVF reduces heat losses towards the sky, guaranteeing temperature on the internal wall higher than the UF. The surface temperature on the insulation of the UF is 4 °C lower than the one that occurs in OVF, for both exposures and the status of calm wind.

Such a result indicates that the OVF reduces the risk of condensation on the thermal insulation compared to the UF. As a general rule, the increase of wind velocity reduces the heating of the façades due to the solar radiation, as a consequence the temperatures on the most external layer decrease.

4.1.3. Velocity profiles

The velocity profile (left side in Fig. 5), is referred to the air duct for the OVF, while it is referred to the region near the wall for the UF.

The profile of velocity, within the cavity of the OVF and for the region near to the UF, points out significant differences as a function of the wind status, façade exposure as well as the time of the day.

Most intense winds generate into the cavity a velocity profile typical of forced convection, independently by the time of the day and the façade exposure. Consequently, the airflow more effectively cools the surfaces facing the channel.

Similar observations can be done for the UF, the increase of the external wind causes the increases of the velocity on the façade (orange and light-blue continue lines) and consequently the cooling effect.

Otherwise, for the calm wind condition the profile of velocity into the channel has noteworthy dependence by the time of the day (red and blue dotted lines) as well as the façade exposure.

The velocity profiles show that both during the day and the night

times, an upward airflow is generated into the cavity.

During the daytime, the airflow into the channel generates two distinct profiles of velocity, one on the external and the other on the inner side of the wall-channel. Indeed, the two surfaces facing the cavity have temperatures higher than the outdoor air, so a twofold buoyancy effect is generated (Garay et al., 2017, Sanjuan et al., 2011).

The most intense velocity is reached on the external side since it has the highest temperature.

Similar effects are observed for both the façade exposures. However, the velocity profile is more flattened for the East -facing façades due to the less intense solar irradiance compared the South exposure.

During the night-time, a single upward profile of velocity is observed within the channel due to the higher temperature on the inner wall (TS_{4-UVF}) in comparison to the outdoor air.

The previous analysis indicates that the OVF, in comparison to the UF, leads to a reduction of the solar gain during the day time, while it allows maintaining higher temperature during night time.

4.1.4. Heat fluxes

Finally, the performances of the OVF and UF are compared evaluating the heat fluxes which flow through both the façades. The heat fluxes towards the indoor space ($Q_{OVF/UF,indoor}$), which is computed as a function of the temperature gradient between the indoor temperature (T_i) and internal superficial temperature ($TS_{1-OVF/UF}$), as well as towards the outdoor environment ($Q_{OVF/UF,outdoor}$), which is computed as a function of the temperatures on the external layer, as above defined, ($TS_{4-OVF/UF}$), the outdoor temperature (T_o) and the sky temperature (T_{sky}), are shown in Fig. 6. The daily heat fluxes, ($Q_{OVF/UF,indoor}$ (dashed lines) as well ($Q_{OVF/UF,outdoor}$ (continuous lines) are depicted as a function of the exposure and the status of wind.

In Fig. 6 the incoming heat fluxes have a positive sign whereas the outgoing heat fluxes have a negative sign.

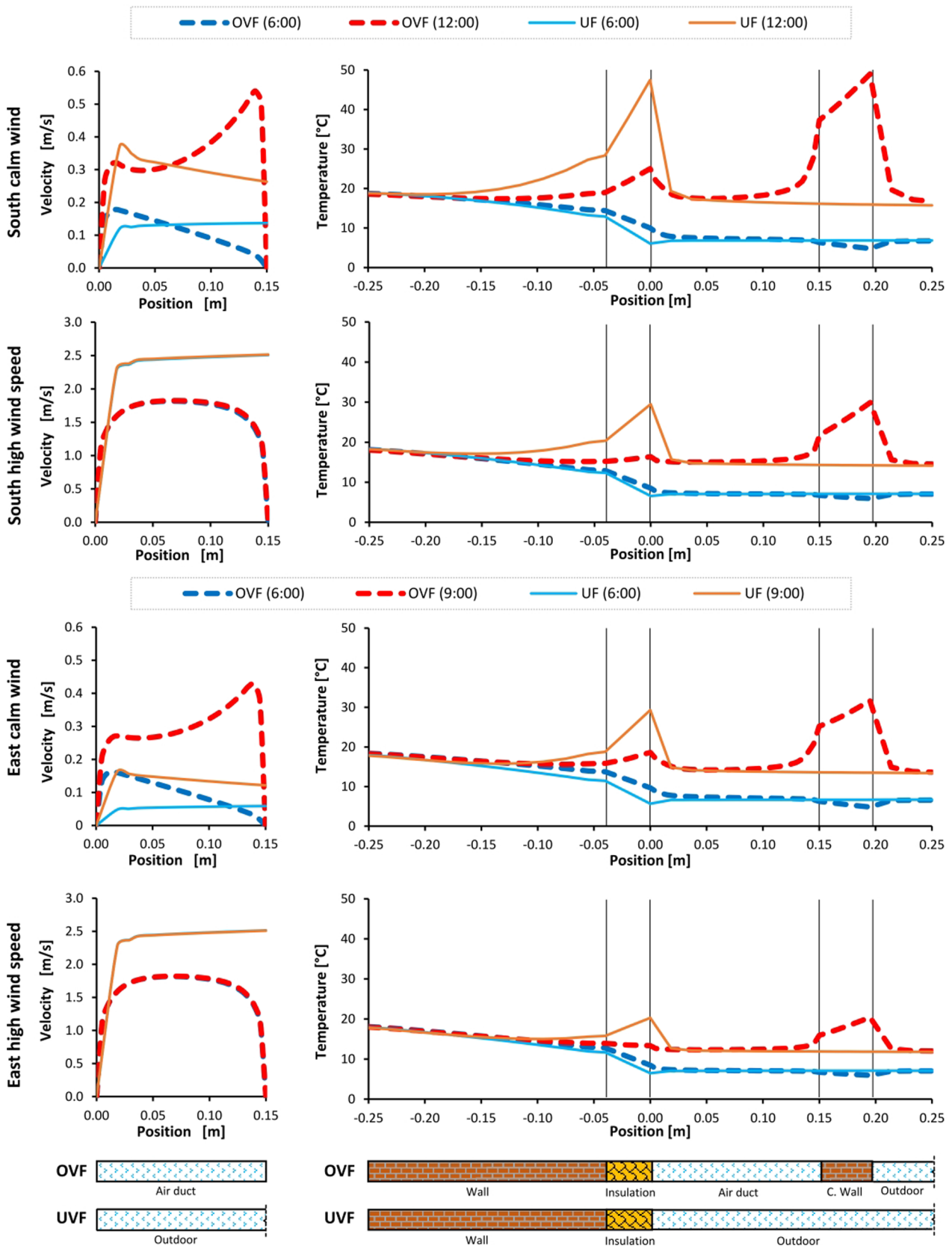


Fig. 5. Velocity and Temperature profiles of the OVF and UF at specific hours of the day for each scenario.

It is possible to observe that the two exposures give rise to different heat flux timelines coherently with the solar path. The differences between $(Q_{OVF/UF})_{outdoor}$ and $(Q_{OVF/UF})_{indoor}$ depend by the thermal

inertia of the façade, which generates the time lag and the attenuation of the heat fluxes transferred to the indoor.

In general, the heat fluxes are most powerful for the UF, so the

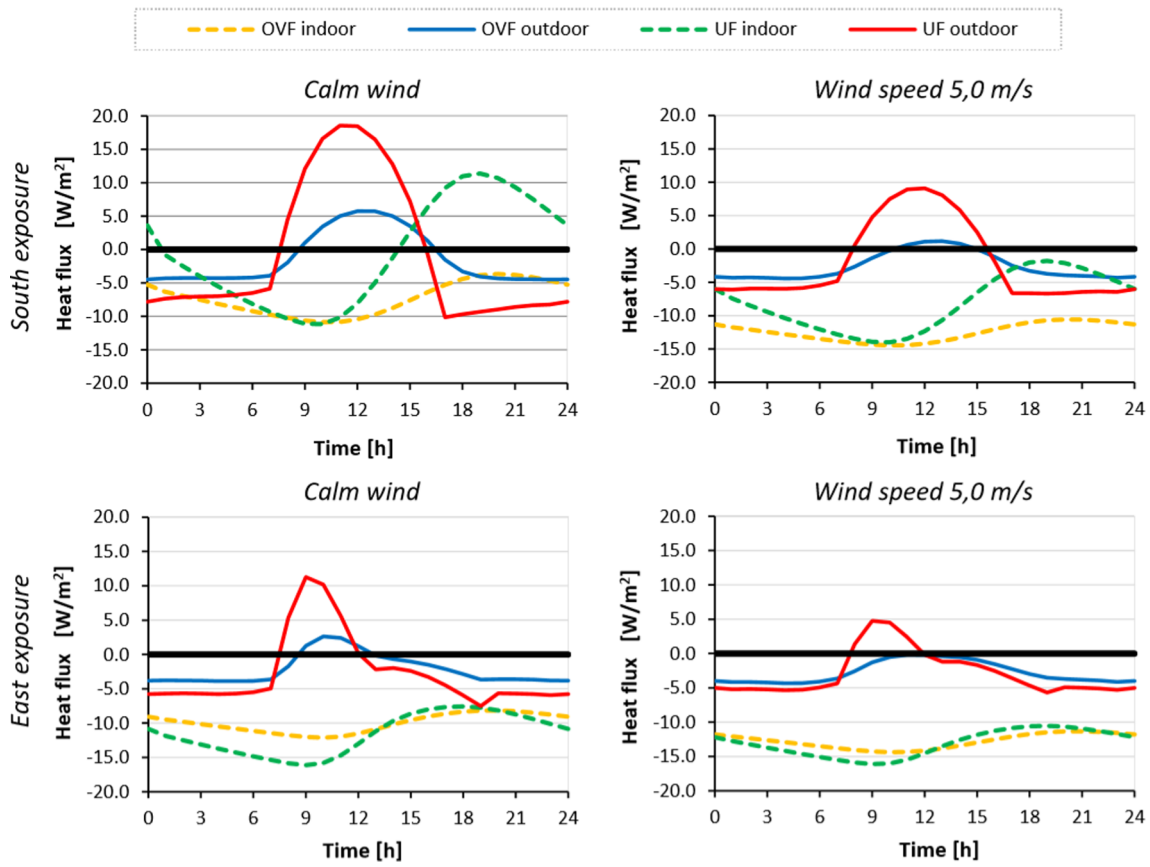


Fig. 6. UF and OVF's hourly thermal fluxes for each scenario during a sunny winter day.

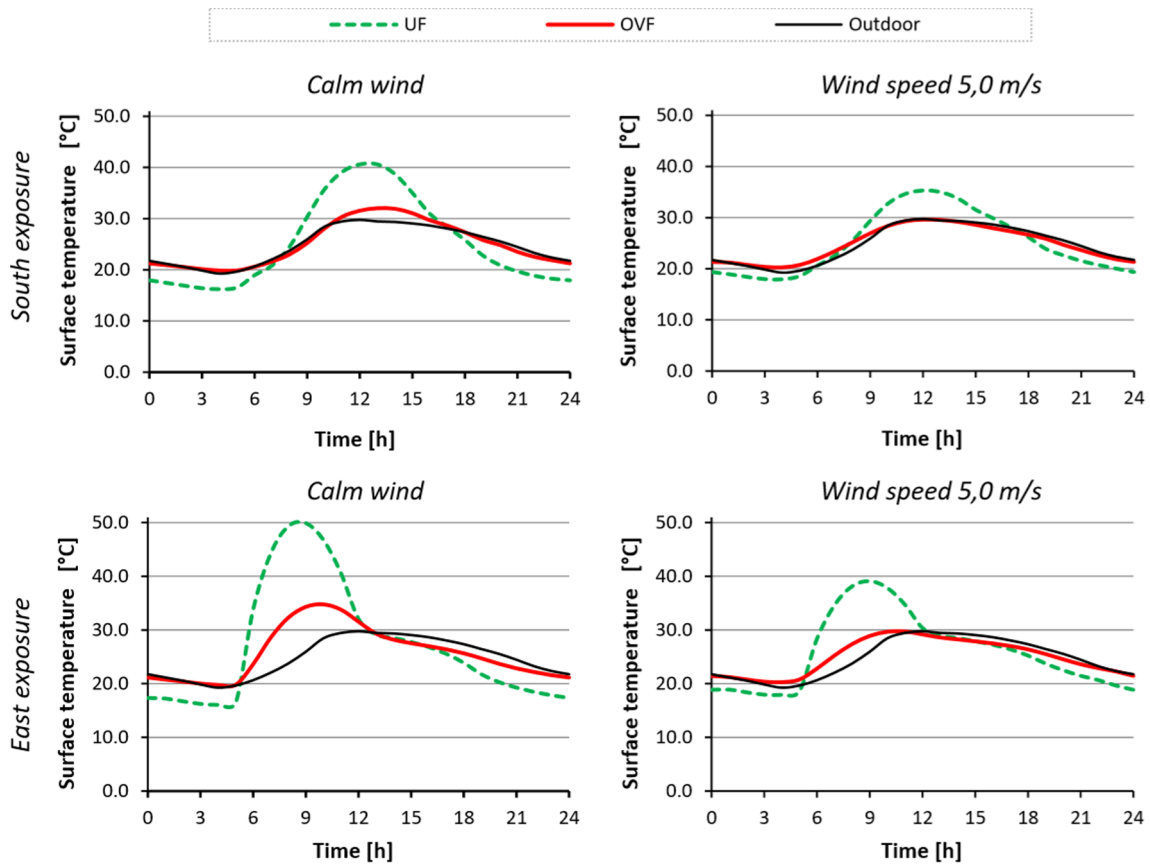


Fig. 7. Hourly surface temperature of the OVF and UF during a summer day for each scenario.

counter-wall of the OVF shields the internal wall of the façade ensuring greater separation from the external environment.
 The most strength wind reduces the magnitude of the heat fluxes

towards the outdoor for both the exposures.
 The screen effect of the external skin diminishes the solar gains during the daylight hours, the highest decrease happens for the South

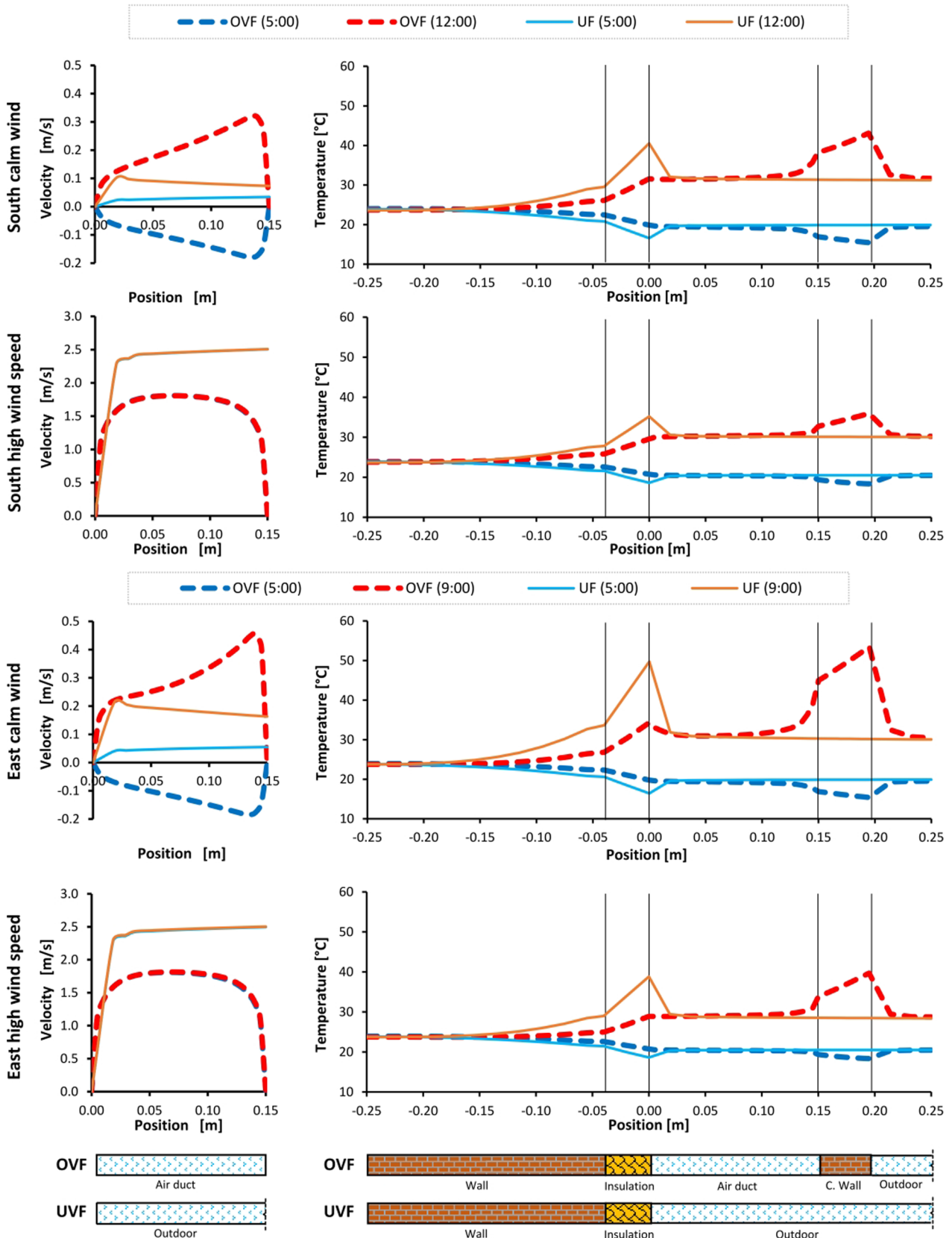


Fig. 8. Velocity and Temperature profiles of the OVF and UF at specific hours of the day for each scenario.

exposure and the status of calm wind, being of 17.9 and 5.1 W/m² respectively for the UF and OVF at noon, with a difference of 12.8 W/m².

It has to be remarked that the solar gains are not always converted in an effective energy saving as they may lead just to an overheating of the indoor space during the daytime period in winter.

Most intense winds reduce the solar gains, of about 50.0% for the UF and about 80.0% for the OVF in comparison to the status of calm wind. The OVF shows the highest solar gains decrease because of the counter wall transfer the solar energy by radiation to the internal wall, and consequently, the decrease of the temperature on the external surface has a higher impact.

During the nighttime, the thermal losses of the UF (Q_{UF})_{outgoing,w} are always higher than that one of the OVF (Q_{OVF})_{outgoing,w}. The difference among (Q_{UF})_{outgoing} and (Q_{OVF})_{outgoing} are the highest for the South façade and for calm wind day, whereas this difference is minimal for the East façade and windy day.

As an example, for the South Exposure and a calm wind day, the thermal losses of the OVF (Q_{OVF})_{outgoing} are approximately 4.5 W/m², whereas for the same scenario the thermal losses of the UF (Q_{UF})_{outgoing} are about 10.1 W/m², with a reduction of the energy needs of almost 50%, which guarantees a reduction of the peak energy demand for space heating.

4.2. Summer performances

As observed for the winter period, during the summer period the thermal behaviour of both the façades depends on their exposure as well as the wind status.

4.2.1. External daily superficial temperature

Fig. 7 depicts the hourly external surface temperatures for the UF

(TS_{4-UF}) and the OVF (TS_{4-OVF}), as well as the outdoor temperature for the different windiness and façade exposure.

By looking to the East exposure, the superficial temperatures of the OVF are lower than the superficial temperatures of the UF during the daytime period, with differences that reach a maximum of 15 °C for low-wind conditions. Otherwise, the temperatures of the UF are slightly lower than the temperatures of the OVF during the night period.

In general, higher wind velocity, i.e. 5.0 m/s, reduces the superficial temperature of both UF and OVF, besides, the maximum temperature difference between the two façades diminishes to about 10 °C. The façade facing South has similar behaviour of the façade facing East. The main differences are generated by the reduced solar irradiance that hits the South façade during the summer period.

Thus, the OVF allows to remarkably reduces the solar gains in comparison to the UF during the hot summer days.

4.2.2. Profile of temperature across the wall

Fig. 8 shows the temperature and velocity profiles for the different façade orientations and wind conditions.

The East and South façades show similar behaviour. It is evident the reduction of the temperatures of the UVF generated by the airflow within the cavity.

As above mentioned the East façade is hit by the most intense irradiance, so it oriented reach the highest temperatures. During the daytime, the counter-wall of the OVF allows to maintains rather low surface temperatures on the inner wall of the cavity (TS_{4-OVF} = 34 °C), whilst, the external layer of the UF reaches very high temperatures (TS_{4-UF} = 50 °C). During night-time, the superficial temperatures TS_{4-UVF} are comparable to the outdoor air temperature.

4.2.3. Heat fluxes

The daily heat fluxes, (Q_{OVF, UF})_{indoor} (dashed lines) as well (Q_{OVF,}

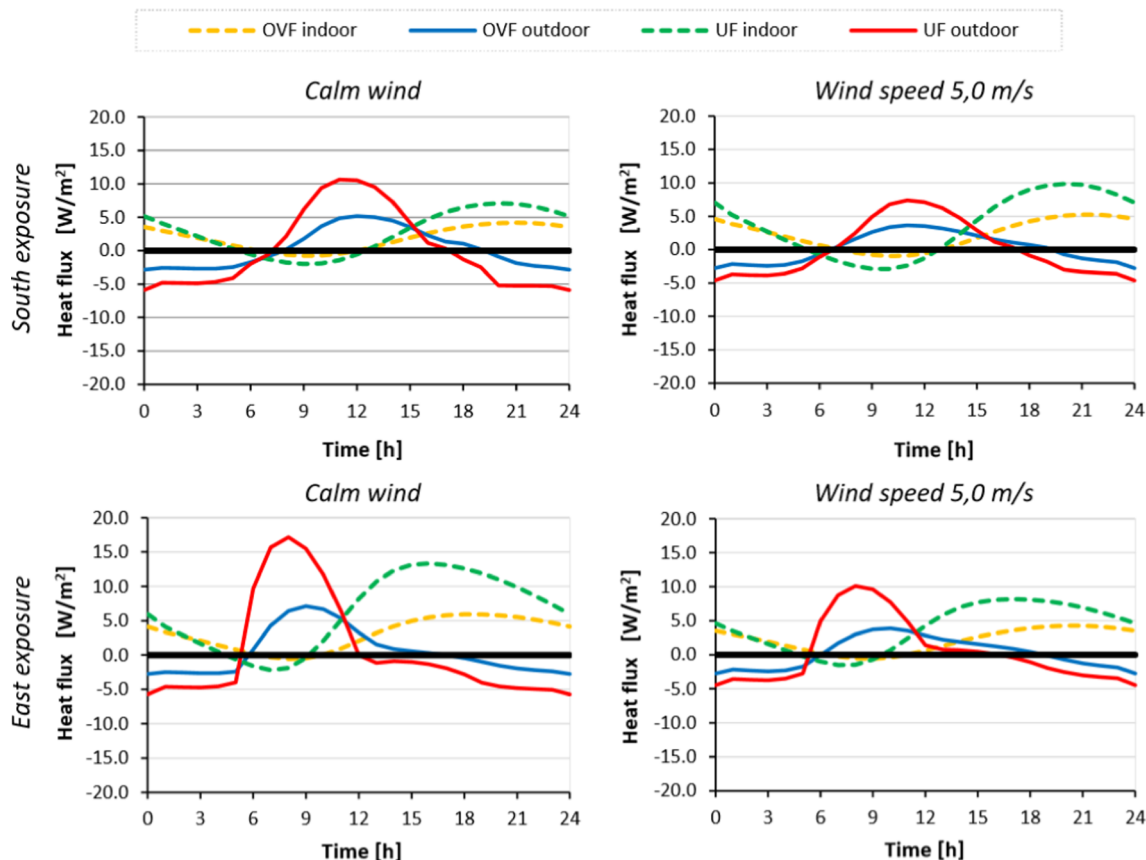


Fig. 9. UF and OVF’s summer thermal fluxes. Façade facing South (top) and East (bottom); Calm wind (left-side) and wind speed of 5.0 m/s (right-side).

$UF_{outdoor}$ (continuous lines) are depicted as a function of the exposure and the windiness.

In Fig. 9 the incoming heat fluxes have a positive sign whereas the outgoing heat fluxes have a negative sign.

In general, the thermal behaviour of the two façades follows a similar trend of that one described during the winter period. One of the main difference is that the East façades are subjected to the highest heat fluxes.

The $(Q_{OVF/UF})_{outdoor}$ is transferred to the indoor space $(Q_{OVF/UF})_{indoor}$ attenuated and delayed as a function of the thermal inertia of the internal wall.

Due to the effect of the counter-wall, the heat fluxes are more powerful for the UF than the OVF. This means that the external layer of the internal wall of the OVF has a less intense fluctuation of its temperature during the day. For the East exposure and the status of calm wind, the OVF allows achieving the highest reduction of the solar gains $(Q_{OVF})_{incoming}$, being 10.0 W/m^2 , thanks to the ventilated channel and the screen effect of the counter wall. It is evident that for all scenarios, the OVF allows diminishing the incoming heat fluxes guarantying the reduction of the peak energy demand necessary for space cooling.

4.3. Energy savings

In this section, the daily heat fluxes, which crosses the two façades and the energy saving, calculated by Eq. (8), are shown in Fig. 10.

As previously mentioned, the analysis of the daily heat fluxes $(Q_{OVF/UV})_{outdoor}$ that crosses the outermost layer of the two façades allows enhancing the different performances between the OVF and UF deriving by the ventilated cavity and the screen effect of the counter-wall.

For the right interpretation of the reported results, it has to be remarked that the daily heat fluxes taken into account are, the outgoing thermal fluxes $(Q_{OVF/UV})_{outgoing,w}$ during the winter day, so the solar heat gains are not reckoned, and the incoming heat fluxes $(Q_{OVF/UV})_{incoming,s}$ during the summer day, thus the night cooling is not reckoned.

It is possible to highlight that, under the previous settings, the OVF gives rise to daily thermal fluxes lesser than the UF for all the examined scenarios.

However, for the winter days, the positive sign of the heat fluxes indicates that the UF has heat gains higher than the UVF. The highest differences

The energy fluxes through the OVF are rather constant for both the winter and the summer days independently by the façade orientation and the wind status, which are around 60.0 and 30.0 Wh/day m^2 respectively dor winter and summer day.

This outcome highlights the role of the combined effect of the counter wall and the ventilation to protecting the internal wall by the environmental forcing.

As a rule, wind calm conditions enhance the energy-saving achievable by the OVF both in winter and summer days, which ranges from 20.0 to 55.0% . The highest ES is achieved during a summer day for the façade facing East/West. On the contrary during a winter day the façade facing South give rise to the highest ES.

These results indicate that for the façades facing from East to West, the adoption of an OVF gives rises to remarkable Energy Saving. More specifically the façades facing South attain the better performance during the winter day, while the façades facing East or West attain the better performance during the summer day.

5. Discussion

In this section, a brief comparison with the results of previous literature studies is presented. Among the experimental and numerical analysis on an OVF (Marinosci, 2011, Marinosci et al., 2011), the Authors observed that the Southside of the OVF during a winter sunny day, at noon reached an external superficial temperature of about $31.5 \text{ }^\circ\text{C}$ (measured) and $34 \text{ }^\circ\text{C}$ (predicted). These temperatures are in good agreement with the temperature calculated in this study, that for the same orientation and at noon is of about $30.5 \text{ }^\circ\text{C}$. The superficial temperatures observed by Marinosci for the façade West oriented under similar weather conditions are again in are in good agreement with that one calculated in the current study for the East facade. The measurement of the air velocity within the cavity developed in the Marinosci's research are presented for low solar radiation and wind velocity, and once more the experimental data are comparable with that one determined in our research for night time and calm wind status.

Other similarities are encountered analyzing the trend of temperature across the air cavity, as well as the timeline.

Giancola (Giancola et al., 2012) presented an experimental study on an OJVF during both the winter and summer period. The temperatures measured within the air cavity are in good agreement with that one calculated in our research when similar weather conditions. Moreover, the comparison between the heat fluxes determined in the work of Giancola, namely heat fluxes conducted to the room, being about 2.5 W/m^2 for a summer day, and of about 9.0 W/m^2 for a winter day, are comparable with the heat fluxes calculated in our study, in terms both of magnitude and pathline, for the East façade and wind velocity of 5.0 m/s , although obtained with of course not the identical boundary conditions.

This discussion not only allows to underline the trustworthiness of

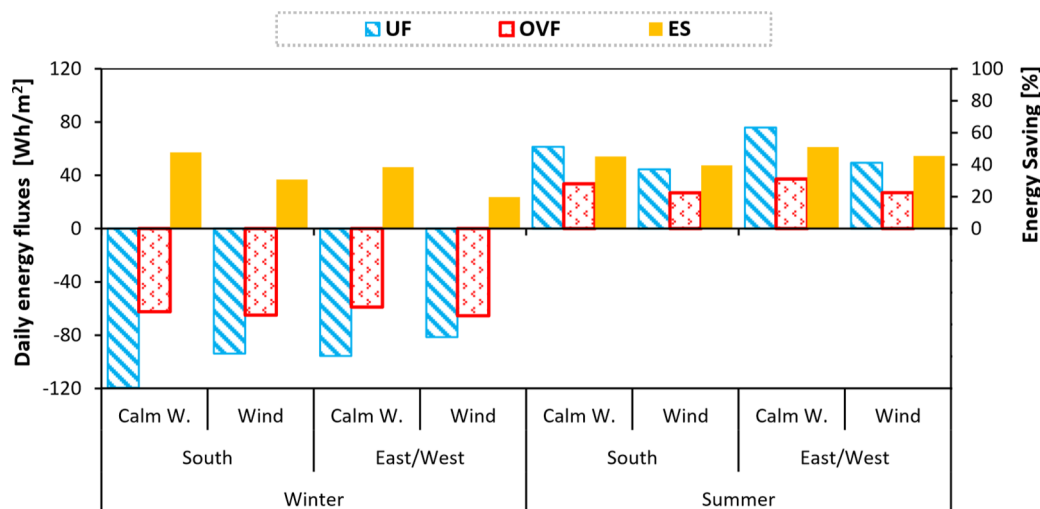


Fig. 10. Daily energy fluxes and Energy saving for the two façades.

the results of the current study but also that the proposed approach could be useful as for the analysis of the thermal behaviour of different kinds of OVF for both the winter and the summer period.

Moreover, it is worth to evidence the novelty of the current research as regards the proposed procedure for comparing the performances of an OVF with a UF with the same stratigraphy.

It is worth remarks, the importance of the utilization of the temperatures on the most external layer of the inner wall for the OVF façade (TS_{4-OVF}), and on the external layer for the UF facade (TS_{4-UF}) for comparing the heat fluxes toward the outdoor environment of both facades ($Q_{OVF, UF, outdoor}$). Such choice is noteworthy since it allows to attain results that are almost independent by the specific stratigraphy of the façade, as evidenced by the comparison with the results of the two above mentioned literature studies.

Finally, the energy-saving achievable by the OVF is defined in such way to take into account only of the outgoing thermal fluxes (i.e. thermal losses) for the winter days ($Q_{OVF, UF, outgoing, w}$ whereas only the incoming thermal fluxes (i.e. heat gains) are taken into account for the summer days ($Q_{OVF, UF, incoming, s}$).

In this way, the performances of the OVF are evaluated without taking into account of the contribute derived by the solar gain for the winter days and the cooling effect obtainable during night-time for the summer days, both effects that are too strictly related to the thermo-physical features of the building where the OVF is applied.

6. Conclusion

In this paper, the thermo-fluid dynamic behaviour of an unventilated façade (UF) and Opaque Ventilated Façade (OVF) were compared. through CFD dynamic simulations considering different exposures and windiness, for both winter and summer weather conditions. In general, it can be pointed out that the thermal behaviour of both the UF and OVF strongly depends on their exposure and wind status.

During the daytime, the outer surface temperatures of the OVF are even 20 °C less than the UF. This outcome indicates an important reduction of the thermal stress on the internal wall constitutive materials.

As a general rule, it has been observed as the increase of the wind speed causes a decrease of the outer surface temperature and consequently of the thermal fluxes exchanged between the façade and the outdoor.

As regards the winter performance, a drawback of the OVF is the fall of the solar gains especially for the South facing façade. However, this aspect could be not substantial as solar gains do not always give rise to effective energy savings as they can just produce the overheating of the indoor space.

During the nighttime, the OVF allows maintaining higher surfaces temperature on the internal wall (TS_{4-OVF}) respect to the UF, so reducing the risk of condensation.

As regards the summer day, the OVF allows diminishing the incoming heat fluxes guarantying the reduction of the peak energy demand for space cooling.

The energy-saving deriving by the use of an OVF is calculated taking into account of only the outgoing thermal fluxes, for the winter day, whereas only the incoming thermal fluxes are taken into account, for the summer day. The outcomes of this study indicate that the OVF allows reducing the thermal fluxes with the outdoor environment during both the winter and summer days.

During the wintertime, the OVF guarantees an Energy Saving being 20.0% for an East/West facing façade under windy conditions and being 50.0% for a South facing façade under calm wind conditions.

During the summertime, the OVF guarantees an Energy Saving almost constant ranging from 40.0 to 50.0% as a function of the façade orientation and wind conditions.

Finally, by looking at the all-year-round performance, the facades facing East or West could be considered as those which allow achieving

the highest energy savings during the summer days, while the façades facing South attain the better performance during the winter days.

Declaration of Competing Interest

The authors declare that they have no known competing financial interests or personal relationships that could have appeared to influence the work reported in this paper.

Acknowledgement

This work was supported by University of Catania “FUNDS FOR UNIVERSITY PLAN FOR RESEARCH 2016/2018 – line 2”, and by the Notice 12/2017 for financing the Ph.D. regional grant in Sicily” as part of Operational Programme of European Social Funding 2014-2020 (PO FSE 2014-2020).

References

- Aketouane, Z., Bah, A., Malha, M., Ansari, O., 2016. Effect of emissivity on the thermal behavior of a double wall facade with a closed cavity. In: International Renewable and Sustainable Energy Conference, Marrakech, Morocco.
- Alonso, C., Oteiza, I., García-Navarro, J., Martín-Consuegra, F., 2016. Energy consumption to cool and heat experimental modules for the energy refurbishment of façades. *Three Case Stud. Madrid, Energy Build.* 126, 252–262.
- ANSYS Fluent User's guide, release Fluent 16.1, ANSYS, Inc., 2015, a.
- ANSYS Fluent UDF manual, release 16.1, ANSYS, Inc., 2015, b.
- Arce, J., Jiménez, M.J., Guzmán, J.D., Heras, M.R., Alvarez, G., Xamán, J., 2009. Experimental study for natural ventilation on a solar chimney. *Renewable Energy* 34 (12), 2928–2934.
- Ascione, F., 2017. Energy conservation and renewable technologies for buildings to face the impact of the climate change and minimize the use of cooling. *Sol. Energy* 154, 34–100.
- Astorqui, J.S.C., Porras-Amores, C., 2017. Ventilated Façade with double chamber and flow control device. *Energy Build.* 149, 471–482.
- Barbosa, S., Ip, K., 2014. Perspectives of double skin façades for naturally ventilated buildings: a review. *Renew. Sustain. Energy Rev.* 40, 1019–1029.
- Bianco, V., Diana, A., Manca, O., Nardini, S., 2016. Thermal behavior evaluation of ventilated roof under variable solar radiation. *Int. J. Heat Technol.* 34 (2), S346–S350.
- Buratti, C., Palladino, D., Moretti, E., Di Palma, R., 2018. Development and optimization of a new ventilated brick wall: CFD analysis and experimental validation. *Energy Build.* 168, 284–297.
- Castell, A., Farid, M.M., 2014. Experimental validation of a methodology to assess PCM effectiveness in cooling building envelopes passively. *Energy Build.* 8, 59–71.
- Ciampi, M., Leccese, F., Tuoni, G., 2003. Ventilated facades energy performance in summer cooling of buildings. *Sol. Energy* 75, 491–502.
- Collinart, T., Bendouma, M., Glounec, P., 2019. Building renovation with prefabricated ventilated façade element: A case study. *Energy Build.* 186, 221–229.
- De Gracia, A., Castell, A., Navarro, L., Oró, E., Cabeza, L.F., 2013. Numerical modelling of ventilated façades: a review. *Renew. Sustain. Energy Rev.* 22, 539–549.
- Diallo, T.M.O., Zhao, X., Dugue, A., Bonnamy, P., Miguel, F.J., Martinez, A., Theodosiou, T., Liu, J.S., Brown, N., 2017. Numerical investigation of the energy performance of an Opaque Ventilated Façade system employing a smart modular heat recovery unit and a latent heat thermal. *Apply Energy* 205, 130–152.
- Diarce, G., Campos-Celador, Á., Martín, K., Urresti, A., García-Romero, A., Sala, J.M., 2014. A comparative study of the CFD modeling of a ventilated active façade including phase change materials. *Appl. Energy* 126, 307–317.
- Directive 2012/27/EU of the European Parliament and of the Council of 25 October 2012 on energy efficiency, Amending Directives 2009, Directives 2009/125/EC and 2010/30/EU and repealing Directives 2004/8/EC and 2006/32/EC, 2009.
- DTU P50-702 janvier 1997. Règles Th – K: Règles de calcul des caractéristiques thermiques utiles parois de construction, 1997.
- Elarga, H., De Carli, M., Zarrella, A., 2015. A simplified mathematical model for transient simulation of thermal performance and energy assessment for active facades. *Energy Build.* 104, 97–107.
- ENEA, National Agency for New Technologies, Energy and Sustainable Economic Development, Energy Efficiency Tips for Citizens and Professionals, 2015.
- European Environment Agency, Annual European Union Greenhouse Gas Inventory 1990–2012 and Inventory Report, 2014.
- Fernandes Maciel, A.C., Carvalho, M.T., 2019. Operational energy of opaque ventilated façades in Brazil. *J. Build. Eng.* 25, 100775.
- Fuentes, M.K., 1987. A simplified thermal model for flat-plate photovoltaic arrays, Sandia Report: SAND85-0330-UC-63, Albuquerque.
- Gagliano, A., Patania, F., Nocera, F., Signorello, C., 2014. Assessment of the dynamic thermal performance of massive buildings. *Energy Build.* 72, 361–370.
- Gagliano, A., Nocera, F., Aneli, S., 2016. Thermodynamic analysis of ventilated façades under different wind conditions in summer period. *Energy Build.* 122, 131–139.
- Gagliano, A., Giuffrida, S., Nocera, F., Detommaso, M., 2017. Energy efficient measure to upgrade a multi-storey residential in a NZEB. *AIMS Energy* 5 (4), 601–624.

- Gagliano, A., Aneli, S., Nocera, F., 2019. Analysis of the performance of a building solar thermal facade (BSTF) for domestic hot water production. *Renewable Energy* 142, 511–526.
- Garay, R., Arregi, B., Elguezabal, P., 2017. Experimental thermal performance assessment of a prefabricated external insulation system for building retrofitting. *Procedia Environ. Sci.* 38, 155–161.
- Giancola, E., Sanjuan, C., Blanco, E., Heras, M.R., 2012. Experimental assessment and modelling of the performance of an open joint ventilated facade during actual operating conditions in Mediterranean climate. *Energy Build.* 54, 363–375.
- Giancola, E., Soutullo, S., Olmedo, R., Heras, H., 2014. Evaluating rehabilitation of the social housing envelope: Experimental assessment of thermal indoor improvements during actual operating conditions in dry hot climate, a case study. *Energy Build.* 75, 264–271.
- Giancola, E., Nuria, Sánchez M., Friedrich, M., Larsen, O.L., Nocente, A., Avesani, S., Babich, F., Goia, F., 2018. Possibilities and challenges of different experimental techniques for airflow characterization in the air cavities of Façades. *J. Facade Des. Eng.* 6 (3), 34–48.
- Kolaitis, D.I., Malliotakis, E., Kontogeorgos, D.A., Mandilaras, I., Katsourinis, D.I., Founti, M.A., 2013. Comparative assessment of internal and external thermal insulation systems for energy efficient retrofitting of residential buildings. *Energy Build.* 64, 123–131.
- IEA, International Energy Agency. *Energy Technology Perspectives 2012. Pathways to a Clean Energy System.*
- Ibañez-Puy, M., Vidaurre-Arbizu, M., Sacristán-Fernández, J.A., Martín-Gómez, C., 2017. Opaque Ventilated Façades: Thermal and energy performance review. *Renew. Sustain. Energy Rev.* 79, 180–191.
- Leccese, F., Salvadori, G., Barlit, M., 2019. Ventilated flat roofs: A simplified model to assess their hygrothermal behavior. *J. Build. Eng.* 22, 12–21.
- Liang, R., Pan, Q., Wang, P., Zhang, J., 2018. Experiment research of solar PV/T co-generation system on the building facade driven by a refrigerant pump. *Energy* 161, 744–752.
- Mandilaras, I., Atsonios, I., Zannis, G., Founti, M., 2014. Thermal performance of a building envelope incorporating ETICS with vacuum insulation panels and EPS. *Energy Build.* 85, 654–665.
- Marinosci, C., 2011. Dynamic thermal performance of building components and applications of the experimental and theoretical analysis of a ventilated facade. Phd thesis.
- Marinosci, C., Strachan, P.A., Semprini, G., Morini, G.L., 2011. Empirical validation and modelling of a naturally ventilated rainscreen facade building. *Energy Build.* 43, 853–863.
- Nizovtsev, M.B., Belyi, V.T., Sterlygov, A.N., 2014. The facade system with ventilated channels for thermal insulation of newly constructed and renovated buildings. *Energy Build.* 75, 60–69.
- Patania, F., Gagliano, A., Nocera, F., Ferlito, A., Galesi, A., 2010. Thermofluid-dynamic analysis of ventilated facades. *Energy Build.* 42, 1148–1155.
- Photovoltaic Geographical Information System (PV-GIS), Photovoltaic-software.com, 2020.
- Sánchez, M.N., Giancola, E., Suárez, M.J., Blanco, E., Heras, M.R., 2017. Experimental evaluation of the airflow behavior in horizontal and vertical Open Joint Ventilated Facades using Stereo-PIV. *Renewable Energy* 109, 613–623.
- Sánchez, M.N., Giancola, E., Blanco, E., Soutullo, S., Suárez, M.J., 2020. Experimental validation of a numerical model of a ventilated facade with horizontal and vertical open joints. *Energies* 13, 146.
- Sanjuan, Cristina, Suárez, María José, González, Marcos, Pistono, Jorge, Blanco, Eduardo, 2011. Energy performance of an open-joint ventilated facade compared with a conventional sealed cavity facade. *Sol. Energy* 85 (9), 1851–1863. <https://doi.org/10.1016/j.solener.2011.04.028>.
- Seo, W.D., Lee, K.G., 2013. Application plan for an intelligent facade and interactive design of environment-friendly buildings. *Adv. Mater. Res.* 689, 18–21.
- Soutullo, S., Sánchez, M.N., Enriquez, R., Olmedo, R., Jiménez, M.J., Heras, M.R., 2016. Comparative thermal study between conventional and bioclimatic office buildings. *Build. Environ.* 105, 95–103.
- Stazi, F., Ulpiani, G., Pergolini, M., Magni, D., Di Perna, C., 2018. Experimental comparison between three types of opaque ventilated facades. *The Open Constr. Build. Technol. J.* 12, 296–308.
- UNI EN ISO 6946:2008, Componenti ed elementi per edilizia - Resistenza termica e trasmittanza termica - Metodo di calcolo, 2008.
- UNI 11018:2003 - Rivestimenti e sistemi di ancoraggio per facciate ventilate a montaggio meccanico - Istruzioni per la progettazione, l'esecuzione e la manutenzione - Rivestimenti lapidei e ceramic, 2003.
- Yang, H., Xie, Y., Yuan, J., 2019. Potential of self-drying siding with raised air cavities for building envelopes. *Build. Environ.* 152, 172–181.
- Zuazu-Rosa, A., Martín-Gómez, C., Ibañez-Puy, E., Vidaurre-Arbizu, M., Ibañez-Puy, M., 2018. Design, assembly and energy performance of a ventilated active thermoelectric envelope module for heating. *Energy Build.* 176, 371–379.



Analysis of the performance of a building solar thermal facade (BSTF) for domestic hot water production



Antonio Gagliano ^{a, *}, Stefano Aneli ^a, Francesco Nocera ^b

^a Department of Electric, Electronics and Computer Engineering, University of Catania, Catania, Italy

^b Department of Civil Engineering and Architectural, University of Catania, Catania, Italy

ARTICLE INFO

Article history:

Received 6 December 2018

Received in revised form

3 April 2019

Accepted 19 April 2019

Available online 30 April 2019

Keywords:

Building solar thermal facade

DHW energy needs

Thermal performance

TRNSYS simulations

Energy and environmental analysis

ABSTRACT

The installation of solar collectors applied or integrated into the building envelope may represent an interesting opportunity to increase the fraction of the building energy demands supplied through solar energy.

In particular, building solar thermal facades (BSTFs) could be very useful in high-rise buildings, which do not have sufficient spaces where to install a solar plant.

This paper aims to evaluate the energy performances of building solar thermal facades (BSTFs), constructed with two distinct types of solar collectors, flat plate (FPC) and evacuated solar collectors (ETC), through transient simulations, carried out with TRNSYS software, under different climate conditions. Moreover, an economic and LCA analysis on the two types of examined BSTFs were developed.

Additionally, this study presents a preliminary investigation on a prototype of ventilated building solar thermal facade (v-BSTF) built in Ragusa.

The results of such analysis highlight that BSTFs can represent suitable systems for the DHW production with great environmental and economic conveniences due to the short energy and CO₂ payback times.

© 2019 Elsevier Ltd. All rights reserved.

1. Introduction

The diffusion of solar thermal systems for satisfying the energy demand for domestic hot water as well for space heating should be boosted in view to reach the new EU ambitious targets of 32% from renewables by 2030.

In this regard, the provisional deal among the EU countries, foresees a sub-target of an indicative 1,3% yearly increase of renewables in heating and cooling installations, calculated on a period of 5 years starting from 2021 [1]. Thus, the exploitation of solar energy may provide a huge contribution to satisfying the building's energy needs completely or in part through renewable energy [2].

This means that architectural integration of active solar systems (photovoltaics, solar thermal and hybrid systems) will be crucial in the design and operation of buildings and their energy systems [3]. Building integration of solar collector technology, however, has to

be foreseen during the early design stage to replace conventional cladding solutions.

In this way, S. Kalogirou [4], gave a survey of possible solutions of PV and STS integration on the building roofs and façades. Indeed, Chr. Lamnatou et al. [5], revealed that the majority of the models is about BIPV and skin façades while there are very few studies on BIST systems. Thereby, more investigations on energetic, thermal, optical simulations for BIST installations particularly for active systems (e.g. active solar thermal collectors) are necessary.

Fully integrated façade or roof systems have to provide the same protective features as conventional building skins (thermal insulation and moisture, wind, and water protection) while generating significant renewable energy throughout their service life as part of the building. Buonomano et al. [6] analysed the energy and economic performance of roof and/or façades Building Integrated flat-plate Photovoltaic and Thermal (BIPVT) collectors for residential applications. They have developed a simulation model for multi-story residential buildings in different European climates. As result, they found out that the adoption of BIPVT panels produces a decrease of the primary energy demands from 67.0% to 89.0%, depending on the weather and the building-plant configuration.

* Corresponding author.

E-mail addresses: antonio.gagliano@dieei.unict.it (A. Gagliano), stefano.aneli@unict.it (S. Aneli), fnocera@unict.it (F. Nocera).

The market for Building Integrated Solar Thermal (BIST) collectors is increasing, mainly in countries such as Germany and Austria, where proper incentives have advanced the development of energy-generating building envelopes [7].

The International Energy Agency, Solar Heating and Cooling Programme has supported the task Solar Energy and Architecture (IEA SHC Task 41), which led to providing design criteria and guidelines for achieving high-quality architecture for buildings integrating solar energy systems [8].

F. Motte et al. [9] affirmed that the aesthetic of solar thermal collectors can be an obstacle to their development and limits the growth of the market. Consequently, they presented a new-patented concept of flat plate solar collector totally integrated into a gutter. The new complete solar collector consists of several short modules connected serially.

Maurer et al. [10] presented a general methodology to evaluate the economic benefits of building integrated solar thermal systems. They demonstrated that any thermal energy offset by the BIST generates a saving that reduce the building's operational cost. Moreover, the BIST system can reduce the overall construction material costs and may offer additional revenue in the form of financial incentives and tax credits.

Albanese et al. [11] evaluated the performances for an experimental passive solar space heating system utilising heat pipes. Such system transfers heat through an insulated wall from an absorber outside the building to a storage tank inside the building. The heat pipe system provided significantly higher solar fractions than the other passive options in all climates with the most advantageous performances in cold and cloudy climates. Buonomano et al. [12] analysed the energy performance of a low-cost water solar collector prototype, designed for the integration into building façade. It has been found out that the building integrated solar thermal collectors influences the HVAC energy demand and the indoor hygrothermal comfort in a passive way.

Beccali et al. [13] carried out transient simulations for a south-façade integrated solar air collectors in two different Italian sites characterized by different climatic conditions (Milan and Palermo). They showed that the BIST positively affects the yearly energy balance particularly for climates where the heating demand is prevalent.

Other researches focused on Finite Element Models (FEM) or Transient System Simulation (TRNSYS) model calculation of integrated component overall performance.

Specifically, Hassan et al. [14] presented a new design for BIST, based upon thermal performance, functional integration, composite behavior, environmental design, durability, sustainability, reliability, flexibility, ease, and speed of construction, and cost-effectiveness. Antoniadis et al. [15], proposed a study on the optimization of a building integrated solar thermal system with seasonal storage using TRNSYS. Two distinct type of solar collectors and two different building integration options were investigated: a roof integrated flat plate solar array and a vacuum tube solar array either integrated into the façade.

Many studies are focused on the thermal performances of Solar Domestic Hot Water System (SDHW). Such topic is worth of relevance considering that in new housing the hot water production reaches sometimes 30.0% of overall energy consumption. Thus satisfying DHW energy needs through solar thermal system became a primary objective for reaching the NZEB target.

Notton et al. [16] stated that in the Mediterranean area, a solar thermal plant can satisfy up to 80.0% of the hot water energy demands with minimal operational and management expense.

Motte et al. [17] estimated the effect of adding a PCM into a building-integrated solar thermal collector in view to improve the thermal performances of an SDHW system.

Gagliano et al. [18] monitored and investigated the performances of a pilot PVT plant for DHW production. Other studies investigated the economic viability of solar systems in both residential [4] and non-residential buildings. Chow et al. [19] analysed the performances of a flat-plate collectors integrated into the facades of a high-rise residential building in Hong Kong.

Buonomano et al. [20] developed a new simulation model for the dynamic energy performance analysis of multi-zone buildings of a non-residential NZEB with Building Integrated PhotoVoltaic (BIPV) and PhotoVoltaic/Thermal (BIPV/T) device.

Life-cycle impact assessment (LCA) studies have been also developed for both building added (BAST) and BIST system. S. Kalogirou [21] investigated the environmental benefits of utilising solar energy instead of conventional sources of energy, the different emissions resulting from the solar system operation are estimated and compared to those of a conventional fuel system.

The energy and the life cycle assessment (LCA) of a solar thermal collector for sanitary water demand has been investigated following the international standards of series ISO 14040 by Ardenete et al. who demonstrated the great energy convenience of such technology [22].

Starting from the results of previous research, Ardenete et al. considered an energy balance between the employed energy during the collector life cycle and the energy saved thanks to the collector use. They estimated that, even in pessimistic scenarios, the energy and emission payback times are lower than 4.0 years [23].

Life-cycle impact assessment studies (LCA) for both building added (BAST) and BIST system are based on embodied energy and embodied carbon emissions [24].

The aim of this study is to evaluate the viability of façade solar collectors used for DHW production in different climate contexts. Thus, the energy and environmental analysis of evacuated tube solar thermal collectors (ETC) and flat plate solar-thermal collectors are compared and analysed by means of the software TRNSYS.

Considering that there is a lack of literature studies, which investigate the overall performances of façade solar collectors, it is worth of interest to evaluate the variation of the energy performances of vertical BSTFs under different climate conditions. The performances of the two types of examined BSTFs are also evaluated through an LCA and economic analysis.

Moreover, some preliminary results of the survey carried out on the prototype of a ventilated solar facade (v-BSTF) developed within the research project "Solar Collector Continue Façade (FCCS)", supported by "PO FERS Sicilia 2007/2013 Research line 4.1.1.1", are presented.

This paper has the following structure. After the introduction, in the second paragraph a brief discussion on the LCA analysis of building integrated/applied solar thermal systems is proposed. The third paragraph illustrates the methodologies and the structure of the project in TRNSYS. The fourth and fifth paragraphs describe the study specification and the results of the energy and environmental analysis carried out considering two distinct scenarios: BSTF constructed with FPC or ETC. Finally, a case study of a prototype of a ventilated solar facade added in the building envelope (vBSTF) is presented.

2. Life-cycle of building integrated/applied solar thermal systems

LCA studies allow comparing design alternatives that are different in terms of environmental impacts. A life cycle study is usually segmented into four distinct phases: product, construction, use, and end-of-life. The product phase is relative to the picking up, the transportation and the manufacture of raw materials into products.

The construction phase consists of the transportation of the products to the final destination and the construction–installation processes. The use stage includes energy and water requirements, maintenance, and material substitution. The end-of-life refers to the decommissioning and the waste processing of solar system products.

In order to assess the life-cycle impacts assessment (LCIA) of a solar thermal facade, the energy produced and delivered inside or exported outside the building system must be included.

Fig. 1 shows the typical stages of an LCA study applied to a building integrated/applied solar thermal system.

The Ecoinvent database is one of the sources most used on LCA studies about building integrated or added façade solar systems by LCA experts.

2.1. Life-cycle inventory databases

The life-cycle inventory (LCI) analysis requires the quantification of the inputs of water, energy and raw materials, and discharges to air, land, and water.

Life Cycle Environmental Impact Assessment has the aim to assess the potential environmental impacts of the system throughout the life cycle of the product. Thus, environmental and human health consequences along with resource depletion have to be addressed.

The environmental indicators used to evaluate the environmental impacts are Global Warming Potential (GWP), Ozone Depletion Potential (ODP), Acidification Potential (AP); Eutrophication Potential (EP); Photochemical Ozone Creation Potential (POCP); Abiotic Depletion Potential of Fossil resources (ADP_FF); Embodied Renewable energy (ER).

A broad LCIA study was carried out assuming as reference the average solar technologies available in Switzerland [25]. Such study was conducted by SimaPro 7.3 software and Ecoinvent 2.2 database. Table 1 summarizes the environmental impacts and the energy used to produce 1.0 m² of FPC and ETC solar collectors and one piece of different building added solar systems.

Another comprehensive environmental analysis of solar systems was developed by Carlsoon et al. [26]. They used the Eco-indicator 99 (EI99) [27], IPCC_{100a} [28] as well as the cumulative energy demand indicator (CED). Table 2 summarizes some of the results of such study (see Table 3).

The IPCC_{100a} indicates the number of greenhouse gases emitted into the atmosphere during the production of one energy unit (e.g. kg CO_{2,eq.} per 1 MJ of energy produced).

The Eco-indicator 99 method assesses the environmental effects in terms of damage to human health, ecosystem quality, and resources and it is expressed in points (pt.).

The cumulative energy demand indicator represents the energy necessary for system material/component manufacture, installation, material disposal, and transportation during all the life cycle phases.

The above-mentioned studies [25,26] provide quite similar results in regard to the emission of CO₂ (kg CO_{2,eq.}), respectively indicated in terms of GWP and IPCC_{100a}, as well as between the values of ADP_FF and CED.

In the light of the previous scrutiny, it is possible to assume that data in Tables 1 and 2, in accordance with [25], are valid at European scale “given the fact that there are only slight differences between the technologies used within the European countries”.

Moreover, it is worth emphasizing that the environmental performance of FPC and ETC differed significantly. The production and installation of an ETC solar system determine life-cycle impacts lower than that one of an equivalent FPC solar system.

Metallic copper and aluminum make the largest contribution to the environmental load for solar collectors. However, if secondary metals are used, the contribution to the environmental load of the metallic part of the solar collectors are significantly reduced.

3. Methodology

In this section, firstly, the solar thermal system is illustrated, and then the TRNSYS model is presented.

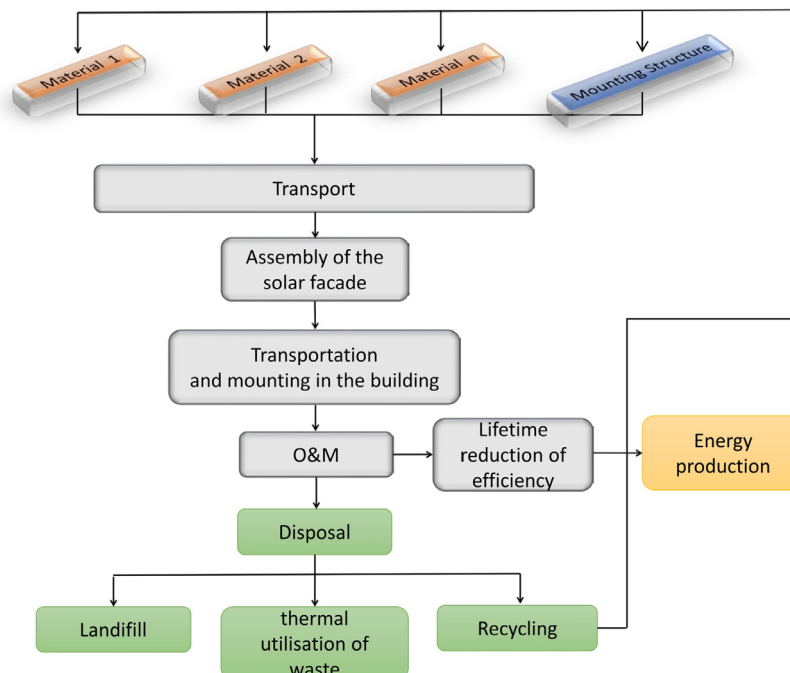


Fig. 1. Typical stages of an LCA study applied to a building-integrated solar thermal system elaborated from Ref. [25].

Table 1
LCIA of solar collectors and building added solar systems (redrafted from Ref. [25]).

Solar thermal collectors/systems	Life-cycle impact category					EP [kg PO ₄ equiv.]	Embodied Energy	
	ADP	GWP [kg CO ₂ equiv.]	ODP [kg CFC-11 equiv.]	AP [kg SO ₂ equiv.]	POCP [kg C ₂ H ₄ equiv.]		ADP_FF [MJ equiv.]	ERE [MJ equiv.]
Flat plate collector	6.81E-01	1.02E+02	9.69E-06	9.76E-01	5.00E-02	6.65E-01	1.52E+03	2.46E+02
Evacuated tube collector	6.74E-01	9.03E+01	8.42E-06	7.81E-01	3.26E-02	6.55E-01	1.48E+03	1.38E+02
Solar system, flat plate collector, one-family house, domestic hot water	9.83E+00	1.33E+03	1.35E-04	8.77E+00	6.24E-01	5.93E+00	2.13E+04	2.55E+03
Solar system, flat plate collector, one-family house, combined system	1.95E+01	2.74E+03	3.52E-04	1.98E+01	1.34E+00	1.39E+01	4.35E+04	5.29E+03
Solar system with evacuated tube collector, one-family house, combined system	1.77E+01	2.35E+03	3.06E-04	1.58E+01	1.03E+00	1.25E+01	3.90E+04	3.68E+03

Table 2
Environmental analysis of solar system (redrafted from Ref. [26]).

Solar thermal collectors/systems	Ecoindicator 99 EI99 (pt)	IPCC _{100a} (kg CO ₂ eq)	cumulative energy demand CED (GJ)
Flat plate collector	17.2 (7.8) ^R	89 (54) ^R	1.6 (1.0) ^R
Evacuated tube collector	15.3 (8.4) ^R	74.59 (72.5) ^R	1.46 (1.4) ^R
Solar system, FPC (12.8 m ²); storage 1.0 m ³	418 (262) ^R	2539 (1891) ^R	67.6 (54.9) ^R
Solar system, ETC (8.2 m ²); storage 1.0 m ³	318 (226) ^R	1912 (1696) ^R	57.0 (51.5) ^R

^R Use of 100% secondary metals as alternative to primary metals.

Table 3
Features of the two typologies of thermal collectors.

Panel type	η_0 (-)	a_1 (W/m ² K)	a_2 (W/m ² K ²)
Glazed flat plate	0.803	3.550	0.035
Evacuated-tube	0.789	1.550	0.007

3.1. Description of the simulated solar plant

The thermal energy produced by the solar collectors is stored in the solar tank and then used for DHW production (see Fig. 2) when requested. An auxiliary heater will provide the necessary energy for heating up the water in order to reach the set-point temperature (45 °C).

The thermal power “ P_{th} ” transferred from the solar collectors to the solar tank is calculated by equation (1), as a function of the mass flow rate m_s , the water specific heat C and the difference between

the inlet and the outlet temperatures in the storage tank.

$$P_{th} = m_s \cdot C \cdot (T_{in} - T_{out}) \quad (1)$$

The thermal efficiency of the solar collectors is calculated, in accordance with the European standard EN 12975, by equation (2).

$$\eta_{th} = \eta_0 - a_1 \cdot \frac{(T_m - T_a)}{G_k} - a_2 \cdot \frac{(T_m - T_a)^2}{G_k} \quad (2)$$

where η_0 , a_1 and a_2 are the parameters that characterize the solar panel, while T_m , T_a , and G_k are respectively the average temperature of solar panel, environmental air temperature and incident solar radiation.

Energy provided by the auxiliary (E_{aux}) is calculated by:

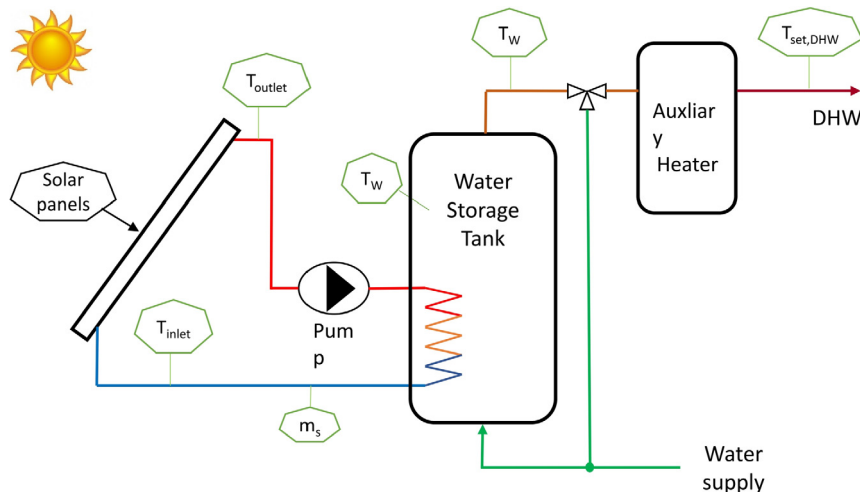


Fig. 2. Scheme of the solar system.

$$E_{aux} = \int \dot{m}_w \cdot C \cdot (45 - T_w) \cdot dt \quad (3)$$

where \dot{m}_w is the flow rate of DHW required by the user and T_w is the temperature of the water at the outlet of the storage tank.

Then, the valuable energy produced by the solar system is determined by the difference between the energy demand for DHW production (E_{DHW}) and the energy supplied through the auxiliary heater [29].

$$E_{th} = E_{DHW} - E_{aux} \quad (4)$$

The fraction of the energy demand for DHW production supplied by the solar systems is evaluated by:

$$f = \frac{E_{DHW} - E_{aux}}{E_{DHW}} \quad (5)$$

3.2. TRNSYS simulations

The model of the solar system created in TRNSYS software [30] through the graphical user interface ‘Simulation Studio’, consists of various components organized by joining the outputs of the one to the input(s) of the other(s).

Thus, distinct components describe the solar thermal loop (i.e. solar panels, storage tank, unit pump, and controller) as well as the management of the energy demand (i.e. DHW load, thermal mixing, and auxiliary heater).

Inputs and outputs parameters are the temperatures of the fluid at the inlet/outlet of the solar collectors, the solar panel thermal efficiency, the temperature in the thermal storage, the auxiliary energy demand. Fig. 3 shows the flow diagram of the solar system created in TRNSYS.

The solar collector receives hourly meteorological data as inputs from the Type 109 data reader in the standard TMY2 format. The On/Off controller receives inputs of the fluid temperature that exits the collector and the temperature of the fluid at the bottom of the storage tank. The output control function is connected with the pumps, thus switching it on or off, allowing or not the charging of the tank (Type 60).

The DHW tank subsystem includes the components that define the request for DHW (Type 4c), as well as a temperature-controlled flow diverter (Tempering Valve - Type 11b) used to regulate the flow stream at the required temperature T_{set} . When the enthalpy level from the solar tank is insufficient for achieving the minimum required temperature, the flow stream goes to the auxiliary heating

system.

As previously explained two distinct BSTF configurations are simulated, in the first the solar collectors used are flat plate model (scenario 1), while in the second configuration the solar collectors used are evacuated tube model (scenario 2).

Consequently, Type 1 describes the solar collector subsystem, under scenario 1, while Type 71 describes the evacuated tube collector, under scenario 2.

4. Study specifications

In this section of the study, the results of the simulations of a BSTF (tilt angle of 90°), facing South, located in four different Italian cities, that are Ragusa, (lat $36^\circ55'$) Catania (lat. $37^\circ30'$), Rome (lat. $41^\circ53'$) and Milan (lat. $45^\circ28'$), are illustrated.

The analyses carried out evaluate the fraction of DHW energy demand that can be satisfied through BSTF constructed with two distinct typologies of solar collectors, FPC (scenario 1) and ETC (scenario 2), under different climatic conditions.

In both scenarios, the BSTFs have an area of 4.0 m^2 , which was chosen as a reference for an Italian residential unit with a DHW consumption of about 200 l/day. Table 3 shows the technical data of commercial collectors available in the Italian market assumed in the simulations. The hourly consumption profile is that suggested by the standard EN 15316:2007.

The climatic differences among the four cities can be pointed out comparing the average monthly radiation and temperature data, as well the number of heating degree-days. These data were obtained from the PV-GIS monthly radiation tool [31].

As regard, the number of Heating Degree Day, Milan has the highest HDD (2404), which are about two times higher than that one of Rome and Ragusa (1415 and 1324) and almost three times the HDD of Catania (833).

As regard the air temperature the greatest differences of temperature among the cities emerge during the winter period, when up to 10°C between Milan and Catania is observed.

Fig. 4 depicts the global solar irradiance that hits a vertical surface in the winter and summer solstices under clear sky conditions [31].

The solar irradiance on a south-facing vertical solar façade on a sunny winter day is higher than the solar irradiance on a sunny summer day; the maximum daily solar irradiance in winter is even twice the maximum daily solar irradiance in summer.

The solar irradiance has quite modest differences among the four cities both in winter and summer days. This means that such position of the solar collectors smooths the dependence of the solar radiation by the latitude. During summer days, the solar irradiance reaches the highest values in Milan and the lowest in Catania and Ragusa, so the southern cities are the most penalized during the hot season.

Fig. 5 shows the solar radiations collected by the vertical solar façade during all year round in the investigated cities.

As previously observed, the values of solar radiation do not reach the highest values during the summer months, except for Milan. More specifically, the solar radiation in Ragusa, Catania, and Rome in June is less than the solar radiation in December of about 46.0%, 42.0% and 17.0%.

While, the highest monthly solar radiations are achieved during the spring and autumn months in all the investigated cities. During the summer period a vertical solar façade has modest performance especially in the sites with the lowest latitudes. Milan, which is the most northern city compared to the other investigated cities, has the greatest values of monthly solar radiation from May to July.

During the cold season, however, it has the most frequent worst meteorological conditions that reduce the beam irradiance,

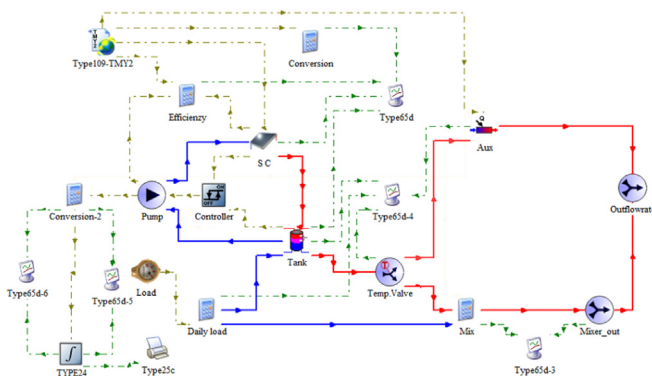


Fig. 3. TRNSYS assembly of the simulated solar system.

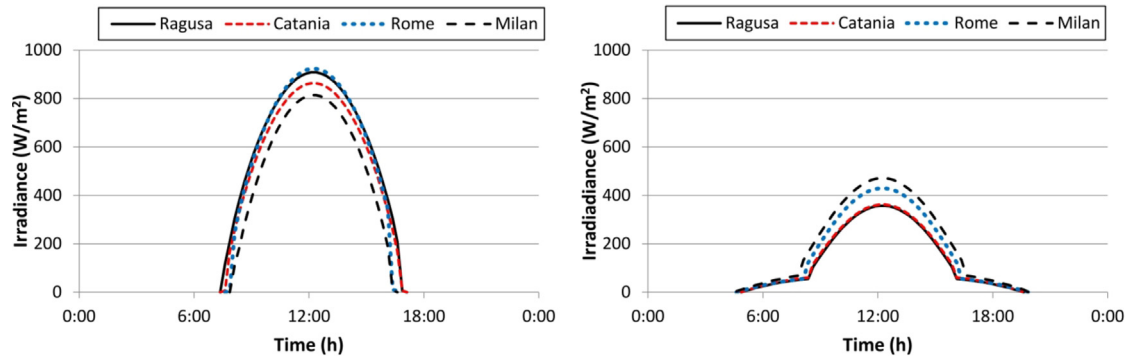


Fig. 4. Solar radiation on winter solstice (left-side) and summer solstice (right-side).

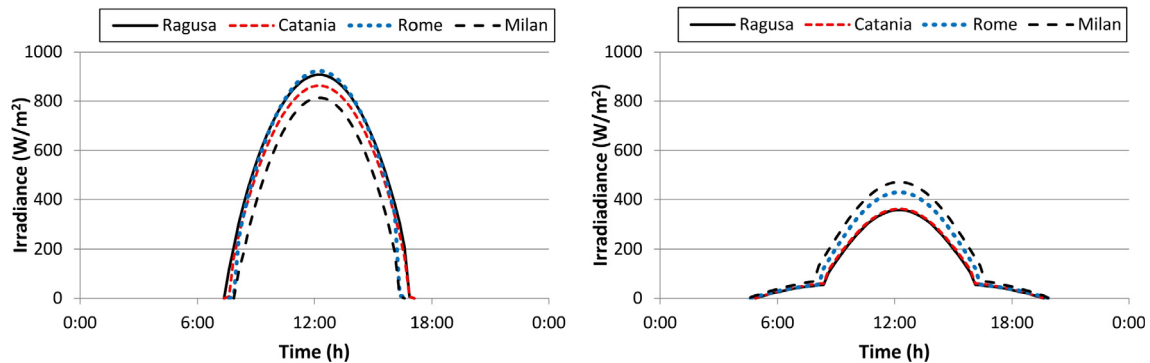


Fig. 5. Comparison of monthly solar radiation.

especially at the highest latitude. For this reason, the lowest values of solar radiation have been detected in Milan during the winter months.

5. Simulation results

In this section, some of the results of transient simulations carried out for the two scenarios are shown and commented.

It has to be underlined that in this study the thermal fluxes occurring between the solar thermal facade and the building envelope are not investigated.

5.1. Winter period

The transient simulations allow calculating the main parameters that characterize the performances of the BSTF per each month, city and scenario.

As an example, the results obtained during a winter week (January 20–27) in Ragusa and Milan, which respectively could be assumed as representative for temperate and cold climate, are shown in the following.

Fig. 6 depicts the outlet temperatures from the solar collectors under scenario 1 ($T_{o,s1}$ dotted red line) and scenario 2 ($T_{o,s2}$ dotted light blue line), the ambient air temperatures (T_a , green line), the solar irradiance (I_b , black line), as well as the temperatures in the solar tank (T_{s1} , red line and T_{s2} light blue line), in Ragusa.

Fig. 7 shows the same parameters in Milan.

During this week, it is possible to observe the effect of different sky conditions on the thermal behavior of these solar systems.

As regards Ragusa, under scenario 1 the temperatures in the solar tank, T_{s1} , are constantly higher than 30 °C, with the highest values that do not exceed 50 °C.

Under scenario 2 the temperatures in the solar tank, T_{s2} , are constantly higher than 35 °C, with the highest values that do not exceed 65 °C.

The daily variation of the temperatures in the solar tank is quite similar in both scenarios with differences of almost 10 °C, during the whole period.

Analogous considerations may be pointed out for the outlet temperatures from the solar collectors, it is confirmed that $T_{o,s2}$ is always higher than $T_{o,s1}$.

As regards Milan, during the same observed winter week the solar irradiance as well as the outdoor temperatures are lower than that in Ragusa.

In particular, the last three days represent very cloudy sky conditions for which only the diffuse component of the solar radiation is present. Consequently, the two solar systems do not produce any useful energy.

Once again, the daily variation of the temperatures in the solar tank during the whole period are quite similar in both scenarios.

Thus, comparing equivalent scenarios, a BSTF installed in Ragusa allows reaching solar tank temperatures that are at least 10 °C higher than that attained in Milan.

Fig. 8 shows, for both scenario1 and 2, the hourly thermal energy provided by the solar plants (E_{th}) and that one supplied by the auxiliary heater (E_{aux}) installed in Ragusa. Fig. 9 shows the same parameters in Milan.

In the above graphs, the areas subtended by the curves correspond to the daily energy needs for DHW production.

Under scenario 1, although the energy supplied by the solar system guarantees great daily coverage factors, higher than 0.7, the auxiliary heater has to function all the days. In particular in the morning and in the late hours of the day.

Otherwise, under scenario 2 the daily coverage factors

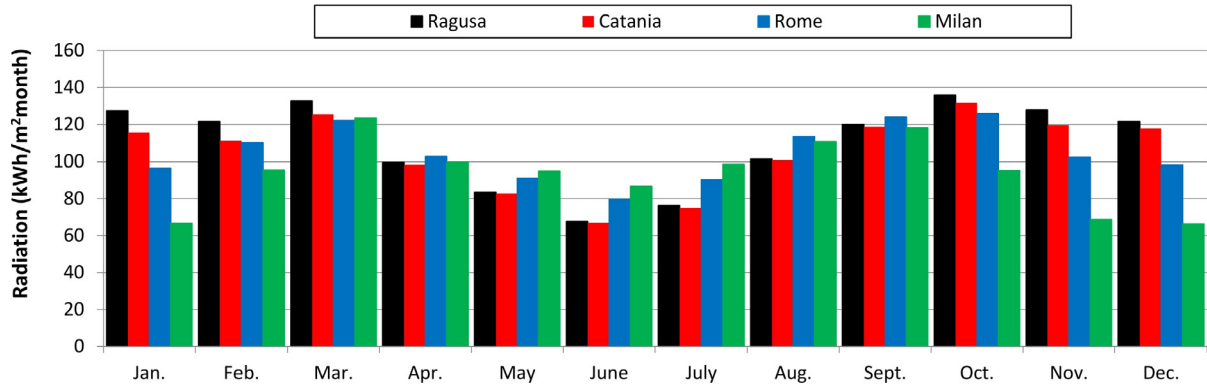


Fig. 6. Weather-data (solar irradiance and ambient temperature) and solar plant operating temperatures (tank and collectors) during a winter week in Ragusa.

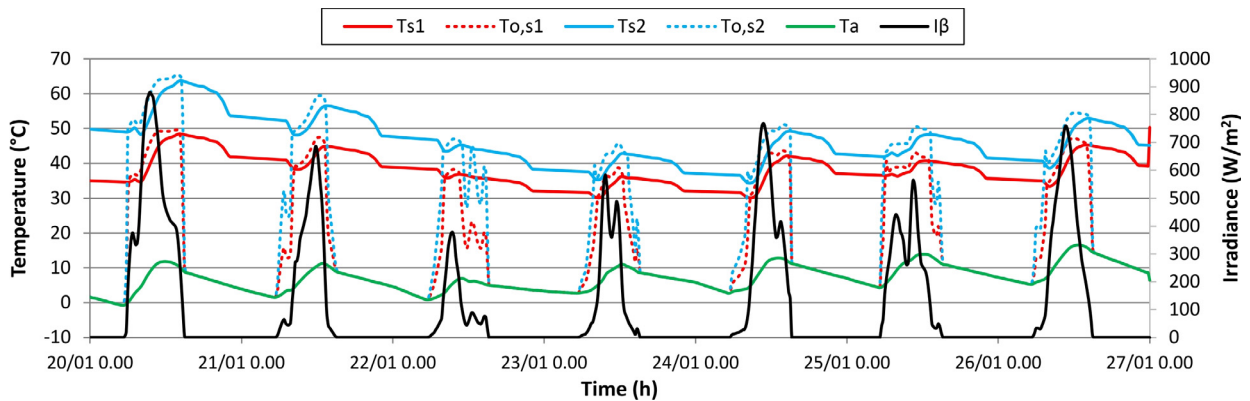


Fig. 7. Weather-data (solar irradiance and ambient temperature) and solar plant operating temperatures (tank and collectors) during a winter week in Milan.

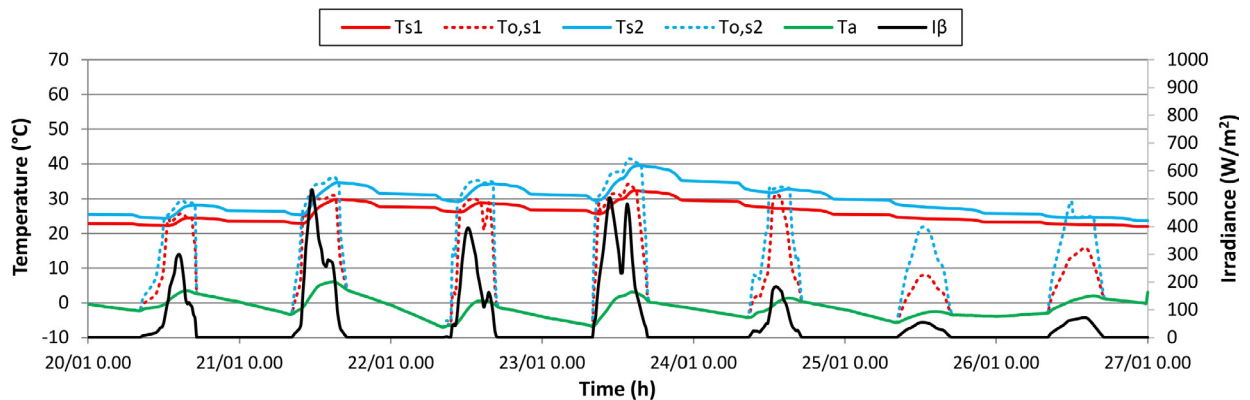


Fig. 8. Energy fluxes during a winter week in Ragusa.

significantly increase. In fact, during four days the DHW energy requirements are totally supplied through the solar system ($f = 1.0$), and in the other three days, the energy supplied by the auxiliary heater is very small.

The performances of the BSTF installed in Milan are modest compared with that one of Ragusa. In particular, under the scenario 1 the thermal power supplied by the solar plant is very scarce, just in one day the solar system provides of about 0.65 kW, which is about 40.0% of the peak value for the DHW demand.

Under scenario 2, the performances of the system, although remain modest, increase significantly reaching a thermal power of about 1.1 kW that is about 70.0% of the peak value for the DHW

demand. This outcome evidences that the ETC solar collectors exploit better their features in the coldest climates.

Generally, the scarce performances obtained from both the two solar systems are related to the low values of solar radiation and air temperatures as previously highlighted.

It is interesting to underline that the energy provided by the solar plant is strictly coupled with the daily trend of the DHW needs, which have peaks values in the early morning and in the late evening.

5.1.2. Summer period

Similarly, the same analysis showed for the winter season are

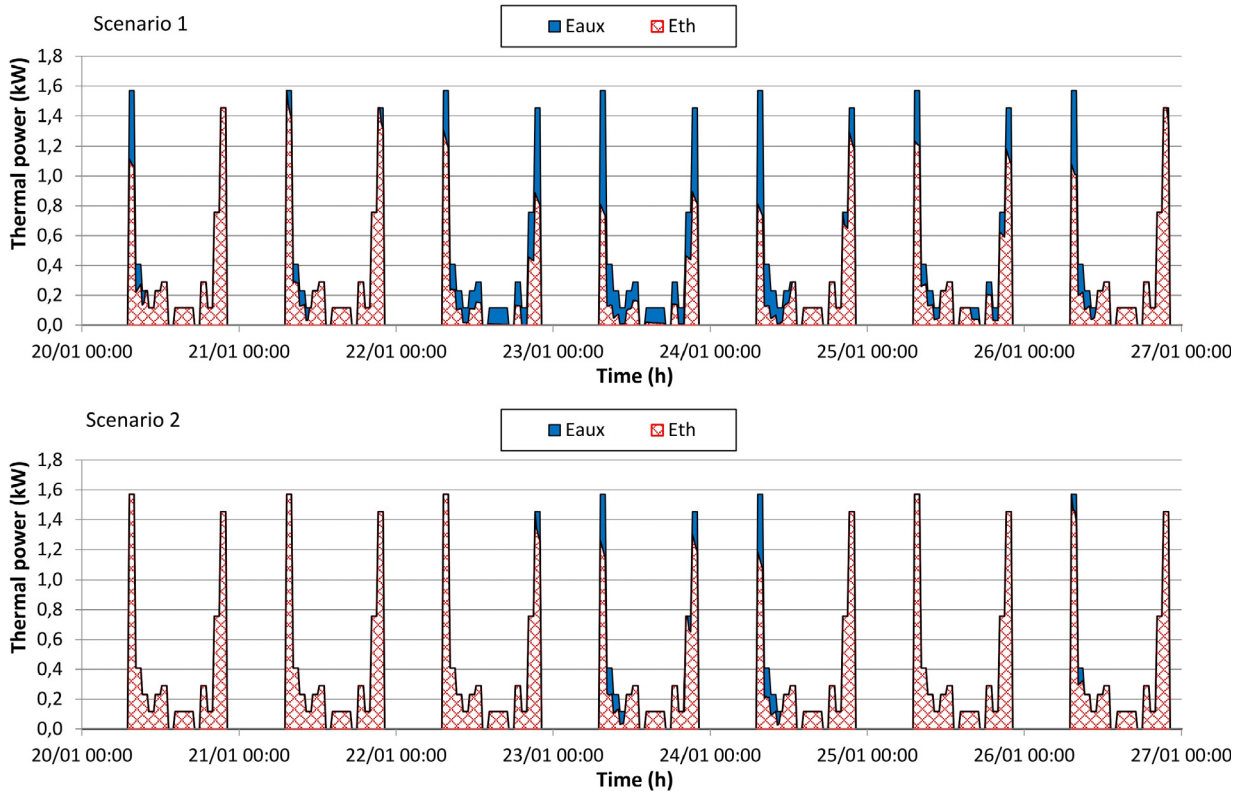


Fig. 9. Energy fluxes during a winter week in Milan.

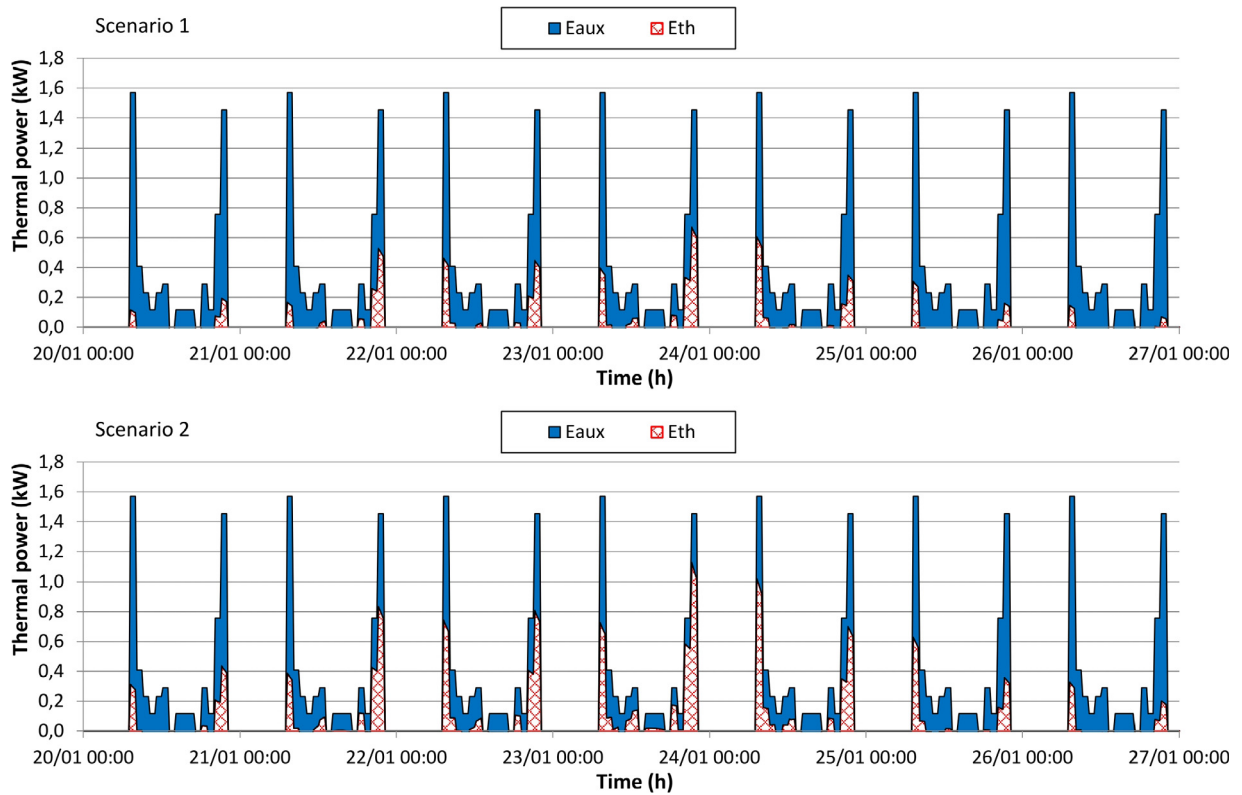


Fig. 10. Weather-data (solar irradiance and ambient temperature) and solar plant's operating temperatures (tank and collectors) during a summer week in Ragusa.

proposed in the summer period (20–27 June).

Fig. 10 depicts the outlet temperatures from the solar collectors under scenario 1 ($T_{o,s1}$ dotted red line) and scenario 2 ($T_{o,s2}$ dotted light blue line), the ambient air temperatures (T_a , green line), the solar irradiance (I_β , black line), as well as the temperatures in the solar tank (T_{s1} , red line and T_{s2} light blue line), in Ragusa.

Fig. 11 shows the same parameters in Milan.

As regards Ragusa, under the scenario 1 the temperatures in the solar tank, T_{s1} , ranges from 32.0 to 42.0 °C, while under the scenario 2, T_{s2} , ranges from 35.0 to 45.0 °C.

The daily variation of the temperatures in the solar tank is quite similar in both scenarios with differences less than 5.0 °C, during the whole period.

Analogous considerations may be pointed out for the outlet temperatures from the solar collectors, it is confirmed that $T_{o,s2}$ is always higher than $T_{o,s1}$.

These outcomes confirm that the two BSTFs have energy performances that are not so different between the winter and the summer period in Ragusa.

This is due to the reduced irradiance that strikes a vertical surface south exposed during the summer period. The maximum daily values of irradiance are of about 50.0% lesser than that observed during a sunny winter day.

As regards Milan, during the same observed summer week the solar irradiance that strikes the solar façade is higher than in Ragusa, while the outdoor temperatures are similar.

Once again, the daily variation of the temperatures in the solar tank is quite similar in both scenarios, during the whole period.

Under the scenario1 the temperatures in the solar tank, T_{s1} , are continuously higher than 32.0 °C, with peak values that reach 47.0 °C, while under the scenario 2 the temperatures achieved in the solar tank, T_{s2} , are permanently higher than about 5.0 °C respect to the scenario1.

Thereby, rather unexpectedly, the solar tank temperatures in Milan are 5.0 °C higher than that one achieved in Ragusa.

As previously discussed, this outcome indicates that the reductions of the performances of a vertical solar façade are greatest in cities with low latitude (e.g. Ragusa).

Fig. 12 shows the hourly thermal power supplied by the solar plants (E_{th}) and that one supplied by the auxiliary heater (E_{aux}), in Ragusa during the summer week (June 20–27).

Fig. 13 depicts the same data in Milan.

Under scenario 1, although the energy supplied by the solar system guarantees great daily coverage factors, higher than 0.8, the auxiliary heater has to function all the days.

Under scenario 2 the daily coverage factors further increase, but anyway in all days it is necessary to supply a little amount of energy

by the auxiliary heater.

These outcomes confirm that the two BSTFs have energy performances that are not so different between the winter and the summer period in Ragusa.

During the summer season, the daily coverage factors show substantial increase respect to the winter season thanks to the high values of the irradiances and of the air temperatures.

Under scenario 2 the performances of the BSTF are a bit better respect to scenario 1.

Even in Milan, the solar plants do not allow fully balancing the energy demand for DHW. This reveals the mandatory use of an auxiliary energy source.

It is worth of interests to underline that during such summer week, the solar plants in Ragusa and Milan achieve almost similar performances.

5.1.3. Yearly performances

In this section of the study, the yearly performances of the solar façade are presented. Fig. 14 shows the monthly coverage factor values “f” for both the scenarios analysed.

It can be observed that the coverage factors “f” in Catania, Ragusa, and Rome are quite similar during the whole year. As regard, Milan, under scenario 1 the coverage factor “f” has modest values during the winter period. Coverage factors less than 10% area chived during the coldest months. Otherwise, under scenario 1 during the mid and the summer seasons the coverage factors “f” reach values of about 0.60, while under scenario 2 a value of about 0.70 is achieved.

As expected, the higher values of “f” are reached during the mid-season and the use of the ETC allows achieving the highest performance.

It is important to note that solar systems installed on the south-facing façade allow reducing the fluctuations of the coverage factor throughout the year, especially when evacuated tube collectors are used. Moreover, during the summer, the reduced solar irradiance that hits the vertical surfaces avoids overproduction and therefore energy waste.

Table 4 shows the yearly thermal energy supplied by the solar panels (E_{th}), the auxiliary energy supplied by the auxiliary system (E_{aux}) as well as the coverage factor (f), for the different scenarios and cities. The percentage differences in the energy yields between the two scenarios are also indicated.

In Ragusa, Catania, and Rome a vertical BSTF constructed with 4.0 m² of flat plate collectors allows to satisfy up to 65.0% of the energy needs for DHW requirements. On the other hand, in Milan just about 44.0% of the DHW demand is satisfied. This quite modest outcome is due to multiple factors, such as limited solar radiation,

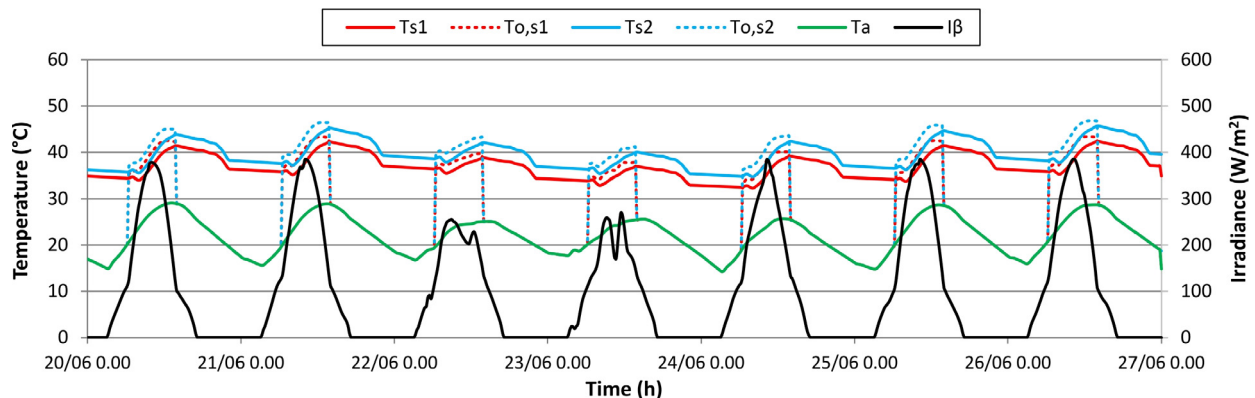


Fig. 11. Weather-data (solar irradiance and ambient temperature) and solar plant's operating temperatures (tank and collectors) during a summer week in Milan.

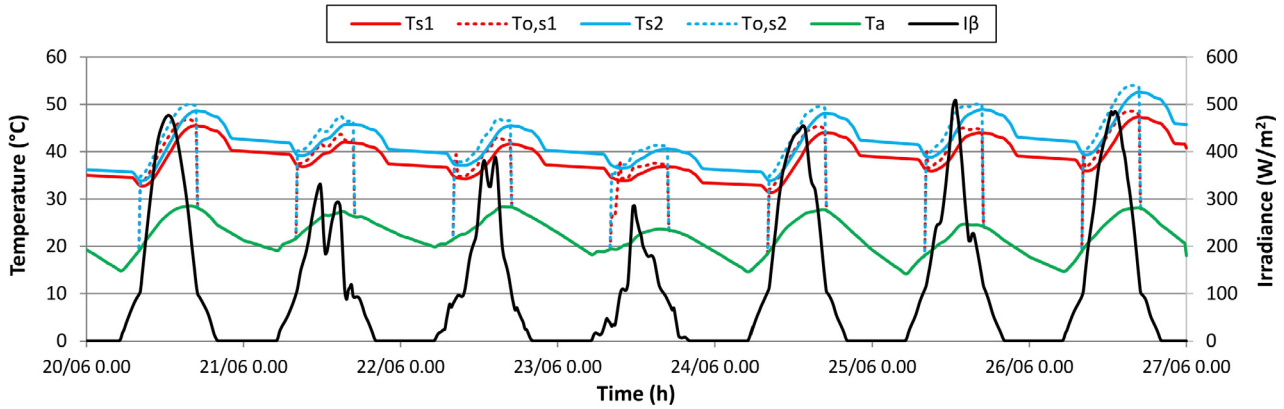


Fig. 12. Energy fluxes during a summer week for Ragusa.

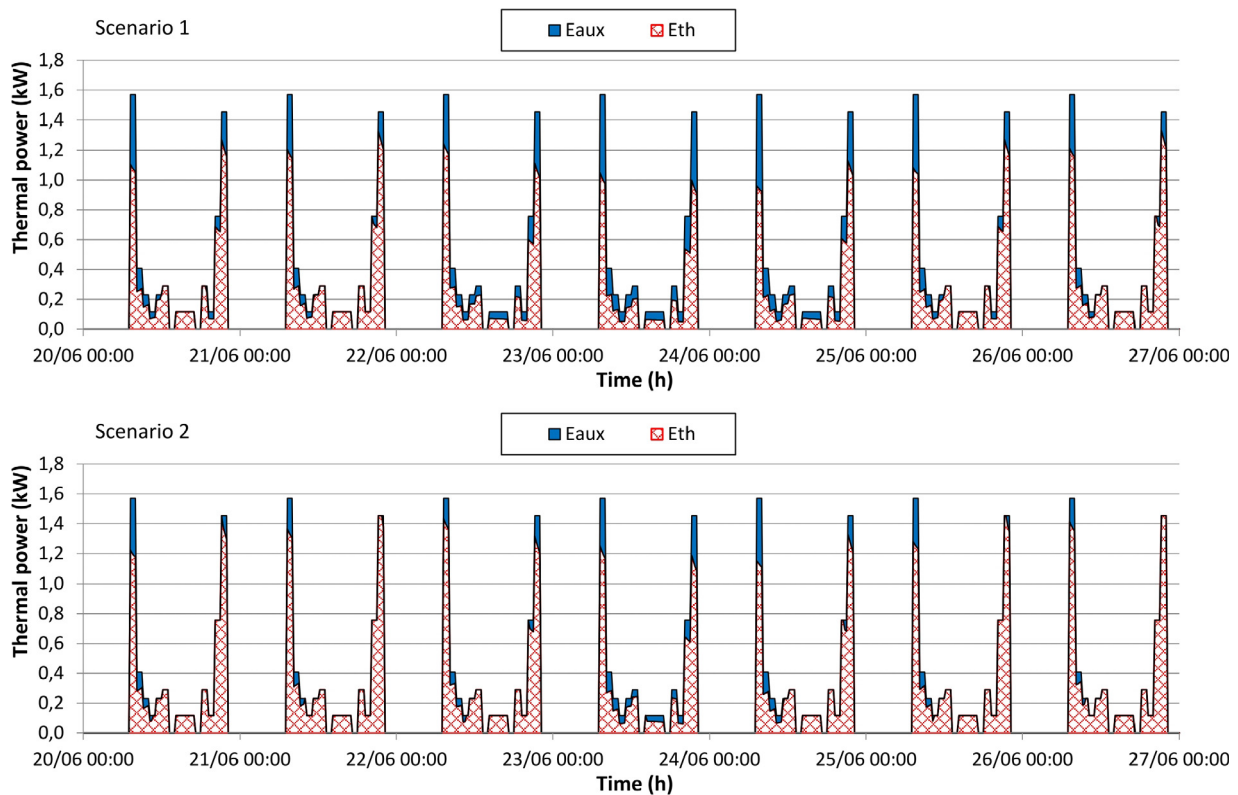


Fig. 13. Energy fluxes during a summer week for Milan.

cool air temperatures and few days with clear sky compared to the other cities, during the winter months.

The use of ETC improves the performances of the solar facades of about 15.0% in Ragusa, 13.0% in Catania and 14.0% in Rome, it allows reaching a yearly “f” factor of 0.76.

In Milan, where the coldest climate limits the efficiency of flat plate collectors, the use of ETC allows boosting the yearly “f” factor up to 0.57 with an increment of 28.0%.

It is possible to highlight that the differences among the performances of the solar facades are not directly related to the values of the HDD. Indeed, in Ragusa and Roma, the coverage factor is about the same of Catania, although the HDD of Ragusa and Roma are about 1.5 times the number HDD of Catania.

The accuracy of the results obtained through TRSNYS software is proved by numerous literature studies [32,33].

5.1.4. Economic analyses

In this section, a simplified economic analysis of the two alternatives is proposed. In particular, the Payback time (PBT) due to the extra expenses necessary for installing the ETC into the BSTF solar façade, as they have costs higher than that of the flat plate collector, has been calculated. A difference of cost between the two typologies of the solar collectors (ΔC) of 120,00 Euro/m² has been evaluated.

PBT is calculated as:

$$PBT = \frac{\Delta C}{ES_{ETC} - ES_{FPC}} \quad (7)$$

where

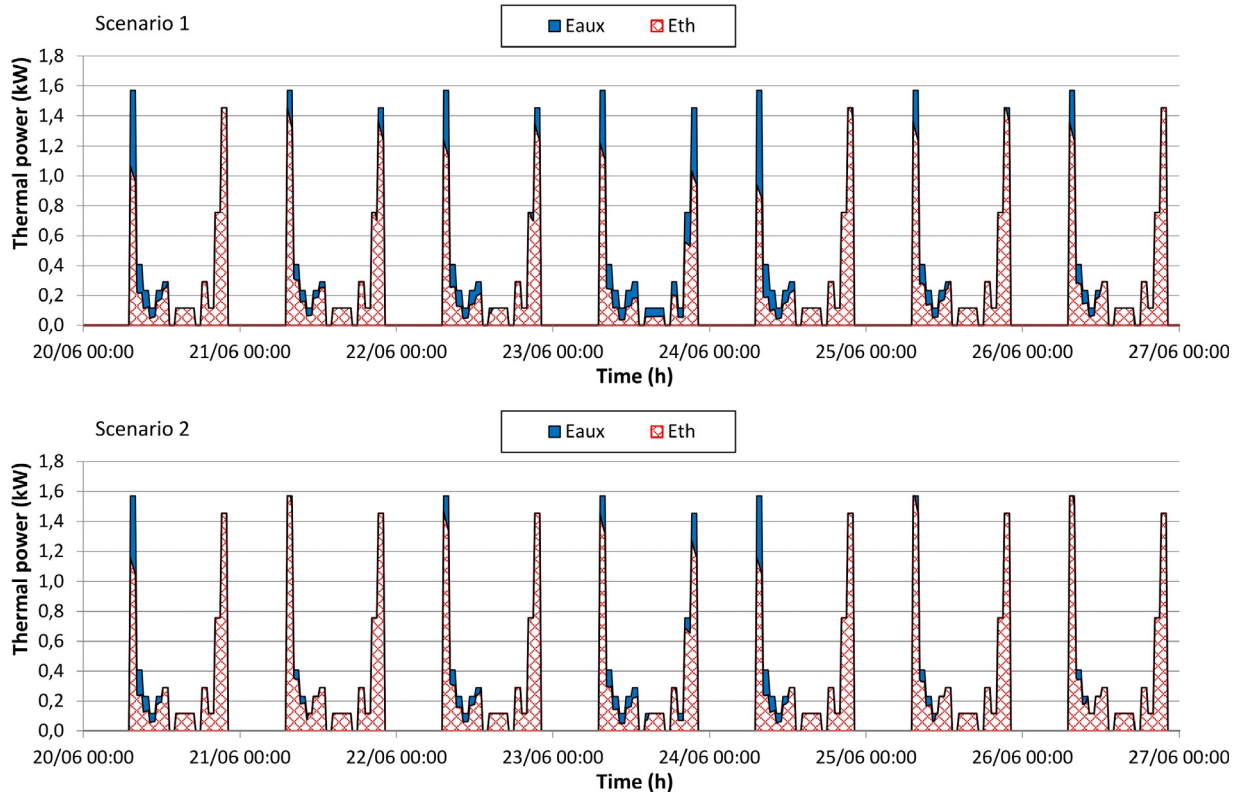


Fig. 14. Coverage factor of DHW demand for the two scenarios.

Table 4
Annual result for various scenarios analysed.

	Scenario 1			Scenario 2			% Difference		
	E _{th} (kWh)	E _{aux} (kWh)	f (-)	E _{th} (kWh)	E _{aux} (kWh)	f (-)	ΔE _{th}	ΔE _{aux}	Δf
Ragusa	1943	1028	0.65	2247	724	0.76	15.6	-29.5	15.6
Catania	1999	972	0.67	2263	708	0.76	13.2	-27.2	13.2
Rome	1994	977	0.67	2281	690	0.77	14.4	-29.3	14.4
Milan	1312	1659	0.44	1685	1286	0.57	28.4	-22.5	28.4

ΔC is the cost difference between ETC and FPC (Euro)
 ES_{ETC} is the economic saving under scenario 2 (ETC).
 ES_{FPC} is the economic saving under scenario 1 (FPC)

For each scenario, the economic savings ES has been calculated by the product of E_{th}, (shown in Table 4) per the cost of the thermal energy, assumed 90,00 €/MWh.

The difference between the energy saving achievable by the two systems (ΔES) determines the payback time necessary for compensating the extra expenses necessary for installing the ETC into the BSTF. Table 5 summarizes the main outcomes of this analysis (see Table 6).

Table 5
Economic comparison between the two scenarios.

	Scenario 1	Scenario 2	Difference	Payback time
	ES _{FPC} (€/y)	ES _{ETC} (€/y)	ΔES (€/y)	year
Ragusa	174,87	202,23	27,4	17.54
Catania	179,91	203,67	23,8	20.20
Rome	179,46	205,29	25,8	18.58
Milan	118,08	151,65	33,6	14.30

The installation of the evacuated tube solar collectors (ETC) instead of the flat plate collectors (FPC) involve payback times of about 20.0 years in Catania, and of about 18.0 years in Ragusa and Roma meanwhile in Milan the payback time is less than 15.0 years.

These outcomes highlight that the use of the ETC has the best economic feasibility in Milano, under the current financial scenario.

Thus, the use of the ETC in BSTF system could be suggested in localities that has HDD of about 2400.0 that are the values of the HDD in Milan.

5.1.5. Energy and emission payback times

In this section of the study, the energy and emission payback time are calculated using the literature data showed in Ref. [26].

The energy payback time (EPBT), defined as the time necessary for a solar installation to ‘pay back’ the same amount of energy equivalent to that required for the production/operation of the renewable plant itself [22], is calculated as:

$$E_{PBT} = \frac{E_{in}}{E_{useful} - E_{O\&M}} \tag{8}$$

where

Table 6
IPCC_{100a} and CED for the two solar systems under investigation.

Solar thermal collectors/systems	IPCC _{100a} (kg CO ₂ eq)	Cumulative energy demand CED (GJ)
Solar system, FPC (4.0 m ²); storage 0.4 m ³	1074	18.5
Solar system, ETC (4.0 m ²); storage 0.4 m ³	917	7.36

E_{in} is the primary energy needed for system material/component manufacture, installation, material disposal, and transportation during all the life cycle phases (GJ);

E_{useful} is yearly energy output of the solar thermal system (GJ per year);

$E_{O\&M}$ is the energy consumed during the use phase of the solar thermal system (GJ per year).

The overall impacts of the solar system during its life cycle and the emission savings are assessed through the emission payback-time (EM_{PBT}). EM_{PBT} is the time for a solar installation to avoid the same amount of emissions equivalent to that required for the production/operation of the renewable plant itself for the generic pollutant.

The emission payback-time related to CO₂eq emission is calculated by the following equation:

$$EM_{PBT,CO_2eq} = \frac{EM_{CO_2eq}}{EM_{S,CO_2eq} - EM_{O\&M,CO_2eq}} \quad (9)$$

where

EM_{CO_2eq} is the global emissions of CO₂eq related to the production, assembly, transport, maintenance and disposal of the solar plant (kg CO₂eq);

EM_{S,CO_2eq} is the yearly emission saving of CO₂eq. (kg CO₂eq/year);

$EM_{O\&M,CO_2eq}$ is the yearly emission of CO₂eq related to the use of the renewable plant (kg CO₂eq/year).

The data necessary for calculating E_{PBT} and EM_{PBT} , which are IPCC_{100a} and CED were derived from Ref. [26]. Since the actual volume of the solar tank installed in the investigated systems (0.4 m³), is different by the reference solar tank (1.0 m³), it was introduced the corrective factor $1/2.5^{0.5}$ for calculating the number of materials employed.

The amount of aluminum in the collector frames was assumed proportional to the solar collector area.

Data reported in Table 7 have been calculated under the following assumptions.

The energy consumed during the use phase of the solar system ($E_{O\&M}$), which is estimated in 0.75 GJ/year, as well as yearly emission of CO₂eq related to the use of the renewable plant ($EM_{O\&M,CO_2eq}$) is not included in the two environmental descriptors.

The yearly emission savings (EM_{S,CO_2eq}) are calculated evaluating the emissions of a conventional system (e.g. a domestic gas boiler)

Table 7
Energy and environmental payback time per the two solar façades.

	Scenario 1	Scenario 2	Scenario 1	Scenario 2
	E_{PBT}	E_{PBT}	EM_{PBT}	EM_{PBT}
Ragusa	2.96	1.00	2.75	2.01
Catania	2.87	0.99	2.67	2.00
Rome	2.88	0.99	2.68	1.98
Milan	4.66	1.38	4.22	2.74

that delivers as much energy as that supplied by the solar system. Thus, for domestic gas boilers, a global warming factor of 215.0 gCO₂ eq per kWh of useful heat [34] is assumed.

The yearly emissions of CO₂eq ($EM_{O\&M,CO_2eq}$) deriving by the use of the renewable plant, descends by the electricity consumed by the pumps, which were calculated adopting a specific emission of 287.0 gCO₂eq per kWh [34].

The energy payback-time related to the scenario1 (FPC) is higher than the energy payback-time of scenario 2 (ETC). This result depends not only by the greatest energy supplied by the ETC but also and mainly on the fewer primary energy needed for system materials/components assembly. Scenario 2 allows attaining EPBTs that are always lesser than 1.4 years, while scenario 1 has EPBTs that are of about 3.0 years and even more than 4.5 years in Milan.

As regard, the emission payback times the differences between the two scenarios are smaller. Scenario 2 confirms the best performances, with EPBTs that are lower than 2.0 years with the exception of Milan that has an EPBT of about 2.7 years. Once again, under scenario 1, Milan has an EPBT higher than 4.0 years.

Evidently, the use of secondary metals as an alternative to primary metals reduces the environmental impact of the FPC collectors smoothing the disproportion between the environmental impacts of the two solar technologies.

However, both the two solar façades have short energy and emission payback times in comparison with the life cycle of a solar system that is at least 20.0 years. Thus, the positive judgments, revealed by the short payback time values for both energy and CO₂, allow affirming that vertical solar façades represent suitable systems for DHW production with great environmental convenience.

6. Experimental v-bstf prototype

In this section, the prototype design and data collected through the monitoring system are illustrated.

6.1. Prototype design

Under the research project “Solar Collector Continue Façade” (FCCS), funded by the POR FERS Sicilia 2007/2013- Research line 4.1.1.1, two BSTF prototypes were designed and tested.

These two BSTF prototypes, depicted in Fig. 15, are installed into the industrial building of the EUROINFISSI Company, in Ragusa. They are constructed with an aluminum frame specifically designed to be coupled with the solar plate collector type Viessmann Vitosol 200-FM. The designed BSTF may be integrated or, merely overlaid into the façade in case of building renovation.

One of the two BSTF prototype, namely v-BSTF, is mounted leaving a ventilated gap between the FPC and the building envelope.

The ventilated solar thermal façade (v-BSTF) has a total gross surface of 7.50 × 2.40 m and it is constituted by six solar panels, subdivided into two arrays. The v-BSTF is north-west oriented.

The v-BSTF is part of a solar thermal plant, designed for DHW production, equipped with a solar storage tank with a capacity of 1,000.0 L. The hydronic circuit is managed through a control system that switches on/off the solar pump by controlling the outlet

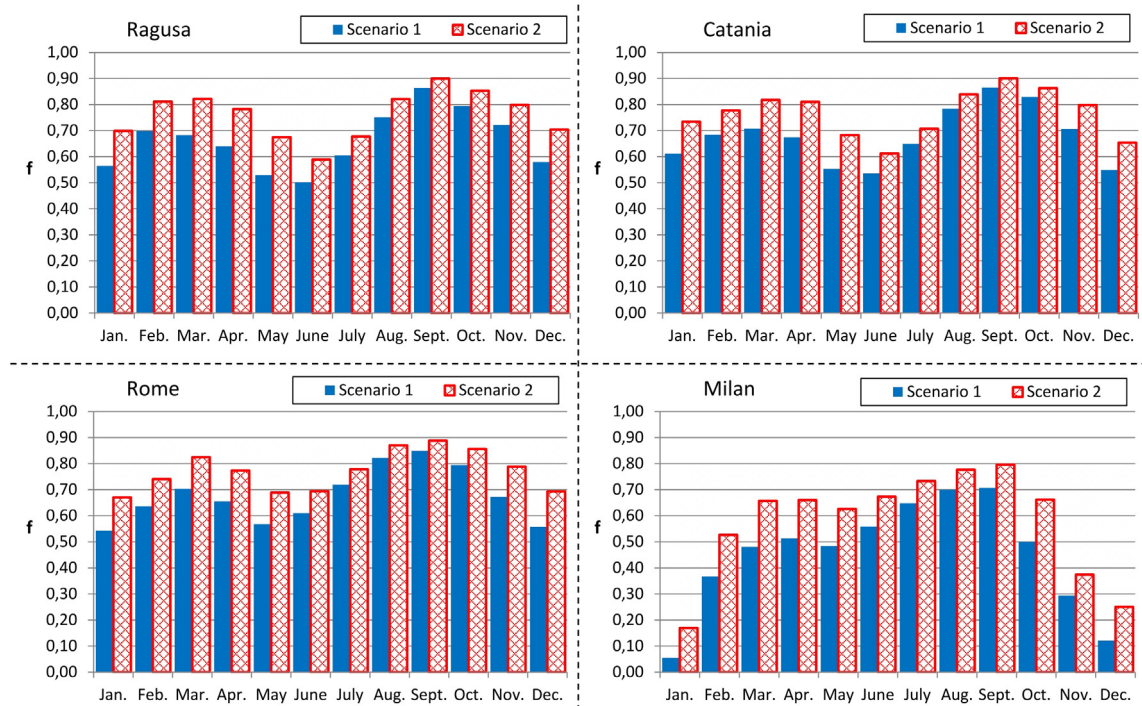


Fig. 15. Map of the building (left side); photo of the two BSTF prototypes (right side).

temperature from the solar collector and the temperature in the lowest part of the solar storage tank.

Nearby the pilot v-BSTF, a meteorological station equipped with a set of sensors for the measurements of the outdoor air temperature, global radiation on the vertical plane, wind speed and direction was installed. Moreover, the superficial temperatures on the back of the solar collectors and on the building wall and the air velocity are measured at different heights into the air gap. The air pressure difference between the inlet and outlet sections of the air gap, the superficial temperature on the front of the solar collector and the air temperature in the indoor space were also measured. All the measured parameters were recorded in a data logger [16].

LSI Lastem manufacturer commercializes all the components of the monitoring system.

Fig. 16 depicts the different sensors installed.

Fig. 17 depicts the cross section and the front view of the v/BSTF installed.

Moreover, the positions and the name of the sensors installed on the v-BSTF facade are indicated. The placement of the temperature sensors was conceived for the purpose to evaluate the vertical gradient of the temperatures, on the surface facade and on the rear of the v_BSTF, generated by the airflow in the air gap.

The comparison of the temperatures measured with sensor TS₇ with the temperatures measured on the building façade (TS₁, TS₃, and TS₅) allows evaluating the difference of temperature on a surface directly exposed to the sun rays and on a shaded surface. Moreover, the lag and fluctuation of the peak temperatures can be evaluated on the above mentioned surfaces.

The sensors that measure the surface temperature are called TS_i (i = 1, 2 ... 7). They are installed in the middle part of each solar panel, three in adherence to the building wall (TS₁, TS₃, and TS₅), others three in the back of the solar plate panel (TS₂, TS₄, and TS₆). The sensor TS₇ is installed into the front face of the lower solar panel of the v/BSTF.



Fig. 16. Features of the main sensors installed.






	Outdoor air temperature	Air temperature	Total radiation	Wind speed and direction	Surface temperature
					
Measuring range	-50÷70°C	-50÷70°C	0÷2000W/m ²	>0.36m/s	-50÷70°C
Accuracy	0.10°C	0.10°C	±5%	1.5%	0.15°C
Response time	30s	30s	23s	0.48s	35s

Fig. 17. Section and front view of the v-BSTF façade with the installed sensors.

The comparison of the temperatures measured with sensor T_{S7} with the temperatures measured on the building façade (T_{S1} , T_{S3} , and T_{S5}) allows evaluating the difference of temperature of a surface directly exposed to the sun rays and a shaded surface. Moreover, the time shift between the peaks of temperatures in those surface may be pointed out.

6.2. On-site measurements

Fig. 18 depicts the data collected through the monitoring system during six winter days. The upper part of this figure shows the solar irradiance and the environmental temperature, while the lower part shows the temperatures measured by the sensors.

It is possible to observe that during these sunny days the

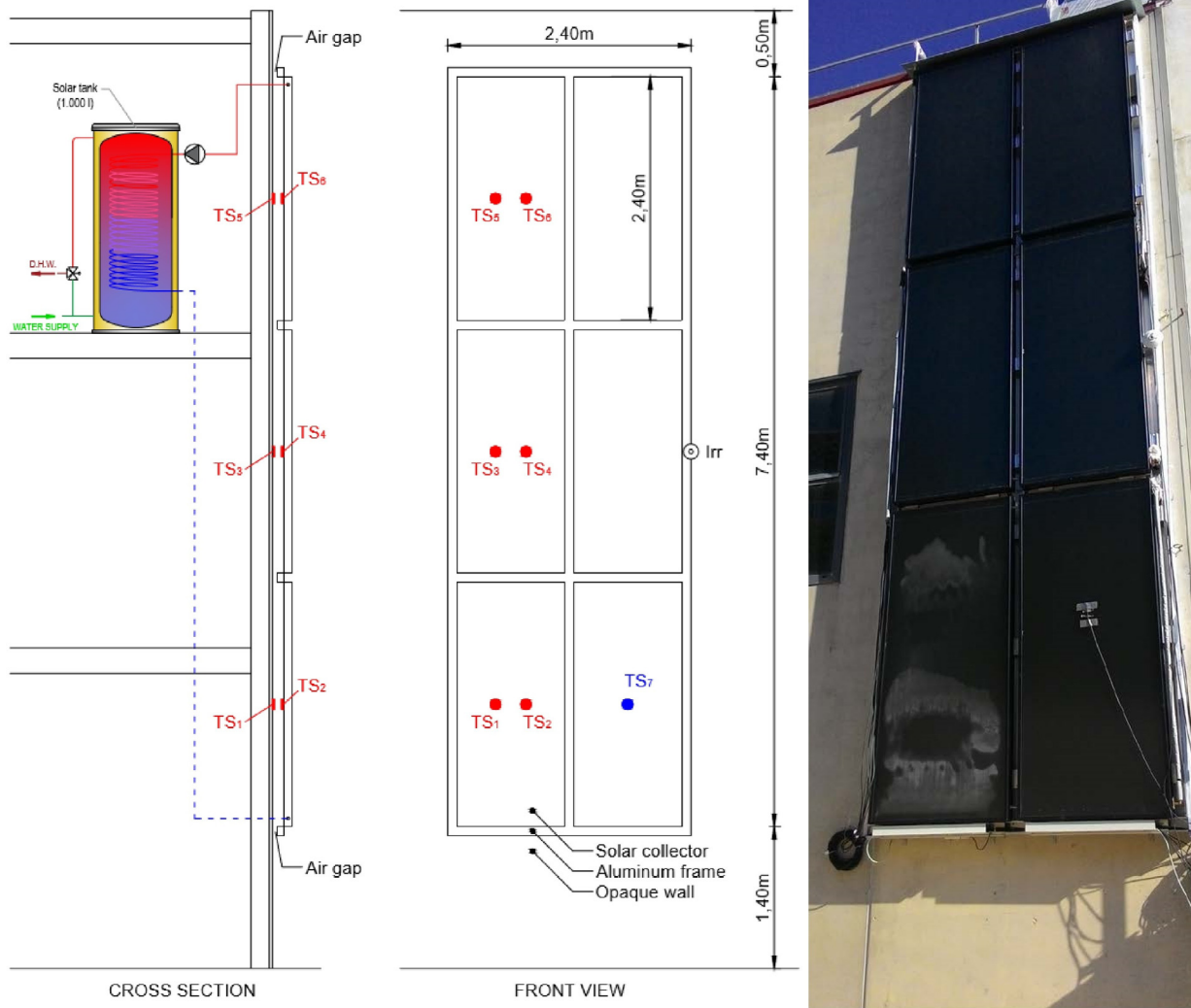


Fig. 18. Experimental data measured on the v-BSTF.

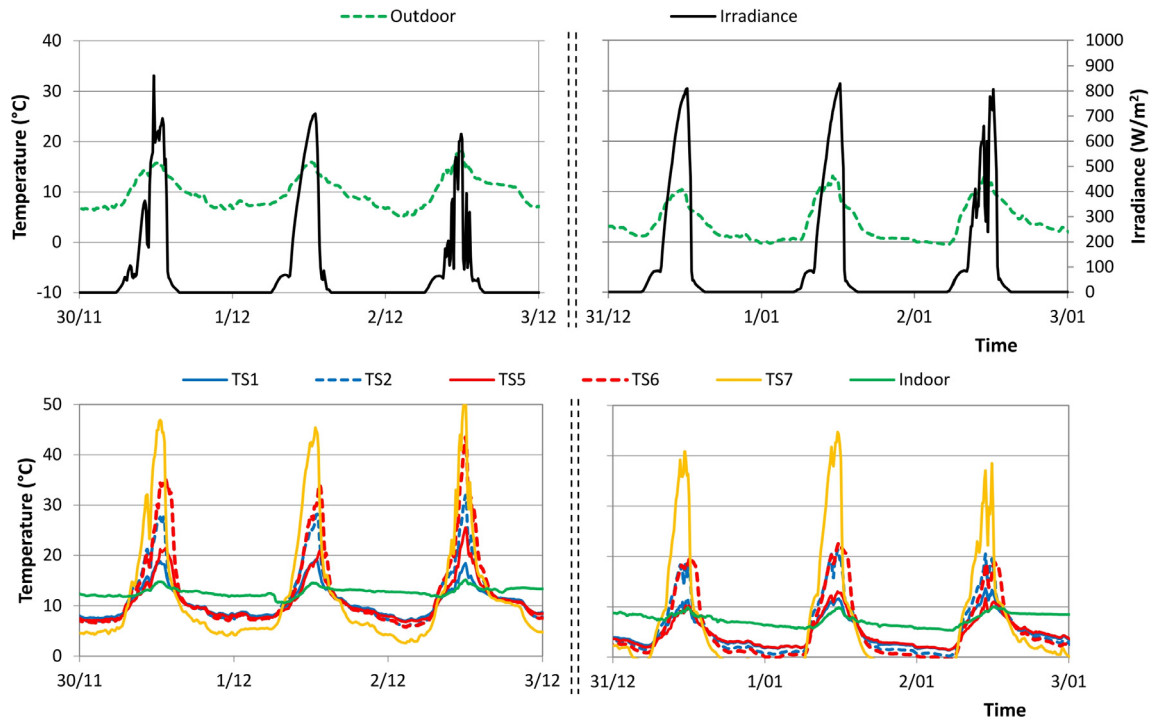


Fig. 19. The monitored data during the 1st December.

thermal behavior of the v/BSTF is quite similar.

Fig. 19 shows the details of the monitored data during one of these days (1st December).

It is possible to notice that the superficial temperature (T_{s7}) on the front of the solar panel is the highest during day-time (the surface is heated by the solar radiation) and it is the lowest during night-time (the surface is cooled by radiative losses versus the skydome). Such temperature has the highest thermal drop.

On the back of the solar collectors, the highest temperature is reached in the upper part of the solar facades (T_{s6}).

This means that the surrounding air is heated flowing out in the ventilated air gap. The temperatures differences between the highest and the lowest sensor ($T_{s6} - T_{s2}$) increase during the daytime reaching a maximum of about 10 °C about at 13:30.

The temperatures measured on the building facade, (T_{s1} and T_{s5}), once again increase moving from the bottom up of the building façade, reaching a temperature difference of about 5 °C ($T_{s5} - T_{s1}$) at 13:30.

During daytime, these temperatures (T_{s1} , and T_{s5}) are permanently higher than the outdoor air temperatures. During night-time a reversal behavior occurs, since the superficial temperatures on the building facade (T_{s1} and T_{s5}) are about 5 °C higher than T_{s7} and close to the outdoor temperature. This result designates a reduction of the radiative heat-losses from the wall surface to the skydome in comparison with a façade directly exposed to the skydome.

Finally, it has to be remarked that the solar façade causes a decrease of the solar gains during the winter period, since a part of the solar energy that strikes the facade is used for heating the fluid in the solar circuit.

However, as well known this shortcoming may be neglected considering that only a low percentage of the solar radiation that strikes the opaque façade is useful for reducing the building thermal load. And also, that during night-time the v-BSTF allows reducing the heat losses through the building envelope as previously mentioned.

During the summer period the combined effect of shading and

ventilation deriving by the adoption of v-BSTF allows achieving remarkable energy savings, up to 50.0% [35].

7. Conclusions

This study evaluates the viability of solar thermal plant added to the building facades (BSTF) under different climate conditions. Thus, the energy and environmental analysis of vertical solar thermal facade constructed with flat plate solar collector or evacuated tube solar collector (ETC) used for DHW production have been investigated through numerical simulations by TRNSYS software.

In particular, the performances of the solar façades were investigated in four different Italian cities. The simulations were conducted considering the DHW requirements of a typical Italian family. The results of simulations provide the temperatures reached in the thermal storage, the energy supplied by the solar plant as well as the auxiliary energy supplied.

The comparison among the different cities shows that the BSTF allows reducing the fluctuations of the coverage factor “ f ” throughout the year, especially when evacuated tube collectors are used. Moreover, during the summer, the reduced solar radiation that hits the vertical surfaces avoids thermal energy overproduction and therefore the risk of overheating and the consequent energy waste.

The yearly analysis highlights that under the scenario 1, BSTF constituted by just 4.0 m² of FPC, the coverage factors “ f ” of about 67.0% in Catania and Roma, 65.0% in Ragusa and 44.0% in Milan are achieved.

Otherwise, under scenario 2, BSTF constituted by just 4.0 m² of ETC, an increase of the performance especially in the coldest city (Milan) is obtained. The coverage factors reach values of about 57.0% in Milan and more than 76.0% in the other investigated cities.

The proposed simplified economic analysis highlights that the installation of the ETC instead of the FPC involves payback time of about 20.0 years in Catania, Ragusa and Roma, which does not

justify the adoption of the ETC in such cities. In Milan, the payback time is less than 15 years that may be acceptable under the economic point of view instead.

Both the two BSTF have energy and emission payback times less than 2 years, which are very short in comparison with the life cycle of such solar systems.

The high fraction of the DHW energy requirements supplied through the BSTF, as well as the short energy and CO₂ payback times, allow affirming that a vertical solar façade represents a suitable system for DHW production with great environmental conveniences.

Acknowledgments

This research was developed under the research project Solar Continue Collectors Façade (FCCS) funded by POR FESR Sicilia 2007/2013 - Research line 4.1.1.1. bis.

References

- [1] The International Energy Agency IEA, Key World Energy Statistics, 2015, 2015.
- [2] A. Savvides, C. Vassiliades, A. Michael, S. Kalogirou, Siting and building-massing considerations for the urban integration of active solar energy systems, *Renew. Energy* 135 (May 2019) 963–974.
- [3] I. Visa, A. Duta, M. Moldovan, Outdoor performance of a trapeze solar thermal collector for facades integration, *Renew. Energy* 137 (2018).
- [4] S.A. Kalogirou, Building integration of solar renewable energy systems towards zero or nearly zero energy buildings, *Int. J. Low Carbon Technol.* 10 (2015).
- [5] C. Lamnatou, J.D. Mondol, D. Chemisana, C. Maurer, Modelling and simulation of Building-Integrated solar thermal systems: behaviour of the coupled building/system configuration, *Renew. Sustain. Energy Rev.* 48 (2015).
- [6] A. Buonomano, F. Calise, A. Palombo, M. Vicidomini, BIPVT systems for residential applications: an energy and economic analysis for European climates, *Appl. Energy* 184 (2016).
- [7] H. Gajbert, Solar Thermal Energy Systems for Building Integration, 2008.
- [8] M.C. Munari Probst, C. Roecker, Towards an improved architectural quality of building integrated solar thermal systems (BIST), *Sol. Energy* 81 (2007).
- [9] F. Motte, G. Notton, C. Cristofari, J.L. Canaletti, Design and modelling of a new patented thermal solar collector with high building integration, *Appl. Energy* 102 (2013).
- [10] C. Maurer, C. Cappel, T.E. Kuhn, Simple models for building-integrated solar thermal systems, *Energy Build* 103 (2015).
- [11] M.V. Albanese, B.S. Robinson, E.G. Brehob, M. Keith Sharp, Simulated and experimental performance of a heat pipe assisted solar wall, *Sol. Energy* 86 (2012).
- [12] A. Buonomano, C. Forzano, S.A. Kalogirou, A. Palombo, Building-façade integrated solar thermal collectors: energy-economic performance and indoor comfort simulation model of a water based prototype for heating, cooling, and DHW production, *Renew. Energy* 137 (2018).
- [13] M. Beccali, G. Leone, P. Caputo, S. Ferrari, Building integrated solar thermal design: assessment of performances of a low cost solar wall in a typical Italian building, *Energy Procedia* 91 (2016).
- [14] M.M. Hassan, Y. Beliveau, Design, construction and performance prediction of integrated solar roof collectors using finite element analysis, *Constr. Build. Mater.* 21 (2007).
- [15] C.N. Antoniadis, G. Martinopoulos, Optimization of a building integrated solar thermal system with seasonal storage using TRNSYS, *Renew. Energy* 137 (2018).
- [16] G. Notton, F. Motte, C. Cristofari, J.L. Canaletti, Performances and numerical optimization of a novel thermal solar collector for residential building, *Renew. Sustain. Energy Rev.* 33 (2014).
- [17] F. Motte, G. Notton, C. Lamnatou, C. Cristofari, D. Chemisana, Numerical study of PCM integration impact on overall performances of a highly building-integrated solar collector, *Renew. Energy* 137 (2017).
- [18] A. Gagliano, G.M. Tina, F. Nocera, A.D. Grasso, S. Aneli, Description and performance analysis of a flexible photovoltaic/thermal (PV/T) solar system, *Renew. Energy* 137 (2018).
- [19] T.T. Chow, K.F. Fong, A.L.S. Chan, Z. Lin, Potential application of a centralized solar water-heating system for a high-rise residential building in Hong Kong, *Appl. Energy* 83 (2006).
- [20] A. Buonomano, G. De Luca, U. Montanaro, A. Palombo, Innovative technologies for NZEBs: an energy and economic analysis tool and a case study of a non-residential building for the Mediterranean climate, *Energy Build.* 82 (2016).
- [21] S.A. Kalogirou, Environmental benefits of domestic solar energy systems, *Energy Convers. Manag.* 45 (2004).
- [22] F. Ardenete, G. Beccali, M. Cellura, V. Lo Brano, Life cycle assessment of a solar thermal collector, *Renew. Energy* 30 (2005).
- [23] F. Ardenete, G. Beccali, M. Cellura, V. Lo Brano, Life cycle assessment of a solar thermal collector: sensitivity analysis, energy and environmental balances, *Renew. Energy* 30 (2005).
- [24] C. Lamnatou, G. Notton, D. Chemisana, C. Cristofari, Life cycle analysis of a building-integrated solar thermal collector, based on embodied energy and embodied carbon methodologies, *Energy Build.* 84 (2014).
- [25] C. Lamnatou, D. Chemisana, R. Mateus, M.G. Almeida, S.M. Silva, Review and perspectives on Life Cycle Analysis of solar technologies with emphasis on building-integrated solar thermal systems, *Renew. Energy* 75 (2015).
- [26] B. Carlsson, H. Persson, M. Meir, J. Rekstad, A total cost perspective on use of polymeric materials in solar collectors - importance of environmental performance on suitability, *Appl. Energy* 125 (2014).
- [27] M. Goedkoop, R. Spriensma, The Eco-Indicator 99 - A Damage Oriented Method for Life Cycle Impact Assessment: Methodology Report, third ed., 2001.
- [28] T. Barker, Climate Change 2007 Synthesis Report: an Assessment of the Intergovernmental Panel on Climate Change, 2007.
- [29] A. Gagliano, G.M. Tina, S. Aneli, S. Nizetić, Comparative assessments of the performances of PV/T and conventional solar plants, *J. Clean. Prod.* 219 (2019).
- [30] S.A. Klein, TRNSYS 16 (2006).
- [31] JRC European Commission, Photovoltaic geographical information system (PVGIS), Joint Research Centre – JRC; Institute for Energy and Transport – IET, 2017.
- [32] S.A. Kalogirou, Y. Tripanagnostopoulos, Hybrid PV/T solar systems for domestic hot water and electricity production, *Energy Convers. Manag.* 47 (2006).
- [33] R.L. Shrivastava, V. Kumar, S.P. Untawale, Modeling and simulation of solar water heater: a TRNSYS perspective, *Renew. Sustain. Energy Rev.* 67 (2017).
- [34] ISPRA, Italian Greenhouse Gas Inventory1990–2015, National Inventory Report, 2017, 2017.
- [35] A. Gagliano, F. Nocera, S. Aneli, Thermodynamic analysis of ventilated façades under different wind conditions in summer period, *Energy Build.* 122 (2016).

Assessment of the electrical and thermal performances of a building integrated photovoltaic thermal plant.

Antonio Gagliano*, Giuseppe Marco Tina, Stefano Aneli
Department of Electrical, Electronic and Computer Engineering
University of Catania, Catania, Italy
e-mail: antonio.gagliano@unict.it

ABSTRACT

An ambitious goal for the building sector is the fulfilment of the buildings energy demand through renewable energy sources (RESs). However, due to the lack of available spaces, different kinds of RESs could not find the necessary surfaces where they can be installed. Therefore, it becomes more and more necessary to think about the integration of solar systems into the building envelope and to use systems that allow a high conversion rate of solar radiation into primary energy. Photovoltaic/thermal (PV/T) plants, which generate simultaneously electrical and thermal energy, allow very efficient exploitation of solar energy.

This research aims to evaluate the energy production of a PV/T system integrated into the building façade (BIPVT), as well as the interaction with the heat fluxes through the building envelope. Such analysis has been carried out by dynamic analysis, using the TRNSYS software, having as references a residential building located in the Mediterranean area. The results of the study indicate that a PV/T system installed on a south-facing façade allows providing more than 170 kWh of electrical energy and about 50 kWh of thermal energy for a square meter of PV/T collector. Moreover, the BIPVT plant slightly increases the demand for space heating and reduces those for cooling, globally the total energy demand is reduced by approximately 65%.

KEYWORDS

BIPVT, solar hybrid system, building energy, thermal fluxes, electricity from the grid, experimental validation, TRNSYS.

1 - INTRODUCTION

The development of technology and the economy is not yet able to reverse the trend of increasing energy consumption in the construction sector. Since there is no technical alternative that eliminates energy consumption in the construction sector, it is necessary to directly produce energy from renewable sources through systems integrated into the building envelope.

Building-Integrated PhotoVoltaic (BIPV) or Solar Thermal (BIST) systems integrate solar PV or Thermal panels as part of the building envelope (e.g. roof, windows, facades and shading devices) [1-4]. Renewable energy generated by these systems contributes to reducing the energy demand of the building and can also be fed/sold to the grid. Furthermore, integrated systems must present ease of architectural and aesthetic integration.

The analysis of a vertical BIST system for DHW production was performed considering four different Italian cities [5]. The findings of this study pointed out that 4.0 m² of FPC are enough to satisfy more than 67% of the DHW demand of a family in the hottest cities and that 4.0 m² of ETC allow satisfying more than 57% of the demand even in cold cities. Furthermore, the BIST allows reducing the fluctuations of the coverage factor throughout the year. Besides, during the summer the reduced solar radiation that hits the vertical surfaces avoids the risk of overheating into the

building. BIPV allows reducing energy consumption due to HVAC by about 28% in hot regions [6]. A drawback of BIPV systems is the higher PV operating temperature in comparison with stand-alone installation [7]. This effect may be reduced using PVT collectors, which produce electricity and low-temperature heat, available for Domestic Hot Water (DHW) and space heating [8] and cooling [9] purposes, where the thermal efficiency can reach 55% [10].

Hybrid photovoltaic/thermal (PV/T) solar collectors take advantages by the solar energy unconverted in electrical energy by a PV module, enhances the energy yield per unit area of roof or façade. They constitute a very interesting technology for increasing the distributed generation and the integration of renewable energy in buildings.

Gagliano et al. [11] have carried out a comparison among the performances two alternatives systems, a PV plant and an ST plant, which generates electrical and thermal energy, and a PV/T plant that produces in cogenerative way thermal and electrical energy. Buonamano et. Al [12] have studied the installation of PVT integrated into the south-facing façade into a non-residential high-rise building, finding a reduction of 46% for the electricity required and of about 10% for DHW and about 28% for space heating.

A PVT roof-mounted system designed to feed the DHW requirements for a multi-housing building is presented in [13]. A key factor for increasing the penetration of renewable energies is their storage. Lamnatou et al. [14] have evaluated which are storage systems most appropriate for BIPV and BIPVT applications, emphasizing the environmental profile of the different storage materials. Several papers are available in the literature regarding the energy analyses of BIPV systems [15] and BIPVT systems [16]. Otherwise few studies deal with the optimization of the whole design of PVT systems integrated into a vertical façade, as well as the variations on the thermal fluxes exchanged through the façade where these systems are implemented.

Therefore, further experimental and analytical studies should be carried out to improve the knowledge with BIPVT systems, based on PV/T water collector, installed on vertical facades.

To cover this lack of knowledge, the present work investigates the thermal behaviour and the energy yield of a BIPVT plant installed in a multi-floor residential building for domestic hot water production. The main novelty of this study consists in the optimization of the ratio between the surface of the PVT water collector and the volume of the thermal storage through a simulation model developed in TRNSYS.

The performances of the WISC PVT module have been described by the tuning of one of the type already available in TRNSYS starting from the experimental data derived by the pilot PVT plant installed at the University of Catania.

Moreover, the proposed BIPVT model takes into account the temperature effect on the PVT electrical production, as well as the heat fluxes exchanged between the PVT module and the other components of the façade the building.

A preliminary experimental analysis on a pilot PVT plant installed in the city of Catania, Italy has been conducted to test the accuracy of the TRNSYS simulation model.

As results, the heating and cooling energy demand, as well as the annual withdrawal of electricity from the electrical grid for the building with and without the BIPVT plant and the different analysed scenario, are evaluated.

The performances of the BIPVT are also described using both consolidated key performance indicator, as well as novel parameters.

2 - METHODOLOGY

This study aims to evaluate the performance of a solar energy source (PV/T systems) installed in the building facades. This could be a suitable solution for multi-storey buildings where the roof surface maybe not enough to install solar plants for all the residential units present.

2.1 - System layout and model description

This study proposes the comparison between a building equipped with BIPVT system and the same building that is not provided with a solar plant, that is the baseline configuration.

In the baseline configuration, it is assumed that the various energy demand (DHW production, space heating and cooling, artificial lighting and other requirements) are provided by an electrical boiler for the DHW production, electrical heat pumps/chillers for space heating and cooling, whilst the electricity is provided by the national grid.

The BIPVT system integrated into the façade is put in place without any ventilated chamber between the PV/T panels and the building facade. The electrical energy produced will be used to satisfy the electrical requirements while the thermal energy is devoted to DHW production. In particular, if the thermal energy produced is less than the demand an auxiliary electrical heater provides the complementary energy requested.

Figure 1 shows the layout adopted for the reference building and the building equipped with BIPVT.

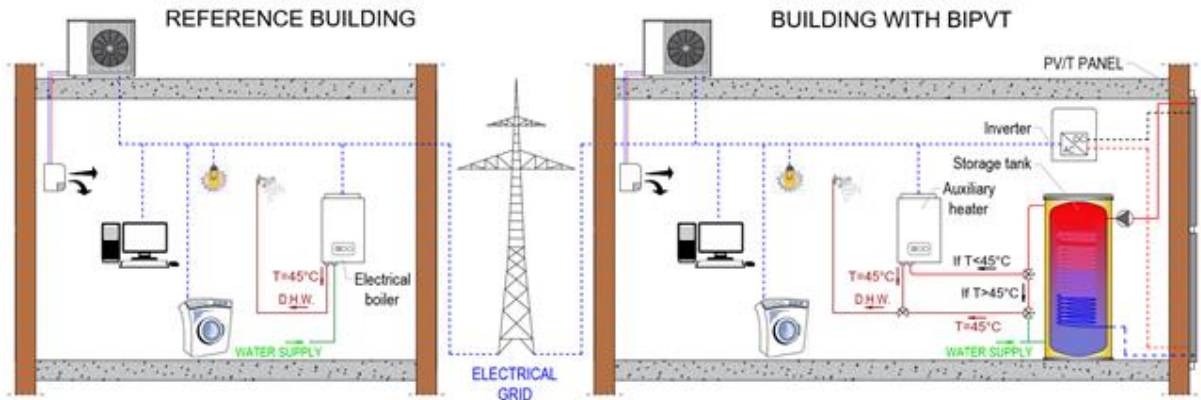


Figure 1. System layout for building with and without BIPVT

As shown in figure 1, the PV/T panels are connected to a solar storage tank through pipes equipped with a pump and a control unit (forced circulation system). The storage tank is a vertical type with the serpentine heat exchanger placed in the lower part of the tank. Tap water from the mains (T_{sup}) enters at the bottom of the tank, while hot water is drawn from the higher part of the tank ($T_{t,out}$). If $T_{t,out}$ is greater than the temperature required by the user ($T_{setpoint}$), the adjustment devices mix it with tap water from the aqueduct. Otherwise, if $T_{t,out}$ is less than $T_{setpoint}$, the auxiliary heater provides the energy necessary to reach the setpoint temperature.

Finally, the electricity supplied by the PV/T panels is converted by an inverter device that operates at the maximum power point (MPP) and it is used directly for the building electrical demand or conveyed to the electrical grid. The topic was studied considering a quasi-steady state approach implemented by TRNSYS software [17].

2.2 - Energy yields and Key Performance Indicators

The electrical and thermal energy produced by a PV/T source can be evaluated using a metric based on the First Law of Thermodynamics.

The eq. 1 allows to calculate the net electricity product ($E_{el,PV/T}$) during a fixed period, where the η_{inv} is the efficiency of the inverter device fixed equal 95%, η_{el} represents the electrical efficiency of panel calculated with eq. 2, A is the surface of the panel, G the total incident irradiation and P_{pump} the power for pumping the coolant fluid.

$$E_{el,PV/T} = \int_0^t (\eta_{inv} \cdot \eta_{el} \cdot A \cdot G - P_{pump}) dt \quad (1)$$

$$\eta_{el} = \eta_{STC} [1 - \beta(T_{PV} - T_{STC})] \quad (2)$$

with η_{STC} efficiency at the Standard Test Conditions (STC), β thermal decay coefficient, T_{PV} temperature of the PV cells and T_{STC} temperature at STC.

The thermal energy ($E_{th,panel}$) produced by PV/T panel can be estimated by applying the thermal balance equations to the fluid passing through the panels (eq. 3).

Moreover, the energy-saving obtained for the DHW production is calculated by eq. 4.

$$E_{th,panel} = \int_0^t \dot{m}_{PV/T} \cdot C_f \cdot (T_{p,out} - T_{p,in}) dt \quad (3)$$

$$E_{DHW,PV/T} = \int_0^t \dot{m}_{DHW} \cdot C_w \cdot (T_{m,out} - T_{sup}) dt \quad (4)$$

where $\dot{m}_{PV/T}$ and \dot{m}_{DHW} are respectively the mass flowrates circulating in the PV/T circuit and that required for DHW, C_f and C_w indicate respectively the specific heat of the coolant fluid and that of the water, $T_{p,out}$ and $T_{p,in}$ are the temperatures of the fluid at outlet and inlet of the PV/T panels, $T_{m,out}$ and T_{sup} are the temperatures of the water from the storage and of the feed water. Finally, the energy provided by the auxiliary (E_{aux}) is calculated by:

$$E_{AUX} = \int_0^t \dot{m}_{DHW} \cdot C_w \cdot (T_{setpoint} - T_{m,out}) dt \quad (5)$$

One of the main Key Performance Indicators (KPI) of energy production plants from renewable sources is the demand coverage factor (f), that is the ratio between the energy supplied by the system and that required by users. Therefore, the coverage factors are calculated for electricity (f_{el}), DHW (f_{DHW}) and global demand (f_{TOT}).

$$f_{el} = 100 \cdot \frac{E_{el,PV/T}}{E_{el,load}} \quad [\%] \quad (6)$$

$$f_{DHW} = 100 \cdot \frac{E_{DHW,PV/T}}{E_{DHW,load}} \quad [\%] \quad (7)$$

$$f_{TOT} = 100 \cdot \frac{E_{el,PV/T} + E_{DHW,PV/T}}{E_{el,load} + E_{DHW,load}} \quad [\%] \quad (8)$$

where $E_{DHW,load}$ and $E_{el,load}$ are respectively the DHW and the total electrical demand, calculated as:

$$E_{el,load} = \frac{E_{el-Heating}}{COP} + \frac{E_{el-Cooling}}{EER} + E_{el-apps} \quad (9)$$

In a PV/T installation, the electrical performances depend by the temperature of the working cells, which in turn depends on the solar irradiation (G). Thus, it is worth of interest to introduce a KPI, namely $T_{char,PV}$ (eq. 10), which allows evaluating the working temperature of the PV cells weighted by G .

$$T_{char,PV} = \frac{\int T_{PV} \cdot G \cdot dt}{\int G \cdot dt} \quad (10)$$

To determine the thermal level of the water supplied by the solar system to satisfy users demand, the KPI $T_{char,DHW}$, is defined using the eq. 11, where the temperature of the water coming from the solar system is weighed for the instantaneous water flow required by the user for the DHW demand.

$$T_{char,DHW} = \frac{\int T_{m,out} \cdot \dot{m}_{DHW} \cdot dt}{\int \dot{m}_{DHW} \cdot dt} \quad (11)$$

Finally, the $T_{char,panel}$, which indicates the coolant thermal level achieved in the panels, is calculated using eq. 12.

$$T_{char,panel} = \frac{\int T_{f,av} \cdot G \cdot dt}{\int G \cdot dt} \quad (12)$$

where $T_{f,av}$ is the average temperature of the fluid inside the PV/T panels.

The thermal efficiency is calculated by [18]

$$\eta_{th} = \eta_0 - a_1 \frac{\Delta T^*}{G} - a_2 \frac{\Delta T^{*2}}{G} \quad (13)$$

where η_0 is the optical efficiency, a_1 is the heat loss coefficient, a_2 is the temperature dependence of the heat loss coefficient, G is the total solar irradiance, ΔT^* is the difference between the average temperature of the fluid inside the PV/T panels and the ambient temperature.

2.3 – Case study

The case study refers to a multi-family house, well-representative of conventional Italian constructions, located in the South-Italy (Catania).

The features of the building envelope were chosen according to those of the buildings built in the period 1970-2000 in southern Italy, which correspond to about 50% of the building stock.

The analysis of the building energy demand is referred to an apartment placed on intermediate floors, with a floor area of 100.0 m² and net volume of 300 m³.

This apartment has three walls facing the outdoor environment, to East, South and West orientation, each with an area of 30.0 m², of which 9.0 m² constituted by glazed surfaces.

Table 1 shows the main features of the components of the building envelope.

Table 1. main features of the components of the building envelope

U_{wall}	Wall surface mass	U_{glass}	SHG	Air infiltrations	Sensible and Latent Heat gains
[W/(m ² K)]	[kg/m ²]	[W/(m ² K)]	[-]	[vol/h]	[W/person]
0.587	227.0	2.83	0.755	0.52	77.0, 55.0

The number of occupants is 0.04 per square meter as suggested by the UNI 10339 norm. The heating period goes from December 1st to March 31st; the cooling period is set from June 1st to September 30th, the setpoint temperature are set respectively to 20°C and 26°C.

The building energy demands are of 712.0 and 1,442 kWh respectively for the space heating ($E_{el,heating}$) and cooling ($E_{el,cooling}$) respectively for the baseline scenario.

The total consumption for DHW is 152.5 l/day, according to the Italian regulation [UNITS11300-2], with the daily profile defined by the standard EN 15316:2007. Finally, the $T_{setpoint}$ is fixed at 40 °C and the T_{sup} is 15 °C.

The BIPVT plant is realized with twelve water WISC PV/T mono-crystalline (c-Si) modules. This PV/T module has an electrical efficiency of 15.4% at Standard Test Conditions (STC), temperature coefficient (β) of 0.44%. and peak power of 250 W.

The parameters used for calculating the thermal efficiency by equation 13, are the optical efficiency $\eta_0 = 0.55$ and the coefficient $a_1 = 15.76 \text{ W(K}\cdot\text{m}^2)$.

The BIPVT is installed in the façade facing south and has a net surface of 19.92 m², with an installed peak power of 3.0 kWp. The electrical energy demand is determined by energy demand for space heating and cooling, and that one necessary for the common household appliances $E_{el,app}$, this last are is fixed equal to 3,000 kWh/y [19].

3 –MODELIZATION OF THE WISC PV/T COLLECTOR

In this study, the Wave PV/T panels produced by DualSun is taken as a reference as they are used in the pilot PV/T plant installed at the DIEEI of the University of Catania. All the characteristics of this plant and the monitoring system are described in [20]. Therefore, there is the availability of huge experimental data that are used to validate the results carried out through the simulations.

The type 563 available into TRNSYS software libraries is used for simulating the studied BIPV/T system, since it may be connected to the multi-zone building model. Consequently, the influence of the PVT collector on the building heating and cooling loads can be assessed.

This type needs of the following input parameters main geometric characteristics, thermal resistances of the various layers that make it up and the electrical characteristics of the module.

The outputs of type 563 are the thermal and electrical efficiency, the outlet fluid temperature and the collector efficiency curve of the PVT panels.

The first objective of this study is to evaluate the effectiveness of the results of this type with the observed experimental data. Figure 2 shows the plot of the experimental values observed in different periods of the year and with a specific mass flow rate of 0.30 kg/(min·m²) as a function of the ratio $\Delta T^*/G$.

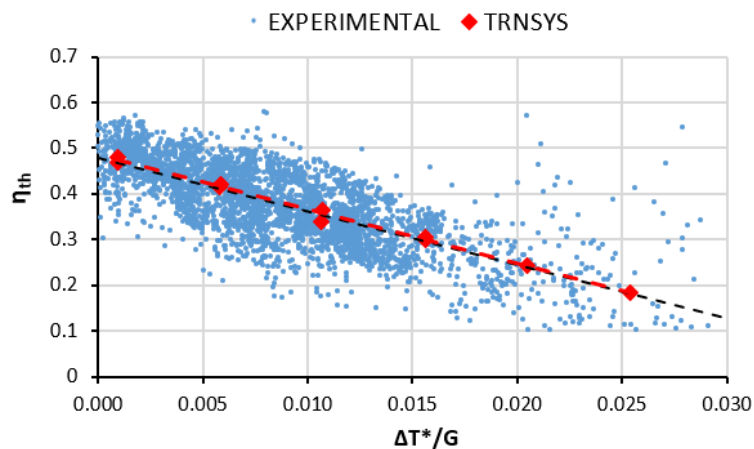


Figure 2. Thermal curves comparison between experimental and simulated values

As it is possible to observe there is a great dispersion of the value of the thermal efficiency, so a best-fit curve has been determined, which is characterized by a coefficient, η_0 of 0.48 and a_1 of 11.6 W(K·m²), which are rather different by the results carried during the laboratory tests. However, as they are referred to real operating conditions that take into account the ageing effect, we have decided to use these data for characterizing the performance of the investigated PV/T collector.

Thus, the input parameter used by the type 563 have been tuned in such a way to replicate the experimental data. As it can be observed, the simulated data provide an accurate evaluation of the efficiency curve of the investigated PV/T collector, indeed, the curve obtained by the interpolation of the simulated values in TRNSYS (red dashed line), overlaps almost perfectly that obtained by the interpolation of the experimental data (black dashed line).

4 – RESULT AND DISCUSSIONS

4.1 - Sizing of the storage tank in a BIPVT

The performances of the BIPVT plant are investigated analysing the effect of different volume storage on the energy yield provided by the investigated system.

All the simulations have been performed utilising higher resolution hourly weather data for Catania [21]. The specific mass flow rate of 0.30 kg/(min·m²) was determined after sensitivity analysis, which is within the range of the values suggested by Duffie and Beckman [18].

As regards the volume of the thermal storages it strongly influences the performance, larger is the volume higher is the efficiency of the PVT collector, while the temperature of the produced water has an inverse trend. Thus, the volume of the storage is varied from 10 to 50 litres per square meter of PV/T panel. The analysis is limited to 50 l/m² since larger volume does not increase the energy output, as will be illustrated in the following.

Figure 3 shows the sensitivity analysis carried out in terms of electrical yields (left side) calculated by eq. 1, the thermal yields generated by the PVT panel ($E_{th,panel}$) and the useful energy for DHW production ($E_{DHW,PV/T}$) calculated by eq. 3 and 4.

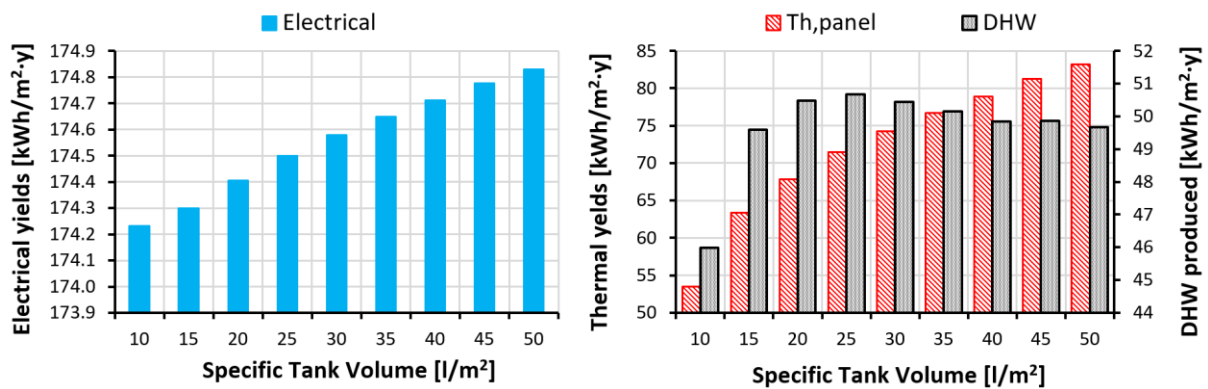


Figure 3. Annual electrical (left) and thermal (right) energy yield per m² of PV/T panel.

It is observed that either the electrical energy and the thermal energy increases with the increase of the specific volume. This result is quite obvious since the higher is the volume of the tank the lower are the operating temperatures and consequently either the electrical and the thermal efficiency. Otherwise, focusing the analysis on the thermal energy derivable for DHW, which take into account of the enthalpic content of the hot water, it is observed that E_{DHW} has a maximum for the specific volume of 25 l/m². The decreases of E_{DHW} is mainly due to the increase in the thermal losses from both the storage tank and the PV/T collectors.

An equivalent analysis has been carried out observing the variation of the energy demands for space heating and cooling, as well for the total building energy needs deriving by the summation of the needs for space heating, cooling and DHW production. Figure 4 shows the yearly energy needs per square meter of the floor as a function of the specific volume tank.

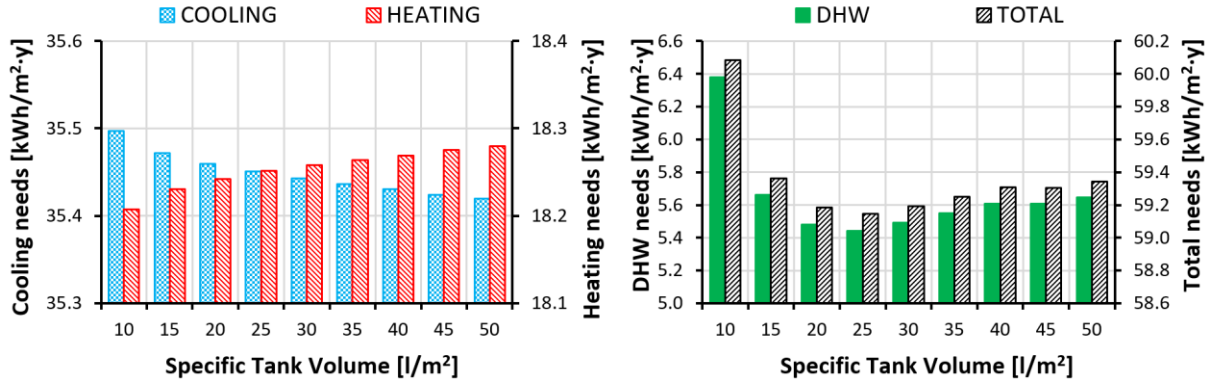


Figure 4. Specific cooling, heating, DHW and total yearly energy needs.

It can be highlighted that the specific energy needs for space cooling ($E_{Cooling}$) and heating ($E_{Heating}$), as predictable, have an opposite behaviour, $E_{Cooling}$ decreases as the volume of the tank increases while $E_{Heating}$ increases. This is due to the decrease in the average temperatures of the coolant fluid inside the BIPVT facade as the tank volume increases. Otherwise, the energy demand for DHW has a minimum for the specific volume of 25 l/m². The total energy demand (E_T), given by the summation of $E_{Cooling}$, $E_{Heating}$ and E_{DHW} , has the minimum value, of 59.15 kWh/y m², for a specific volume of the tank of 25 l/m² of PV/T area.

Finally, figure 5 shows, the variation of the coverage factors f_{EL} , f_{DHW} and f_{TOT} , on the left side, and the characteristic temperatures for the PV cell ($T_{char,PV}$), the coolant fluid ($T_{char,PVT}$) and the DHW ($T_{char,DHW}$) on the right side, as a function of the specific volume of the storage tank.

The variation of the coverage factor confirmed the results obtained through the previous analysis, i.e the electrical f_{EL} increases as the specific tank volume (V_{ST}) increases up to 65.2%, while the f_{DHW} reaches the maximum value, of 65%, for $V_{ST} = 25$ l/m². The opposite trends of these two coverage factors determine the finding that f_{TOT} is almost constant for $V_{ST} > 25$ l/m², so an increase of the volume storage determines an ineffective oversizing of the system.

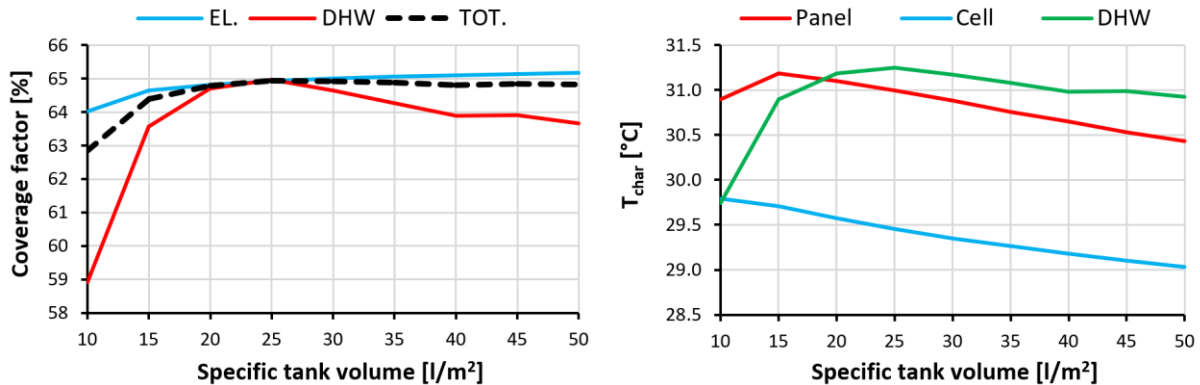


Figure 5. characteristic temperatures.

As regards the $T_{char,panel}$, it reaches its maximum value for the specific tank volume (V_{ST}) of 0.15 l/m², while it decreases almost linearly for $V > 0.15$ l/m².

Otherwise, the $T_{char,cell}$ decreases almost linearly with the increase of the volume storage.

Finally, the $T_{char,DHW}$ has its maximum for the specific volume of the tank of 25 l/m² of panels.

Therefore, for the investigated BIPVT façade, which utilises WISC PV/T panels, the analysis conducted highlight that a thermal tank with a specific volume of 25 l/ m² of PVT panel allows maximising the overall producibility of the system, the thermal level of the water produced for DHW and minimizes the overall energy demand of the building.

This outcome has great significance as it indicates that the volume of the water tank per unit area of a PVT collector is about half of the minimum values of 50 l/m² suggested by [18].

4.2 – Energy demand for the building with and without BIPVT

This section compares the all-year-round energy requirements of the building with and without the BIPVT system. The BIPVT plant has been designed utilising the optimized value defined in the previous section. Figure 6 shows the daily electrical and thermal energy demand for the two-building configurations. In particular, the yellow area depicts the electric demand for typical households appliances (e.g. lighting, TV, dishwasher and so on) supposed constant during the year, the green area indicates the energy consumption for DHW, assumed as constant for the baseline configuration; the red and the blue area indicates the energy demand for space heating and cooling. Finally, the black dotted curve indicates the electricity produced by the BIPVT plant.

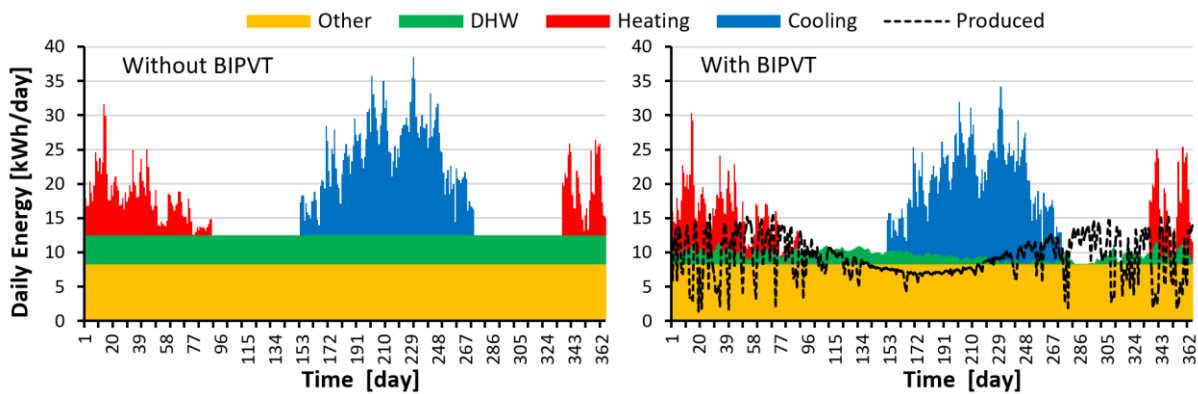


Figure 7. Daily energy demand for the baseline and the BIPVT scenario.

It is possible to observe as the total daily electrical demand for space heating and cooling is extremely variable during the days and according to the seasons.

The dotted black line, which represents the power production of the BIPVT plant is also extremely variable, with minimum values of 1.4 kWh/day for cloudy days and maximum of 15.5 kWh/day for sunny days. It can be highlighted as the daily energy demand for DHW production for the building with the BIPVT plant are significantly reduced in comparison with the baseline configuration. As previously underlined the energy requirements for space heating and cooling between the two configurations are very modest, as evidenced in Table 2.

During the midseason, the electricity produced exceeds the demand of the building, Otherwise, during the winter and summer period, the electricity production is not sufficient for balancing the large electrical demand requested for satisfying the heating and cooling load.

Globally, the BIPVT plant generates 3,354.0 kWh of electric energy and 1009.0 kWh of thermal energy for DHW production. This means that a BIPVT plant installed on a façade facing sud generate 168.0 kWh/m² (1,118 kWh/kWp) of power production and 50.5 kWh/m² of thermal energy for DHW production.

Figure 7 shows the coverage factors for electrical, thermal and total energy demand achieved by using the proposed BIPVT system.

The coverage factor for the electrical demand, f_{el} , varies from about 40% during the summer, up to the total fulfilment of the electric demand during the mid-seasons, when there is no demand of electricity for heating or cooling.

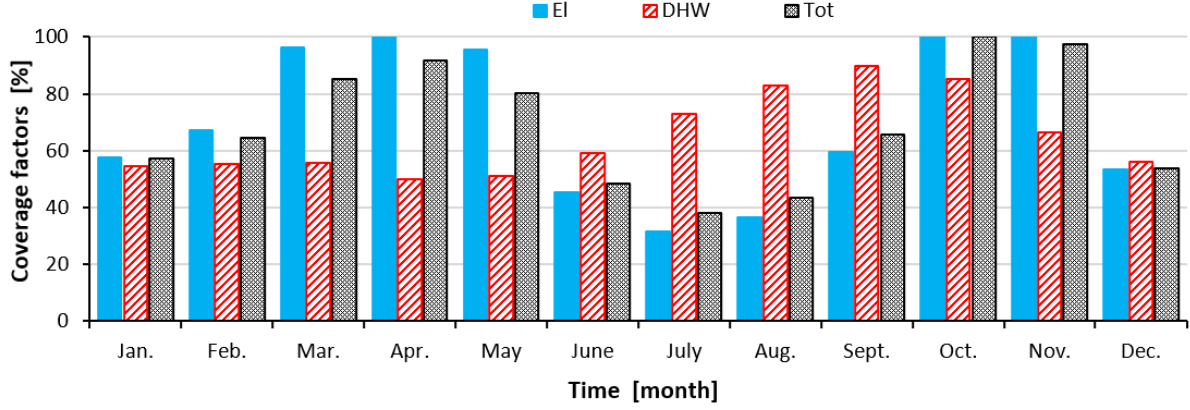


Figure 7. Monthly coverage factor.

The f_{DHW} is always higher than 50%, it reaches 90% for the months between August and October, thanks to either the high solar radiation, which hit the south façade and the outdoor air temperatures. Looking at f_{Tot} , it exceeds 80% in spring and autumn, with the highest yearly peak in October. These results suggest that for improving the performance of a BIPVT system, the use of thermal insulated PV/T collectors is suggested. Indeed these PV/T collectors allow achieving better performance during the cold season without negatively affecting the electrical production due to the low air temperatures. In Table 2, the annual electric requirements for air conditioning, differentiated for space heating and cooling ($E_{el-Heating}$ and $E_{el-Cooling}$), electrical household appliances (E_{el-app}), the annual energy for DHW production (E_{DHW}), and the electricity drawn from the grid, for the two configurations are indicated. It is also indicated the percentage difference between the two building configurations, calculated by eq. 14.

$$\Delta E = \frac{E_{BIPVT} - E_{baseline}}{E_{baseline}} \quad (14)$$

Table 2. Comparison of the energy demand for the two-building configurations

	$E_{el-Heating}$ [kWh]	$E_{el-Cooling}$ [kWh]	E_{el-app} [kWh]	$E_{el-grid}$ [kWh]	E_{DHW} [kWh]
Baseline	712	1,442	3,000	5,159	1,553
BIPVT	730	1,418	3,000	1,805	544
$E_{BIPVT} - E_{baseline}$	18	-24	-	-3,354	-1,009
ΔE (%)	2.51	-1.68	-	-65.01	-64.97

Globally, the installation of BIPVT increases the energy required for space heating of 18 kWh, that is about 2.5%, and decreases that one for space cooling of 24 kWh, that is 1.7%.

These results indicate that the investigated BIPVT does not meaningful modify the thermal fluxes exchanged through the building facades. The energy demand either for DHW production and electrical demand are reduced by about 65%.

Moreover, it is interesting to observe that the electrical power production for the studied BIPVT façade fulfils the energy demand for the common household electrical appliances (i.e. 3,000 kWh) with a modest surplus. Finally, it has to be highlighted these results are obtained with the ratio between the peak power of the BIPVT and the annual electricity demand of 0.58 Wp/kWh.

5 - CONCLUSION

Through a semi-stationary approach, carried out using TRNSYS software, the performances of Building Integrated PhotoVoltaic/Thermal system (BIPVT) installed in the south of Italy has been investigated. The analysed BIPVT plant, installed in the south façade of a building located in the city of Catania (IT), is equipped with 22.00 m² of PV/T panels, with electric peak power of 3,000 Wp. One of the first results of this study is the draw-up of the procedure for tuning the TRNSYS type 563 in such way to attain results that are effective for the PV/T type used in this study.

To this aim, the experimental data collected in the pilot PV/T system installed in the University of Catania are used. A second outcome has been derived through the sensitivity analysis conducted for evaluating the effect of the volume storage on the overall performance in of the BIPTV systems. This analysis has highlighted that the adoption of a specific volume of 25 l/m² of PV/T collectors allows achieving better energy performances.

This information is of crucial importance for the design of a BIPVT plant as it indicates that the volume of the water tank per unit area of a PVT collector is about half of the minimum values of 50 l/m² suggested by literature studies.

As regards the energy demand for space heating and cooling, it is highlighted that the installation of a solar facade has very modest effects. Globally, an increase of the energy demand for space heating of 18 kWh, and decreases of 24 kWh for space cooling, which represent a variation of about 2.5% and 1.7% respect to respective energy demand.

As regards the energy demand either for DHW production and power, these are reduced by approximately 65%. However, it is interesting to observe that the electrical power production fulfils the energy demand for the common household electrical appliances (i.e. 3,000 kWh). This finding indicates that a ratio of 0.58 Wp/kWh between the peak power of PV/T and the electrical load is indicated to balance production and demand. Future development of this research foresees the analysis of BIPVT system built with thermal insulated PV/T collectors since this typology of PV/T collectors allows to achieve better performance during the winter period without negatively affecting the electrical performance due to the low air temperatures.

ACKNOWLEDGMENT

This research is funded by “the Notice 12/2017 for financing the Ph.D. regional grant in Sicily” as part of the Operational Program of European Social Funding 2014-2020 (PO FSE 2014-2020).

This work was also financed by the University of Catania within the project "Piano della Ricerca Dipartimentale 2016–2018" of the DIEEI of the University of Catania

NOMENCLATURE

Latin symbols	
<i>A</i> Surface Area (m ²)	<i>G</i> Irradiance (W/m ²)
<i>a</i> heat loss coefficient of thermal panel	<i>m</i> mass flowrate (kg/s)
<i>C</i> specific heat (J/(kg·K))	<i>P</i> power (W)
<i>E</i> energy (Wh)	<i>T</i> Temperature (°C)
<i>f</i> coverage factor of need	<i>t</i> time (s)
Greek symbols	
β thermal decay coefficient (°C ⁻¹)	Δ difference (dimensionless)
η efficiency (dimensionless)	

REFERENCES

1. Edelman, M., Lundgren, M., Nigel, K., Frontini, F., Munari Probst, M.C., Scogniamiglio, A., Giovanardi, A., Roecker, C., Snow, M., Farkas, K., Maturi, L., Zanetti, I., Wall, M., SOLAR

- ENERGY SYSTEMS IN ARCHITECTURE - integration criteria and guidelines, *Report T.41.A.2: IEA SHC Task 41 Solar energy and Architecture*, 2012.
2. Jelle, B.P., Breivik, C., State-of-the-art building integrated photovoltaics, *Energy Procedia*, vol 20, pp 68-77, 2012.
 3. Ritzen, M., Vroon, Z., Geurts, C., Building integrated photovoltaics, *Photovoltaic solar energy: from fundamentals to applications*, Wiley, Chichester, pp. 579-589, 2017.
 4. Peng, C., Huang, Y., Wu, Z., Building-integrated photovoltaics (BIPV) in architectural design in China, *Energy and Buildings*, Volume 43, Issue 12, Pages 3592-3598, 2011
 5. Gagliano, A., Aneli, S., Nocera, F., Analysis of the performance of a building solar thermal facade (BSTF) for domestic hot water production, *Ren. Energy*, Vol. 142, pp 511-526, 2019.
 6. Salameh, T., El Haj Assad, M., Tawalbeh, M., Ghenai, C., Merabet, A., Öztop, H.F., Analysis of cooling load on commercial building in UAE climate using building integrated photovoltaic facade system, *Sol. Energy*, Vol 199, pp 617-629, 2020
 7. Memari, A.M., Iulo, L.D., Solnosky, R.L., Strultz, C.R., Building integrated photovoltaic systems for single family dwellings: innovation concepts, *Open J. of Civil Eng.*, vol 4, pp 102-119. DOI: 10.4236/ojce.2014.42010
 8. Buonomano, A., Calise, F., Palombo, A., Vicidomini, M., BIPVT systems for residential applications: An energy and economic analysis for European climates, *Applied Energy*, Vol. 184, pp 1411-1431, 2016.
 9. Buker, M.S., Mempo, B., Riffat, S.B., Experimental investigation of a building integrated photovoltaic/thermal roof collector combined with a liquid desiccant enhanced indirect evaporative cooling system, *Energy Conv. and Manag.*, Vol. 101, pp 239-254, 2015.
 10. Debbarma, M., Sudhakar, K., Baredar, P. Comparison of BIPV and BIPVT: A review *Resource-Efficient Technologies*, Vol 3, Issue 3, pp 263-271, 2017.
 11. Gagliano, A., Tina, G.M., Aneli, S., Nizetic, S., Comparative assessments of the performances of PV/T and conventional solar plants, *J. of Cleaner Prod.*, Vol 219, pp 304-315, 2019.
 12. Buonomano, A., Calise, F., Palombo, A., Vicidomini, M., Transient analysis, exergy and thermo-economic modelling of facade integrated photovoltaic/thermal solar collectors, *Ren. Energy*, Vol 137, pp 109-126, 2019.
 13. Del Amo, A., Martínez-Gracia, A., Bayod-Rújula, A.A., Antoñanzas, J., An innovative urban energy system constituted by a photovoltaic/thermal hybrid solar installation: Design, simulation and monitoring. *Ap. Energy*, Vol 186, Part 2, pp 140-151, 2017.
 14. Lamnatou, C., Notton, G., Chemisana, D., Cristofari, C., Storage systems for building-integrated photovoltaic (BIPV) and building-integrated photovoltaic/thermal (BIPVT) installations: Environmental profile and other aspects, *Sc.of The Tot Env.*, Vol 699, 2020,
 15. Shukla, A.K., Sudhakar, K., Baredar, P., A comprehensive review on design of building integrated photovoltaic system, *En. and Buildings*, Vol 128, pp 99-110, 2016.
 16. Ibrahim, A., Fudholi, A., Sopian, K., Othman, M.Y., Ruslan, M.H., Efficiencies and improvement potential of building integrated photovoltaic thermal (BIPVT) system, *En. Conv. and Manag.*, Vol 77, pp 527-534, 2014.
 17. Klein, S.A., Beckman W. A., et al., TRNSYS, A Transient Simulation Program. ASHRAE 82, 1976.
 18. Duffie, J.A., Beckman W.A., Solar engineering of thermal processes. 2nd ed. New York: John Wiley & Sons; 1991.
 19. Gagliano A., Patania F., Nocera F., Capizzi A., Galesi A., GIS-based decision support for solar photovoltaic planning in urban environment- Sustainability in Energy and Buildings, 2013
 20. Gagliano, A., Tina, G.M., Nocera, F., Grasso, A.D., Aneli, S., Description and performance analysis of a flexible photovoltaic/thermal (PV/T) solar system, *Ren. Energy*, Vol 137, Pages 144-156, 2019.
 21. <https://ec.europa.eu/jrc/en/pvgis>

A novel building ventilated façade with integrated bifacial photovoltaic modules: analysis of the electrical and thermal performances

Giuseppe Marco Tina
DIEEI
Università degli studi di Catania
Catania, Italy
giuseppe.tina@unict.it

Fausto Bontempo Scavo
DIEEI
Università degli studi di Catania
Catania, Italy
faustobontempo@hotmail.it

Stefano Aneli
DIEEI
Università degli studi di Catania
Catania, Italy
stefano.aneli@unict.it

Antonio Gagliano
DIEEI
Università degli studi di Catania
Catania, Italy
agagliano@dii.unict.it

Abstract—The Energy Performance of Buildings Directive (EPBD) is, together with the energy efficiency directive, the main legislative instrument to promote the buildings energy performance and to boost renovation within the EU. EPBD requires that all new buildings have to reach the objective to be nearly Zero-Energy Buildings (nZEBs) by 2020. The concept of nZEBs focuses on firstly improving the energy performance of the building envelope and, then, integrating Renewable Energy Sources (RESs) to cover the remaining energy demand. In this context, photovoltaic (PV) systems provide a reliable solution for electricity supply either in existing or new buildings. Building Integrated Photovoltaic (BIPV) systems have the twofold advantage of increasing the prospects of renewable energy in the built environment, whilst providing savings in materials and construction time by replacing traditional building elements. Recently, bifacial PV cells have attracted interest because of their potential to increase PV modules power production. Integration of bifacial PV modules into a building façade represents a significant step forward in the application of this relatively new technology. Such façade can serve not only as a renewable source of electricity acting as an active system but also it contributes to reducing the building cooling needs acting as a passive system. In this paper, a multilayer one-dimension dynamic thermal model of monofacial glass-back sheet and bifacial glass-glass PV modules integrated into a building façade is presented. Given the geometry and PV technologies of the considered facades, as well as Catania (Italy) weather conditions, it has been shown that the bifacial glass-glass PV modules can produce an energy yield of about 5% more than the monofacial PV module.

Keywords— *Renewable energy, photovoltaic, BIPV, ventilated, façade, bifacial.*

I. INTRODUCTION

The façades of buildings are one of the most technologically complex components of a building, both from an architectural point of view, as they must show the aesthetic and engineering value as they play a significant role in protecting and maintaining the internal thermal conditions.

Currently, the construction sector is responsible for around 40% of global energy consumption in many developed and developing countries [1,2]. As a result, improving energy efficiency in buildings has become one of the core programs of government sectors towards sustainable city development.

Over the years, various practices have been adopted to improve performance, including the implementation of ventilated façades, which have multiple advantages, such as reducing the building's energy needs [3]. A greater effect can be found in Mediterranean climates with hot summers and mild winters.

The ventilated façade is made up of an interior and exterior wall with an air gap between them where the outdoor air flows. The airflow can be generated either through natural convection or by mechanical means. The heat gain on the interior wall is limited through the cooling obtained by the ventilation into the air gap [4,5]. The heat gain through the inner wall reduces as the distance between the two layers is made larger [6].

Ventilated façades differ from each other in the characteristics and the criteria with which they are made, for example, the material of the external surface which can be transparent or opaque, active (photovoltaic modules, vegetation etc...) or passive (bricks, glass etc ..), the size of the cavity, as well as the size of the openings of the air inlet channel and so on. Hawala has made a detailed classification concerning the different types of façade in [7].

One of the most recent solutions of ventilated façades is the realization of the external surface of the wall, using photovoltaic modules. By integrating these systems into buildings, there is a double effect, reducing the heat input in the building and producing electricity from renewable sources [8].

The most common photovoltaic panels are opaque and can, therefore, act as shading devices [9]. A more recent technology that is making its way into buildings are semi-transparent PVs that can be incorporated into the glass [10,11].

The advantages of semi-transparent photovoltaic systems include an increase in daytime lighting compared to more opaque façades, a reduced heat gain compared to double transparent glass and on-site electricity generation.

If, moreover, high-performance photovoltaic modules such as bifacial ones are installed, the overall energy yield of the system is also increased as a share of energy is also produced from the rear surface of the photovoltaic module.

So bifacial modules, compared to traditional monofacial solar panels, allow increasing the power density per unit area [12].

In [13] it is stated that it is possible to obtain up to 50% more energy than monofacial PV modules by simultaneously collecting the albedo radiation coming from the roof and surrounding surfaces closest to the PV module, using a concentration device that increases albedo radiation.

The bifacial modules have a lower LCOE than the classic monofacial modules [14]. Furthermore, they're often more durable because both sides are UV resistant, and potential-induced degradation (PID) concerns are reduced when the bifacial module is frameless. They have a longer lifetime for the glass-glass structure compared with the traditional glass-back sheet module configurations, because double glass modules have lower cell temperature [15], and the rear glass can still stand in unfavourable environments. Balance of system costs (BOS) is also reduced when more power is generated from bifacial modules in a smaller array footprint.

To obtain energy gains due to bifaciality, installations of highly reflective internal wall surfaces are suggested to reflect as much solar radiation as possible on the rear face of the module. Soria in [16] has shown to obtain a maximum energy gain, relative to a bifacial module installed in vertically wall to 20 %.

In the present study, different alternatives of active façades are investigated under the point of view of (i) thermal behaviour of PV module, (ii) electrical yields and (iii) thermal exchange between PV panels and building envelope.

In detail, four active façades systems were considered:

- unventilated active façade with an integrated monofacial module, (BIPV);
- ventilated active façade with an integrated monofacial module (V-BIPV);
- ventilated active façade with an integrated bifacial module (V-BIbPV);
- ventilated active façade with an integrated bifacial module and reflective treatment in the internal wall (Vr-BIbPV) with a reflection coefficient r_{wall} equal to 0.7.

This numerical study has been carried out by simulations in Matlab® environment, considering the weather dynamic conditions of a Mediterranean city.

The main goal of this research is to identify the type of active façade which maximizes electricity production considering different periods of the year, but in the meantime, we want to highlight how the different active façades influence the thermal fluxes exchanged through the building envelope.

II. METHODS

The study of performance and thermal behaviour of several active façades was conducted using numerical models developed in Matlab® environment.

The features of the active façades were chosen starting from the characteristics of two pilot façades which are going to be realized in the laboratories of the DIEEI department of the University of Catania (Italy). Therefore, the geometric configuration, the exposure of the façades, the characteristics of

the photovoltaic modules as well as the property of internal wall, replicate the features of the ongoing experimental system.

A. Numerical models

The developed numerical models allow to evaluate the thermal behaviour and performance of the active façade system in dynamic state conditions and are based on energy balance equations.

The heat fluxes exchanged among the layers that compose the active façades and the fluxes exchanged with the external environment are governed by the three basic mechanisms of heat transfer: radiation, convection, and conduction.

For the studied active façades, the following thermal fluxes occur: convection and thermal radiation between the inner slab of the façade and the indoor environment; conduction through the different layers of the inner wall; convection between the outer slab of the inner wall and the air in the cavity; convection between the rear part of PV module and the air in the cavity; thermal radiation between the outer slab of the inner wall and the rear side of PV module; conduction through the different layers that make up the PV module; convection and thermal radiation between the front side of PV module and the outdoor environment.

The main difference between a ventilated and an unventilated active façade lies in the air gap. Indeed, in the ventilated active façade the air can circulate freely, as the interspace is in contact with the outside through an opening.

Figure 1 shows a graphic representation of the unventilated active façade and the ventilated active façade. In the case of unventilated active façade (BIPV) it has been assumed that the monofacial PV module is installed in adherence to the wall of the building and that the air present between the tedlar and the external layer of the wall is trapped inside the frame of the PV panel

Three alternatives active ventilated façades were studied. The V-BIPV is realised with opaque monofacial PV modules, in which the rear layer is made of tedlar material. The V-BIbPV is realised with a semi-transparent bifacial PV module, in which the rear layer is made up of a layer of glass. Finally, the Vr-BIbPV is again realized with a semi-transparent bifacial PV module differs with the addition of a high reflection paint posed on the outermost surface of the interior wall.

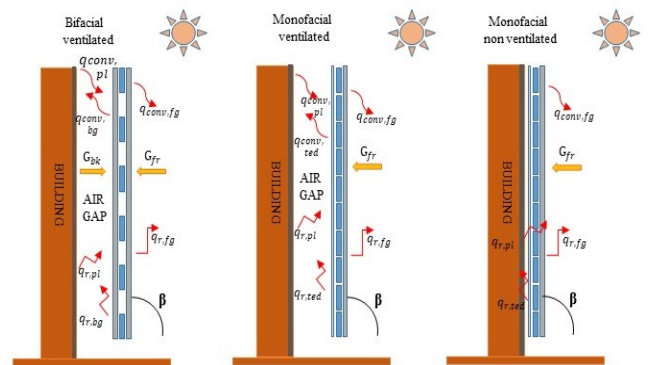


Fig. 1. Schematic representation of the modeled configurations: (a) V-BIbPV and Vr-BIbPV (b) V-BIPV (c) BIPV

In Figure 1 the terms q_{conv} and q_r refer to the heat fluxes on both sides of the PV module, described by the subscripts “fg”,

“bg”/“ted”, due to the convection and radiation phenomena respectively. G_{fr} and G_{bk} represent the solar irradiance that hit the module on the front and the backside respectively.

For each layer (ith) that compose the active façade, the following energy balance has been written:

$$\frac{dE_i}{dt} = \dot{E}_{incoming} - \dot{E}_{outgoing} \quad (1)$$

Where the first member indicates the stored energy in the layer ith, $E_{incoming}$ and $E_{outgoing}$ indicate respectively the incoming and the outgoing energy fluxes.

The balance equations are simultaneously solved using the ode45 function in Matlab, modified via the fourth-order Runge Kutta method. The simulations were conducted using 1440 daily time steps (time step equal 1 minute).

The conductive heat fluxes are taken into account using Fourier's formulation (eq. 2).

$$\dot{Q}_{cd} = -\lambda A \frac{\Delta T}{\delta} \quad (2)$$

where λ , δ and A are the thermal conductivity, layer thickness and surface of the considered layer, ΔT indicates the temperature gradient.

The radiative exchanges with the skydome have been calculated using the Stefan-Boltzmann law and the ground (eq. 3). The view factor is equal to 1/2 being the panel/façade placed vertically. The ground temperature is calculated using the eq. 4. The radiative fluxes between the two layers separated by the air gap are calculated using the view factor for flat and parallel surfaces (eq. 5). Whereas, the convective exchanges are calculated using the eq. 6 [17]:

$$\dot{Q}_{rad,fg-sky/gr} = \frac{1}{2} \sigma_0 \varepsilon_{fg} A (T_{fg}^4 - T_{sky/gr}^4) \quad (3)$$

$$T_{gro} = T_{air} + \frac{\alpha_{gr} G_H}{h_{gr}} \quad (4)$$

$$\dot{Q}_{rad} = \frac{\sigma_0 A (T_1^4 - T_2^4)}{\frac{1}{\varepsilon_1} + \frac{1}{\varepsilon_2} - 1} \quad (5)$$

In eq. 5 σ_0 is the Stefan-Boltzmann constant, ε represent the emissivity of the layer, α_{gr} the absorptivity coefficient of ground, G_H the total horizontal irradiation and h_{gr} the convection coefficient.

$$\dot{Q}_{conv} = 0.85 \left(1.959 + 1.517 |T - T_{airgap}|^{\frac{1}{3}} + 1.33 w_{airgap} \right) \quad (6)$$

In Eq. 6, T is the temperature of the layer facing the airgap, T_{airgap} is the average temperature of the air inside the gap, w_{airgap} is the average air velocity in the chamber.

In the case of an unventilated cavity, the Newton formula (eq. 7) is used where the convection coefficient (h) is set equal to 11.1 W/(m²K) [18].

$$\dot{Q}_{conv} = hA(T - T_{airgap}) \quad (7)$$

For the convective exchanges with the outdoor environment, calculated using eq. 7, the convective coefficient

(h) is calculated using different expressions as reported in [19, 20].

As regards the irradiation incident on the façade (G_{fr}), it is given by the sum of the radiation incident on the vertical surface (G_V) plus the reflected part by the ground (eq. 8).

$$G_{fr} = G_V + \alpha_{gr} G_H \quad (8)$$

In the case of semi-transparent (bifacial) PV modules, the part of solar irradiation entering the chamber that hits the internal wall is calculated through eq. 9, where τ_{fg} is the transmission coefficient of the glass and PF is the packing factor, i.e. ratio between the total PV cells area and the PV module area.

$$G_t = \tau_{fg} G_{fr} (1 - PF) \quad (9)$$

Finally, the incident solar irradiation on the rear of the semi-transparent module (G_{bk}) is calculated using eq. 10, where r_{wall} indicates the reflective coefficient of the internal wall.

$$G_{bk} = r_{wall} G_t \quad (10)$$

The electrical efficiency of the PV module has been calculated starting from the cell temperature:

$$\eta = \eta_{STC} [1 - \beta_0 (T_{pv} - T_{STC})] \quad (11)$$

The electrical power is calculated using eq. 12 and eq. 13 respectively for monofacial and bifacial modules.

$$P_{elm} = \eta \cdot A \cdot G_{fr} \quad (12)$$

$$P_{elb} = \eta \cdot A \cdot G_{fr} + \eta \cdot BF \cdot A \cdot G_{bk} \quad (13)$$

Where BF is the bifaciality factor and is defined as follows:

$$BF = \frac{\eta_{STC,bk}}{\eta_{STC,fr}} \quad (14)$$

B. Case studies

The scenarios analysed refer to an active façade with or without a ventilation chamber, and with different types of the PV modules (i.e. monofacial and bifacial) and the reflective coefficient of the internal wall.

The ventilated active façades have an air gap of 10 cm thickness, where the air is free to circulate in any climatic condition.

For the scenario, V-BibPV, the reflective coefficient of the internal wall was assumed of 0.2 and 0.7 for the Vr-BibPV scenario a highly reflective paint is posed on the internal side of the air gap.

In all scenarios, the façade has dimensions of 1.0 m wide and height equal to the length of the PV module (about 2.0 m). The physical properties of each layer are shown in Table 1.

The building wall is made up of 20 cm of brick and 2 cm of plaster. To take into account the variation of the temperature into the wall, it is divided into 6 homogeneous layers. Two of them are constituted by plaster with a thickness of 1cm and the other four are constituted by a section of 5 cm of brick. The temperature inside the building is kept at 20 °C during the wintertime, 26°C during the summertime. The 1 surface thermal resistance on the internal side of the building is posed to 0.13 m²K/W [21].

TABLE I. MODEL LAYERS CHARACTERISTICS OF PV FAÇADE

Symbol	$A_{fg/bg}$	$L_{fg/bg}$	$W_{fg/bg}$	$\delta_{fg/bg}$	$C_{fg/bg}$	$\rho_{fg/bg}$	$\lambda_{fg/bg}$	$\alpha_{fg/bg}$	$\tau_{fg/bg}$	$\epsilon_{fg/bg}$	
Front/back Glass	1.975	1.979	0.998	0.003	980	2300	1.0	0.03	0.90	0.89	
Symbol	A_{pv}		BF	δ_{pv}	C_{pv}	ρ_{pv}	λ_{pv}	α_{pv}	η_{STC}	β_0	
PV cells (pv)	1.797		>85	0.00035	0.757	2.330	168.0	0.93	17.0	0.038	
Symbol	A_{ted}	L_{ted}	W_{ted}	δ_{ted}	C_{ted}	ρ_{ted}	λ_{ted}	α_{ted}			
Tedlar		1.979	0.998	0.0002	1.200	1.500	0.2	0.90			
Symbol		L_{gap}	W_{gap}	$\delta_{gap vent}$	C_{gap}	ρ_{gap}	$\lambda_{gap unvent}$	$\delta_{gap unvent}$			
Air gap		2.0	1.0	0.10	1.005	1.20	0.026	0.02			
Symbol	L_w	W_w	δ_{pl}	δ_{brick}	C_{brick}^{pl}	ρ_{pl}	λ_{brick}	λ_{pl}	λ_{brick}	ϵ_{pl}	Γ_{wall}
Inner wall	2.0	1.0	0.02	0.2	1000	1800	600	1.0	0.4	0.7	0.2/0.7

C. Weather data

This study was carried out considering the active façades located in the city of Catania (37° 30' 0" N - 15° 6' 0" E). The weather data (i.e. solar irradiation, wind speed, and air temperature) used for the implementation of the numerical model were taken from PV-GIS database [22].

All comparisons were done considering the façades facing south and evaluating the performance during three "representative" clear days: winter solstice, spring equinox and summer solstice. Figure 2 shows the daily outdoor temperature, the daily incident solar irradiation on the façades (continuous line) and the solar irradiation on the horizontal plane (dashed line).

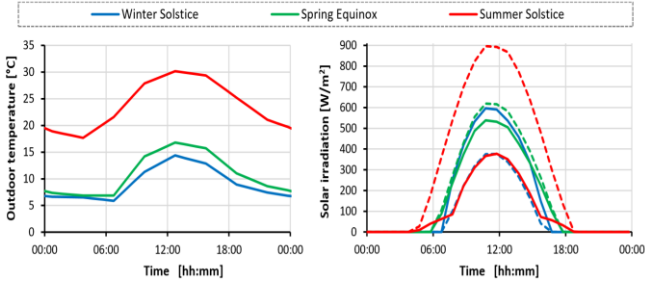


Fig. 2. Temperature (left) and solar irradiation (right) for the three reference days.

III. RESULTS AND DISCUSSIONS

This section compares the thermodynamic behaviours and the energy performance for the studied technologies of active façades.

A. Thermal and performance behaviour of the integrated PV modules

Figure 3 shows the main results obtained for the four technologies analysed considering the three climatic seasons described above. In detail, on the left side, the comparisons of the temperature of the photovoltaic cells are shown, while on the right side the electrical efficiencies (dashed lines) and the electric power (continuous lines) are shown.

The patterns of the plotted variables do not depend evidently on the considered studied days (equinox and solstices) whereas the numerical values are different (see for example the values at sunrise and sunset time and noon).

Observing the cell temperatures, it is noted that the BIPV has the maximum values because there is no ventilation behind the modules since they are directly integrated into the building envelope. In the ventilated active façades the cell temperatures are much lower than in the BIPV with differences sometimes even higher than 5°C. For the V-BiBIPV, the lowest temperatures are achieved. In fact, in the V-BIPV technology, the tedlar layer blocks much of the solar radiation incident on it, heating up, while in the bifacial panels, the rear glass (which replaces the tedlar) allows most of it to pass, guaranteeing temperatures of about 1-2°C lower than the same geometry equipped with a conventional PV panel. Finally, V-BiBIPV and Vr-BiBIPV have very similar cell temperatures, with a temperature increase in the case of maximum Vr-BiBIPV of 0.5°C, caused by the higher solar radiation incident on the back of bifacial modules.

The electrical efficiency is strongly influenced by the temperature of the cells (eq. 11), therefore a similar behaviour can be observed but opposite to that seen for the temperature of the modules. In the case of BIPV, the modules have the lowest efficiency, while rear ventilation increases their efficiency in the case of V-BIPV. Finally, the adoption of the bifacial module generates, albeit minimal, a further increase in efficiency compared to the case of the V-BIPV.

The electric power produced depends on the available solar irradiation and the electrical efficiency (eq. 12 and 13), therefore in line with what was previously seen, in the case of BIPV the lower values are obtained, while the ventilation in the V-BIPV allows an increase of approximately 1.5% during peak hours compared to the same module installed without an air gap, thanks to the increase in electrical efficiency. The use of the bifacial modules allows a further increase in the produced power, as the module benefits from the increase in incident solar irradiation in the backside, with an increase in power in the peak hours of 2.9% compared to the same geometry with a conventional module (V-BIPV) and 4.4% compared to BIPV. Finally, the adoption of reflective material in the outer envelope of the wall allows the Vr-BiBIPV to further increase performance, with an increase in peak power of 7.4%, 5.7% and 2.9% compared, respectively, to BIPV, V-BIPV and V-BiBIPV.

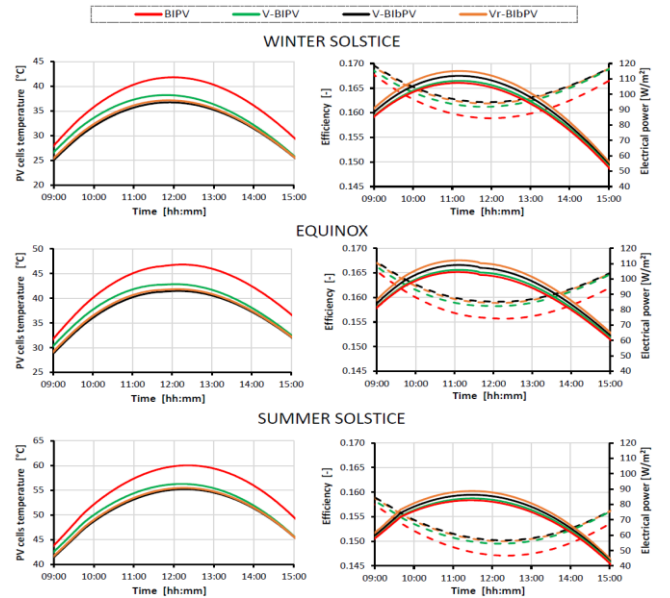


Fig. 3. Daily profiles of cell temperature, efficiency and electrical power.

B. Thermal behaviour of the "active façade" system

The difference in the thermal behaviour of the "active façade" system affects the heat flux through the wall, as well as the profile of the temperatures within the wall and the layers of the active façades.

Figure 4 shows the temperature profiles for the three days analyzed at the centre of the wall, observed during the two solstices at noon.

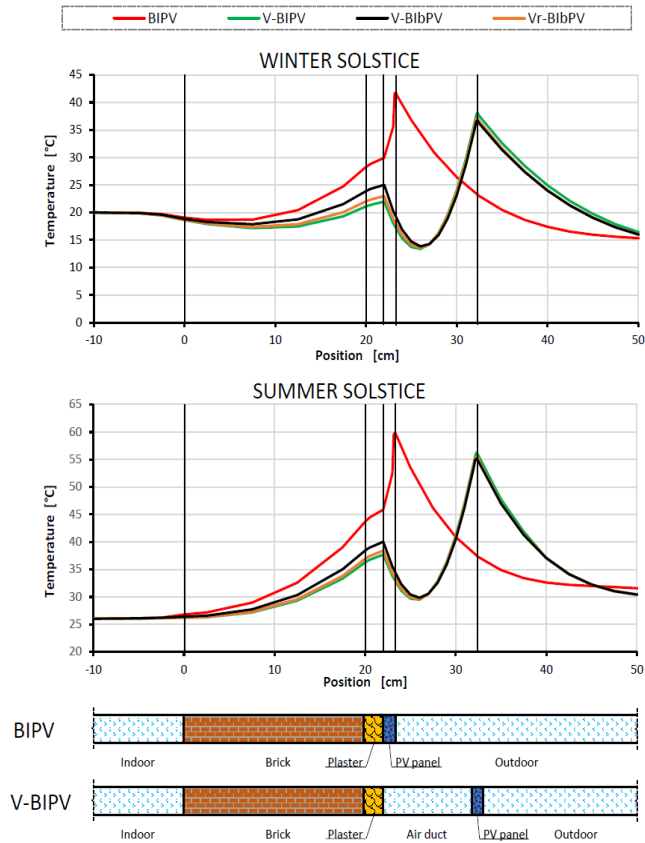


Fig. 4. Temperature into the whole façade at noon, during winter and summer day.

In the case of ventilated active façades, the superficial temperature on the internal side of the air gap is significantly lower than that one of the unventilated façade (BIPV), thanks to airflow that cools the wall, so a modest amount of heat is transferred to the building wall.

Otherwise, in the case of BIPV, the lack of ventilation in the backside of the panel generates an increase of the temperatures of the panel (as previously highlighted). This behaviour allows active ventilated façades to reduce thermal loads during the summer season, but which can also lead to the reduction of solar gains during the winter season. By comparing in detail the three active ventilated façades, it is noted that the maximum temperatures of the building envelope occur in the case of V-BiBpV, since the back glass allows that from it a part of solar radiation hit directly the wall. In the case of Vr-BiBpV, the use of the reflective surface reflects part of the incident irradiation on the wall, thus reducing the heat absorption. Finally, the use of the conventional module (V-BIPV) achieves the lowest temperatures, because it completely enables the solar radiation to directly hit the wall.

C. Equations Energy production and thermal energy requirements

As the technology adopted varies, the performance in terms of the power generated, as well as the thermal fluxes through the walls of the building.

Figure 5 shows the comparison of the four technologies analyzed, considering the daily electrical energy produced (at left) and the daily thermal fluxes through the wall (at right), where the negative value corresponds to outgoing flux (heat losses) and positive if the flux is towards inside (gains).

The results on the daily power yields reflect what has been already highlighted examining the instantaneous powers, thus among the four scenarios, the lowest power production occurs in the case of BIPV. The ventilated active façades exceed the power production compared to the BIPV scenario of about 1.2% in the case of V-BIPV, about 3.9% in the case of V-BiBpV and of about 7% in the case of Vr-BiBpV.

Moreover, the ventilated active façades compared with the BIPV scenario cause an increase of the heat losses during the winter season, while strongly reduce the heat gains during the summer season. Therefore, the choice of the most appropriate system must be calibrated looking to the needs of the building user and the climatic conditions of the site.

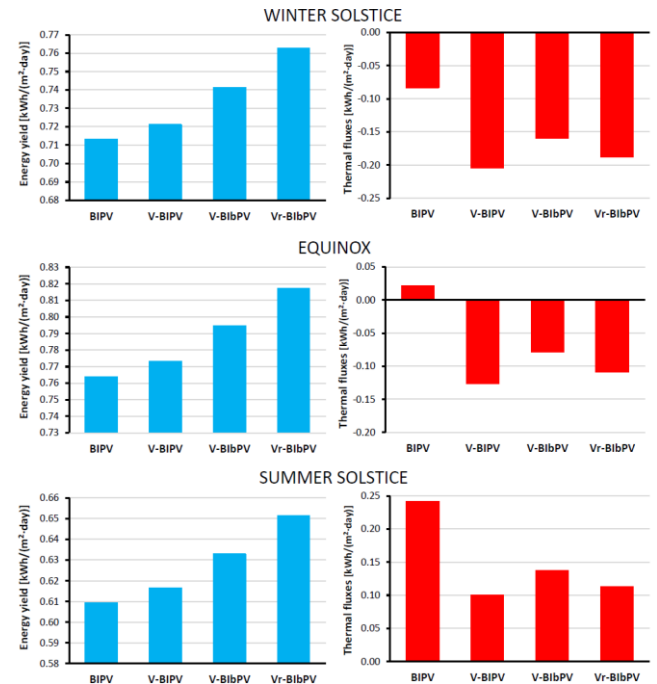


Fig. 5. Daily electrical yields and daily thermal fluxes through the façade.

IV. CONCLUSION

In this study, the thermal and electrical performances of four active façades systems, that are an unventilated active façade with an integrated monofacial module, (BIPV), a ventilated active façade with an integrated monofacial module (V-BIPV); two ventilated active façade with an integrated bifacial module, (V-BiBpV and Vr-BiBpV). These last two façades differ for the reflective treatment in the internal wall, rwall, which are respectively 0.2 and 0.7. These analyses are carried out by developing numerical models in Matlab[®]. The simulations have been conducted considering the weather climate in the city of Catania Italy) during the winter and summer solstices and the spring equinox. The obtained results have evidenced that the use of the bifacial modules allows

increasing the produced power, as such modules benefit from the incident solar irradiation in the backside. Specifically, an increase of the PV power in peak hours of 2.9% compared to the same geometry with a conventional module (V-BIPV) and 4.4% compared to BIPV have been calculated. Moreover, the adoption of reflective material in the outer envelope of the wall allows the Vr-BibPV to further increase performance, with an increase in peak power of 7.4%, 5.7% and 2.9% compared, respectively, to BIPV, V- BIPV and V-BibPV. Other findings of this study are the analysis of the heat fluxes transmitted through the façade. It has been pointed out that the ventilated active facades compared with the BIPV scenario cause an increase of the heat losses during the winter season, while strongly reduce the heat gains during the summer season. Therefore, the choice of the most appropriate system must be calibrated looking to the needs of the building user and the climatic conditions of each site. Further development of this study will be the built of an experimental setup for testing the effective performances of the investigated systems as well as of the numerical model proposed

ACKNOWLEDGMENT

This research was conducted with the financial support of the MIUR by the Notice 12/2017 for financing the industrial PhD "PON FSE-FESR RICERCA E INNOVAZIONE 2014-2020 AZIONE I.1 and by the Notice 12/2017 for financing the Ph.D. regional grant in Sicily" as part of Operational Program of European Social Funding 2014-2020 (PO FSE 2014-2020).

NOMENCLATURE

Latin symbols	
<i>A</i> Surface Area (m ²)	PF packing factor (dimensionless)
<i>a</i> albedo	G Irradiance (W/m ²)
BF Bifaciality factor	h Convective coefficient
C Heat Capacity (J/K)	H Horizontal
<i>c</i> Specific heat (J/kgK)	T Temperature (°C)
<i>r</i> reflection coefficient	w wind speed (m/s)
Greek symbols	
α Cell absorptivity (dimensionless)	β Tilt angle (°)
β₀ thermal coefficient (°C ⁻¹)	λ Thermal conductivity (W/m·K)
ε Emissivity (dimensionless)	σ Boltzmann constant (W/m ² ·K ⁴)
γ Coefficient of solar radiation (dimensionless)	τ Transmissivity (dimensionless)
η Electrical efficiency (dimensionless)	ρ Density (kg/m ³)
Abbreviations	
STC Standard Test Conditions	m Monofacial
NOCT Normal Operating Cell Temperature	b Bifacial
fr front	bk back
Subscripts	
bg Back glass surface	gr Ground
cd Conduction	mod Module
el electrical	pv Photovoltaic
conv Convection	Wall wall
fg Front glass surface	r Radiative
ted Back tedlar surface	pl plaster

REFERENCES

- [1] Cuerda E, Pérez M, Neila J. Façade typologies as a tool for selecting refurbishment measures for the Spanish residential building stock. *Energy Build* 2014;76:119–29
- [2] Aflaki A, Mahyuddin N, Mahmoud ZA-C, Baharum MR. A review on natural ventilation applications through building façade components and ventilation openings in tropical climates. *Energy Build* 2015;101:153–62.
- [3] A. Gagliano, F. Nocera and S. Aneli, "Thermodynamic analysis of ventilated façades under different wind conditions in summer period", *Energy and Buildings*, vol. 122, pp. 131-139, 2016. Available: 10.1016/j.enbuild.2016.04.035.
- [4] Guillén IG-LV, Fran JM, López-Jiménez PA. Thermal behavior analysis of different multilayer façade: numerical model versus experimental prototype. *Energy Build* 2014;79:184–90.
- [5] Patania AG F, Nocera F, Ferlito A, Galesi A. Thermofluid-dynamic analysis of ventilated façades. *Energy Build* 2010;42:1148–55
- [6] Ciampi MLF, Tuoni G. Ventilated façades energy performance in summer cooling of buildings. *Sol Energy* 2003;75:491–502.
- [7] E. Halawa et al., "A review on energy conscious designs of building façades in hot and humid climates: Lessons for (and from) Kuala Lumpur and Darwin", *Renewable and Sustainable Energy Reviews*, vol. 82, pp. 2147-2161, 2018. Available: 10.1016/j.rser.2017.08.061.
- [8] Attoye, D.E.; Tabet Aoul, K.A.; Hassan, A. A Review on Building Integrated Photovoltaic Façade Customization Potentials. *Sustainability* 2017, 9, 2287.
- [9] Yoo S-H, Lee E-T. Efficiency characteristic of building integrated photovoltaics as a shading device. *Build Environ* 2002;37:615–23.
- [10] Chae YT, Kim J, Park H, Shin B. Building energy performance evaluation of building integrated photovoltaic (BIPV) window with semi-transparent solar cells. *Appl Energy* 2014;129:217–27.
- [11] Park K, Kang G, Kim H, Yu G, Kim J. Analysis of thermal and electrical performance of semi-transparent photovoltaic (PV) module. *Energy* 2010;35:2681–7.
- [12] T. Liang et al., "A review of crystalline silicon bifacial photovoltaic performance characterisation and simulation", *Energy & Environmental Science*, vol. 12, no. 1, pp. 116-148, 2019. Available: 10.1039/c8ee02184h
- [13] R. Guerrero-Lemus, R. Vega, T. Kim, A. Kimm and L. Shephard, "Bifacial solar photovoltaics – A technology review", *Renewable and Sustainable Energy Reviews*, vol. 60, pp. 1533-1549, 2016. Available: 10.1016/j.rser.2016.03.041.
- [14] C. Rodríguez-Gallegos, M. Bieri, O. Gandhi, J. Singh, T. Reindl and S. Panda, "Monofacial vs bifacial Si-based PV modules: Which one is more cost-effective?", *Solar Energy*, vol. 176, pp. 412-438, 2018. Available: 10.1016/j.solener.2018.10.012
- [15] M. Lamers et al., "Temperature effects of bifacial modules: Hotter or cooler?", *Solar Energy Materials and Solar Cells*, vol. 185, pp. 192-197, 2018. Available: 10.1016/j.solmat.2018.05.033.
- [16] B. Soria, E. Gerritsen, P. Lefillastre and J. Broquin, "A study of the annual performance of bifacial photovoltaic modules in the case of vertical façade integration", *Energy Science & Engineering*, vol. 4, no. 1, pp. 52-68, 2015. Available: 10.1002/ese3.103.
- [17] Víctor Manuel Soto Francés, Emilio José Sarabia Escriva, José Manuel Pinazo Ojer, Emilie Bannier, Vicente Cantavella Soler, Gonzalo Silva Moreno, Modeling of ventilated façades for energy building simulation software, *Energy and Buildings*, Volume 65, 2013, Pages 419-428, ISSN 0378-7788, <https://doi.org/10.1016/j.enbuild.2013.06.015> (<http://www.sciencedirect.com/science/article/pii/S0378778813003538>)
- [18] UNI EN ISO 6946:2018: Building components and elements - Thermal resistance and thermal transmittance - Calculation methods